James De Clerck *Editor*

Experimental Techniques, Rotating Machinery, and Acoustics, Volume 8

Proceedings of the 33rd IMAC, A Conference and Exposition on Structural Dynamics, 2015

SEM

Springer

Conference Proceedings of the Society for Experimental Mechanics Series

James De Clerck

Editor

Experimental Techniques, Rotating Machinery, and Acoustics, Volume 8

Proceedings of the 33rd IMAC, A Conference and Exposition on Structural Dynamics, 2015

Springer

Editor
James De Clerck
The Enterprise Program
Michigan Technological University
Houghton, MS, USA

Printed on acid-free paper

Preface

Experimental Techniques, Rotating Machinery & Acoustics, represents one of ten volumes of technical papers presented at the 33rd IMAC, A Conference and Exposition on Structural Dynamics, 2015 organized by the Society for Experimental Mechanics, and held in Orlando, Florida February 2–5, 2015. The full proceedings also include volumes on Nonlinear Dynamics; Dynamics of Civil Structures; Model Validation and Uncertainty Quantification; Sensors and Instrumentation; Special Topics in Structural Dynamics; Structural Health Monitoring & Damage Detection; Shock & Vibration Aircraft/Aerospace, Energy Harvesting; and Topics in Modal Analysis.

Each collection presents early findings from experimental and computational investigations on an important area within Structural Dynamics. *Topics in Modal Analysis I* represents papers on enabling technologies for Modal Analysis measurements such as Sensors & Instrumentation, and applications of Modal Analysis in specific application areas. Topics in this volume include:

Experimental Techniques
Processing Modal Data
Rotating Machinery
Acoustics
Adaptive Structures
Biodynamics
Damping

The organizers would like to thank the authors, presenters, session organizers, and session chairs for their participation in this track.

Houghton, MS, USA   J. De Clerck

Contents

Chapter 1
A Computational Model to Investigate the Influence of Spacing Errors on Spur Gear Pair Dynamics

Murat Inalpolat

Abstract In this paper, a computational model is developed to investigate the influence of tooth spacing errors on the dynamics of spur gear pairs. This finite element based computational model implicitly includes periodically-time varying gear mesh stiffness and nonlinearities caused by tooth separations in resonance regions. The model can simulate the long period transmission error induced dynamic response from a spur gear with different spacing error patterns and predicts both time domain histories and frequency-domain spectra of dynamic mesh force and dynamic transmission error. The dynamic responses due to both deterministic and random teeth spacing errors are predicted and compared to the previously generated results from a lumped parameter model capable of utilizing experimentally measured transmission error as the realistic excitation mechanism. This study also enables creation of an extensive database of dynamic response spectra of gear pairs under the influence of spacing errors that will later be utilized for investigating the diagnostics of gear pairs.

Keywords Spacing errors • Dynamics • Nonlinear effects • Contact • Manufacturing

1.1 Introduction

Gear manufacturing constitutes the decision and imposition of a certain quality level. The imposed quality level is specified based upon the requirements of the application and even the gears with the highest quality levels will have certain amount of manufacturing errors (tolerances). These manufacturing errors and tolerances contribute to the loaded transmission error that affects the meshing dynamics of gear pairs. Moreover, it is design and sometimes assembly dependent how these different amounts of errors on gears in mesh act upon each other and affect the resultant gear dynamics. Consequently, understanding the role and effect of different gear design and manufacturing based errors and tolerances on the transmission errors of gears is important. One of the most significant contributors to the gear transmission error is the tooth spacing errors. Gear tooth spacing error is defined as the circumferential position error of one gear tooth flank with respect to the previous tooth flank as illustrated in Fig. 1.1 [1]. Here, consecutive teeth are located on a reference diameter (usually pitch diameter) of a gear. In an ideal situation, a particular gear has Z number of teeth that have identical involute profiles that are equally spaced around the pitch diameter. Existence of spacing error means that some of the tooth profiles are angularly misplaced from their ideal position with respect to the teeth adjacent to them. The reference tooth (index) is chosen as Tooth-1 in Fig. 1.1 without loss of generality. The right hand side flank of Tooth-1 is the reference profile (flank) when certain amount of torque acting in the clockwise direction is assumed to exist on this gear. The circular distances, S1 and S2, between the right flanks of Tooth-1 and Tooth-2 and also between Tooth-2 and Tooth-3, where both flanks intersect the reference diameter are both equal to a circular pitch p ($p = \pi.m$) for a gear with ideal geometry. If S1 deviates from the nominal circular pitch p then the difference is interpreted as the spacing error ε_1 for Tooth-2. Similarly, if S2 has a different value than p then it is interpreted as the spacing error ε_2 for Tooth-3.

Gear tooth spacing errors arise during the manufacturing processes and in many cases have periodicities related to the cutting or heat treatment process in addition to the random components [2]. Periodicities in transmission error function are usually low order and tend to result in amplitude and phase modulation of the gear dynamic mesh forces. If transmission error is of this form, there will be a number of sidebands with significant energy content located around the tooth mesh order and its multiples. It is vital to understand the degree of modulations as it is a reflection of the type and amount of manufacturing errors that exist on the gears.

M. Inalpolat (✉)
Structural Dynamics and Acoustic Systems Laboratory, University of Massachusetts Lowell, One University Avenue, Lowell, MA 01854, USA
e-mail: Murat_Inalpolat@uml.edu

Fig. 1.1 Illustration of the tooth spacing errors
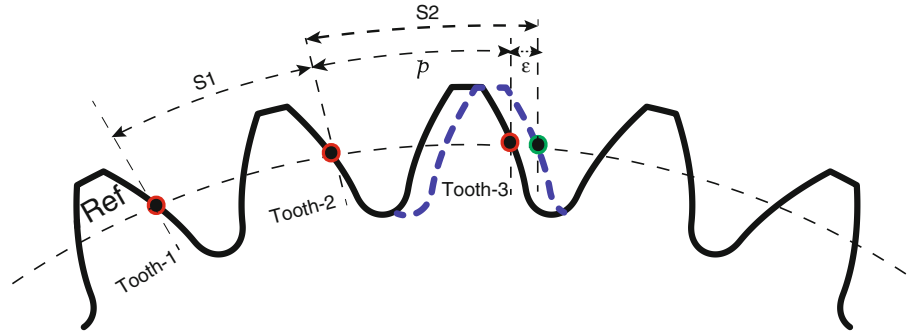
Spacing errors modify the transmission error as it will cause a certain gear tooth profile to be misplaced on the reference diameter, either coming into contact earlier or later with the corresponding tooth on the other gear in mesh compared to its expected timing under ideal conditions. This translates the contact in time that can significantly change the dynamics of the gears as the dynamic excitation phase continuously changes and instantaneous contact ratio becomes lower or higher than expected at different times causing either overloading or contact loss of the tooth in mesh. Consequently, complicated spacing error patterns that interact with each other on gears in mesh could significantly alter the resultant life of gears under operation and affect the overall system reliability. Besides, spacing errors are time-invariant but may be assembly dependent errors depending on their designs. Interaction of one gear having certain spacing errors with the other gear having different spacing errors depends on how they are assembled (clocked) and may alter the resultant gear pair dynamics and noise for the gears with a non-hunting-tooth design. The frequency spectra for the gears with spacing errors usually exhibit a broad-band energy distribution due to deviations from the perfectly repetitive nature of the transmission error. Thus, it is not sufficient to use limited Fourier series amplitudes of transmission error to simulate the meshing dynamics any more. The proper means of simulating indexing errors would be to apply the errors over the total rotation of both pinion and gear. This would require running the gears through their total hunting period. Nevertheless, worst case spacing errors occur when the respective errors of the pinion and gear match up.

Although spacing errors are quite influential on gear pair dynamics, the work published on the subject matter is sparse. Remmers developed an analytical method to study the effect of tooth spacing errors, load, contact ratio and profile modifications on the gear mesh excitations [2]. He indicated that random tooth spacing errors may be used to reduce the gear mesh excitations at certain frequencies. Mark derived expressions for Fourier series coefficients of all components of static transmission error including harmonic and non-harmonic coefficients of gear defects of concern. He used Fourier transforms of tooth pair stiffness and surface deviations from perfect involute to come up with the expressions mentioned [3]. Later, Mark utilized the mathematical expressions developed in this work to study mesh transfer functions of gears with different surface and profile deviations [4]. Kohler and Regan and later Mark discussed components of the frequency spectrum for gears with pitch errors based on analytical approaches and agreed on the fact that existence of the components depends on loading conditions and if the only deviation from perfect tooth geometry is due to pitch errors then frequency spectrum of corresponding transmission error function will have no components at the mesh frequency harmonics [5–7]. Padmasolala et al. carried out simulations to study the effectiveness of profile modification for reducing dynamic loads in gears with different tooth spacing errors and showed that linear tip relief is more effective in reducing dynamic loads on gears with relatively small spacing errors whereas parabolic tip relief becomes more effective when the amplitude of the spacing error increases [8]. Wijaya studied effects of spacing errors and run-out on the dynamic load factor and the dynamic root stress factor of an idler gear system [9]. C. Spitas and V. Spitas studied the overloading conditions of gears and effect of tip relief on the dynamics of gears with assumed indexing errors [10]. In their individual studies, first Milliren and later Handschuh experimentally investigated the influence of various gear errors on the quasi-static transmission errors and root stresses of spur gears [11, 12]. They used a common test rig to determine the effects such as spacing errors and lead wobble on the quasi-static behavior of spur gear pairs.

In this study, the influence of tooth spacing errors on dynamics of spur gear pairs is investigated using a deformable body dynamic model. The advantage of utilizing this previously self-proven computational tool is that it becomes possible to avoid some of the inevitable experimental influences on the data obtained through experiments. It is not possible to completely isolate one or a few different types of tolerances from the rest when using gears that are procured for experiments. This becomes possible with a computational tool and is vital in understanding the signature due to individual errors and tolerance types from the diagnostics perspective. Gears with no tolerances ("perfect gears") and with a variety of different spacing error patterns were simulated for predicting and comparing for their static and dynamic transmission error behaviors. The existing sparse literature on the spacing errors and their influence on spur gear dynamics and diagnostics lack a computational investigation to predict the static and dynamic transmission error of gear pairs, which has been the main motivation for this study.

1.2 The Deformable-Body Dynamic Model

A finite element based computational model is used in all of the subsequent quasi-static and dynamic simulations. This novel modeling scheme utilizes a relatively coarse mesh template at the non-contact regions. The contact zone is modeled using a semi-analytical approach and thus avoids the need for highly refined meshes and also the re-meshing that would be required for each different contact position in space [13]. This combined semi-analytical surface integral/finite element formulation makes this solution scheme a much faster one compared to the traditional finite element based analysis tools while keeping the precision that is required for a contact analysis. A separate local reference frame is attached on each gear body and finite element computations are done separately for each individual gear in this analysis scheme. The gear mesh stiffness, gear body displacements and tooth forces are calculated implicitly for each time step. The elastic gear deformations are superimposed on the rigid body displacements as they are comparatively much smaller. The local coordinate frames that are attached on each gear follow the rigid body motion of the gear that they are attached. This way, it becomes possible to write the finite element nodal displacement vector x_{fi} for gear i in the form of a set of linear differential equations as:

$$M_{ffi}\ddot{x}_{fi} + C_{ffi}\dot{x}_{fi} + K_{ffi}x_{fi} = f_{ffi} \tag{1.1}$$

In Eq. 1.1, f_{ffi} is the external force/load vector, C_{ffi} is the damping matrix based on the Rayleigh damping model [14]. The damping matrix is proportional to the mass and stiffness matrices and can be written as $C_{ffi} = \alpha M_{ffi} + \beta K_{ffi}$, where α and β are constant coefficients and $\alpha = 479$ and $\beta = 1.4 \ 10^{-7}$ were used here. If the rigid body motions are considered and thus represented by x_{ir}, then Eq. 1.1 can be replaced by:

$$\begin{bmatrix} M_{ffi} & M_{fri} \\ M_{rfi} & M_{rri} \end{bmatrix} \begin{Bmatrix} \ddot{x}_{fi} \\ \ddot{x}_{ri} \end{Bmatrix} + \begin{bmatrix} C_{ffi} & C_{fri} \\ C_{rfi} & C_{rri} \end{bmatrix} \begin{Bmatrix} \dot{x}_{fi} \\ \dot{x}_{ri} \end{Bmatrix} + \begin{bmatrix} K_{ffi} & K_{fri} \\ K_{rfi} & K_{rri} \end{bmatrix} \begin{Bmatrix} x_{fi} \\ x_{ri} \end{Bmatrix} = \begin{Bmatrix} f_{fi} \\ f_{ri} \end{Bmatrix} \tag{1.2}$$

The equations of motion for the pinion ($i = 1$) and for the gear ($i = 2$) are assembled into the overall system equations of motion in the matrix form as:

$$M\ddot{x} + C\dot{x} + Kx = F \tag{1.3}$$

The overall system (gear pair) equations of motion are numerically solved in the time domain using the Newmark time-discretization and integration scheme [14]. This model considers either the pinion (input) or the gear (output) as the reference signal to determine output and input TE signals (both in µrad), or as a linear displacement along the line of action as

$$e(t) = r_p\theta_p(t) - r_g\theta_g(t) \tag{1.4}$$

where r_p and r_g represent the base radii and $\theta_p(t)$ and $\theta_g(t)$ represent the rotational displacements of pinion and gear, respectively.

1.3 Computational Test Cases

A unity ratio spur gear pair is modeled using the finite element based deformable-body dynamic model is shown in Fig. 1.2. This gear pair is intentionally utilized as the same gear pair was recently used in a subsequent study that constitutes a comparative baseline for the current investigation and serves as the baseline gear geometry with "no spacing error" [15]. This unity-ratio spur gear pair has an operating center distance of 150 mm and a theoretical contact ratio of 1.8. Basic gear parameters for these gears are listed in Table 1.1. A total of 9 test cases with gears having different spacing error patterns formed the inventory for the computational test matrix. The computational test matrix includes the cases listed as:

Case 1: Baseline gears with no spacing errors (compared to results from [15]).
Case 2: Pinion has a spacing error pattern of 0 15 0 µm, gear has no error.
Case 3: Pinion and gear both have a spacing error pattern of 0 15 0 µm.
Case 4: Pinion has a spacing error pattern of 0 15 0 µm and gear has a spacing error pattern of 0 −15 0 µm.
Case 5: Pinion has a spacing error pattern of 0 −15 0 µm and gear has a spacing error pattern of 0 15 0 µm.
Case 6: Pinion and gear both have a spacing error pattern of 0 −15 0 µm.

Fig. 1.2 Deformable-body computational model of the unity spur gear pair
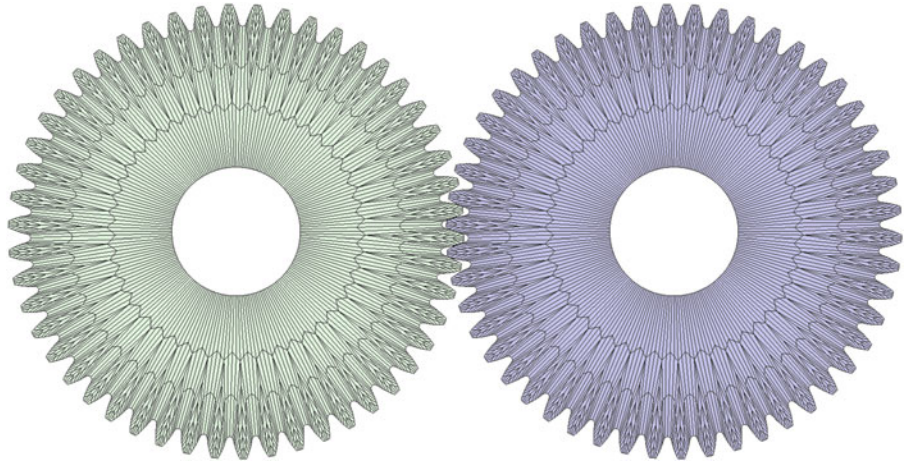
Table 1.1 Basic parameters of the gears used in this study

Parameter	Value
Number of teeth	50
Normal module [mm]	3
Pressure angle [deg]	20
Pitch diameter [mm]	150
Base diameter [mm]	140.95
Major diameter [mm]	156
Minor diameter [mm]	140.68
Circular tooth thickness [mm]	4.64
Active facewidth [mm]	20
Tip relief magnitude [mm]	0.012
Starting roll angle of tip relief [deg]	20.9

Case 7: Pinion has a sinusoidal indexing (spacing also sinusoidal) error pattern with a peak value of 15 μm, gear has no error.

Case 8: Pinion and gear both have sinusoidal indexing error patterns (spacing also sinusoidal) with a peak value of 15 μm.

Case 9: Pinion and gear both have random spacing error patterns with a tolerance range of $[-15\ 15]\ \mu$m.

In some of these cases, the spacing error was placed in the negative direction, which refers to the tooth entering mesh later than expected. The negative directions of the errors are obtained by removing additional material from the teeth with no error in a manufacturing environment. Likewise, if a tooth enters mesh earlier than nominal compared to the previous tooth, the spacing error is positive. Cases 2 through 6 include gears with discrete tooth (on a single particular tooth) spacing errors. In Case 7, a computational test was carried out where only the pinion has a sinusoidally-varying tooth indexing (accumulated spacing errors between the index tooth and each of the other teeth) errors that is in mesh with a gear with no error. Moreover, two more realistic cases where two gears having various different spacing errors were studied. In Case 8, both the pinion and the gear were created to have sinusoidally-varying tooth indexing errors. This is mostly caused by imperfections of the gear cutting tool and the manufacturing process. In Case 9, both the pinion and the gear were created to have random spacing errors within the range of $[-15, 15]\ \mu$m.

1.4 Results and Discussion

In this section, the influence of spacing errors on dynamic response of gear pairs is presented utilizing predicted static and dynamic transmission error time histories and corresponding frequency spectra. Dynamic transmission error (DTE) predictions are compared to the baseline quasi-static transmission error (STE) predictions of the gear pairs to gain more insight into the influence of dynamic effects on the transmission error and on gear characteristic frequencies that are essentially the key features for diagnostics. Here, results are reported in terms of DTE, while the model is also capable of predicting gear dynamic mesh force and displacements, as well as dynamic bearing forces and bearing displacements. First, the deformable-body model was run to predict the DTE spectrum of the baseline gear pair to identify the off-resonant
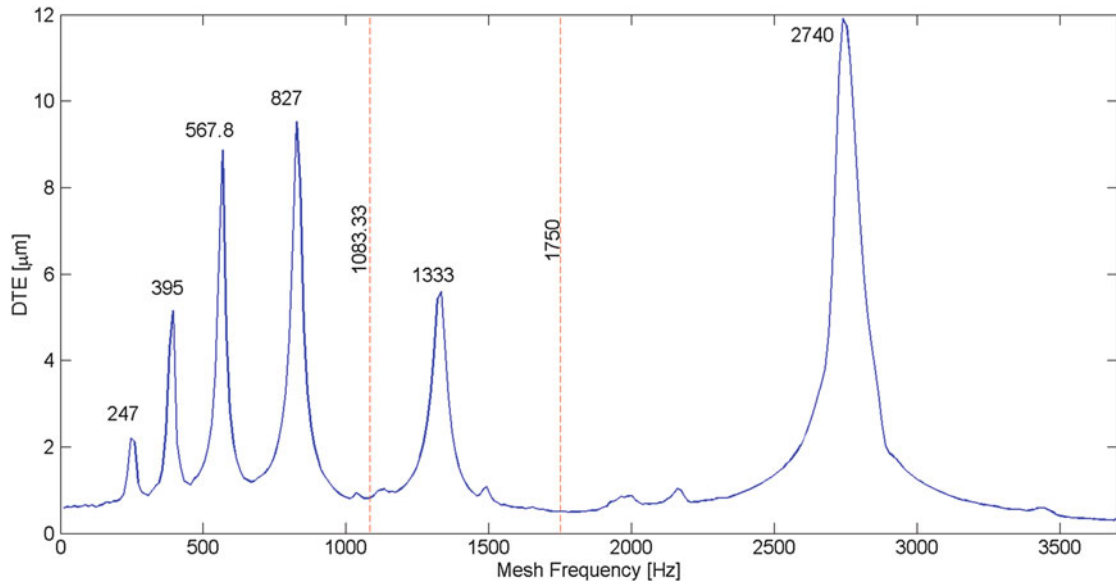
Fig. 1.3 The DTE spectrum of the gear pair with the baseline geometry
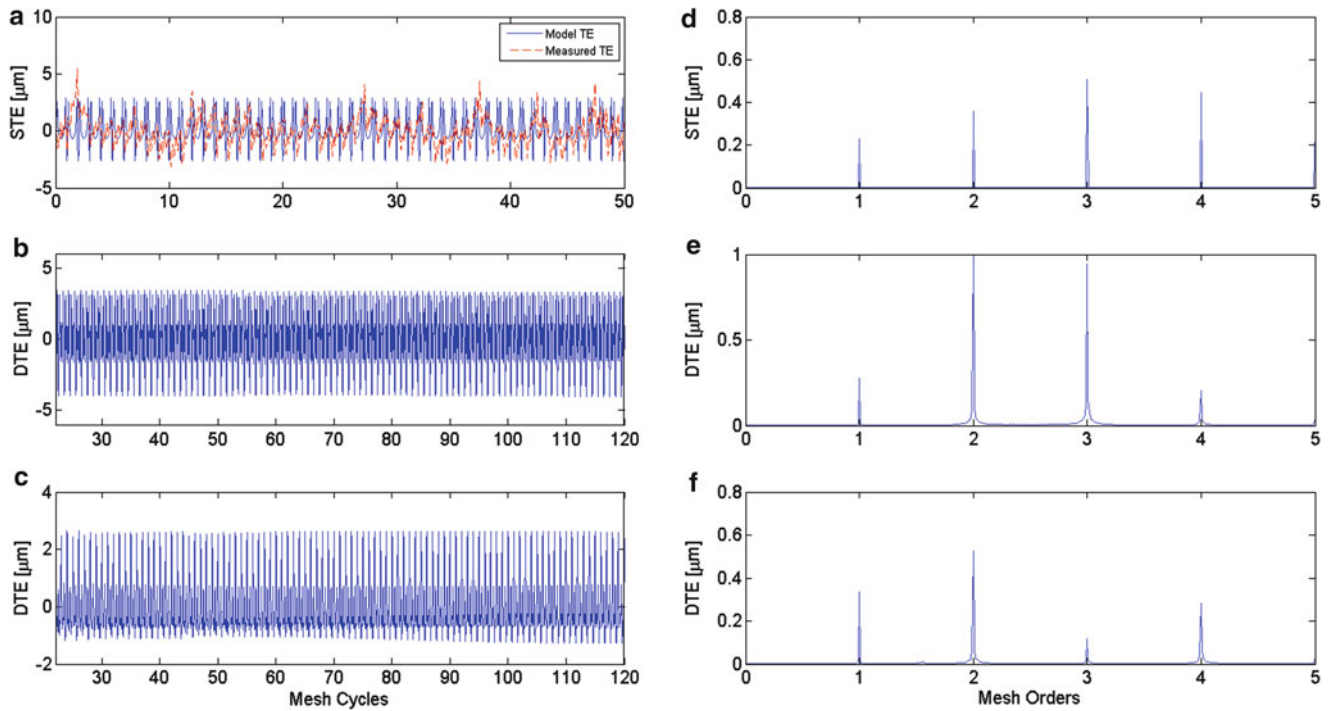
Fig. 1.4 Predicted STE (**a**) versus measured STE (in *red* and *dashed*), along with predicted DTE time histories from Case 1 at 1,300 and 2,100 rpm (**b**, **c**) and corresponding frequency spectra (**d**–**f**)

speed (frequency) ranges of the system within which specific frequencies were chosen for further analysis. The off-resonant frequencies that were used for further analysis are 1,083 Hz (1,300 rpm) and 1,750 Hz (2,100 rpm). At these off-resonant speeds (away from any system natural frequencies and parametric resonance frequencies), magnification on the TE due to the gear pair dynamics can be clearly observed without the extra amplifications due to mesh resonances and potentially nonlinear effects as can be observed from Fig. 1.3.

Although numerous predictions were carried out, a subset of the results are reported here to illustrate the importance of incorporating spacing errors into the gear dynamics and diagnostics considerations. Simulation results from Case 1 which included the baseline gears with no spacing errors are shown in Fig. 1.4.

Fig. 1.5 Predicted STE (**a**) along with predicted DTE time histories from Case 2 at 1,300 and 2,100 rpm (**b**, **c**) and corresponding frequency spectra (**d**, **f**)

In Fig. 1.4, the predicted STE time history is given between gear mesh cycles 0–50 whereas the DTE time histories are presented for a wider mesh cycle ranged low frequency shoft orders are intentionally excluded in the plots. The relatively narrow mesh cycle range (corresponds to one full rotation of both gears) was intentionally chosen in Fig. 1.4a such that the presentation is clear as only this plot includes a comparison between previously measured STE [15] and the computationally predicted STE for the same gear pair. Figure 1.4a indicates that there is up to 2 μm difference between the peak to peak values of both traces (excluding the very first peak which includes a slight amplification only in the beginning of the measurements and does never repeats itself in terms of its amplitude). This is expected as despite all the efforts of eliminating them, these gears that were measured for their STE levels still had limited amount of tooth spacing errors and run-out along with other tolerance variations on them. One advantage of using the computational approach is that it is possible to avoid these additional factors completely and really capture distinct features of the gear dynamics and diagnostics under the influence of spacing errors. The transient effects taking place for the initial cycles of the predicted DTE is intentionally excluded for all the DTE results presented (starts from mesh cycle #20). Predicted STE and DTE traces were presented within the same mesh cycle ranges to clearly demonstrate the dynamic magnification as well as speed (and thus dynamic) effects. In Fig. 1.5, STE and DTE time histories and corresponding frequency spectra from Case 2 are presented following the same sequence in Fig. 1.4. Case 2 included a gear with no spacing errors and a pinion with a spacing error of 15 μm at tooth #45. The peaks that are seen in the STE time trace given in Fig. 1.5a exhibit how the discrete spacing error of the particular tooth on the gear comes in mesh (although not completely in-phase with each other due to contact ratio) and causes a sudden increase in the predicted STE once during a complete rotation of the gear, i.e. once in every 50 mesh cycles. The same trend was observed when using the analytical model in a previous study [15].

The fact that one of the teeth has discrete spacing error whereas all the other teeth have perfect spacing breaks the rotationally symmetric nature of the meshing action and affects the resulting dynamical behavior of the gear pair. This can essentially be observed from Fig. 1.5a–c, when the same gear pair was used but was run at sequentially increasing speeds (10 rpm, 1,300 rpm and 2,100 rpm). Interestingly, in Fig. 1.5b, c, when the gears were rotating at 1,300 and 2,100 rpm, the time traces exhibit how more than once mesh cycle was affected due to a single discrete spacing error on the gear. Under dynamic conditions, teeth do not only deflect due to the applied external load but also oscillate about this pre-deflected position under the influence of dynamic loads. Moreover, spacing errors cause time and phase lags or leads on the mesh timing which can cause dynamic loads to get magnified and become more impulsive. Gear contact ratio enriches the gear pair dynamics as it is the most important design parameter that affects when and how much particular tooth will carry load.
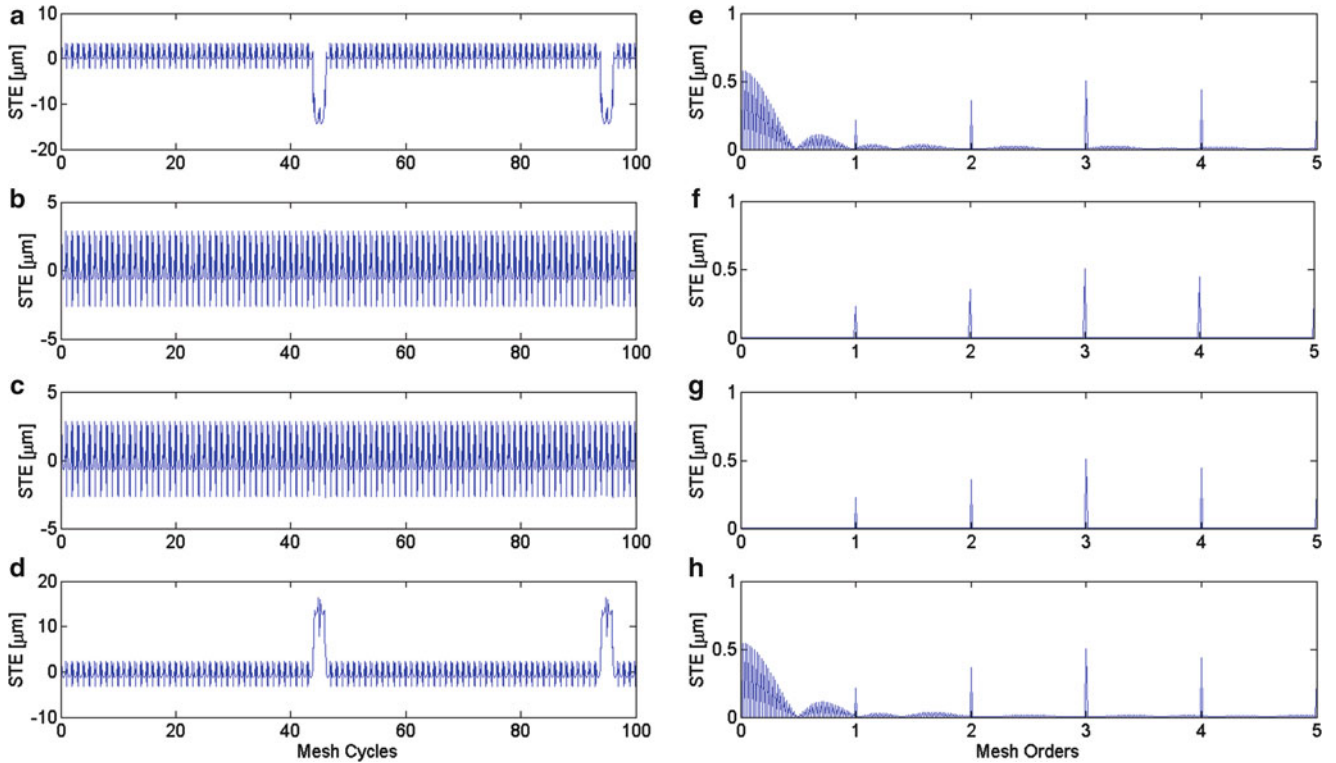
Fig. 1.6 Predicted STE time histories from (**a**) Case 3, (**b**) Case 4, (**c**) Case 5, and (**d**) Case 6 and (**e, h**) their corresponding frequency spectra

It is also important to note how the more energized broad-band shaft-order regime and its physical reasoning due to the spacing error. In Fig. 1.5d–f, shaft order (orders lower than the fundamental mesh order) peaks and its integer multiples are revealed. The main reason is that the teeth with discrete spacing error repeats and leaves its signature once in every rotation of the gear, modifying the frequency spectrum. The peaks revealed at integer multiples of the shaft orders are due to the amplitude and phase modulation of the TE.

In Fig. 1.6, STE predictions from Cases 3 through 6, where a discrete spacing error pattern of $0-\pm15-0$ μm was used on the pinion and the gear, are presented in a comparative way. The predictions at dynamic conditions were excluded as the primary goal of this particular analysis is to reinvigorate the understanding of the worst (and the best) theoretical case of the spacing errors on both gears with a single tooth having spacing error that are coming together. It is observed from Fig. 1.6 that when the pinion and gear both have a single tooth with spacing error of the same amount and with same sense, they constitute the worst case scenario. For these two cases the teeth on both gears are coming into mesh earlier or later than expected simultaneously and they both contribute to a larger TE value. It is the opposite with the results from Case 4 and 5 as revealed in Fig. 1.6b, c.

In Fig. 1.7, results from Case 7, which includes a pinion with a sinusoidally-varying indexing error pattern (distribution) and a gear with no error, are presented. The effect of having sinusoidally-varying indexing errors on the pinion gives rise to STE and DTE predictions similar to a case where the pinion could have had pitch line run-out. Frequency spectra given in Fig. 1.7d–f exhibit the strong harmonic content as well as the relatively weak resonant activity (when compared to Case 2).

In Case 8, both the pinion and the gear have sinusoidally-varying tooth indexing error patterns. This represents a more realistic case where the same cutting tool (i.e. hob) with a certain wear pattern is used to cut both pinion and the gear. Figure 1.8 exhibits an interesting fact that when two gears with sinusoidally-varying indexing errors with a phase angle between them mesh together, the resulting STE and DTE may be lower compared to Case 7 with only planet gear having spacing errors. This phase angle is essentially the angle (geometric shift) between the sine waves that both the pinion and the gear tooth spacing error patterns exhibit. If the pinion teeth that have the peak error values (peak points of a sine wave) always mesh between the corresponding teeth on the gear with the peak values, they would add up to a higher TE value. In Fig. 1.8, a case where the peak values had a 180° phase angle in-between and thus minimized TE was demonstrated. On a separate note, no sideband peaks are revealed in Fig. 1.8d–f as the carrier frequency (modulation process requires a carrier and a modulator signal) due to the tool wear (essentially a sine wave) has a frequency equal to rotational frequency of the gear and thus coincides with the preexisting gear mesh frequency and its harmonics, not adding additional frequency content.
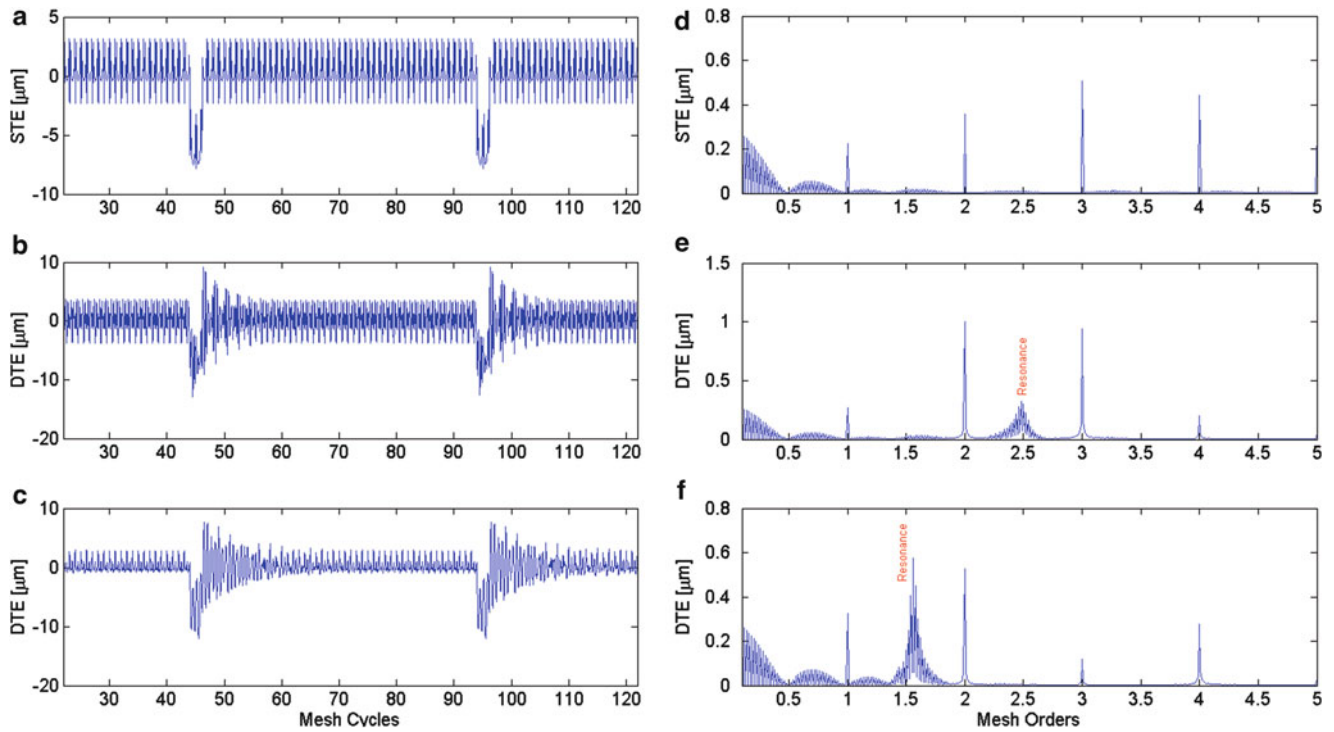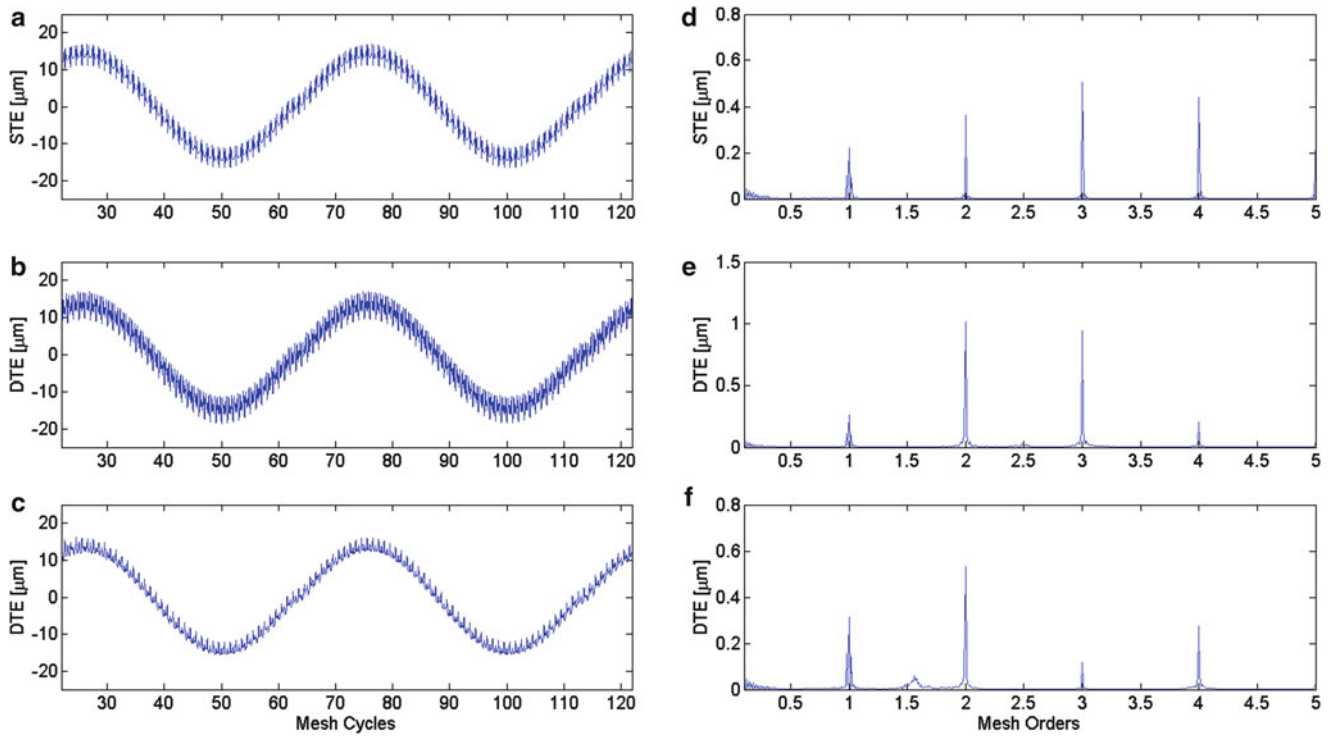
Fig. 1.7 Predicted STE (**a**) along with predicted DTE time histories from Case 7 at 1,300 and 2,100 rpm (**b**, **c**) and corresponding frequency spectra (**d**, **f**)
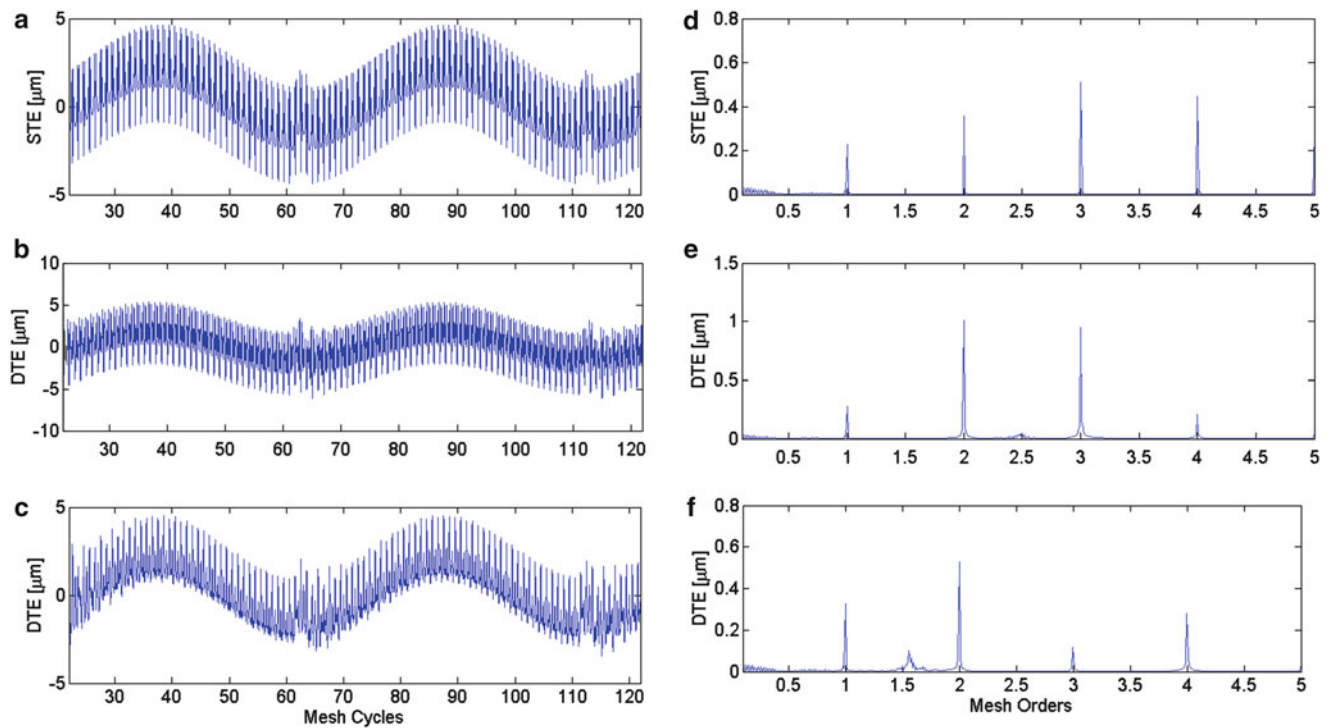
Fig. 1.8 Predicted STE (**a**) along with predicted DTE time histories from Case 8 at 1,300 and 2,100 rpm (**b**, **c**) and corresponding frequency spectra (**d**, **f**)
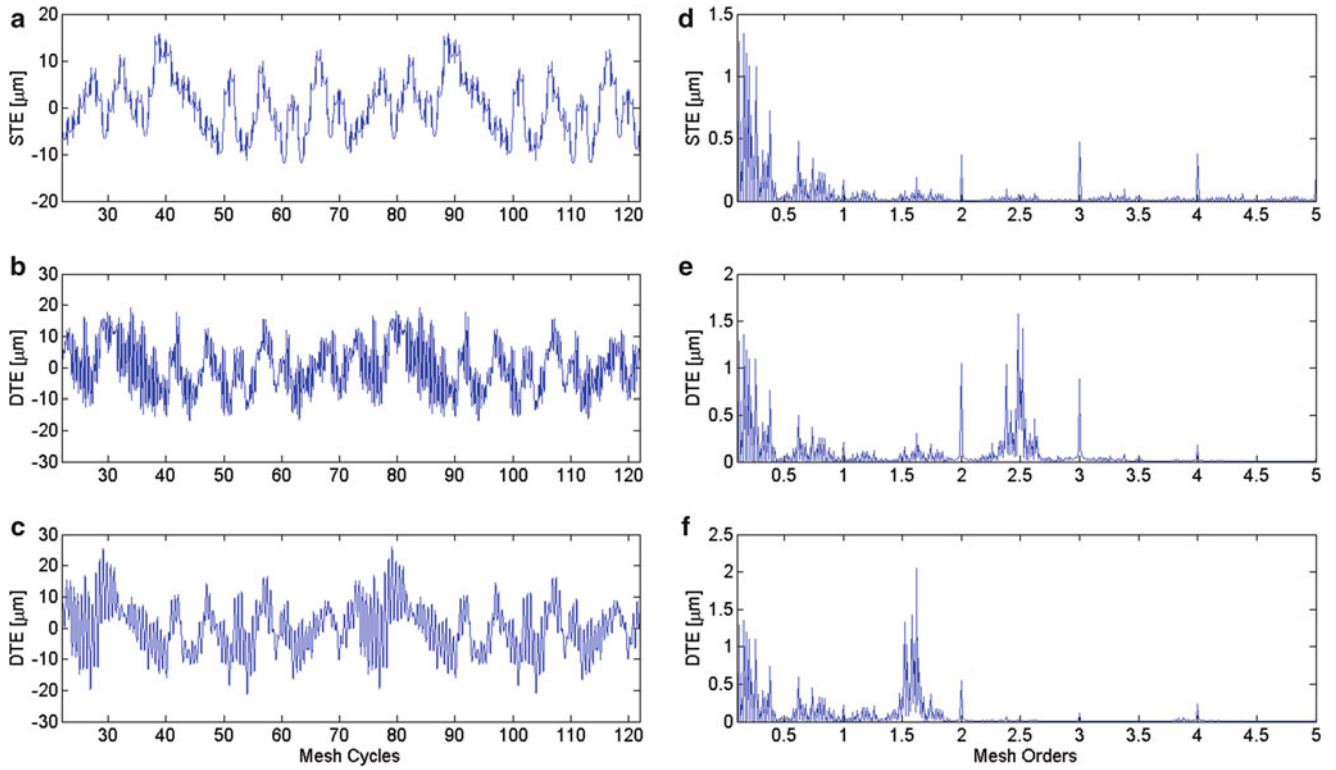
Fig. 1.9 Predicted STE (**a**) along with predicted DTE time histories from Case 9 at 1,300 and 2,100 rpm (**b**, **c**) and corresponding frequency spectra (**d**, **f**)
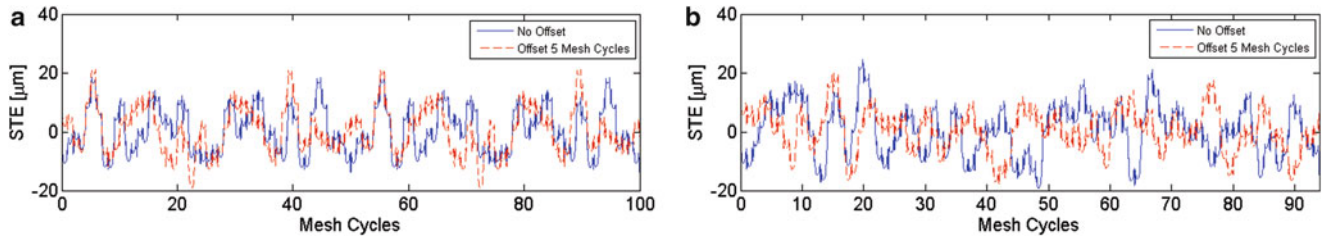
Fig. 1.10 The influence of assembly on (**a**) a non-hunting tooth design gear set, (**b**) a hunting tooth design gear set

In Case 9, both the pinion and the gear was generated to have random spacing errors within the range of $[-15, 15]$ μm. The random error pattern is definitely more representative of the real spacing error patterns observed on the gears manufactured using regular gear cutting operations such as hobbing, shaping etc. Although randomly distributed, spacing errors were kept between the range $[-15, 15]$ μm. As seen both from the time traces and the corresponding spectra in Fig. 1.9, random spacing error patterns cause a truly broad-band excitation activating the resonant peaks and shaft orders regardless of the gear speeds.

Parallel axis gears are predominantly designed to have a so-called "hunting-tooth" design, where the number of teeth on the pinion and the gear do not have common factors. It is preferable that gears have a "hunting-tooth" design as this way any tooth on either gear will contact every tooth on the other gear before coming into mesh with the same tooth again. This spreads the wear and failure potential evenly over all the gear teeth, thus increasing the life of the gearbox. Figure 1.10 exhibits a comparison of STE time histories for two slightly different gear designs, one with a non-hunting tooth (Fig. 1.10a) and the other with a hunting-tooth (Fig. 1.10b) design. The non-hunting tooth gear pair ($Z_p = 50$ and $Z_g = 50$) was first simulated following the baseline configuration that has been used in this study and later when the gear was shifted by 5 tooth mesh cycles and repositioned (reassembled) while pinion was kept in position. Results indicate that assembly has an important influence on the STE and thus dynamic response for gears with non-hunting tooth design. It can be observed from Fig. 1.10b that STE of hunting-tooth design that is exemplified here ($Z_p = 47$ and $Z_g = 51$) was not affected by the variation in the assembly position. The STE time trace obtained from the baseline hunting-tooth gear design (called as "No offset in Fig. 1.10b") repeats itself but only shifted in time by 5 mesh cycles.

1.5 Conclusion

In this study, a deformable-body model was developed to predict the spur gear pair dynamics. This model uses a unique solution methodology that combines the precision of the finite element technique and the speed of a surface-integral based analytical technique at different regions of the geometric model. This methodology makes it possible to obtain gear pair dynamic response both at steady-state and transient speed conditions in a fast and accurate manner. First, gears with deterministic (discrete and later sinusoidally-varying) and stochastic spacing errors were simulated for their STE and DTE and resulting gear pair dynamics was compared against a baseline gear pair with no spacing errors. Cases with gears having limited discrete spacing errors increase the dynamic response during limited number of mesh cycles thus increasing the dynamic response. Their frequency spectra are enriched by additional shaft order peaks due to amplitude and frequency modulations caused by the perturbed transmission error excitation. Cases with random indexing errors exhibit even broader-band response, having peaks at shaft order and its integer multiples along with mesh order and its harmonics. They exhibit significantly more energy content at frequencies lower than the fundamental mesh frequency. The broader-spectrum is caused by the broad-band TE excitation causing a frequency modulated dynamic mesh force spectrum. Finally, it is shown that gears with realistic (having random contributions) indexing errors may generate different vibroacoustic spectra when assembled differently (different clocking etc.) depending on their design parameters. Next steps in this research effort include investigating the influence of spacing errors on the system response from the diagnostics perspective.

References

1. AGMA Technical Standards, ANSI/AGMA 2015-1-A01
2. Remmers EP (1978) Gear mesh excitation spectra for arbitrary tooth spacing errors, load and design contact ratio. ASME J Mech Des 100:715–722
3. Mark WD (1978) Analysis of the vibratory excitation of gear systems: basic theory. J Acoust Soc Am 63(5):1409–1430
4. Mark WD (1979) Analysis of the vibratory excitation of gear systems II: tooth error representations, approximations, and application. J Acoust Soc Am 66(6):1758–1787
5. Kohler H, Regan R (1985) The derivation of gear transmission error from pitch error records. Proc IME C J Mech Eng Sci 199(C3):195–201
6. Mark WD (1987) The role of the discrete Fourier transform in the contribution to gear transmission error spectra from tooth spacing errors. Proc IME C J Mech Eng Sci 201(C3):227–229
7. Kohler H, Regan R, Mark WD (1987) The derivation of gear transmission error from pitch error records-discussion. Proc IME C J Mech Eng Sci 201(C3):230–232
8. Padmasolala G, Lin HH, Oswald FB (2000) Influence of tooth spacing error on gears with and without profile modifications, NASA/TM-2000-210061 PTG-14436
9. Wijaya H (2001) Effect of spacing errors and run-out on transverse load sharing and dynamic factors and idler gear dynamic analysis, MS thesis, The Ohio State University, Columbus
10. Spitas C, Spitas V (2006) Calculation of overloads induced by indexing errors in spur gearboxes using multi-degree-of-freedom dynamical simulation. Proc Inst Mech Eng K J Multi-body Dyn 220:273–282
11. Milliren M (2011) An experimental investigation into the various errors on the transmission error and root stresses of spur gears, MS thesis, The Ohio State University, Ohio
12. Handschuh M (2013) An investigation into the impact of random spacing errors on static transmission error and root stresses of spur gear pairs, MS thesis, The Ohio State University, Ohio
13. Vijayakar SM (1990) A combined surface integral and finite element solution for a three dimensional contact problem. Int J Numer Methods Eng 34:525–545
14. External2D (2014) Advanced Numerical Solutions, Inc., Hilliard
15. Inalpolat M, Handschuh M, Kahraman A (2014) Impact of indexing errors on spur gear dynamics. In: International gearing conference 2014, Lyon

Chapter 2
Drill Vibration Suppression Through Phase-Locked Loop Control

Nicholas Martinez, Jermaine Chambers, Michelle Gegel, Eric Schmierer, and Alex Scheinker

Abstract The drilling process produces vibrations that have adverse effects in a variety of applications, including precision machining, dental procedures, oil string operations, and explosives neutralization. This research seeks to prototype a rotating drill that actively suppresses the vibrations transmitted to the drilling target. The dynamics of the uncontrolled drilling system are first modeled in the axial direction of the drill tool. Then a phase-locked loop control is proposed which, along with sensors and actuators, serves to reduce vibrations during the drilling process by directly applying a forcing function out of phase with the excitation. To achieve versatility in application, the controller design includes adaptive capabilities such that, throughout a drilling process, the control system will measure the modal frequencies and adjust accordingly. The results of this study can lead to the production of drilling devices that minimally disturb the drilled object and produce superior surface finish.

Keywords Drilling dynamics • Phase-locked loop • Vibration suppression • Extremum-seeking function • Adaptive control

2.1 Introduction

In a wide range of fields, undesired vibrations resulting from the drilling process pose numerous issues including poor precision manufacturing, structural damage, and human discomfort. There are three sources of vibration in the drilling process: free, forced, and self-excited [1]. Free vibrations are excited by an impulse or step force applied to the system. Some examples of system impulse include impact of the drilling apparatus, use of a broken bit, and an electrical short circuit in a motor or generator. Forced vibrations are excited by periodically applied, transient, and external forces. The most common periodic force in the drilling process is rotating unbalances in machinery including spindle rotation or machining dynamics. Self-excited vibrations are often referred to as chatter and can occur at certain combinations of depth-of-cut and spindle speed. This phenomenon may be caused by several mechanisms including friction between the tool and work piece, mode coupling, and thermodynamics of the cutting process. Chatter due to these physical mechanisms is often classified as primary chatter. Secondary chatter, often the most influential source of excitation in the drilling process, is caused by surface waviness on the work piece from the previous cutting passes [2, 3]. This research is aimed at cancelling forced vibrations as they were measured to be the most prominent.

One of the undesired effects of vibration is Hand-Arm Vibration Syndrome (HAVS). HAVS is a disease that involves sensory, motor, circulatory, and musculoskeletal disorders and is often diagnosed to those regularly working with vibrating handheld tools. *Vergara* [4] attempted to detect the safety problems directly related to vibrations transmitted to the hand-arm

---

N. Martinez
Department of Mechanical Engineering, University of New Mexico, Albuquerque, NM 87131, USA

J. Chambers
Department of Mechanical Engineering, Prairie View A&M University, Prairie View, TX 77446, USA

M. Gegel
Department of Mechanical Engineering, Missouri University of Science and Technology, Rolla, MO 65409, USA

E. Schmierer (✉)
Applied Engineering and Technology, Los Alamos National Laboratory, Los Alamos, NM 87545, USA
e-mail: schmierer@lanl.gov

A. Scheinker
RF Engineering, Los Alamos National Laboratory, Los Alamos, NM 87545, USA

system. It was found that about 15 % of the tools exceed the action limits according to the International Organization for Standardization (ISO5349). In most cases, workers did not perceive these limits as problematic introducing an additional risk. In dentistry, large vibratory amplitudes produced by pneumatic drills can cause a phenomenon known as vibration induced white finger (VWF), a disorder that affects the blood vessels in the fingers, toes, ears, and nose. Technicians experiencing long daily exposure often endure the following symptoms: loss of feeling and control in fingers; tingling and numbness; pale and cold skin; and pain [5]. Technicians are not the only individuals in the dental industry affected by residual drilling vibrations. Dentists are continually trying to create an environment that is comfortable for patients. Fear of pain is the leading reason for individuals not seeking dental care [6]. *Takamori* performed a basic study on vibrations during tooth preparations caused by high-speed drilling and results yielded a frequency spectrum near the high sensitivity of hearing with tooth vibrations greater than other novel techniques [6]. This study suggests a potential factor in provoking pain during a routine dental procedure. Besides drilling problems observed in medical applications, some applications require minimal vibration in order to successfully complete the task. Explosive Ordnance Disposal (EOD) personnel may be endangered by drilling vibrations when rendering hazardous explosive devices safe. In particular, improvised devices that include vibration sensitive triggers are of significant concern. Thus, technology aimed to reduce drilling vibrations is needed to eliminate the numerous issues encountered in the drilling process.

The two methods of suppressing vibration consist of passive and active damping. Passive damping refers to energy dissipation within the structure by add-on damping devices. Conversely, active damping refers to energy dissipation from the system by external means, which in this research involves cancelling the vibration via sensing and controlling components [7]. When applied to different systems or to a system whose dynamics vary with time, passive damping is no longer an effective method in vibration control. Thus, a majority of the prior work aiming to dissipate vibrations in rotating machinery takes an active damping approach. The most popular approach is to suppress the unwanted vibration with a control algorithm and a highly responsive actuator, such as a piezoelectric ring-stack actuator [8]. A piezoelectric actuator is a solid-state ceramic actuator that converts electrical energy directly into linear motion with virtually unlimited resolution. In the research performed by *Park et al*. a collocated piezoelectric stack actuator and sensor along with an adaptive positive position feedback (PPF) control was used to suppress vibration in lathe operations [8]. The experimental results showed reduced chatter and significant improvement in surface finish. The drilling process, however, is different in that the tool rotates rather than the work piece.

Numerous vibratory control schemes have been investigated; in particular, the simulation study comparing the application of an active force control (AFC) strategy and the classic proportional-integral-derivative (PID) control scheme in a vibration suppression system [7]. The AFC operates by computing the estimated disturbance force from the mass acceleration, the actuator force and an estimation of the estimated virtual mass. *Hassan* et al. modeled a portable handheld machine and monitored the accompanying residual vibrations. The vibrations produced were effectively suppressed by applying the AFC strategy. The AFC strategy yielded a much more robust performance when compared to the conventional PID control scheme [7].

In the research of *Rios-Gutierrez*, a positive acceleration feedback control (PAF) was introduced to suppress mechanical vibrations. This control algorithm is ideal under circumstances where displacement sensors, such as laser vibrometers, are not readily available. Compact sensors such as accelerometers are widely used and often available in the lab. Furthermore, the PAF controller conveniently requires an accelerometer as the sole sensing metric. The PAF control scheme was validated on an experimental setup of a small scale, three-story structure [9]. Unlike the positive position and positive velocity feedback controllers (PPF and PVF), the PAF does not roll-off; subsequently, this must be taken into consideration when using this type of controller since it can disturb the higher modes of the system [9].

The control developed for this research falls into the category of phase-locked loop (PLL) control. In general terms, a PLL generates an output signal that is directly related to the phase of the input, although many varieties of PLL's exist. The main components of a PLL consist of a phase detector, filter, and oscillator, all of which can be implemented in either analog, digital, or software formats. PLL's are commonly used in radio, telecommunications, computers, and other electronic applications. *Algrain M.* utilized PLL's in a simple, yet effective approach for suppressing periodic vibration in structures [10]. This control system canceled selective frequencies by applying counter-actuation, of equal magnitude but in the opposite direction of the excitation. Sensing was performed by two inexpensive accelerometers; one accelerometer provided feedback on the combined effects of the excitation and actuation while the other measured only the excitation, as part of a feedforward configuration. The feedback and feedforward components served different purposes. Although a feedback loop offered desirable synchronizing qualities, this loop operated on an error signal which was being driven to zero, such that low signal-to-noise-ratios degradated the overall performance. To improve immunity to noise, a second accelerometer was included as part of a feedforward loop which operated on the much stronger signal from the disturbance excitation. In conjunction with feedback and feedforward control, PLL's were employed to target dominant frequencies

and determine the optimal output phase. Experimental testing achieved attenuation levels as high as 30 dB, confirming the effectiveness of this control design which was also economical, robust, highly stable, and did not require a system model [10].

Similar to *Algrain's* approach, this research pursued a system that targets dominant frequencies and uses PLL control to actuate out-of-phase with the excitation. Thus the advantages of low-cost, robustness, stability and lack of a need for a system model, transfer over to the drilling application presented here. In addition to the novelty of applying this control scheme to a drilling process, this work implements the entire control system in software which offers more flexibility over analog or digital circuitry. The proposed control system is an attractive solution to drill vibrations because the method is effective, conceptually simple, easy to expand, and inexpensive to construct.

2.2 Experimental Setup

A Jet JDP-15MF axial drill press was used as the analyzed system for this research, see Fig. 2.1. Modal analysis of the drilling apparatus showed that the attached fixture platform used to hold the drilling target was the source of the largest acceleration amplitude when in operation [12]; accordingly, an external fixture was recommended in order to isolate the drilling target from the dynamics of the supporting plate. To better represent real-world drilling scenarios, the external fixture, also shown in Fig. 2.1, was fabricated using 80/20 Inc. industrial erector set. The drilling target, an aluminum 6061-T6 plate ($30.5 \times 30.5 \times 0.318$ cm), was then assembled onto the fixture by bolting four bolts of 0.794 cm diameter onto each corner of the plate.

Modal analysis was performed on the drilling target, to characterize the dynamics of the uncoupled system. PCB Piezotronics accelerometers were attached to the drilling target for data acquisition and a National Instruments (NI) PXI -1000B chassis was used along with NI LabVIEW Real-Time (RT) software. The LabVIEW RT module extends LabVIEW graphical programming to create applications that run with deterministic real-time performance, which is essential for high-speed control implementation.

Rather than an array of accelerometers, a collocated sensor/actuator was implemented such that a single accelerometer was placed directly in line with the actuator. The first experimental setup consisted of dual shakers where one shaker excited the plate with a known disturbance input and the other suppressed this known disturbance. In the second experimental setup, the controlled excitation was eliminated and the system was coupled to the drilling head through drill bit contact with the
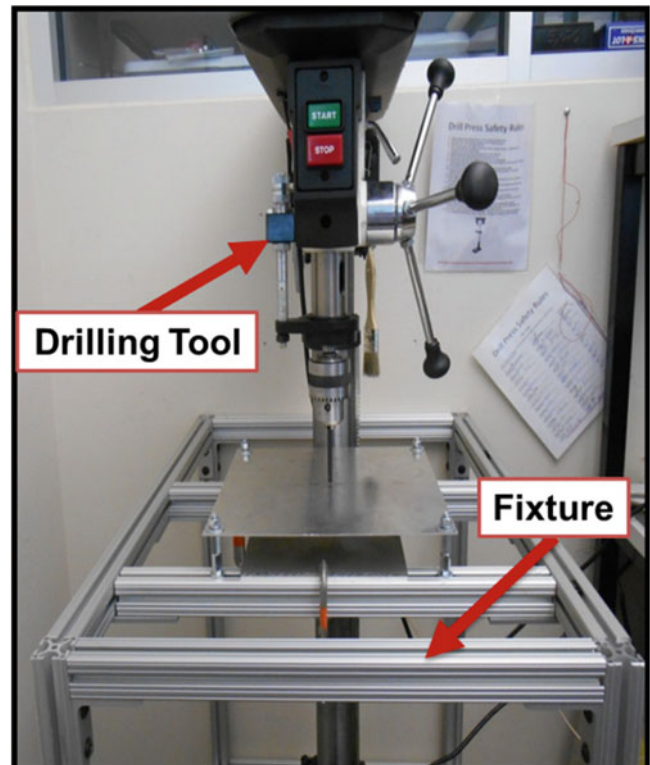
Fig. 2.1 Jet JDP-15MF drill press and drilling target fixture
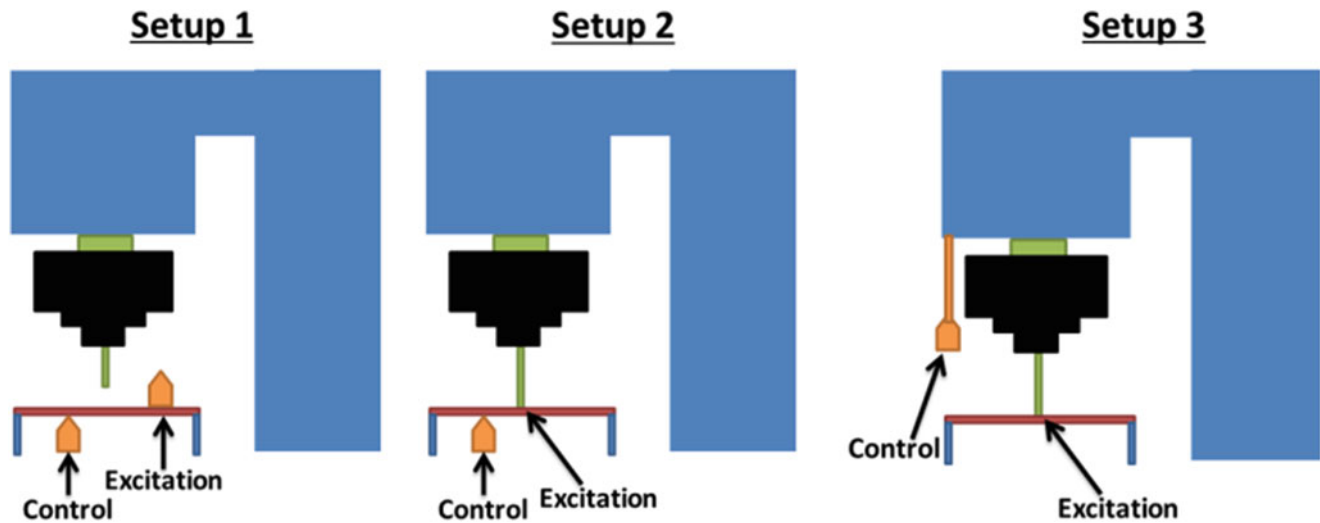
Fig. 2.2 Experimental configurations

Fig. 2.3 Two degree of freedom drill system MSD model
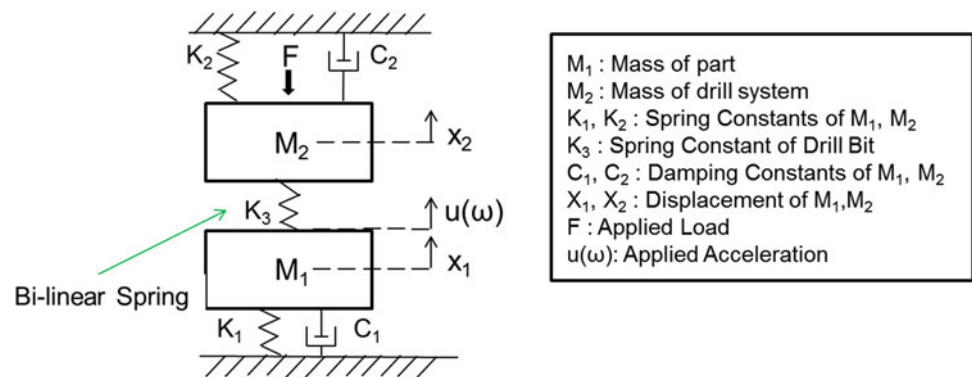
plate. Once the system was coupled, the excitation was now generated by the powered drilling machine. The control actuator was still located underneath the plate and its function was equivalent to Setup 1. In the third setup, the control actuator was removed from under the plate and instead suspended from the stock or non-rotating portion of the spindle. Here the actuator performs the same function as a dynamic vibration absorber which is tuned to reduce or eliminate the vibration of an excited system. This setup introduces a control system directly integral to the drilling tool as desired. A schematic of the described experimental test setups are shown in Fig. 2.2.

2.3 Model Development

In previous work [12], a parametric study and Rational Polynomial Fraction method were used to estimate fundamental behavior of the drilling system to create a refined numerical model for simulating the drilling process. Through this development, the stiffness and damping coefficients of the plate and drill press as well as the stiffness of the drill bit were determined [12]. A constant force and varying acceleration were the inputs driving the model. The varying acceleration described the disturbance input of the system and was simulated as a summation of two sinusoids containing frequency components relative to the rotational speed of the drill. It is important to note that the amplitudes and phase angles were assumed to be constant, time invariant parameters. System parameters of the model development described above were used when developing baseline simulations with different control algorithms (Fig. 2.3).

2.4 Constructing Elaborate Disturbance Input

The proposed idea for vibration suppression involved actuating out-of-phase with the drill excitation such that the actuation and excitation destructively interfere. First, the signal from the accelerometer was analyzed to determine the nature of the excitations to be cancelled. Then a matching signal was output to the actuator and the effects of changing the output's phase were examined.

To study the nature of the drill excitation, an accelerometer was situated on top of the plate which maintained contact with the running drill. A Fast Fourier Transform was performed on the acceleration signal which indicated that the vibrations induced in the plate contained multiple frequency components. A dominant peak consistently appeared at the motor's operational speed of 30 Hz and another noticeable peak emerged at the frequency of the spindle rotation, which could be adjusted by reconfiguring the belt assembly. The mode from the spindle speed occupied a rather low frequency range, about 3–60 Hz. Higher frequency harmonics of the motor and spindle rotation also emerged regularly. In order to monitor the time histories of these frequency components, digital band pass filters were applied to the accelerometer signal and the resulting filtered signals displayed irregular fluctuations in amplitude. With multiple frequency components and amplitudes, it was postulated that the acceleration signal could be approximated by Eq. 2.1.

$$\sum_{i=1}^{n} A_i \cos(\omega_i t + \phi_i) \tag{2.1}$$

A_i = amplitude
ω_i = frequency component
ϕ_i = phase angle

After determining the nature of the drill's excitation, the ability to construct a matching signal was then pursued. An accelerometer signal was read into the LabVIEW environment where an FFT operated on the data. Using the magnitude information from the FFT, the program was able to identify the peak frequency for each manually-specified frequency range. In this experiment, the user specified four ranges such that the program selected four peak frequencies. With these peak frequencies and their corresponding magnitudes, the program generated a sinusoid for each of the four selected components. The sinusoids were then summed and compared to the original accelerometer signal, as displayed in the Fig. 2.4. By inspection, the reconstructed signal closely matches the original accelerometer reading. Thus, the signal can be reasonably approximated by the summation shown in Eq. 2.1, with n = 4 and where $\omega_1, \ldots, \omega_4$ correspond to the four largest frequency components of the signal.
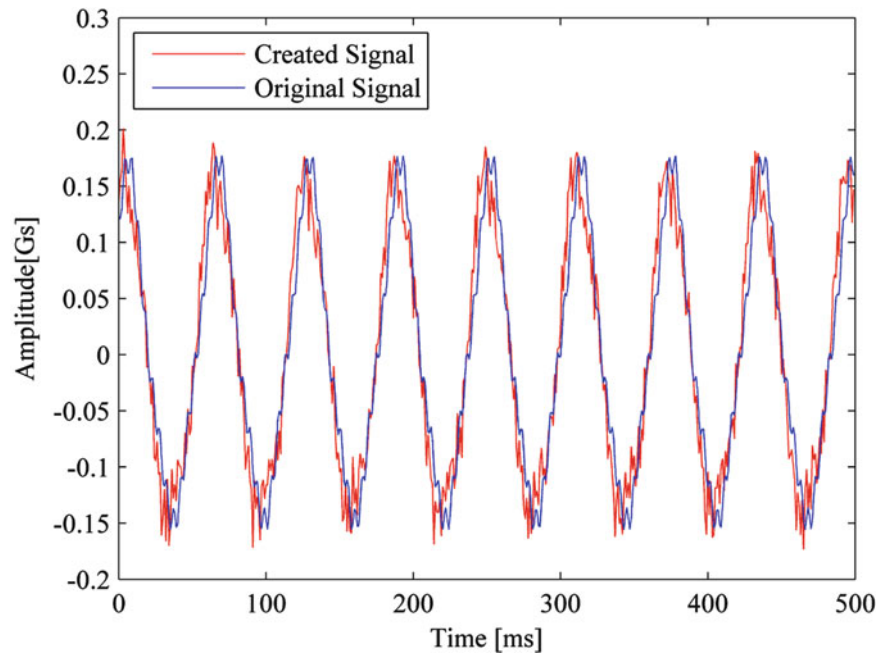
Fig. 2.4 Input signal reconstruction based on the four most dominant frequency components
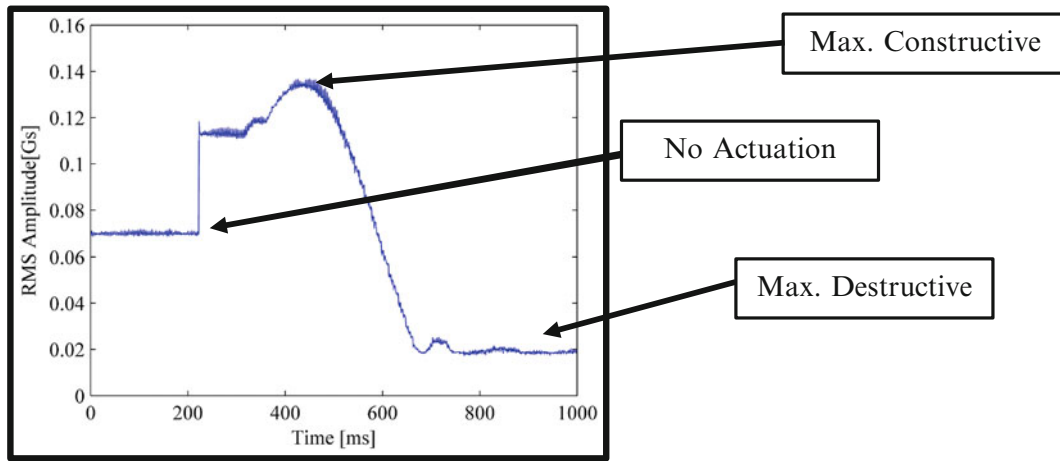
Fig. 2.5 Manual phase shift: RMS of raw acceleration signal

2.5 Manual Phase-Shift Experiment

In further experimentation, a shaker actuator was placed on top of the plate such that the accelerometer now measured the combined effects of the drill and actuator, in the configuration of Setup 1. A signal was reconstructed from the accelerometer input, as described in Sect. 2.4, and was routed from the LabVIEW environment to the shaker. The program included an indicator that displayed an updating RMS of the raw accelerometer signal. The RMS value was expected to reach a maximum when the excitation and actuation added constructively and decrease when the two added out-of-phase. With both the drill and actuator in operation, the RMS was observed to oscillate at a slow rate (less than 10 Hz). This RMS oscillation was attributed to a phase drift in the drill excitation, since the phase of the shaker output was constant with time. The realization of a phase drift in the excitation revealed a need for the output to adapt its phase with time.

To test the viability of the phase-cancellation idea, the effects of a drifting excitation phase were temporarily eliminated by replacing the drill excitation with a constant phase excitation from a second shaker. In this case, users could shift the output's phase manually and observe how the RMS acceleration responded. As the user swept through a range of phase angles, the RMS value exhibited maximum and minimum values corresponding to constructive and destructive interference respectively, see Fig. 2.5. For this particular experiment, the minimum RMS value was observed to be about 0.02 g's, 71 % reduction from the unactuated value of 0.07 g's. Significant reduction in amplitude was also apparent when comparing the time histories of the controlled and uncontrolled signals, as shown in Fig. 2.6. These results confirmed that manually-controlled out-of-phase cancellation succeeded in suppressing vibrations in the plate.

2.6 Controller Development

The phase drift experienced by the drill excitation required that the output signal track with the time-varying phase of the excitation. A software-based phase-locked loop was implemented in LabVIEW to accomplish this. Although typical phase-locked loops cannot lock to the phase unless the initial offset is within a certain range, here an extremum-seeking algorithm is implemented, which is robust in that there are no requirements on the initial value [11]. Described below are the mathematical expressions employed in this PLL algorithm. First, the excitation frequency component of interest is characterized as the sinusoid in Eq. 2.2, where ω_0 is the peak frequency selected from the FFT and ϕ is the unknown time-variant phase angle. Note that the amplitude A(t) is a function of time as observed in the initial accelerometer measurements. Equation 2.3 represents the match generated by the algorithm which has the same form as original signal. Although the signals in Eqs. 2.2 and 2.3 share the same frequency, $\phi(t)$ in Eq. 2.2 represents the unknown phase while $\widehat{\phi}(t)$ denotes the generated match. The amplitude of the matched signal is taken as the RMS of previous samples. To quantify the discrepancy between the actual signal and the generated match, the cost function shown in Eq. 2.4 compares the two [11]. Lastly, the cost function is incorporated into the extremum-seeking function, Eq. 2.5, where the discrepancy between the original signal and the match is minimized.

Fig. 2.6 Single frequency cancellation
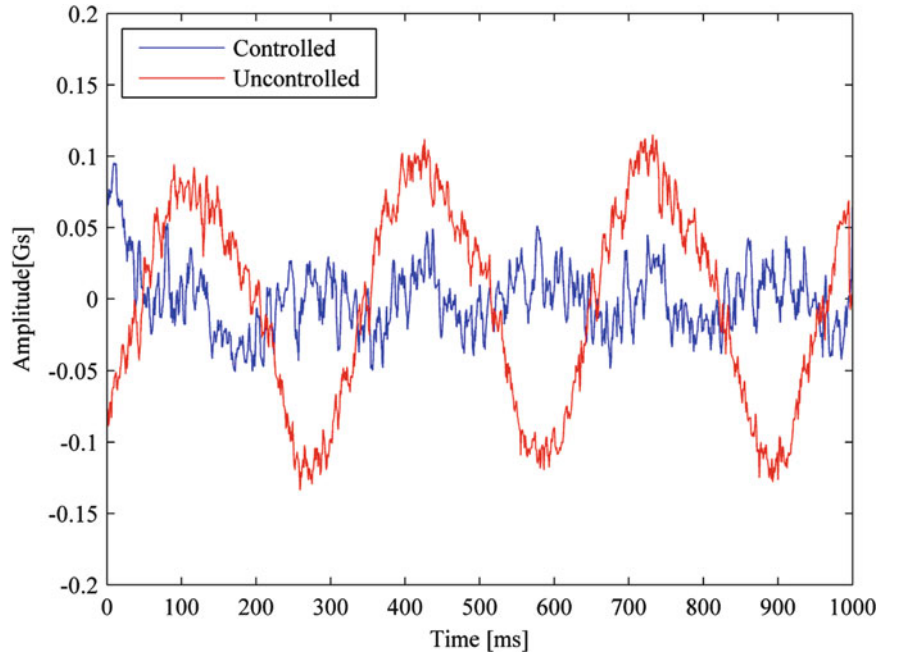
$$\textit{Signal to match} \qquad A(t) \cos \left(\omega_0 t + \phi(t)\right) \tag{2.2}$$

$$\textit{Generated match} \qquad A_{RMS}(t) \cos \left(\omega_0 t + \widehat{\phi}(t)\right) \tag{2.3}$$

$$\textit{Cost} \quad Cost\left(\widehat{\phi}(t)\right) = \left| A_{RMS}(t) \cos \left(\omega_0 t + \widehat{\phi}(t)\right) - A(t) \cos \left(\omega_0 t + \phi(t)\right) \right| $$
$$+ \left| A_{RMS}(t) \cos \left(\omega_0 t + \widehat{\phi}(t)\right) - A(t) \cos \left(\omega_0 t + \phi(t)\right) \right|^2 \tag{2.4}$$

$$\textit{Extremum} - \textit{seeking function} \quad \frac{\partial \widehat{\phi}}{\partial t} = \alpha \sqrt{\omega} \cos \left(\omega t\right) - k \sqrt{\omega} \sin \left(\omega t\right) * Cost\left(\widehat{\phi}(t)\right) \tag{2.5}$$

$A(t) =$ disturbance amplitude
$A_{RMS}(t) =$ root mean squared of disturbance amplitude
$\omega_0 =$ targeted frequency
$\phi(t) =$ disturbance phase
$\widehat{\phi}(t) =$ matched phase
$\alpha =$ perturbation size
$\omega =$ perturbation frequency

These equations were incorporated into a LabVIEW program, using a finite difference approximation for the partial derivative in Eq. 2.5. Points were sampled one at a time from the accelerometer, band pass filtered to represent a single frequency component, and sent through the block diagram depicted in Fig. 2.7. For each iteration, the program compares a new sample to the previously generated match, calculates a value for the cost function, and then adjusts $\widehat{\phi}$ so as to minimize this cost. The first time the loop executes, the initial value of $\widehat{\phi}$ is arbitrary. Convergence and tracking takes place as, on average, $\widehat{\phi}$ performs a gradient descent of the cost function.

2.7 Phase Detector Application

The points generated in this manner by the phase-lock-loop were plotted against the original input signal in LabVIEW (Fig. 2.8) and the graphs indicate that the generated signal successfully locks on to the phase of the input. The amplitude of

Fig. 2.7 Adaptive phase lock algorithm

$$\frac{d\hat{\varphi}(t)}{dt} = \alpha\sqrt{\omega}\cos(\omega t) - k\sqrt{\omega}\sin(\omega t)Cost(\hat{\varphi}(t))$$

$$\omega >> \frac{d\varphi(t)}{dt}, \quad \omega >> \omega_0$$

$$\frac{d\bar{\bar{\varphi}}(t)}{dt} = -\frac{k\alpha}{2}\frac{d}{d\bar{\varphi}}Cost(\bar{\bar{\varphi}}(t))$$
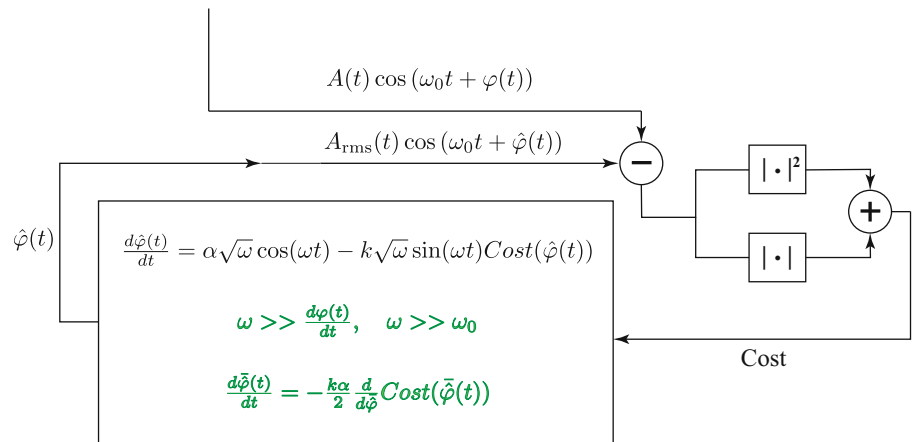
Fig. 2.8 Phase lock assessment. Created signal locks in-phase with the input signal
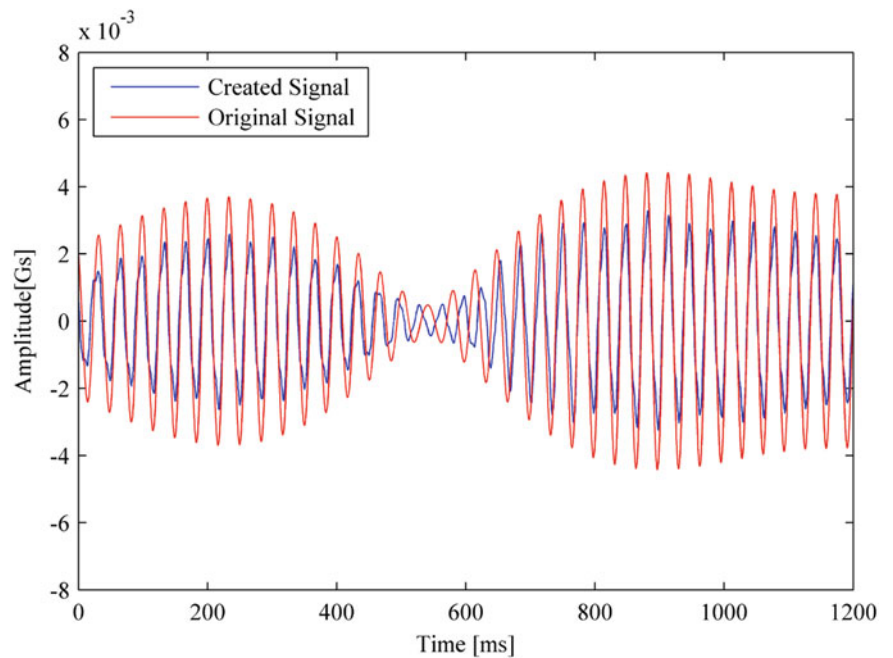
the match signal also tracks with the envelope of the input disturbance; the generated amplitude shown is smaller than the original signal by a scaling factor of $\sqrt{2}$ for easier visual comparison.

Once the control locks onto the phase and amplitude of the targeted frequency component, the output signal must be shifted to produce destructive interfere. Assuming the accelerometer and actuator are physically collocated, the phase difference to produce destructive interference would be 180° for each frequency included in the summation.

2.8 Adaptive Control System

In the overall system, as diagramed in Fig. 2.9, each of the following processes operate on the acquired samples to generate an output: (1) FFT, (2) Max peak finder, (3) Adaptable Bandpass filter, (4) RMS, (5) Extremum-seeking function. This control system can adapt to three different aspects of the excitation: frequency, phase, and amplitude. The controller's ability to adapt to the dominant frequencies and filter around them was demonstrated in Experiment 1 while the phase and amplitude adaptability were demonstrated in Experiment 3. However, combining these functionalities into a unified control system presented challenges with software timing, available hardware, and overall project timing constraints.
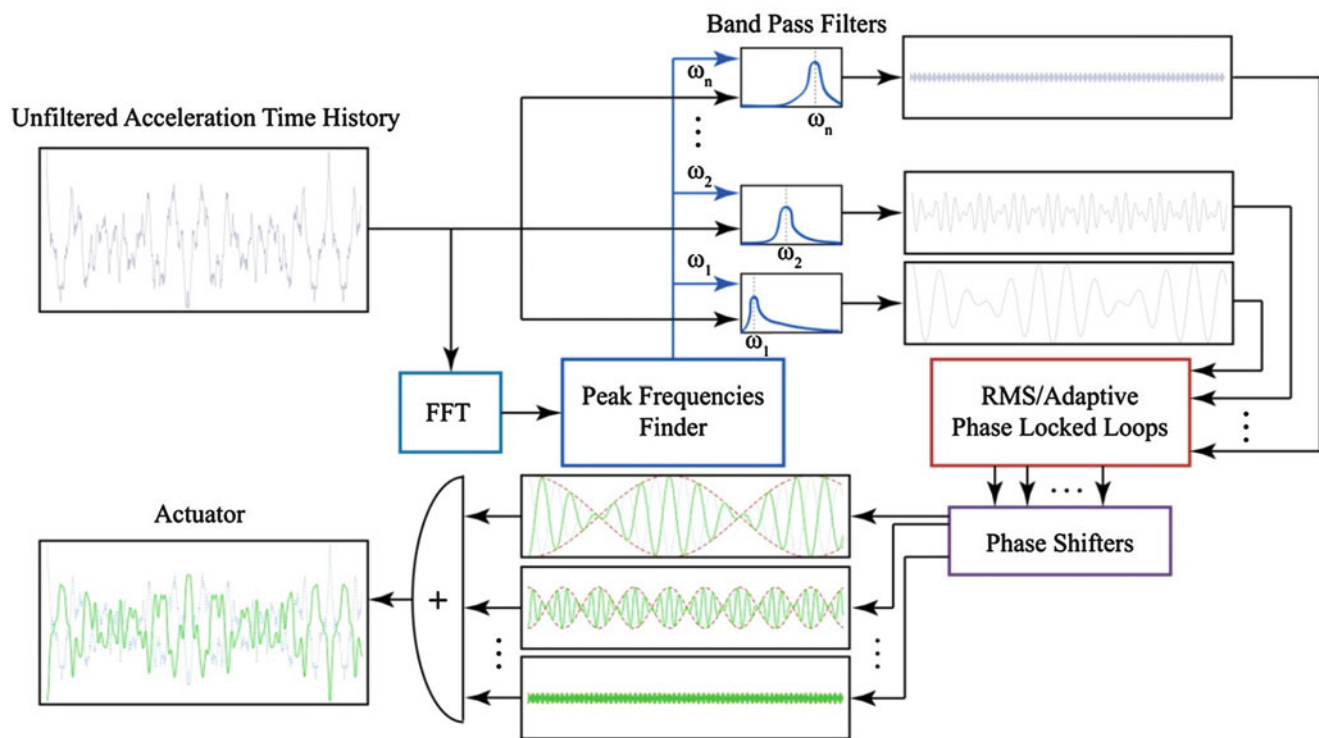
Fig. 2.9 Overall system block diagram

2.9 Challenges with Software Implementation and Future Work

Since this suppression scheme depends on phase adjustments, the output waveform must maintain deterministic timing. The program simultaneously reads in a single point and writes out another. The rate at which these single samples are acquired must be fast enough to sufficiently characterize the frequencies of interest. For example, to characterize the 30 Hz component of the incoming signal with 10 pts per cycle would require a sampling rate of 300 Hz. While sampling rates of this order are perfectly achievable from a hardware perspective, software execution requires additional considerations. The control processing for each point must occur within a single sample period so the sampling rate is limited by the speed of software execution. Typically, a time-critical loop is made more efficient by confining all user-interface interaction to a separate, lower-priority thread on the processor, an advanced programming technique. Although the program receives points one at a time, several of the control system blocks require an accumulation of points: the FFT, digital filter and amplitude RMS. Further investigation is required to determine whether the number of accumulated points adversely affects processing speed and the ideal number of points to accumulate for these different processes. Also for experimental purposes, it would be desirable to allow the user to change the control parameters on the fly such as the perturbation size of the extremum-seeking function. Since this feature would not warrant inclusion in the time-sensitive loop, the lower-priority and time-critical loops must interact with each other.

Depending on hardware system delays and the physical locations of the actuator and accelerometer, the optimal output phase for to destructively interfere with the excitation at the point of measurement may not be 180°. Thus, a necessary addition to the proposed phase-locked loop would be the ability to automatically compensate the phase of the output to minimize the measured vibrations, rather than assume a phase difference of 180°.

The actuator selected for this application must be capable of withstanding highly dynamic loads. The piezoelectric stack actuators initially employed in this work lost responsiveness after a few hours of experimental driving, despite remaining within the voltage limits specified by the manufacturer. Alternatively, the electromechanical shakers used in place of the piezoelectric actuators involve complicated transfer characteristics such that the driving voltage does not always produce the desired response from the armature. To precisely control the actuator's response would require including a separate controller for the shaker in addition to the algorithm proposed here.

In this research, the controller's effectiveness at damping a single frequency was demonstrated but this could easily be extended to damp multiple peak frequencies simultaneously. Although significant improvement in vibration levels

was observed by damping the single highest frequency, actuating at two frequencies inconsistently resulted in negligible improvement. This lack of improvement could be attributed to imprecise control of the shaker. Thus, if multiple frequency components are to be cancelled, the actuator must be capable of responding to complex waveforms or multiple actuators must be used, one for each frequency.

Further experimentation with a cutting drill bit rather that a blank would be beneficial because the excitation frequency, amplitude, and phase induced in the plate are expected to vary more dramatically as the drill bit penetrates. In theory, the proposed phase-locked loop control would adapt to these time-varying quantities as demonstrated in the case with the bit blank.

2.10 Conclusion

This research investigated the implementation of a software-based phase-locked loop control to suppress axial vibrations in a drilling process. Experiments confirmed the ability of the control system to identify peak frequencies, to suppress vibrations by actuating out of phase, to remain locked to a shifting phase, and to track with the amplitude's envelope. Future work includes combining these adaptable capabilities into a single system, adding the ability to optimize the phase of the output, selecting actuators that can accommodate lower frequencies and complex waveforms, and experimenting with a cutting drill bit.

References

1. Siddhpura M, Paurobally R Experimental investigation of chatter vibrations in facing and turning processes. World Acad Sci Eng Technol 7: 2013-06-28
2. Wani AS, Sagavkar GS, Bhate VK (2013) Vibration analysis of drilling operation. Int J Stud Res Technol Manag 1(2):163–175
3. Faassen RPH, van de Wouw N, Oosterling JAJ, Nijmeijer H (2003) Prediction of regenerative chatter by modeling and analysis of high-speed milling. Department of Mechanical Engineering, Eindhoven University of Technology
4. Vergara M, Sancho JL, Rodriguez P, Gonzalez-Perez A (2008) Hand-transmitted vibration in power tools: accomplishment of standards and users' perception. Int J Ind Ergon 38:652–660
5. Branner AJ (1986) Dose response relationships for hand-transmitted vibration. Scand J Work Environ Health 12:284–288
6. Takamori K1, Furukawa H, Morikawa Y, Katayama T, Watanabe S (2003) Basic study on vibrations during tooth preparations caused by high-speed drilling and Er:YAG laser irradiation. US National Library of Medicine National Institutes of Health, Wiley-Liss, Inc.
7. Hassan MF, Mailah M, Junid R, Alang NA (2010) Vibration suppression of a handheld tool using intelligent active force control (AFC). In: Proceedings of the world congress on engineering, vol II, WCE June 30–July 2, 2010, London, U.K
8. Park G, Radecki PP, Farinholt KM, Bement MT (2010) Vibration suppression in cutting tools using a collocated piezoelectric sensor/actuator with an adaptive control algorithm. J Vib Acoust 132 051002–051010
9. Rios-Gutierrez M, Silva-Navarro G (2010) Suppression of mechanical vibrations in a building like structure by means of a piezoelectric patch actuator and positive acceleration feedback. 2010 7th international conference on electrical engineering computing science and automatic control (CCE)
10. Algrain M, Hardt S, Ehlers D (1996) A phase lock loop based control system for suppressing periodic vibration in smart structural systems. Department of Electrical Engineering and Center for Electro-Optics, University of Nebraska
11. Scheinker A Simultaneous stabilization and optimization of unknown, time-varying systems. In: Proceedings of the 2013 American control conference 17–19 June 2013, pp 2637–2642, Washington, DC
12. Winter B, Stevens G, Lu R, Flynn E, Schmierer E (2014) Nonlinear modeling for adaptive suppression of axial drilling vibration. In: IMAC XXXII conference proceeding, February 3–6, 2014, Orlando, Florida

Chapter 3
Towards the Selection of Balancing Planes to Attain Low Vibrations in Flexible Rotor Motor Systems

Sumit Singhal and Kumar Vikram Singh

Abstract Electric motors with variable frequency drives have several kinds of excitations, such as mechanical unbalance and electromagnetic forces between the rotor and stator. They cause undesirable lateral vibrations in induction motors during their operation. The vibration can be minimized by careful selection of balancing planes that are required to keep vibrations low at various operating speeds in the case of an induction motor rotor. It is important to note that arbitrary selection of balancing planes may not be feasible due to manufacturing, assembly and existing motor design constraints. In this research, a rotordynamic model is developed for simulating free and forced response of the industrial scale motor-rotor system operating at super-critical speed. The accuracy of this model is verified with the experimental modal analysis data. Subsequently, this model is used to design for selecting balancing planes to minimize the vibration at critical and operating speeds. This paper describes a complete process for achieving a suitable balancing through parametric study. The effects of residual unbalance on the vibrations at the super critical operating speeds are also highlighted. Research is currently underway in formulating and solving associated optimization problems for estimating optimal balancing for a range of operating speeds as well as multiple modes of interest.

Keywords Rotordynamics • Vibrations • Balancing • Flexible rotor • High speed

3.1 Introduction and Background

High-speed electric motor systems with variable frequency drives are frequently used to drive rotating systems. Controlling centrifugal forces and rotordynamic vibrations (or acoustics) when rotation speeds are high are two major challenges in rotating machinery design and reliability. To overcome these challenges, designers must address two key points. First, the rotor must have sufficient mechanical strength to withstand centrifugal forces. Second, the designer must take the natural frequencies of the system into account. In order to comply with API [1, 2] specification, all critical frequencies should be separated from the nearest operating speeds by 15 % to reduce excessive vibration. Critical frequencies can be handled in two ways. First is called "stiff rotor design", where the rotor is operated below the first critical speed. This option requires sturdy construction and thick shafts. Alternatively, for "flexible rotor design", the rotor is driven at the speeds in between the critical speeds associated with multiple modes.

Construction of Large Induction Motor The main components of a shaft-rotor core system are the shaft, steel sheets, copper/aluminum rods, end connector and axial vents. The shaft is made of carbon steel bar stock such as AISI 1045, 4140 or 4340. The shaft is made to ensure strength and resistance to deflection. The rotor core consists of numerous, thin, circular, laminated electric steel sheets. These sheets are compressed with enough force to keep them as one solid piece. Aluminum and copper are used to process rotor cores. Aluminum is cast into the solid rotor core, and copper bars are hammered and shrink-fitted into the solid rotor core. Because most flexible rotor motors are currently made with the copper bars, this material is be used for this analysis. Axial vents are also present and vary in size and amount. They are primarily used to keep the rotor core from overheating and thermal vibration instability.

S. Singhal (✉)
Siemens, Norwood, OH, USA
e-mail: sumit.singhal@siemens.com

K.V. Singh
Mechanical and Manufacturing Engineering Department, Miami University, Oxford, OH, USA
e-mail: singhkv@miamioh.edu

Fig. 3.1 Induction motor rotor
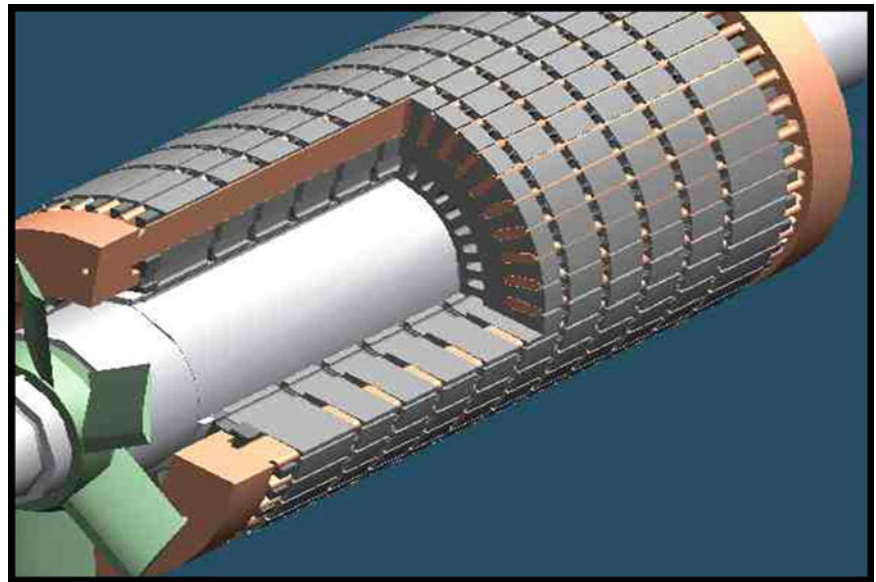
Sources of Mechanical Unbalance in Induction Motor Rotors An excess mass on one side of the rotor, causing asymmetry in the rotation, is the main cause unbalance. Rotor balance involves the entire rotor structure, which is made up of a multitude of parts, including the shaft, rotor laminations, end heads, rotor bars, end connectors, retaining rings (where required) and fans as shown in Fig. 3.1. Unbalance in the motor rotor is attributed to the following:

1. Tolerances in fabrication, machining, and assembly.
2. Variations within materials such as voids, porosity, density and finishes.
3. Nonsymmetrical structure during operation such as shifting of parts due to rotational stresses, aerodynamic forces and temperature changes.

Balancing problems can be minimized by precision manufacturing technology. For motors, rotor punching must be precision manufactured with close concentricity. The punching must be stacked square with the bore, uniformly pressed and clamped in position when shrunk on the shaft to prevent movement with speed change. Rotor bars are shimmed and/or swaged so they are tight in the slots. There are other less common methods to assure tight rotor bars, such as heating the core and chilling the bars. End connectors should be induction brazed symmetrically to the bars so they can help eliminate variations in balance due to thermal change. In induction motors, the rotor core is usually the source and location of the unbalance, as the remaining rotor shafts are machined to within very precise tolerances.

Lateral Vibration and Balancing in the Induction Motors API 684 emphasizes that achieving a balanced condition for a rotating assembly is a fundamental element of maximizing machinery reliability. Several kinds of excitations exist that can cause lateral vibrations in induction motors. Unbalance of rotating machinery is the most common cause of equipment vibration. Lower unbalance is always desired as it produces low level vibrations and causes insignificant stresses in the rotating assemblies, bearings and support systems while increasing the reliability of the rotating machinery. Large high-speed induction motors operating on variable frequency drives with flexible rotordynamic designs are often required to pass through the critical speed.

API 684 [1] standard, describes balancing as "A procedure for adjusting the radial mass distribution of a rotor so that the mass centerline (principal inertial axis) approaches or coincides with the rotor's rotational axis, thus reducing the lateral vibration of the rotor due to unbalanced inertia forces and forces on the bearings, at once-per-revolution frequency (1X)." Furthermore, per ISO 11342 [3] standard, the aim of balancing any rotor is to achieve satisfactory running when installed on site. In this context 'satisfactory running' means that not more than an acceptable magnitude of vibration is caused by the unbalance remaining in the rotor.

A Note on the Selection of Number of Correction Planes Dan Hartog in 1930 [4] postulated that for speeds higher than about half of the first critical speed, the rotor assumes deformations which cannot longer be neglected since they create new centrifugal forces in addition to ones caused by the original unbalance. Hartog also concluded that a flexible rotor design can be balanced in two planes for a single speed only and that, as a rule, these machines will become unbalanced at any

other operating speed. API 541 [2] also states that a minimum of three planes are required for balancing a flexible shaft induction motor. It can be concluded that more than two planes are required for flexible rotor induction motor running on variable frequency drive. However, ISO 11342 [3] describes a criteria for using a two-plane balance for elastic rotors with rigid sections and states that: "If the unbalance in the rotor is distributed within the substantially rigid section of the rotor and the unbalance corrections are also made within this section, then the rotor will be balanced for all speeds".

As highlighted above that usually a minimum of three balancing planes are needed to attain low vibration levels in most flexible rotor designs that operate above the first flexure mode of vibration. It is the aim of this work to show that in certain cases; by carefully choosing two planes for balancing, low vibrations in an induction motor rotor at various operating speeds can be attained. This is achieved by experimental testing, finite element modelling and analysis of an industrial scale motor, as described in Sect. 3.2. Once the modal properties of the motor is validated, this model is further used for rotordynamic analysis and balancing. Different cases to achieve balancing are highlighted with the actual experimental results in Sect. 3.3 and potential balancing planes are obtained, followed by the conclusion and future work for this research.

3.2 Rotordynamic Testing and Modelling of Induction Motor Rotor

The dynamics of an induction motor rotor-bearing system is governed by the following set of equations in a matrix form

$$\mathbf{M\ddot{x}} + \mathbf{C\dot{x}} + \mathbf{Kx} = \mathbf{f} \tag{3.1}$$

where, $\mathbf{M}$, $\mathbf{K}$ and $\mathbf{C}$ are the mass, stiffness and damping matrices, respectively, and $\mathbf{f}$ is the external excitation force vector acting on the rotor-bearing system. In order to include the effect of magnetic forces, the structural stiffness matrix is added with matrix representing negative stiffness on the rotor core section due to magnetic pull acting on the rotor [5]. External force vectors are typically either excitations caused by mass unbalance or electromagnetic forces created by magnetic eccentricity (uneven air gap). Finite element based modeling is used to predict the natural frequencies of such systems and to simulate the steady state and transient vibration response of the rotor-motor system. In this study experimental modal analysis as well as finite element modeling and simulations are conducted simultaneously to identify the rotor-motor dynamic characteristics.

3.2.1 Mode Identification Through Experimental Modal Analysis

First, in order to estimate the influence of a rotor core on the deflection shape of the rotor shaft, an experimental modal analysis was conducted on rotor-shaft with various boundary configurations, as shown in Fig. 3.2. The deflection shapes of the shaft at the first three flexural bending modes are computed and they are shown in Fig. 3.3. Due to symmetric boundary conditions, first bending mode results in maximum deflection in the middle (anti node) and zero displacement at nodes.

A similar experimental modal analysis was conducted with the rotor core and axial fans shrunk on the shaft as shown in Fig. 3.4. The boundary conditions and placement of sensors were the same each time the experiment was conducted to ensure that each experiment was performed under the same conditions. Comparing Figs. 3.3 and 3.4, we can see that the deflection shape of the shaft changes significantly. The addition of a laminated copper cage does not only add mass, but also add flexural stiffness to the rotor shaft. As observed from Fig. 3.4, the addition of the laminated copper cage results in increasing the rigidity at the section of the shaft where rotor core was shrunk. Addition of such flexure rigidity by laminations and their effects on resulting natural frequencies and mode shapes could be estimated by the method shown by the authors in [6]. It is shown that depending on the design and manufacturing process, a magnetic core can add between 2 % and 6 % flexural stiffness to the rotor shaft. This can lead to significant changes in the critical speed predictions, if rotor core stiffness is not considered in rotor dynamic analysis. In the subsequent finite element analysis the effect of laminated core is included to incorporate the effects of core-laminates.
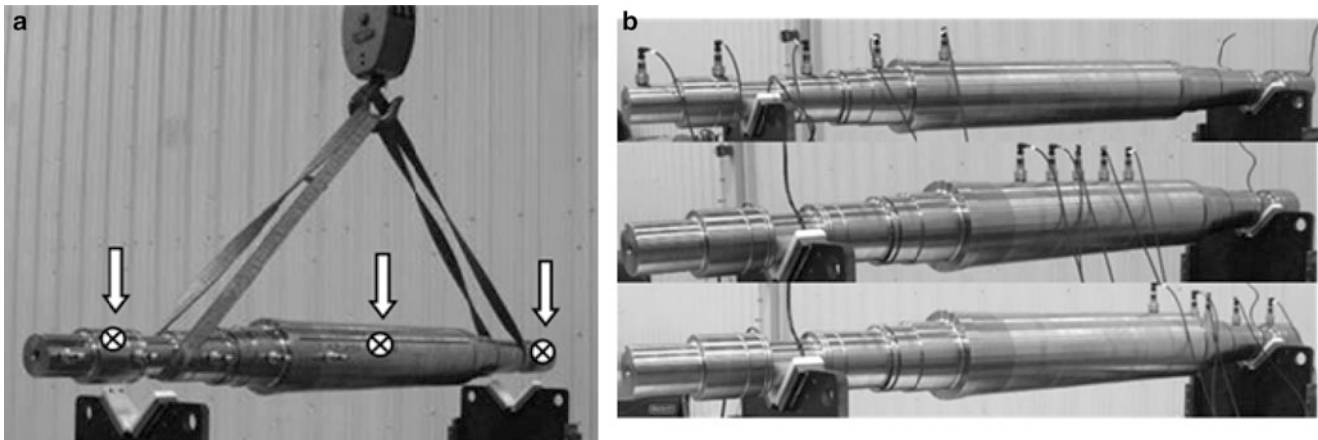
Fig. 3.2 (**a**) Free-free shaft mounting configuration supported by straps: *arrows* indicate "Top" and "Side" impact locations (**b**) sensor mounting configuration for mode extraction

Fig. 3.3 (**a**) Deflection shape of the shaft (**b**) deflection shape of the complete rotor
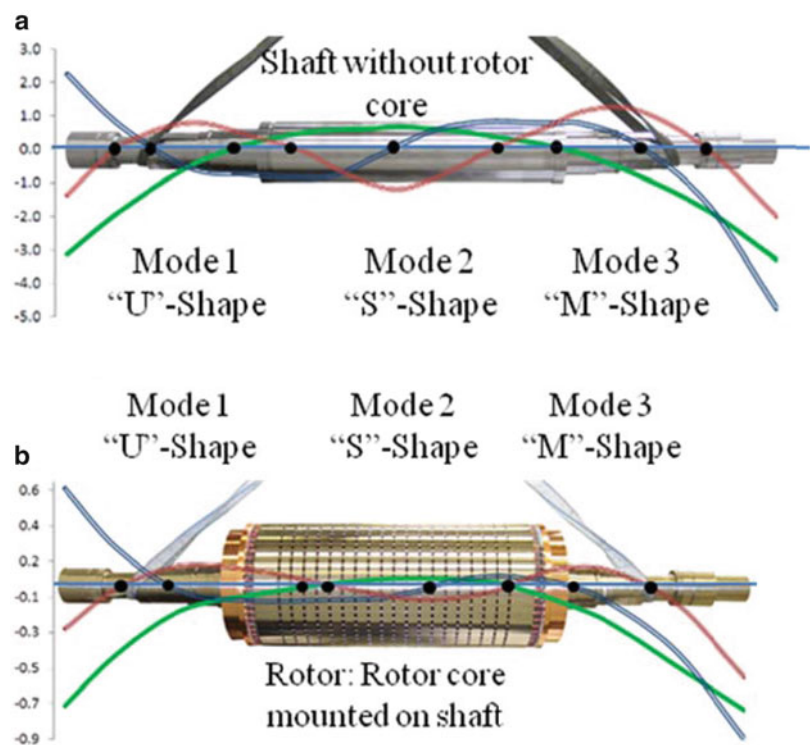
3.2.2 Finite Element Modeling for Rotordynamic Simulation

After the identification of modal parameters, mathematical model of the rotor-bearings systems was constructed for rotor dynamics analysis to estimate the critical speeds and forced vibration analysis. Following parameters was used for FEM motor model.

Motor Data

Rated Power: 4,000 HP; Rated Speed: 3,600 rpm; Rotor Weight: 1,100 kg;
Residual Unbalance: Per API 541
Bearing Type: Plain Cylindrical
Hydrodynamic Lubrication Oil Type: ISO VG 32
Lubrication System: Natural Cooling
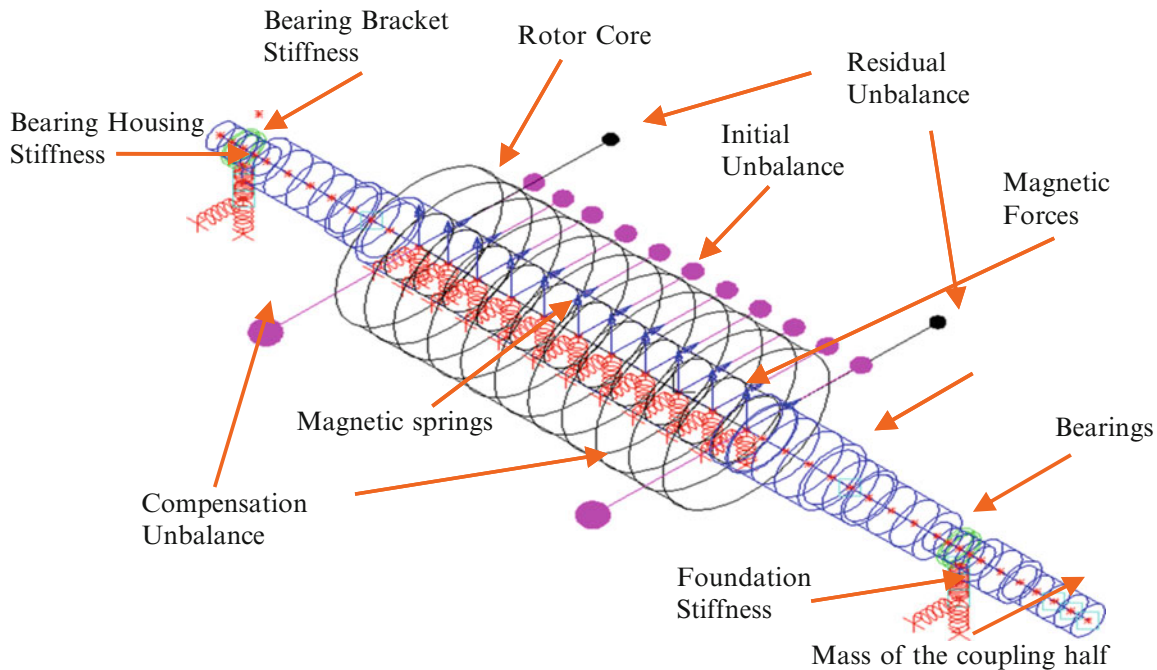
Fig. 3.4 Finite element rotordynamic model

The finite element rotordynamic program VARFEM which employs the MADYN solver to calculate the natural frequency and forced vibration response of the induction motor was used for study. This rotordynamic model consists of the shaft and rotor laminations modeled as beam elements. Magnetic attraction between rotor and stator was modeled as negative spring constant and magnetic forces were modeled as rotating forces, as outlined in [5]. Oil lubricated hydrodynamic bearing is also included in the critical speed and vibration response calculation. Bearing housing and bracket stiffness are estimated from the experiments and are included in the rotordynamic model. Both direct and cross-coupled stiffness of the rotordynamic oil film is calculated using SBCALC program, as well as the damping coefficients.

Foundation stiffness for the rotordynamic model is based API 541[2] criteria for massive foundation, where the foundation is considered massive if the vibration of the motor feet is less than 30 % of the vibration of the bearing housing. The rotordynamic model also considers the stiffening effect due to the presence of the active core in the rotor as well as the mass and inertia of flexible couplings and axial fans. The rotordynamic model contains initial mechanical unbalance due to manufacturing tolerances distributed over the entire rotor core. Correction unbalance and residual unbalance are applied at locations where correction weights would be applied during an actual balancing process. For the forced vibration response, the API 541, criterion of maximum permissible residual unbalance of ISO .67G is applied to the rotordynamic model. The result is the actual response of the rotor during field operation, which also corresponds to G 0.67 balancing quality grade according to ISO 1940 [3]. For lateral critical speed analysis and unbalance response tests, however, API 541 requires four times the permissible residual unbalance to be applied on the rotor. Dynamic electromagnetic forces are distributed along the rotor core and applied at each node as shown in Fig. 3.4. This rotordynamic model accommodates electromagnetic forces acting on the rotor due to uneven air gap generated during manufacturing as well as stack up tolerances for different components.

3.2.3 Rotordynamic Analysis

3.2.3.1 Damped Critical Speed and Stability Analysis

The natural frequency of the rotor-bearing system is calculated at its maximum operating speed of 3,600 rpm, including the effects of electromagnetic forces. The first critical speed is found when the rotor spinning at 2,400 rpm (40 Hz) and is shown in Fig. 3.5a. The associated mode shape demonstrates horizontal vibration at the bearings. This is called "the bearing mode" as the bearings usually have less horizontal stiffness than vertical stiffness. The second critical speed occurs at 2,820 rpm

Fig. 3.5 (**a**) Bearing mode at
40 Hz, (**b**) bending mode at
47 Hz
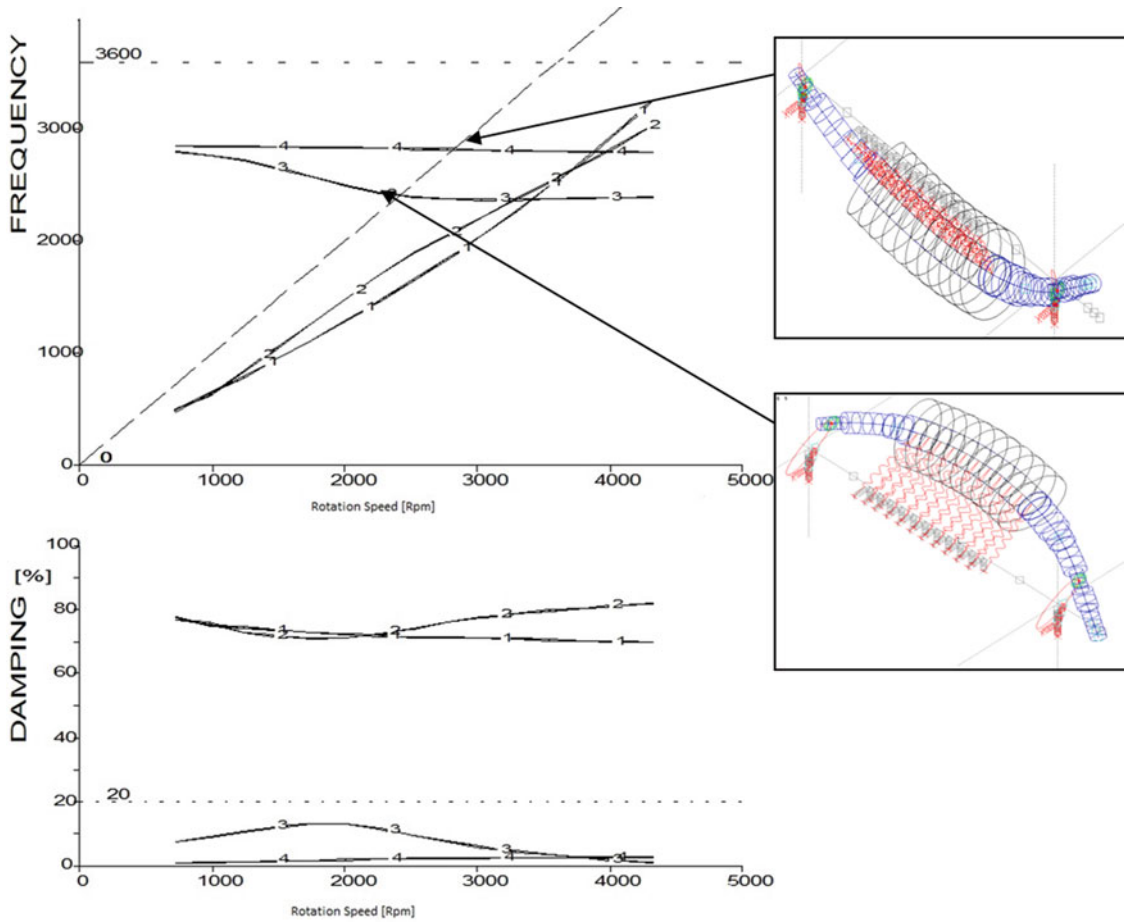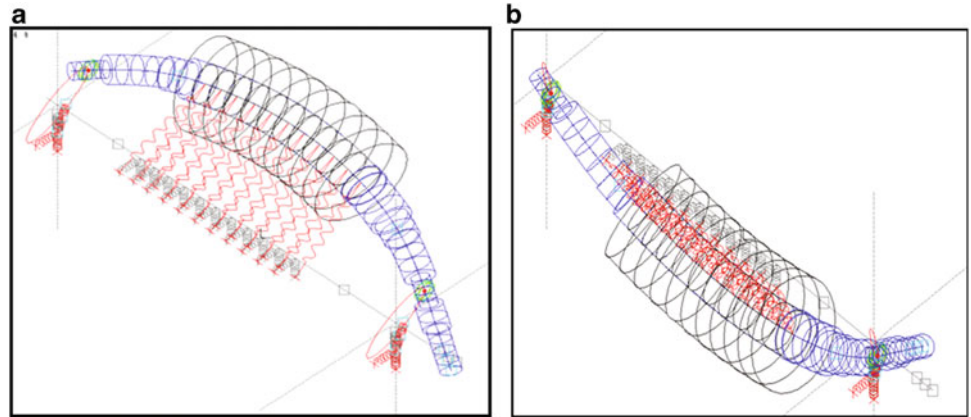
Fig. 3.6 Critical speed map

(47 Hz) which is the first flexural bending mode of the rotor-motor system, as shown in Fig. 3.5b. At this speed most of the bending occurring at the rotor core portion of the shaft and much less deflection in the bearings. The critical speed map of the rotor-bearing system is shown in Fig. 3.6 which demonstrates the effect of rotational speeds on first few natural frequencies of the system. The first two "rigid body oil film modes" which are highly damped are not considered to be critical speed per API 684 [1] and does not require any separation margin from the operating speed for the safe operation.

Therefore, Mode 3 and Mode 4 which are the horizontal and vertical critical speeds, occurring at 2,400 and 2,820 rpm respectively, as shown in Fig. 3.5a, b are considered here. Since the critical speed has 15 % separation margin from the operating speed of 3,600 rpm, the rotor design is safe to operate at 3,600 rpm per API. It is also important to note from Fig. 3.6 that damping of Mode 3 becomes zero at 4,400 rpm. At this speed, the stability limit has been reached for Mode 3.

At this speed, the rotor can go into self-excited rotordynamic instabilities, such as oil whip. Stability of the induction motor system limit can be increased by using tighter bearing clearance, changing the oil inlet temperature or using different bearing type such as tilting pad, lobe or active magnetic bearings [7–9].

3.2.3.2   Steady State Response

By assuming the unbalance in the rotor, as described in Sect. 3.2.2, forced vibration rotordynamic analysis is performed and peak to peak shaft vibration amplitude relative to bearing housing vibration is obtained for range of rotational speeds. The vibration amplitude and associated phase are computed at the bearing locations for this speed range and they are plotted in Fig. 3.7a, b respectively. It is evident that the maximum vibration amplitude occurs at the critical speeds. High vibrations at critical speeds could cause catastrophic failure of mechanical components.

3.2.3.3   Goals for Balancing

For safe and reliable operation of the machine shaft, peak to peak vibration amplitude at the bearings should not be greater than bearing clearance. API 541 [2] states that the maximum shaft relative peak to peak vibration amplitude at the critical speed should not exceed 80 % of designed diametric bearing clearance or 2.8 mils whichever is less, with four times the maximum permissible residual unbalance per plane. In order to prevent rotor to stator contact, rotor vibration should not exceed the radial air gap at any speed below the normal operating speed, even while passing through the critical speed in flexible rotor design. API 541 limits the maximum peak to peak vibration of the rotor in a large induction motor to 1.2 mils at one times the rotational speed and overall vibration to 1.5 mils for 3,600 rpm rotor speed.

In addition to robust rotordynamic design, proper balancing techniques and low residual unbalance are required to attain low vibration rotating machinery. By following maximum vibration criteria as discussed in earlier section, API 541 [2] allows maximum residual unbalance to be less than 4 W/N, which corresponds to an ISO 1940 balancing grade of 0.7. During rotordynamic analysis, the residual unbalance value as well as the location of the correction planes showed great influence on the vibration response of the same rotor structure. API 541 [2] specifies that for better vibration characteristics of induction motors, all flexible rotor designs require a minimum of balancing planes, with one plane positioned in the center of the rotor core. Adding a center plane in the rotor would significantly upgrade the motor design as special manufacturing and balancing techniques are required. This is uncommon to see, however, because a larger motor is required to accommodate the higher driven load requirement and the addition of a center plane requires the removal of any active magnetic material from the motor. Consequently, it is important to optimize the locations of the balancing planes and in some cases modify the rotor shaft design to achieve low vibration. From the well tested rotordynamic model and unbalance response analysis, it is possible to optimize the location of a balancing correction plane.

In contrast to API 541 specifying a three-plane balance for flexible shaft rotors, ISO 11342 [3] section 6.5.2 states criteria for two-plane balancing of elastic rotors with rigid section,

> If the unbalance in the rotor is distributed within the substantially rigid section of the rotor and the unbalance corrections are also made within this section, then the rotor will be balanced for all speeds.

3.3   Estimating Optimized Balancing Planes

Experimental modal analysis concludes that an induction motor rotor with shaft and core results in a substantially more rigid section in the rotor. Most of the unbalance in the rotor is distributed in this section of the rotor. Hence, per ISO 11342, if a correction was made in this rigid portion of the shaft, the rotor will be balanced for all speeds with two place balance. Therefore, three-plane balance as called for by API 541 specification should not be required for these scenarios.

To verify this argument, a parametric study is carried out with the same finite element model of the rotor describes in Sect. 3.2. For this rotor, the first critical speed is at 2,400 rpm and the second critical speed is at 2,820 rpm. According to API 541, since the rated operating speed is 3,600 rpm and this induction motor is over critical speed, this machine will require at least three correction planes with one plane at the center of rotor core.

The criteria for acceptable balancing correction planes for this study are:
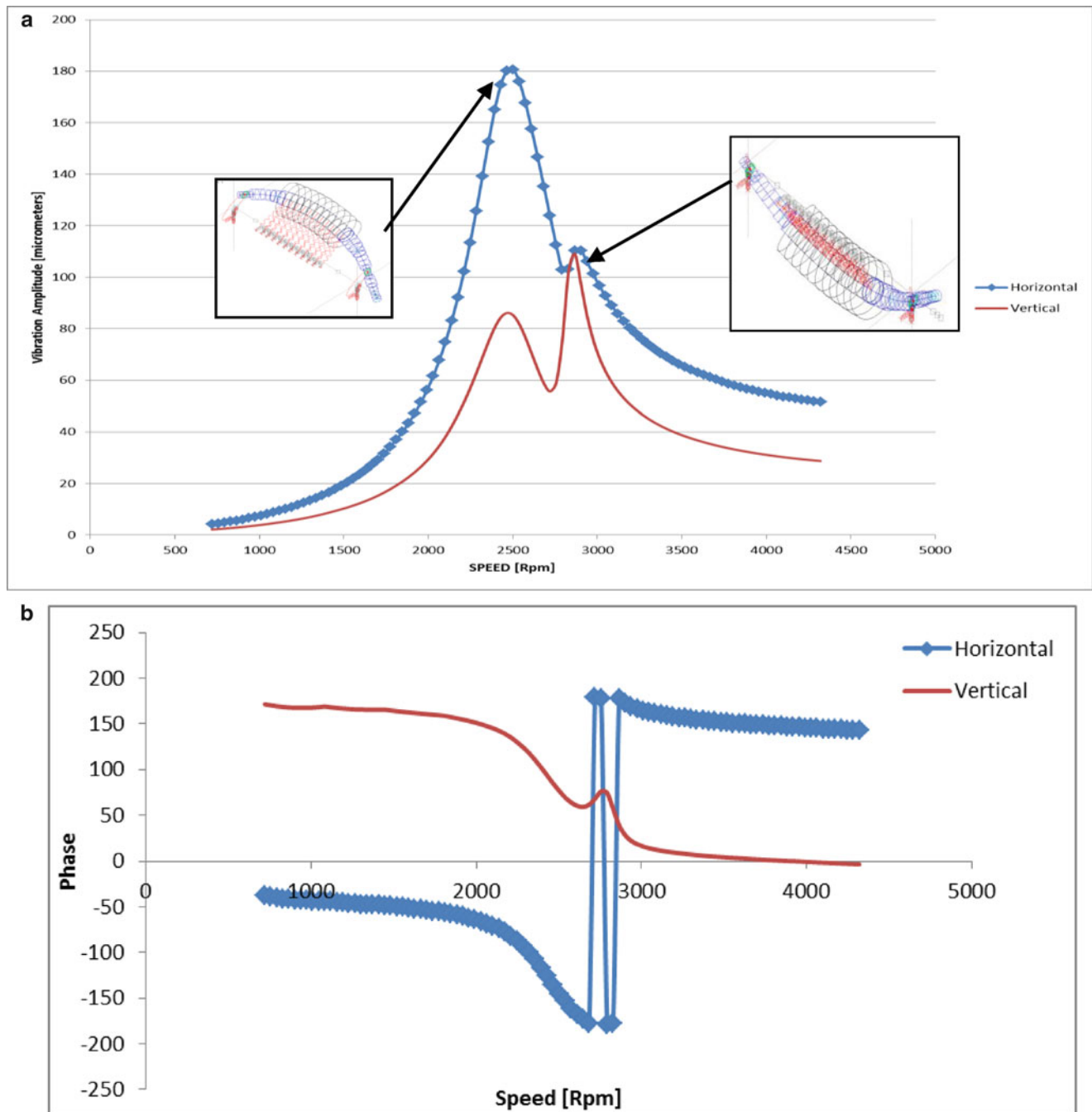
Fig. 3.7 (**a**) Vibration amplitude at bearing locations due to initial unbalance, (**b**) phase at bearing locations due to initial unbalance

1. Shaft relative peak to peak vibration amplitude at the critical speed should not exceed 80 % of designed diametric bearing clearance, or 2.8 mils, whichever is less, with four times the maximum permissible residual unbalance per plane., according to API541 4.3.5.3
2. Shaft relative peak to peak vibration amplitude at the rated operating speed should meet API 541 vibration limit.

Three cases of balancing planes are considered for this analysis and forced vibrational response are computed for the range of rotational speeds for all these cases. Balancing planes for each cases are chosen as per the standards as well as with the consideration of practical constraints associated with the rotor-motor design. The description of these cases and associated balanced response are presented her. The unbalance response for all three cases are shown in Fig. 3.9a, b.

Fig. 3.8 (**a**) Two correction planes on rigid section, (**b**) three correction planes on rigid section including one in center of core, (**c**) two correction planes away from the rigid section of the core
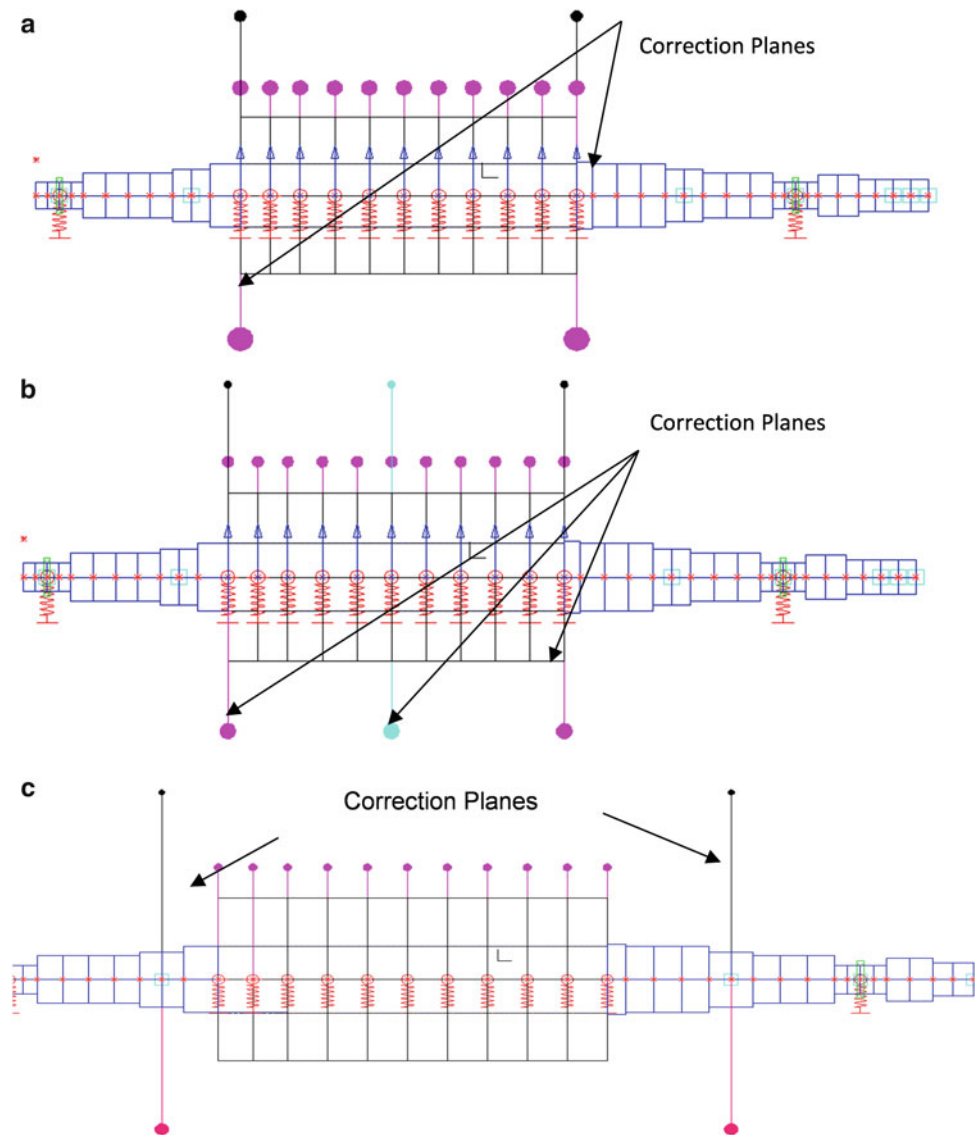
Case (1): Two Balancing Planes Close to the Core on the Rigid Section In this design configuration, two correction planes are located on the either side of the rigid section of the core as shown in Fig. 3.8a. According to ISO 11342, this configuration should give satisfactory vibration amplitude for flexible shaft rotor at all speeds. The unbalance response for this case as shown in Fig. 3.9a, shows that relative peak to peak vibration amplitude of the system at the rated operating speed is 17 micrometers, or 0.67 mils, which is well below API 541 vibration limit of 1.2 mil for one time rotational speed vibration limit. It is also clear that while passing through the critical speeds, vibration is 32 micrometers, or 1.25 mil, which is also well below API criteria.

Hence, with two correction balancing planes close to the core on the rigid section, it is possible to meet API vibration limit and the industry standard of ISO 11342 for flexible rotor balancing is satisfied.

Case (2): Three Balancing Planes on the Rigid Portion of the Core In this design configuration, two correction planes are located on the either side of the core and one correction plane is located at the center of core, as shown in Fig. 3.8b. This design configuration meets API 541 design criteria for flexible rotor design. Correction balances and residual unbalances are divided equally between three planes for the rotordynamic simulation.

From the unbalance response analysis shown in Fig. 3.9a, b, we can see the relative peak to peak vibration amplitude of that shaft at the rated operating speed is 12 micrometers, or 0.5 mils. While passing through the critical speed, vibration is 25 micrometers (or 1.2 mil), which is still below API criteria. Three correcting balancing planes on the core show slight improvement in vibration amplitude.
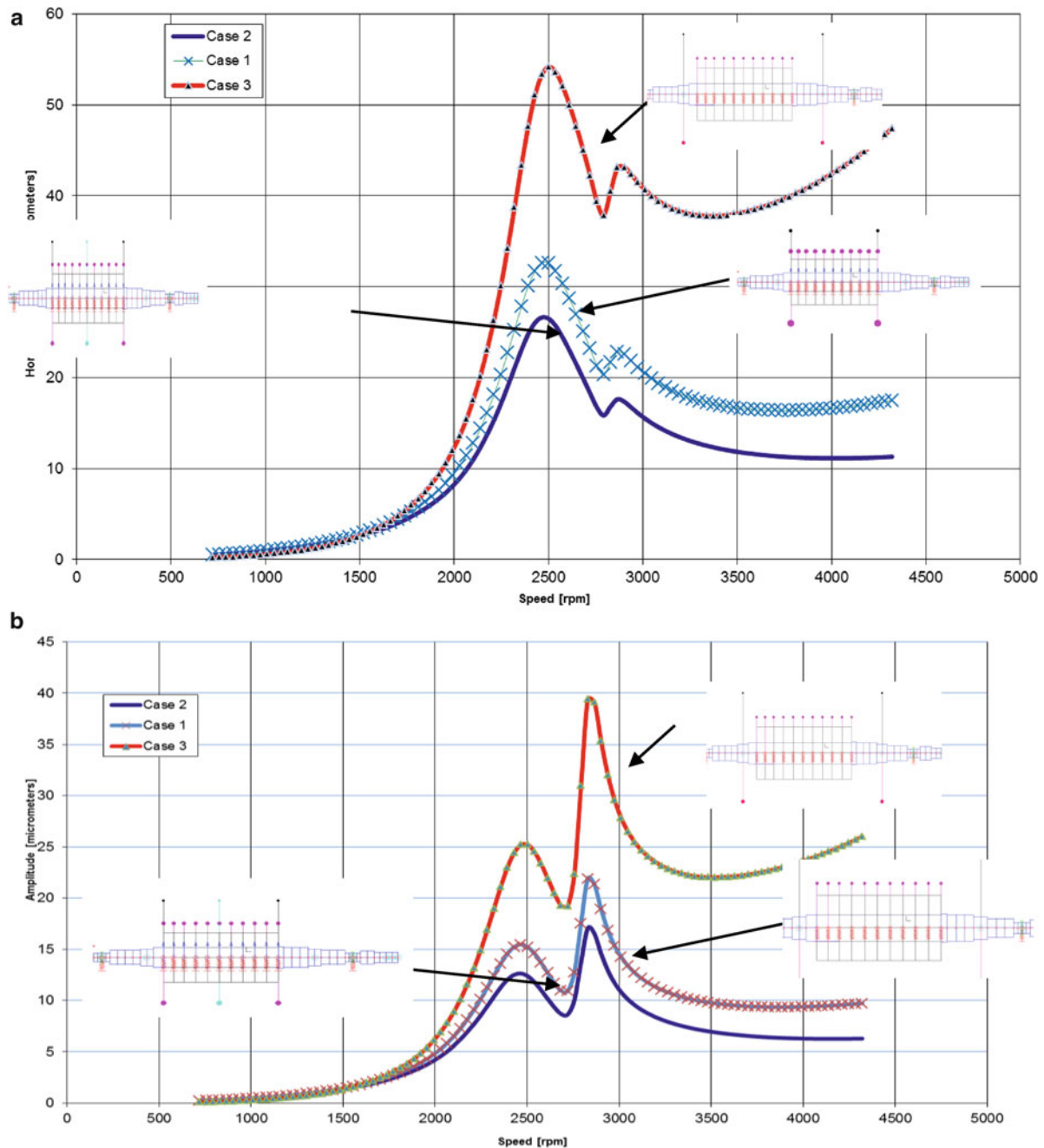
Fig. 3.9 (**a**) Horizontal direction unbalance response with different balancing planes locations, and, (**b**) vertical direction unbalance response with different balancing planes locations

It is important to note that the addition of a center balancing plane in the rotor could significantly impact the existing motor design as special manufacturing and balancing techniques are required. This is uncommon and not practical because a larger motor is required to accommodate the higher driven load requirement and the addition of a center plane requires the removal of any active magnetic material from the motor. Although three balancing plane offer more reduction in vibration amplitudes compared to Case I, the associated cost vs. performance should be considered when making a design decision.

Case (3): Balancing Plane on the Fan Away from the Rigid Section of the Rotor Core   For this example, two correction planes are located on either side of the rigid section of the core, much closer to the bearings, as shown in the Fig. 3.8c. These planes are very easy to access from assembly and manufacturing.

From the unbalance response shown in Fig. 3.9a, b, it is evident that shaft relative peak to peak vibration amplitude at the rated operating speed is 40 micrometers, or 1.5 mils, which is well above API 541 vibration limit of 1.2 mil for one time rotational speed vibration limit. When passing through the critical speed, vibration is 55 micrometers (or 2.3 mil), which is close to API criteria. It can therefore be deduced that although rotordynamic design meets the critical speed separation criteria, it does not meet low vibration criteria for operating speeds. Correction planes are located away from the location of initial unbalance; hence vibration increases due to internal bending caused by mechanical unbalance.

The parametric case studies presented here highlighted the fact that in order to determine the optimized balancing planes practical considerations of the rotor-motor design as well as the industrial standards both needs to be carefully considered. Although more balancing plane presents lower vibration scenarios, various other two plane balancing configurations may also be able to satisfy the balancing requirements in a cost-effective manner. For flexible rotors balancing at both critical speeds as well as operating speeds needs to be ensured.

3.4 Conclusions and Future Work

In induction motors, several kinds of excitations that cause lateral vibrations exist. In addition to mechanical excitations such as mechanical unbalance, electromagnetic forces between rotor and stator can influence the lateral vibrations of the rotor. The addition of a laminated copper cage not only adds mass, but also adds flexural stiffness to the rotor shaft. The addition of a laminated copper cage results in the rigid portion at the section of the shaft where the rotor core was shrunk. The deflection characteristics of the shaft changes with the addition of a magnetic core. Neglecting core stiffness can lead to significant errors in critical speed predictions during rotor dynamic analysis.

In addition to robust rotordynamic design, proper balancing techniques and low residual unbalance are keys to attaining low vibration in rotating machinery. It is possible to meet API vibration limits and statements of ISO 11342 for flexible rotor balancing with two balancing planes close to the location of initial unbalance, which is also the rigid section of interest. Although three balancing planes on the core show slight improvement in vibration amplitude, it is important to note that the addition of a center balancing plane in the rotor could significantly upgrade the motor as special manufacturing and balancing techniques are required which may not be practical. This is uncommon to see, however, because a larger motor is required to accommodate the higher driven load requirement and the addition of a center plane requires the removal of any active magnetic material from the motor. If balancing planes are located away from the location of initial unbalance, vibration increases due to internal bending caused by mechanical unbalance. The parametric case studies presented here highlighted the fact that in order to determine the optimized balancing planes practical considerations of the rotor-motor design as well as the industrial standards both needs to be carefully considered. Although more balancing plane presents lower vibration scenarios, various other two plane balancing configurations may also be able to satisfy the balancing requirements in a cost-effective manner. For flexible rotors balancing at both critical speeds as well as operating speeds needs to be ensured.

Considering all of this, cost vs. performance should be considered for making a design decision. Research and experiments are currently underway to formulate and solved constrained optimization problems with practical location and weight constraints on the balancing mass by using the influence coefficient method and modal balancing as shown in [10, 11].

References

1. API 684 (2005) API standard paragraphs – rotordynamic tutorial: lateral critical speeds, unbalance response, stability, train torsionals and rotor balancing, 2nd edn. American Petroleum Institute, Washington, DC
2. API 541 (1995) Form-wound squirrel cage induction motors–250 horsepower and larger, 4th edn. American Petroleum Institute, Washington, DC
3. ISO 11342 (1998) Mechanical vibration – methods and criteria for the mechanical balancing of flexible rotors. The International Organization for Standardization, Geneva
4. Hartog D (1956) Mechanical vibration, 4th edn. McGraw Hills, New York
5. Werner U, Binder A (2006) Rotor dynamic analysis of asynchronous machines including the finite-element-method of engineering low vibration motors. In: International symposium on power electronics, electrical drives, automation and motion SPEEDAM, Taormina, pp 20–28
6. Singhal S, Singh KV, Hyder A (2011) Effect of laminated core on rotor mode shape of large high speed induction motor. IEMDC, pp 1552–1556
7. Singhal S, Khonsari M (2005) A simplified thermohydrodynamic stability analysis of journal bearings. Proc Inst Mech Eng J J Eng Tribol 219(3):225

8. Singhal S, Mistry R (2009) Oil whirl rotordynamic instability phenomenon-diagnosis and cure in large induction motor. In: Petroleum and chemical industry conference, record of conference papers – industry applications society 56th annual, Anaheim, 14–16 Sept 2009, pp. 1–8
9. Eaton D, Rama J, Singhal S (2010) Magnetic bearing applications & economics. In: Petroleum and chemical industry conference (PCIC), record of conference papers industry applications society 57th annual, San Antonio, 20–22 Sept 2010, pp. 1–9
10. Friswell MI, Penny JE, Garvey SD (2010) Dynamics of rotating machines. Cambridge University Press, Cambridge
11. Prabhu BS, Sekhar AS (2008) Dynamic analysis of rotating systems and applications. Multi-Science Publication, Essex

Chapter 4
Experimental Acoustic Modal Analysis of an Automotive Cabin

G. Accardo, M. El-kafafy, B. Peeters, F. Bianciardi, D. Brandolisio, K. Janssens, and M. Martarelli

Abstract In the automotive industry, one of the most important comfort requirements in designing a high quality vehicle is to avoid or minimize the noise in the passenger compartment. Therefore, an ever increasing interest exists to predict the interior acoustic behavior by means of accurate simulation models both to improve the vehicle NVH performance and to reduce the development cycle for new products. Nevertheless, nowadays the level of accuracy of such models is not sufficient to replace the design prototype phase with an all-digital phase, so experimental methods in which an acoustic characterization is performed based on measurements play an important role in understanding the modelling challenges, improving the overall modelling know-how and, more in general, in comprehension of the physical behaviour.

By means of a case study on a fully trimmed sedan car, this paper discusses the acoustic modal analysis equipment requirements and testing procedure. Due to specific acoustic modal analysis challenges, such as the high modal damping ratios and the need to use a large number of sound sources spread around the cabin to get a sufficient excitation of the modes, the modal parameter estimation is often a non-trivial task. Here the modal parameters (i.e. resonance frequency, damping ratio, mode shape, and modal participation factor) will be estimated by the new ML-MM method, a multiple-input multiple-output frequency-domain maximum likelihood estimator based on a modal model formulation. The performance of the ML-MM method will be compared to more classical modal parameter estimation methods.

Keywords Acoustic modal analysis • Interior car sound • Sound source • Fully trimmed sedan car • Vibro-acoustics effect

4.1 Introduction

In the past few decades, the reduction of interior noise levels in automotive cabins has become a very active research area, mainly encouraged by the need for weight reduction and the current trend towards environmentally compatible hybrid-electric power train concepts. Moreover the interior sound quality of a car is one of the most important decision factors for customers when purchasing a new car. Therefore, the interior sound quality has to be carefully considered and controlled in the design process. To improve the interior noise performance, CAE predictions have gained importance, especially in the early development stage when it is still possible to make changes without negatively affecting the vehicle development

G. Accardo (✉) • B. Peeters • F. Bianciardi • K. Janssens
Siemens Industry Software NV, Interleuvenlaan 68, B-3001, Leuven, Belgium
e-mail: giampiero.accardo@siemens.com; bart.peeters@siemens.com; fabio.bianciardi@siemens.com; karl.janssens@siemens.com

M. El-kafafy
Siemens Industry Software NV, Interleuvenlaan 68, B-3001, Leuven, Belgium

Acoustic and Vibration Research Group, Vrije Universiteit Brussel, Pleinlaan 2 B, B-1050, Brussels, Belgium

Faculty of Engineering – Mattaria, Helwan University, Helwan, Egypt
e-mail: melkafaf@vub.ac.be

D. Brandolisio
Siemens Industry Software NV, Interleuvenlaan 68, B-3001, Leuven, Belgium

Department of Mechanical Engineering, KU Leuven, Kasteelpark Arenberg 41-3001, Leuven, Belgium
e-mail: daniele.brandolisio@kuleuven.be

M. Martarelli
Faculty of Engineering, Università degli Studi eCampus, Novedrate, CO, Italy
e-mail: milena.martarelli@uniecampus.it

time. An acoustic finite element (FE) model of a vehicle cavity is an important component of a structural-acoustic numerical model for interior noise simulation. This model can be used to fine-tune the structural and acoustic design of the cavity to achieve specific NVH objectives. It can also be used as a diagnostic tool to identify the potential noise sources and also to evaluate the effectiveness of the proposed design modifications. It is obvious that the effectiveness of this approach greatly depends on the accuracy of the predictions made using such a model. Hence in order to understand the modelling challenges and improve the overall modelling know-how of which the car will benefit in the development phase, the experimental acoustic characterization of the cabin plays a crucial role. When performing an interior acoustic study, it is important to relate the acoustic responses to the intrinsic system behaviour of cabin cavity. This can be done by means of Acoustic Modal Analysis [1, 2], i.e. modal parameter estimation methods decompose the system behaviour into a set of individual resonance phenomena, each characterized by a resonance frequency, damping ratio, participation factor and mode shape. The experimental data set to derive this model from consists of a set of Frequency Response Functions (FRFs) between a set of reference (i.e. acoustic source input) degrees of freedom and all response (i.e. microphone output) degrees of freedom [3].

Specific acoustic modal analysis challenges are the high modal damping ratios resulting in highly overlapping modes with complex mode shapes and the use of a large number of references distributed around the cabin to get a sufficiently homogenous sound field.

Due to all these features, traditional modal parameter estimation methods may prove less suited for such data. Thus, a method overcoming the difficulties that the classical methods face when fitting an FRF matrix consisting of many (i.e. four or more) columns is needed. Recently, Yoshimura et al. published different studies on the experimental challenges related to the application of Acoustic Modal Analysis to an automotive cabin. They also proposed a non-linear least squares (NLS) method that is able to process FRF data with many references [4, 5].

This paper focuses on the experimental modal analysis of an automotive cabin. Here modal parameters will be firstly estimated by the well-known LMS Polymax method [6], and secondly by the ML-MM estimator, where the error between the modal model equation and the measured FRF data is minimized in a maximum likelihood sense [7, 8].

The paper is organized as follows. In Sect. 4.2 a brief overview about the theoretical background on Acoustic Modal Analysis is described. Using a discretized formulation, one can see that an analogy exists between acoustic and mechanical systems. Thanks to this equivalence, the classical approach can be used also in the acoustic modal analysis case, if one uses the correct variables. In Sect. 4.3 the case study on a fully trimmed car is introduced. Test preparation, set-up and measurements are described in detail. In order to have an idea on the expected acoustic modes, a numerical model was created and used for a preliminary analysis. This model was instrumental to study the proper distribution of sources and to prepare the geometry of the microphones capturing pressure response inside the cavity. Measurement points, sources and their respective location will be presented.

After the validation of the measurement chain, Sect. 4.4 discussed the modal parameter estimation. Two different methods are used for this purpose: firstly LMS Polymax and secondly ML-MM. Furthermore, a study on the influence of the number of references is carried out with Polymax and described in this section. The results previously obtained by the two methods are compared in terms of curve fitting, mean error, values of the modal parameters and mode shapes. Finally, in Sect. 4.5 some concluding remarks are given.

4.2 Theory of Acoustic Modal Analysis

In this section, only a brief theoretical overview is given. Many references can be consulted for further details about the model formulations describing the dynamic behaviour of (vibro-) acoustic systems, such as [9, 10].

Here boundaries of the enclosure will be modeled as rigid walls, so the dynamic behaviour of a pure acoustic system will be recalled.

By considering a three-dimensional closed acoustic system with rigid or finite impedance but non-vibrating boundaries, the governing equation of the system, excited by a point monopole of volume velocity at r_0 can be written in the form [9]:

$$\nabla^2 p\left(r, t\right) - \frac{1}{c^2} \ddot{p}\left(r, t\right) = -\rho \dot{q} \delta\left(r - r_0\right) \tag{4.1}$$

where p is the sound pressure, which is a function of space r and time t; c is the speed of sound; ρ is the density of the medium; and q is the volume velocity. The boundary condition over the rigid surface S is

$$\frac{\partial p}{\partial n} = 0 \text{ over } S \tag{4.2}$$

where n is the internal unit normal to S.

The discretization of the continuous acoustic wave equation is based on the finite element formulation. The acoustic domain of volume V is represented by an assemblage of acoustic finite elements. The pressure distribution within an element is interpolated in terms of the nodal pressures by using shape functions. Variational formulation based on the differential Eq. (4.1), boundary condition (4.2) and FE discretization gives the M^f, C^f and K^f matrices. To preserve the analogy with a structural finite element model, the matrix M^f is called the acoustic mass matrix, although it represents a compressibility matrix, relating the pressure to a displacement; the matrix C^f is the acoustic damping matrix, induced by the impedance boundary condition; the matrix K^f is called the acoustic stiffness matrix, although it represents an inverse mass or mobility matrix, relating the pressure to an acceleration. Assuming now that a number of point monopoles of known volume velocity are placed in the cavity and the sound pressure across the volume is sampled at an appropriate number of points, it can be shown that the continuous wave equation can then be substituted by its discrete equivalent:

$$M^f \ddot{p} + C^f \dot{p} + K^f p = -\rho \dot{q} \tag{4.3}$$

It is noted that in the present formulation, one-way coupling between the structure and the interior acoustic domain is assumed. This approximation is acceptable for the cases where the acoustic loading on the structures is negligible, like in automotive NVH applications, where air is the medium [11]. It can be seen that the discrete governing equation above is equivalent to the discrete mechanical equations of motions, with M^f, C^f, K^f in the role of mass, damping, and stiffness matrices; p in the role of displacement; and $\dot{q}$ in the role of force.

Taking the Laplace-transform and assuming zero initial conditions we get:

$$\left[s^2 M^f + s C^f + K^f\right] \cdot p(s) = -\rho s q(s) \tag{4.4}$$

As usual in structural dynamics, the inverse of the matrix term can be substituted by the frequency response function $H(s)$:

$$p(s) = -\rho s H(s) \cdot q(s) \tag{4.5}$$

One can prove that the FRF-matrix can be expressed as a partial fraction expansion of modal parameters [12]:

$$H(s) = \sum_{r=1}^{N_m^f} \frac{Q_r \phi_r \phi_r^T}{s - \lambda_r} + \frac{Q_r^* \phi_r^* \phi_r^{*T}}{s - \lambda_r^*} \tag{4.6}$$

where N_m^f are the number of modes, ϕ_r the r-th modal vector, Q_r the modal scaling factor for the r-th mode, and λ_r the system pole for the r-th mode. Substituting now s by $j\omega$ and using Eq. (4.5) it is obvious that the modal parameters of the system can be gained from the FRF measurements where the sound pressures across the volume are referenced to the volume velocities of the sources. The expressions (4.4), (4.5), and (4.6) are in complete analogy with those being used in structural dynamics, therefore, it can be concluded that the classical modal parameter estimation approach can be followed also in the acoustic modal analysis case.

An interesting expansion towards coupled vibro-acoustic modal analysis is provided in [13].

4.3 Acoustic Modal Analysis Test Campaign

In this section, before describing the test campaign carried out to extract the acoustic modes of the cavity of a fully trimmed sedan car (Fig. 4.1) and extracting the modal parameters, a preliminary analysis with a Finite Element (FE) model is presented. Such a model will be used as a baseline to know the number and shapes of the acoustic modes of the system. The selected car for this case study is property of Siemens Industry Software and often used for NVH research purposes.

The description of the measurements will focus on the experimental set-up, its validation and the followed experimental procedure.

4.3.1 Preliminary Analysis

An acoustic FE model of the interior car cavity with rigid boundaries (Fig. 4.2) was created in LMS Virtual.Lab Acoustics, in order to know preliminarily the mode shapes and the number of acoustic modes expected in the frequency range of interest,

Fig. 4.1 Fully trimmed car used
in the case study
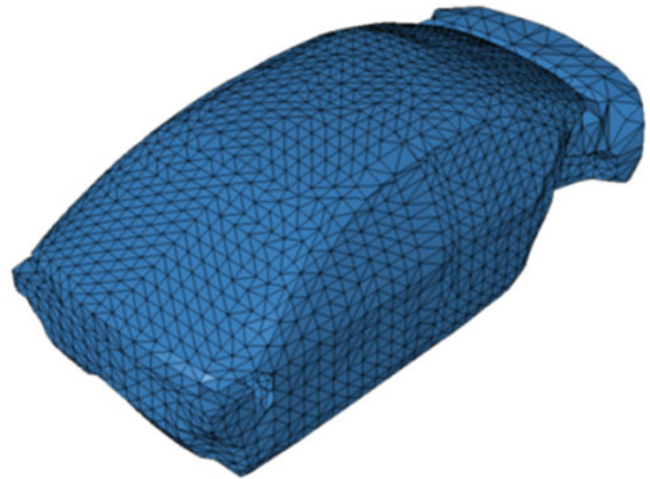

Fig. 4.2 CAE cavity model

Fig. 4.3 Cavity cross-section
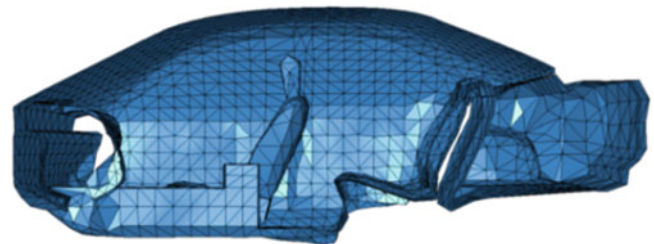
0–200 Hz. The internal cavity was modeled with more than 65,000 solid tetrahedral elements and more than 130,000 degrees of freedom. As visible in Figs. 4.2 and 4.3, the model includes also the geometry of the seats and the trunk compartment. Even though the rigid-walled assumption is not realistic due to the fact that the actual cabin consists of a number of flexible panels and surfaces with sound adsorbing material, the rigid-walled acoustic modes still provide a benchmarking for investigating the acoustic modal difference due to the structure-acoustic interaction [14]. Suitable physical characteristics of the air are defined for the fluid elements.

Hence under the assumption of rigid boundaries, the real eigensolution analysis shows that there are 10 uncoupled eigenmodes in the frequency range of interest (Table 4.1 and Fig. 4.4):

Let us highlight that the above model does not take into account any trim materials and any flexible boundary walls, so the eigenmodes from this rough model are not expected to be very close to the real ones. Nevertheless, at this first stage, this model is extremely useful to have an idea on the number of the modes and on their shape. Furthermore, information from the numerical model about the mode shapes are fundamental: (i) to know where to locate properly the sources in order to avoid nodal lines; (ii) to have a preliminary geometry of the measurement points; (iii) to select meaningful modes and address the dominant acoustic modes in such a coupled system where the FRFs are also influenced by the resonance of the structural system which has a rather higher modal density than the acoustic one [5, 15]. No FE model updating process will be performed on this model in the current paper, referring to possible future works for this purpose.

Table 4.1 CAE eigenfrequencies

#	Frequency [Hz]	Mode shape
1	≈0	Rigid body
2	44.53	I longitudinal
3	85.81	I longitudinal & rigid body trunk
4	112.42	I lateral
5	128.42	II longitudinal & rigid body trunk
6	141.06	I longitudinal & I lateral
7	150.20	I longitudinal & I lateral & I lateral trunk
8	155.57	I vertical
9	178.03	II longitudinal & I lateral & I lateral trunk
10	181.97	
11	201.20	I lateral & I vertical & I lateral trunk
12	205.98	III longitudinal

Fig. 4.4 CAE mode shapes – amplitude and phase
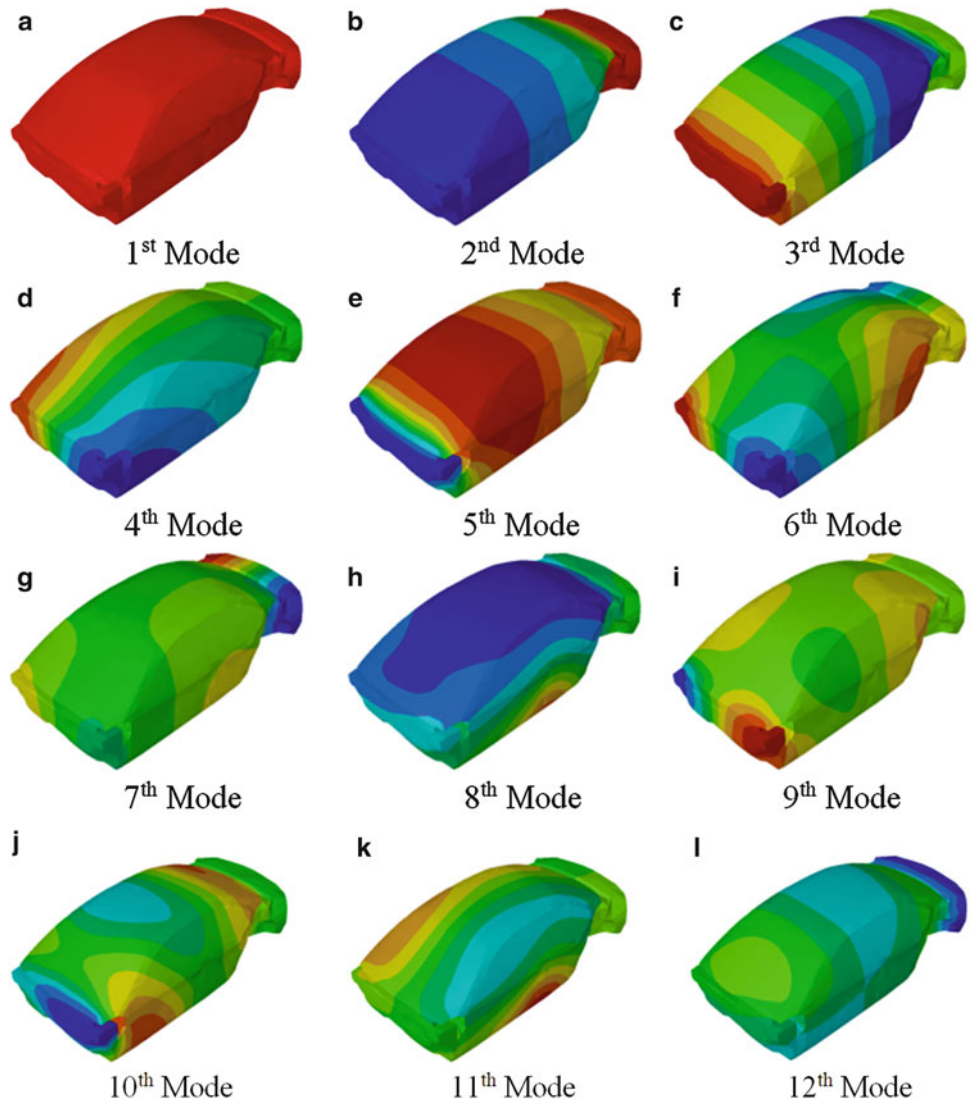
4.3.2 Experimental Set-Up

Multiple acoustic excitation tests were carried out inside the cavity of the sedan car already shown in Fig. 4.1. Thirty-four microphones located both on a roving array with spacing equal to around 20 cm and near to boundary surfaces captured the responses simultaneously. A total of 18 runs were performed to measure the pressure distribution over the entire cavity
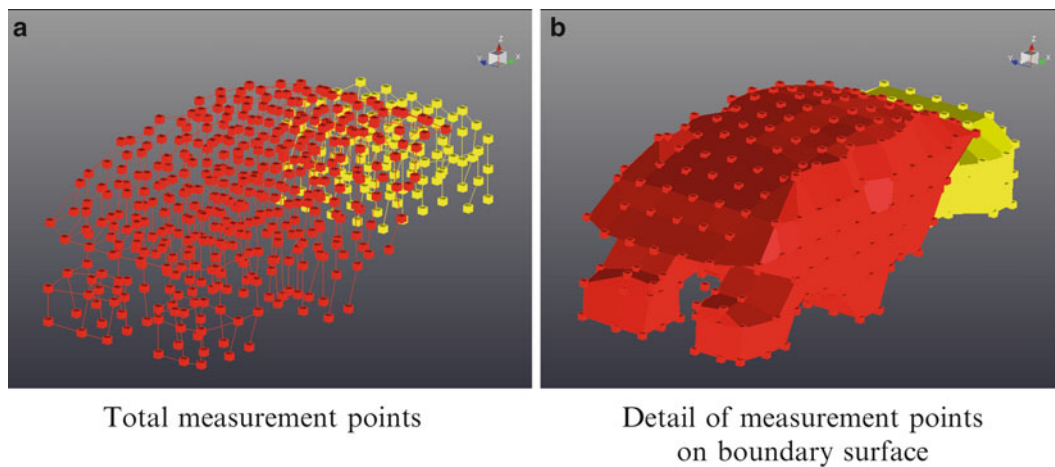
Fig. 4.5 Measurement points
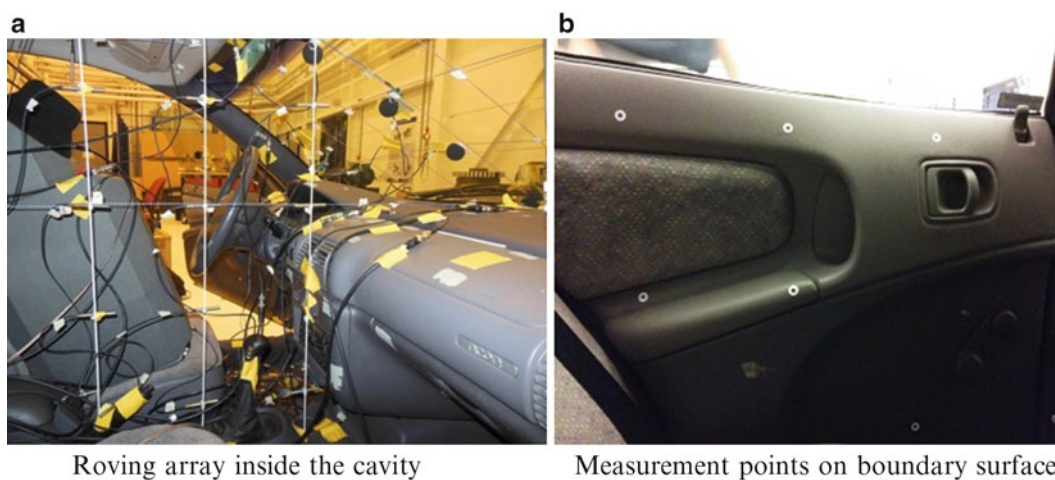
Fig. 4.6 Roving arrays

(both cabin and trunk). For each run, up to 12 loudspeakers switched on sequentially were used for acoustic excitation. A sequential excitation was preferred to a simultaneous excitation mainly to minimize the correlation between the inputs, and also the number of averages (hence time) to have good values of signal-to-noise-ratio [16].

In this section, a detailed description of the set-up used in the test campaign is given.

4.3.2.1 Measurement Points

The accurate description of the acoustic modes can be achieved by placing roving arrays of microphones at as different locations as possible in the vehicle, in order to increase the observability of the modes and to have more degrees of freedom to be used for the correlation and updating of the FE numerical model.[1] The pressure responses were measured both at the boundary surface and inside the cavity by positioning the microphones approximately every 20 cm (Figs. 4.5 and 4.6). The mesh of measurement points was preliminarily defined by means of the CAE model. Afterwards, the coordinates were updated to reflect the actual test scenario. Sensors were placed also in extreme positions, such as in foot regions, between the windshield and the dashboard, and in the hat shelf region, making a total of 526 measurement points. The same spacing and approach were followed for the trunk as well.

---

[1]A reasonable accuracy of the geometrical coordinates of the sensor locations is also need for the FE correlation and updating.

Fig. 4.7 Reference distribution

a

Side view

b

Front view

c

Back

d

Top view

Fig. 4.8 LMS Qsources

a

Miniature Volume Source (Q-IND)

b

Low Mid Frequency Source (Q-LMF)

Twelve further microphones located 2 cm away from the acoustic sources were kept fixed to check the repeatability of the measurements. Additionally, four uni-axial accelerometers were placed on the structure at fixed locations again in order to check the repeatability and also to analyze vibro-acoustic coupling effects.

4.3.2.2 Sources
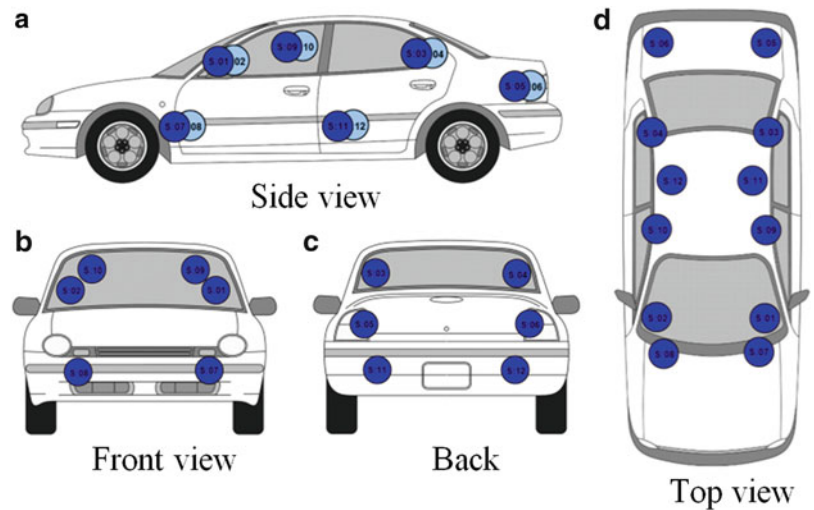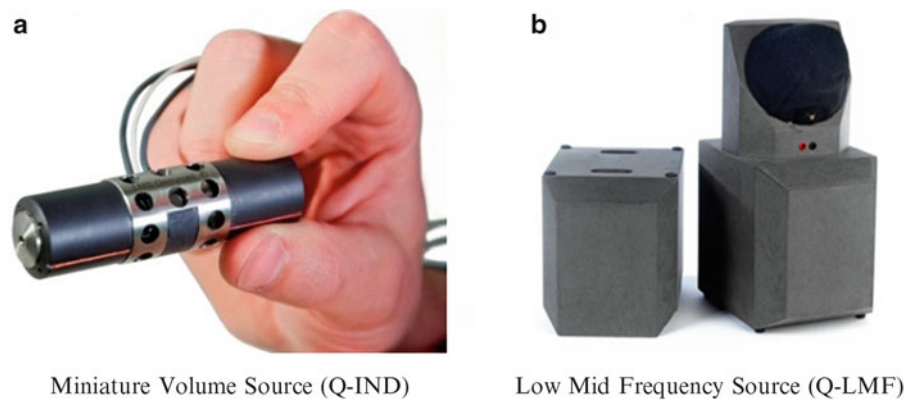
Calibrated volume acceleration sound sources are necessary to measure acoustic FRFs that are required in Acoustic Modal Analysis. Sound sources have to be omnidirectional and have a negligible size in order not to influence the field, above all in the higher frequency ranges [17]. As showed numerically in [3] and experimentally in [4, 5], an appropriate source distribution over the entire cavity is required to excite properly the acoustic modes. Indeed few sources do not allow the right identification of the mode shapes: distortions in the neighbourhood of the excitation point are strongly observed.

For this reason, a rather large amount of sources were used to excite as many modes as possible: up to 12 volume velocity sources were set in geometrically symmetric locations, close to the edges, corners and at the maximum amplitude locations to avoid nodal lines and excite close to pressure maxima on the boundaries. Locations of the mentioned excitation points are shown in Fig. 4.7.

Two different kinds of LMS Qsources (Fig. 4.8) were available: LMS Qsources Miniature Sources (Q-IND) and LMS Qsources Low-Mid Frequency Source (Q-LMF). The Q-LMF sources have the advantage to provide high noise levels of excitation (extremely high coherence) in low frequency range, but, on the other hand, they have the disadvantage to have a non-negligible size, as shown in Fig. 4.9. Nevertheless, the choice of using such sources was driven to the requirement of better exciting the lower frequency range. An analysis on the influence of these sources is reported below.

The **LMS Q-IND** sources have been developed to acquire acoustic and vibro-acoustic FRFs at low and mid frequencies in an accurate way without disturbing the acoustic behaviour of the passenger cavity. Due to its miniature size, such a source has no body diffraction and emits the noise as a monopole source in the frequency range between 50 and 5,000 Hz. As shown
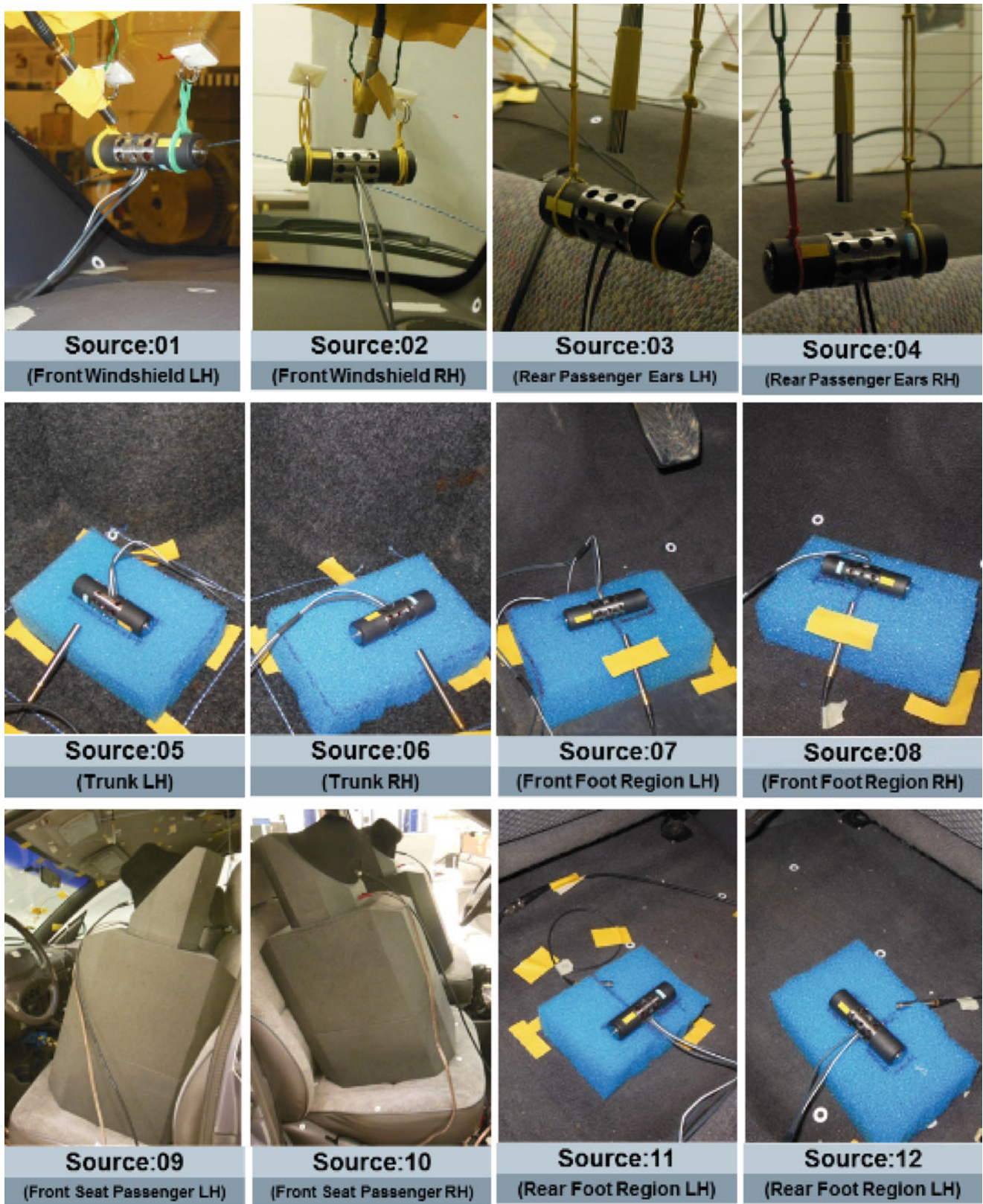
Fig. 4.9 Source locations

Fig. 4.10 Q-IND: directivity of the sound source

Directivity plot
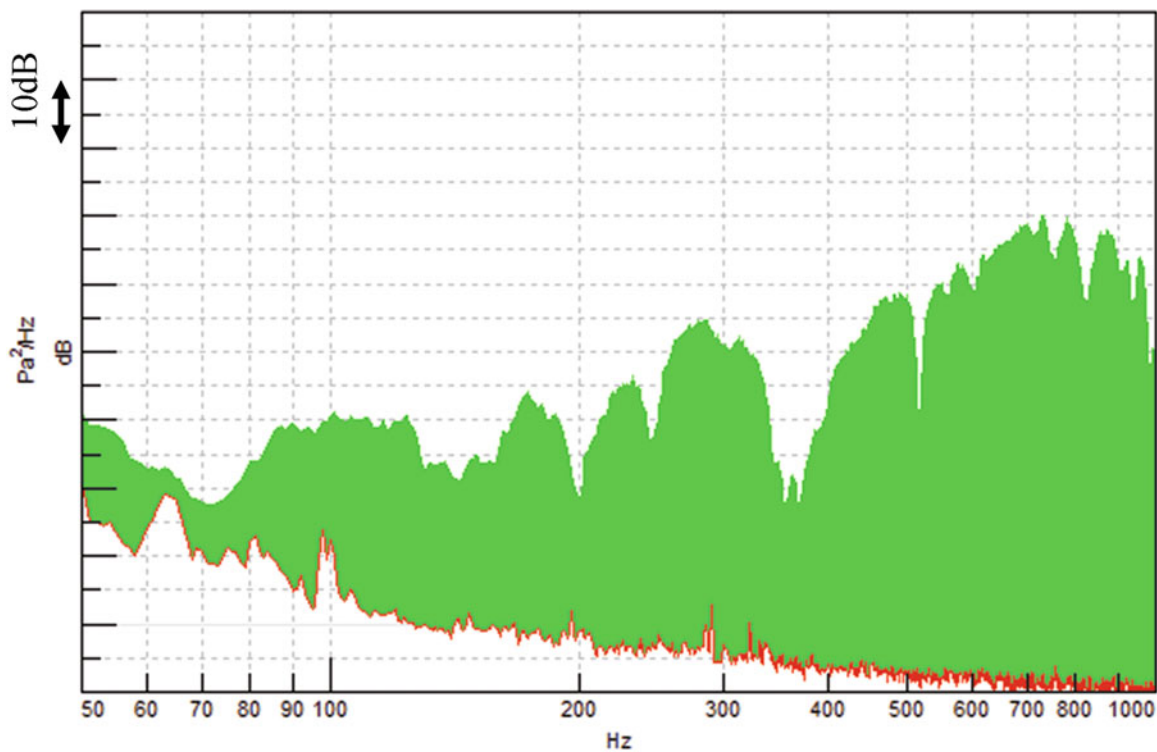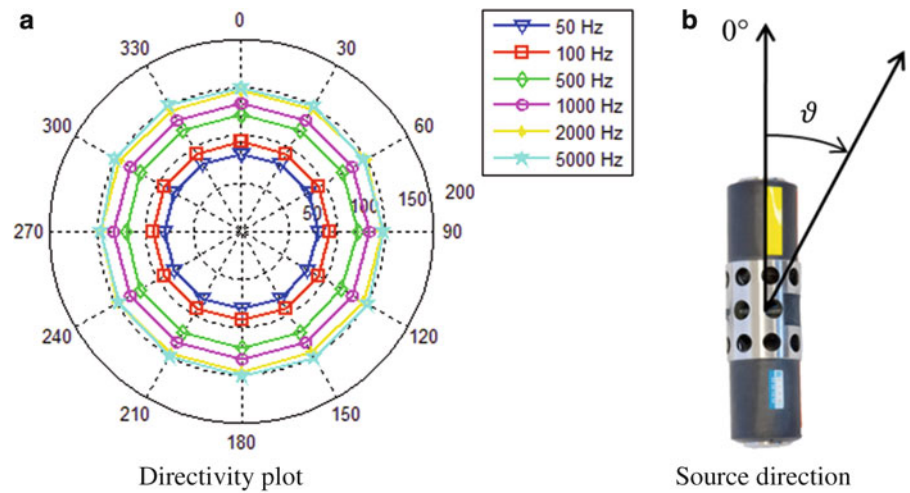
Source direction

Fig. 4.11 Q-IND: noise level versus background noise

in the directivity plot[2] in Fig. 4.10, the emitted sound does not attenuate along different directions up to several kHz; hence the source can be properly used as a monopole. The source incorporates electro-dynamic actuators and an internal sound source strength sensor. It outputs a volume displacement signal.

Figure 4.11 shows a comparison between a microphone response in the trunk when the source is active and when the source is switched off. Above 50 Hz, the artificial noise generation results in a response that is up to 50 dB higher, at certain frequency lines, guaranteeing a sufficient signal to noise ratio necessary for an accurate FRF measurement.

---

[2]The directivity plot is based on FRF in 1/3 octaves by using white noise as excitation signal. The distance from the sound-source to the recording microphone was 50 cm in semi free-field condition. The measurements have been carried out in semi-anechoic test laboratories at the LMS Engineering Services facilities in Belgium.
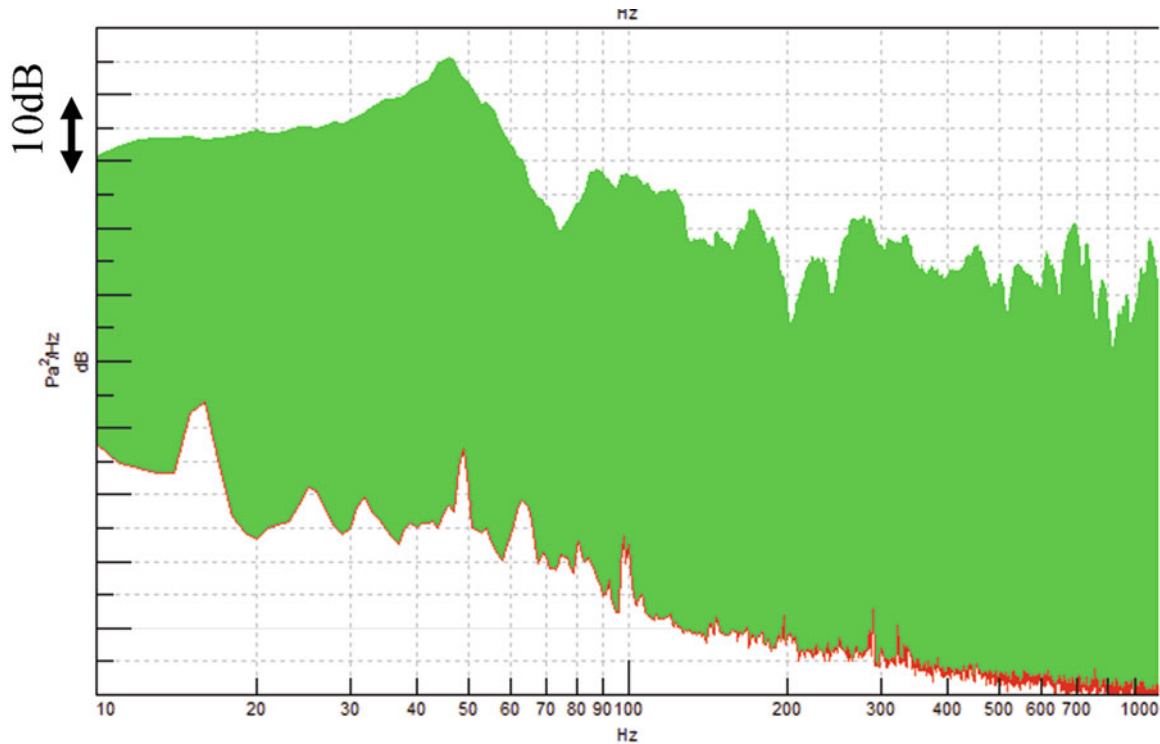
Fig. 4.12 Q-LMF: noise level versus background noise

The **LMS Q-LMF** sources are designed to be used in the frequency range between 10 and 1,000 Hz covering an important frequency band in vehicle development. Because most applications are for seat positions, these devices are optimized for quick positioning on a seat with the acoustic center at ear location (compliant with ISO5128). The unique properties of this low/mid-frequency source include compact, human body diffraction simulation, omnidirectional, time-stable sensitivity and high noise levels compared to measured background noise, as visible in Fig. 4.12.

Coster et al., in [18], reported that the effect of the source body diffractions and source directivity are negligible up to 100 Hz in free-field condition. As visible in Fig. 4.13, the presence of these sources inside the cavity influences the acoustic field from 80 Hz onwards.

So it's worth to underline that the FRFs will be partially affected by the presence of the Q-LMF sources. For this reason, Q-LMF have been kept fixed on the front seats during the whole test campaign in order not to introduce measurement data inconsistencies by varying volume distortions. However, a numerical simulation taking into account the sources located as in the real scenario (Figs. 4.14 and 4.15), has shown that the eigenfrequencies are only slightly shifted in the frequency range of interest. Comparing the eigenfrequencies in Table 4.2, one can observe that the maximum relative error between the values of the two models is always less than 3 % for the first eight modes. Furthermore, the MAC values in Fig. 4.16 are really near to 1, hence the mode shape distortion is still reasonable, for the first eight modes. Let's note, from Table 4.2 and Fig. 4.16, that only the 9th and 10th modes are mainly influenced by the presence of the Q-LMF sources: their order seems to be switched.

Hence error on the measurements due to the presence of such bigger sources can be considered rather limited.

Further details about source performances will be shown in the next section.

4.3.3 Set-Up Validation

4.3.3.1 Excitation Signal Level

The quality of modal analysis relies critically on the quality of the measured FRFs. So assessment on the quality of experimental data becomes essential. Hence, before starting the actual testing, a first set of measurements was performed to validate requirements such as efficiency of the inputs, reciprocity, repeatability and linearity.
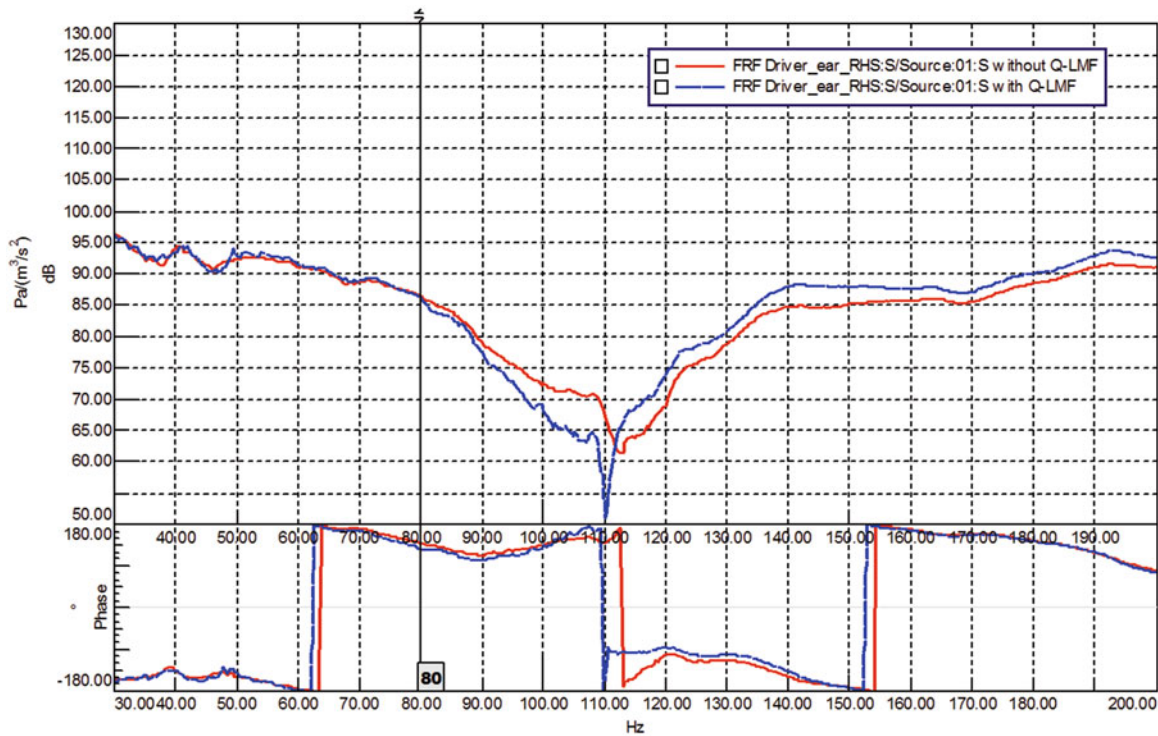
Fig. 4.13 Volume distortion due to the presence of Q-LMF sources

Continuous random white noise was chosen as excitation signal. The H1 estimator was used to compute the FRFs based on 150 averages.

Typical input autopower spectra expressed in volume acceleration are shown in Fig. 4.17. One can observe that an acceptable level of energy goes into the system over the frequency band of interest.

4.3.3.2 FRFs Reciprocity

Because of the symmetry, the FRF matrix, which is mathematically the inverse of the dynamic stiffness matrix, will also be symmetric. Hence FRF data from a measurement should be identical if we exchange the locations of input and output. Theoretically, this property can be traced back to the symmetry of mass, stiffness and damping. Reciprocity was checked in order to assess the reliability and accuracy of the measured FRFs. Figure 4.18 shows an example of reciprocity check: one can see that the amplitude and phase are nearly the same for both cross frequency response functions over the whole frequency range of interest.

4.3.3.3 Repeatability

Since during the test procedure doors and trunk were opened several times, the repeatability of the measurements was constantly monitored throughout the entire test campaign. This was mainly to ensure that the dynamic behaviour of the system and the whole measurement set-up system were time-invariant [19, 20]: certain FRFs were measured for each run, just to check the that neither the system nor the test set-up have experienced any significant changes. Figure 4.19 shows that the dynamic behaviour of the system was constant and that the testing conditions were kept unaltered throughout the measurement.

Fig. 4.14 Model with Q-LMF sources – CAE mode shapes (amplitude and phase)
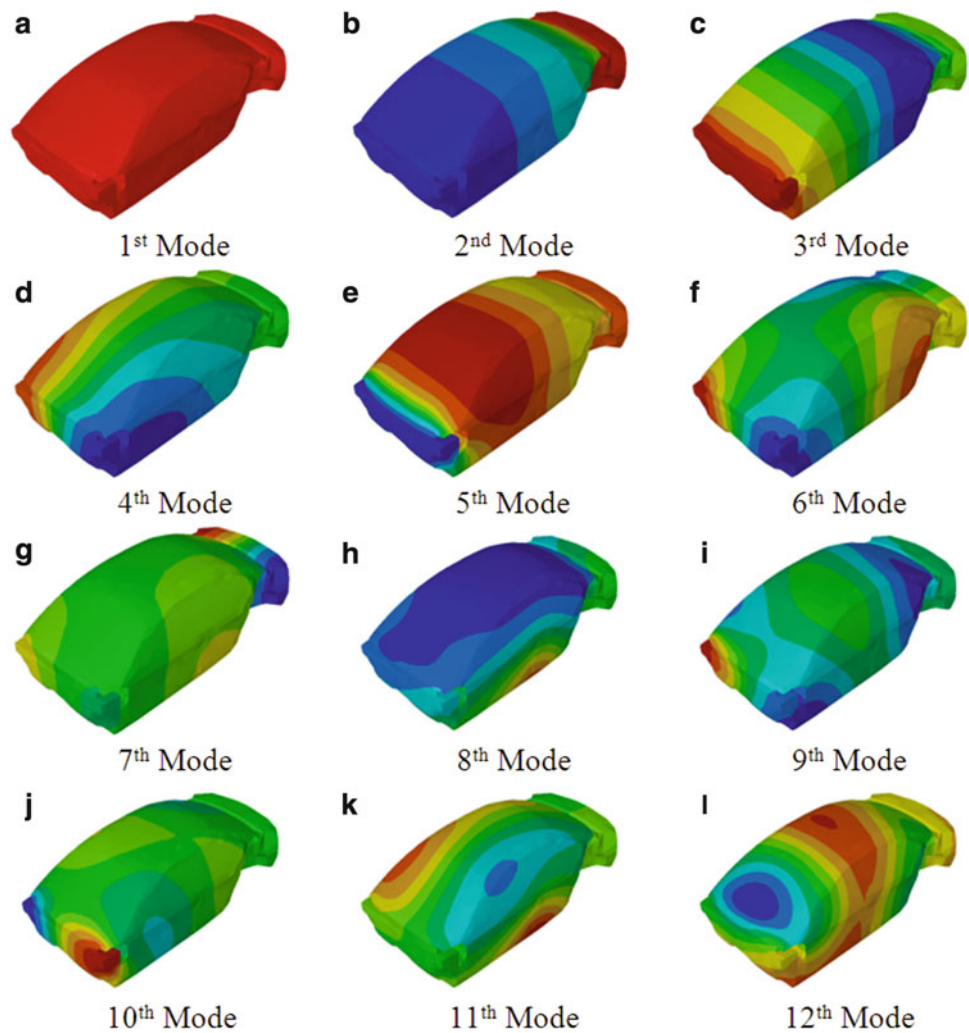
Fig. 4.15 Cavity cross-section and Q-LMF location
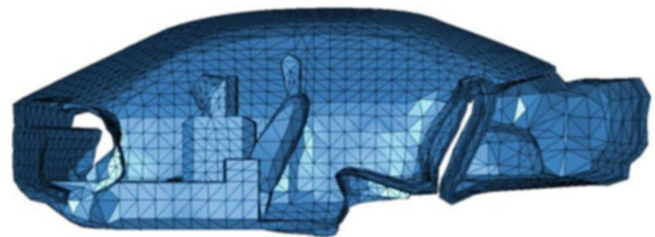
4.3.3.4 Linearity

As a last check, the linearity of the system was tested: measuring the FRFs at difference force levels can partly check non-linearity. Indeed if the system is linear, FRFs are independent of excitation amplitudes. As visible in Fig. 4.20, the FRFs from the same location measured with different excitation levels show the uniformity of the curve and the linear behaviour of the system.

The validation of the entire measurement chain has proven the good quality of the measurement method being used. By checking the auto-powers of the inputs, the cross frequency responses (reciprocity), the consistencies of the data throughout the measurements (repeatability) and the system responses for different input levels (linearity), the proper excitation of the system, the reliability of the inputs, and the assumption of time-invariant linear system are guaranteed.

Table 4.2 CAE model without Q-LMF vs. CAE model with Q-LMF

#	CAE model without Q-LMFs		CAE model with Q-LMFs	
	Frequency [Hz]	Mode shape	Frequency [Hz]	Mode shape
1	≈ 0	Rigid body	≈ 0	Rigid body
2	44.53	I longitudinal	44.72	I longitudinal
3	85.81	I longitudinal & rigid body trunk	84.19	I longitudinal & rigid body trunk
4	112.42	I lateral	109.42	I lateral
5	128.42	II longitudinal & rigid body trunk	130.10	II longitudinal & rigid body trunk
6	141.06	I longitudinal & I lateral	140.07	I longitudinal & I lateral
7	150.20	I longitudinal & I lateral & I lateral trunk	149.98	I longitudinal & I lateral & I lateral trunk
8	155.57	I vertical	153.53	I vertical
9	178.03	II longitudinal & I lateral & I lateral trunk	177.37	
10	181.97		178.80	II longitudinal & I lateral & I lateral trunk
11	201.20	I lateral & I vertical & I lateral trunk	199.71	I lateral & I vertical & I lateral trunk
12	205.98	III longitudinal	204.00	III longitudinal

Fig. 4.16 CAE model without Q-LMF vs. CAE model with Q-LMF – MAC matrix
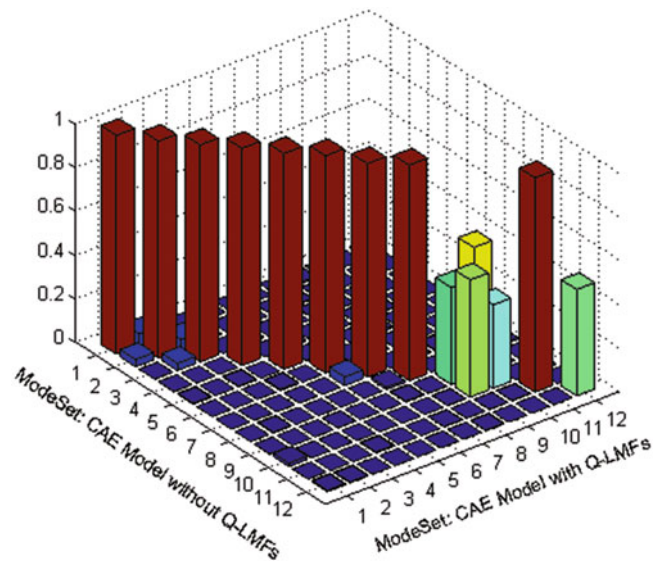
4.4 Experimental Modal Analysis

In this section the modal parameters of the cavity are firstly estimated by LMS Polymax. A study on the influence of the number of references is performed and the main challenges of analyzing acoustic modal analysis measurement data are presented.

Secondly the new frequency-domain maximum likelihood estimator based on a modal model formulation (ML-MM) is applied to the case with 12 references and the modal parameters are compared with those estimated by the previous method.

4.4.1 Results with Polymax and Influence of Number of References

An important issue to be addressed when processing acoustic modal analysis data is the identification of pre-dominantly acoustic modes in FRFs with a rather high modal density. Even if purely acoustic FRFs have been measured, the modal density is high since the acoustic cavity is coupled to a flexible body and also the resonances of the structural system (mainly panel vibrations from the windshield, the roof, . . .) show up in the microphone measurements. So, as already observed in [4], among the several coupled natural frequencies, the number of effective acoustic eigenvalues must be narrowed down to a level that is around the number of uncoupled acoustic eigenvalues computed analytically or numerically. For this purpose the data acquired by accelerometers placed on strategic positions (windshield, roof, trunk, side windows, . . .) can help to
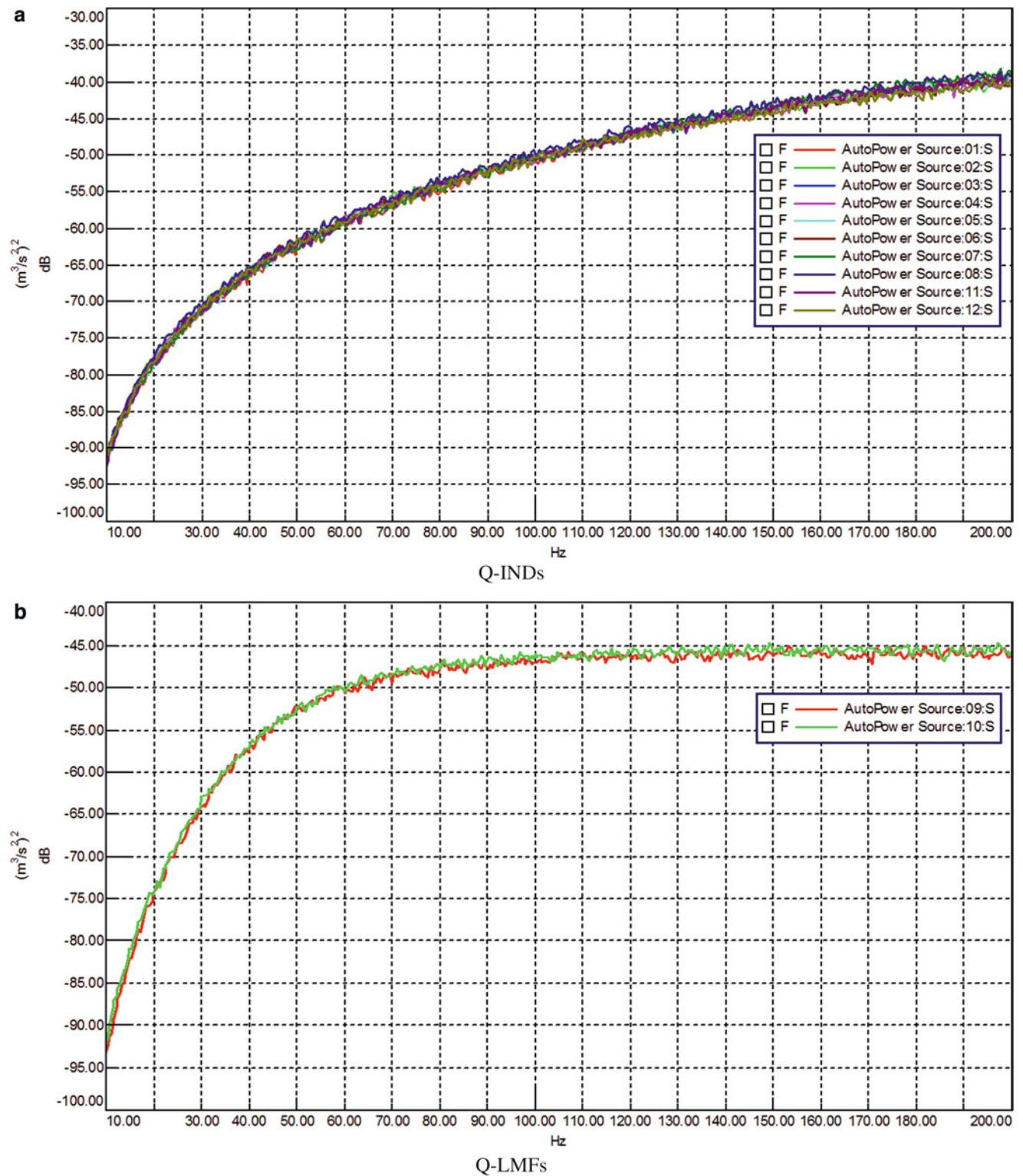
Fig. 4.17 Autopower spectra with continuous random white noise excitation

distinguish the dominant acoustic modes: analyzing the structural driving points FRFs, the main peaks in these FRFs can be considered to be structural modes. If these frequencies are also revealed in the acoustic FRFs, then they can be assumed as not purely acoustic. Moreover, the high damping of the cavity involves lower and wider peaks in FRFs resulting in highly overlapping modes. Finally, possible data inconsistencies, due to the fact that the different runs were performed in different
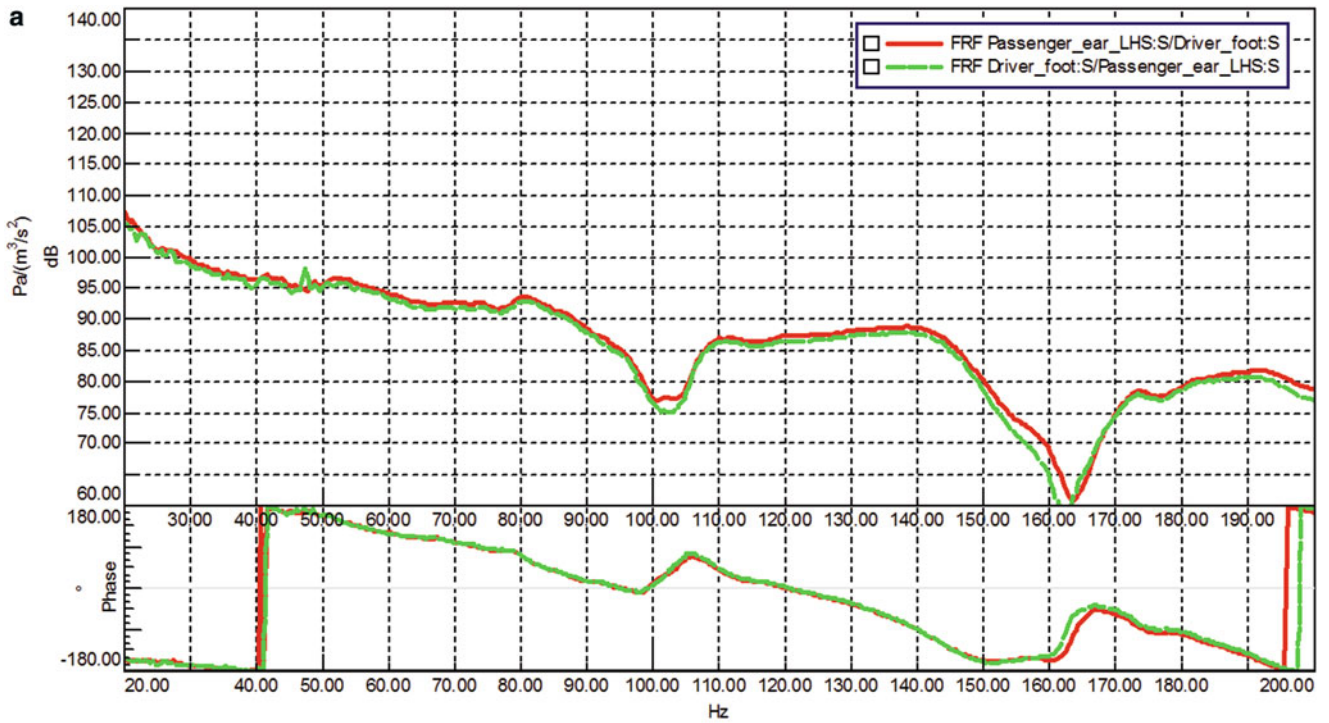
Passenger_ear_LHS – Driver_foot reciprocity
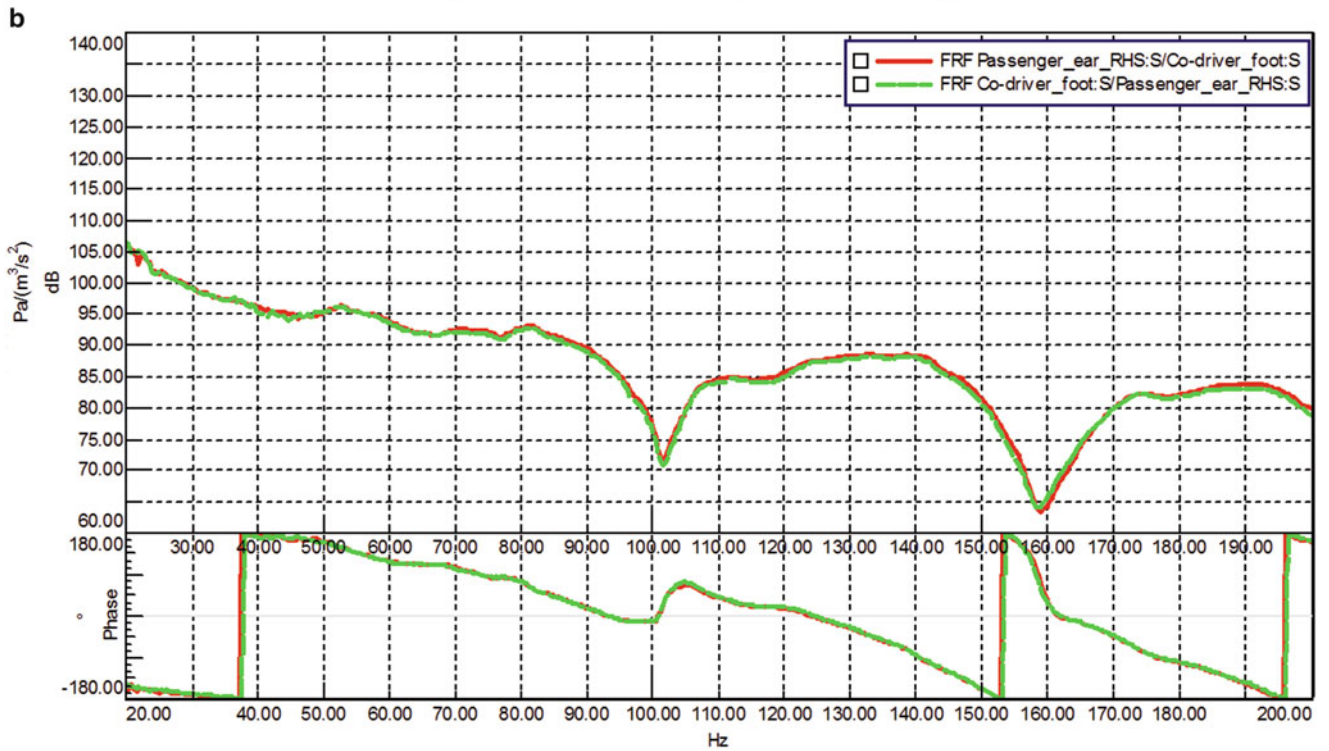
Passenger_ear_RHS – Co-driver_foot reciprocity

Fig. 4.18 Reciprocity check
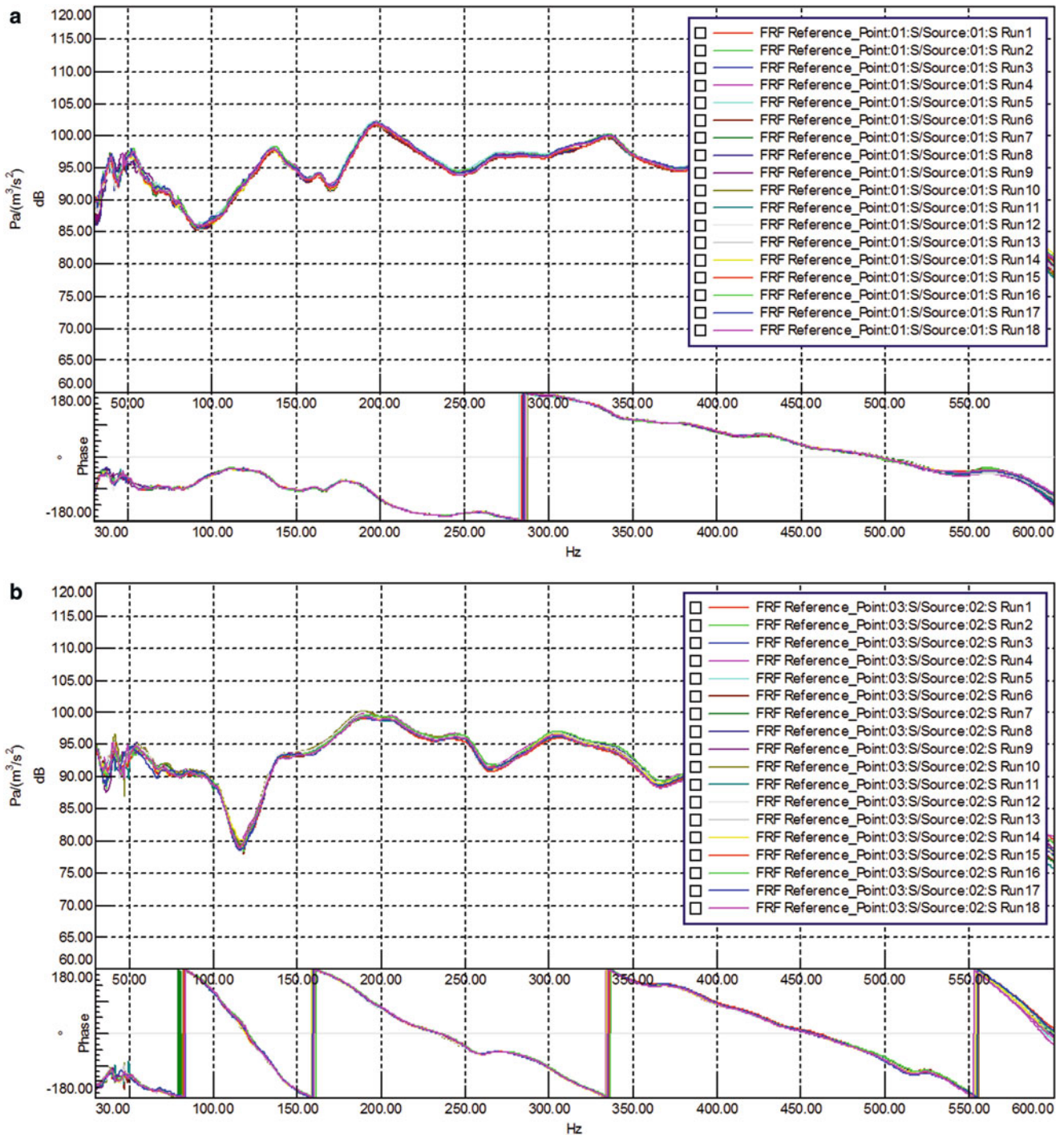
Fig. 4.19 Examples of repeatability check

days, can cause resonance frequencies to vary within the test database and when analyzed altogether, can cause a rather unclear stabilization chart, and hence a non-trivial selection of the right stable pole – or more precise, the right stable pole does not exist as such, there are multiple stable poles identifying the same mode.

As already said, a further difficulty to identify acoustic mode shapes is also due to the shortage of speakers to excite all the dominant modes [5]. Hence different cases, with 6, 10 and 12 references (Fig. 4.21), are analyzed in order to study the influence of number of references on the proper excitation of the acoustic modes.
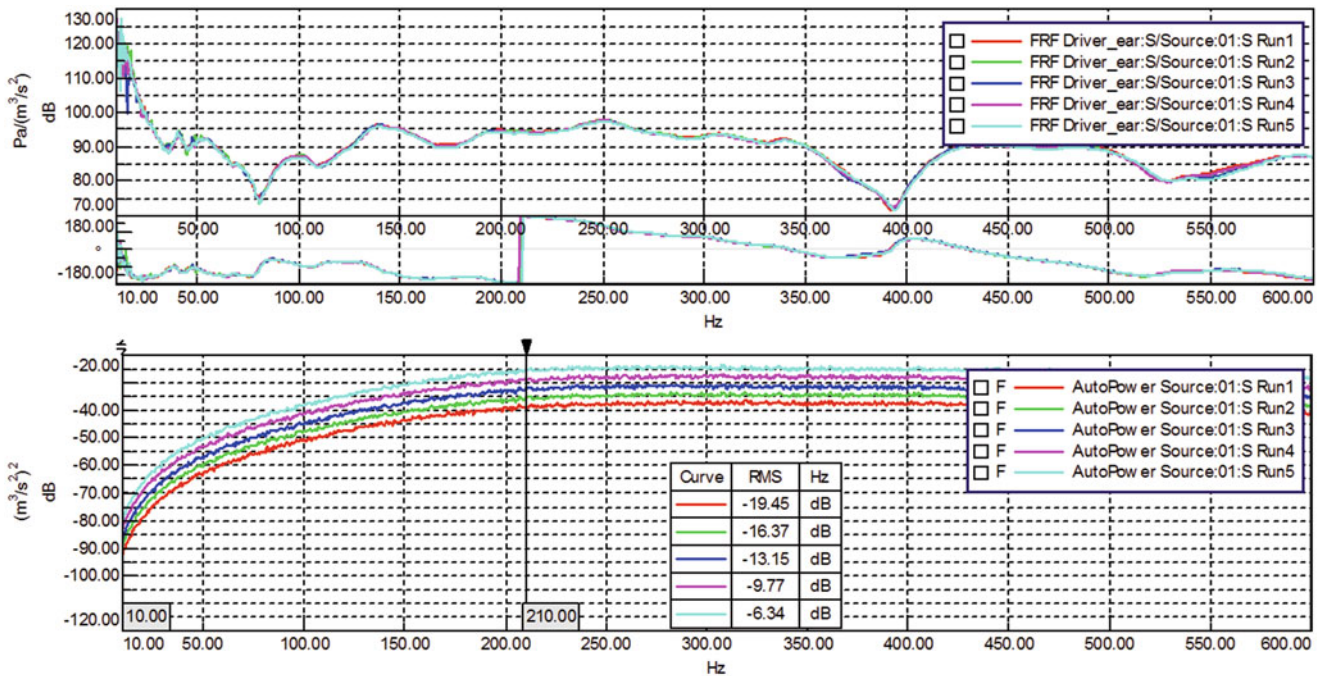
Fig. 4.20 Linearity check
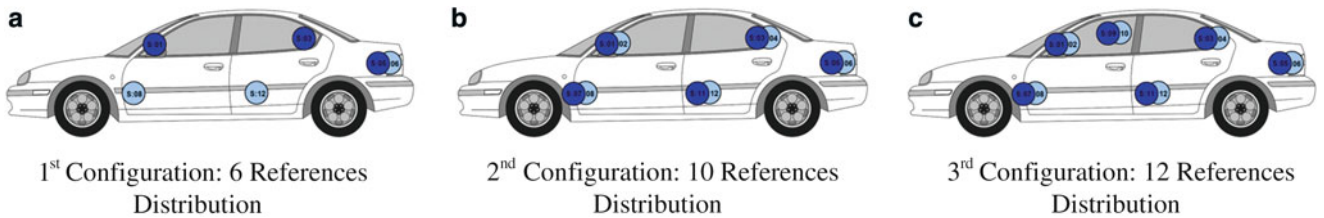
Fig. 4.21 References layouts

Whereas the Q-LMF sources are able to excite well the low frequency range, resulting in a really high coherence from 15 Hz onwards (Fig. 4.22b), the Q-IND sources can emit a strong signal only from 50 Hz onwards. The coherence is indeed rather low up to 30 Hz (Fig. 4.22a). Hence modal parameters are extracted in the frequency range from 40 to 200 Hz, excluding the acoustic rigid body mode (1st Mode) around 12 Hz.

Modal parameters are extracted using a total of $526 \times N_i$ (with N_i the number of references in each configuration) FRFs simultaneously. Nine pure acoustic modes are well identified in this frequency range with 12 references (Fig. 4.23). Most of the expected modes are extracted in the 3rd configuration, whereas 1 mode is not extracted in the 1st configuration. A global improvement of the mode shapes is observed when increasing the number of references: the nodal lines become clearer and mode shapes gain more symmetry. On average, one can see that out of diagonal elements of AutoMAC matrix get lower when increasing the amount of references, as a result of a less correlation with themselves. Figures 4.24 and 4.25 show an example of this general trend. In Table 4.3, the results obtained for each configuration are summarized. Let's observe that all the modes below 140 Hz are always successfully identified, whereas an increasing number of references is needed to better extract the pure acoustic modes in higher frequencies. Finally, one can observe that three adjacent modes around 150 Hz are well extracted in the last two configurations. Nevertheless, their order is a bit different in the two cases (Fig. 4.26).

As experienced before, it was quite challenging for classical modal parameter estimation methods to curve-fit an FRF matrix with so many columns (12 references) (Fig. 4.27). The mean fitting error was around 9 % for the 3rd configuration, so modal data could be affected by a non-negligible error. Therefore, a new iterative frequency-domain solver that has the potential to overcome the difficulties with many references was also used and briefly illustrated in the next section.

Q-IND (Source:01)

Q-LMF (Source:09)
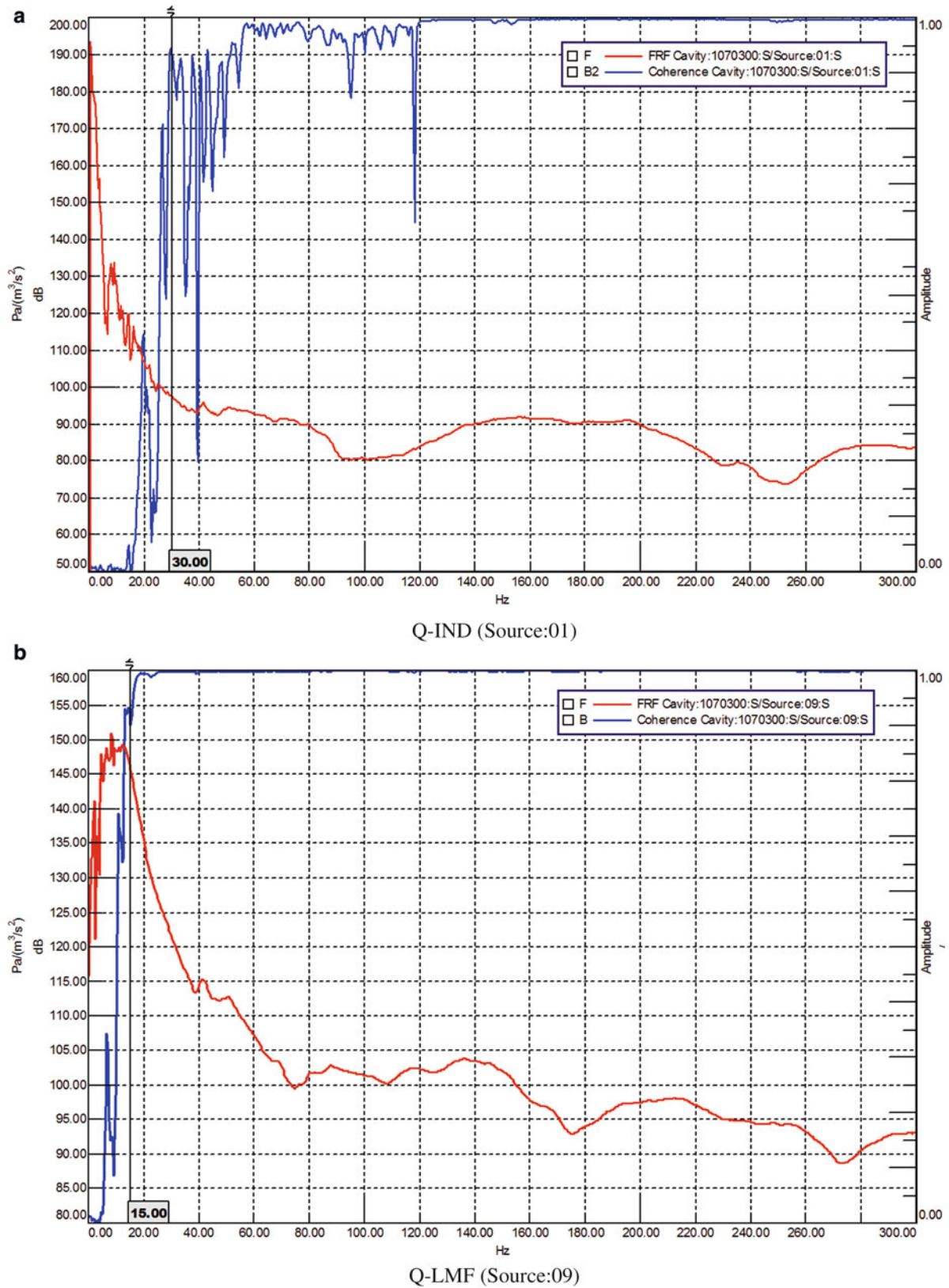
Fig. 4.22 Some coherence examples

a 2nd Mode (52.54 Hz, 14.46%)

b 3rd Mode (78.12 Hz, 12.46%)

c 4th Mode (96.08 Hz, 9.22%)

d 5th Mode (138.04 Hz, 6.31%)

e 6th Mode (145.74 Hz, 4.72%)

f 7th Mode (148.37 Hz, 9.24%)

g 8th Mode (149.97 Hz, 4.72%)

h 9th Mode (194.22 Hz, 7.82%)

i
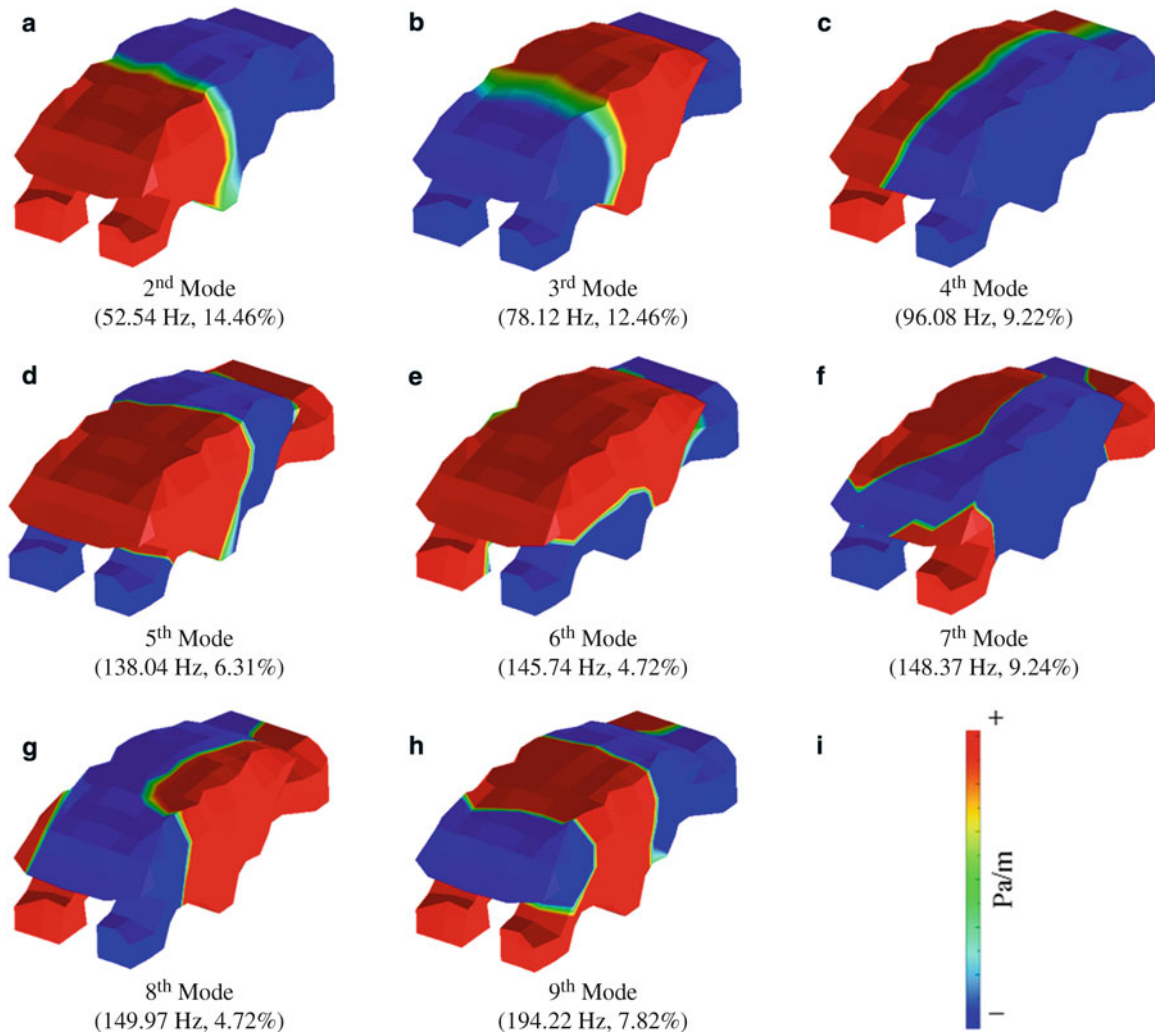
Fig. 4.23 Mode shapes – amplitude and phase (12 references)

Fig. 4.24 II longitudinal mode

a 1st Configuration

b 2nd Configuration
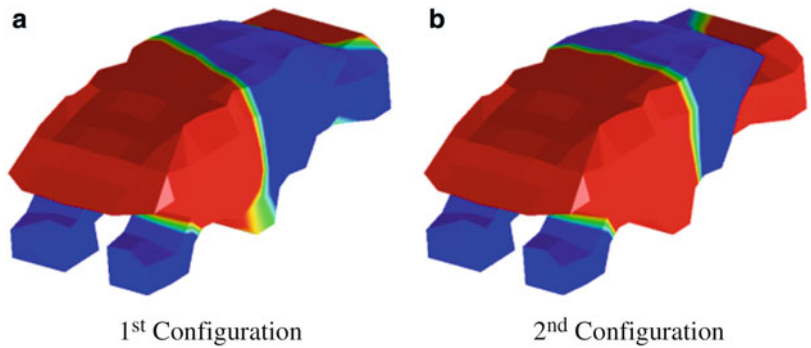
4.4.2   Maximum Likelihood Estimation Based on the Modal Model (ML-MM)

Before showing the results obtained by the new solver, a brief theoretical overview of the method is reported below. Then the results are shown and summarized.

Fig. 4.25 I vertical mode

1st Configuration 2nd Configuration
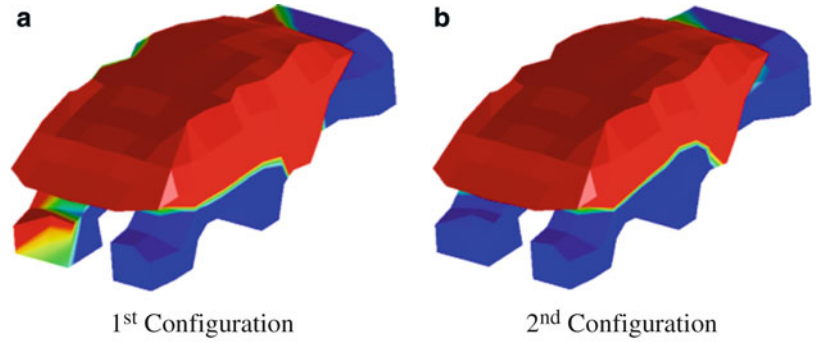
Table 4.3 Comparison of modal parameters

6 references			10 references			12 references			
#	Frequency [Hz]	Damping [%]	#	Frequency [Hz]	Damping [%]	#	Frequency [Hz]	Damping [%]	Mode shape
2	53.36	14.46	2	53.72	15.38	2	52.54	12.89	I longitudinal
3	77.78	11.79	3	78.71	11.67	3	78.12	12.46	I longitudinal & rigid body trunk
4	95.61	8.43	4	95.91	8.72	4	96.08	9.22	I lateral
5	139.15	7.48	5	139.21	7.05	5	138.04	6.31	II longitudinal & rigid body trunk
			6	148.26	6.48	8	149.97	4.72	I longitudinal & I lateral
6	149.79	11.47	7	149.60	10.34	6	145.74	11.72	I vertical
7	151.41	6.46	8	149.82	9.27	7	148.37	9.24	I longitudinal & I lateral & I lateral trunk
8	192.86	6.34	9	194.21	6.74	9	194.22	7.82	III longitudinal

1st Configuration 2nd Configuration 3rd Configuration
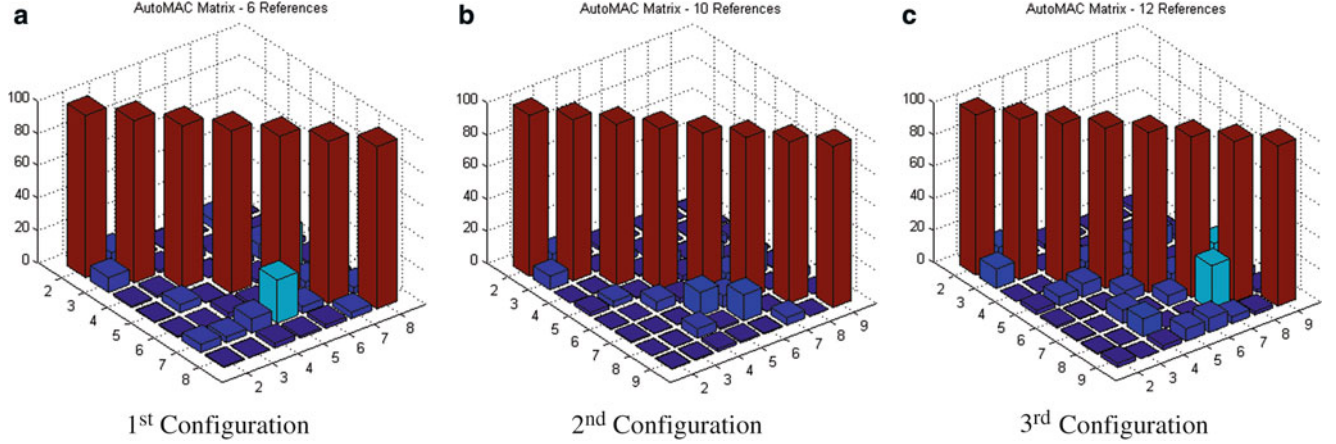
Fig. 4.26 AutoMAC for different configurations

4.4.2.1 Theoretical Background

The ML-MM method [7, 8, 21] is a multiple-input multiple-output (MIMO) frequency-domain estimator providing global estimates of the modal model parameters. In the first step of the ML-MM estimator, initial values of all the modal parameters (i.e. poles, mode shapes, participation factors, and upper and lower residuals) have to be specified. In the next step, the error between the modal model equation and the measured data is minimized in a maximum likelihood sense. Assuming the different measured FRFs to be uncorrelated, the ML-MM cost function to be minimized can be formulated as:

$$K_{ML-MM}(\theta) = \sum_{o=1}^{N_0} \sum_{k=1}^{N_f} E_o(\theta, \omega_k) E_o^H(\theta, \omega_k) \tag{4.7}$$
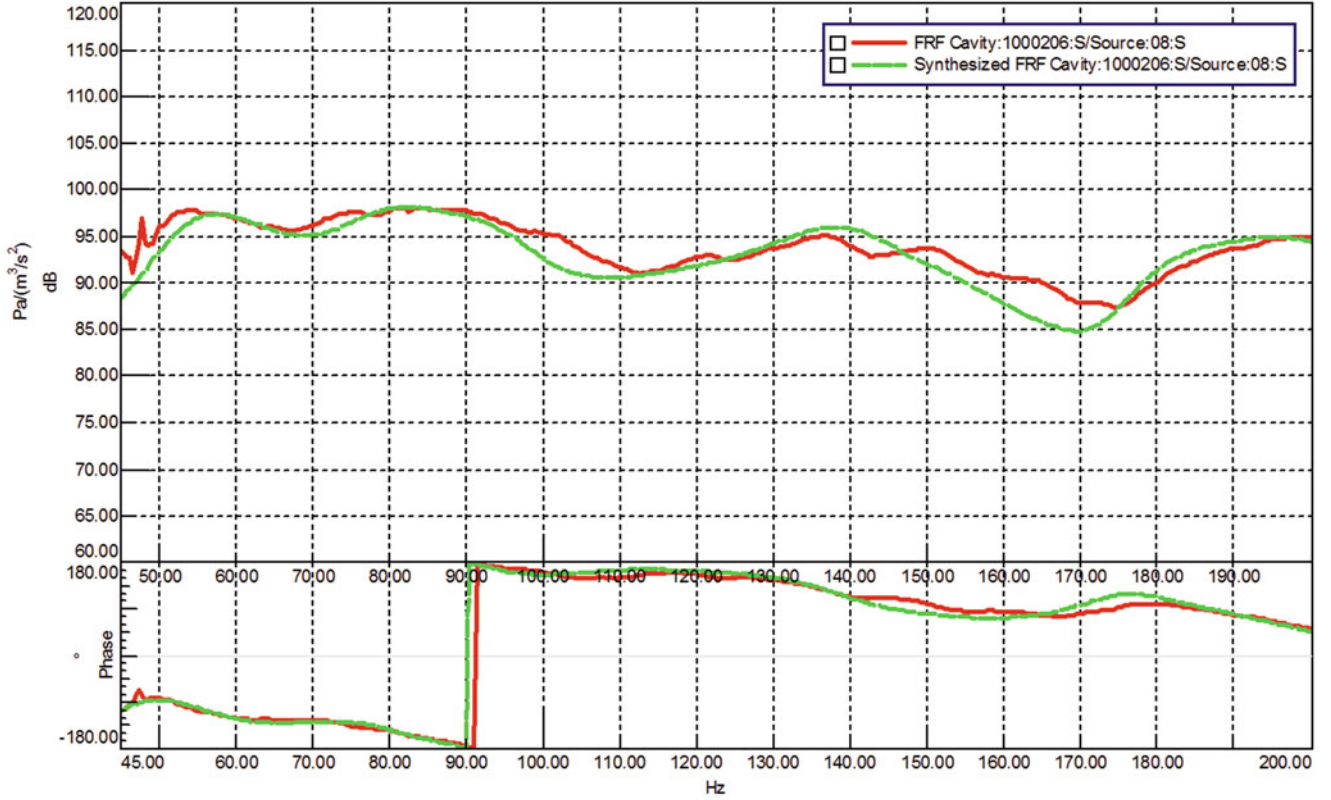
Fig. 4.27 Example of synthetized curve

where $()^H$ stands for the complex conjugate transpose of a matrix (Hermitian), N_o the number of outputs, N_f the number of frequency lines, ω_k the circular frequency, and $E_o(\theta, \omega_k)$ the weighted error equation corresponding to the o-th output degree of freedom (DOF) given as follows:

$$E_o(\theta, \omega_k) = \left[\frac{H_{o1}(\omega_k) - \widehat{H}_{o1}(\theta, \omega_k)}{\sqrt{var(H_{o1}(\omega_k))}} \cdots \frac{H_{oN_i}(\omega_k) - \widehat{H}_{oN_i}(\theta, \omega_k)}{\sqrt{var(H_{oN_i}(\omega_k))}} \right] \in \mathrm{C}^{1 \times N_i} \tag{4.8}$$

where $H_{oi}(\omega_k) \in \mathrm{C}$ the measured FRF, $\widehat{H}_{oi}(\theta, \omega_k) \in \mathrm{C}$ the modeled FRF, $var(H_{oi}(\omega_k))$ the variance of the measured FRF for output o and input i and N_i is the number of inputs.

Assuming displacement FRFs, $\widehat{H}(\theta, \omega_k) \in \mathrm{C}^{N_o \times N_i}$ can be represented using the modal model formulation as follows:

$$\widehat{H}(\theta, \omega_k) = \sum_{r=1}^{N_m} \left(\frac{\psi_r L_r}{s_k - \lambda_r} + \frac{\psi_r^* L_r^*}{s_k - \lambda_r^*} \right) + \frac{LR}{s_k^2} + UR \tag{4.9}$$

with N_m the number of identified modes, $\psi_r \in \mathrm{C}^{N_o \times 1}$ the r-th mode shape, λ_r the r-th pole, $s_k = j\omega_k$, $()^*$ stands for the complex conjugate of a complex number, $L_r \in \mathrm{C}^{1 \times N_i}$ the r-th participation factor, $LR \in \mathrm{C}^{N_o \times N_i}$ and $UR \in \mathrm{C}^{N_o \times N_i}$ the lower and upper residual terms. The lower and upper residual terms are modeling the influence of the out-of-band modes in the considered frequency band. The maximum likelihood estimates of θ (i.e. $\psi_r, L_r, \lambda_r, LR$, and UR) will be obtained by minimizing the above-mentioned cost function $k_{ML-MM}(\theta)$. This will be done using the Gauss-Newton optimization algorithm. To ensure convergence, the Gauss-Newton optimization is implemented together with the Levenberg-Marquardt approach, which forces the cost function to decrease [22]. To start the optimization algorithm, initial values for all the modal parameters are estimated by LMS Polymax method. More details about the ML-MM method (e.g. mathematical implementation, uncertainty derivation, ...) are presented in [7, 8, 21].

Table 4.4 Comparison of modal parameters

Polymax			ML-MM			
#	Frequency [Hz]	Damping [%]	#	Frequency [Hz]	Damping [%]	Mode shape
2	52.54	12.89	2	51.06	13.82	I longitudinal
3	78.12	12.46	3	81.44	14.94	I longitudinal & rigid body trunk
4	96.08	9.22	4	97.24	10.65	I lateral
5	138.04	6.31	5	137.79	7.25	II longitudinal & rigid body trunk
6	145.74	11.72	6	148.66	13.70	I vertical
7	148.37	9.24	8	150.74	11.79	I longitudinal & I lateral & I lateral trunk
8	149.97	4.72	7	149.34	6.57	I longitudinal & I lateral
9	194.22	7.82	9	195.13	6.05	III longitudinal

4.4.2.2 Results and Comparison

Modal parameters are again extracted using a total of 526×12 FRFs simultaneously. The analysis was stopped after 20 iterations.

As visible in Fig. 4.28, the curve fit improves drastically, with a mean fitting error around 2 %. Again nine pure acoustic modes are well identified in this frequency range. As visible in Table 4.4 and Fig. 4.29, the extracted modes are perfectly in line with those already estimated by Polymax, but the quality of the mode shapes seems to increase in terms of symmetry and similarity with the numerical ones. The AutoMAC matrix in Fig. 4.30b shows a really good independency of the eigenvectors estimated by ML-MM. It is also observed that the out of diagonal elements have lower values with respect to those from the AutoMAC matrix obtained with Polymax (Fig. 4.30a). Looking at Table 4.4 and Fig. 4.31, one can observe that the 7th and 8th modes are reversed in the two analyses. Some differences between Polymax and the ML-MM method can be seen in terms of the frequencies and damping estimates. Actually, these differences are reflected as an improvement in the goodness of the fit between the measured and the synthesized FRFs.

4.5 Conclusions

In this paper an intensive test campaign carried out to characterize the interior acoustic field of an automotive cabin is presented. Equipment and test procedure are described in detail. A CAE model of the cavity was used to study the optimal source distribution in order to place the exciters close to the antinodes. The geometry of the measurement points was also initially defined with the help of the CAE model and afterwards based on the true microphone locations. Such an FE model proved extremely useful both to quantify the influence of the Q-LMF sources on the interior acoustic field and to serve as a baseline on the expected pure acoustic modes. Once the measurement chain was validated, FRFs were measured between 526 microphones on roving arrays and 12 sources switched on sequentially.

Modal parameters are estimated in the frequency range between 40 and 200 Hz by two different methods: Polymax and ML-MM. Ten acoustically dominant modes are identified by both methods and seem to be in line with the numerical ones in terms of mode shapes. The modes extracted by the two methods are really comparable, although their order is reversed in some case. Nevertheless, ML-MM provides superior FRF synthesis results and, hence, more reliable values, as also shown by the more "natural" and symmetric mode shapes.

A study on the number of sources to be used in order to identify properly the acoustically dominant modes is reported as well. It has been observed that, whereas the lower modes (up to 140 Hz) are always well identified, the extraction of higher modes requires a large amount of sources. This is even more true when modes are present that are closely spaced in frequency.

Future studies will consist in further numerical analyses in order to better understand and quantify the vibro-acoustic coupling effects and the actual role of the damping in such a system. Updating of the acoustic cavity FE model based on test results, is also a very challenging task and subject of future investigations.
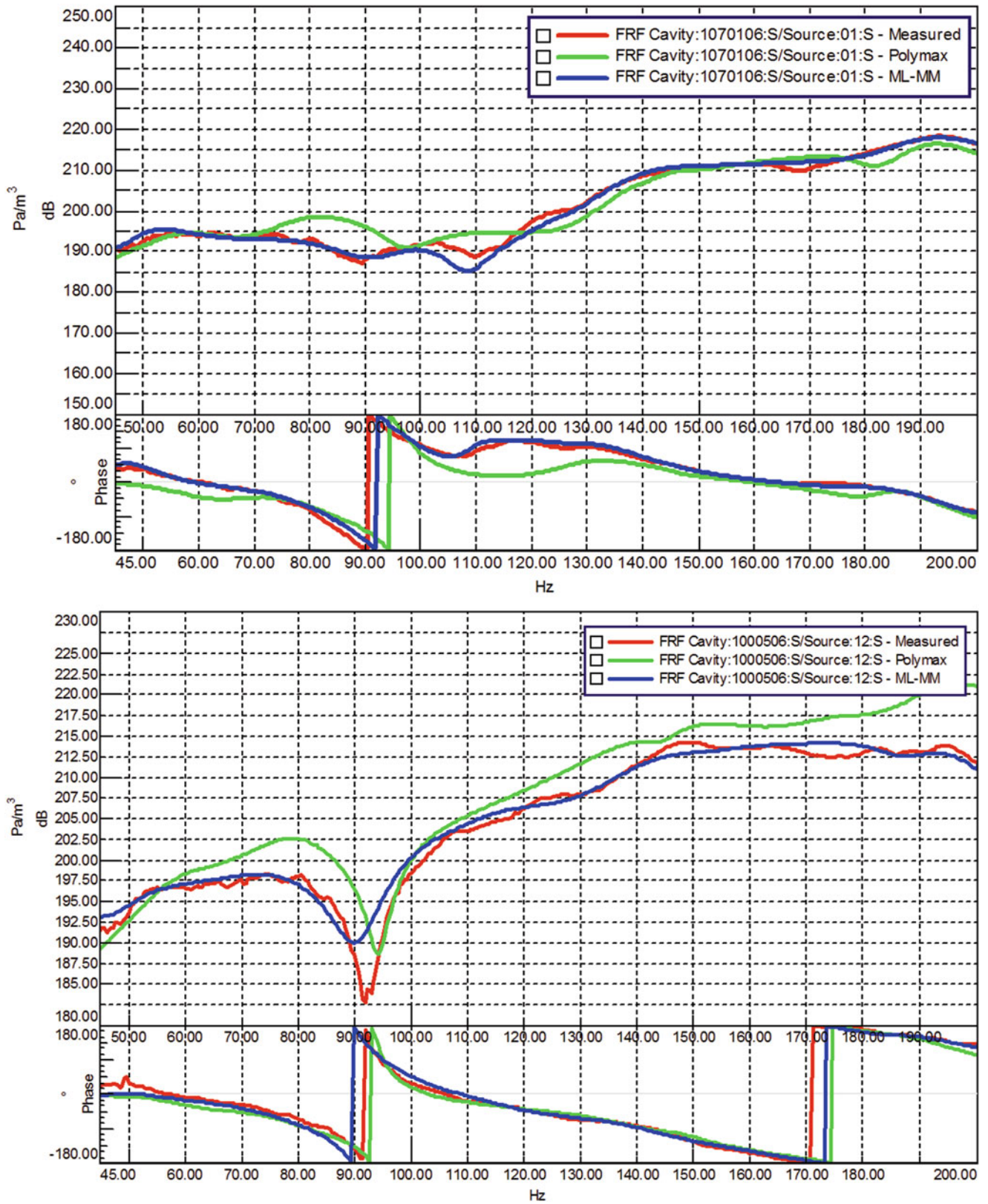
Fig. 4.28 Improved curve fitting
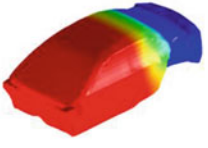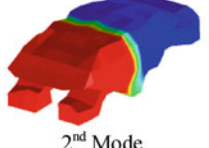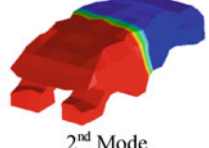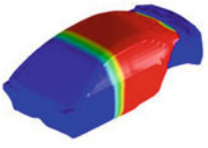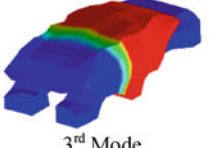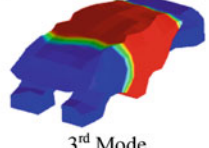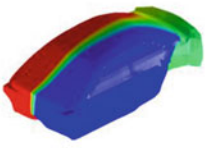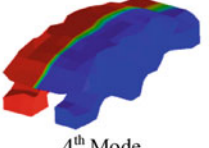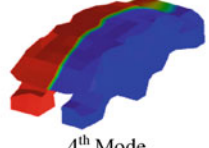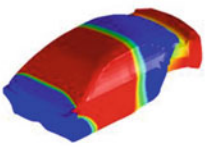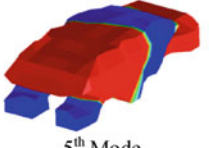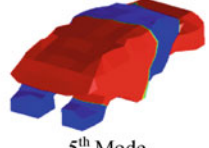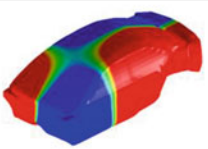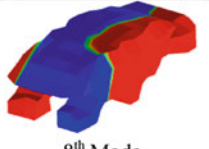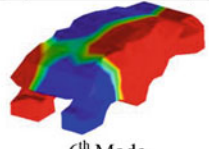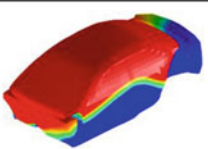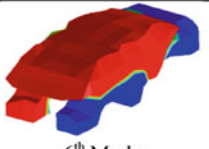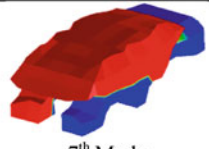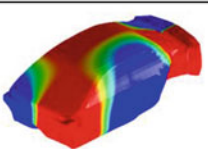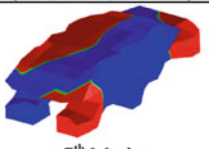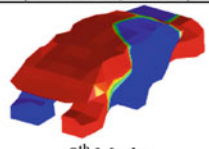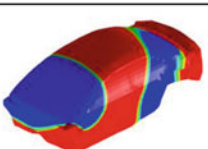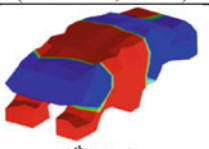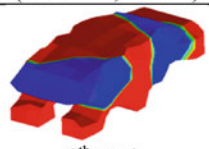
Numerical Modes (CAE Model)	Experimental Modes (Polymax)	Experimental Modes (ML-MM)	Mode Shape
	2nd Mode (52.54 Hz, 12.89%)	2nd Mode (51.06 Hz, 13.82%)	I Longitudinal
	3rd Mode (78.12 Hz, 12.46%)	3rd Mode (81.44 Hz, 14.94%)	I Longitudinal & Rigid Body Trunk
	4th Mode (96.08 Hz, 9.22%)	4th Mode (97.24 Hz, 10.65%)	I Lateral
	5th Mode (138.04 Hz, 6.31%)	5th Mode (137.79 Hz, 7.25%)	II Longitudinal & Rigid Body Trunk
	8th Mode (149.97 Hz, 4.72%)	6th Mode (148.66 Hz, 13.70%)	I Longitudinal & I Lateral & I Lateral Trunk
	6th Mode (145.74 Hz, 11.72%)	7th Mode (149.34 Hz, 6.57%)	I Vertical
	7th Mode (148.37 Hz, 9.24%)	8th Mode (150.74 Hz, 11.79%)	I Longitudinal & I Lateral & I Lateral Trunk
	9th Mode (192.22 Hz, 7.82%)	9th Mode (195.13 Hz, 6.05%)	III Longitudinal

Fig. 4.29 Mode shapes – comparison (The discrepancies between the CAE and test geometry in the front part of the cavity are not due to a different modelling of the car. The region between the foot area and the dashboard is present in the real scenario as well, but hardly accessible to the sensors)
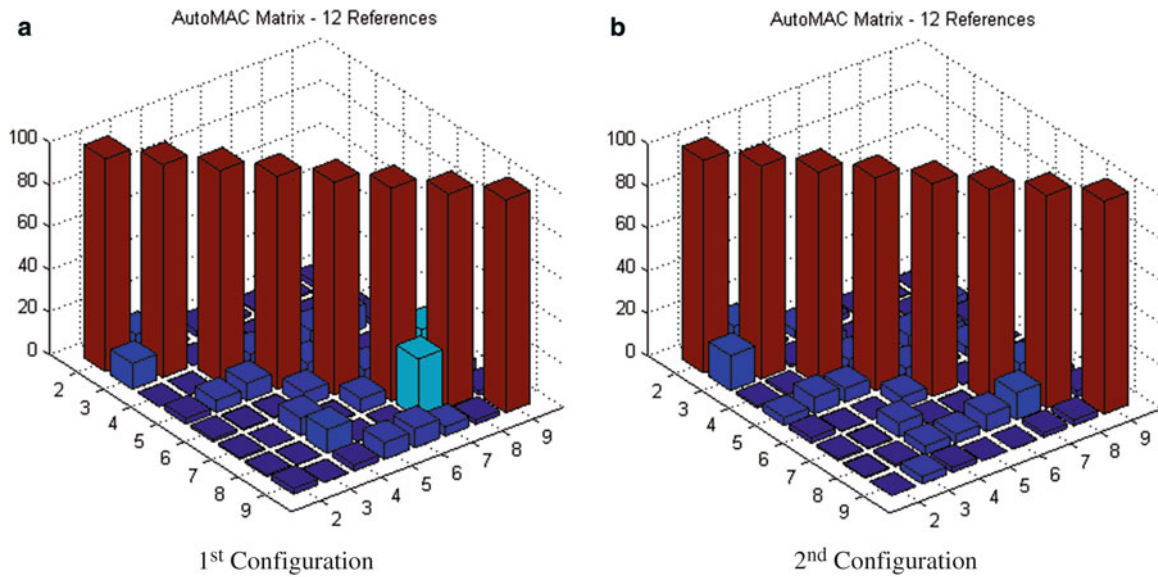
Fig. 4.30 AutoMAC matrices

Fig. 4.31 MAC between Polymax and ML-MM
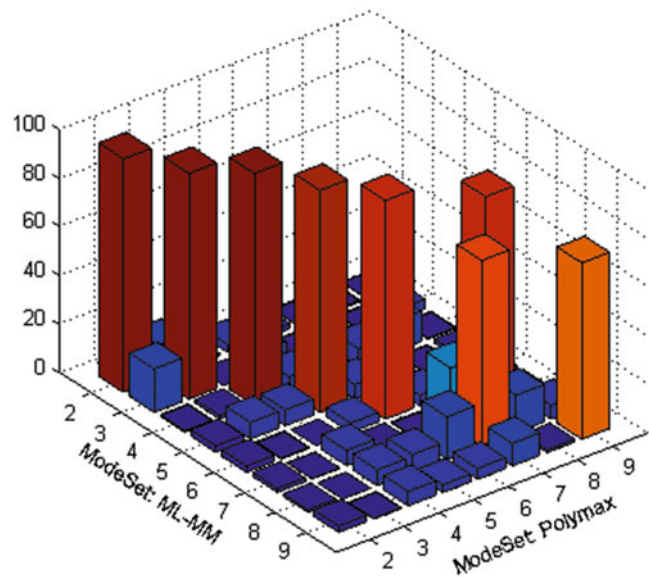
References

1. Sung TMSH, Nefske DJ, Le-The H, Bonarens F (1999) Development and experimental evaluation of a vehicle structural-acoustic trimmed-body model. SAE technical paper 1999-01-1798
2. Sanderson MA, Onsay T (2007) CAE interior cavity model validation using acoustic modal analysis. SAE technical paper 2007-01-2167
3. Peeters B, El-kafafy M, Accardo G, Knechten T, Janssens K, Lau J, Gielen L (2014) Automotive cabin characterization by acoustic modal analysis. In: Proceedings of JSAE spring annual conference, Yokohama, Japan 114–20145437
4. Yoshimura T, Saito M, Maruyama S, Iba S (2012) Modal analysis of automotive cabin by multiple acoustic excitation. In: Proceedings of ISMA, Leuven, Belgium
5. Tsuji H, Maruyama S, Yoshimura T, Takahashi E (2013) Experimental method extracting dominant acoustic mode shapes for automotive interior acoustic field coupled with the body structure. SAE technical paper 2013-01-1905
6. Peeters B, Van der Auweraer H, Guillame P, Leuridan J (2004) The PolyMAX frequency-domain method: a new standard for madal parameter estimation. Shock Vib 11:395–409
7. El-Kafafy M, De Troyer T, Peeters B, Guillame P (2013) Fast maximum-likelihood identification of modal parameters with uncertainty intervals: a modal model-based formulation. Mech Syst Sign Proc 37:422–439
8. El-Kafafy M, Guillame P, De Troyer T, Peeters B (2012) A frequency-domain maximum likelihood implementation using the modal model formulation. In: Proceedings of SYSID, Brussels

9. Fahy F, Gardonio P (1985) Sound structural vibration. Radiation, transmission and response. Academic, London
10. Ohayon R, Soize C (1998) Structural acoustics and vibration. Mechanical models, variational formulations and discretizations. Academic, London
11. Dhandole S, Modak SV (2012) A constrained optimization based method for acoustic finite element model updating of cavities using pressure response. Appl Math Model 36:399–413
12. Heylen W, Lammens S, Sas P (2012) Modal analysis. Theory and testing. PMA – K.U. Leuven, Belgium
13. Wyckaert K, Augusztinovicz F, Sas P (1996) Vibro-acoustical modal analysis: reciprocity, model symmetry, and model validity. J Acoust Soc Am 100(5):3172–3181
14. Xu H, Dickinsons O, Wang J, Kang H (2014) Acoustic cavity modal analysis for NVH development of road machinery cabins. In: Proceedings of the 32nd international modal analysis conference, Orlando
15. Tsuji H, Enomoto T, Maruyama S, Yoshimura T (2012) A study of experimental acoustic modal analysis of automotive interior acoustic field coupled with the body structure. SAE technical paper 2012-01-1187
16. Brandt A (2011) Noise and vibration analysis: signal analysis and experimental procedures. Wiley, Hoboken, West Sussex, UK
17. Wyckaert K, Meulewaeter L (1996) On the influence of finite acoustic source dimensions on acoustical frequency response funcions inside an enclosed cavity. In: Proceedings of ISMA, Leuven, Belgium
18. Coster C, Nagahata D, van der Linden PJG (2010) On the accuracy reciprocal and direct vibro-acoustic transfer-function measurements on vehicles for lower and medium frequencies. In: Proceedings of ISMA, Leuven, Belgium
19. He J, Fu ZF (2001) Modal analysis. Butterworth-Heinemann, Oxford
20. Ewins DJ (2000) Modal testing: theory, practice and application. Research Studies Press Ltd, Philadelphia
21. El-kafafy M, Accardo G, Peeters B, Janssens K, De Troyer T, Guillame P (2015) A fast maximum likelihood-based estimation of a modal model. In: Proceedings of the 33rd international modal analysis conference, Orlando
22. Eykhoff P (1979) System identification: parameter and state estimation. Wiley, Bristol

Chapter 5
Uncorrelated Noise Sources Separation Using Inverse Beamforming

Claudio Colangeli, Paolo Chiariotti, and Karl Janssens

Abstract The separation of a measured sound field in uncorrelated sources distributions can be very useful when dealing with sound source localization problems. The use of the Principal Component Analysis (PCA) principle, combined with a Generalized Inverse Beamforming (GIBF) technique, offers the possibility to resolve complex and partially correlated sound sources distributions.

Despite very promising, this approach appears still to be optimized and the influence of a number of potentially influent parameters is to be understood. In this paper a developed GIBF algorithm is combined with a PCA and firstly tested on a simulated problem, then applied on gradually more complex real cases. A sensitivity analysis on some relevant parameters is carried out in order to evaluate the robustness of the developed algorithm and the effectiveness of the used PCA.

Keywords Beamforming • Inverse beamforming • Sound source identification • Principal component analysis • Array methods

List of Acronyms

PCA   Principal Component Analysis
GIBF Generalized Inverse Beamforming
SVD   Singular Values Decomposition
MAC   Modal Assurance Criterion
CSM   Cross-Spectral Matrix
APS   Auto Power Spectrum
GCV   Generalized Cross-Validation function

5.1 Introduction

The use of Generalized Inverse Beamforming (GIBF), offers the possibility to resolve complex and partially correlated sound sources distributions if used in combination of a PCA of the acoustic field [1]. This makes it particularly suitable in problems of sound source localization where many causes of noise, uncorrelated each other, are active at the same time [2, 3]. This for several reasons: first of all an inverse approach allows defining the most appropriate radiation model [4, 5] for the case in study, allowing also to quantify the strength of the noise sources active in the field; moreover the accuracy in localizing point as well as distributed noise sources is rather constant in frequency.

These undoubted advantages justify the interest in such methodologies, despite a series of drawbacks:

– The inverse formulation leads most of the times to ill-posed problems requiring an effective regularization strategy.
– The decomposition of the acoustic field in uncorrelated sources by means of PCA may be not always ideal.

C. Colangeli (✉) • K. Janssens
Siemens Industry Software NV, Interleuvenlaan 68, 3001 Leuven, Belgium
e-mail: claudio.colangeli@siemens.com

P. Chiariotti
Università Politecnica delle Marche, Via Brecce Bianche 1, 60131 Ancona, Italy
e-mail: p.chiariotti@univpm.it

The influence of such variables on the performances of the technique is still to be deepened. In order to do so, the proposed formulation of GIBF is tested through a sensitivity analysis. A set of optimal values for such parameters will be proposed as well as some guidelines to be used in the application of the method.

5.2 PCA for Uncorrelated Noise Sources Separation

Considering, as in Fig. 5.1, two uncorrelated sources $s_1(t)$ and $s_2(t)$ whose spectra are $S_1(\omega)$, $S_2(\omega)$, and two microphones m_1 and m_2 receiving the abovementioned sources: $P_1(\omega)$ and $P_2(\omega)$, the CSM (C_M) between the signals at the microphones of such a problem is given by the Eq. (5.2).

$$\begin{pmatrix} P_1 \\ P_2 \end{pmatrix} = \begin{bmatrix} G_{11} & G_{21} \\ G_{12} & G_{22} \end{bmatrix} \begin{pmatrix} S_1 \\ S_2 \end{pmatrix} \tag{5.1}$$

$$C_M = \begin{bmatrix} (S_1 G_{11} + S_2 G_{21})(S_1 G_{11} + S_2 G_{21})^* & (S_1 G_{11} + S_2 G_{21})(S_1 G_{12} + S_2 G_{22})^* \\ (S_1 G_{12} + S_2 G_{22})(S_1 G_{11} + S_2 G_{21})^* & (S_1 G_{12} + S_2 G_{22})(S_1 G_{12} + S_2 G_{22})^* \end{bmatrix} \tag{5.2}$$

Assuming uncorrelated sources we have $i \neq j \Rightarrow S_i S_j^* = 0$. Moreover: $G_{kl} G_{mn}^* = 1 \iff k = m \wedge l = n$. So:

$$C_M = \begin{bmatrix} S_1{}^2 + S_2{}^2 & S_1{}^2\left(G_{11}G_{12}^*\right) + S_2{}^2\left(G_{21}G_{22}^*\right) \\ S_1{}^2\left(G_{12}G_{11}^*\right) + S_2{}^2\left(G_{22}G_{21}^*\right) & S_1{}^2 + S_2{}^2 \end{bmatrix}$$
$$= S_1{}^2 \begin{bmatrix} 1 & G_{11}G_{12}^* \\ G_{12}G_{11}^* & 1 \end{bmatrix} + S_2{}^2 \begin{bmatrix} 1 & G_{21}G_{22}^* \\ G_{22}G_{21}^* & 1 \end{bmatrix} \tag{5.2.1}$$

The CSM, is by definition Hermitian, so its eigenvalue decomposition can be obtained in the form (5.3):

$$C_M = E S E^\dagger \tag{5.3}$$

$$E = \begin{bmatrix} G_{11} & G_{21} \\ G_{12} & G_{22} \end{bmatrix} \qquad S = \begin{bmatrix} S_1{}^2 & 0 \\ 0 & S_2{}^2 \end{bmatrix} \tag{5.4}$$

Comparing the Eq. (5.3) and the (5.2.1), the matrices E and S are obtained in Eq. (5.4) showing that the APS of the uncorrelated sources active in the field are eigenvalues for the CSM (see also [2]) and the corresponding eigenvectors depend on their radiation model. This interesting result will be combined with GIBF using the just described PCA to:

- Ascertain the number of uncorrelated sources active in the field.
- Retrieve their strength by means of their corresponding eigenvalue of the CSM.
- Filter out the background noise by discarding the lowest eigenvalues of CSM.
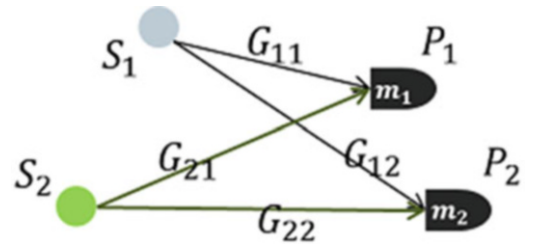
Fig. 5.1 Sources (S_1 and S_2) radiation towards microphones (P_1 and P_2)

5.3 Generalized Inverse Beamforming Formulation

It is proposed a formulation of GIBF for processing phased microphones array measurements aiming at identifying (localization and quantification) the noise sources in an acoustic field. The idea is to reconstruct the measured acoustic field through the superimposition of a distribution of ideal sources disposed in a so-called target grid.

Sources distribution :

$$a_i = \begin{bmatrix} \hat{a}_1 \ \ldots \ \hat{a}_N \end{bmatrix}^T \tag{5.5}$$

Receiver distribution :

$$v_i = \begin{bmatrix} \hat{v}_1 \ \ldots \ \hat{v}_M \end{bmatrix}^T \tag{5.6}$$

Radiation matrix :

$$\{A\}_{m,n} = \frac{e^{-ikr_{mn}}}{4\pi r_{mn}} \tag{5.7}$$

r_{mn} is the distance between the mth of the M microphones and the nth of the N target grid points.

What demonstrated in Sect. 5.2 is here exploited for decomposing the acoustic field at the microphones position in uncorrelated sources distributions through the SVD of the CSM. Considering the Eq. (5.3), this is done as follows:

$$V = \begin{bmatrix} v_1 \ \ldots \ v_l \end{bmatrix} = \sqrt{S}E \tag{5.8}$$

$$Aa = V \tag{5.9}$$

With: $a = [a_1, \ldots, a_i, \ldots, a_l] \in \mathbb{C}^{N \times l}, \ \ V \in \mathbb{C}^{M \times l}$, 1: number of not negligible eigenvalues of the CSM.

The unknowns, in (5.9), are the sources distributions a_i related to each eigenmode $\sqrt{s_i}e_i$. So the inverse problem $a = A^{-1}V$ must be solved. For optimizing the solution is adopted the algorithm proposed in [1, 6], formulating per each significant eigenmode v_i the problem $Aa_i = v_i$ and applying the following algorithm:

1. Calculate the initial source vector, a_i by inverting the radiation matrix: $a^0_i = (\{A\}_{M*N})^{-1}v_i$
2. Reorder and truncate (10 %) the source vector a^k_i, discarding the smallest terms
3. Calculate a new source vector: $a^k_i = \left(\{A\}_{(0.1^k)M*N} \right)^{-1} v_i$
4. Repeat (2) and (3) until a wanted number of sources is reached.

The Tikhonov's approach will be used for inverting the ill-conditioned radiation matrix. In this paper a robust criterion in the choice of the regularization factor λ is adopted taking advantage of the properties of the SVD of A.

$$A \in \mathbb{C}^{M \times N},$$

$$A = U\Sigma X^{\dagger} = \sum_{i=1}^{M} u_i \sigma_i x_i^{\dagger} \tag{5.10}$$

$$U \in \mathbb{C}^{M \times M} = \begin{bmatrix} u_1 \ \ldots \ u_M \end{bmatrix}$$

$$\sigma = \text{diag}(\Sigma) = \begin{bmatrix} \sigma_1 \ \ldots \ \sigma_M & 0 \ \ldots \ \sigma_N = 0 \end{bmatrix} \in \mathbb{R}$$

$$X \in \mathbb{C}^{N \times N} = \begin{bmatrix} x_1 \ \ldots \ x_N \end{bmatrix}$$

The candidate regularization factors are chosen among a set of logarithmically distributed regularization parameters between the highest and the lowest non-zero singular value of the radiation matrix A.

Recalling that: $\sigma = \begin{bmatrix} \sigma_1 \ldots \sigma_M \end{bmatrix}$, that $U = \begin{bmatrix} u_1 \ldots u_M \end{bmatrix}$ and $v_i = \begin{bmatrix} v_1 \ldots v_M \end{bmatrix} = \sqrt{s_i} e_i$, the most effective filter factor for regularizing the posed ill-conditioned problem can be selected by minimizing the following quasi-optimality function (5.12) (see reference [7]):

$$f_{cand}(n)_j = \frac{\sigma_j{}^2}{\sigma_j{}^2 + \lambda_{cand}(n)^2} \tag{5.11}$$

$$Q\left(\lambda_{cand}(n)\right) = \sqrt{\sum_{j=1}^{M} \left(1 - f_{cand}(n)_j\right) f_{cand}(n)_j \frac{u_j{}^\dagger v_i}{\sigma_j}} \tag{5.12}$$

$$n = 1, \ldots, Nr$$

$$j = 1, \ldots, M$$

Once λ_k is obtained at each iteration k of the algorithm, the matrix inversion can be obtained per Singular Values or, alternatively, by regularized pseudo-inversion of A:

$$a^k{}_i = \sum_{j=1}^{M} \frac{\sigma_j{}^2}{\sigma_j{}^2 + \lambda_k{}^2} \frac{u_j{}^\dagger v_i}{\sigma_j} x_j \tag{5.13}$$

$$
\begin{aligned}
\text{M} < \text{N} \rightarrow a^k{}_i &\approx A^\dagger \left(AA^\dagger + \lambda_k{}^2 I\right)^{-1} v_i \\
\text{M} > \text{N} \rightarrow a^k{}_i &\approx \left(A^\dagger A + \lambda_k{}^2 I\right)^{-1} A^\dagger v_i
\end{aligned}
\tag{5.14}
$$

In the presented work Eqs. (5.11), (5.12) and (5.13) are used and compared with other regularization strategies.

5.4   Quantification and Localization of the Sources Strength Active in the GIBF Maps

In this section is presented a novel method for localization and quantification of the sources in a GIBF map. This approach is based on the crucial assumption that the APS of each uncorrelated source active in the field is an eigenvalue for the CSM. Referring to Sect. 5.2 and to Refs. [2, 3], the strength q_m of the source distribution in the GIBF map which is related to the mth eigenvalue of the CSM can be estimated using Eq. (5.15):

$$q_m = \frac{s_m - s_M}{MR_r} \tag{5.15}$$

Where:

s_m: m-th eigenvalue of the CSM
s_M: minimum eigenvalue (noise)

$$R_r = (1/4\pi r)^2$$

r: distance array-source grid
M: Number of microphones

The idea is to find the relation between the estimation of the source strength given by the Eq. (5.15) and the one obtained processing the GIBF map, under the following hypothesis (valid for monopole radiation):

Fig. 5.2 Example of centroids localization in the GIBF map
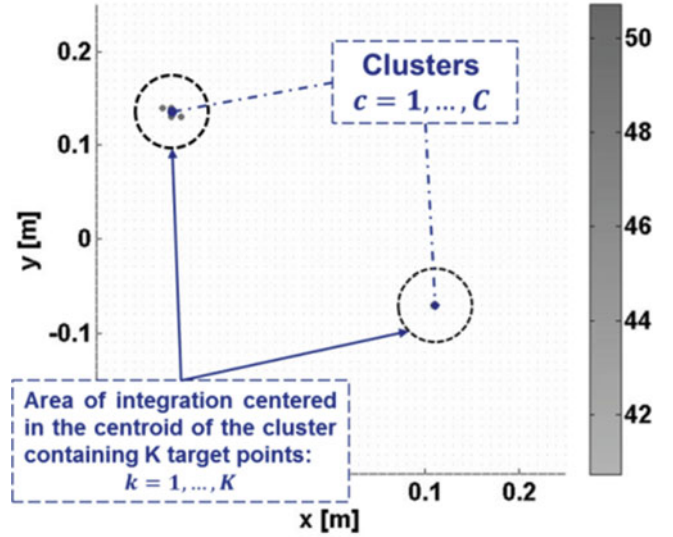
– A source is represented by a cluster of monopoles.
– The monopoles of a cluster have uniform phase (per frequency line) within the cluster.

The proposed algorithm is summarized below referring to Fig. 5.2:

1. Localization of the C clusters in the GIBF map and their centroids;
2. Consider areas of integration: $cluster(k = 1, \ldots, K)_c$;
3. Sum contributions:

$$P_c = \sum_{k}^{K \epsilon\ cluster_c} a_m\left(cluster(k)_c\right) \tag{5.16}$$

K: number of the monopoles belonging to the cluster;
4. Comparison with the eigenvalue estimation: $\left|P_c - \sqrt{q_m}\right| < \Delta \Rightarrow cluster(k)_c$ is a source distribution.

5.5 Simulated and Real Test Case Scenarios

This sensitivity analysis has been carried out taking as test case a simulated problem of a loudspeakers panel 0.5 m $\times$ 0.5 m and an array of 36 microphones placed at a distance of 0.6 m from the panel.

The same scenario has been replicated in reality using a true loudspeakers panel and the same array geometry used for the simulation. The loudspeakers used in the tests are those identified with number 2 and 4 in Fig. 5.3. From now on these sources will be called Source#1 and Source#2 respectively and considered belonging to an area of tolerance of a radius of 0.05 m. The scenarios presented are summarized in Table 5.1 and Fig. 5.4.

5.6 Sensitivity Analysis

The cross-influence of all the combinations of the following parameters on the GIBF algorithm has been studied:

– Number of averages taken for CSM (AVG): 1,000,667,500,333,100,50,33,10.
– Background noise in data (SNR_{dB}): 50,40,30,20,17,10,7,0.

The signals sample rate is Fs = 20,480 Hz. The beamforming simulation has been carried out in time domain by simulating the delays at the different microphone positions. In all the GIBF calculations has been considered a target grid points distribution equally spaced in the calculation plane with a spatial resolution of 0.01 m. The CSM has been calculated keeping
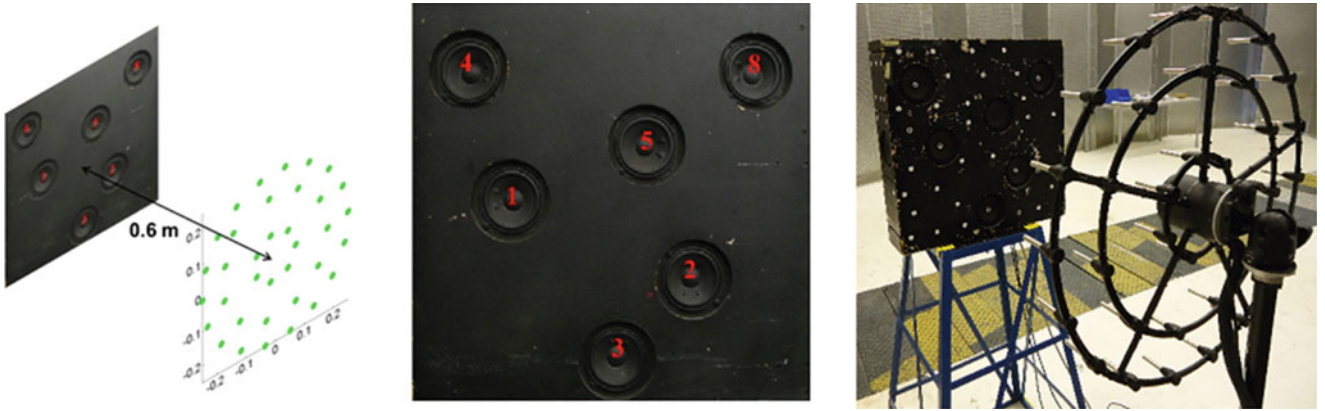
Fig. 5.3 Simulated and real test case on the used loudspeakers panel

Table 5.1 List of the Scenarios presented in this study

Scenario	Source#1	Source#2
a	Random noise	Electric engine noise
b	Random noise	Uncorrelated random noise (same noise level)
c	Random noise	Uncorrelated random noise $\downarrow 10 dB_{SPL}$
d	Random noise	
e	Sine @ 1 kHz	

Fig. 5.4 Sources locations and respective areas of tolerance
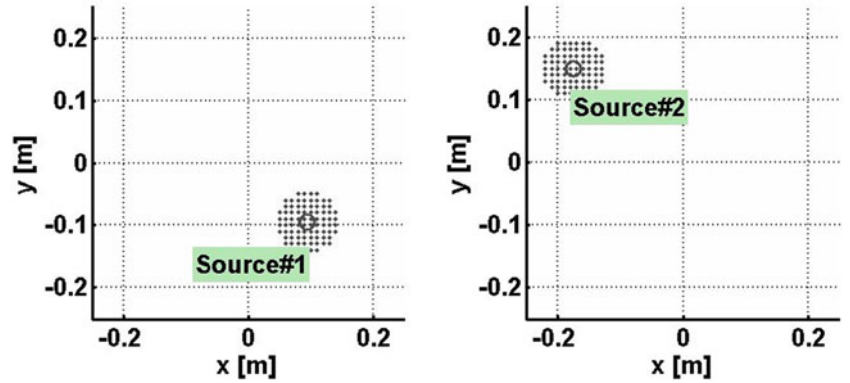
a frequency resolution of 10 Hz. This choice is driven by an analysis on this parameter which is not reported because did not show clearly identifiable trends, but it demonstrated that 10 Hz is a good compromise for strength estimation and calculation time. If not differently specified, the results described below will be presented at a frequency of 1 kHz.

5.6.1 Eigenmodes of the CSM and GIBF Solution for Uncorrelated Sources

Equation (5.4) has shown that the APS of the uncorrelated sources active in the acoustic field are eigenvalues for the CSM. This feature can be exploited for deciding the number and which uncorrelated sources to be used to reconstruct the sound field. This operation will tell information also about the background noise present in the data and if the number of averages taken for computing the CSM is enough for correctly filter it out through the PCA.

According to Eqs. (5.8) and (5.9), since the solution a_i is related to the ith eigenmode of the CSM, its propagation Aa_i towards the array is by definition orthogonal to any other eigenmode of the CSM.

If there are S relevant sources active in the field, it must be:

$$Aa_i, v_j = 0 \ \forall \ j \neq i, \text{ with } j = 1, \ldots, S \tag{5.17}$$
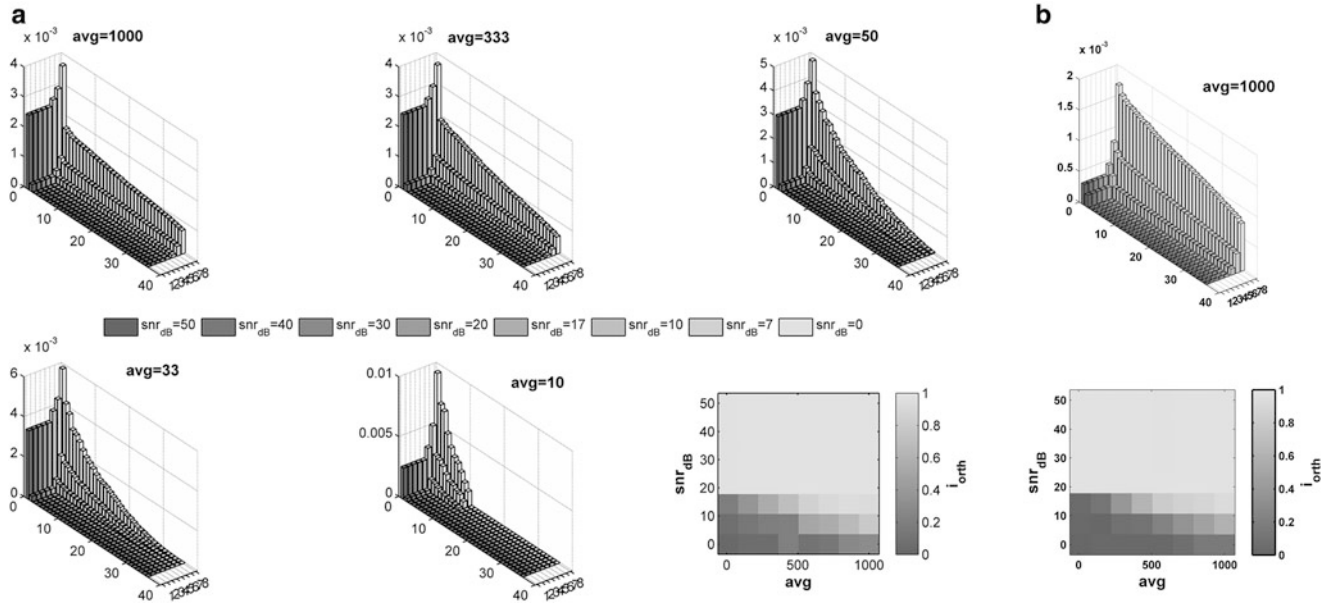
Fig. 5.5 Eigenvalues trend (AVG vs. SNR) and indicator i_{orth} for scenario c (**a**) and scenario b (**b**)

This property can be used for verifying the results. Let us define the following indicator Eq. (5.17) whose trend is shown in Fig. 5.5a bottom right and in Fig. 5.5b bottom.

$$i, j = 1, \ldots, S \;\rightarrow\; i_{orth} = \det\left(MAC\left\{v_j, Aa_i\right\}\right) = \begin{cases} 1 \rightarrow \text{solutions are orthogonal} \\ < 1 \rightarrow \text{solution are not orthogonal} \end{cases} \tag{5.18}$$

Figure 5.5 also shows, in two scenarios, the eigenvalues of the CSM ranked in a descended order and grouped per SNR and different number of averages showing that, for GIBF applications, the number of averages should be at least $avg = 10 * M$ (M is the number of microphones), for having the main eigenvalues stable for quantification purposes.

As expected the SNR has a strong influence on the i_{orth} therefore on the solution. Uncorrelated sources with different frequency content permit to tolerate slightly more severe SNR conditions.

5.6.2 Localization, Separation and Quantification

GIBF results for scenario a and scenario b (with real measurements) in the frequency range 800–5,000 Hz and applying $avg = 500$, are shown in Figs. 5.6 and 5.7.

In the case of scenario a (Fig. 5.6), since the frequency content of the two uncorrelated sources is rather different, the identification of the sources is optimal. Figure 5.7 shows a real test case where the two sources APS are very similar producing two effects: difficulty in reconstructing the spectra of the sources (obtained using reference microphones placed in the proximity of the loudspeakers) and presence of numerical ghost images in the GIBF map.

The indicator for evaluating the correct localization of the sources is defined as follows:

$$i_{loc}(m) = \frac{\sum_{n' \in Source\#1} a_m\left(n'\right) + \sum_{n'' \in Source\#2} a_m\left(n''\right)}{\sum_{n=1}^{N} a_m(n)} \tag{5.19}$$

The idea is to compare what is inside the areas of tolerance of the two sources with what is all over the GIBF map. In a similar way the quantification can be evaluated. In this case the energy content inside the sources areas is compared with the estimation of the sources strength done through the corresponding eigenvalues. With the notation used in Eqs. (5.15) and (5.16), the strength estimation indicator can be defined as follows:
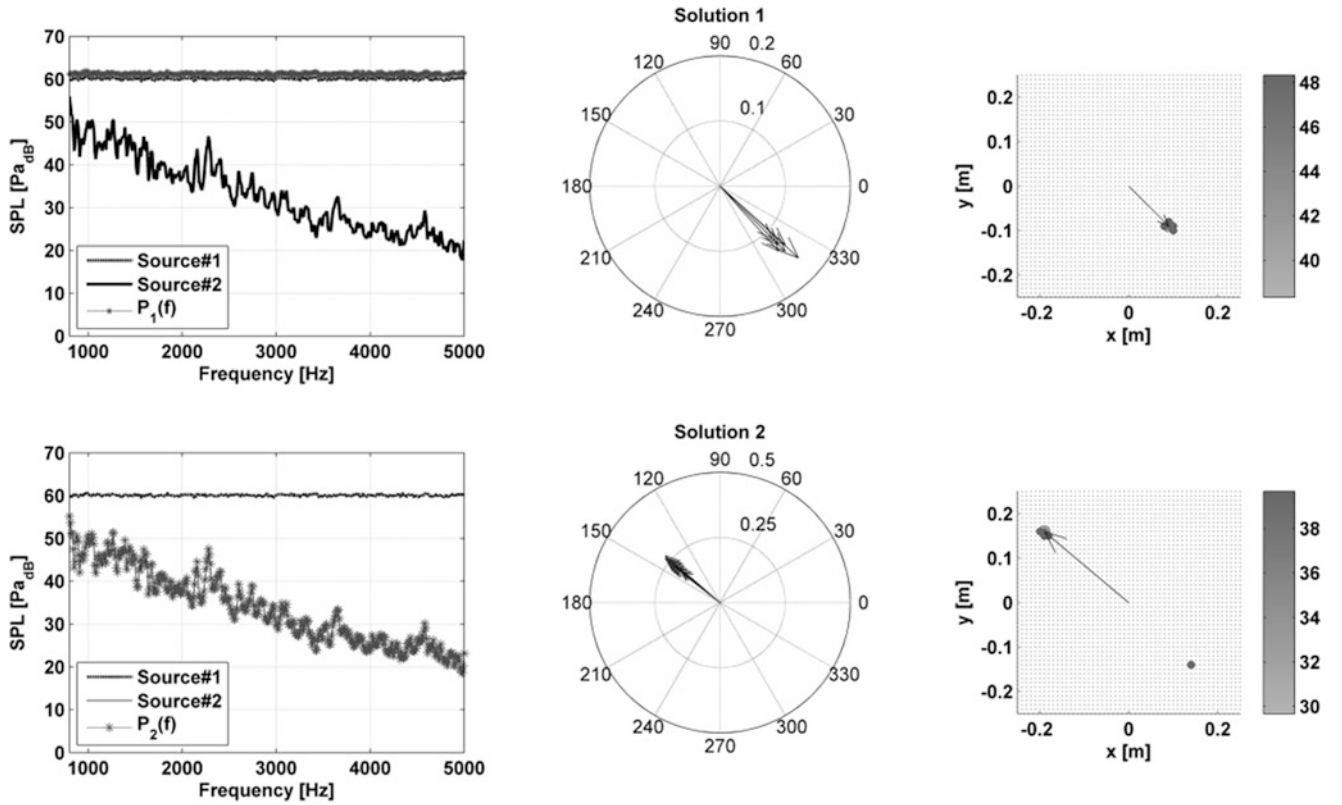
Fig. 5.6 Scenario a. GIBF calculated in the range 800 Hz–5 kHz. Quantification compared with the actual spectra of the sources. Localization shown through a compass plot showing an *arrow* per each spectral line calculated, pointing the retrieved coordinate of the source. An example of beamforming map is shown at 1 kHz

$$i_{str}{}^{(m,1)} = \frac{\sum_{n' \in Source\#1} a_m(n')}{\sqrt{q_m}} \qquad i_{str}{}^{(m,2)} = \frac{\sum_{n'' \in Source\#2} a_m(n'')}{\sqrt{q_m}} \qquad m = 1, \ldots, S \qquad (5.20)$$

S is the number of GIBF solutions calculated and it is equal to the number of relevant eigenvalues in the CSM.

Figure 5.8 shows that the sources are correctly localized in both scenarios b and c for SNR >20 dB.

In the scenario c, where one of the uncorrelated sources is stronger than the other, is visible also that the sources are always correctly separated and the quantification. Indeed the conditions of correct separation and quantification described in Eq. (5.21) are fulfilled.

$$\begin{cases} i_{loc} \cong 1 \\ i_{str}{}^{(1,2)} = 0 = i_{str}{}^{(2,1)} \\ i_{str}{}^{(1,1)} = 1 = i_{str}{}^{(2,2)} \end{cases} \qquad (5.21)$$

For scenario b, despite less evident, the trend of the indicators is the same, but with major presence of numerical issues.

5.6.3 Regularization Strategy

In Sect. 5.3 are described the adopted regularization strategy and matrix inversion techniques used so far. Referring to [2], different alternative regularization strategies have been tested and presented here: quasi-optimality, GCV, L-Curve, Lagrange.

Figure 5.9 presents a comparison between the methods in presence of a sinusoidal source at 1 kHz and 1 Pa amplitude placed at the coordinate: [0.095 m −0.095 m] in the shown maps (scenario e). The most effective are the quasi-optimality and GCV functions. The L-Curve still allows localizing the source with a less clear pattern.

Fig. 5.7 Sources spectra calculated with GIBF and compared with reference microphones spectra in a real test case. Example of localization maps without CTC (**a**)
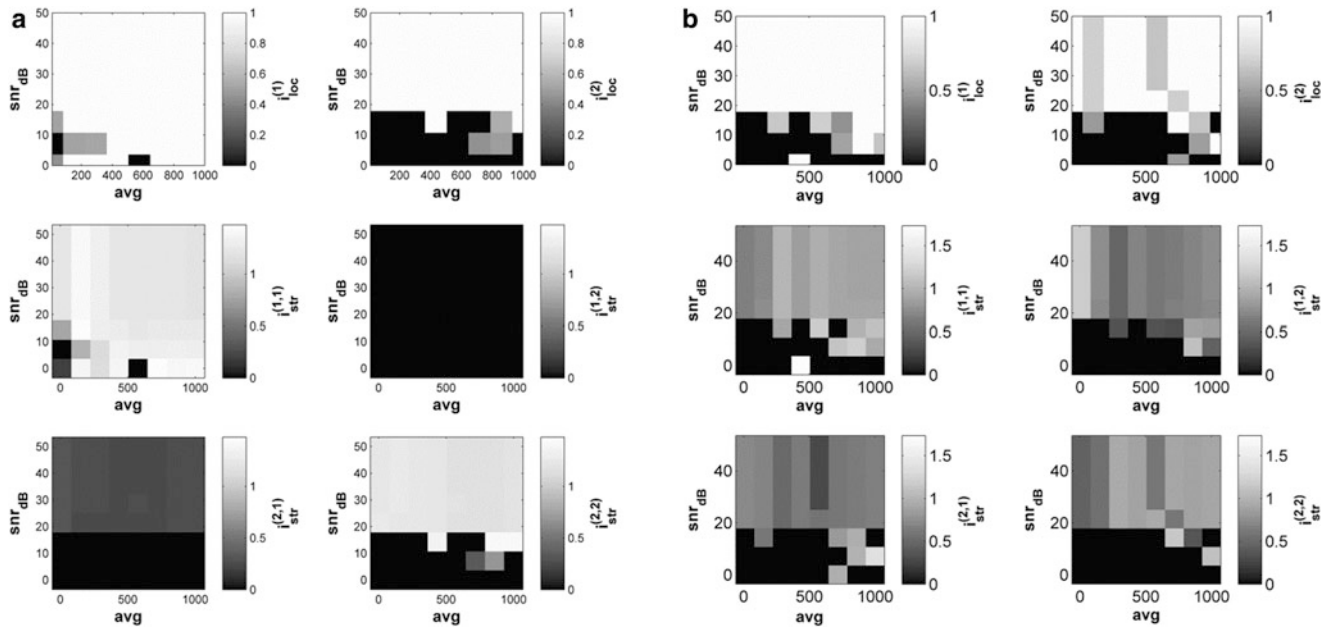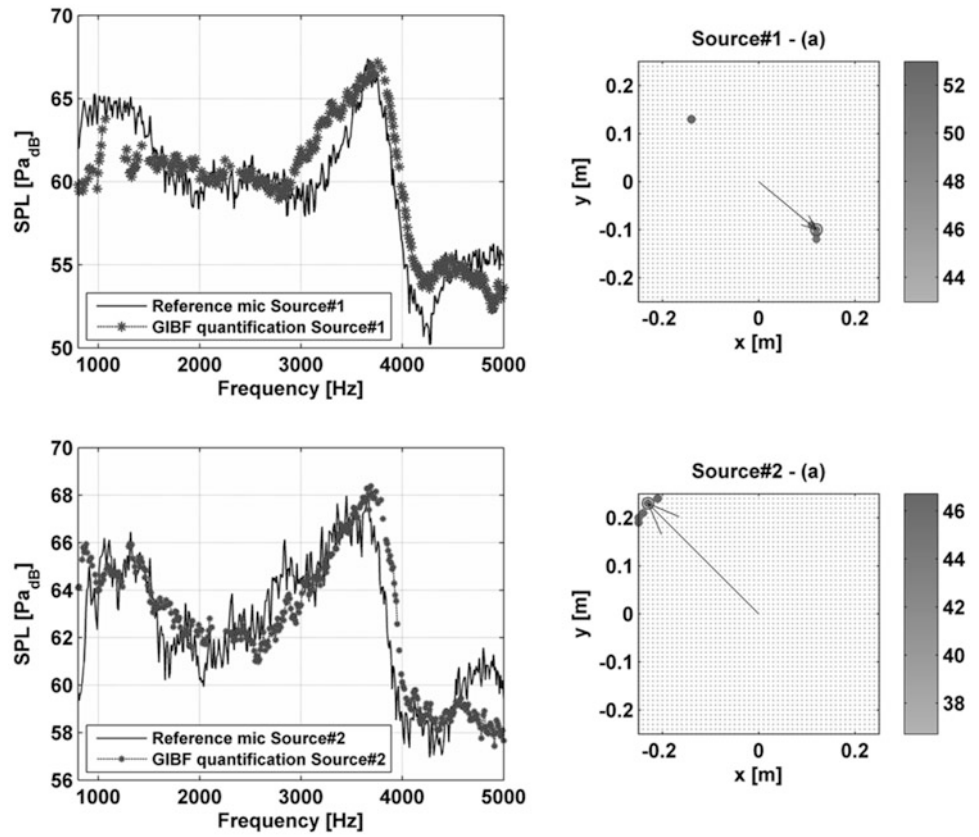
Fig. 5.8 i_{loc} and i_{str} for scenario c (**a**) and for scenario b (**b**). AVG versus SNR

Figure 5.10 shows the trend of the chosen regularization factor during the iterative process of the GIBF algorithm in the four cases. Quasi-optimality and GCV functions yield a similar regularization factor after the first iterations.

The strength of the source is 90 dB. The strength estimation using the different regularization strategies is shown in Table 5.2. The use of Eq. (5.14) instead of Eq. (5.13) has also demonstrated the same trend.

Fig. 5.9 GIBF with different regularization strategies using Eq. (5.13) for matrix inversion
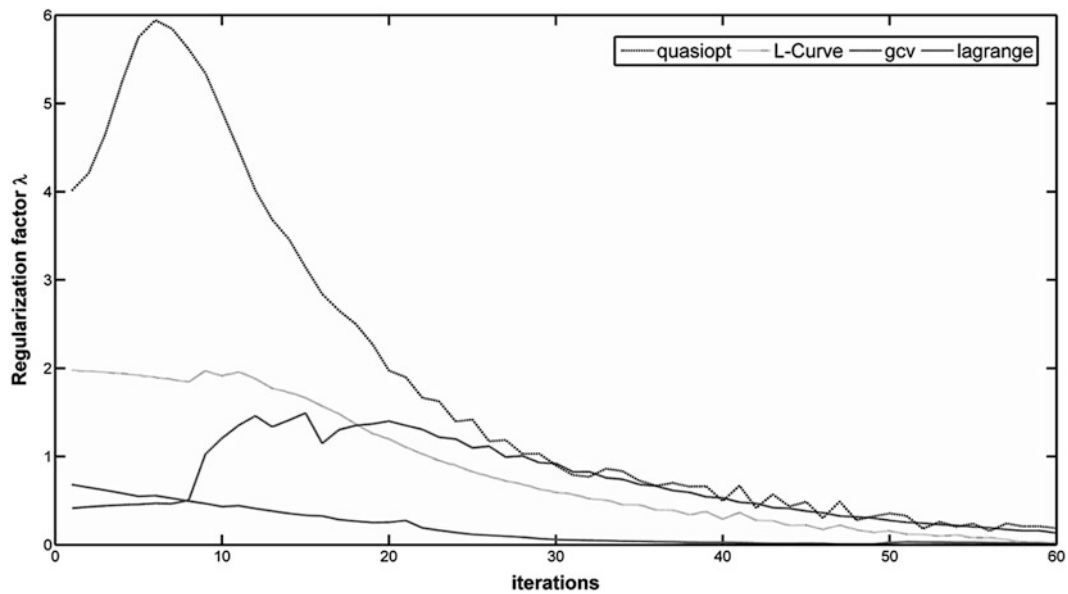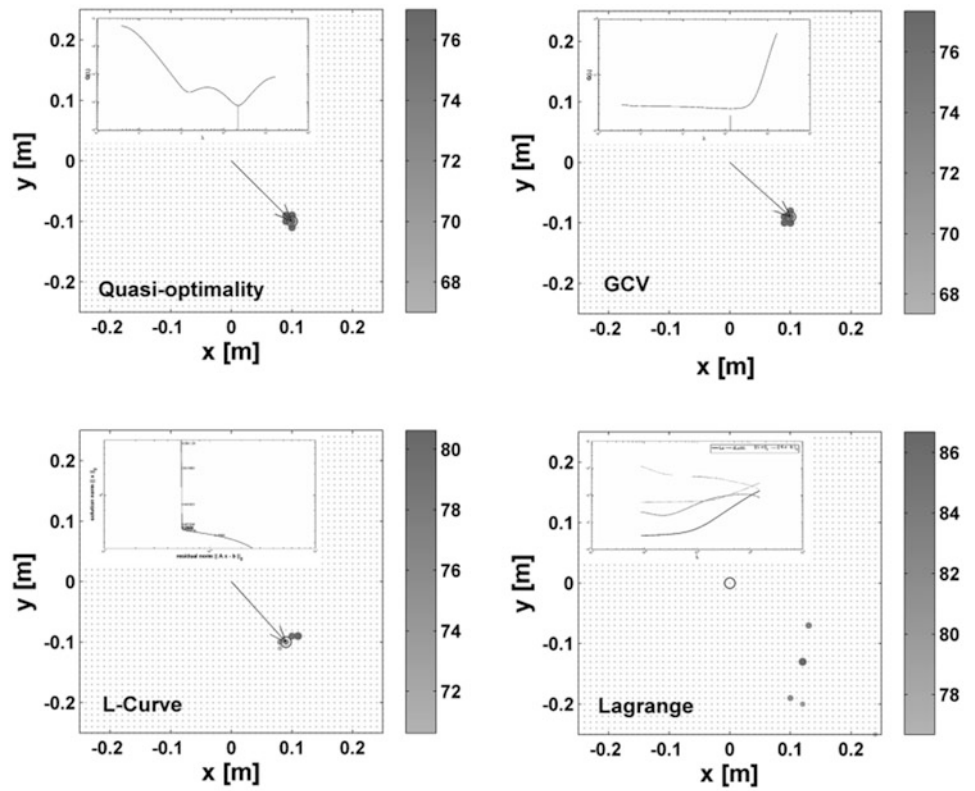
Fig. 5.10 Trend of regularization factor during GIBF iterations

Table 5.2 Strength estimation using GIBF with different regularization strategies

1. Quasi-opt	**2.** GCV	**3.** L-curve	**4.** Lagrange
90.8 dB	**90.9 dB**	**91 dB**	**/**
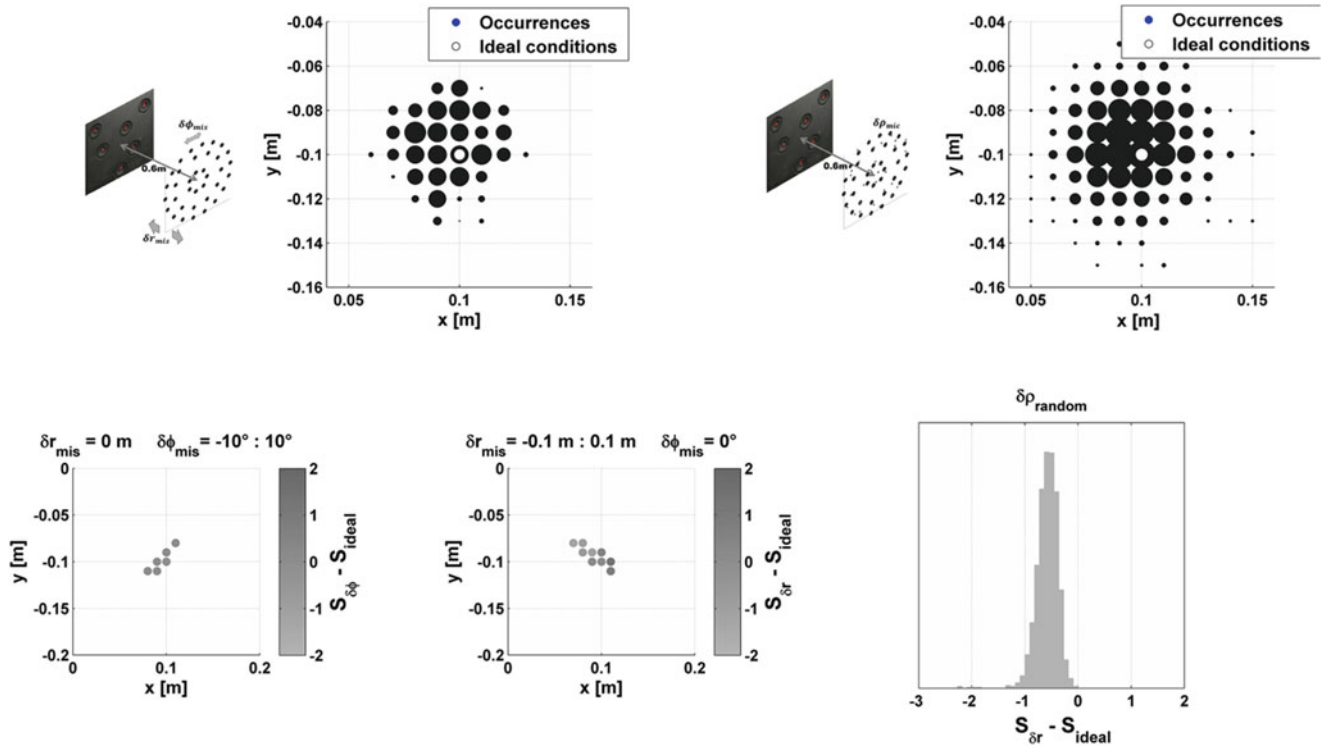
Fig. 5.11 GIBF with wrong positioning of the array (*top-left* and *bottom-left*) and GIBF with wrong positioning of microphones within the array (*top-left* and *bottom-left*)

5.6.4 Influence of Wrong Positioning of the Array and Its Microphones

The robustness of the algorithm to wrong specifications of the geometry has been tested by simulating the most common errors: wrong positioning of the array in the space, wrong positioning of the microphones within the array. In the first analysis the array error in positioning is made varying in the range: $r_{ideal} + \delta r_{mis} = 0.6m \pm 0.1m$ with a 0.01 m step for the distance to the target grid and $\Phi_{ideal} + \delta \Phi_{mis} = 0° \pm 10°$ with a step of 0.1 ° for the error in angle positioning. In the second case the position of each microphone is made randomly varying within a sphere of radius $\delta \rho_{mic} = 0.01$ m centered at the microphone ideal position The size of the dots in the maps in Fig. 5.11 is proportional to the number of occurrences in which the source has been localized in that position. In both analyses the localization error is within an area of about 0.05 m radius. The color of the dots in the graphs at the bottom-left side of Fig. 5.11 is proportional to the difference of the obtained source strength and the one in the ideal position (S_{ideal}). The quantification error is almost not present in the case of angle error, while, as expected, it is proportional to the distance error of the array from the target in the second case. Regarding the random case (Fig. 5.11 bottom-right), in the majority of the cases the source strength is slightly underestimated ($S_\delta - S_{ideal}$ is presented in dB).

5.7 Conclusions

The sensitivity analysis allowed better understanding the influence of most of the relevant parameters in the performances of the formulated GIBF combined with the PCA of the CSM. The main results can be summarized as follows:

– Computing the CSM taking a sufficient number of averages is crucial for correct source quantification and separation. A suitable rule of thumb is taking at least 10*M averages with M sensors in the array. Even though, if the uncorrelated sources spectra are similar, the separation may be not optimal.
– The localization, quantification and separation performances of GIBF are similarly influenced by the presence of background noise in the array measurements. A reasonable threshold is: $SNR \geq 20dB$.

– The conducted analyses on frequency resolution for calculating the CSM didn't show a clear trend, nevertheless 10 Hz resulted to be a good compromise for correctly reconstruct the spectra of the sources.
– The regularization strategy adopted for solving the inverse problem dramatically influences the results and it is crucial, for GIBF, to select the optimal regularization factor at each step of the iterative process. The analysis demonstrated that good options are the so-called quasi-optimality function or GCV function.
– A wrong positioning of the array, or of some microphones within it, introduces errors limited in an area of a 0.05 m radius for localization and a possible wrong estimation of the source within a $\pm 2dB$ range.

What shown in this analysis demonstrates the applicability of GIBF combined with PCA of the CSM for resolving complex acoustic fields, in presence of multiple uncorrelated sources, also with strong background noise. This makes it suitable for applications where these features are needed such as automotive applications, interior beamforming and aeroacoustics.

References

1. Suzuki T (2008) Generalized inverse beamforming algorithm resolving coherent/incoherent, distributed and multipole sources. In: 14th AIAA/CEAS aeroacoustics conference (29th AIAA aeroacoustics conference), Vancouver, 5–7 May 2008
2. Muller TJ (2002) Aeroacoustic measurements. Springer, Berlin
3. Zavala P (2012) Aeroacoustic source and moving source identification. PhD thesis, Faculty of Mech. Eng., University of Campinas, Sao Paulo
4. Dougherty RP (2011) Improved generalized inverse beamforming for jet noise. In: 17th AIAA/CEAS aeroacoustics conference, AIAA 2011–2769
5. Zavala P, De Roeck W, Janssens K, Arruda JRF, Sas P, Desmet W (2010) Monopole and dipole identification using generalized inverse beamforming. In: 16th AIAA/CEAS aeroacoustics conference, Stockholm, Sweden
6. Zavala P, De Roeck W, Janssens K, Arruda JRF, Sas P, Desmet W (2011) Generalized inverse beamforming with optimized regularization strategy. Mech Syst Signal Process 25:928–939
7. Hansen PC (1994) Regularization tools: a matlab package for analysis and solution of discrete ill-posed problems. Num Algorithms 6:1–35

Chapter 6
Active Noise Control Experiment Minimising Radiation of Active Energy

Uli Krause and Delf Sachau

Abstract The test set-up consists of so-called primary loudspeakers simulating the noise source and so-called secondary loudspeakers belonging to the active noise system (ANS). The ANS has two accelerometers and one microphone per secondary speaker. The microphone is located in the near sound field of the secondary loudspeaker. One accelerometer is fixed onto the loudspeaker cone. The other accelerometer is attached to the noise source. The control algorithm contains an adaptive feed-forward scheme for the amplitude of the control signal and an approach to compensate phase deviations. The ANS is tested in a configuration with two primary and two secondary loudspeakers.

Keywords Adaptive control • Acoustics • Active control • Adaptive structures • Sound intensity

6.1 Introduction of Adaptive Control of Active Sound Energy

Active noise control (ANC) is a nice approach and handy system when low frequency noise has to be attenuated and weight and space are limiting requirements. Typically only microphones are used in active noise systems (ANS). The acquired sound pressure is minimized, but the sound pressure is only the potential part of the acoustic energy. Our approach is different and minimizes the flow of active acoustic energy into an interior. This is achieved by minimizing the active sound power of all sound sources, which are, in particular, dominant noise sources and that of the ANS. Figure 6.1 shows the concept able to minimize the active sound power. The vibrating structure is divided into several elemental (primary) sources, each with its own phase shift. From each primary source the accelerations $a_\mathrm{p}(t)$ are taken and fed to the controller. The sound power of each secondary source is calculated from measured pressures $p_\mathrm{s}(t)$ and accelerations $a_\mathrm{s}(t)$ inside the digital controller. The control signal $y(t)$ is adapted so that the active sound intensity of each speaker becomes zero. This zero power phenomenon is widely known [1–3], but not, to the knowledge of the authors, experimentally verified for multichannel systems.

6.2 Controller Scheme

Figure 6.2 shows the controller which has been used in the experiments. The equations are discussed by means of a two by two system to keep the notation as simple as possible. The controller uses a complex feed-forward scheme with an filtered-reference-least-mean-square (FxLMS) algorithm [4]. These minimizes the column matrix of errors

$$e(k) = a_\mathrm{s}^\mathrm{m}(k) - \mathrm{diag}\left\{\kappa_\mathrm{sol}^\mathrm{c}\right\} a_\mathrm{p}^\mathrm{m}(k), \tag{6.1}$$

where $\kappa_\mathrm{sol}^\mathrm{c}$ are entirely real amplifications and $a_\mathrm{s}^\mathrm{m}(k)$, $a_\mathrm{p}^\mathrm{m}(k)$ denote discrete Fourier transforms at frequency bin k of secondary and primary source accelerations. The diag{•} operation creates a diagonal matrix from a column matrix. As reference $X(k)$ one of the primary source accelerations is selected, which is possible because the two signals belong to one noise source and so are correlated. By adaptation of the control $y^\mathrm{m}(k)$ with the complex filter weights $w(k)$ times reference $X(k)$ the errors $e(k)$ is minimized. The request of zero power output is enabled by ensuring zero active sound intensity at every secondary source

U. Krause • D. Sachau (✉)

Helmut-Schmidt-University, University of the Federal Armed Forces Hamburg, Holstenhofweg 85, Hamburg, 22043 Germany

e-mail: dsachau@hsu-hh.de

Fig. 6.1 Concept for active minimization of active energy
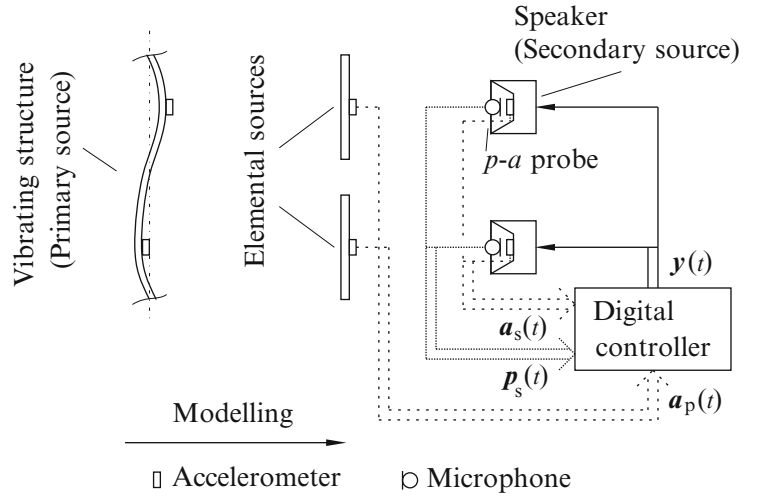
Fig. 6.2 Block diagram of controller
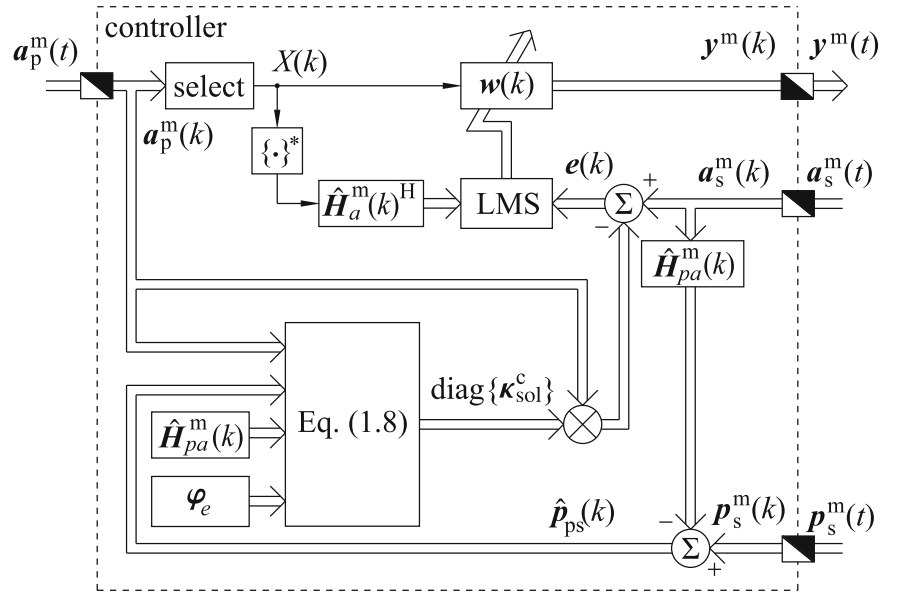
$$i_{\text{s}} = \begin{bmatrix} I_{\text{s1}} \\ I_{\text{s2}} \end{bmatrix} = \mathbf{0}. \tag{6.2}$$

The active sound intensities are calculated according to

$$i_{\text{s}} = -\frac{1}{2\omega}\text{diag}\left\{\left.1\right/\Lambda_1, \left.1\right/\Lambda_2\right\}\text{Im}\left\{\text{diag}\left\{\text{diag}\left\{e^{-j\varphi_e^1}, e^{-j\varphi_e^2}\right\} p_{\text{s}}^{\text{m}}(k)\right\}\left(a_{\text{s}}^{\text{m}}(k)\right)^*\right\}, \tag{6.3}$$

where $\varphi_e(j\omega)$ is the phase error and $\Lambda(j\omega)$ denotes the amplitude error of the measured complex sound intensity $C_c^m(j\omega)$ from the true sound intensity $C_s(j\omega)$ at angular frequency ω in the form [5]

$$C_{\text{s}}^{\text{m}}(j\omega) = C_{\text{s}}(j\omega)\,\Lambda(j\omega)\,e^{j\varphi_e(j\omega)}. \tag{6.4}$$

The minus sign in the terms $e^{-j\varphi_e^1}$ and $e^{-j\varphi_e^2}$ point out that with these terms a correction of the phase errors φ_e is included in (6.3). The amplitude error is not important as only (6.2) has to be guaranteed. Multiplying (6.2) with

$$-2\omega\text{diag}\{\Lambda_1, \Lambda_2\} \tag{6.5}$$

from the left yields

$$\text{Im}\left\{\text{diag}\left\{\text{diag}\left\{e^{-j\varphi_e^1},\ e^{-j\varphi_e^2}\right\}\boldsymbol{p}_s^m(k)\right\}\left(\boldsymbol{a}_s^m(k)\right)^*\right\} = \boldsymbol{0}. \tag{6.6}$$

The superposition of pressures at the secondary sources

$$\boldsymbol{p}_s^m = \boldsymbol{p}_{sp}^m + \widehat{\boldsymbol{H}}_{pa}^m \boldsymbol{a}_s^m, \tag{6.7}$$

where $\widehat{\boldsymbol{H}}_{pa}^m$ is a model of the complex transfer matrix from pressures to accelerations is inserted in (6.2). The required secondary source amplifications can afterwards be calculated from the system of equations (6.6). The result is given by

$$\boldsymbol{\kappa}_{sol}^c = -\boldsymbol{A}^{-1}\text{Im}\left\{\text{diag}\left\{\text{diag}\left\{e^{-j\varphi_e^1},\ e^{-j\varphi_e^2}\right\}\widehat{\boldsymbol{p}}_p^m(k)\right\}\left(\boldsymbol{a}_p^m(k)\right)^*\right\} \tag{6.8}$$

with

$$\boldsymbol{A} = \text{Im}\left\{\text{diag}\left\{\left(\boldsymbol{a}_p^m(k)\right)^*\right\}\text{diag}\left\{e^{-j\varphi_e^1},\ e^{-j\varphi_e^2}\right\}\widehat{\boldsymbol{H}}_{pa}^m(k)\text{diag}\left\{\boldsymbol{a}_p^m(k)\right\}\right\}. \tag{6.9}$$

6.3 Results

The experiments were conducted in a laboratory with low reverberation, see Fig. 6.3 right. The sound pressure is measured in the whole monitoring volume by a robot equipped with class 1 measuring microphones (Fig. 6.3).

The measuring setup for the sound intensity measurement is shown in Fig. 6.4. A sound intensity probe from Microflown has been used. The probe is able to measure particle velocity in three Cartesian coordinate directions instantaneously. Measurements were conducted at two planes, see Fig. 6.4.

Figure 6.5 shows the active sound intensity vector diagrams at a frequency $f = 315$ Hz. When comparing Fig. 6.5a, b left as well as right a reduction in active sound intensity is found. The direction of the active sound intensity vectors changes when secondary sources are active (ANS on). The reductions in length of the sound intensity vectors on the second measuring plane behind the secondary sources is larger than on plane 1.

The active sound power is analyzed with

$$P = \int_A \overrightarrow{I} \cdot d\overrightarrow{A} \tag{6.10}$$
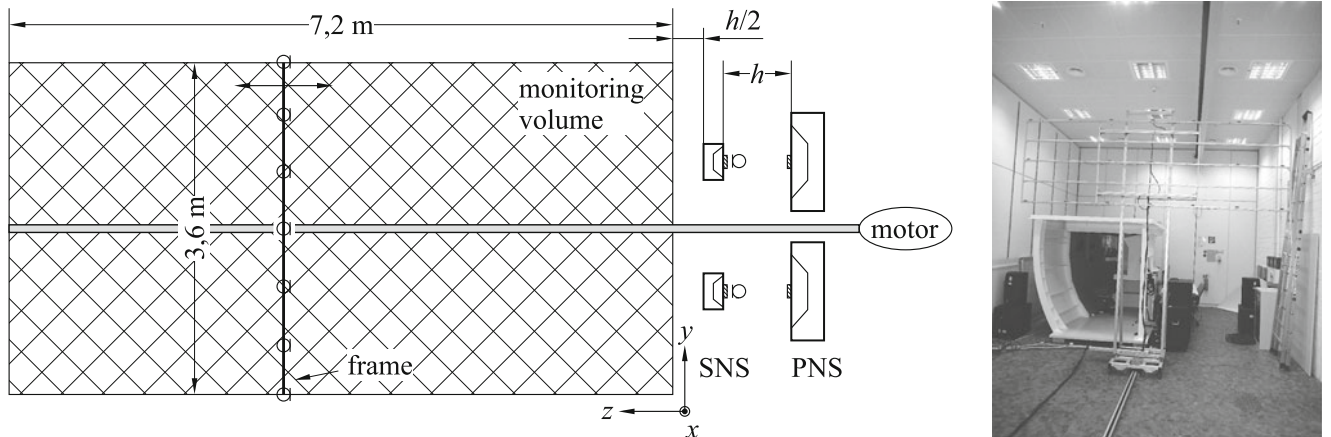
Fig. 6.3 Sound pressure measuring setup
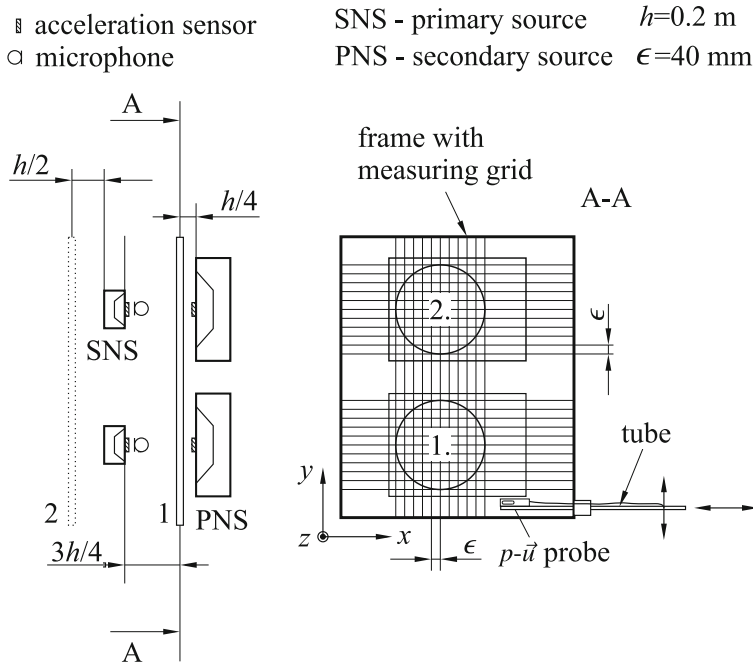
Fig. 6.4 Sound intensity measuring setup
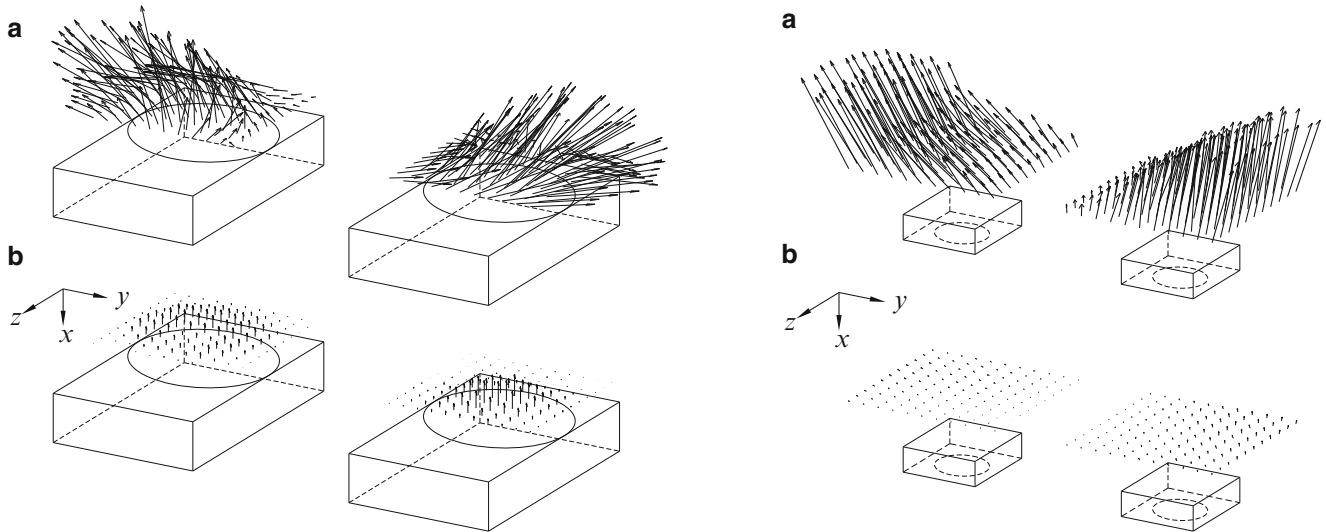
Fig. 6.5 Active sound intensity vector diagrams (**a**) with ANS off, (**b**) with ANS on

by evaluating Eq. (6.8) over the measurement surfaces. This yields the values of Table 6.1. The reduction in sound power level L_W decreases with increasing h/λ, where λ is the wavelength and h is the distance of primary and secondary sources, see Fig. 6.5 left.

The mean sound pressure level over all measuring points of the sound pressure map was calculated, see Table 6.2. A significant reduction in mean sound pressure level is achieved by the proposed approach. Similar to the results of measured sound power a decrease of the reduction in mean sound pressure level is found for increasing h/λ, which is plausible.

Table 6.1 Sound power level L_W
(a) for measurement plane 1, (b)
for measurement plane 2 when
ANS on/off

h/λ	L_W in dB on/off
(a)	
0.18	70.2/79.3
0.12	69.7/76.5
0.06	68.5/76.9
(b)	
0.18	54.5/63.7
0.12	46.9/61.7
0.06	40.1/60.1

Table 6.2 Spatial mean sound
pressure level $\overline{L}_p$ in laboratory
when ANS on/off

h/λ	$\overline{L}_p$ in dB on/off
0.18	62.0/77.4
0.12	53.5/73.0
0.06	53.2/76.3

6.4   Conclusions

The conducted experiments of the sound intensity based control algorithm showed the feasibility of the proposed concept. Further investigations might focus on stability regarding environmental perturbations.

References

1. Böhme S, Sachau D (2010) Single channel system for adaptive power minimization. In: Proceedings INTERNOISE 2010, Lisboa
2. Tanaka N, Takahashi K (2009) Active acoustic power control using zero power strategy. In: Proceedings INTERNOISE 2009, Ottawa
3. Elliott SJ, Joseph P, Nelson PA, Johnson ME (1991) Power output minimization and power absorption in the active control of sound. J Acoust Soc Am 90(5):2501–2512
4. Haykin S (2001) Adaptive filter theory. Prentice Hall, New Jersey
5. Fahy F (1998) Sound intensity. Spon Press, London

Chapter 7
Active Control of Transformer Noise by MIMO Algorithm

J.M. Liu and W.D. Zhu

Abstract The Transformer Noise is called hum mainly constructed by harmonic waves of 100 Hz, 200 Hz, 300 Hz, . . . , 1,400 Hz, 1,500 Hz. If each harmonic wave of a fixed frequency is stable to some extent measured at the position of error microphone, by producing the some amplitude wave with negative phase through the secondary source (the active control speaker), the noise at the position of error microphone will be greatly reduced. To reduce more than one position's noise, many active control speakers will be used, so the MIMO (Multi input Multi output) Frequency Response Function (FRF) matrix and MIMO algorithm are needed. In the paper, the relationship between preciseness of FRF and the stability of control system is discussed. The method to obtain the precise FRF matrix and the MIMO algorithm of ANC (Active Noise Control) are introduced. The algorithm is verified by field experiment with 2 speakers and 2 error microphones, the total noise in each microphone is reduced 6–10 dB at different time, the harmonic wave amplitude of fixed frequency can reduce 10–30 dB. The effect is prominent comparing to the results of other papers in active control of transformer noise.

Keywords Active noise control • Electrical transformer • MIMO • Stability • FRF

7.1 Introduction

Electrical industry is very important for the national economic development. The noise problems in this industry become more pressing. As the amounts of using electricity increases in urban city in recent years, many electrical transformers are installed near the residential area. The hum noise produced by the electric transformer which can reach as high as 80 ~100 dB [1], disturbing the living of people nearby. To control the noise of transformer is no time to delay.

In Fig. 7.1, is the electrical transformer installed in City Jinan of China, near the residential area. The hum noise produced by the transformer is illustrated as Fig. 7.2.

The hum noise of the transformer is caused by the vibration of iron core driven by magnetic flux, called the magnetic noise. The base frequency is 2 times of electric current wave, in china, it is 100 Hz. Besides the base frequency, there are high orders of harmonic waves. The noise mainly concentrates on 100 Hz, 200 Hz, 300 Hz, . . . ,1.4 kHz, 1.5 kHz. The bigger the volume of the transformer, the peaks are higher in lower frequency district; the smaller the volume of transformer, the peaks are higher in upper frequency district. The level of noise is in positive ratio with the flux intensity of iron core, the greater the power, the higher of the noise level.

The noise problem of electrical transformer had been studied by some institutes of large company such as Westinghouse and General Electronic as early as 1930s [2–6]. The studied subjects include the mechanism of transformer vibration and noise, acoustic characteristic and the means of suppressing noise, mainly based on the tests and the summarization of the experience.

Active Noise Control (ANC), also called suppressing noise with sound source, means using the secondary speaker manually to cancel the original primary noise [7]. This concept is first put forward by American Paul Lueg [8] and patented in 1934, to suppressing the noise according to sound wave cancellation of Yong's interference principle. Till 1950s with the electronic technology development, Olson, Conover etc. [9, 10] devised the test apparatus of ANC according to Lueg's thoughts. In 1970s by the help of modern control technology, Jessel, Swinbanks etc. [11–14] had made stable developments in depressing 1 dimensional conduit noise by ANC. After 1980s, with the appearance of high speed DSP chips, the ANC

J.M. Liu (✉)
China Orient Institute of Noise & Vibration, Beijing 100085, China
e-mail: liujm@coinv.com

W.D. Zhu
University of Maryland, Baltimore, MD 20250, USA

Fig. 7.1 Electrical transformer

Fig. 7.2 The spectrum of transformer noise
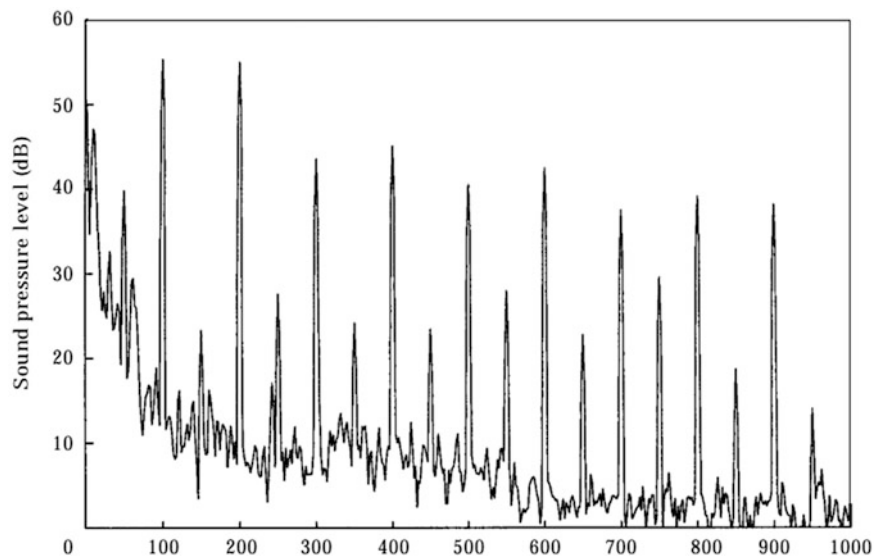
is developing toward the direction of adaptive and surpassing noise in 3 dimensions. By now, the ANC has experienced the "Design—Test—Theorization and Application" developing process, a lot of study outcomes in many applying fields have been obtained.

Active control the noise of the electrical transformer is the application of ANC, that suppress noise in 3 dimensions. In recent study, Limin Zhang, Jiancheng Tao etc. decrease one harmonic frequency wave noise of transformer in 100 Hz, in the field, illustrated as Fig. 7.3 [15]. In ANC, the harmonic wave of low frequency is easier to depress than high frequency, for the wave of low frequency varied speed is slower.

This paper mainly discussing the stable problem of MIMO control system in ANC for electric transformer. One 2 error microphones and 2 secondary speakers ANC control system has completed applied in the field, all the harmonic wave amplitude of fixed frequency have been reduce 10–30 dB, in the 2 error microphones' position, the total noise reduce 6–10 dB with original noise level about 60 dB. These 2 positions can be expanded to many positions according to MIMO control system concept, so in a finite space, the noise can be depressed in a whole.

7.2 MIMO Algorithm of Active Control of Transformer Noise and Stability Study

The Transformer Noise is called hum mainly constructed by harmonic waves of 100 Hz, 200 Hz, 300 Hz, ..., 1,400 Hz, 1,500 Hz. If each harmonic wave of a fixed frequency is stable to some extent measured at the position of error microphone, by producing the some amplitude wave with negative phase through the secondary source (the active control speaker), the noise at the position of error microphone will be greatly reduced. To reduce more than one position's noise, many active

control speakers will be used, so the MIMO (Multi input Multi output) Frequency Response Function (FRF) matrix and MIMO algorithm are needed. In measurement, A weighting curve can be used to measure the sound level. From 100 to 1,500 Hz range, 6–15 harmonic single frequencies may be chosen to control.

The measured preciseness of FRF from the secondary source to the error microphone is closely related to the MIMO control system stability. In the field, to obtain the precise FRF of in each harmonic wave, produce a single frequency harmonic wave in each secondary source, assure the amplitude of sound measured at the nearest error microphone will 20 dB greater than the background noise, the measured time is more than 10 s for each frequency from 100 to 1.5 kHz. By this way, a MIMO FRF matrix will be obtained for each fixed frequency.

When the FRF matrix is obtained, the active control can proceed. To present sound level measured at error microphones, compute the amplitude and phase of DA for each frequency, the DA new vector add the old vector, is the control vector, and also is the old vector for next control loop. In the beginning, the old vector is 0.

The sampling frequency for AD and DA is 10,240 Hz, for each 1,024 points, adjust the control wave, the Loop Time of control is 0.1 s.

When the DA amplitude surpass the threshold value set previously (for example, 2,000 mv), the control will stop, and measure the FRF matrix again. When the location of secondary sources or error microphones changed, this situation will happen.

There are secondary sources with number m (DA channel number is m), which are used to control error microphones with number n, here m<=n. According to least square method, for each harmonic wave, there is

$$
\begin{bmatrix} H_{11} & H_{12} & \cdots & H_{1m} \\ H_{21} & H_{22} & \cdots & H_{2m} \\ \vdots & \vdots & \ddots & \vdots \\ H_{n1} & H_{n2} & \cdots & H_{nm} \end{bmatrix} \begin{Bmatrix} F_1 \\ F_2 \\ \vdots \\ F_m \end{Bmatrix} = \begin{Bmatrix} Y_1 \\ Y_2 \\ \vdots \\ Y_n \end{Bmatrix}
\tag{7.1}
$$

The solutions is

$$
F = \left(H^H H \right)^{-1} H^H Y
\tag{7.2}
$$

Here $*^H$ means transform conjugate.

Let complex matrix $B = \left(H^H H \right)^{-1} H^H$, thus

$$
F = BY
\tag{7.3}
$$

The dimension of B is $m \times n$

Considering MIMO system, the FRF from secondary source to error microphone in each fixed frequency is constant complex, using complex H_{ji} to represent the element of FRF matrix, here i is the order number of secondary source (speaker) or DA channel, j is the order number of error microphone, or AD channel. For a fixed frequency, the noise vector measured at error microphone is a complex vector $A = \begin{Bmatrix} A_1 \\ A_2 \\ \vdots \\ A_n \end{Bmatrix}$. For the first time control, to compute the DA complex vector $D = \begin{Bmatrix} D_1 \\ D_2 \\ \vdots \\ D_m \end{Bmatrix}$, the equation is

$$HD + A = 0 \tag{7.4}$$

The least square solution is $D = -BA$.

Here H is measured FRF matrix, assuming H' is the real FRF matrix, after 1st loop control, the left noise vector $\Delta A = \begin{Bmatrix} \Delta A_1 \\ \Delta A_2 \\ \vdots \\ \Delta A_n \end{Bmatrix}$ is

$$\Delta A = \left(I - H' B \right) A \tag{7.5}$$

Here I is $n \times n$ unit matrix.

Let complex matrix $C = I - H' B$, the matrix dimension is $n \times n$

$$C = I - H' \left(H^H H \right)^{-1} H^H \tag{7.6}$$

Thus the left noise after 1st loop control is

$$\Delta A = CA \tag{7.7}$$

The control correcting vector $\Delta D = \begin{Bmatrix} \Delta D_1 \\ \Delta D_2 \\ \vdots \\ \Delta D_m \end{Bmatrix}$ will be

$$\Delta D = -B \Delta A \tag{7.8}$$

The real control vector for next control loop is $D + \Delta D$.

If background noise A keeps stable, after k times loop control, the left noise vector will be

$$\Delta A = C^k A \tag{7.9}$$

The control correcting vector can still be solved be Eq. (7.8).

Due to $\left| C^k \right| = |C|^k$, if $|C| < 1$, the MIMO control system will be stable.

To keep the MIMO control system stable, at lest the following condition must be guaranteed.

$$\left| I - H' \left(H^H H \right)^{-1} H^H \right| < 1 \tag{7.10}$$

Fig. 7.4 Stable circle
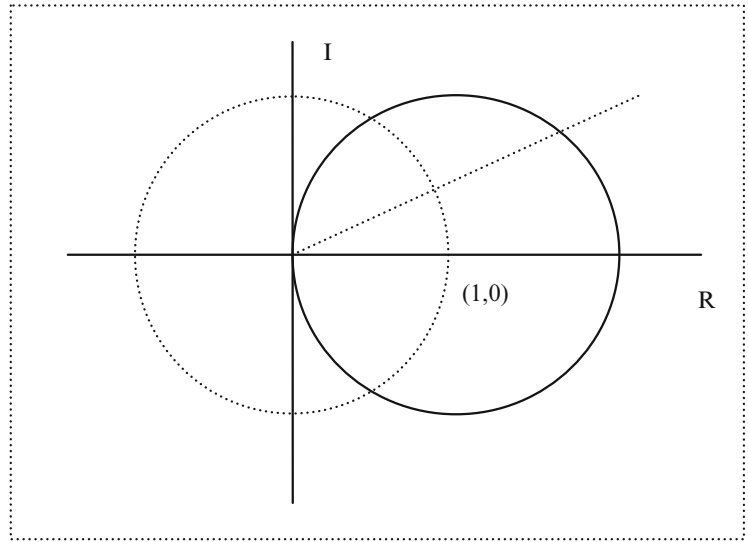
Fig. 7.5 Appratus Connecting
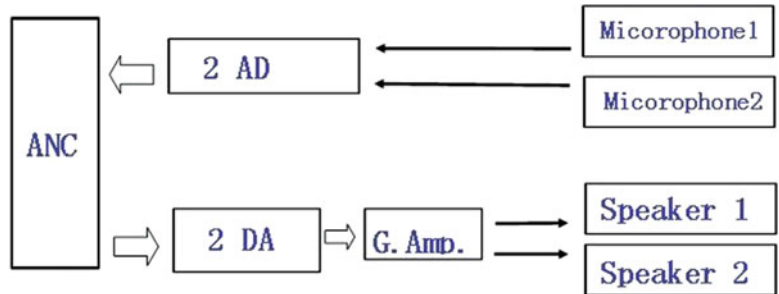
This condition depends on the preciseness of measured FRF matrix.

For 1×1 system, there is only one element in matrix C, the Eq. (7.10) simplified as

$$\left| 1 - H'/H \right| < 1 \tag{7.11}$$

Illustrated as Fig. 7.4, in the complex plane, only point H'/H is within the circle (the real line circle) of center is at point (1,0) and radius equals 1, the control system is stable.

Closer to point (1,0) is point H'/H, the better the control effect.

If the phase error between H' and H is more than 90°, H'/H will be in the left plane, the control system will be unstable.

Assume the phase of H'/H keeps constant, illustrated as dotted line in Fig. 7.4. If the amplitude of H increases, point H'/H will close to the origin, the system is stable. But if the amplitude of H decrease, point H'/H will go far away from the origin, once the amplitude surpasses the cross point of dotted line and real line circle, the system will be unstable. In real control system, the gain amplifier control the amplitude of H', when the gain amplifier decrease, amplitude of H' will also decrease, the phase of H' keeps unchanged, H'/H will close to the origin, the system is stable. By adjust gain amplifier to 0, the noise level without ANC can be measured, then the gain amplifier can adjust to the original position, the control will work again. In this process, the control system will keep stable. If the phase error of H'/H is 0, when the amplitude of H'/H is below 2, the system is stable, that means the amplitude stable range of H is $\left(0.5 \left| H' \right|, +\infty \right)$.

In the real control system, the noise is not strictly stable, and for the MIMO system, there are coupling factors, so the stable condition will be stricter than discussed above.

Fig. 7.6 The installation of
speakers and microphones in field

Table 7.1 The contrast of ANC effect

f(Hz)	100	200	300	400	500	600	700	800	900	1,000
Origin (dB)	73.10	58.70	61.11	59.40	56.43	54.99	41.62	42.82	44.32	43.68
ANC (dB)	45.71	35.71	45.38	35.39	46.35	47.31	29.49	36.66	33.25	40.13
Decrease (dB)	27.39	22.99	15.73	14.01	10.08	7.68	12.13	6.16	11.07	3.55

7.3 Field Application

Two secondary sources with gain amplifier and 2 error microphones, constructing a 2×2 MIMO ANC system, is applied in the field, to control the electric transformer, in City Qingdao of China. Figure 7.5 is the illustration diagram of apparatus connection, and Fig. 7.6 is the installation picture of speakers and microphones. In Fig. 7.6, two speakers are in work state, the others are reserved for future using. The distance of speaker to error microphones is 1.5 m. Both distances of 2 error microphones and 2 speakers are 2.5 m. The gain amplifier and computer which run the ANC module are put in the office.

Table 7.1 is the contrast for each harmonic wave before ANC control and after ANC control.

Figure 7.7 is the noise level without ANC control, Fig. 7.8 is the noise level after ANC control.

7.4 Discussion

For electric transformer ANC control, at each frequency, a MIMO FRF can be measured. The preciseness of FRF decides the control stability. If one of the frequencies is not stable, the control system will not work.

The preciseness of measured FRF is decides by measured method, the best way to measure FRF is produce a strong single harmonic sound in only one of the speaker at one time.

The gain amplifier characteristic is very important, except the low noise, in low frequency and high frequency the amplitude curve should be flat.

The distance of error microphone to secondary source will greatly influence the control system stability. The shorter the distance, the more preciseness of measured FRF, the more stable of the control system.

The phase preciseness of measured FRF is very important for ANC control, the phase stable range depends on the measured FRF amplitude. Increase the measured FRF amplitude artificially, the stable phase range will increase, but the control speed will decrease, so the control effect will be weakened. When the amplitude of measured FRF increases greatly or the gain amplifier turns to near 0, the stable phase range will increase to $(-90, 90)$.

By increasing the secondary sources number and error microphones number, in a limited space, the noise will be suppressed, only if the density of error microphones is enough.

Fig. 7.7 Without ANC control
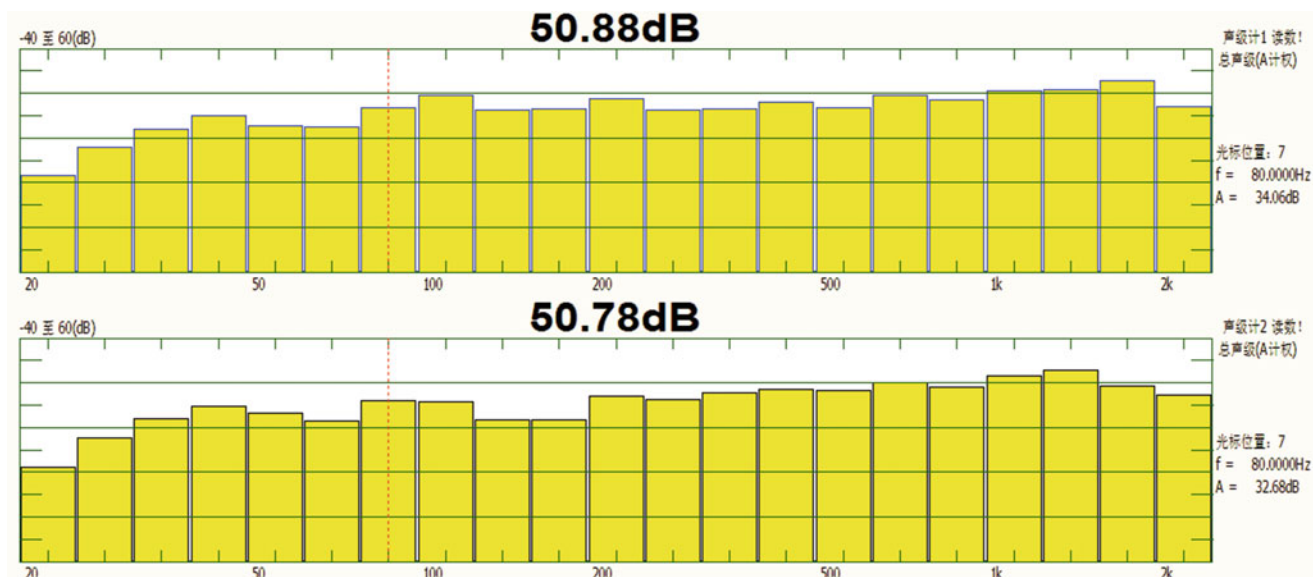
Fig. 7.8 With ANC control

The total control effect is closely depending on the level of origin noise, for high level noise, the control effect will be more efficient. For about 60 dB background noise, decrease 10 dB by ANC is not difficult.

References

1. Beranek B (1979) A method for predicting the audible noise emissions from large outdoors power transformers. IEEE Trans Power Apparat Syst 98(3):1109–1112
2. Kerr HW, Palmer S (1964) Large power transformers. IEE Electron Power 10(4):53–54
3. Kerr HW, Palmer S (1964) Developments in the design of large transformer. IEE Electron Power 11(5):823–832
4. Musonni F (1968) Transformer base vibrations. Electr World 61(13):37–41
5. Oppenheim A, Wasserman S (1964) Understanding acoustic enclosure systems. IEEE Trans Electr Ind 23(11):79–81
6. Chalmers A (1964) Plate steel reduces noise level. Electr World 161(14):138

7. Tian Jing (1991) The base concept of active noise control and developing foreground. Noise Vib Control (Chinese) 11(5):90–95
8. Lueg P (1936) Process of silencing sound oscillation. US Patent 2,043,416
9. Olson HF, May EG (1953) Electronic sound absorber. J Acoust Soc Am 25(6):1130–1136
10. Conover WB, Ringlee RJ (1955) Recent contributions to transformer audible noise control. Power Apparat Syst Part III Trans Am Inst Electr Eng 74(3):77–90
11. Jessel MJM, Mangiante GA (1972) Active sound absorbers in an air duct. J Sound Vib 23(3):383–390
12. Canevet G (1978) Active sound absorption in an air conditioning duct. J Sound Vib 58(3):333–345
13. Eghtesadi K, Hong WKW, Leventhall HG (1983) The tight coupled monopole active attenuator in a duct. Noise Control Eng J 20(1):16–20
14. Swinbanks MA, Vib JS (1973) The active control of sound propagation in long ducts. J Sound Vib 27(3):411–436
15. Limin Zhang, Jiancheng Tao, Xiaojun Qiu (2012) Active control of transformer noise with an internally synthesized reference signal. J Sound Vib 331:3466–3475

Chapter 8
Numerical Prediction Tools for Low-Frequency Sound Insulation in Lightweight Buildings

Juan Negreira and Delphine Bard

Abstract Lightweight wooden-framed constructions have steadily increased their market share in Sweden during the last two decades. Achieving acoustic and vibration comfort in wooden-based buildings is, however, still a challenging task. Wood is high in both strength and stiffness in relation to its weight, but its variability has repercussions on how sound propagates, this triggering sound insulation problems. Even if buildings comply with present-to-day regulations, complaints amid residents often arise due to low frequency noise, as it is outside the scope of the standards (where no analyses are performed below 50 Hz). In this investigation, laboratory acoustic sound insulation measurements carried out on a facade element according to the current standards, are intended to be reproduced and calibrated by means of the finite element method. In doing so, the first steps of a numerical predictive tool mimicking the real specimen, from 0 to 100 Hz, are presented. This will enable further research about phenomena occurring in the far low end of the frequency range, which is believed to be the cause of most nuisances reported by residents. Reliable predictive tools for addressing acoustic issues during the design phase avoid additional costs of building test prototypes and ensure a better acoustic performance.

Keywords Lightweight • Finite element method • Prediction tools • Low frequency noise • Sound transmission

8.1 Introduction

Multi-storey residential wooden framed building drastically gained popularity in Sweden since the year 1994, after a century-old ban regarding their construction (due to numerous urban fires in the 1800s) was lifted. Their vibration and acoustic performance was initially approved by applying the exact same regulations as for concrete buildings, even despite of their different behaviour; without thoroughly investigating whether the existent standardised sound insulation evaluation methods were appropriate. Yet those buildings complying with the regulations, complaints among the residents often arise due mainly to low frequency noise (below 100 Hz) which is left out of the scope of the norms. This indicates that the standardised single number evaluation of sound insulation should not be considered as neutral with respect to building technique and materials [1]. Consequently, the frequency range of analysis was increased down to 50 Hz in the year 1999. The requirements in Sweden thus currently demand measurements and evaluation in the extended frequency range 50–3,150 Hz, whereas in other countries the standardised range still applies, i.e. 100–3,150 Hz.

Investigations performed lately in the frame of the Swedish project AkuLite aimed at highlighting the importance of including low frequencies when evaluating sound insulation in lightweight buildings. In [1], statistical analyses between objective measured parameters (accelerations, deflections, etc.) and subjective ratings of people living in the apartments that were measured, were performed. A total of ten relatively new buildings (less than 10 years) were measured; four of them having a traditional wooden framework and flooring boards, one having a cold-formed thin-walled steel framework, four being made of cross laminated timber (CLT) and one having walls and floors made of massive concrete cast in-situ. Regarding airborne sound insulation, the rating $R'_w + C_{l,50-3100}$ [2–4] was proven to be adequate as compared with subjective perception, yet being important that the frequency of analysis starts at 50 Hz, as the correlation given by the statistical parameter R^2 decreased considerably from 73 % to 58 % when starting at 100 Hz. No further improvement in the correlation was found when including frequencies down to 20 Hz. When analysing the impact sound, however, including frequencies down to 20 Hz improved the correlation of measurements to occupants' rating of annoyance from 32 % using $L'_{n,w} + C_{l,50-2500}$ [5] to 85 %

_____

J. Negreira (✉) • D. Bard
Department of Construction Sciences, Lund University, John Ericssons väg 1, 22363 Lund, Sweden
e-mail: juan.negreira@construction.lth.se

when including a new proposed spectrum adaptation term $L'_{n,w} + C_{l,\text{Akulite},20-2500}$. The latter highlights the importance of including low frequencies in the evaluation of such problems and paves the way for more research to be carried out in, for example, other type of buildings, and also preferably from different countries (i.e. not just Sweden) [1].

In this investigation, a preliminary parameter study of a double leaf wall in terms of airborne sound transmission is performed. The long-term aim with the knowledge stemming from this study, is to eventually create reliable prediction tools which can mimic the low frequency behaviour of more complex construction elements such as facades. This was performed by means of the finite element (FE) method, which has been proven to be a powerful tool to address low frequency problems in an accurate manner (e.g. [6]). Research and development in the field of building acoustics has thus far being mainly carried out in terms of measurements, but the introduction and development of accurate predictive tools has a big potential in terms of economics, since issues can be tackled during the design phase instead of in test buildings and mockups, and also to obtain better buildings from an acoustic point of view.

8.2 Governing Theory

8.2.1 Structure-Acoustic Analysis

By deriving independent FE formulations for both the acoustic (referred to as F) and the structural domain (denoted as S) and eventually imposing continuity conditions in terms of displacements and pressures at the domain-separating boundaries, structure-acoustic systems can be analysed. Note that linear problems are being considered for both domains, due to the amplitudes of the vibrations dealt with being relatively small. More details of FE formulations than the ones presented here can be found, e.g. [7, 8].

8.2.1.1 Structural Domain

The differential equation of motion for the continuum formulation of a three-dimensional solid, occupying the domain Ω_S, is given by

$$\tilde{\nabla}^T \boldsymbol{\sigma}_S + \mathbf{b}_S = \rho_S \frac{\partial^2 \mathbf{u}_S}{\partial t^2}, \tag{8.1}$$

$\boldsymbol{\sigma}_S$ being the matrix representation of the stress tensor, $\mathbf{b}_S$ the body force vector, ρ_S the mass density, $\mathbf{u}_S$ the displacement vector, $\tilde{\nabla}$ a differential operator matrix and t the time. A FE discretisation and use of Galerkin's method results in the following FE formulation

$$\mathbf{M}_S \ddot{\mathbf{a}}_S + \mathbf{K}_S \mathbf{a}_S = \mathbf{f}_{l,S} + \mathbf{f}_{b,S}, \tag{8.2}$$

$$\mathbf{M}_S = \int_{\Omega_S} \mathbf{N}_S^T \rho_S \mathbf{N}_S \, dV, \qquad\qquad \mathbf{K}_S = \int_{\Omega_S} (\tilde{\nabla}\mathbf{N}_S)^T \mathbf{D}_S \tilde{\nabla}\mathbf{N}_S \, dV,$$

$$\mathbf{f}_{l,S} = \int_{\Omega_S} \mathbf{N}_S^T \mathbf{b}_S \, dV, \qquad\qquad \mathbf{f}_{b,S} = \int_{\partial\Omega_S} \mathbf{N}_S^T \mathbf{t}_S \, dS. \tag{8.3}$$

where $\mathbf{M}_S$ is the mass matrix, $\mathbf{K}_S$ is the stiffness matrix, $\mathbf{a}_S$ is the nodal displacement vector, $\mathbf{f}_{l,S}$ is the body load vector, $\mathbf{f}_{b,S}$ is the boundary load vector, $\mathbf{N}_S$ contains the FE interpolation functions, $\mathbf{D}_S$ is the constitutive stress-strain matrix and $\mathbf{t}_S$ is the surface traction vector. Note that the term $\mathbf{C}_S \dot{\mathbf{a}}_s$ has been omitted here, where $\mathbf{C}_S$ is the damping matrix. The latter terms would normally be added to the left-hand side of Eq. (8.2) to account for viscous forces present in the structure.

8.2.1.2 Acoustic Fluid Domain

Apart of the already mentioned assumption of small displacements, the governing equations of the acoustic fluid are derived assuming the fluid to be irrotational and inviscid. The motion of the fluid in the acoustic fluid domain Ω_F, choosing the acoustic pressure as the primary variable (other primary variables e.g. fluid displacement could be employed) is governed by the equation of motion and the continuity equation [9]:

$$\rho_0 \frac{\partial^2 \mathbf{u}_F}{\partial t^2} + R \frac{\partial \mathbf{u}_F}{\partial t} + \nabla p_F = 0, \tag{8.4}$$

$$\frac{\partial p_F}{\partial t} + \rho_0 c_0^2 \nabla \cdot \frac{\partial \mathbf{u}_F}{\partial t} = 0, \tag{8.5}$$

where ρ_0 is the static density, R is the flow resistivity, ∇ is the gradient operator, p_F is the acoustic pressure and c_0 is the speed of sound. By differentiating Eq. (8.5) with respect to time and inserting Eq. (8.4), the wave equation in the acoustic fluid domain is obtained as

$$\frac{1}{c_0^2} \frac{\partial^2 p_F}{\partial t^2} + \frac{R}{\rho_0 c_0^2} \frac{\partial p_F}{\partial t} - \nabla^2 p_F = 0. \tag{8.6}$$

Performing again a FE discretisation and use of Galerkin's method results in an FE formulation in the acoustic fluid domain, given by

$$\mathbf{M}_F \ddot{\mathbf{p}}_F + \mathbf{C}_F \dot{\mathbf{p}}_F + \mathbf{K}_F \mathbf{p}_F = \mathbf{f}_{b,F}, \tag{8.7}$$

$$\mathbf{M}_F = \frac{1}{c_0^2} \int_{\Omega_F} \mathbf{N}_F^T \mathbf{N}_F \, dV, \qquad\qquad \mathbf{C}_F = \frac{R}{\rho_0 c_0^2} \int_{\Omega_F} \mathbf{N}_F^T \mathbf{N}_F \, dV,$$

$$\mathbf{K}_F = \int_{\Omega_F} (\nabla \mathbf{N}_F)^T \nabla \mathbf{N}_F \, dV, \qquad\qquad \mathbf{f}_{b,F} = \int_{\partial\Omega_F} \mathbf{N}_F^T \mathbf{n}_F^T \nabla p_F \, dS, \tag{8.8}$$

where $\mathbf{p}_F$ is the nodal pressure vector, $\mathbf{f}_{b,F}$ is the boundary load vector and $\mathbf{n}_F^T$ is the boundary normal vector, pointing outwards from the acoustic fluid domain.

8.2.1.3 Coupling of Domains

At the domain-separating boundaries connecting the structural to the acoustic fluid domain ($\partial\Omega_{SF}$), continuity conditions in terms of both displacements and pressures are prescribed as

$$\mathbf{u}_S \mathbf{n}_F = \mathbf{u}_F \mathbf{n}_F, \tag{8.9}$$

$$\sigma_S|_{n_F} = -p_F, \tag{8.10}$$

where $\sigma_S|_{n_F}$ is the stress normal to $\partial\Omega_{SF}$. The spatial coupling matrix is defined as

$$\mathbf{H}_{SF} = \int_{\partial\Omega_{SF}} \mathbf{N}_S^T \mathbf{n}_F \mathbf{N}_F \, dS, \tag{8.11}$$

and the boundary load vectors at $\partial\Omega_{SF}$ can then be rewritten as

$$\mathbf{f}_{b,S} = \mathbf{H}_{SF} \mathbf{p}_F, \tag{8.12}$$

$$\mathbf{f}_{b,F} = -\rho_0 \mathbf{H}_{SF}^T \ddot{\mathbf{a}}_S - R \mathbf{H}_{SF}^T \dot{\mathbf{a}}_S. \tag{8.13}$$

Using Eqs. (8.12) and (8.13) in combination with Eqs. (8.2) and (8.7) results in the structure-acoustic system of equations

$$\begin{bmatrix} \mathbf{M}_S & \mathbf{0} \\ \rho_0 \mathbf{H}_{SF}^T & \mathbf{M}_F \end{bmatrix} \begin{bmatrix} \ddot{\mathbf{a}}_S \\ \ddot{\mathbf{p}}_F \end{bmatrix} + \begin{bmatrix} \mathbf{C}_S & \mathbf{0} \\ R\mathbf{H}_{SF}^T & \mathbf{C}_F \end{bmatrix} \begin{bmatrix} \dot{\mathbf{a}}_S \\ \dot{\mathbf{p}}_F \end{bmatrix} + \begin{bmatrix} \mathbf{K}_S & -\mathbf{H}_{SF} \\ \mathbf{0} & \mathbf{K}_F \end{bmatrix} \begin{bmatrix} \mathbf{a}_S \\ \mathbf{p}_F \end{bmatrix} = \begin{bmatrix} \mathbf{f}_{l,S} \\ \mathbf{0} \end{bmatrix} + \begin{bmatrix} \mathbf{f}_{b,S} \\ \mathbf{f}_{b,F} \end{bmatrix}, \tag{8.14}$$

where $\mathbf{f}_{b,S}$ and $\mathbf{f}_{b,F}$ contain contributions from the parts of the domain boundaries $\partial\Omega_S$ and $\partial\Omega_F$, respectively, that are separated from the interface boundary $\partial\Omega_{SF}$.

8.2.2 Porous Material Models

Different types of mineral wools are often introduced in walls and facades of lightweight buildings so as to improve thermal and acoustic insulation. The way waves propagate is modified when they impinge in the porous material, as they are forced to travel a longer distance, i.e. a dampening effect taking place due to friction at the surface of the fibres. A porous material can be modelled by either using empirical models (i.e. formulae based on experimental power laws), or analytical models (where assumptions about the geometry and behaviour of the structural frame and the interaction with the air are taken). For more information about this matter, see e.g. [10].

In [10], the influence of including acoustic media in floor, ceiling, and wall cavities of lightweight wooden buildings was studied for impact loads. The main conclusion drawn there from the numerical studies is that acoustic media affect the vibration transmission and must then be considered when performing low-frequency vibration analyses. Generally, the transmitted vibrations are overestimated if air alone is included in the cavities, meaning that the insulation present in reality in the structural elements should also be considered, as it introduces a more realistic dampening effect. In line with the latter, a comparative study between three different ways of modelling insulation was also carried out in [10], the conclusion being that in their valid frequency ranges, the different methods for modelling the porous material that were tried yield very similar results. Based on the latter statement, in the subsequent analyses only one model was considered (the analytical model with rigid structural frame) due to its wider frequency rage of validity (the two empirical models tried give unphysical behaviour at lower frequencies).

8.2.2.1 Equivalent Acoustic Fluid Model: Rigid Structural Frame—Model Description

Phenomenological equivalent acoustic fluid models can be adopted sometimes if the wave lengths are much larger than the characteristic dimensions of the microstructure, avoiding the practically impossible task of modelling the exact microstructure of porous materials. Different assumptions regarding the geometry and behaviour of the structural frame and the interaction between the frame and the acoustic fluid must be adopted, see [11, 12]. The model presented in here considers the porous materials as an equivalent acoustic fluids, their being analysed with the numerical methods employed for acoustic fluids and are integrated in a structure-acoustic model in a straightforward manner by modifying the coefficients in Eq. (8.5). Also, these models involve two properties of the structural frame, namely the porosity ϕ and the structure factor K_S, also known as the tortuosity. ϕ is the ratio of fluid volume to total volume, while K_S is defined as $\rho_e = K_S \rho_0$, relating the density of the acoustic fluid in the pores to an effective density ρ_e of the equivalent acoustic fluid. With a rigid structural frame, the equation of motion and the continuity equation in Eqs. (8.4) and (8.5), respectively, become

$$K_S \rho_0 \frac{\partial^2 u_F}{\partial t^2} + R \frac{\partial u_F}{\partial t} + \nabla p_F = 0, \tag{8.15}$$

$$\phi \frac{\partial p_F}{\partial t} + \rho_0 c_0^2 \nabla \cdot \frac{\partial u_F}{\partial t} = 0. \tag{8.16}$$

By differentiating Eq. (8.16) with respect to time and inserting Eq. (8.15), the wave equation for the equivalent acoustic fluid is obtained as

$$\frac{K_S \phi}{c_0^2} \frac{\partial^2 p_F}{\partial t^2} + \frac{R \phi}{\rho_0 c_0^2} \frac{\partial p_F}{\partial t} - \nabla^2 p_F = 0, \tag{8.17}$$

which is similar the wave equation for an acoustic fluid given in Eq. (8.6), the coefficients being modified by the properties of the structural frame. In Eq. (8.6), R accounts for the dissipation of energy in an acoustic fluid domain in a smeared approach, whereas in Eq. (8.17) it is a property of the structural frame.

8.3 Double Leaf Wall

Even though the final aim is to create a FE prediction tool for a facade element which can eventually be used to improve its performance, it was first considered that a simpler model should be used to analyse some general parameters influencing the modelling in terms of a parametric study. Thus, an intensive study was undertaken in a double leaf wall. The results stemming from here will then be used in Sect. 8.4.
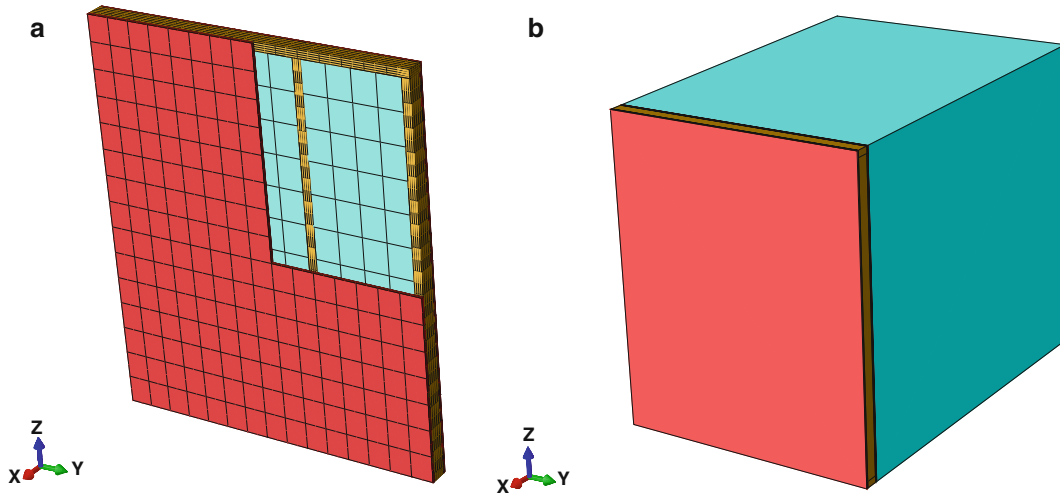
Fig. 8.1 FE model employed in the parametric analysis. The gypsum boards are shown in *red*, the studs and beams in *brown*, and the acoustic media (air and insulation) in *light blue*. (**a**) Double leaf wall. (**b**) Wall and receiving room model (Color figure online)

Table 8.1 Properties of the solid materials

Wood	E_1=8,500	E_2=E_3=350	G_{12}=G_{13}=700	G_{23}=50	ν_{12}=ν_{13}=0.2	ν_{13}=0.3	ρ=432
Gypsum board	E=2,000	ν=0.2	ρ=692.3	–	–	–	–
Air	K=141,360	ν=0.3	ρ=1.2	–	–	–	–
Porous material	R=6,000	ϕ=0.96	α=1.1	–	–	–	–

The elastic E and bulk K moduli are given in [MPa], the densities ρ in [kg/m^3] and the resistivity R in [Nm^{-4}s]. The other quantities are dimensionless

8.3.1 Finite Element Model

A section of a wooden double leaf wall was modelled in the commercial FE software Abaqus [13], see Fig. 8.1a. The wall panel consisted of a $2200 \times 1845 \times 90$ mm^3 wood frame covered with one 13 mm thick gypsum plate on each side, creating a model with three cavities between the plates and the vertical studs. The centre-to-centre distance between the studs was set to 600 mm, their cross-section being 90×45 mm^2. Full interaction between parts was considered, and the outer frame of the double leaf wall was pinned all around. The properties for the materials were either provided by the manufacturers or measured in the laboratory, see Table 8.1. The computational mesh for all structural parts was obtained using solid 3D stress finite hexahedral elements with 20 nodes and quadratic interpolation. Regarding the acoustic media, linear acoustic hexahedral elements with eight nodes were utilised. The element size for all parts was decided based on the wavelengths expected to occur in the model at the higher frequency of interest, i.e. 100 Hz. Damping was included in the model, its matrix being constructed as a linear combination of the stiffness and mass matrices by means of Rayleigh damping [14].

Also, a room attached to the wall, the so-called receiving room was modelled on the opposite side of the excitation, its dimensions being $2200 \times 1845 \times 2500$ mm^3. An eigenvalue analysis showed the first three room modes to occur at 68.1, 77.8 and 92.4 Hz, which fall within frequency range of analysis (0–100 Hz). The boundary conditions considered in the free sides on the room was $\nabla \mathbf{p} = 0$, i.e. rigid reflecting surfaces. The whole model can be seen in Fig. 8.1b.

Note that in this first investigation, knowledge on the behaviour of the structure was gained by investigating the parameters affecting the response, this eventually enabling a more refined model to be developed on the basis of these findings. Thus, the relative differences between the modelled results being of greater importance than the absolute correlation between the output from the simulations and the existent measurements.

The wall was excited by a diffuse field of amplitude 1 Pa on one side of the wall with frequencies ranging from 0 to 100 Hz. In order to evaluate and to compare results from the analyses performed, the sound pressure level was evaluated in the receiving room as

$$L_p(\mathrm{f}) = 10 \cdot \log \left(\frac{\sum_{i=1}^{n} \tilde{p}_{\mathrm{RMS}_i}^2(\mathrm{f})}{\mathrm{n} \cdot \tilde{p}_{\mathrm{REF}}^2} \right), \tag{8.18}$$

Fig. 8.2 Diffuse field excitation
in Abaqus [13]
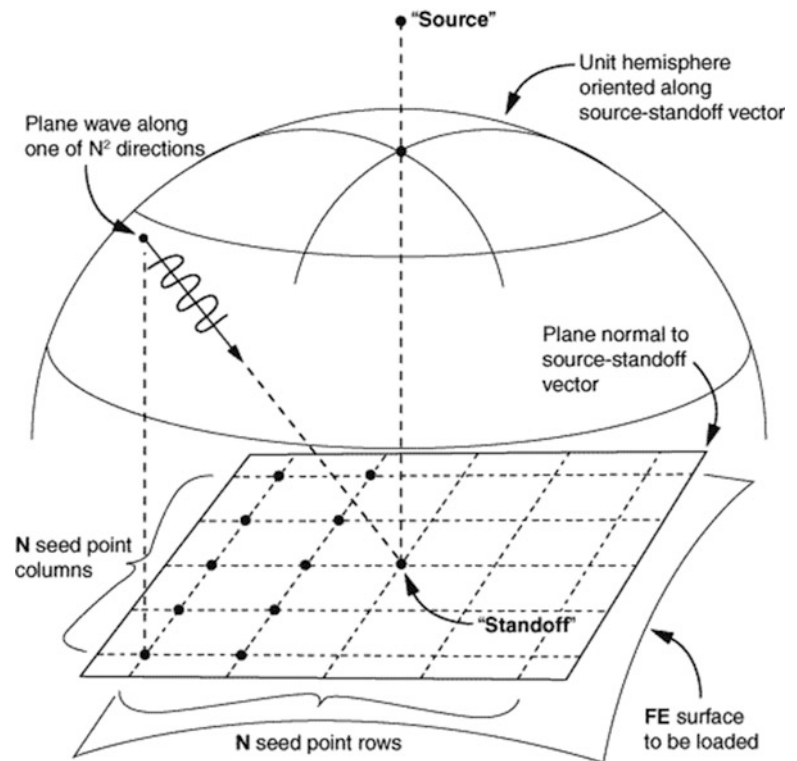
where $\tilde{p}_{\mathrm{RMS}_i}$ (f) is the root mean square (RMS) in Pascals of the sound pressure level at each frequency and n is the number of evaluation nodes in the FE model. The reference pressure p_{REF} is $2 \cdot 10^{-5}$ Pa [15]. As evaluation points, all nodes in the receiving room (if not otherwise stated) were considered, so as to have a good average of the sound pressure level.

8.3.2 Diffuse Field in the Low Frequencies

The assumption of having a diffuse field excitation from the sending room does not strictly apply in the frequency range of interest here (even though in laboratory conditions it is closer than for in-situ measurements) . The Schroeder frequency marks the cross-over between the low frequency region, where separate modes dominate, and the high frequency region, dominated by dense modal overlap with statistical properties. For typical residential listening environments, it normally falls between 100 and 200 Hz [16], hence a non-diffuse field being probably present for our case in reality in the frequency range of interest.

The basic assumption of diffuse-field theory is that the sound field in the room is diffuse, its being so if the following two conditions are fulfilled [16]:

- At any position in the room the reverberant sound waves are incident from all directions with equal intensity (and random phase relations).
- The reverberant sound field is the same at every position in the room.

A perfect diffuse field can be obtained by summing up the effect of an infinite number of uncorrelated plane waves whose directions are equally spatially spread. In Abaqus, the diffuse field loading condition is approximated by a number of deterministic incident plane waves coming from angles distributed over a hemisphere encapsulating the loaded surface, see Fig. 8.2. One must specify a seed number N (N^2 being the deterministic incident plane waves travelling along vectors distributed over the hemisphere so that the incident power per solid angle approximates a diffuse incident field), a source and a standoff point. The latter two points primarily orient the loaded surface with respect to the incoming reverberant field. The hemisphere is centered at the standoff point, and its apex is the source point [13].

Laboratory measurements of airborne sound insulation in building elements are dealt with in ISO 140-3 [3], whereas for field measurements ISO 140-4 [4] applies. Even though in the laboratory diffuse field conditions can be improved by

Fig. 8.3 FE model of the facade element. The outer part of it is the double gypsum layer (in *red* colour). (**a**) Detail of the facade. (**b**) Open facade with acoustic media (Color figure online)
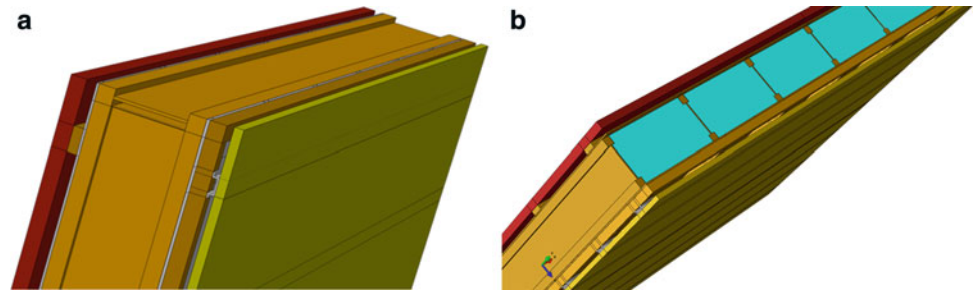
Table 8.2 Reference model

Acoustic media	Air and insulation in the wall cavities
Seed number	30 seeds (i.e. 900 incident plane waves)
Source point	1.6 m away from the wall
Standoff point	2 cm away from the wall
Load type	Diffuse field on wall surface
Evaluation points	All nodes in the receiving room
Receiving room volume	$\approx 10\,\mathrm{m}^3$
Sending room	Not included

the installation of diffusers in both sending and receiving room and also because of the fact that the rooms are larger than $50\,\mathrm{m}^3$, the latter is unfortunately not the case of in-situ measurements, as many dwellings have rooms of less than $50\,\mathrm{m}^3$. Both norms allow measurements in diffuse field conditions to be taken down to 50 Hz, the guidances presented there advised to not be followed for rooms of volumes less than $50\,\mathrm{m}^3$ due to the lack of repeatability and non diffuse field conditions. Several investigations aimed at proposing reliable methods with increased repeatability and reliability in the low-frequency range, i.e. in the 50, 63 and 80 Hz third octave bands, even for smaller rooms, namely for example [17, 18].

In the investigation presented here, and keeping in mind that laboratory measurements are to be mimicked (i.e. more control over the diffuse field), a diffuse field excitation was considered in the FE model for the parametric study (Fig. 8.3).

8.3.3   Results: Parametric Study

A parametric study was carried out in the double leaf wall described in Sect. 8.3.1. A reference model was considered (cf. Table 8.2), several parameters being varied subsequently, one at the time, so as to check their influence in the results with respect to the reference one. Again, note that the parametric studies here do not aim at exactly predict the sound pressure levels in the receiving room, but rather to gain understanding about the model. Thus, establishing relative differences between different models is the main aim in here.

Influence of inclusion of acoustic media: In first instance, a comparison in the sound transmission through the wall when adding acoustic media was carried out. The cavities were modelled in three different ways: with no acoustic media (i.e. just structural vibrations being considered), filled with air alone and filled with insulation, as it is normally the case in reality (thus this latter was chosen as the reference model).

The results presented in Fig. 8.4a depict the necessity of including acoustic media in the cavities of walls when studying sound transmission. The frequency response curve drastically changes if just structural vibrations are considered as compared with considering air alone or insulation. If one compares the curves where acoustic media are modelled, their shape remains fairly similar, simply slight differences in amplitude being present.

The latter conclusion is in accordance to [10], where it was concluded that acoustic media affect the vibration transmission in wooden lightweight buildings. In there, however, just impact loads acting on the floor were studied, therefore the importance of including this small investigation as well to see whether or not that conclusion applies as well in the case of airborne sound transmission.

Influence of the number of seeds: The number of seeds (see Sect. 8.3.2 and Fig. 8.2 for further explanation) was varied so as to find a balance between the computational cost and the accuracy of the solution. Looking at the results shown in Fig. 8.4b, one can see that a 900 incident plane waves provide reliable results in terms of convergence of the response, since
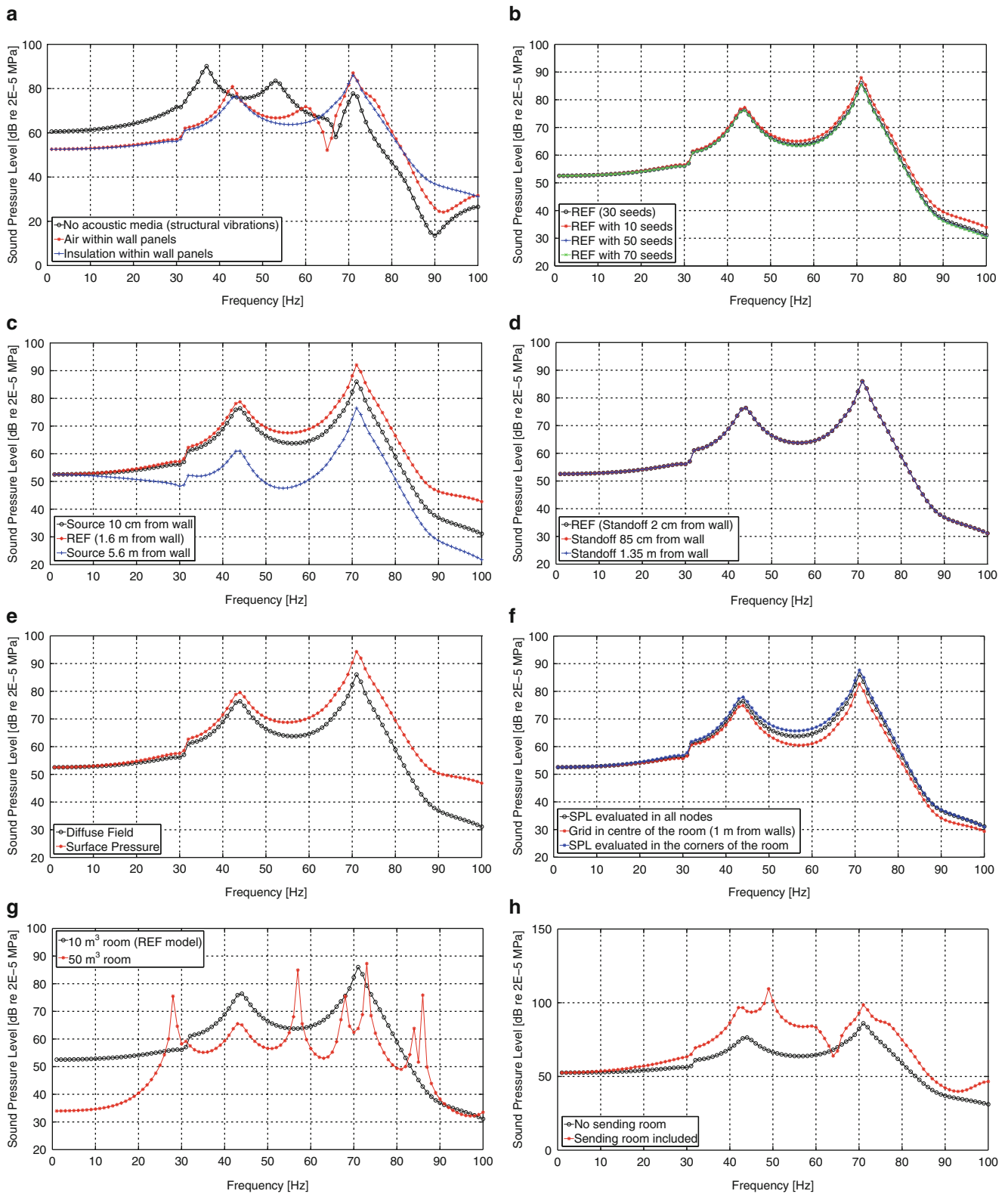
Fig. 8.4 Results of the different parametric studies performed. Please note that the axis' scales may differ. (**a**) Influence of acoustic media. (**b**) Influence of number of seeds. (**c**) Influence of source point position. (**d**) Influence of standoff point position.(**e**) Influence of loading type. (**f**) Influence of evaluation points. (**g**) Influence of the receiving room size. (**h**) Influence of including the sending room

the curve is almost superimposed with those considering 2,500 and 4,900 plane incident waves (50 and 70 seeds respectively). Considering just ten seeds (100 plane incident waves), however, does not yield such a close agreement.

Influence of the source point position: The influence of the position of the source point (see Sect. 8.3.2 and Fig. 8.2 for clarification) was also investigated. As it could be expected beforehand, the sound pressure level in the receiving room diminishes the further away from the wall the source point is set. The curves keep, nevertheless, the same shape, being the amplitudes the only thing varying (i.e. one curve could be, in principle, obtained from the other by just multiplying one of them times a factor, due to linearity), see Fig. 8.4c. This highlights the importance of selecting the source point at the same distance from the wall as the loudspeaker was placed when performed measurements, if accurate output from simulations is to be obtained.

Influence of the standoff point position: The position of the standoff point (see Sect. 8.3.2 and Fig. 8.2 for further explanation) was also varied. Its influences is, as seen in Fig. 8.4d, negligible. Its position should, however, be taken fairly close and not superimposed to the surface where the incident waves are impinging for a more accurate definition of the diffuse field [13].

Influence of loading type: A surface pressure loading was tried as compared to the diffuse field. As seen in Fig. 8.4e, the curves are very similar in shape, but they diverge with increasing frequency, probably due to the fact that non-perpendicular incident waves are not considered when a surface pressure is modelled. Modelling the exact excitation is thus also (as it could be beforehand expected) a key issue if reliable prediction tools are to be developed.

Influence of evaluation points: Measuring sound insulation in the very low frequency range is a substantial challenge. The position of the source as well as the microphone placements can have a strong influence on the transmission since diffuse field conditions are usually not met in medium-sized rooms, yielding repeatability problems. In the laboratory, this can be somehow alleviated by installation of diffusers, but in-situ measurements very seldom offer that possibility. As one can see in Fig. 8.4f, there is a considerable difference if the sound pressure level is evaluated in the corners as compared to if it is assessed in the corners. This difference is probably not larger here due to the small size of the room, the mismatches being larger if a bigger room was involved. An average of the sound pressure over all the nodes will probably yield more accurate results than just selecting some of them, as high-pressure areas would be somewhat compensated by lower pressures zones of the room.

Influence of size of the receiving room: A possible option to reduce computation time could be to first simulate the wall subjected to a diffuse field excitation, the structural displacements on the other side of the wall (after the transmission) being used in a subsequent analysis as input, where the room alone would just be analysed. By doing so, modifications in either in the building element or in the room alone could be performed, its saving computation time. The latter statement depends, however, on the degree of interaction between the receiving room and the construction element. If pressure waves in the room impinge back on the wall creating new incoming pressure waves, the aforementioned technique is not valid and therefore the whole system should be modelled.

In Fig. 8.4g, results for two different sizes of the receiving room are presented. It can be seen that, when varying the receiving room size, a totally different sound pressure field is obtained. This is due in part to the different size of the room (a change in geometry obviously implies a different dynamic behaviour from an acoustic point of view) but also probably due to larger interaction between the construction element and the room (this has to be further studied). Hence, it can be concluded that a receiving room should be included in the FE analyses. The room should be as accurate as possible in terms of dimensions, absorption and the like (remember that here rigid reflecting surfaces are considered).

Influence of modelling the sending room: Very much in the same way as there can be interaction between the construction element and the receiving room, the former could also interact with the sending room, and so it was tried. In the case under study here, it all indicates, see Fig. 8.4h, that there is indeed the need for also modelling the sending room. The differences in the results can be in part due to waves scattering through the sending room, instead of ideally impinging the wall when no room was included.

The fact of including the sending room is, in terms of computation time, a daunting task, as the number of degrees of freedom will quickly increase when including both rooms in the model, its exceeding the computer resources to solve the problem in a reasonable amount of time. This should also be further investigated.

8.4 Ongoing Work: Facade Element

With the knowledge gained from the conclusions drawn from Sect. 8.3.3, a more refined model of a facade element was created. The ultimate aim, as previously mentioned, is to find a FE model which can mimic measurement results performed in a laboratory environment. When doing so, modifications on the facade element will be performed so as to improve the element's acoustic performance.

A facade element of dimensions $3620 \times 2720 \times 460\,\text{mm}^3$ was modelled in the commercial FE software Abaqus [13], see Fig. 8.3. All parts were individually created and assembled as shown in Fig. 8.3. The facade element consisted on the materials are, from exterior to interior: 22×145 wooden panels, 28×70 wooden studs c600 (horizontal), Masonite board 6.4 mm, Masonite studs R300 c600 (vertical), glassfiber 170 mm, Masonite R40 8 mm, 45×45 wooden studs C600 (vertical), glassfiber 45 mm, Gyproc AP profile c400 (horizontal), glassfiber 25 mm and $2\times$ gypsum boards 13 mm type GN. The analysis conditions are the same as for the double leaf wall, i.e. full interaction between parts was considered, the outer frame was pined, Rayleigh damping considered and the FE mesh established with the same type of elements. The only exception was the receiving room, this time being $200\,\text{m}^3$ large, as it was the case of the measurements we were provided with. The analyses are being currently undertaken.

8.5 Discussion and Conclusions

FE simulations have a big potential to be used as a prediction tool in order to address acoustic issues during the design phase of the buildings. This would allow structural modifications of the construction before the building is actually erected, its saving costs and time to the builders. The challenge is, however, how to model different issues so that the output from simulations mimics the real behaviour of the construction element in question. Even if research has grown and been performed in the past years in matters related to such issues, there is still a long way to go until the behaviour of lightweight buildings, especially in the low frequency range, is understood and therefore properly simulated.

In this investigation, a parametric study of a double leaf wall was performed in terms of airborne sound transmission. Several issues influencing the response were varied trying to gain understanding on the modelling part. Even though the long term aim is to model and predict more complex construction elements, the double leaf wall was first chosen due to its lower calculation time as compared to those.

The results which stem from the previous studies are being currently applied to a more complicated construction element, namely a facade element which is intended to be modelled, calibrated against measurements and further developed and improved. The results are promising, paving the way towards a reliable predictive tool, yet a long way to go until all modelling issues are understood and able to be implemented.

References

1. Ljunggren F, Simmons C, Hagberg K (2014) Correlation between sound insulation and occupants' perception – proposal of alternative single number rating of impact sound. Appl Acous 85:57–68
2. International Organization for Standardization ISO 717-1, Acoustics – Rating of sound insulation in buildings and of building elements – Part 1: airborne sound insulation, 1996
3. International Organization for Standardization ISO 140-3, Acoustics – Measurement of sound insulation in buildings and of building elements – Part 3: Laboratory measurements of airborne sound insulation of building elements, 1995
4. International Organization for Standardization ISO 140-3, Acoustics – Measurement of sound insulation in buildings and of building elements – Part 4: Field measurements of airborne sound insulation between rooms, 1998
5. International Organization for Standardization ISO 717-2, Acoustics – Rating of sound insulation in buildings and of building elements – Part 2: impact sound insulation, 2013
6. Negreira J, Flodén O, Bard D (2012) Reflection and transmission properties of a wall-floor building element: comparison between finite element model and experimental data. In: Proceedings of acoustics Hong Kong
7. Ottosen N, Petersson H (1992) Introduction to the finite element method. Pearson Education Ltd., Harlow
8. Bathe KJ (2006) Finite element procedures. Prentice Hall, New York

9. Sandberg G (1986) Finite element modelling of fluid-structure interaction (PhD thesis), Lund University, Division of Structural Mechanics
10. Flodén O, Vibrations in lightweight structures – efficiency and reduction in numerical models. Lund University, Division of Structural Mechanics, 2014
11. Zwikker C, Kosten CW (1949) Sound absorbing materials. Elsevier, Amsterdam
12. Morse PM, Ingard KU (1968) Theoretical acoustics. Princeton University Press, New Jersey
13. Dassault Systèmes, Abaqus documentation, Version 6.12, 2012
14. Chopra AK (1995) Dynamics of structures. Prentice Hall, Upper Saddle River
15. Hopkins C (2007) Sound insulation. Elsevier, London
16. Hodgson M (1996) When is diffuse-field theory applicable? Appl Acoust 49(3):191–201
17. Hopkins C, Turner P (2005) Field measurement of airborne sound insulation between rooms with non-siffuse sound fields at low frequencies. Appl Acoust 66(12):1339–1382
18. Fothergill LC (1980) Recommendations for the measurements of sound insulation between dwellings. Appl Acoust 13:171–187

Chapter 9
Reduction of Radiating Sound from CFRP Laminated Plates with Orthotropy

Nobuyuki Okubo, Yuki Izumi, Takeshi Toi, Hideyuki Muramatsu, and Yuji Naito

Abstract CFRP is being positively introduced because of its light weight with sufficient stiffness for example in vehicle body but from acoustic aspect more investigations are needed. In order to grasp the vibration and acoustic feature of flat and curved CFRP laminated plates with orthotropy, the difference from isotropic material such as steel is clarified using experimental modal analysis. As a result CFRP is found to possess a dominant radiating sound mode shape at specific frequency. Then based on the FE model of the CFRP plate, a small CFRP patch with optimum anisotropy is designed to attach for effective reduction of the sound and finally its performance is verified in experiment.

Keywords Radiating sound • CFRP laminated plate • Fiber direction • Orthotropic • Anisotropy

9.1 Introduction

In modern vehicle design, the improvement of fuel consumption is strongly demanded for clean environment and therefore for lighter body weight, Carbon Fiber Reinforced Plastics, CFRP is widely introduced because of its high specific tensile strength and specific rigidity compared with metal. Especially at strength required parts, CFRP laminated plates consisted of thin sheet with fiber and resin, so called prepreg are adopted. This laminated plate is anisotropy with respect to fiber direction and at curved section Young's modulus is varied due to different fiber density and direction [1]. As a result if the vehicle components with isotropic metal are simply replaced by CFRP laminated plates, problems arise in terms of vibration and noise.

References are found that the breathing vibration mode to increase the radiating sound is appeared when the shape is changed from flat to curved in case of isotropic metal [2], the optimum design of curvature is proposed to reduce the sound radiation power [3] and the radiating sound due to breathing mode is reduced by adding bead at the panel [4] which is difficult to apply to CFRP because of cutting the fiber.

In this paper first the vibration and sound characteristic of CFRP plate are grasped by experimental modal analysis and then the FE model is created to simulate the same characteristics for the improvement of radiating sound. Finally the reduction of radiating sound is proposed based on this FE model.

CFRP laminated plate used in this paper is orthotropic three layers manufactured by autoclave method with flat and curved in longitudinal direction shape. The dimension is length $700 \times$ width $500 \times$ thickness 1.32 mm, curvature radius 854 mm and thickness of one prepreg is 0.44 mm. The fiber direction is notified as [±45] for 45°/−45°, [0/90] for 0°/90° and the right foot subscript n such as [±45]$_n$ stands for n layers [1].

N. Okubo (✉) • Y. Izumi • T. Toi
Chuo University, 1-13-27 Kasuga, Bunkyo-ku, 112-8551 Tokyo, Japan
e-mail: okubo@mech.chuo-u.ac.jp

H. Muramatsu
Toyota Technical Development Co., Tokyo, Japan

Y. Naito
Toyota Technocraft Co., Ltd., Tokyo, Japan

9.2 Vibration and Sound Characteristic of CFRP Plate

9.2.1 Experiment Condition

Figure 9.1 shows the flow of experimental modal analysis and Fig. 9.2 does the measurement points. The test plate is set in hemi-anechoic room hung by nylon cord from jig on the base as free-free condition. The input is given by an impact hammer and the response is captured by a light weight acceleration pick up (mass: 0.5 g) and five 1/2 microphones (distance from the plate: 50 mm) and FFT analyzer is used to calculate FRF. Note that Sum FRF of vibration in this paper stands for summation of all FRFs at 165 measurement points and Sum FRF of sound at five microphones.

9.2.2 Comparison of Vibration and Sound Characteristic with SUS and CFRP

First the sum FRF of vibration and that of sound in 1/3 octave band are compared with SUS and CFRP in case of flat plate as shown in Fig. 9.3 where CFRP is larger than SUS in both. For 10–800 Hz range, overall value of CFRP averaged over 4 different layers is 4.0 dB larger than that of SUS in vibration sum FRF and also 14.0 dB larger in sound sum FRF. This means that rather than vibration problem, the sound problem is apt to be serious in case of CFRP.

9.2.3 FRF Comparison of Flat and Curved Plate

The vibration and sound FRF are compared with flat and curved plate. Figure 9.4 shows the difference in case of $[\pm 45]_3$ where the vibration FRFs are almost the same but the sound FRFs reveal that the curved shows much larger than the flat especially in high frequency range, 500–800 Hz. Figure 9.5 also shows the sound FRFs with other layer type of CFRP and the same trend is observed.
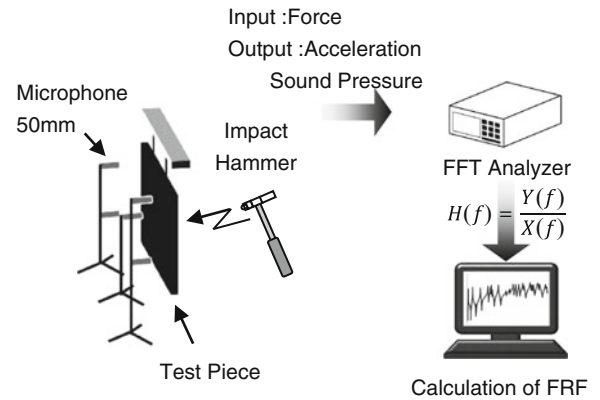
Fig. 9.1 Flow of experimental modal analysis
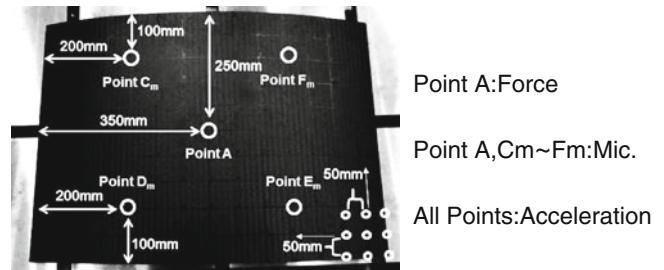
Fig. 9.2 Measurement point

Fig. 9.3 Sum FRF of flat plates
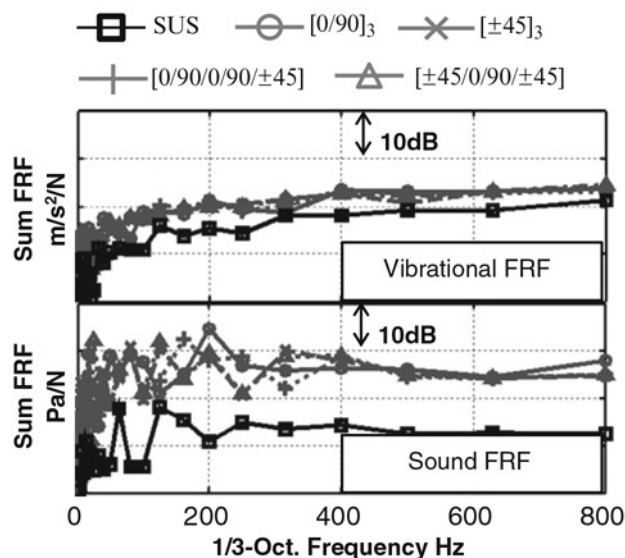
Fig. 9.4 Sum FRF of [±45]₃
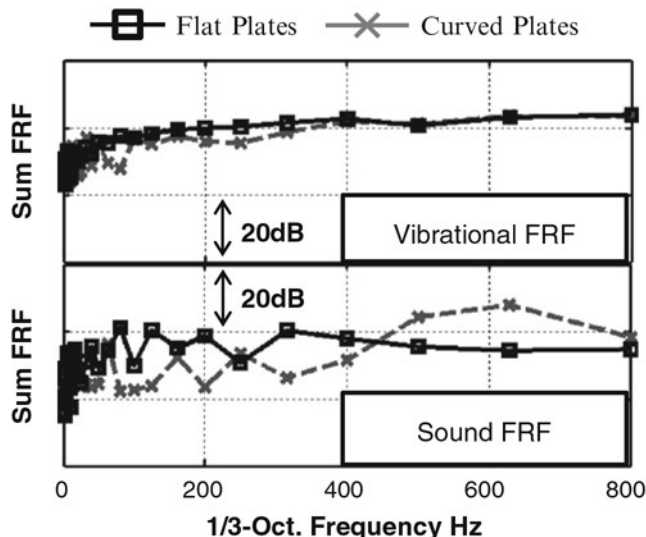
9.2.4 Influence of Anisotropy to Sound FRF

In order to gain insight about the difference in sound FRF in high frequency range, narrow band sound FRF is shown in Fig. 9.6 for four fiber direction types. It is seen that the largest peak frequency is different with respect to the fiber direction type and Fig. 9.7 shows the corresponding mode shape. These mode shapes are so called breathing mode where the center of the plate is vibrating in phase and radiating sound efficiently.

9.3 FE Model of the Plate

9.3.1 Modeling the CFRP Laminated Plate

The material property is determined by specimen test of rectangular piece of the CFRP laminated plates in the same lot and the classical laminated plate theory is applied [1]. The specimen of [0/90]₃ is used to calculate Young's modulus, E_L, E_γ and Poisson's ratio ν_{LT} and that of [±45]₃ for Young's modulus E_{45} and Poisson's ratio ν_{45}. The shear modulus in plane, G_{LT} is defined as,

Fig. 9.5 Sum FRF
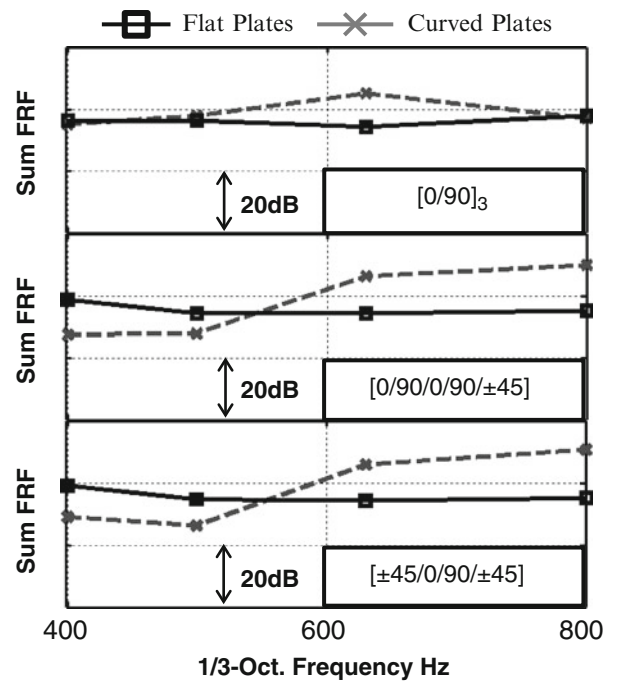
Fig. 9.6 Sound FRF (Driving point A)
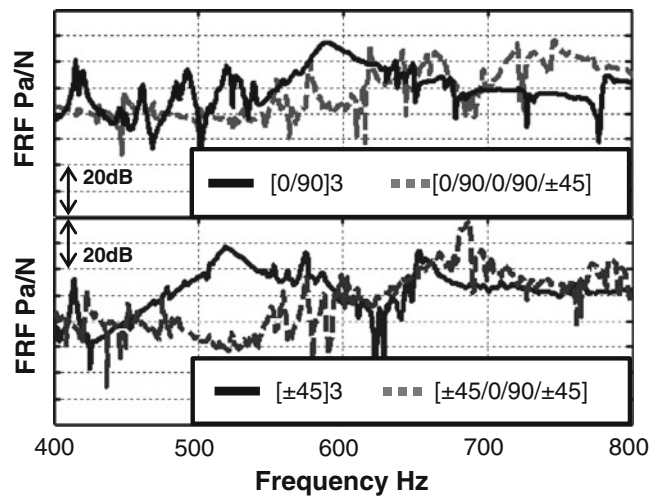
$$\frac{1}{G_{LT}} = \frac{4}{E_{45}} - \frac{1}{E_L} - \frac{1}{E_T} + \frac{2v_{LT}}{E_L} \tag{9.1}$$

And that out of plane, G_{LZ} and G_{TZ} are assumed the same as G_{LT} for simplicity.

Based on these material properties the FE model of the plate is created for eigenvalue analysis and frequency response analysis. Then BE model is used for radiating sound analysis. The boundary condition is free-free as the same experimental condition and an impulse force is acted at the center of the plate and radiating sound is calculated 50 mm apart from the center.

9.3.2 Comparison of Analysis and Experiment

The comparison of vibration and sound FRF by analysis and experiment is shown in Fig. 9.8 and the Modal Assurance Criterion, MAC in Fig. 9.9. Up to 600 Hz range both FRF agree well and also mode shapes are matched well. Also for other three fiber direction types, high accurate FE models are obtained.

Fig. 9.7 Dominant radiating mode

[0/90]$_3$: 586Hz   [0/90/0/90/±45] : 746Hz

[±45]$_3$: 522Hz   [±45/0/90/±45] : 687Hz

Fig. 9.8 Sound FRF (Driving point A)

(▬ Experiment ▪▪▪ Analysis : [±45]$_3$)

FRF

20dB   Vibrational FRF

FRF

20dB   Sound FRF

0   100   200   300   400   500   600
Frequency Hz

Fig. 9.9 Modal assurance criterion

(Analysis vs. Experiment : [±45]$_3$)

22   100 %

Mode Number
of Analysis

0   22   0 %

0   **Mode Number**   22
of Experiment
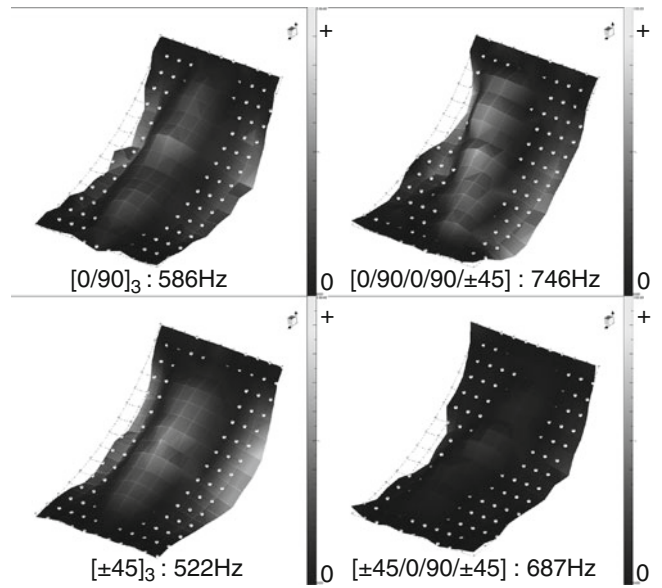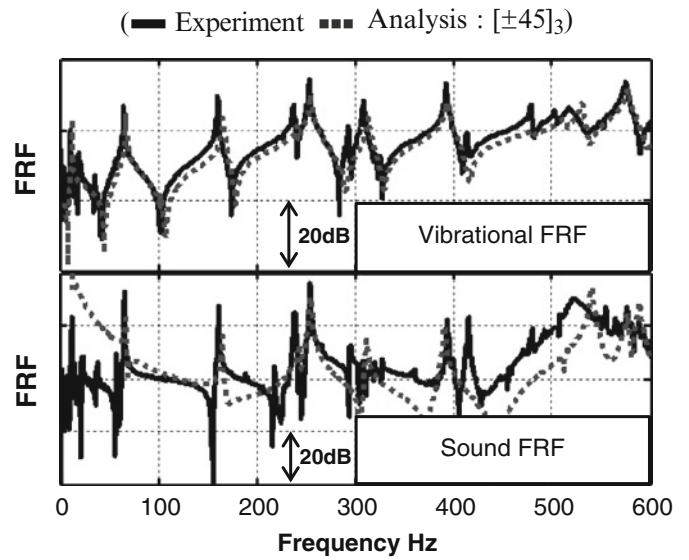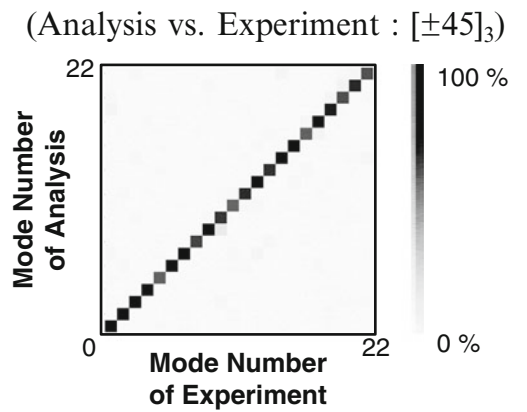
9.4 Reduction of Radiating Sound

9.4.1 Flow of Reduction

Since the dominant mode shape at specific frequency which causes the radiating sound are found, the area of large amplitude at the center of the plate is aimed to decrease as shown in the flow of reduction of radiating sound in Fig. 9.10. The idea is that a small CFRP plate, called patch, 180 mm square size with 1.32 mm thickness (0.44 mm prepreg three layer) which corresponds 1/10 total volume is adhered to the center of the plate. The radiating sound analysis of CFRP plate with patch is conducted by FE model mentioned before in order to consider the optimum design of fiber direction of the patch.

9.4.2 Design of Anisotropy

It is important to consider the fiber direction of the patch with respect to the base CFRP plate because it changes the rigidity. By using the FE model, the radiating sound due to breathing mode shape under consideration (base plate $[\pm 45]_3$) is calculated when the patch angle is changed by $1°$ step and Fig. 9.11 shows the result of down value of sound FRF. Compared with the original plate without the patch, $45°$ patch angle achieves 12.0 dB down and $10°$ does 14.6 dB down, namely 2.6 dB more improvement is expected.

9.4.3 Verification by Experiment

In order to verify the prediction by simulation, CFRP plate with patch is manufactured. Figure 9.12 shows the measured comparison of sound FRF with the original without the patch, $45°$ patch angle (the worst denoted patch $[\pm 45]_3$) and $10°$ (the optimum patch $[10/-80]_3$). The reduction of radiating sound form the original at peak frequency is observed 6.4 dB from the original without the patch to patch $[\pm 45]_3$ ((a) vs. (b) in the figure) and 7.6 dB from the original to patch $[10/-80]_3$ ((a) vs. (c)) and 1.2 dB difference between patch $45°$ and $10°$ ((b) vs.(c)). The similar trend predicted by analysis is verified in experiment. Concerning the overall value for 10–800 Hz range, the patch $[\pm 45]_3$ gains 8.8 dB down and the optimum patch $[10/-80]_3$ does 9.0 dB down from the original. This indicates that the reduction of radiating sound is especially effective at the specific frequency of breathing mode shape.

Fig. 9.10 Flow of reduction of radiating sound pressure
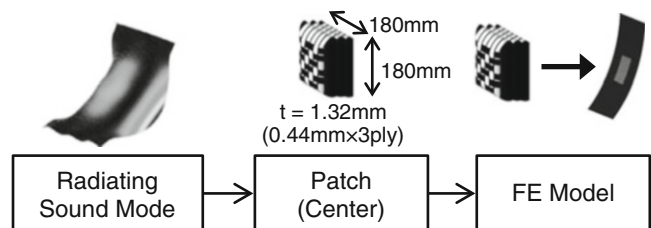
Fig. 9.11 Optimal design of $[\pm 45]_3$ with respect to angle of patch
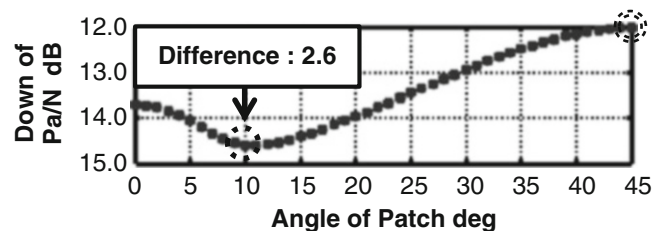
Fig. 9.12 Measured Sound FRF of Patch Model

(▬ Non-Patch ×××Patch $[\pm45]_3$ ▮▮▮ Patch $[10/\text{-}80]_3$)
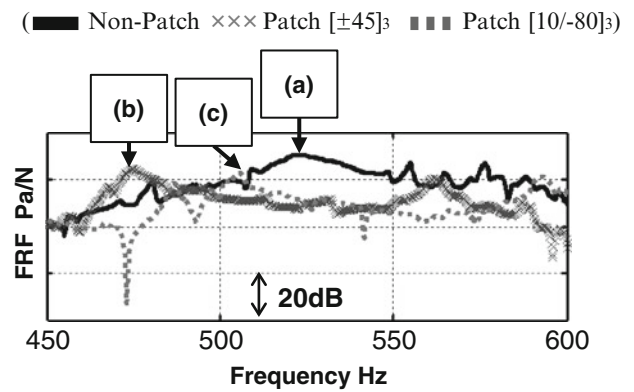
Fig. 9.13 Experimental setup (Enclosed)
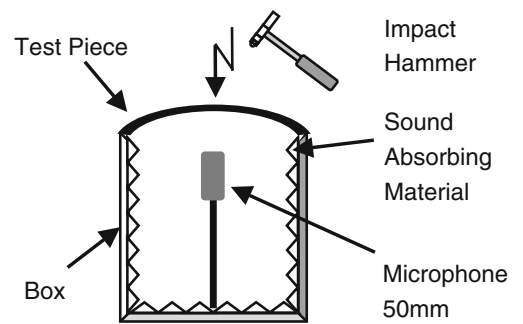
Fig. 9.14 Measured sound FRF of patch model (Enclosed)

(▬ Non-Patch ×××Patch $[\pm45]_3$ ▮▮▮ Patch $[10/\text{-}80]_3$)
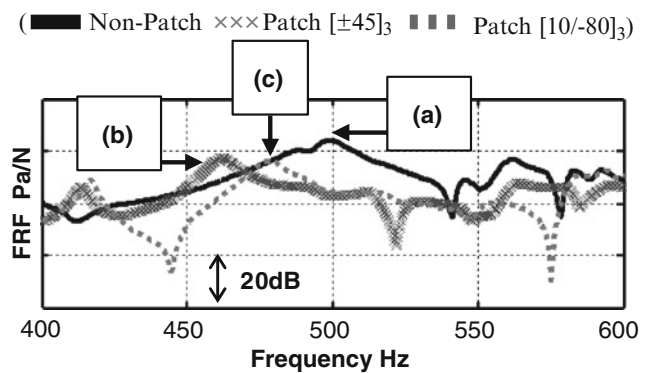
9.4.4 Reduction in Enclosed Space

The previous consideration is made for radiating sound in open space so the enclosed space is dealt with next as shown in Fig. 9.13. In order to avoid the cavity acoustic mode and vibration of the wall, sound absorbing materials are covered inside expect the CFRP plate. Figure 9.14 shows the measured sound FRF between the input force and the acoustic pressure at the microphone inside. The reduction of radiating sound form the original without the patch at peak frequency is observed 7.0 dB by the patch $[\pm45]_3$ ((a) vs.(b)) and 7.9 dB by the optimum patch $[10/-80]_3$ ((a) vs. (c)) and 0.9 dB difference between them ((b) vs. (c)). The overall value for 10–800 Hz range is improved by 4.6 dB down for patch $[\pm45]_3$ and 4.5 dB down for patch $[10/-80]_3$ respectively.

9.4.5 Change of the Breathing Mode Shape

The change of the breathing mode shapes are compared with the original without the patch, patch $[\pm45]_3$ and the optimum patch $[10/-80]_3$ as shown in Fig. 9.15. In case of patch $[\pm45]_3$, the center of the plate is modified from the peak to node but in case of optimum patch $[10/-80]_3$ the amplitude of wider area are suppressed which results more effective reduction of radiating sound.

Fig. 9.15 Dominant radiating mode $[\pm 45]_3$

Non-Patch 522Hz · Patch $[\pm 45]_3$ 475Hz · Patch $[10/-80]_3$ 506Hz

Table 9.1 Material property

Material	Young's modulus	Density
Anisotropy (CFRP)	$E_L = E_T = 57.0$ GPa	1,515.0 Kg/m^3
Isotropy (Aluminum)	$E = 63.2$ GPa	2,710.0 Kg/m^3

Fig. 9.16 Comparison of radiating sound pressure level and patch mass
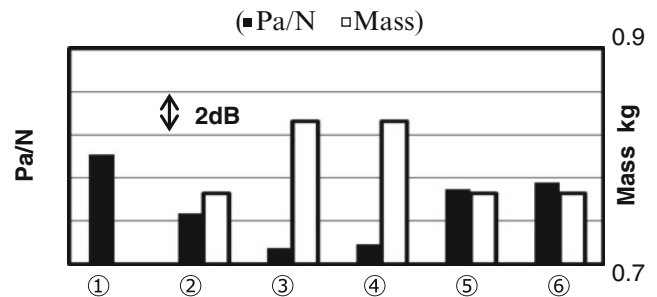
9.4.6 Tradeoff Against Mass Effect

The radiating sound can be reduced by increasing mass of the plate in general and therefore the tradeoff between mass and the patch effect are discussed. The following six cases including isotropy patch (aluminum) are dealt with in the calculation of radiating sound. The material property for anisotropy and isotropy used are indicated in Table 9.1.

- Original CFRP without patch (base plate $[\pm 45]_3$)
- Anisotropy patch with optimum $[10/-80]_3$
- Isotropy patch
- Isotropy patch but equivalent CFRP rigidity
- Isotropy patch but equivalent CFRP mass (thin thickness)
- Isotropy patch but equivalent CFRP rigidity and mass

Compared with the original, case ② to ⑥ are succeeded to reduce the radiating sound. Case ③ and ④ achieve large reduction but mass is increased much which is inappropriate in terms of light weight design. Case ②, ⑤ and ⑥ are the same mass but ② is more effective in reduction of radiating sound because of anisotropy (Fig. 9.16).

9.5 Conclusions

1. The vibration and sound characteristics of CFRP laminated plate with orthotropy are clarified by experiments.
2. The FE model of the CFRP plate can be created based on the experimental results.
3. By making good use of the FE model, the optimum angle of fiber direction of small patch CFRP plate adhered in the center can be predicted in order to reduce the radiating sound.
4. The reduction of radiating sound by CFRP patch is confirmed by experiments.

References

1. Fukuda H et al (1989) Mechanics of composite material. Kokinshoten, Tokyo, 233p
2. Scott JFM et al (1992) Vibration of an elastic strip with varying curvature. Philos Trans R Soc Lond Ser A Math Phys Eng Sci 339(1655): 587–625
3. Kaneda S et al (2001) Reduction of radiating sound power by optimal design of curvature of vibrating plate. J BEM 18:13–18
4. Nakajima J et al (2010) Reduction of booming noise due to panel radiation. JSAE (54–10):14–16
5. JIS K 7164: Test for tensile property

Chapter 10
Rotating Disc Model for Complex Eigenvalue Analysis of Brake Squeal

Yujian Wang, Yongchang Du, and Pu Gao

Abstract Modelling of disc rotor is a key step in building a disc brake model for squeal analysis. While braking, the disc is rotating and other components are fixed and there are sliding contact between the pads and the disc. In the most common used complex eigenvalue analysis method, the moving load nature was normally ignored. In this paper a modal based rotating disc model is purposed. Modal parameters of stationary disc were calculated from finite element model. The frequency response function of rotating disc, under which the disc was excited and corresponding responses to be observed at spatial fixed points, was derived. The equivalent modal parameters, which represent the dynamic properties of rotating disc suffering moving loads, were studied. Because of rotating, each mode of the disc split to two complex modes and becomes the superposition of two travelling waves. The conclusion agrees with those from analytical method.

Keywords Disc brake • Squeal • Rotating • Moving load • Modal parameter

10.1 Introduction

Disc brakes may suffer from noise. High performance systems with high friction levels are especially vulnerable in this respect. Reducing the friction level may not be an option, so alternative means of solving the problem have been the aim of much research and development. A number of theories have been formulated to explain the mechanisms of brake squeal, and numerous studies have tried with varied success to apply them to the dynamics of disc brakes [1, 2].

Because of the complex geometries and boundary/loading conditions of the components involved in brake squeal, finite element (FE) model is used in most cases and complex eigenvalue analysis is preferred to study the dynamic behavior. For the squeal of disc brake system, Liles was the first person who utilized complex eigenvalue analysis using FE method to predict disk squeal propensity [3]. Guan constructed FE models for all the brake components, built substructure (component) modal synthesis system model, found the influential component modes through substructure modal participation analysis, sensitivity analysis and feed-in energy analysis and finally improve the design of the bracket [4–7]. Similar approaches were adopted by other researchers, i.e. Nack [8], Yuan [9], Kung [10], Goto et al. [11].

Though much work was done on the issue of squeal, it requires continuous study and investigation to refine the prediction accuracy of brake models. For example, the model of disc is worthy of attention. This is a complicated problem by the fact that the disc is rotating and the pads and caliper are fixed and the nature of the contact between the pads and the disc. Historically, in the study of brake squeal, the moving load nature normally has been ignored in the belief that squeal which tends to occur at low disc speeds does not warrant this complication [4, 12]. In complex eigenvalue analysis method, i.e. Guan's modal synthesis model [4], the dynamic behavior of disc is represented by its stationary modal parameters and the effect of rotating is only embodied in the relentlessly one-direction friction forces on pad / disc interface. Ouyang et al. [12, 13] proposed to treat the disc vibration and squeal as a moving load problem and put forward an analytical-numerical combined method. In their works, the disc brake was conceptually divided into two parts: the rotating disc, which was approximated as an annular, thin plate and solved by an analytic method, and nonrotating components, which was solved by FE method. Then the complex eigenvalues of disc brake including the moving loads can be predicted.

This paper proposes a preliminary study of a modelling method of disc that can represent the rotating effect. Stationary disc FE model is built and modal parameters is calculated. The frequency response function of rotating disc, under which

Y. Wang • Y. Du (✉)
State Key Laboratory of Automotive Safety and Energy, Tsinghua University, Beijing, China
e-mail: duyc@tsinghua.edu.cn

P. Gao
School of Vehicle and Energy Engineering, Yanshan University, Qinhuangdao, China

Fig. 10.1 Finite element model
of the stationary disc
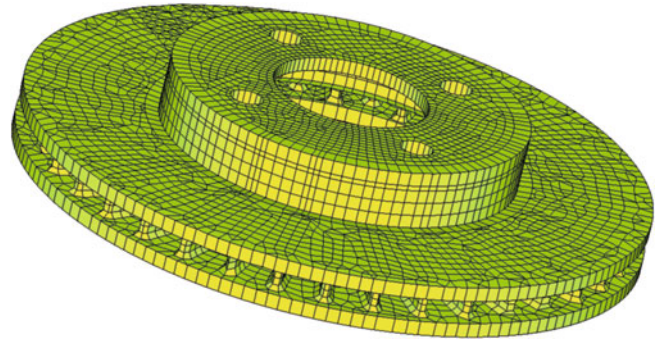
Table 10.1 Modal frequencies
of axial ND type disc modes

Modal shape	1ND	2ND	3ND	4ND	5ND	6ND	7ND
Modal frequency (Hz)	1,300.1	1,471.2	2,835.9	4,491.2	6,193.6	7,903.9	9,649.4

the disc is excited and corresponding responses to be observed at spatial fixed points, is derived. The equivalent modal parameters, which represent the dynamic properties of rotating disc suffering moving loads, will be studied. Comparison will be made between the results in this paper and those from analytical disc models.

10.2 Finite Element Model of the Disc

The target disc is from a passenger car's front brake. FE model is built, as illustrated in Fig. 10.1. It consists of nearly 8,500 elements. The FE model is validated through the comparison of modal parameters predicted from FE model and those from experimental modal analysis under free-free boundary conditions and a tuning process of the material properties of the model. After that, proper constraints are applied to FE mode to calculate modal parameters to be used for squeal analysis. Table 10.1 lists the modal frequencies of axial nodal diameter (ND) type modes of the disc.

10.3 Rotating Dynamics and Modal Extraction

In disc brake system, the disc rotates yet the components coupled with the disc are stationary. In most cases, it's convenient to model the brake in a fixed coordinate system. So a model that can describe the dynamic properties of rotating disc in fixed coordinate system is preferred. In this paper, a modal approach is proposed based on a study of dynamic responses of a rotating disc.

Because most squeal occur in the low speed range (for common passenger cars, when the vehicle speed is 50 km/h, the rotating speed of disc is approximately 100 rad/s, which is far lower than its critical speed), gyroscopic and centrifugal effects are very small and can be omitted.

Since the disc is rotary symmetric, the modal shapes of a disc are in the form of trigonometric functions. To simply the problem, the disc is divided to a series of concentric circular rings. For a certain ring, when it's in stationary state, its rth modal frequency is ω_r and the corresponding modal shape can be express as

$$\phi_{pr} = \phi_{lr} \cos r\theta_{lp} \quad (r = 1, \ldots N) \tag{10.1}$$

where r is the mode rank, N is the account of modes, ϕ_{lr} is the rth modal shape coefficient of exciting point l, ϕ_{pr} is that of measuring point p, θ_{lp} is the central angle between l and p.

The transfer function between point p and l can be expressed as

$$H_{lp}(s) = \sum_{r=1}^{N} \frac{\varphi_{lr}\varphi_{pr}}{s^2 + \omega_r^2} = \sum_{r=1}^{N} \left(\frac{A_{lpr}}{s - j\omega_r} + \frac{A_{lpr}^*}{s + j\omega_r} \right) \tag{10.2}$$

where A_{lpr} is the rth residue.

$$A_{lpr} = -\frac{j\varphi_{lr}\varphi_{pr}}{2\omega_r} \tag{10.3}$$

The impulse response function of the system is the transverse Laplace Transform of $H_{lp}(s)$

$$h_{lp}(t) = L^{-1}\left[H_{lp}(s)\right] = \sum_{r=1}^{N} A_{lpr}e^{j\omega_r t} + A_{lpr}^{*}e^{-j\omega_r t} = \sum_{r=1}^{N} \frac{\phi_{lr}\phi_{pr}}{\omega_r}\sin\omega_r t = \sum_{r=1}^{N} \frac{\phi_{lr}^{2}}{\omega_r}\cos r\theta_{lp}\sin\omega_r t \tag{10.4}$$

Omitting subscript l and p, and considering central angle θ_{lp} as an argument of function h, Eq. 10.4 becomes

$$h\left(t, \theta_{lp}\right) = \sum_{r=1}^{N} \frac{\phi_{lr}^{2}}{\omega_r}\cos r\theta_{lp}\sin\omega_r t = \sum_{r=1}^{N} h_{0r}(t)\cos r\theta_{lp} \tag{10.5}$$

where $h_{0r}(t)$ represents the impulse response function of the exciting point

$$h_{0r}(t) = \frac{\phi_{lr}^{2}}{\omega_r}\sin\omega_r t \tag{10.6}$$

Divide the ring to evenly spaced points naming 0, 1, 2 …. The central angle between adjacent points is $\Delta\theta$. The ring rotates counterclockwise at Ω rad/s, as shown in Fig. 10.2. At the beginning all the points on the ring are in their balancing position. Suppose the ring is excited by a unit pulse force $\delta(t)$ at a spatial fixed point l. Examine the response of ring at spatial fixed point p. When time $t = 0$, fixed point l coincides with moving point 0 and point p coincides with point n.

When $t = 0$, the response of point p is actually the response of point n

$$x(0) = h\left(t, \theta_{lp}\right) * \delta(t)\big|_{t=0} = h\left(0, \theta_{lp}\right) = 0$$

When $t = \Delta t = \Delta\theta / \Omega$, the ring rotates over $\Delta\theta$. Now point n + 1 coincides with point p, so the response is

$$x\left(\Delta t\right) = h\left(t, \theta_{lp} + \Delta\theta\right) * \delta(t)\big|_{t=\Delta t} = h\left(\Delta t, \theta_{lp} + \Delta\theta\right) = \sum_{r=1}^{N} h_{0r}\left(\Delta t\right)\cos r\left(\theta_{lp} + \Omega\Delta t\right)$$
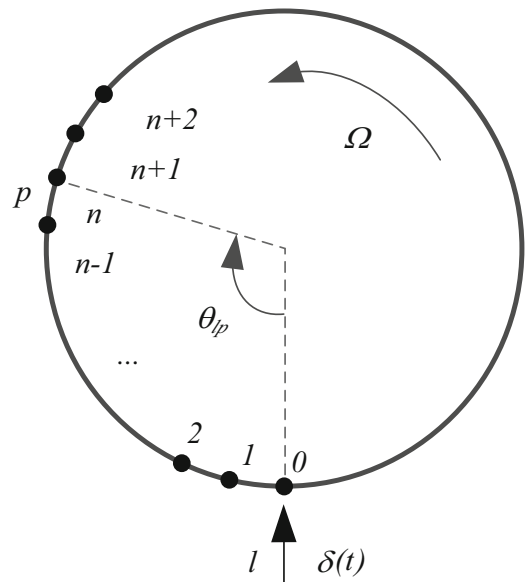

Fig. 10.2 Ideal ring to illustrate dynamics of rotating disc

When t $= 2\Delta t$, the ring rotates over another $\Delta\theta$. Now point n $+ 2$ coincides with point p, so the response is

$$x\left(2\Delta t\right) = h\left(t, \theta_{lp} + 2\Delta\theta\right) * \delta(t)\big|_{t=2\Delta t} = h\left(2\Delta t, \theta_{lp} + 2\Delta\theta\right) = \sum_{r=1}^{N} h_{0r}\left(2\Delta t\right) \cos r\left(\theta_{lp} + 2\Omega\Delta t\right)$$

. . .

So after i steps, time is t $= i\Delta t$, the response will be,

$$x\left(i\,\Delta t\right) = h\left(t, \theta_{lp} + i\,\Delta\theta\right) * \delta(t)\big|_{t=i\,\Delta t} = h\left(i\,\Delta t, \theta_{lp} + i\,\Delta\theta\right) = \sum_{r=1}^{N} h_{0r}\left(i\,\Delta t\right) \cos r\left(\theta_{lp} + i\Omega\Delta t\right)$$

Let $\Delta\theta \to 0$, we can derive the response measured at point p at continues time t.

$$x(t) = h\left(t, \theta_{lp} + \Omega t\right) = \sum_{r=1}^{N} h_{0r}(t) \cos r\left(\theta_{lp} + \Omega t\right) \tag{10.7}$$

Note that Eq. 10.7 is the measured response under a unit pulse excitation, so the equivalent impulse response function of rotating ring in the circumstance excited at fixed point l and measured at fixed point p can be expressed as

$$\overline{h}(t) = \sum_{r=1}^{N} h_{0r}(t) \cos r\left(\theta_{lp} + \Omega t\right) = \sum_{r=1}^{N} \frac{\phi_{lr}^{2}}{\omega_r} \sin \omega_r t \cos r\left(\theta_{lp} + \Omega t\right)$$

$$= \sum_{r=1}^{N} \frac{\phi_{lr}^{2}}{2\omega_r} \left[\sin\left[\left(\omega_r + r\Omega\right) t + r\theta_{lp}\right] + \sin\left[\left(\omega_r - r\Omega\right) t - r\theta_{lp}\right]\right] \tag{10.8}$$

The equivalent transfer function $\overline{H}(s)$ is the Laplace Transform of $\overline{h}(t)$

$$\overline{H}(s) = L\left[\overline{h}(t)\right] = L\left[\sum_{r=1}^{N} \frac{\phi_{lr}^{2}}{2\omega_r} \left[\sin\left[\left(\omega_r + r\Omega\right) t + r\theta_{lp}\right] + \sin\left[\left(\omega_r - r\Omega\right) t - r\theta_{lp}\right]\right]\right.$$

$$= \sum_{r=1}^{N} \frac{1}{2}\frac{\varphi_{lr}^{2}}{\omega_r} \left[\frac{\left(\omega_r + r\Omega\right)\cos r\theta_{lp} + s\,\sin\,r\theta_{lp}}{s^2 + \left(\omega_r + r\Omega\right)^2} + \frac{\left(\omega_r - r\Omega\right)\cos r\theta_{lp} - s\,\sin\,r\theta_{lp}}{s^2 + \left(\omega_r - r\Omega\right)^2}\right]$$

$$= \sum_{r=1}^{N} \frac{A_{r1}}{s - s_{r1}} + \frac{A_{r1}^{*}}{s - s_{r1}^{*}} + \frac{A_{r2}}{s - s_{r2}} + \frac{A_{r2}^{*}}{s - s_{r2}^{*}} \tag{10.9}$$

where

$$\begin{cases} s_{r1} = j\left(\omega_r + r\Omega\right) \\ A_{r1} = \frac{1}{4}\frac{\varphi_{lr}^{2}}{\omega_r}\left(\sin\,r\theta_{lp} - j\,\cos r\theta_{lp}\right) \end{cases} \begin{cases} s_{r2} = j\left(\omega_r - r\Omega\right) \\ A_{r2} = \frac{1}{4}\frac{\varphi_{lr}^{2}}{\omega_r}\left(-\sin\,r\theta_{lp} - j\,\cos r\theta_{lp}\right) \end{cases}$$

Each item in the accumulative factor of Eq. 10.9 is a transfer function of two modes. So the equivalent modal parameters can be extracted as

$$\begin{cases} \overline{\omega}_{r1} = \left(\omega_r + r\Omega\right) \\ \overline{\varphi}_{lr1} = \frac{\sqrt{2}}{2}\sqrt{\frac{\left(\omega_r + r\Omega\right)}{\omega_r}}\varphi_{lr} \\ \overline{\varphi}_{pr1} = \frac{\sqrt{2}}{2}\sqrt{\frac{\left(\omega_r + r\Omega\right)}{\omega_r}}\varphi_{lr}\left(\cos r\theta_{lp} + j\,\sin r\theta_{lp}\right) \end{cases} \begin{cases} \overline{\omega}_{r2} = \left(\omega_r - r\Omega\right) \\ \overline{\varphi}_{lr2} = \frac{\sqrt{2}}{2}\sqrt{\frac{\left(\omega_r - r\Omega\right)}{\omega_r}}\varphi_{lr} \\ \overline{\varphi}_{pr2} = \frac{\sqrt{2}}{2}\sqrt{\frac{\left(\omega_r - r\Omega\right)}{\omega_r}}\varphi_{lr}\left(\cos r\theta_{lp} - j\,\sin r\theta_{lp}\right) \end{cases} \tag{10.10}$$

It can be seen from Eq. 10.10 that mode r of the ring splits to two modes due to rotating. The modal frequencies are $(\omega_r + r\Omega)$ and $(\omega_r\text{-}r\Omega)$ respectively. The two frequencies will change with rotation speed. The variation of modal frequency is proportional to the rank r. The higher the rank, the more the modal frequency will change.

The expressions of φ_{pr1} and φ_{pr2} include imaginary parts, indicating that both modes are complex modes. So there's no standing nodal point of the mode shape. For mode r_1, the nodal point travels backward relative to rotation, and for mode r_2, forward.

So when the rotating disc is suffering a fixed load, its vibration should contain responses from the split modes. As illustrated in Eq. 10.10, one travels backward, the other forward. This result is in good agreement with those reported in the literature [14–16].

10.4   Conclusion

This paper presents a preliminary study of a modelling method for rotating disc based on its modal parameters. First, FE model is used to calculate the modal parameter in stationary status. Then equivalent modal parameters, which represent the dynamic properties of rotating disc suffering moving loads, were derived. Because of rotating, each mode of the disc split to two complex modes and becomes the superposition of two travelling waves. The conclusion agrees with those from analytical method.

References

1. Kinkaid NM, O'Reilly OM, Papadopoulos P (2003) Automotive disc brake squeal. J Sound Vib 267(1):105–166. doi:10.1016/S0022-460X(02)01573-0
2. AbuBakar AR, Ouyang H (2006) Complex eigenvalue analysis and dynamic transient analysis in predicting disc brake squeal. Int J Veh Noise Vib 2(2):143–155
3. Liles G (1989) Analysis of disc brake squeal using finite element methods. SAE technical paper 891150, doi:10.4271/891150
4. Guan D, Jiang D (1998) A study on disc brake squeal using finite element methods. SAE technical paper 980597, doi:10.4271/980597
5. Zhu X, Guan D (1993) The experimental and simulational analysis on drum brake squeal by structurally closed-loop coupling model. SAE technical paper 931879, doi:10.4271/931879
6. Guan D, Su X, Zhang F (2006) Sensitivity analysis of brake squeal tendency to substructures' modal parameters. J Sound Vib 291(1):72–80. doi:10.1016/j.jsv.2005.05.023
7. Guan D, Huang J (2003) The method of feed-in energy on disc brake squeal. J Sound Vib 261(2):297–307. doi:10.1016/S0022-460X(02)01074-X
8. Nack W (1999) Brake squeal analysis by finite elements. SAE technical paper 1999-01-1736, doi:10.4271/1999-01-1736
9. Yuan Y (1996) An eigenvalue analysis approach to brake squeal problems. In: Proceedings of the 29th ISATA conference automotive braking systems, Florence
10. Kung S, Dunlap KB, Ballinger RS Complex eigenvalue analysis for reducing low frequency brake squeal. SAE technical paper 2000-01-0444
11. Goto Y, Amago T, Chiku, K et al (2004) Experimental identification method for interface contact stiffness of FE model for brake squeal. In: Proceedings of IMechE international conference- braking. Professional Engineering Publishing Ltd. UK, pp 143–155
12. Ouyang H, Cao Q, Mottershead JE et al (2003) Vibration and squeal of a disc brake: modelling and experimental results. Proc Inst Mech Eng D J Automob Eng 217(10):867–875. doi:10.1243/095440703769683270
13. Ouyang H, Li W, Mottershead JE (2003) A moving-load model for disc-brake stability analysis. J Vib Acoust 125(1):53–58. doi:10.1115/1.1521954
14. Nayfeh AH, Jilani A, Manzione P (2001) Transverse vibrations of a centrally clamped rotating circular disk. Nonlinear Dyn 26(2):163–178
15. Ouyang H, Mottershead JE (2001) Unstable travelling waves in the friction-induced vibration of discs. J Sound Vib 248(4):768–779
16. Ouyang H, Mottershead JE (2004) Dynamic instability of an elastic disk under the action of a rotating friction couple. J Appl Mech 71(6): 753–758. doi:10.1115/1.1795815

Chapter 11
Validation of Closed-Loop Coupling Disc Brake Model for Squeal Analysis

Pu Gao, Yongchang Du, and Yujian Wang

Abstract Disc brake squeal remains an elusive problem in the automotive industry and developing a model that will predict unstable squeal-noise dynamics with reasonable accuracy is in urgent need. In this paper, a two stage validation method of closed-loop coupling disc brake model for squeal analysis using complex eigenvalue analysis is presented. At component level, finite element (FE) models are verified through the comparison of FE calculation and modal test results. At the system level, optimization method is adopted. Experiment modal analysis of stationary disc brake system with brake line pressure and brake torques applied is conducted. Then an optimization process is initiated to minimize the differences between modal frequencies predicted by the stationary model and those from test. Thus model parameters more close to real situation are found. Unstable mode prediction results of validated model are compared with those from brake noise bench test. The validated model can predict most of the squeal frequencies and the real part represent the occurrences of squeal. The method presented in this paper is proven to be valid and effective.

Keywords Disc brake • Squeal • Closed-loop coupling model • Validation • Finite element

11.1 Introduction

The automotive industry is faced with continuous increasing requirements regarding safety, reliability and acoustics. Thereby the NVH (noise, vibration and harshness) characteristic of brake systems becomes more important. Brake squeal noise is one of the important NVH issues experienced during braking. Due to its complex nature brake squeal has been a challenging problem for researchers and engineers since 1930s [1].

Researchers have applied many mathematical methods for this problem. CEA (complex eigenvalue analysis) is one of the most common used methods. Liles is the first person who introduced CEA to assess the stability of a disc brake system [2]. Guan and her research group built closed-loop coupling model for both drum and disc brake system based on modal synthesis method and developed analysis a set of methods such as substructure modal composition analysis, substructure modal parameter sensitivity analysis, feed-in energy analysis, etc... These methods can analyze the influence of components' structural parameters to squeal and determine which one is dominant. The analysis results reached good agreement with those from test [3–6].

It includes two steps to build a closed-loop coupling model. The first step is to obtain modal parameters of brake components (substructures) which are calculated through FE (finite element) methods in most cases. The second step to construct the system model basing on modal synthesis method [4]. It's obvious that the validation of the developed model should also include component level and system level. In component level, the geometry and material properties as well as dynamic characteristics of components should be well described in its FE model. In system level, the key issue is that the coupling matrix should accurately represent the complex interactions of components when squeal occurs.

A few discussions of the validation of analysis model can be found in public literatures. Component level validation is performed in most of these works [4, 7, 8]. In system level, the coupling parameters are often determined from experience and the validity of their values is unsure. AbuBaker built a disc brake system FE model. Besides component level validation, he also performed system level validation by comparing predicted and experimental results of the stationary disc brake assembly. The updating the spring stiffness of coupling components was based on a trials and errors process [9].

P. Gao
School of Vehicle and Energy Engineering, Yanshan University, Qinhuangdao, China

Y. Du (✉) • Y. Wang
State Key Laboratory of Automotive Safety and Energy, Tsinghua University, Beijing, China
e-mail: duyc@tsinghua.edu.cn

This paper presents a two level validation process of a closed-loop coupling disc brake model. Component level FE models are built and verified through the comparison of FE calculation and modal test results. System level validation is performed through an optimization process. Experiment modal analysis of stationary disc brake system with brake-line pressure and brake torques applied is conducted. Modal parameters are extracted. Then an optimization process is initiated to minimize the differences between experimental and model predicted modal frequencies. Unstable mode prediction results of initial and validated models are calculated and compared with those from brake noise bench test. The comparison shows the improvement of predicting accuracy.

11.2 Component Level Model and Validation

The target system is a front disc brake of a passenger vehicle. It consists of disc rotor, outer pad (finger pad), inner pad (piston pad), caliper, guiding pins, bracket and steering knuckle, as shown in Fig. 11.1.

All the components are divided into five substructures, which are, A: Outer pad, B: Disc rotor, C: Inner pad, D: Caliper and guiding pins, E: Bracket and steering knuckle. FE models of these substructures are built. The geometry of FE models are from manufacture's CAD data. So in component level validation material properties are the main concern.

First the density of the material is tuned to make the mass of the FE model and the real component equal. Then experiment modal analysis of all components in free-free boundary condition is performed. Modal parameters in same condition are calculated from FE model. ND (nodal diameter) type mode shapes are selected from the results and compared with those from modal test. The Young's modulus parameters are tuned to reduce relative errors between the two set of results. For example, for the validation of disc model, having tuned the material properties, the maximum relative error is 1.41 %. The comparison results are listed in Table 11.1.
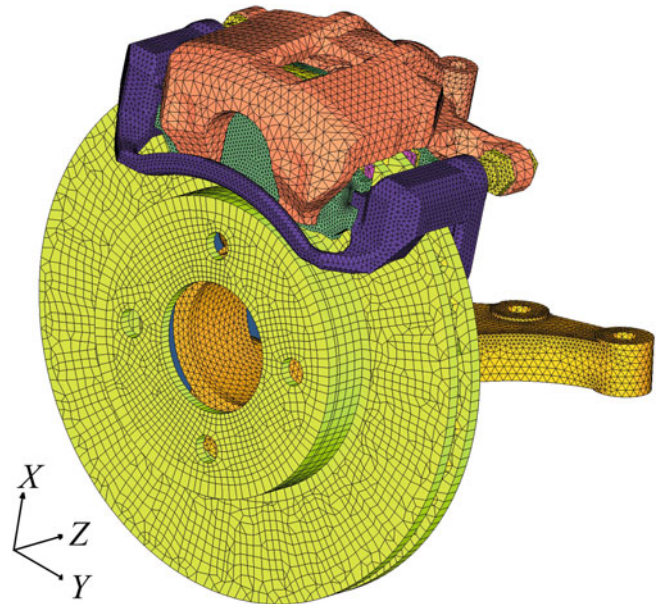
Fig. 11.1 Target brake system

Table 11.1 Modal results of the disc at free-free boundary condition

Mode	2ND	3ND	4ND	5ND	6ND	7ND
Test(Hz)	1,210	2,760	4,407	6,128	7,848	9,675
FE(Hz)	1,215	2,791	4,469	6,182	7,896	9,705
Error(%)	0.37	1.12	1.41	0.88	0.61	0.31

11.3 System Level Validation

11.3.1 Closed-Loop Coupling Model

Closed-loop coupling brake model is based on modal synthesis method. The dynamic behavior of brake components is expressed in the form of modal parameters which are calculated from their individual FE model. Then the components are assembled to become a system model [4, 10].The free vibration equation of the brake system is:

$$M\ddot{u} + \left(K - K_f\right)u = 0 \tag{11.1}$$

Where M and K are discretized mass and stiffness matrix respectively, u is nodal displacement vector, K_f is coupling matrix referring to the relationship between components, which includes spring and friction coupling. K_f is an asymmetric matrix. Constructing coordinate transformation equation as:

$$u = \Phi q \tag{11.2}$$

where

$$\Phi = \begin{bmatrix} \Phi_A & & & & \\ & \Phi_B & & & \\ & & \Phi_C & & \\ & & & \Phi_D & \\ & & & & \Phi_E \end{bmatrix}$$

Φ_A Φ_E are modal shape matrices of components which are modal mass normalized; q is modal coordinate vector in component mode space Φ.

From Eqs. 11.1 and 11.2 it can derived:

$$\ddot{q} + K_{sys}q = 0 \tag{11.3}$$

$$K_{sys} = \begin{bmatrix} \lambda_A & & & & \\ & \lambda_B & & & \\ & & \lambda_C & & \\ & & & \lambda_D & \\ & & & & \lambda_E \end{bmatrix} - \Phi^T K_f \Phi \tag{11.4}$$

where diagonal matrices λ_A λ_E are modal frequency matrices of each component.

Complex eigenvalues and corresponding eigenvectors can be obtained by eigenvalue analysis of Eq. 11.3. The modes of which eigenvalues have positive real parts are unstable modes, and may result in squeal. The imaginary part of the eigenvalue represents the unstable frequency.

K_f is the coupling matrix. For coupling surface between friction material of brake pad and disc rotor, the coupling matrix of a coupled node pair is:

$$K_f = \begin{bmatrix} -K_1 & 0 & K_1 & 0 \\ -\mu K_1 & 0 & \mu K_1 & 0 \\ K_1 & 0 & -K_1 & 0 \\ \mu K_1 & 0 & -\mu K_1 & 0 \end{bmatrix} \tag{11.5}$$

where K_1 is coupling stiffness between friction block and disc rotor and μ is friction factor.

For coupling surface between backplane of inner pad and caliper, the coupling matrix is:

Fig. 11.2 Modal test system of
stationary disk brake
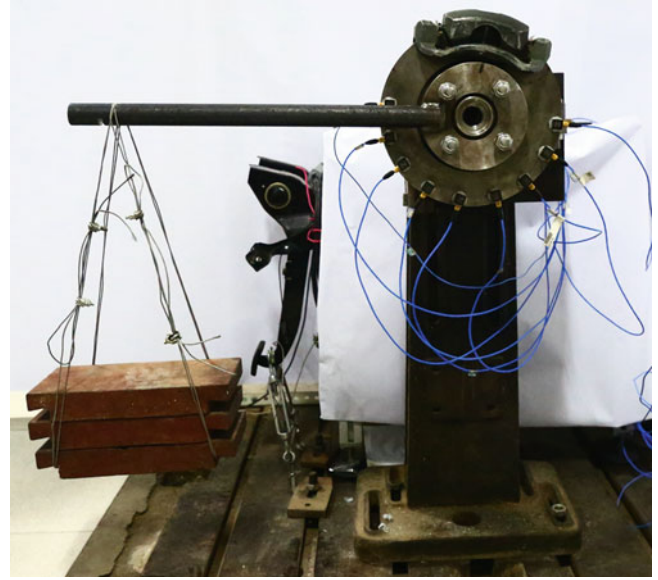
$$\boldsymbol{K}_f = \begin{bmatrix} -K_2 & 0 & K_2 & 0 \\ 0 & 0 & 0 & 0 \\ K_2 & 0 & -K_2 & 0 \\ 0 & 0 & 0 & 0 \end{bmatrix} \tag{11.6}$$

where K_2 is coupling stiffness between backplane of inner brake pad and caliper housing.

$\boldsymbol{K}_f$ consists of coupling stiffness and friction factor. Determining the coupling stiffness values is an important task in the modeling process. To improve the correlation between model predicted and experimental results, the contact stiffness should reflect the actual situations when squeal occurs.

11.3.2 Stationary Modal Test

Modal test of stationary brake assembly is performed to provide validation criteria for the coupled brake system model. So except that the disc is not rotating, all other conditions are made to be closer to that when squeal occurs. The brake is fixed on a firm stand. When testing, certain brake-line pressure is applied to the system. Equivalent brake torques is added to the system through loading bar to make the coupling of components better approaches to real brake situations. A picture of the modal test system of stationary disc brake assembly is shown in Fig. 11.2.

After a few trials, it's found that the modal shape of axial modes of the disc rotor is more regular and significant than others. So in the test, 3 dimensional accelerometers are places along the lower half of the disc's outer edge. The axial response of these points are recorded and used to identify modal parameters of the system.

Based on past experience, we believe that the model to be used for prediction and optimization would produce many modes with similar disc modal shapes and very close modal frequencies. This may introduce confusion to the following work. So some additional accelerometers are placed on caliper fingers and bracket, which are not shown in Fig. 11.3. These signals are used to align the tested and model predicted modes. Totally 13 sensors are used in the test.

Below 6.5 kHz five axial modes, which shapes are regular and smooth and which the modal insurance factors are relative high, are extracted. Modal frequencies and modal shapes are listed in Table 11.2.

Of all the five modes in Table 11.3, the last three modes are chosen for the following optimizing.

Fig. 11.3 Objective function F versus Iteration steps curve
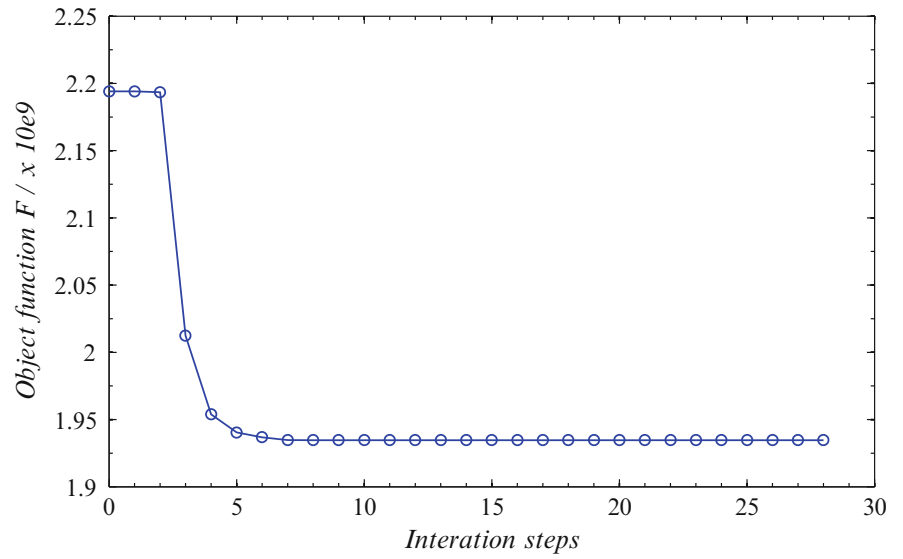
Table 11.2 Modal test result of stationary disc brake

Rank	Modal frequency/Hz	Modal shape[a]
1	1,185.84	
2	1,853.70	
3	2,613.83	
4	4,244.76	
5	6,218.61	

[a]For simple and clarity, axial modal shape is shown in radial deformation

11.3.3 Optimization

The objective of optimization in this paper is to search for better values of coupling stiffness K_1 and K_2 to make the model prediction more accordant with above stationary test results.

Table 11.3 Calculated and test modal frequencies

Seq.	Test result (Hz)	calculated result (Hz)	
		Before optimization	After optimization
1	2,613.83	2,763.91	2,647.33
2	4,244.76	4,268.46	4,290.98
3	6,218.61	6,225.52	6,214.95

Table 11.4 Final values of coupling stiffness

Component 1	Component 2	Coupling stiffness (N/m)
Friction block	Disc rotor	4.9×10^7
Inner pad backplane	Caliper	2.6×10^7

As the initial disc model is for squeal analysis, where sliding friction coupling exist, it should be modified to represent the stationary disk brake assembly in the test. Since the disc doesn't rotate and no sliding friction exists, the asymmetric friction related items in Eq. 11.5 will disappear. The coupling matrix K_f becomes symmetric. So the real parts of eigenvalues of the system (Eq. 11.3) will be all zeros, which means that all predicted modes are stable in this circumstance.

The objective function F of optimization is defined as the variance between modal frequencies calculated from the revised stationary model and those from the test.

$$F = \sum_{j=1}^{N} \left[W_j \left(f_{jl} - f_{je} \right)^2 \right] \tag{11.7}$$

Where f_{jl} is jth predicted modal frequency, f_{je} is jth test modal frequency, W_j is the corresponding weighting coefficient.

$$W_j = \left(f_{1e}/f_{ie} \right)^2 \tag{11.8}$$

So the optimization problem can be formulated as

$$Min : F \tag{11.9}$$

The optimization variables are K_1 and K_2, for clarity, the stiffness values between friction blocks of pads and disc and between inner pad backplane and caliper housing, respectively.

Since the Young's modulus of the friction block is lower than that of the disc, K_1 mainly depends on the former [10]. Its local stiffness is derived from static force/deformation relation of its FE model and is used as the initial value of K_1, which is approximately 3.17×10^7 N/m.

Concerning K_2, because the piston is not considered in the closed-loop coupling disc brake model [10], K_2 represents the volume elastic stiffness of brake oil and pipe-line system, which is estimated to be within (5×10^6 5×10^7 N/m).

The optimization problem is solved using modified sequential quadratic program (SQP) type algorithm provided in the Matlab optimization toolbox. Its basic idea is to transform the constrained optimization problem into an easier sub-problem that can then be solved and used as the basis of an iterative process. The newest version of this method is focused on the solution of the Karush-Kuhn-Tucker (KKT) equations. The KKT equations are necessary conditions for optimality for a constrained optimization problem. If the problem is a so-called convex programming problem, then the KKT equations are both necessary and sufficient for a global solution point. The solution of the KKT equations forms algorithms that attempt to compute the Lagrange multipliers directly. Constrained quasi-Newton methods guarantee super-linear convergence by accumulating second-order information regarding the KKT equations using a quasi-Newton updating procedure.

The variation of objective function F following iteration steps is illustrated in Fig. 11.3. It can be seen that the objective function F drops dramatically and converges after a few steps of iteration.

Modal frequencies calculated from stationary model before and after optimization and those from stationary modal test are listed in Table 11.3. It shows that through optimizing the coupling stiffness values, the model predicted modal frequencies are closer to test modal frequencies. From this result we can believe that now the coupling stiffness values are better approximations of real situations.

The final determined coupling stiffness values are shown in Table 11.4.

Fig. 11.4 Bench test and model
predicted results
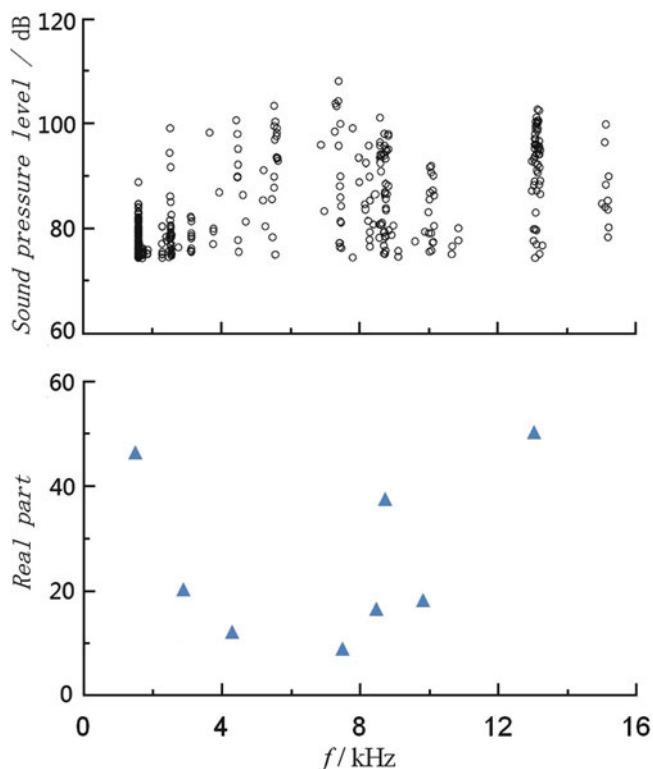
11.4   Correlation Between Model Prediction and Brake Squeal Test

After the two stage validation process, the obtained brake system model should be a better representation of the target brake system. The predicted unstable modes and results from brake squeal bench test are compared and presented in Fig. 11.4.

The upper part of Fig. 11.4 is the result of bench squeal test. The horizontal axle is the noise frequency and the vertical is the measured sound pressure level of squeal. A circle in the figure represents a squeal occurrence. It shows that squeal occurs at 1.6, 2.7, 4.3, 5.5, 7.5, 8.7, 10, and 13 kHz. The greatest occurrences are at 1.6, 2.7, 8.7, and 13 kHz.

The lower part of Fig. 11.4 is the result of unstable modes predicted from the validated models. It includes 8 unstable modes, among which 1.6 , 2.7, 4.3, 7.5, 8.7, 10, and 13 kHz match test results. The real part of 13 kHz mode has the greatest value / squeal occurrence. The real parts of 1.6 and 8.7 kHz modes are close to that of 13 kHz mode. Obviously the validated model predicts most of the squeal frequencies and the real part can represent, to some extent, the occurrences of squeal. The method presented in this paper is proven to be valid and effective.

11.5   Conclusion

- A two stage validation method of closed-loop coupling disc brake model for squeal analysis using complex eigenvalue analysis is presented. At component level, FE models are verified through the comparison of calculation and modal test results. At the system level, optimization method is used adopted to minimize the differences between modal frequencies predicted by the model and those from experiment modal analysis of stationary disc brake assembly with brake line pressure and brake torques applied.
- The validated model can predict most of the squeal frequencies and the real part represent the occurrences of squeal.

References

1. Kinkaid NM, O'Reilly OM, Papadopoulos P (2003) Automotive disc brake squeal. J Sound Vib 267(1):105–166
2. Liles GD (1989) Analysis of disc brake squeal using finite element methods. SAE technical paper 891150
3. Zhu X, Guan D (1993) The experimental and simulational analysis on drum brake squeal by structurally closed-loop coupling model. SAE technical paper 931879
4. Guan D, Jiang D (1998) A study on disc brake squeal using finite element methods. SAE technical paper 980597
5. Guan D, Huang J (2003) The method of feed-in energy on disc brake squeal. J Sound Vib 261(2):297–307
6. Guan D, Su X, Zhang F (2006) Sensitivity analysis of brake squeal tendency to substructures' modal parameters. J Sound Vib 291(1):72–80
7. Ripin ZBM (1995) Analysis of disc brake squeal using the finite element method, University of Leeds
8. Lee YS, Brooks PC, Barton DC et al (1998) A study of disc brake squeal propensity using a parametric finite element model//IMECHE conference transactions, pp 191–201
9. Abu-Bakar AR, Ouyang H (2008) Recent studies of car disc brake squeal. New Research on Acoustics, pp 159–198
10. Jiang D (1998) A study on disc brake squeal. Tsinghua University, Beijing

Chapter 12
Estimation of Torsional Compliance (Stiffness) from Free-Free FRF Measurements: eRCF Theory

Hasan G. Pasha, Randall J. Allemang, Allyn W. Phillips, Alexander Young, and Jeff Poland

Abstract The enhanced rotational compliance function (eRCF) is a useful concept for estimation of static torsional compliance/stiffness of a structure using measured frequency response functions (FRFs) from a structural system with free-free boundary conditions. The eRCF is estimated using FRF measurements involving impact testing in which a four by four (4x4) FRF matrix is acquired at four separate, symmetric locations on a structure. This is in contrast to a traditional, static torsion test that involves constraints applied to two of these four locations and a static torque applied to the other two of these four locations. The traditional, static torsion test requires extensive instrumentation and a two day test procedure while the eRCF method involves minimal instrumentation over several hours. Added masses can be utilized to acquire additional statistical data that estimates the same compliance (stiffness). The theoretical background is presented along with both modeling and experimental cases involving a rectangular plate structure

Notation

Symbol	Description
σ	Standard deviation
Δ	Static deflection (in)
Θ	Angular deflection (rad)
f_{max}	Maximum frequency of the stiffness parameter estimation band (Hz)
f_{min}	Minimum frequency of the stiffness parameter estimation band (Hz)
L_f	Front spacing (in)
L_r	Rear spacing (in)
F	Generalized force magnitude (lb$_f$)
M	Generalized moment magnitude (lb$_f$ in)
$[H(\omega)]$	FRF matrix ($\frac{X}{F}$)
K_T	Static torsional stiffness (lb$_f$ in/deg)
{V}	Moment scaling vector
DOF 1	Left front DOF, z direction
DOF 2	Right front DOF, z direction
DOF 3	Left rear DOF, z direction
DOF 4	Right rear DOF, z direction
DOF 5	Left mid-span DOF, z direction
DOF 6	Right mid-span DOF, z direction
eRCF(ω)	Enhanced Rotational Compliance Function
eFRF(ω)	Enhanced Frequency Response Function

H.G. Pasha • R.J. Allemang (✉) • A.W. Phillips • A. Young
University of Cincinnati-Structural Dynamics Research Lab (UC-SDRL), Cincinnati, OH 45220, USA
e-mail: randy.allemang@uc.edu

J. Poland
BMW Manufacturing Company, Spartanburg, SC 29651, USA

12.1 Introduction

Static structural stiffness is an important criterion in automobile structure design as it impacts vehicle handling, ride comfort, safety and durability. Traditionally, automobile manufacturers used *special test rigs* to estimate stiffness, which require *precise setup* and *expensive instrumentation*. In the past decade, dynamic frequency response function (FRF) measurements with modeling techniques were used to estimate static stiffness [1–3]. Though test setup time and expense associated with the instrumentation are considerably reduced, *heroic technical measures* in terms of user experience and data processing are required to get reasonable stiffness estimates.

As static stiffness information is contained in the measured free-free FRFs, it can be extracted by utilizing *spatial/geometric filtering* and *averaging techniques* [4, 5]. A simple and efficient method to estimate static torsional stiffness from free-free FRFs is developed in this paper. The enhanced Rotational Compliance Function (eRCF) method presented here utilizes spatial/geometric filtering and averaging techniques to enhance response functions and estimate static stiffness. The stiffness estimates obtained from this method were comparable with the analytical results, while requiring significantly less resources.

12.2 Static Torsional Stiffness

Torsional stiffness or *rotational stiffness* K_T is defined as the ratio of applied torque to the angle of twist.

$$K_T = \frac{T}{\theta} \tag{12.1}$$

where, T is the torque (lb_f in or N m) and θ is the angle of twist (deg). Torsional stiffness is expressed in lb_f in/deg or N m/deg.

Torsional stiffness can also be expressed in terms of the modulus of rigidity (a.k.a shear modulus, G: units psi or Pa), the torsion constant (J: units in^4 or m^4) and the characteristic length, L (distance between the fixed end to the point of application of the torque). The product of the torsion constant and modulus of rigidity, $J G$ is more commonly known as *torsional rigidity* [6].

$$K_T = \frac{J G}{L} \tag{12.2}$$

It is evident from Eq. (12.2) that the torsional stiffness is inversely proportional to the characteristic length, in other words, the torsional stiffness value also depends on the test geometry. As a result, multiple torsional stiffness estimates might be required for a structure that has multiple loading locations.

Note that this characteristic length is not included in Eq. (12.1). It is often a convention to present the torsional stiffness, assuming that the characteristic length L is fixed or otherwise known. For a comparative evaluation (i.e. between the model/static testing methods and the enhanced rotational compliance function), the characteristic length is fixed for a given structure and the loading condition. As a result, the characteristic length does not impact the torsional stiffness.

The torsional stiffness of a structure, for example a plate shown in Fig. 12.1, can be calculated using the following expression by performing a static FE analysis or static testing. Consider that the vertices on one end of the plate are constrained and a moment is applied on the other end. The torsional stiffness is defined as

$$K_T = \frac{T}{\theta} \implies \frac{F L_f/2}{\theta} \tag{12.3}$$

where, $\theta = \tan^{-1}\left(\frac{\Delta}{L_f/2}\right)$, is the angular twist, which is expressed in terms of the vertical displacement Δ and the moment arm L_f.

Fig. 12.1 Configuration for estimating torsional stiffness
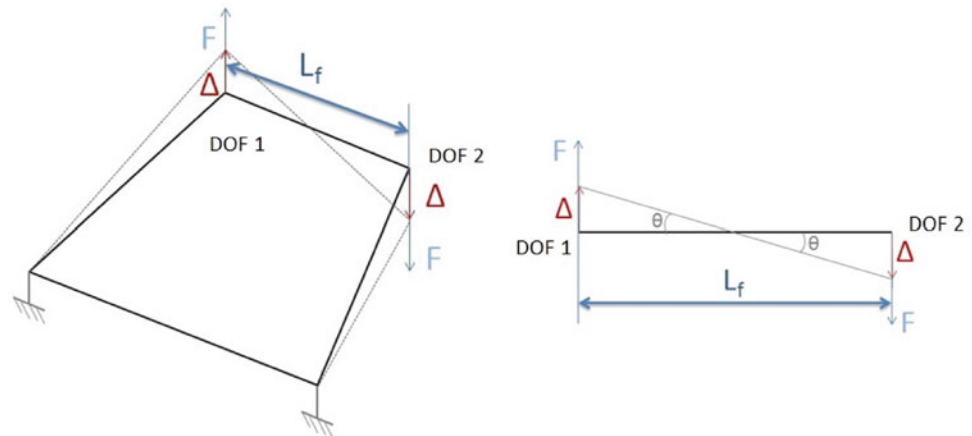
12.3   Enhanced Rotational Compliance Function (eRCF)

12.3.1   General Procedure for Estimating Stiffness using Enhanced Compliance Function Method

The formulation of the enhanced rotational compliance function method for a particular load case involves the following steps:

(1) Develop a free-free system in dynamic equilibrium, which is equivalent to the statically determinate constrained system used in static testing methods
(2) Express the reactions and applied moments/forces in terms of a generalized moment to obtain the moment scaling vector $\{V\}$
(3) Utilize the measured FRFs and the moment scaling vector to formulate the required enhanced compliance function

A system in dynamic equilibrium, which is equivalent to a statically determinate system should be developed for a particular load case. This is achieved by applying equal and opposite force (reaction forces) at the constraint locations. The boundary constraints (fixed to free) at front and rear load/deflection DOFs have no effect on the stiffness estimate as long as the motion at all DOFs is accounted for [7]. The static rotational stiffness is sensitive only to relative motion, end-to-end. Therefore, the boundary constraints can be replaced by reaction moments/forces.

The estimation of static stiffness using an enhanced compliance function involves the following steps:

(1) Measure the acceleration FRFs of the free-free system
(2) Derive the compliance or dynamic stiffness FRFs from the measured acceleration FRFs
(3) Form a reduced (sieved) dataset based on the desired test configuration. A 4x4 system for torsional stiffness estimation is formed.
(4) Compute the enhanced rotational compliance function formulated for the load case, using the measured FRFs and moment scaling vector
(5) Fit an appropriate model to the low frequency region of the enhanced compliance function
(6) Use the model parameters from Step 5 to estimate the static compliance/stiffness

12.3.2   Formulation of the eRCF for Torsion Load Case

In order to simulate a pure torsion load while performing static testing, a commonly used configuration consists of constraints at the rear DOFs. A moment is applied at the front DOFs and the deformations are measured, as illustrated in Fig. 12.2a. The stiffness constraints are applied at the rear DOFs (DOFs 3 and 4), while a moment is applied at front DOFs (DOFs 1 and 2). An equivalent configuration without stiffness constraints for the torsion test is shown in Fig. 12.2b. The constraints at DOFs 3 and 4 are now replaced by a reaction moment ($M_r = F_r \cdot L_r$) at the rear.
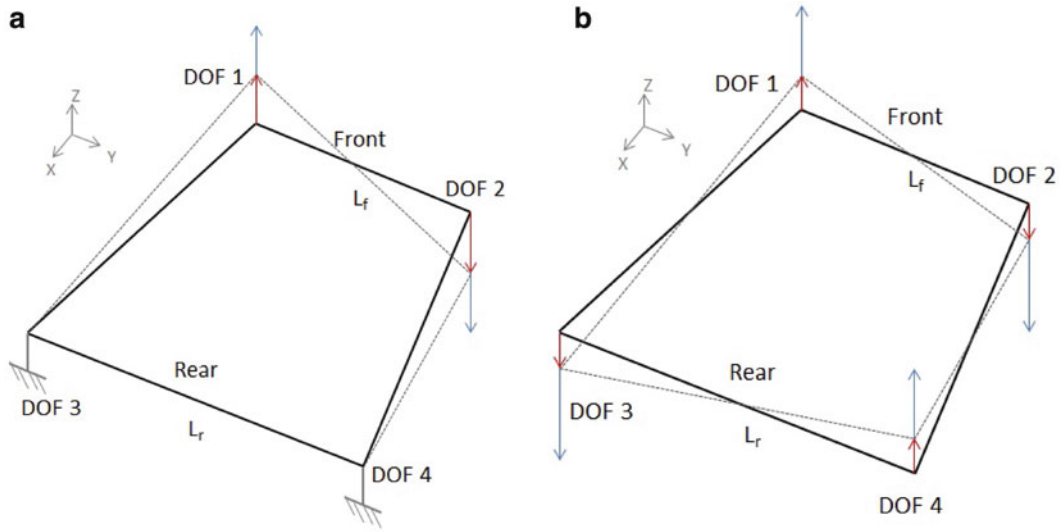
Fig. 12.2 Equivalent configurations for estimating torsional stiffness. (**a**) Fixed-free configuration. (**b**) Equivalent free-free configuration

Fig. 12.3 Load/displacement orientations
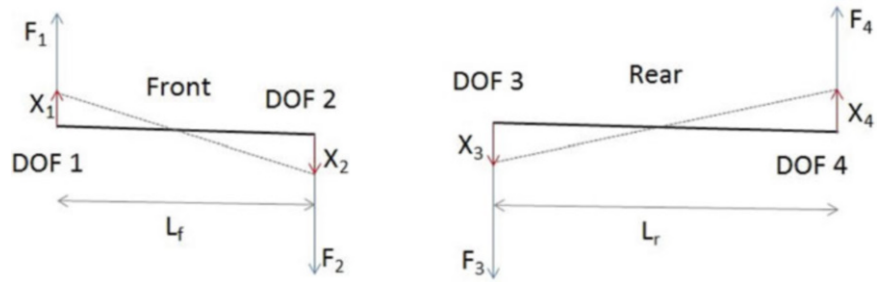
When the moments are applied on the structure, the sum of the applied moments should be equal to zero for the structure to be in equilibrium:

$\circlearrowleft^+$ $\Sigma M_x = 0$

$$M_f = M_r \tag{12.4}$$

$$F_f \cdot L_f = F_r \cdot L_r \tag{12.5}$$

where, M_f, F_f ($= F_1, F_2$), and M_r, F_r ($= F_3, F_4$), are the moments and forces applied at the front and rear DOFs respectively (Fig. 12.3).

Beginning with the fundamental input/output FRF equation,

$$\{X(\omega_i)\}_{4x1} = [H(\omega_i)]_{4x4} \ \{F(\omega_i)\}_{4x1}. \tag{12.6}$$

The force vector $\{F\}$ is rewritten in terms of the generalized moment magnitude (M), applied to the front and the rear of the structure. The frequency notation is dropped for simplicity

$$\{F\} = \begin{Bmatrix} F_1 \\ F_2 \\ F_3 \\ F_4 \end{Bmatrix} \implies \begin{Bmatrix} +\frac{M}{L_f} \\ -\frac{M}{L_f} \\ -\frac{M}{L_r} \\ +\frac{M}{L_r} \end{Bmatrix} \implies M \begin{Bmatrix} +\frac{1}{L_f} \\ -\frac{1}{L_f} \\ -\frac{1}{L_r} \\ +\frac{1}{L_r} \end{Bmatrix} \implies M\{V\} \tag{12.7}$$

where, $\{V\}$ is the *moment scaling vector*.

Therefore,

$$\{X\}_{4\times1} = M \ [H]_{4\times4} \ \{V\}_{4\times1} \,. \tag{12.8}$$

Pre-multiplying both sides by $\{V\}^{\mathsf{T}}$,

$$\{V\}^{\mathsf{T}}_{1\times4} \ \{X\}_{4\times1} = M \ \{V\}^{\mathsf{T}}_{1\times4} \ [H]_{4\times4} \ \{V\}_{4\times1} \,. \tag{12.9}$$

Expanding and reorganizing the terms on the LHS,

$$\mathsf{LHS} \implies \{V\}^{\mathsf{T}}_{1\times4} \ \{X\}_{4\times1} = \frac{X_1}{L_f} - \frac{X_2}{L_f} - \frac{X_3}{L_r} + \frac{X_4}{L_r} \tag{12.10}$$

$$= \frac{X_1 - X_2}{L_f} - \frac{X_3 - X_4}{L_r} \,. \tag{12.11}$$

Expressing the angular deflections in terms of the relative displacements and by applying the small angle assumption, the rotation angles are:

$$\theta_1 = \tan^{-1}\left(\frac{X_1 - X_2}{L_f}\right) \approx \frac{X_1 - X_2}{L_f} \tag{12.12}$$

$$\theta_2 = \tan^{-1}\left(\frac{X_3 - X_4}{L_r}\right) \approx \frac{X_3 - X_4}{L_r} \,. \tag{12.13}$$

Therefore, the LHS of Eq. (12.9) becomes

$$\{V\}^{\mathsf{T}}_{1\times4} \ \{X\}_{4\times1} = \theta_1 - \theta_2 \implies \Delta\theta. \tag{12.14}$$

Organizing the equation into the final form by using the expression in Eq. (12.14) in Eq. (12.9),

$$\Delta\theta = M \ \{V\}^{\mathsf{T}}_{1\times4} \ [H]_{4\times4} \ \{V\}_{4\times1} \tag{12.15}$$

$$\mathsf{eRCF}(\omega_i) \implies \frac{\Delta\theta}{M} = \{V\}^{\mathsf{T}}_{1\times4} \ [H(\omega_i)]_{4\times4} \ \{V\}_{4\times1} \,. \tag{12.16}$$

It has to be noted that in the above equations, all forces, moments, displacements and rotations obey a right hand coordinate rule. Therefore, these terms must be entered into the equations using a common right hand coordinate system and should have positive/negative signs accordingly.

12.4 Experimental Validation

A rectangular steel plate structure was fabricated and the FE models of the plate were validated [8–10]. The validated models were then used to predict the static torsional stiffness using ANSYS®. The measured FRFs from structural tests on the rectangular plate were used to estimate the static torsional stiffness by applying the enhanced rotational compliance function formulated in the previous section.

The analytical predictions were compared with the estimates from the enhanced compliance function method (using both synthesized and measured FRFs). The steps involved in validating the enhanced rotational compliance function method and the results obtained are discussed in detail in the subsequent sections.

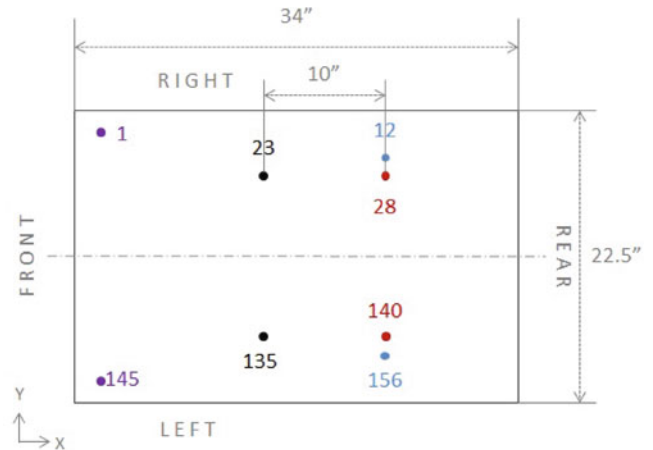**Fig. 12.4** DOF map of the rectangular plate for torsional stiffness estimation

Table 12.1 Rectangular plate DOF description for torsion configurations; $L = 10$ in for both the configurations

Sl	DOF Label Left	DOF Label Right	Distance (in)	Description
1	135	23	14	Front DOFs for Configurations 1 and 2
2	140	28	14	Rear DOFs for Configuration 1 (equal spacing)
3	156	12	18	Rear DOFs for Configuration 2 (unequal spacing)
4	145	1	20	Mass attachment DOFs for 1x and 2x mass cases

12.4.1 Analytical Method

The static torsional stiffness of the rectangular plate can be estimated analytically using the expression in Eq. (12.3). To analytically predict the torsional stiffness, four points on the validated plate model are chosen such that they are symmetric about the centerline. Two configurations were chosen for estimating the torsional stiffness as shown in Fig. 12.4. The geometric details of the selected configurations are given in Table 12.1.

The rotation angle meets the small angle criteria, $\theta = \frac{2\Delta}{L_f}$ rad, where Δ is the vertical deflection at the front DOF. The vertical deflection at the front DOFs is retrieved and the static torsional stiffness is estimated using Eq. (12.3), The static torsional stiffness was estimated to be 3549.33 lb$_f$ in/deg for the *equal spacing* configuration (Configuration 1) and 3619.11 lb$_f$ in/deg for the *unequal spacing* configuration (Configuration 2) (for the no added mass case).

12.4.2 Enhanced Rotational Compliance Function (eRCF) Method

As mentioned in the previous section, two different plate configurations, one with equal front and rear spacing and another with larger rear spacing were considered. FRF data for three perturbed mass cases (no mass, 1x mass and 2x mass cases) for both the configurations was collected.

The perturbed mass cases were utilized to acquire additional statistical data that refined the torsional stiffness estimates. It is evident from the eRCF plots for both the configurations that adding perturbed masses shifted the peaks towards the low frequency region. However, the global characteristics (specifically static torsional stiffness) do not vary considerably.

In order to utilize the eRCF method to estimate the torsional stiffness, a dataset containing the driving-point and the cross-point FRFs should be measured at the locations where the torsional stiffness is to be estimated. Typically, the measured FRFs are acceleration FRFs $\left(\frac{A}{F}\right)$ obtained from an impact test from which compliance functions $\left(\frac{X}{F}\right)$ are derived.

A stiffness estimation toolkit, in which the theoretical eRCF equation (Eq. (12.16)) was implemented, was developed using Matlab$^{\circledR}$. The FRF data was acquired in British units for the rectangular plate. Therefore, a units calibration/conversion value of 386.088 for converting g's to in/s^2 was applied on the acceleration FRFs $\left(\frac{A}{F}\right)$. The distances between front and rear DOFs should be measured and converted in the base displacement units (inch in this case).

Fig. 12.5 eRCF for rectangular plate generated with synthesized FRFs (no added mass cases). (**a**) Configuration 1—Equal spacing $L_f = L_r \implies$ 14 in. (**b**) Configuration 2—Unequal spacing $L_f = 14$ in and $L_r = 18$ in
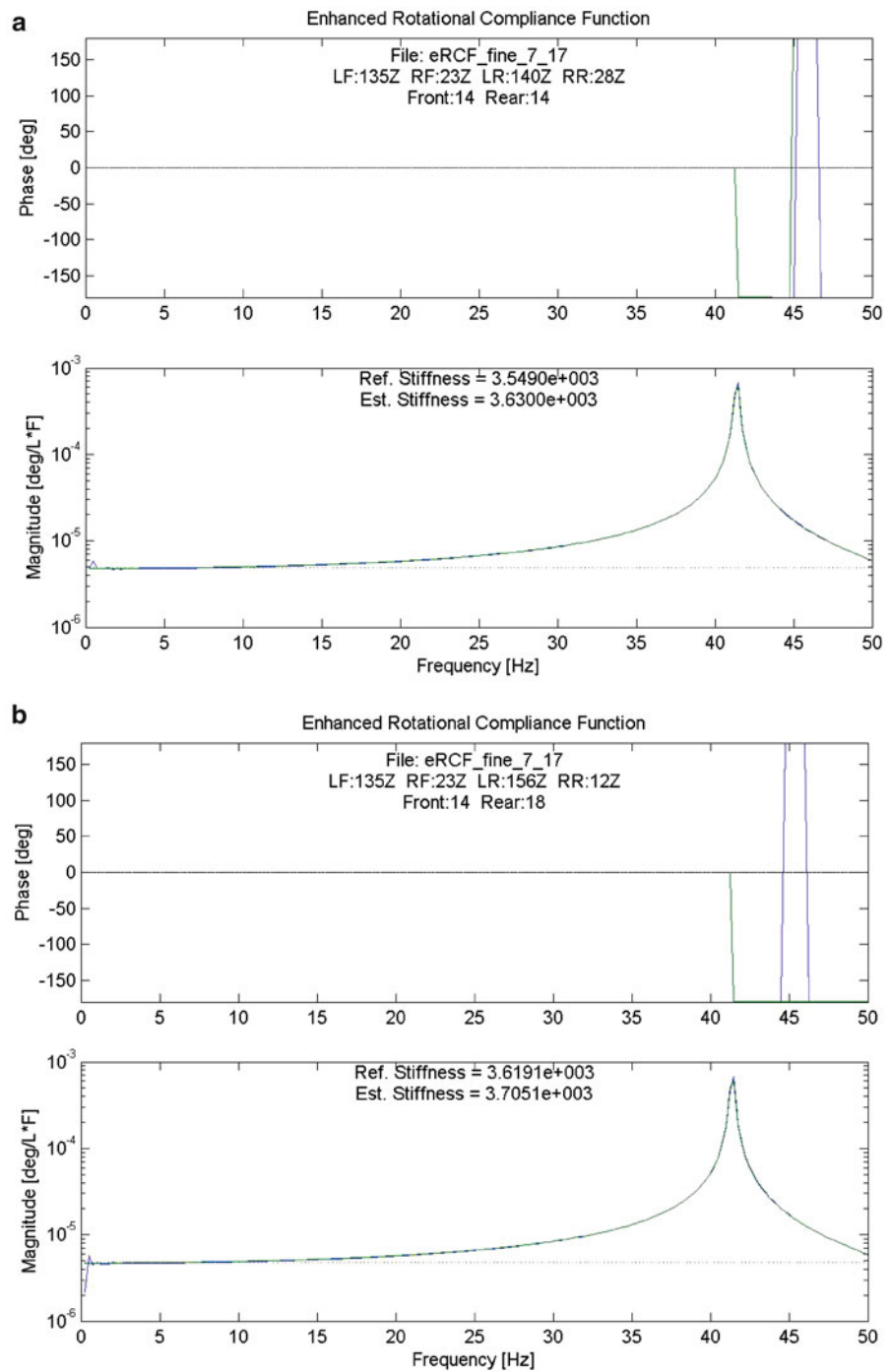
Synthesized FRFs (obtained from the validated FE model), as well as measured FRFs were used to generate the eRCF for the plate torsion configurations. The eRCFs obtained using synthesized FRFs are shown in Fig. 12.5. Individual data fit was performed for each of the perturbed mass case and the plots were overlaid for both plate configurations, as shown in Fig. 12.6.

From the eRCF plots obtained using measured FRFs, it is evident that the effects due to the rigid body modes' modal response and the noise in the low frequency region are reduced when compared to the impedance modeling method.

Fig. 12.6 eRCF for rectangular plate generated with measured FRFs (no mass and added mass cases). (**a**) Configuration 1—Equal spacing $L_f = L_r \implies 14$ in. (**b**) Configuration 2—Unequal spacing $L_f = 14$ in and $L_r = 18$ in
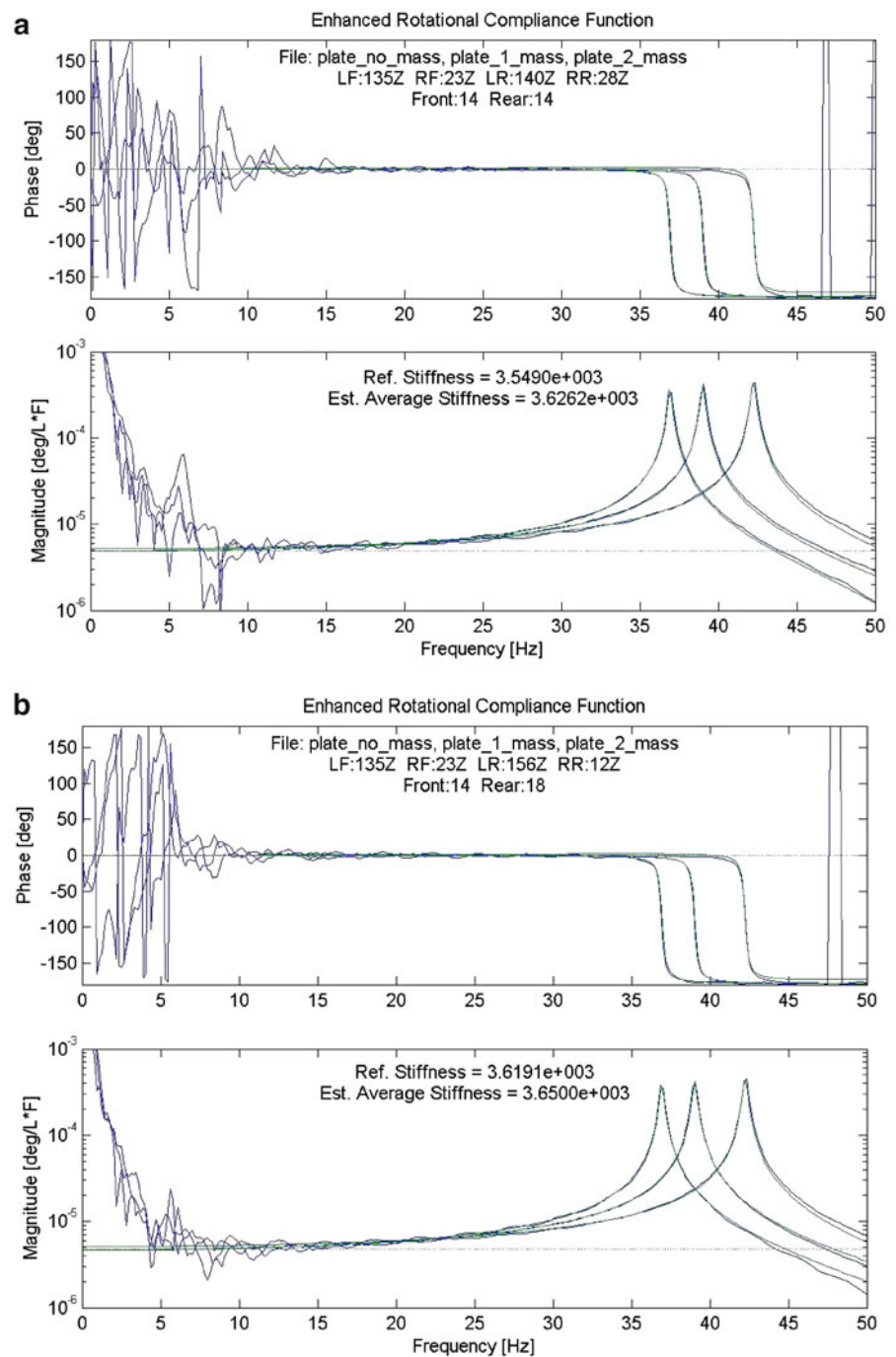
12.5 Results and Discussions

12.5.1 Static Torsional Stiffness Estimation Sensitivity

The stiffness is estimated by fitting a model to the eRCF. In the modal parameter estimation process, modal parameters are extracted after fitting an appropriate model to the data. Unlike modal parameter estimation, no direct use of the modal parameters is involved. The goal is to use an appropriate model and consistent data to be able to estimate the zero frequency compliance.

Typically, reasonable estimates should be obtained by fitting a SDOF model to the first peak of the enhanced compliance function and then extrapolating the value at 0 Hz. The accuracy of the stiffness estimates is dependent on carefully choosing

Table 12.2 Details of the models selected to fit the eRCF method for Configurations 1 and 2

Model	Peaks chosen
SDOF I	First peak
SDOF II	First peak
MDOF I	Peaks one and two

Fig. 12.7 eRCF method parameter estimation with SDOF I model; Configuration 1, no mass case
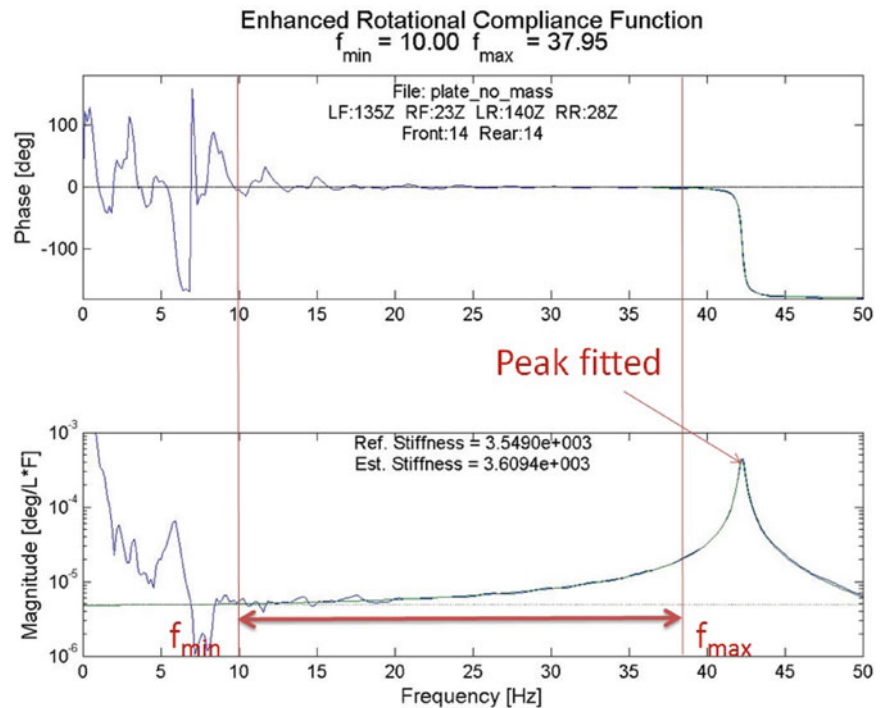
the frequency range where the data is fit. It is required to identify the peak, minimum and maximum frequencies in the desired frequency range for the compliance/stiffness parameter estimation processes. If a poor choice of frequency bandwidth is made, it results in an increased variation in the stiffness estimates.

It is recommended to choose the minimum frequency such that the corresponding phase is nominally 0° to avoid including rigid body response and measurement noise in the model. The maximum frequency should be chosen in the vicinity of the peak being fit.

It was anticipated that by fitting more than just one peak (that predominantly contributes to the static stiffness), a better estimate of torsional stiffness can be achieved. The effect of fitting multiple peaks on the stiffness estimates using various MDOF models along with SDOF models (fitted with different frequency bandwidths) was studied for the eRCF method.

The peaks selected in the different models used to fit the eRCF method for the rectangular plate are listed in Table 12.2. A residual flexibility constant to account for the effect of the high frequency peaks was used in all the models while fitting the eRCFs for the rectangular plate Configurations 1 and 2 (including the perturbed mass cases). A value below the frequency of the first peak was chosen as the maximum frequency (f_{max}) for SDOF I model, the exact value varied depending on which mass perturbed case was being fit.

Allowing the maximum frequency to include the region beyond the resonance should yield acceptable results as the data is usually not contaminated with measurement noise near the peaks. The effect of choosing a maximum frequency value beyond the first peak was studied with SDOF II model. The first two peaks were chosen in the MDOF I model. Example plots to illustrate the minimum and maximum frequencies and the peak (peaks) that was (were) fitted for SDOF I, SDOF II and MDOF I models are shown in Figs. 12.7, 12.8 and 12.9 and the torsional stiffness estimation sensitivity for the rectangular plate is presented in Tables 12.3, 12.4 and 12.5 respectively.

Comparing the results obtained for these models, MDOF I model had the least variation in stiffness estimates in terms of the nominal (average) torsional stiffness value ($\pm 1.43\,\%$). It was also observed that selecting a maximum frequency value above the first peak (SDOF II model) did not significantly yield better results for the torsional stiffness values as compared to SDOF I model.

Fig. 12.8 eRCF method
parameter estimation with SDOF
II model; Configuration 1, no
mass case
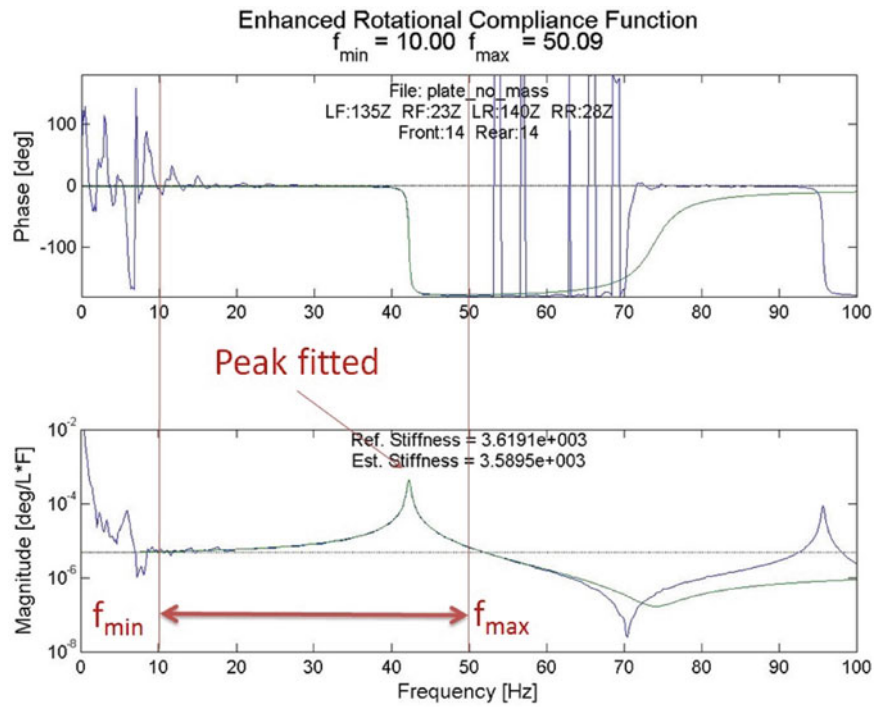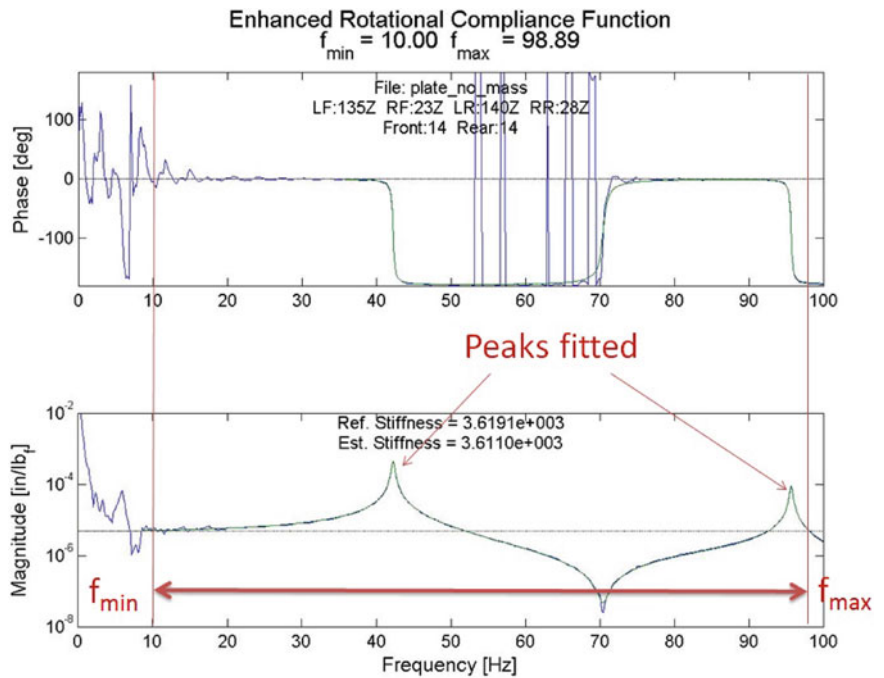

Fig. 12.9 eRCF method
parameter estimation with MDOF
I model; Configuration 1, no
mass case, 2 peaks fitted

12.5.2 Comparison with Results from the Theoretical Model

It is evident from the results for the static torsional stiffness that the theoretical error/uncertainty of the stiffness estimates
from the eRCF method is less than ± 3 % of the nominal torsional stiffness value.

Table 12.3 Parameter estimation sensitivity of eRCF method with SDOF I model (for different f_{min} values); Configuration 1: $K_{T_{ref}}$ = 3549.00 lb_f in/deg and Configuration 2: $K_{T_{ref}}$ = 3619.11 lb_f in/deg

Config.#		f_{max} (Hz)	Static torsional stiffness K_T (lb_f in/deg)					Average $\overline{K_T}$	Std. Dev. σ	$\sigma/\overline{K_T}$ %
			10 Hz-f_{max}	15 Hz-f_{max}	20 Hz-f_{max}	25 Hz-f_{max}	30 Hz-f_{max}			
1	No mass	37.95	3609.40	3609.80	3663.20	3665.50	3666.90	3642.96	30.48	0.84
	1x mass	35.74	3592.20	3682.30	3664.20	3639.00	3693.90	3654.32	40.44	1.11
	2x mass	33.53	3595.70	3651.30	3640.90	3598.70	3419.70	3581.26	93.64	2.61
2	No mass	38.88	3743.30	3732.00	3697.10	3700.60	3674.90	3709.58	27.74	0.75
	1x mass	34.85	3715.70	3701.40	3702.40	3685.00	3781.80	3717.26	37.69	1.01
	2x mass	32.90	3731.70	3660.80	3640.10	3626.90	2955.70	3523.04	319.72	9.08

Table 12.4 Parameter estimation sensitivity of eRCF method with SDOF II model (for different f_{min} values); Configuration 1: $K_{T_{ref}}$ = 3549.00 lb_f in/deg and Configuration 2: $K_{T_{ref}}$ = 3619.11 lb_f in/deg

Config.#		f_{max} (Hz)	Static torsional stiffness K_T (lb_f in/deg)					Average $\overline{K_T}$	Std. Dev. σ	$\sigma/\overline{K_T}$ %
			10 Hz-f_{max}	15 Hz-f_{max}	20 Hz-f_{max}	25 Hz-f_{max}	30 Hz-f_{max}			
1	No mass	50.085	3589.50	3580.00	3461.80	3319.30	3123.10	3414.74	196.36	5.75
	1x mass	50.085	3656.60	3596.00	3622.80	3699.00	3841.40	3683.16	96.48	2.62
	2x mass	50.085	3627.80	3591.40	3562.20	3532.60	3448.20	3552.44	68.10	1.92
2	No mass	50.085	3643.50	3602.70	3582.90	3501.30	3399.40	3545.96	96.92	2.73
	1x mass	50.085	3592.00	3539.30	3487.50	3428.10	3345.20	3478.42	96.14	2.76
	2x mass	50.085	3509.80	3490.60	3412.70	3313.20	3282.00	3401.66	102.31	3.01

Table 12.5 Parameter estimation sensitivity of eRCF method with MDOF I model (for different f_{min} values); Configuration 1: $K_{T_{ref}}$ = 3549.00 lb_f in/deg and Configuration 2: $K_{T_{ref}}$ = 3619.11 lb_f in/deg

Config.#		f_{max} (Hz)	Static torsional stiffness K_T (lb_f in/deg)					Average $\overline{K_T}$	Std. Dev. σ	$\sigma/\overline{K_T}$ %
			10 Hz-f_{max}	15 Hz-f_{max}	20 Hz-f_{max}	25 Hz-f_{max}	30 Hz-f_{max}			
1	No mass	98.89	3611.00	3603.30	3565.90	3538.10	3519.40	3567.54	39.86	1.12
	1x mass	98.89	3599.50	3553.50	3528.50	3500.20	3467.50	3529.84	50.45	1.43
	2x mass	98.89	3675.50	3656.80	3639.30	3618.30	3587.70	3635.52	34.09	0.94
2	No mass	98.89	3640.80	3621.50	3610.40	3587.10	3569.70	3605.9	28.04	0.78
	1x mass	98.89	3611.40	3589.40	3569.70	3551.20	3530.40	3570.42	31.67	0.89
	2x mass	98.89	3558.20	3546.80	3519.00	3495.10	3500.10	3523.84	27.93	0.79

12.5.3 Issues with the eRCF Approach

The quality of the measured data is critical. As double impacts and overloads in high frequency region could severely affect this method, the force/response spectrum and overload indicators should be checked and monitored while acquiring the data. In addition, calibration of the impact hammer and sensors should be performed carefully as they directly affect the stiffness estimates.

12.6 Conclusions

The enhanced rotational compliance function (eRCF) is a simple and efficient method to accurately estimate static torsional compliance/stiffness using measured frequency response functions (FRFs) from a structural system with free-free boundary conditions. The FRF measurements are obtained from impact testing at selected DOFs quickly with minimal instrumentation. These tests involve obtaining a 4x4 FRF matrix at four separate, symmetric locations on a structure for a particular torsional stiffness estimate.

Traditional static torsional tests involve constraints applied to two of these four locations and static loads (moment) applied to the other two of these four locations. These traditional, static torsion tests require extensive instrumentation and a time-consuming procedure. These traditional tests are likely sensitive to the overhung structure problem discussed in this paper.

The theoretical background for eRCF was presented along with validations using both modeling and experimental cases involving a rectangular plate structure. The eRCF method involves minimal instrumentation.

Fitting a MDOF model had the least variation in stiffness estimates in terms of the nominal (average) torsional stiffness value (± 1.43 %). It was also observed that selecting a maximum frequency value above the first peak did not significantly yield better results for the torsional stiffness values as compared to an SDOF model in which the maximum frequency was selected below the first peak.

References

1. Rediers B, Yang B, Juneja V (1998) Static and dynamic stiffness–one test, both results. In: Proceedings of the international modal analysis conference (IMAC) XVI–a conference and exposition on structural dynamics
2. Griffiths D, Aubert A, Green ER, Ding J (2003) A technique for relating vehicle structural modes to stiffness as determined in static determinate tests. SAE Technical Paper Series (2003-01-1716)
3. Deleener J, Mas P, Cremers L, Poland J (2010) Extraction of static car body stiffness from dynamic measurements. SAE Technical Paper Series (2010-01-0228)
4. Allemang RJ, Phillips AW (2012) Static stiffness from dynamic measurements. University of Cincinnati–Structural Dynamics Research Lab (UC-SDRL) (2012)
5. Allemang RJ, Phillips AW (2012) Alternative methods for determining painted body stiffness. University of Cincinnati–Structural Dynamics Research Lab (UC-SDRL) (2012)
6. Beer FP, Johnston Jr ER, DeWolf J, Mazurek D (2011) Mechanics of materials. McGraw Hill Publishing Company, New York
7. Pasha HG (2014) Estimation of Static Stiffnesses from Free Boundary Dynamic (FRF) Measurements. Ph.D. Dissertation, University of Cincinnati
8. Pasha HG, Allemang RJ, Brown DL, Phillips AW (2014) Static torsional stiffness from dynamic measurements using impedance modeling technique. In: Proceedings of the international modal analysis conference (IMAC) XXXII–a conference and exposition on structural dynamics
9. Pasha HG, Allemang RJ, Brown DL, Phillips AW, Kohli K (2014) Support systems for developing system models. In: Proceedings of the international modal analysis conference (IMAC) XXXII–a conference and exposition on structural dynamics
10. Pasha HG, Allemang RJ, Phillips AW (2014) Techniques for synthesizing frfs from analytical models. In: Proceedings of the international modal analysis conference (IMAC) XXXII–A conference and exposition on structural dynamics

Chapter 13
An Estimation of Torsional Compliance (Stiffness) from Free-Free FRF Measurements: eRCF Application

Jeffrey Poland, Alexander Young, Hasan Pasha, Randall Allemang, and Allyn Phillips

Abstract The enhanced rotational compliance function (eRCF) is a useful concept for estimation of static torsional compliance/stiffness of a structure using measured frequency response functions (FRFs) from a structural system with free-free boundary conditions. The eRCF is estimated using FRF measurements from impact testing, namely a four by four (4×4) FRF matrix at four separate, symmetric locations on a structure. A companion paper presents the complete theoretical development and initial analytical and experimental examples. The theoretical background is summarized in this paper along with the results from extensive testing on automotive bodies, involving several tests on the same body style along with tests from different body styles. Comparisons are made to traditional, static torsion tests and a discussion of practical implementation is included.

Keywords Torsional stiffness • Static torsion test • eRCF

13.1 Introduction

Because of the extensive resource effort involved in the historical static torsion stiffness test of an automobile body, an alternative method was sought wherein the torsion stiffness could be determined or characterized using a method involving minimal test resources. The new method could be exploited in the manufacturing environment where production quality control often requires more test subjects than pre-production development testing. A partnership between BMW Manufacturing Co., LLC in Spartanburg, SC and the University of Cincinnati was established to development the method and its application. Using an FRF measurement method, similar to that used for experimental modal analysis was found to be advantageous for several reasons including ease of setup, test time requirements and pre-existing desire to determine modal parameters on the same body in white (BIW). After several trials, the eRCF method was found to be reliable in characterizing the longstanding BMW static method [1].

13.2 Background

A typical torsion static torsion stiffness test rig requires several man-hours of setup with careful attention to boundary and loading conditions, symmetry and sensor placement. Repeatable results are achieved only after these factors are closely controlled. Comparisons from manufacturer to manufacturer are less repeatable due to the idiosyncrasies of respective rigs and the differences in body configuration in the test situation. The concept of applying free-free modal analysis methods (typically using acceleration over force FRFs) to determine static characteristics was tempting for several reasons. The free-free boundary condition, in comparison with the static, is simple and can be easily repeated throughout research or manufacturing facilities. Straightforward free-free modal analysis methods have been attempted [SAE Papers, Griffiths] without sufficient agreement to current static torsional stiffness methods. A more advanced approach that begins with free-free modal analysis methods augmented by impedance and modal modeling technology has been extensively researched and

_____

J. Poland
Acoustic Analyst, BMW Manufacturing Co., LLC, Greer, SC 29651, USA

A. Young • H. Pasha • R. Allemang, Ph.D. (✉) • A. Phillips, Ph.D.
Department of Mechanical and Materials Engineering, College of Engineering and Applied Science, University of Cincinnati
Cincinnati, OH 45221-0072, USA
e-mail: Randall.Allemang@UC.EDU

found to be successful [LMS, BMW SAE References] when extensive resources are available. Unfortunately, this approach is not applicable to potential applications to production quality control situations.

13.3 General Methodology

The new methodology involves developing a virtual measurement that can be estimated quickly from free-free frequency response function (FRF) measurments. This virtual measurement, referred to as an enhanced rotational compliance function (eRCF), is derived from a four by four matrix of acceleration over force FRF measurements taken on a structure in a free-free configuration. Generally, these measurements can be taken using impact testing involving only one hammer and four accelerometers, roving the hammer location over the four accelerometer locations in four measurement cycles. The development of the eRCF is based upon the using a weighted averaging methodology that simulates the application of a moment and the measurement of the rotational response in two planes of interest on the structure. A brief explanation of the method follows. For further details, please note the following references [IMAC eRCF Theory paper, H. Pasha PhD Dissertation].

Assumptions in the application of the eRCF method include that the system is linear, that the front and rear DOFs are symmetric about the centerline, that, beyond the soft support loading, only vertical loads are applied at the DOFs, that rotations meet the small angle criterion, and that the forces and displacements are characteristic of the historic, or traditional, method (Figs. 13.1 and 13.2).

As seen in Eqs. 13.1 and 13.2 below, the distance between front DOFs and rear DOFs determines the moment arm while the FRF measurements hold the displacement/force data. The moment arm vector (Eq. 13.2) also weights, or enhances, the modes which contain torsional shapes between the front and rear DOFs where the FRFs are out-of-phase.

$[H(\omega_i)] =$ Free-Free FRFs in displacement/force units

$L_f =$ Distance between front DOFs
$L_r =$ Distance between rear DOFs

DOF 1 = left front DOF, z direction
DOF 2 = right front DOF, z direction
DOF 3 = left rear DOF, z direction
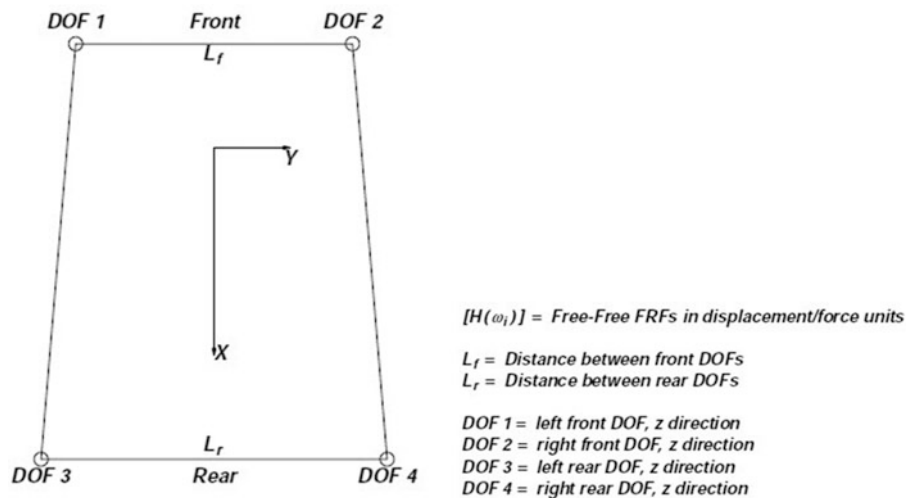DOF 4 = right rear DOF, z direction
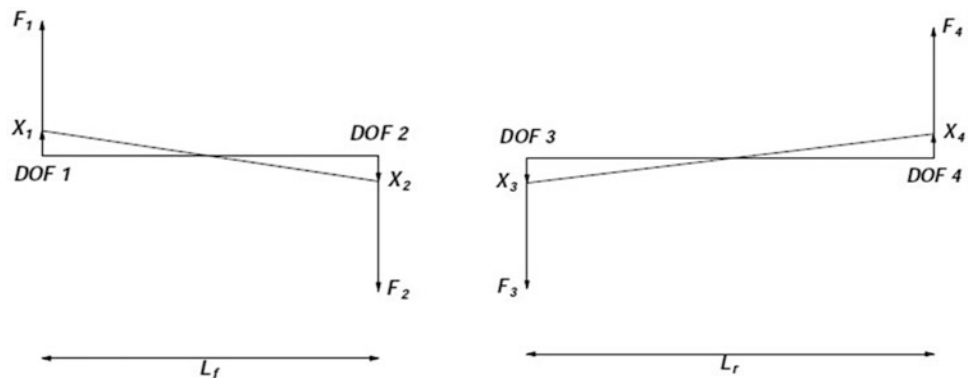
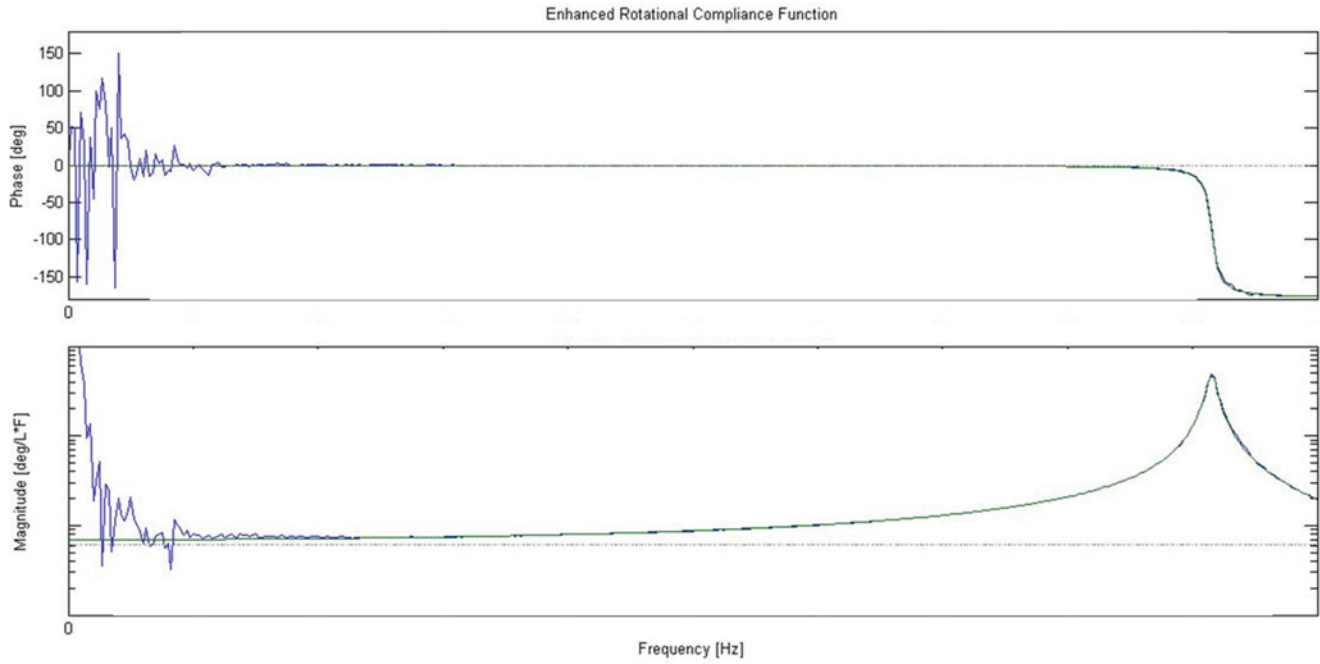**Fig. 13.1** DOF top view

Fig. 13.2 DOF rear view

Fig. 13.3 eRCF visualized

$$eRCF\,(\omega_i) = \frac{\Delta\theta}{M} = \{V\}^T{}_{1\times4}[H\,(\omega_i)]_{4\times4}\{V\}_{1\times4} \tag{13.1}$$

$$\{V\}^T{}_{1\times4} = \{+1/L_f \; -1/L_f \; -1/L_r \; +1/L_r\} \quad \{V\}_{4\times1} = \left\{ \begin{array}{c} +1/L_f \\ -1/L_f \\ -1/L_r \\ +1/L_r \end{array} \right\} \tag{13.2}$$

The static stiffness from the eRCF is calculated by applying a SDOF modal parameter estimation model that includes a residual compliance term to the eRCF. The purpose of the SDOF model with residual compliance is to estimate the torsional stiffness at zero frequency since the actual data, including the eRCF, is very noisy and inconsistent below 10 Hz. The static compliance can be found by utilizing the model at zero Hz and inverting the results to get rotational stiffness in standard units of torque over angle of twist. Note that the use of the model is just to estimate the zero frequency characteristic and no specific use is made of the modal information. A higher order MDOF model with residual compliance can be used if desired. The fit of the model to the data is used as a quality check along with the data characteristics in the low frequency region (zero slope magnitude with zero phase, properly estimating a low frequency, grounded compliance FRF).

Figure 13.3 shows how information from the eRCF is chosen. The top plot shows the phase, from which a stable "flat" region is chosen to fit the residual stiffness. The bottom plot is the magnitude, from which the SDOF peak information is chosen. The blue lines on each plot come from the eRCF while the green line is the model, an SDOF fit with added residual.

Data collection and calculation steps are summarized in the following bullet points:

- Make 4×4 FRF matrix in four passes of 1×4 FRF measurement cycles. The data is acceleration over force on a free-free structure configuration, properly calibrated to appropriate acceleration and force units.
- The 4×4 FRF matrix is processed by Eq. 13.1 with weighting factors that involve the sensor locations, in consistent length units, from Fig. 13.1.
- The frequency range of the eRCF is chosen, consistent with the parameter estimation model. The minimum frequency is normally chosen based upon the low frequency slope and phase characteristics. The high frequency is chosen, dependent on the parameter estimation model, at or beyond the peak of the first observable resonance.

Fig. 13.4 eRCF graphic user interface
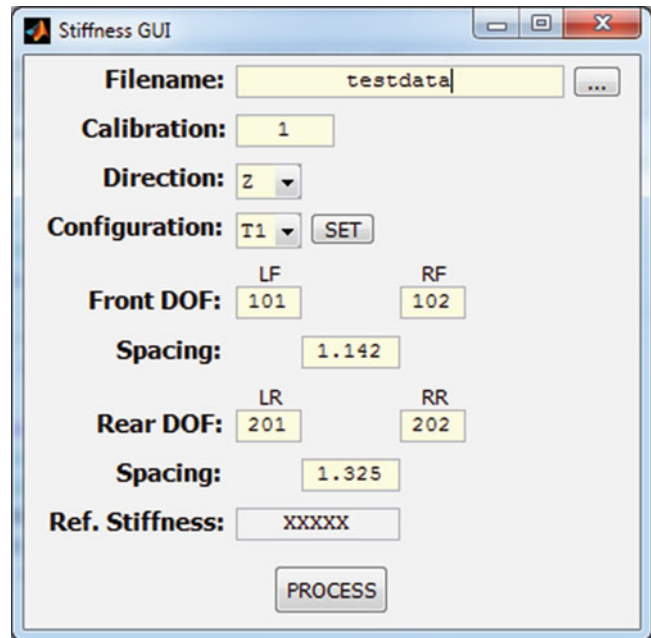
Fig. 13.5 A BMW E70 BIW showing front and rear DOF locations for eRCF measurements

- The match of the synthesized data compared to the estimated eRCF is evaluated for consistency and physical appropriateness.
- The zero frequency compliance is estimated from the zero, or low, frequency value of the model. This value is inverted to get the torsional stiffness in proper units (Fig. 13.4).

13.4 Summary of eRCF Application to Automotive Bodies

Initial testing occurred on an E70 Sports Activity Vehicle (SAV) model test structure which had been well-tested and which was going out-of-production at the time of the BMW-UC project. It served as a consistent test subject while many of the other structures were pre-production or production bodies which would eventually be built into full vehicles. Mass perturbation was also implemented to verify that the method was consistent when mass was perturbed, but not stiffness (Figs. 13.5, 13.6, and 13.7).

Fig. 13.6 Mass addition

Fig. 13.7 Mass additive check

Measurement	Normalized Value
Traditional Method	1.000
eRCF 0 Mass	0.969
eRCF 1 Mass	0.975
eRCF 2 Mass	0.965

Fig. 13.8 eRCF with overloads

Figure 13.8 illustrates a challenge to producing quality driving point FRFs from impact testing, especially in the low fr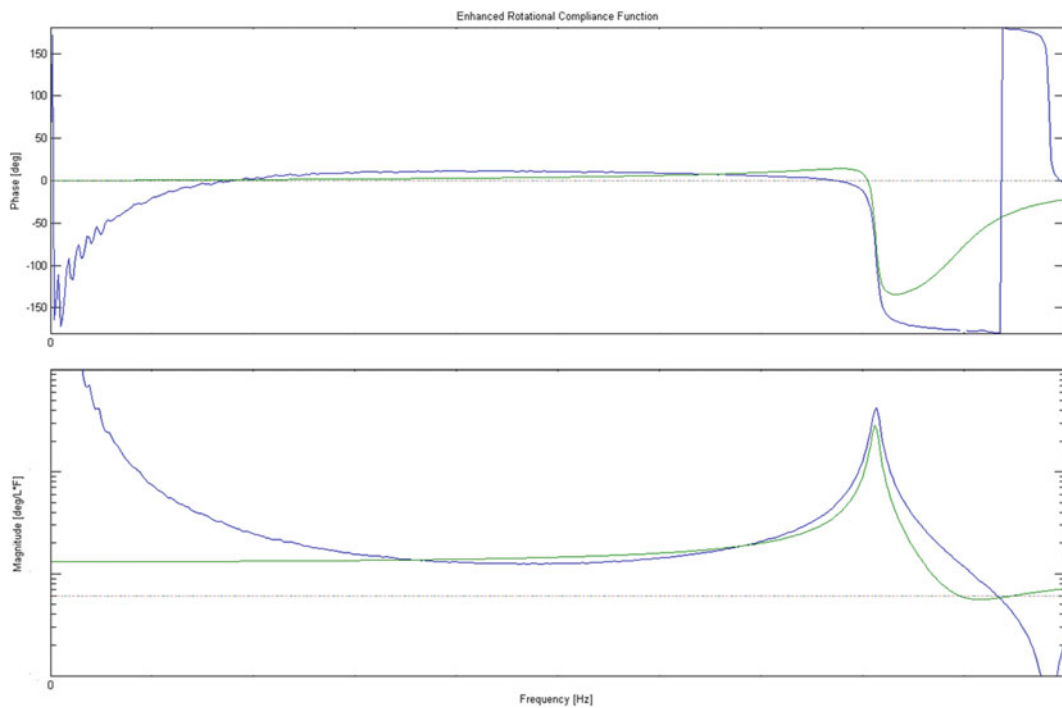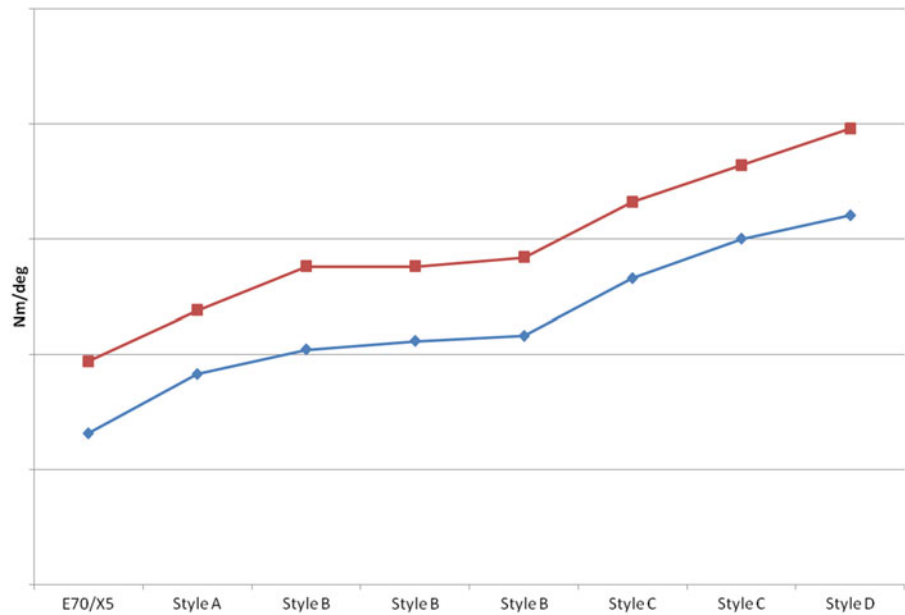equency range. In a related IMAC paper [8], the issue of high frequency overloads associated with such impact testing is discussed. With manual adjustments to the range of certain sensors, this problem can be overcome.

Fig. 13.9 Traditional stiffness result (*red*) versus eRCF (*blue*) for five body styles (color figure in online)

13.5   Results/Significance

Five body styles were tested at the BMW facility in Spartanburg using both the traditional static torsion test method as well as the eRCF method. The following plot summarizes the results (Fig. 13.9):

The body "styles" may be summarized as various versions of the SAV. Differences between bodies which account for the differences in stiffness include overall size, shape (coupe) and whether the body has a sunroof opening or not.

The plot shows a consistent relationship between the eRCF result and the static result from body-to-body. These data suggest that, for the limited number of test subjects, the eRCF can predict the static method within standard uncertainty (3 %). While the sample size is not statistically significant, the eRCF technique is an appropriate tool for production monitoring

13.6   Discussion, Issues, Concerns

An obvious disparity between the two methods is the level of loading seen in the static torsion application versus the impact of a handheld hammer. This can be an important issue depending on the degree of non-linearity that is in the body, the rig attachment hardware and/or the static testing rig.

Another difference is the boundary conditions, namely that the nature of the static rig requires extra constraints, and therefore may impart an additional artificial stiffness to the test subject. Since the eRCF estimate is consistency lower than the static testing estimate, this would support the possibility that the static testing rig is adding stiffness due to the lateral constraint.

The fact that the eRCF estimate shows a consistent relationship to a traditional torsion method is sufficient agreement to provide a benefit. Since the eRCF methodology can be applied with a minimum amount of technology costs (hardware, hardware cost, test time, testing expertise, etc.), the method shows significant potential as a production quality control tool.

13.7   Summary and Future Work

Following this study, the eRCF method was determined to be an appropriate replacement for the historic static test method in the production environment. The method will be used in production monitoring for the body types cited in this study. Future bodies will require calibration with the static test bench and will hopefully provide further verification of the utility of the method. Development of a similar tool to evaluate bending stiffness is under review UC-SDRL.

References/Literature Citations

1. Pasha H, Allemang RJ, Phillips AW (2015) Estimation of torsional compliance (stiffness) from free-free FRF measurments: eRCF theory. Proceedings, International Modal Analysis Conference (IMAC)
2. Rediers B, Yang B, Juneja V (1998) Static and dynamic stiffness – one test, both results. Proceedings of the International Modal Analysis Conference (IMAC) XVI – a conference and exposition on structural dynamics
3. Griffiths D, Aubert A, Green ER, Ding J,A technique for relating vehicle structural modes to stiffness as determined in static determinate tests, SAE technical paper series (2003-01-1716)
4. Deleener J, Mas P, Cremers L, Poland J,Extraction of static car body stiffness from dynamic measurements, SAE technical paper series, (2010-01-0228)
5. Helsen J, Cremers L, Mas P, Sas P (2010) Global static and dynamic car body stiffness based upon a single experimental modal analysis test. Proceedings, ISMA noise and vibration conference, pp 2505–2541
6. Cremers L, Spickenreuther M, Danninger A, Van Herbruggen J (2012) Full car body static and dynamic stiffness identification based on a single detailed modal measurement. LMS European vehicle conference
7. Pasha HG (2014) Estimation of static stiffnesses from free boundary dynamic (FRF) measurements. Ph.D. dissertation, University of Cincinnati, 227 pp
8. Brown DL, Allemang RJ, Phillips AW (2015) Forty years of use and abuse of impact testing: a practical guide to making good FRF measurements. Proceedings, international modal analysis conference (IMAC)

Chapter 14
Estimation of Bending Compliance (Stiffness) from Free-Free FRF Measurements: eBCF Theory

Hasan G. Pasha, R.J. Allemang, A.W. Phillips, A. Young, and J. Poland

Abstract The enhanced bending compliance function (eBCF) is a useful concept for estimation of static bending compliance/stiffness of a structure using measured frequency response functions (FRFs) from a structural system with free-free boundary conditions. The eBCF is estimated using FRF measurements involving impact testing that involve obtaining a six by six (6x6) FRF matrix at six separate, symmetric locations on a structure. This is in contrast to traditional, static bending tests that involve constraints applied to four of these six locations and static loads applied to the other two of these six locations. The traditional, static bending test requires extensive instrumentation and a two day test procedure while the eBCF method involves minimal instrumentation over several hours. The theoretical background is presented along with both modeling and experimental cases involving a rectangular plate structure.

Keywords Static bending stiffness • Enhanced bending compliance function • Bending stiffness sensitivity • Overhang • Off-centered loading

Notation

Symbol	Description
δ	Static deflection (in)
σ	Standard deviation
Δ	Total static deflection (in)
f_{max}	Maximum frequency of the stiffness parameter estimation band (Hz)
f_{min}	Minimum frequency of the stiffness parameter estimation band (Hz)
l_f	Front distance (in)
l_r	Rear distance (in)
F	Generalized force magnitude (lb$_f$)
$[H(\omega)]$	FRF matrix ($\frac{X}{F}$)
K_B	Bending stiffness (lb$_f$/in)
{V}	Force scaling vector
DOF 1	Left front DOF, z direction
DOF 2	Right front DOF, z direction
DOF 3	Left rear DOF, z direction
DOF 4	Right rear DOF, z direction
DOF 5	Left mid-span DOF, z direction
DOF 6	Right mid-span DOF, z direction
eBCF(ω)	Enhanced Bending Compliance Function

H.G. Pasha • R.J. Allemang (✉) • A.W. Phillips • A. Young
University of Cincinnati-Structural Dynamics Research Lab (UC-SDRL), Cincinnati, OH 45220, USA
e-mail: randy.allemang@uc.edu

J. Poland
BMW Manufacturing Company, Spartanburg, SC 29651, USA

14.1 Introduction

Static structural stiffness is an important criterion in automobile structure design as it impacts vehicle handling, ride comfort, safety and durability. Traditionally, automobile manufacturers used *special test rigs* to estimate stiffness, which require *precise setup* and *expensive instrumentation*. In the past decade, dynamic frequency response function (FRF) measurements with modeling techniques were used to estimate static stiffness [1–3]. Though test setup time and expense associated with the instrumentation are considerably reduced, *heroic technical measures* in terms of user experience and data processing are required to get reasonable stiffness estimates.

As static stiffness information is contained in the measured free-free FRFs, it can be extracted by utilizing *spatial/geometric filtering* and *averaging techniques* [4, 5]. A simple and efficient method to estimate static bending stiffness from free-free FRFs is developed in this paper. The enhanced Bending Compliance Function (eBCF) method presented here utilizes spatial/geometric filtering and averaging techniques to enhance response functions and estimate static stiffness. The stiffness estimates obtained from this method were comparable with the analytical results, while requiring significantly less resources.

14.2 Static Bending Stiffness

Bending stiffness K_B, is defined as the ratio of total vertical deflection (Δ) at the load application points to the total static load (F) applied on the structure. Bending stiffness is expressed in lb_f/in or N/m.

Consider the configuration shown in Fig. 14.1. There are four constraints, $DOFs\ 1 - 4$, and the load is applied at $DOFs$ 5 and 6. The bending stiffness is calculated using Eq. 14.1

$$K_B = \frac{F}{\Delta} = \frac{F_5 + F_6}{\delta_5 + \delta_6} \tag{14.1}$$

where, K_B is the static bending stiffness, F is the total applied bending force, Δ is total deflection, F_5 and F_6 are the point loads, δ_5 and δ_6 are the vertical deflections at $DOFs$ 5 and 6 (load application locations) respectively.

Note that the deflection (Δ) due to the bending load depends on the flexural rigidity (EI) of the structure and the characteristic length (span) L for the load case. For a comparative evaluation (i.e. between the model/static testing methods and the enhanced bending compliance function), these properties are fixed for a given structure and the loading condition. As a result, flexural rigidity and the characteristic length do not impact the bending stiffness.

Fig. 14.1 Configuration for estimating bending stiffness
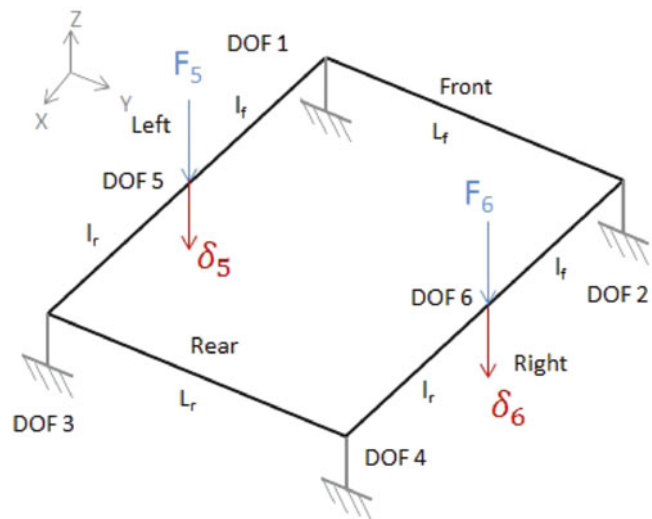
14.3 Enhanced Bending Compliance Function (eBCF)

The global static stiffness of a structure can be extracted from a structural dynamic model of a system, which can be developed using measured frequency response functions obtained from a free-free structural test. Typically, the FRFs measured in the structural test are accelerance FRFs $\left(\frac{A}{F}\right)$. The dynamic compliance FRF $\left(\frac{X}{F}\right)$ or the dynamic stiffness FRF $\left(\frac{F}{X}\right)$ can then be derived from the accelerance FRF by numerical integration. The static stiffness information can be extracted from the dynamic stiffness FRF at 0 Hz.

The limitations of the modal and impedance modeling methods in estimating the static torsional/bending stiffness can be overcome by analyzing an equivalent free-free system. Instead of the boundary constraints (fixed-fixed for bending) applied at certain DOFs in the modal/impedance modeling method, corresponding reaction forces/moments are applied in the enhanced bending compliance function method. An enhanced (virtual) compliance function using free-free FRFs can be developed using a spatial/geometric filtering procedure. The spatial/geometric filtering eliminates torsional characteristics along with some noise and some rigid body mode effects at low frequency while retaining bending characteristics.

A parameter estimation method is required to extract the static compliance/stiffness from the enhanced compliance/stiffness FRF. The compliance/stiffness estimation procedure involves fitting an appropriate model to the enhanced FRF as the data in the low frequency region is noisy. A two-sided single-degree of freedom (SDOF) partial fraction model with a residual flexibility constant can be used to fit the enhanced bending compliance function. Alternatively, a multi-degree of freedom (MDOF) partial fraction model can also be used.

14.3.1 General Procedure for Estimating Stiffness Using Enhanced Compliance Function Method

The formulation of the bending compliance function method for a particular load case involves the following steps:

(1) Develop a free-free system in dynamic equilibrium, which is equivalent to the statically determinate constrained system used in static testing methods
(2) Express the reactions and applied forces in terms of a generalized force to obtain the force scaling vector $\{V\}$
(3) Utilize the measured FRFs and the force scaling vector to formulate the required enhanced compliance function

A system in dynamic equilibrium, which is equivalent to a statically determinate system should be developed for a particular load case. This is achieved by applying equal and opposite force (reaction forces) at the constraint locations. The boundary constraints (fixed to free) at front and rear load/deflection DOFs have no effect on the stiffness estimate as long as the motion at all DOFs is accounted for [6]. The static bending stiffness is sensitive only to relative motion, end-to-end. Therefore, the boundary constraints can be replaced by reaction forces.

The estimation of static stiffness using an enhanced compliance function involves the following steps:

(1) Measure the accelerance FRFs of the free-free system
(2) Derive the compliance or dynamic stiffness FRFs from the measured accelerance FRFs
(3) Form a reduced (sieved) dataset based on the desired test configuration. Typically, a 6x6 system for bending stiffness is formed.
(4) Compute the enhanced bending compliance function formulated for the load case, using the measured FRFs and force scaling vector
(5) Fit an appropriate model to the low frequency region of the enhanced compliance function
(6) Use the model parameters from Step 5 to estimate the static compliance/stiffness

14.3.2 Analysis of a Structure with Two Point-Loads at Mid-Span Location

The eBCF formulation for the case discussed here is based on the following conditions:

(1) Constraints/supports should be on the *edge* of the structure (no overhang)
(2) Bending force should be *centered* between the constraint/support locations so as to produce *symmetric deformation*
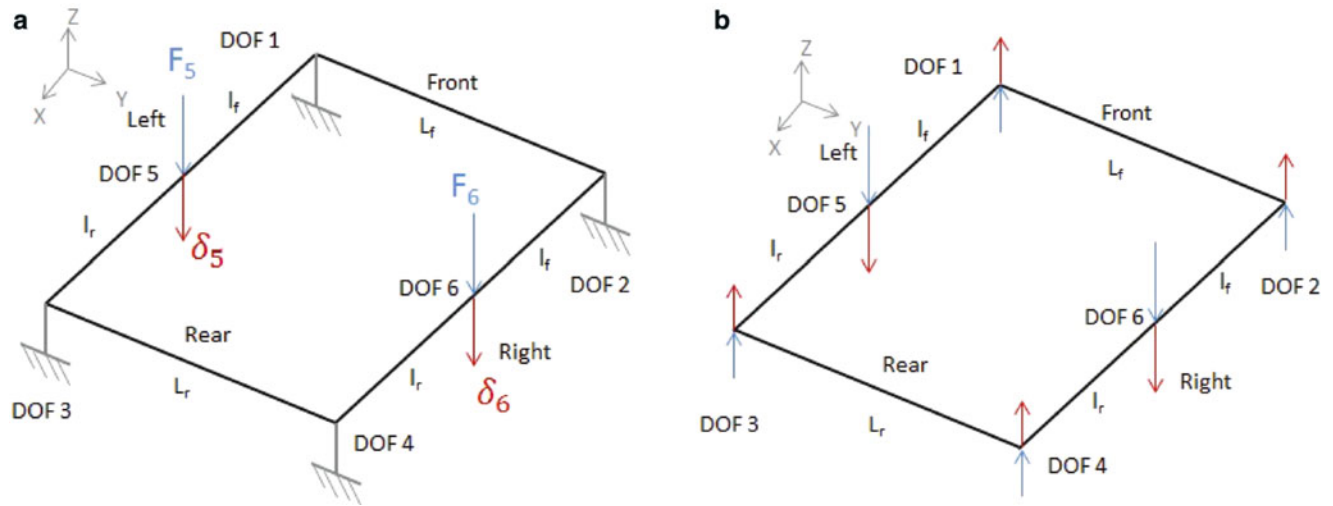
Fig. 14.2 Equivalent configurations for estimating bending stiffness—Two point-loads case. (**a**) Fixed-fixed configuration. (**b**) Equivalent free-free configuration

When the supports are not at the edges, there are *overhung* segments in the structure, which produce a moment at the support locations. These moments have a *stiffening effect* on the structure [6]. When the bending load is not centered between the supports, the deformation is *asymmetric* and the maximum deflection in not at the mid-span location.

For an absolute analysis, when any of the above conditions are violated, this method would have to be adapted by including the effect of the moment due to the overhung segments about the supports and considering the deformed shape of the structure. However, as long as comparative evaluations are being performed, violating the above conditions may not be a concern. If the analysis model and experimental testing have the same overhung inertias, the comparative answer for bending stiffness may be appropriate. For this reason, bending stiffness estimation of structures can be utilized for comparative analysis and not absolute analysis.

Consider the loading shown in Fig. 14.2a. The bending load is applied at two points (DOFs 5 and 6) with boundary constraints applied at four points (DOFs $1 - 4$) on the structure. An equivalent free-free configuration for the bending stiffness load case is shown in Fig. 14.2b. It has to be noted that the force is *centered* ($l_f = l_r$).

The reaction forces at DOFs $1 - 4$ can be expressed in terms of the applied forces at DOFs 5 and 6, for example $\circlearrowleft^+ \Sigma \left(\mathsf{M_y}\right)_{\mathsf{DOF}\ 1} = 0$

$$\mathsf{F}_3(l_f + l_r) = \mathsf{F}_5\, l_f \tag{14.2}$$

$$\mathsf{F}_3 = \mathsf{F}_5\, \frac{l_f}{l_f + l_r} \implies \frac{1}{2}\mathsf{F}_5 \tag{14.3}$$

The forces at DOFs $1 - 6$ can be scaled in terms of the generalized bending force magnitude F applied on the structure. The magnitude of the force applied at DOFs 5 and 6 is $\frac{\mathsf{F}}{2}$. Substituting, $\mathsf{F}_5 = \frac{\mathsf{F}}{2}$ and $\mathsf{F}_6 = \frac{\mathsf{F}}{2}$ yields,

$$\mathsf{F}_1, \mathsf{F}_2, \mathsf{F}_3, \mathsf{F}_4 = \frac{\mathsf{F}}{4} \tag{14.4}$$

14.3.3 Formulation of the eBCF for Two Point-Loads Case

Beginning with the fundamental input/output FRF equation,

$$\{\mathsf{X}(\omega_i)\}_{6\mathrm{x}1} = [\mathsf{H}(\omega_i)]_{6\mathrm{x}6}\ \{\mathsf{F}(\omega_i)\}_{6\mathrm{x}1}. \tag{14.5}$$

The force vector $\{F\}$ is rewritten in terms of the generalized bending force magnitude (F), applied on the structure. The frequency notation is dropped for simplicity.

$$\{F\} = \begin{Bmatrix} F_1 \\ F_2 \\ F_3 \\ F_4 \\ F_5 \\ F_6 \end{Bmatrix} \implies \frac{F}{2} \begin{Bmatrix} -\frac{1}{2} \\ -\frac{1}{2} \\ -\frac{1}{2} \\ -\frac{1}{2} \\ +1 \\ +1 \end{Bmatrix} \implies \frac{F}{2}\{V\} \tag{14.6}$$

where, $\{V\}$ is the *force scaling vector*.

Therefore,

$$\{X\}_{6\times1} = \frac{F}{2} [H]_{6\times6} \{V\}_{6\times1}. \tag{14.7}$$

Pre-multiplying both sides by $\{V\}^T$,

$$\{V\}^T_{1\times6} \{X\}_{6\times1} = \frac{F}{2} \{V\}^T_{1\times6} [H]_{6\times6} \{V\}_{6\times1}. \tag{14.8}$$

Expanding and reorganizing the terms on the LHS,

$$\{V\}^T_{1\times6} \{X\}_{6\times1} = -(X_1 + X_2)\left(\frac{1}{2}\right) - (X_3 + X_4)\left(\frac{1}{2}\right) + X_5 + X_6 \tag{14.9}$$

$$= \left[X_5 - X_1\left(\frac{1}{2}\right) - X_3\left(\frac{1}{2}\right)\right] + \left[X_6 - X_2\left(\frac{1}{2}\right) - X_4\left(\frac{1}{2}\right)\right]. \tag{14.10}$$

It can be recognized that the grouped terms in Eq. (14.10) represent the *static beam deflections*, δ_5 and δ_6, at the load application points, DOFs 5 and 6, on the left and the right side of the plate respectively

$$\delta_5 = X_5 - \left(\frac{X_1}{2}\right) - \left(\frac{X_3}{2}\right) \tag{14.11}$$

$$\delta_6 = X_6 - \left(\frac{X_2}{2}\right) - \left(\frac{X_4}{2}\right). \tag{14.12}$$

Therefore, the LHS of Eq. (14.8) becomes

$$\{V\}^T_{1\times4} \{X\}_{4\times1} = \delta_5 + \delta_6 \implies \Delta \tag{14.13}$$

where, Δ is the total deflection due to the applied bending force F.

Note that for this case, the maximum deflection occurs at the same location as the applied force(s) as the loading is centered.

Organizing the equation into the final form by using the expression from Eq. (14.13) in Eq. (14.8), the eBCF for the two point-loads case is

$$\Delta = \frac{F}{2} \{V\}^T_{1\times6} [H]_{6\times6} \{V\}_{6\times1} \tag{14.14}$$

$$eBCF(\omega_i) \implies \frac{\Delta}{F} = \frac{1}{2} \{V\}^T_{1\times6} [H(\omega_i)]_{6\times6} \{V\}_{6\times1}. \tag{14.15}$$

14.4 Experimental Validation

A rectangular steel plate structure was fabricated and the FE models of the plate were validated [7–9]. The validated models were then used to predict the static bending stiffness by performing static analyses in ANSYS$^®$. The measured FRFs from structural tests on the rectangular plate were used to estimate the static bending stiffness by applying the enhanced bending compliance function formulated in the previous section.

The analytical predictions were compared with the estimates from the enhanced compliance function method (using both synthesized and measured FRFs). The steps involved in validating the enhanced bending compliance function method and the results obtained are discussed in detail in the subsequent sections.

14.4.1 Analytical Method

The validated rectangular plate FE model was used to estimate the bending stiffness for a longitudinal bending configuration, in which four DOFs corresponding to the support locations were constrained and point-loads were applied at two other DOFs. In this configuration, the load was applied at the center of front and rear supports.

The static bending stiffness can be calculated using Eq. (14.1). A static analysis was performed on the validated plate FE model in ANSYS$^®$. Point loads of 1 lb_f were applied at both DOFs 5 and 6 in the vertical direction. The deformation at DOFs 5 and 6 was $\delta_5 = 3.1397 \times 10^{-4}$ in and $\delta_6 = 3.1394 \times 10^{-4}$ in respectively. The static bending stiffness was predicted as 668.18 lb_f/in.

14.4.2 Enhanced Bending Compliance Function (eBCF) Method

An 6x6 free-free FRF dataset for the DOFs shown in Fig. 14.3 was acquired by performing an impact test on the rectangular plate to estimate the bending stiffness.

The theoretical expression in Eq. (14.15) for the eBCF formulated in Sect. 14.3.2 for the two point loads case was implemented in Matlab$^®$. The units calibration/conversion for g's to in/s^2 conversion was applied and the static bending stiffness for the desired configurations was estimated.

The eBCF data in the low frequency region was fitted with a two-sided SDOF partial fraction model with residual flexibility constant. The enhanced bending compliance function (eBCF) and the data fit in the low frequency region are shown in Fig. 14.4, computed with the measured as well as synthesized FRFs. Damping was not modeled; however, a force-exponential window was used while acquiring impact data on the rectangular plate. As a result, the magnitude at the peaks for the eBCF computed with the measured FRFs is low compared to the synthesized case.

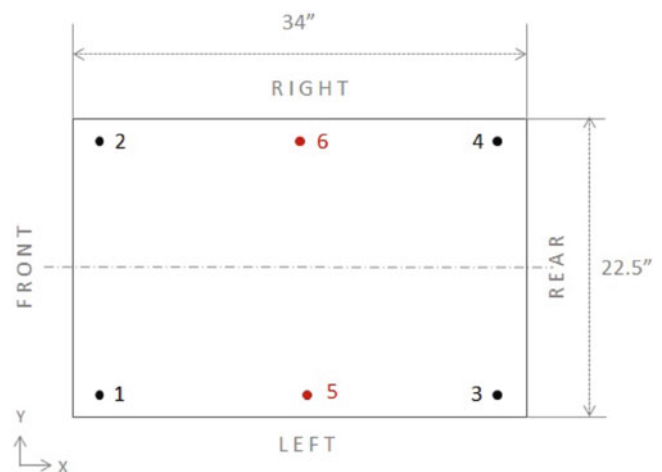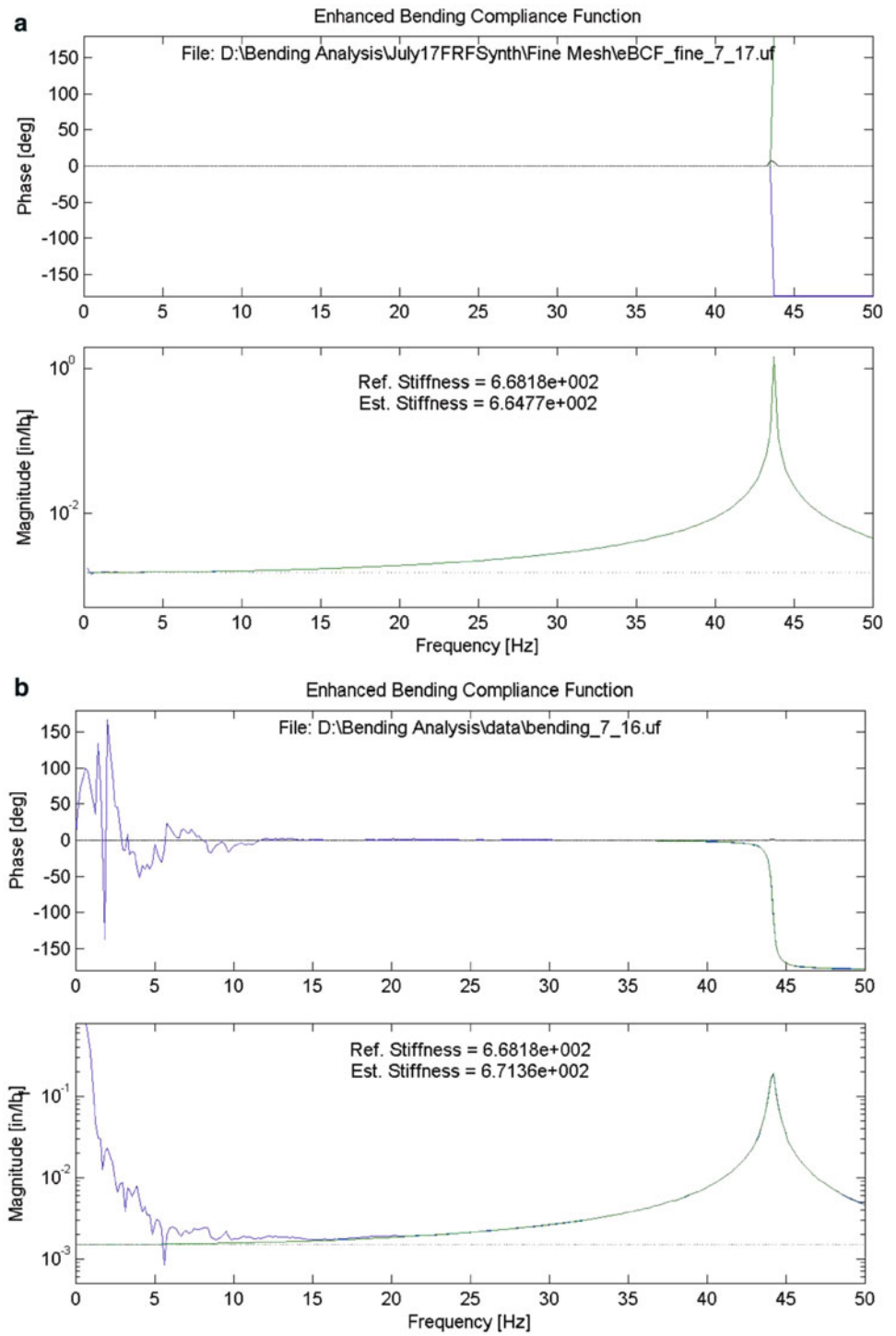**Fig. 14.3** DOF map of the rectangular plate for bending stiffness estimation

Fig. 14.4 eBCF for rectangular plate—longitudinal bending. (**a**) eBCF with synthesized FRFs (**b**) eBCF with measured FRFs

14.5 Results and Discussions

14.5.1 Static Bending Stiffness Estimation Sensitivity

The stiffness is estimated by fitting a model to the eBCF. In the modal parameter estimation process, modal parameters are extracted after fitting an appropriate model to the data. Unlike modal parameter estimation, no direct use of the modal parameters is involved. The goal is to use an appropriate model and consistent data to be able to estimate the zero frequency compliance.

It was anticipated that by fitting more than just one peak (that predominantly contributes to the static stiffness), a better estimate of bending stiffness can be achieved. The effect of fitting multiple peaks on the stiffness estimates using various MDOF models along with SDOF models (fitted with different frequency bandwidths) was studied for the eBCF method. A residual flexibility constant was used in all the models. The peaks selected in the different models used to fit the eBCF are listed in Table 14.1.

The sensitivity of longitudinal bending stiffness obtained by fitting various models for different frequency bandwidths is presented in Table 14.2. On comparing the results, it is evident that the best estimate (based on the average nominal value) for the longitudinal bending stiffness was achieved by fitting the MDOF I model with maximum variation from the nominal (average) bending stiffness value being $\pm 0.17\%$.

The eBCF plots with data fits obtained by fitting the SDOF II and MDOF I models are shown in Figs. 14.5 and 14.6 respectively.

14.5.2 Comparison with Results from Theoretical Model

The theoretical error/uncertainty of the longitudinal bending stiffness estimate from the eBCF method is $\pm 1.08\%$ of the nominal (average) bending stiffness values.

14.5.3 Issues Related to the eBCF Approach

When it is desired to estimate the bending stiffness for stiffer configurations, obtaining good quality data is challenging as the structural response is very low for such cases. The *signal-to-noise ratio* (SNR) is low due to the presence of measurement noise. When the resonance used in the stiffness estimation is too close to the rigid body modes, a relatively smaller frequency bandwidth is available to fit the eBCF data, which compounds this issue. The accuracy of the eBCF method can be poor for such configurations.

Table 14.1 Details of the models selected to fit the eBCF

Model	Peaks chosen
SDOF I	First peak
SDOF II	First peak
MDOF I	Peaks one and two
MDOF II	Peaks one, two and five
MDOF III	Peaks one, two, three and five

Table 14.2 Parameter estimation sensitivity of eBCF method(for different f_{min} values, $K_{B_{ref}} = 668.18$ lb$_f$/in)

Model	f_{max}(Hz)	Static bending stiffness K_B (lb$_f$/in)					Average $\overline{K_B}$	Std. Dev. σ	$\sigma/\overline{K_B}\%$
		15-f_{max}	20-f_{max}	25-f_{max}	30-f_{max}	35-f_{max}			
SDOF I	41.00	661.58	671.36	674.77	680.68	676.77	673.03	7.24	1.08
SDOF II	103.06	688.69	691.72	693.40	695.10	696.49	693.08	3.04	0.44
MDOF I	108.06	687.60	687.27	687.76	688.07	690.17	688.17	1.15	0.17
MDOF II	229.06	700.30	701.01	701.95	702.65	703.53	701.89	1.28	0.18
MDOF III	247.34	700.47	701.33	702.49	703.50	704.73	702.50	1.69	0.24

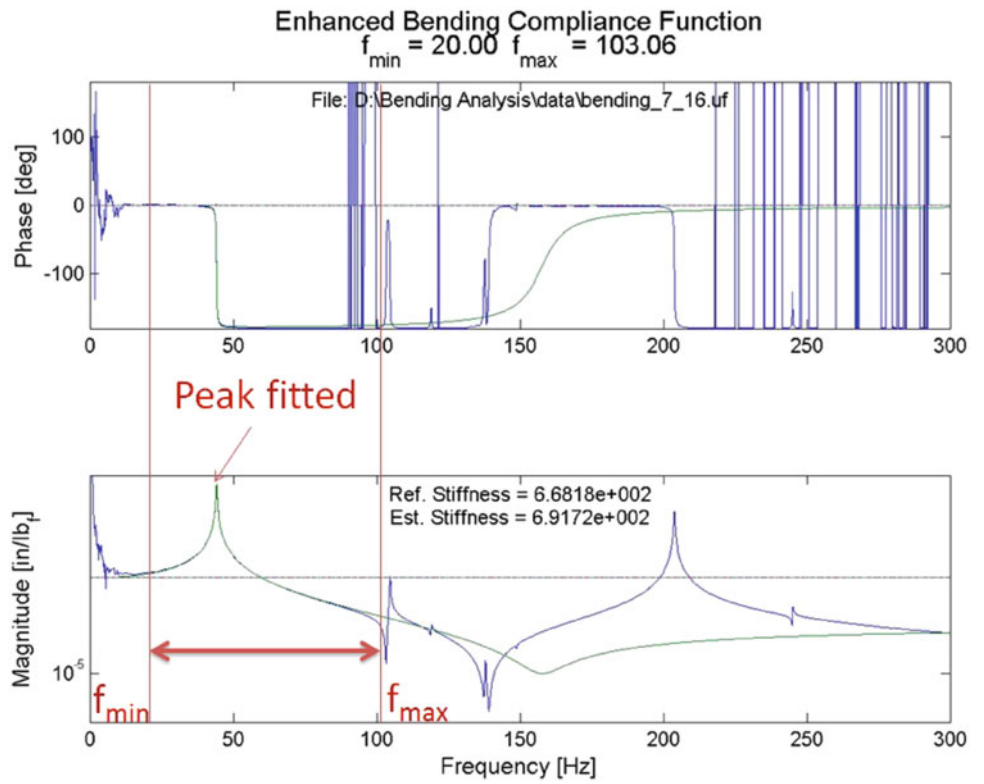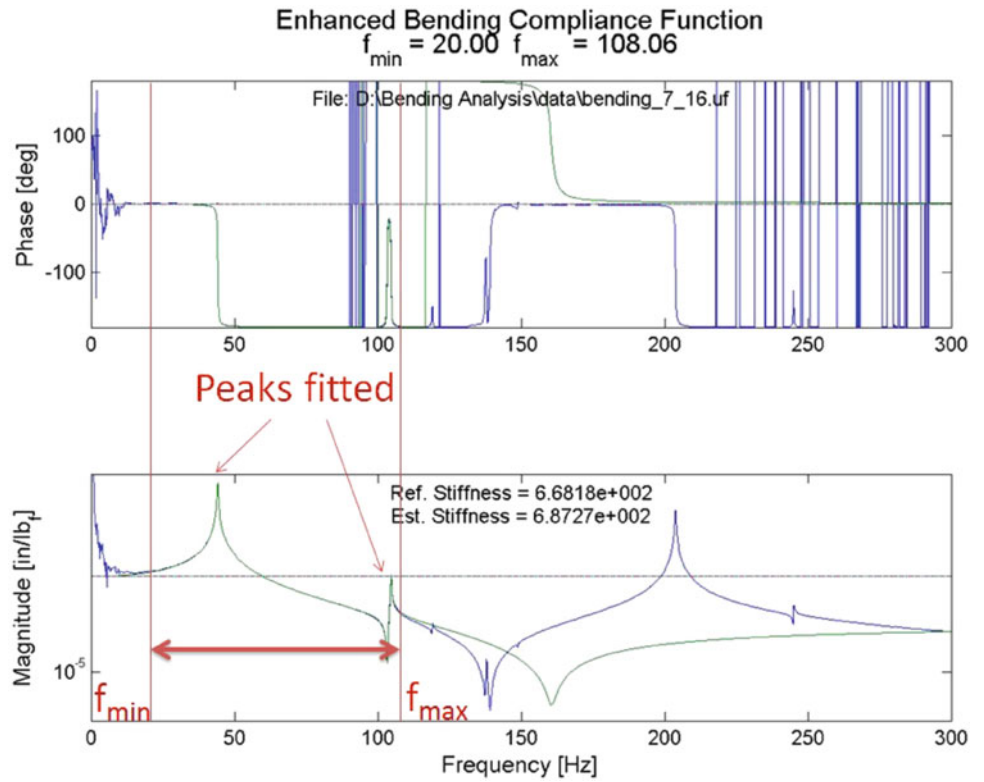**Fig. 14.5** eBCF method parameter estimation with SDOF II model

Fig. 14.6 eBCF method parameter estimation with MDOF I model; first 2 peaks fitted

14.5.4 General Bending Load Cases

The enhanced bending compliance function (eBCF) was formulated in Sect. 14.3.2 for a special bending load case with two point loads, where the loading is at the mid-span locations along the edges and the supports are at the vertices of the structure.

For an overhung structure, the inertia of the overhung segments tends to produce moments that stiffen the structure [6]. In Sect. 14.3.2, the sum of the moments about the supports was equated to zero for deriving the force scaling vector ($\{V\}$). When there are overhanging segments, the moments due to the overhanging segments on the supports should be factored into the force scaling vector.

The static bending stiffness (K_B) is defined as the ratio of the total bending load (F) to the total deflection ($\Delta = \delta_5 + \delta_6$) at the load application points (Eq. (14.16)).

$$K_B = \frac{F}{\Delta} \implies \frac{F_5 + F_6}{\delta_5 + \delta_6} \tag{14.16}$$

When the loading is *not centered*, the maximum deflection does not occur at the load application location. It occurs somewhere between the mid-span location and the load application location depending on the geometry of the structure and the loading. In such cases, the definition for the bending stiffness in Eq. (14.16) can obscure the interpretation of the results for stiffness of the structure. Therefore, an alternate definition for the bending stiffness $K_{B_{max}}$ should be used, which is the ratio of the total load applied to the maximum deformation δ_{max}, as expressed in Eq. (14.17).

The effect of varying the location of loading and the supports on the bending stiffness was studied analytically for a rectangular plate and the results are presented in Appendix A.1.

$$K_{B_{max}} = \frac{F}{\delta_{max}} \implies \frac{F_5 + F_6}{\delta_{max}} \tag{14.17}$$

14.6 Conclusions

The enhanced bending compliance function (eBCF) is a simple and efficient method to accurately estimate static bending compliance/stiffness using measured frequency response functions (FRFs) from a structural system with free-free boundary conditions. The FRF measurements are obtained from impact testing at selected DOFs quickly with minimal instrumentation. Typically, these tests involve obtaining a 6x6 FRF matrix at six separate, symmetric locations on a structure.

Traditional static bending tests involve constraints applied to four of these six locations and static loads applied to the other two of these six locations. These traditional, static bending tests require extensive instrumentation and a time-consuming procedure. These traditional tests are likely sensitive to the overhung structure problem discussed in this paper.

The theoretical background for eBCF was presented along with validations using both modeling and experimental cases involving a rectangular plate structure. The eBCF method involves minimal instrumentation. The theoretical error/uncertainty of the longitudinal bending stiffness estimate from the eBCF method is ± 1.08 % of the nominal (average) bending stiffness values.

A.1 General Bending Load Cases

The effect of varying the location of loading and the supports on the bending stiffness was studied for a rectangular plate using ANSYS® for the cases listed below:

(1) Off-centered loading
(2) Introducing overhang on both sides of the supports by reducing the characteristic length
(3) Removing overhung material on both sides of the supports
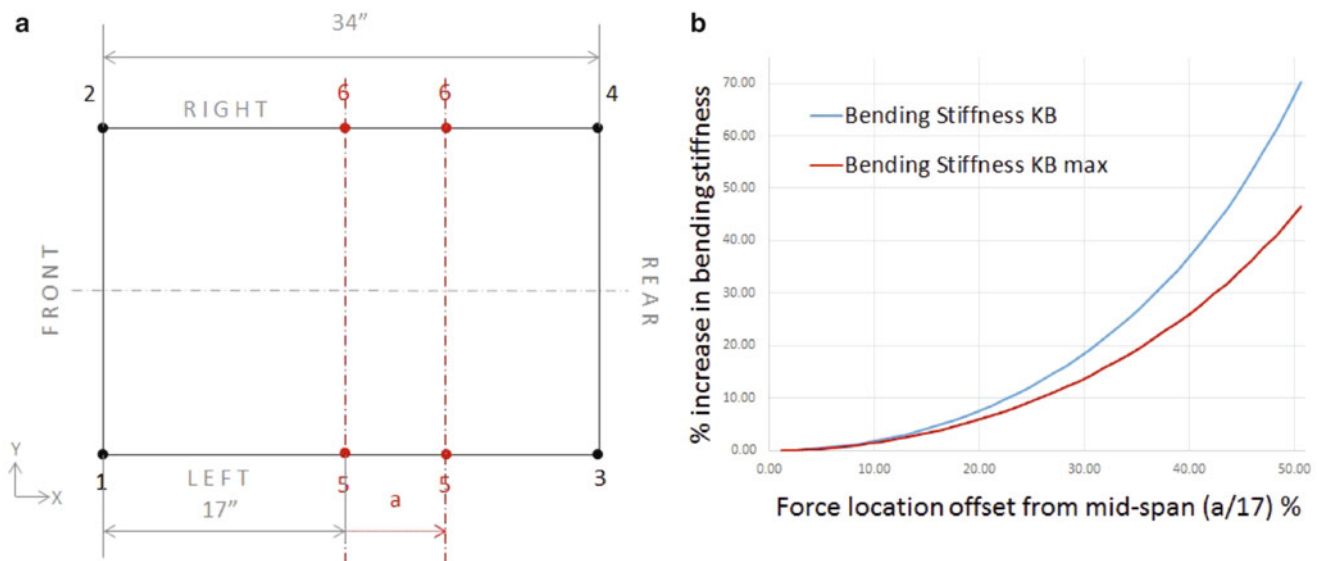(4) Sliding the supports and loading locations (a *double side unequal* overhang)

Fig. 14.7 Effect of off-centered loading on bending stiffness. (**a**) Load case. (**b**) Bending stiffness sensitivity

(5) Introducing overhang on one side of the supports by reducing the characteristic length
(6) Removing overhung material on one side of the supports

   More details are provided in the following sections.

A.1.1   Effect of Off-Centered Loading

As mentioned earlier, when a rectangular plate is loaded at the mid-span location, the maximum deflection is observed at the loading points. However, when the load is applied off-center, the maximum deflection is observed at a location between the load application and the mid-span locations. It is expected that the bending stiffness value would be very sensitive to the loading location when it is off-centered due asymmetric deformation.

   The effect of off-centered loading was studied for a rectangular plate. Consider the load case shown in Fig. 14.7a, the loading location (DOFs $5-6$) is offset from the center. As the force application points are offset from the mid-span location, the bending stiffness increases. Both the estimates of static bending stiffness K_B and $K_{B_{max}}$ are plotted as a function of the percentage offset of the loading points from the mid-span location in Fig. 14.7b.

   As expected, the bending stiffness value increases when the loading is off-centered. It is evident from the results that for a 50 % offset from the center, the bending stiffness based on the deflection at the load application points K_B over-estimates the effect (70.31 % increase in bending stiffness), whereas the bending stiffness based on the maximum deflection $K_{B_{max}}$ estimates an increase in stiffness by 46.52 % compared to the case where the loading is centered. This establishes that the bending stiffness value is highly sensitive to the loading location. When the load is off-centered, an appropriate bending stiffness estimate should be defined for interpreting the results as the maximum deflection is no longer guaranteed to be at the load application points or the mid-span locations.

A.1.2   Effect of Introducing Overhang on Both Sides of the Supports

In the case of a rectangular plate with fixed dimensions, introducing overhanging segments by moving the supports inside would increase the bending stiffness value as the characteristic length is reduced.

   Consider the loading shown in Fig. 14.8a. The supports (DOFs $1-4$), originally at the vertices, are progressively moved inside causing segments of the plate to overhang. The hatched portion in the figure represents the overhanging segments. From the results shown in Fig. 14.8b, it is observed that the bending stiffness increases compared to the case without any overhang.
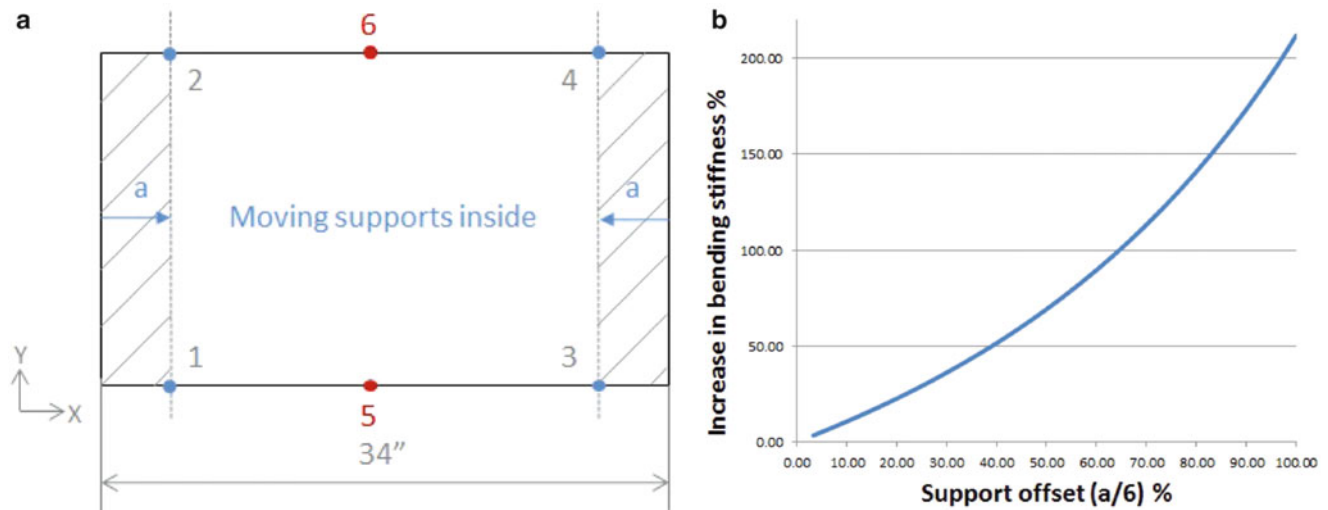
Fig. 14.8 Effect of introducing overhanging material on both sides of the supports. (**a**) Load case (overhung segments are hatched). (**b**) Bending stiffness sensitivity
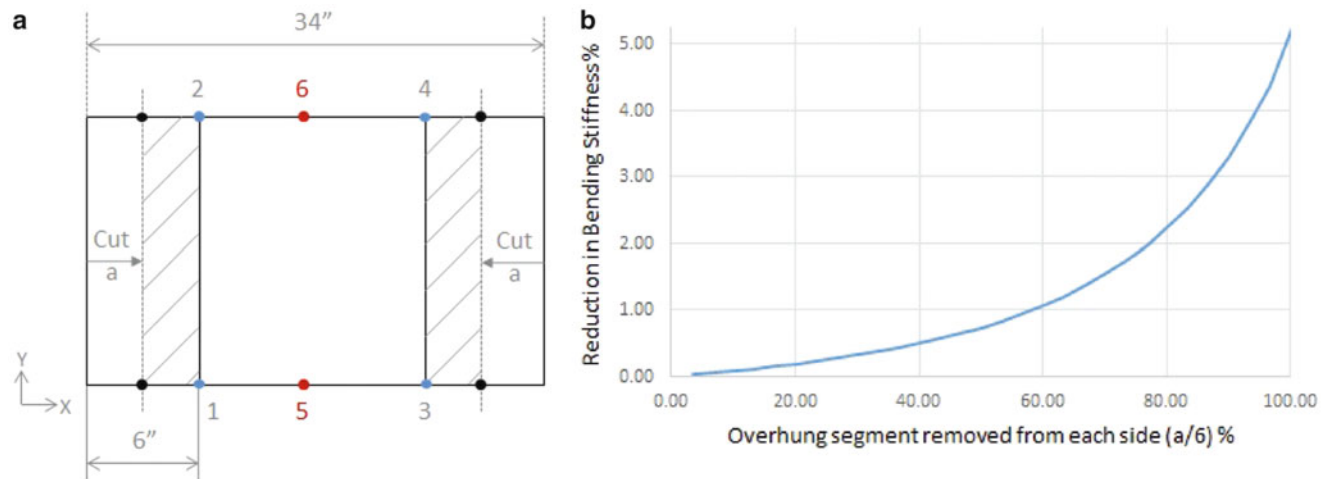

Fig. 14.9 Effect of removing overhanging material on both sides. (**a**) Load case (overhung segments are hatched). (**b**) Bending stiffness sensitivity

The increase in the bending stiffness is plotted as a function of the percentage increase in overhang ($\frac{a}{6}$%). By introducing an overhang of 6 in on each side, the bending stiffness value increases by 211.84 % with respect to the reference case.

A.1.3 Effect of Removing Overhung Material on Both Sides of the Supports

In the previous case discussed in Sec. A.1.2, the effect of reducing the characteristic length (introducing double side overhang) by moving the supports inside was studied. The effect of the removing overhung segments (portion of the plate extending beyond the supports) while the supports are fixed at interior points is discussed here. When there are overhung segments, they introduce moments at the support locations that stiffen the plate. It is therefore expected that removing overhung segments would reduce the bending stiffness value. In addition, when there is material removal, there is an associated reduction in the bending stiffness value.

Consider the loading shown in Fig. 14.9a, DOFs $1 - 4$ represent the support locations and DOFs $5 - 6$ are the loading locations. The case in which there is maximum overhang on both sides of the support ($a = 0$ in) is considered as the reference. A portion (a) of the overhung material (hatched portion in Fig. 14.9a) extending on each side of the supports is removed.
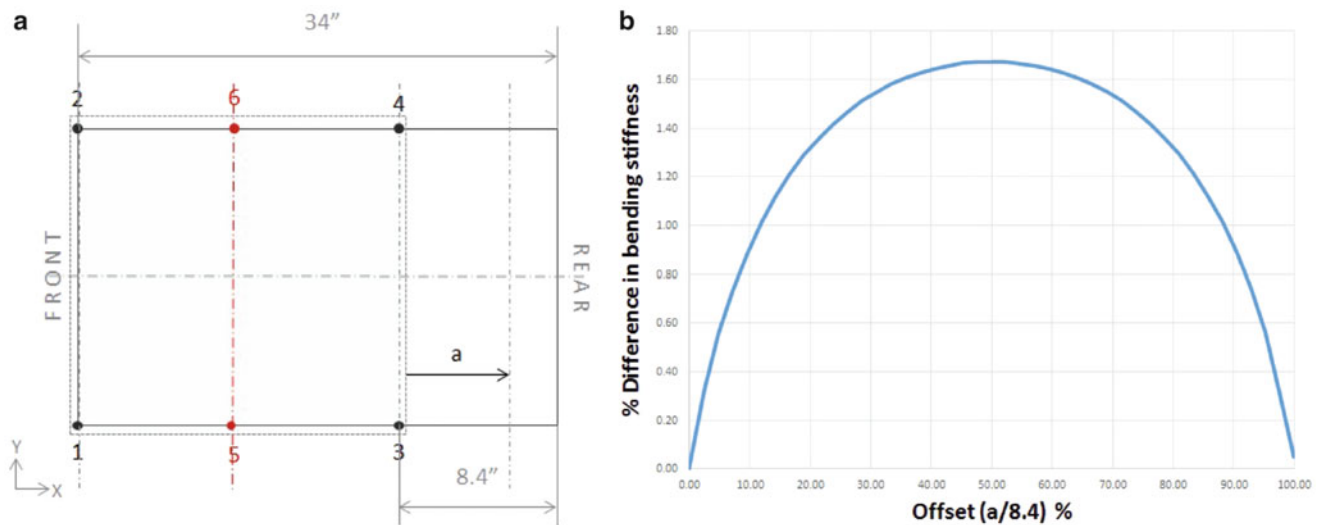
Fig. 14.10 Effect of sliding supports and loading location (double side unequal overhang) on bending stiffness. (**a**) Load case. (**b**) Bending stiffness sensitivity

When the overhung segments are removed completely, the bending stiffness value decreases by 5.14%, as shown in Fig. 14.9b. When the first 50 % (a = 3 in) of the overhung segment is removed on each side, the stiffness value reduces by just 0.73%. However, the bending stiffness value is more sensitive when the remaining 50% of the overhung segments on each side are removed.

A.1.4   Effect of Sliding the Supports and Loading Locations (a Double Side Unequal Overhang)

The effect of moving the loading locations as well as the support locations simultaneously on the bending stiffness is studied. Consider the load case shown in Fig. 14.10a, the loading points (DOFs 5 − 6) and the supports (DOFs 1 − 4) are offset (a) from the front of the plate. There is no appreciable change in the bending stiffness value. The stiffness increases to 1.67 % of the reference value as the supports and loading locations are slided towards the center and reduces on further sliding. The results are presented in Fig. 14.10b.

A.1.5   Effect of Introducing Overhang on One Side of the Supports

In Sect. A.1.2, the effect of moving both the front and the rear supports inside was discussed. The effect of moving just the front supports on the bending stiffness is studied here. As moving the front supports inside would reduce the characteristic length and also introduce an overhanging segment, the bending stiffness is expected to increase.

Consider the loading shown in Fig. 14.11a. The loading is off-centered. The supports (DOFs 1 − 2), originally at the vertices, are progressively moved inside causing a segment of the plate to overhang. The hatched portion in the figure represents the overhanging segment. From the results shown in Fig. 14.11b, it is observed that the bending stiffness increases significantly compared to the case without any overhanging segment.

The increase in the bending stiffness is plotted as a function of the percentage increase in overhang ($\frac{a}{8.4}$ %). By introducing an overhang of 8.4 in on the front, the bending stiffness value increases by 84.83 % with respect to the reference case.
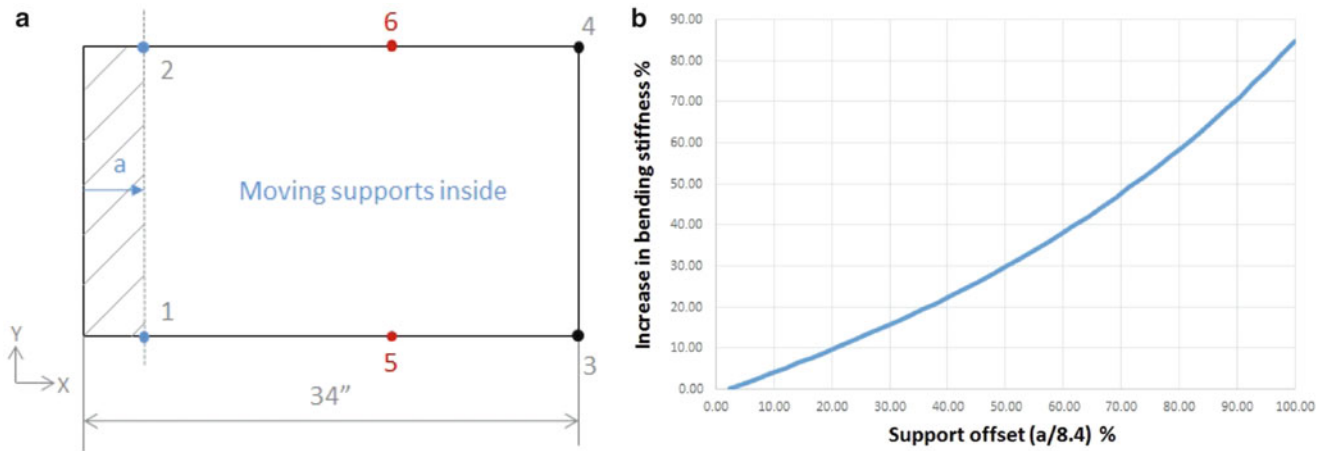
Fig. 14.11 Effect of introducing overhanging material on one side of the supports. (**a**) Load case. (**b**) Bending stiffness sensitivity
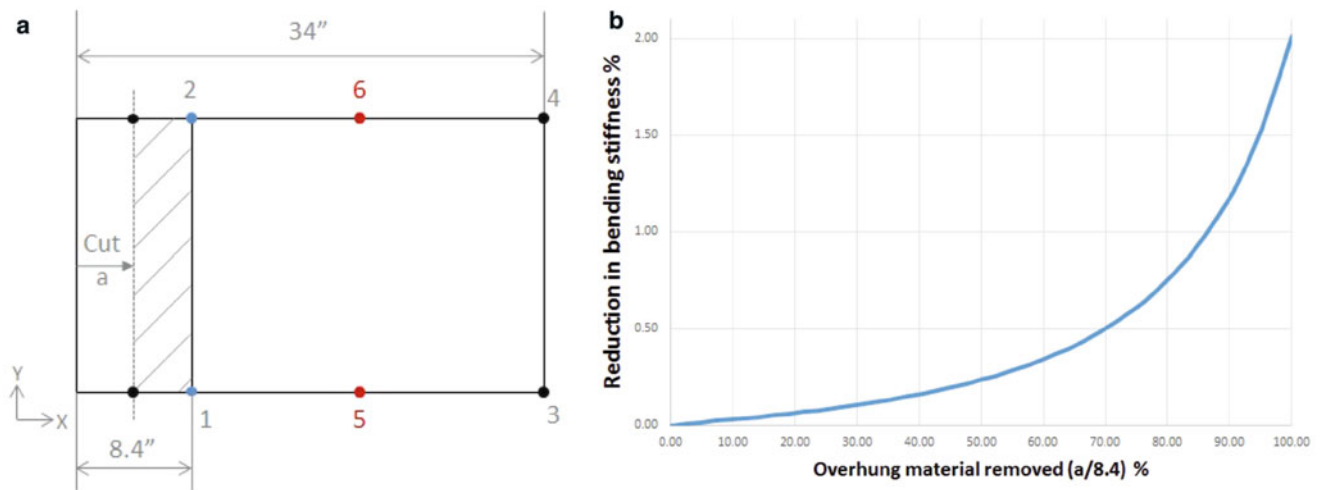

Fig. 14.12 Effect of removing overhanging material on one side. (**a**) Load case (overhung segments are hatched). (**b**) Bending stiffness sensitivity

A.1.6 Effect of Removing Overhung Material on One Side of the Supports

In the previous case Sect. A.1.5, the effect of reducing the characteristic length by moving the front supports inside was studied. The effect of the removing overhung segments from the front with the front supports fixed at interior points on the bending stiffness estimate is studied here. The overhung segment introduces moments at the front support locations that stiffen the plate. Therefore, it is expected that removing the overhung segment would reduce the bending stiffness value.

Consider the loading shown in Fig. 14.12a, DOFs $1 - 2$ represent the front support locations, and DOFs $5 - 6$ are the loading locations. A portion (a) of the overhang material (hatched portion in Fig. 14.12a) extending beyond the front supports is removed. The case in which there is maximum overhang (a = 0 in) is considered as the reference.

When the overhung segments are removed, the bending stiffness value decreases by 1.78 %, as shown in Fig. 14.12b.

A.1.7 Summary

The results for the general bending load cases studied are summarized in Table 14.3.

Table 14.3 Summary of the general bending load cases studied

Case	Description	Off-centered loading	Overhang	Stiffness sensitivity
1	Off-centered loading	Yes	No	Very sensitive
2	Overhang on both sides	No	Double side equal	Very sensitive
3	Removing overhung material on both sides	No	Double side equal	Less sensitive
4	Sliding the supports and loading locations	No	Double side unequal	Less sensitive
5	Overhang on one side	Yes	Single side	Very sensitive
6	Removing overhung material on one side	No	Single side	Less sensitive

References

1. Rediers B, Yang B, Juneja V (1998) Static and Dynamic Stiffness–One test, both results.In: Proceedings of the international modal analysis conference (IMAC) XVI–A conference and exposition on structural dynamics
2. Griffiths D, Aubert A, Green ER, Ding J (2003) A technique for relating vehicle structural modes to stiffness as determined in static determinate tests. SAE Technical Paper Series (2003-01-1716)
3. Deleener J, Mas P, Cremers L, Poland J (2010) Extraction of static car body stiffness from dynamic measurements. SAE Technical Paper Series (2010-01-0228)
4. Allemang RJ, Phillips AW (2012) Static stiffness from dynamic measurements. University of Cincinnati–Structural Dynamics Research Lab (UC-SDRL)
5. Allemang RJ, Phillips AW (2012) Alternative methods for determining painted body stiffness. University of Cincinnati–Structural Dynamics Research Lab (UC-SDRL)
6. Pasha HG (2014) Estimation of static stiffnesses from free boundary dynamic (FRF) measurements. Ph.D. Dissertation, University of Cincinnati
7. Pasha HG, Allemang RJ, Brown DL, Phillips AW (2014) Static torsional stiffness from dynamic measurements using impedance modeling technique. In: Proceedings of the international modal analysis conference (IMAC) XXXII–a conference and exposition on structural dynamics
8. Pasha HG, Allemang RJ, Brown DL, Phillips AW, Kohli K (2014) Support systems for developing system models. In: Proceedings of the international modal analysis conference (IMAC) XXXII–A conference and exposition on structural dynamics
9. Pasha HG, Allemang RJ, Phillips AW (2014) Techniques for synthesizing frfs from analytical models. In: Proceedings of the international modal analysis conference (IMAC) XXXII–a conference and exposition on structural dynamics

Chapter 15
In-Situ Experimental Modal Analysis of a Direct-Drive Wind Turbine Generator

M. Kirschneck, D.J. Rixen, Henk Polinder, and Ron van Ostayen

Abstract The purpose of the support structure of wind turbine generators is to ensure a constant air gap length throughout the circumference of the generator. It is supposed to be light weight and at the same time stiff enough to minimize deformation of the rotor outer surface caused by electro-magnetic forces in the air gap. Reducing weight without compromising the stability and stiffness of the generator requires an in-depth analysis of the dynamic behaviour. In a previous study a model and a calculation method for estimating this behaviour was developed. For validation of this model an in-situ modal testing of a large off-shore wind turbine generator is necessary. The challenges encountered during in-situ dynamic measurements of such a generator are the coupling with the rest of the turbine, the limited accessibility of the structure within the nacelle as well as the large mass of the structure. Various excitation methods were used for the measurements including hammering tests as well as output only measurements during operation and idling of the turbine. This paper presents the challenges encounter during the measurement campaign as well as the results of these measurements.

Keywords Operational modal analysis • Direct-drive wind turbine • Order-based modal analysis

15.1 Introduction

Constructing direct-drive off-shore wind turbines are capital expenditure intensive. Logistic costs are a lot higher off-shore than on-shore. Especially, heavy constructions increase the costs of off-shore installation as they give rise to the need of heavy cranes. Reducing the weight of the turbine decreases, therefore, construction costs as smaller equipment can be used that is more common and thus less expensive to rent. The weight of the nacelle is a key concern as any decrease of the nacelle's weight yields also a reduction of the weight of the tower it is installed on. Consequently, the wind turbine industry has been trying to reduce the weight of the nacelle over the past years.

For direct-drive wind turbines, the largest contributor to the weight of the nacelle is the generator. These are especially heavy in this turbine type, because the low rotation speed of the generator shaft necessitates a high torque in the generator to reach the nominal power output. In the past, the high torque was met by stiff and heavy constructions that only allowed small deformations. More flexible construction concepts came into focus recently [6]. These constructions allow more deformation, making a dynamic analysis of the rotor construction necessary. In a previous study, a calculation method and modelling techniques were introduced for predicting the dynamic behaviour of the rotor [2]. In a previous study, [3], the modal was tried to validate and the dynamics of the rotor structure experimentally determined. However, the results were not satisfactory and thus different methods are used in this paper for an experimental modal analysis.

As in [3] the main problem during the experimental study was the excitation of the structure. This is caused by the size of the structure of interest. The structure of a rotating generator is excited directly by the rotation of the shaft and the higher harmonics of that rotation created by the magnetic forces in the air gap. The resonance frequencies of the structure are, however, so high that only the magnetic forces can excite the resonance frequencies. Just as before in [3] these excitation frequencies were used in most methods shown in this paper for the experimental modal analysis.

M. Kirschneck (✉) • R. van Ostayen
Faculty of Mechanical, Maritime and Materials Engineering, Delft University of Technology, Delft, The Netherlands
e-mail: m.kirschneck@tudelft.nl

D.J. Rixen
Faculty of Mechanical Engineering, Technische Universität München, Germany

H. Polinder
Faculty of Electrical Engineering Mathematics and Computer Science, Delft University of Technology, Delft, The Netherlands

This paper conducts an experimental modal analysis of the generator rotor of the XD-115, a 5 MW direct-drive permanent magnet wind turbine built by XEMC-Darwind. The measurements were conducted in-situ. Various methods were used for excitation including an Order-Based Modal Analysis, an Operational Modal Analysis (OMA) during the yawing of the turbine, and an Operational Modal Analysis during a constant speed operation.

The paper introduces first the measurement set up used during the measurements. Afterwards, it presents the results of the modal analysis and compares the various methods with each other.

15.2 The XD-115

The part of interest for the experimental analysis is highlighted in Fig. 15.1b. That is the part that supports the permanent magnets on the rotor and thus has to withstand the high magnetic forces that are created by the interaction of the magnetic fields of stator and rotor. It consists of a welded steel construction that gives rigidity to the circumference of the outer rotor diameter. Figure 15.2 shows a technical drawing of that part.

The aim of the measurement campaign is to identify the modal parameters of the first modes, including the mode shapes, the damping ration and the frequency. In a preliminary finite element analysis the modes were approximated. The experiments serve as input to update the model and refine its parameters. However, the bearing stiffness, a parameter of the model that is very influential on some of the modes, could not be predicted in the model. This is due to the complexity and the size of the bearing in the XD-115. Therefore, the measurements are also used to identify the bearing parameters and complete the model.

Figure 15.3a shows the set-up of the measurement. Measuring on the rotor and stator side simultaneously required two data acquisition systems (DAQs). One was installed in the rotor (Fig. 15.3b) the other one was connected to the sensors in the rest of the nacelle. A hammer was used for synchronizing the two systems. Its signal was split and fed to both systems. Before the start of the turbine it was disconnected from the rotor DAQ. After the measurements were completed a cross correlation analyse between the two hammer channels at either DAQ would yield the time difference between the two signals. This method has one significant disadvantage. Any delay introduced in either of the DAQs during the measurement cannot be identified. Thus, at the beginning of the measurements the stator and rotor measurements are synchronized, but the longer a measurement is the more likely a time difference at the end is introduced.

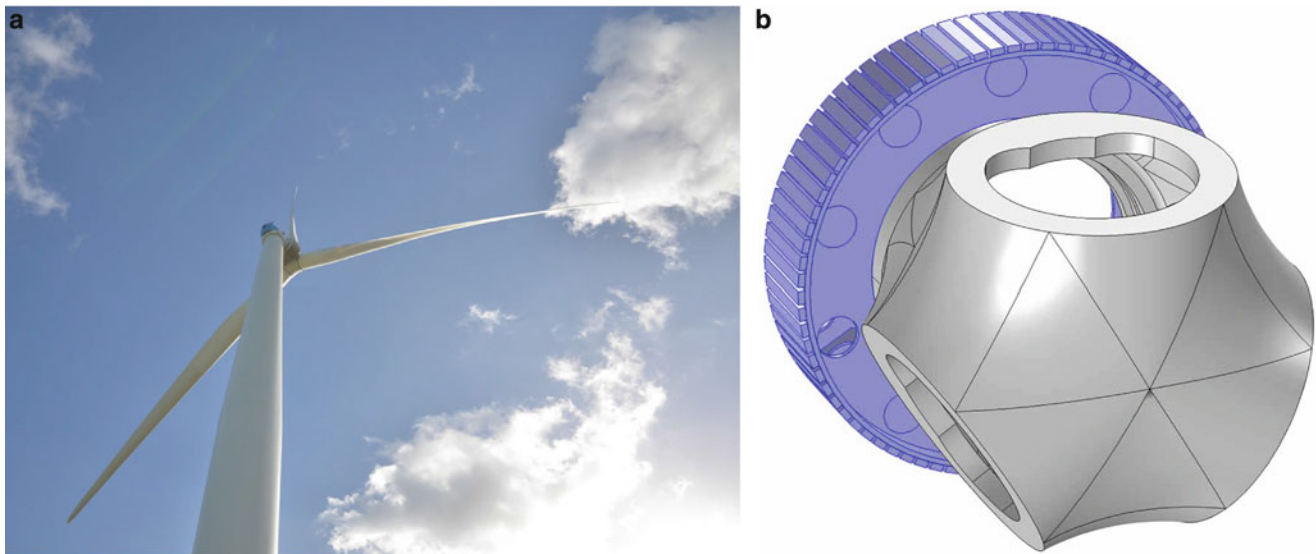**Fig. 15.1** The XD-115 wind turbine, which is used for the measurements. (**a**) The XD-115 wind turbine in Wieringerwerf, North Holland. (**b**) The rotor of the XD-115 without blades. The structure of interest is hilighted in *blue* (Color figure online)
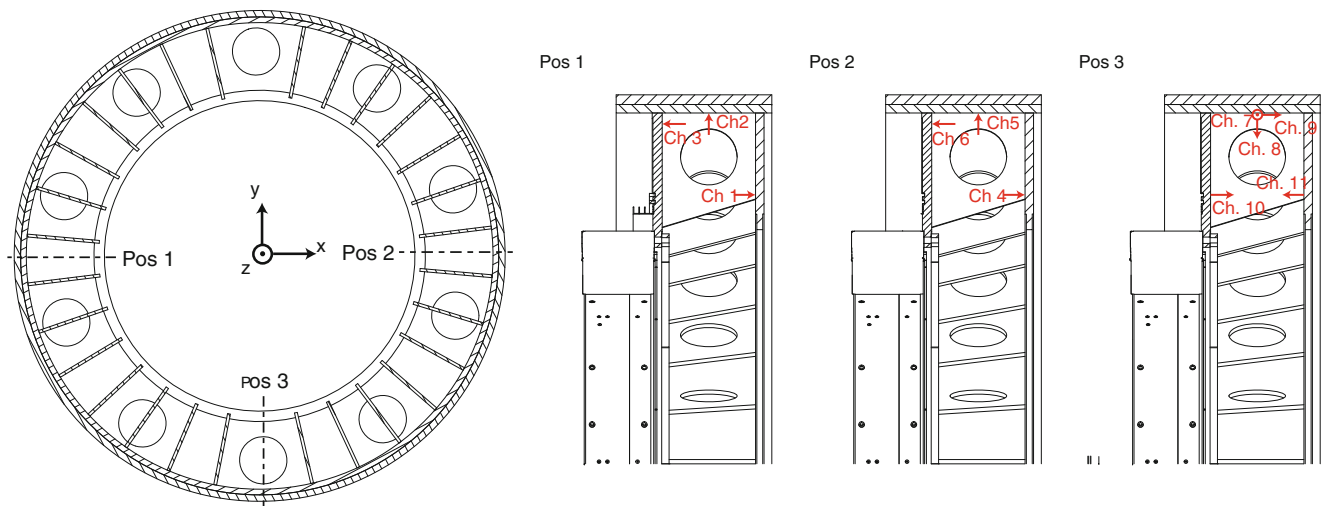
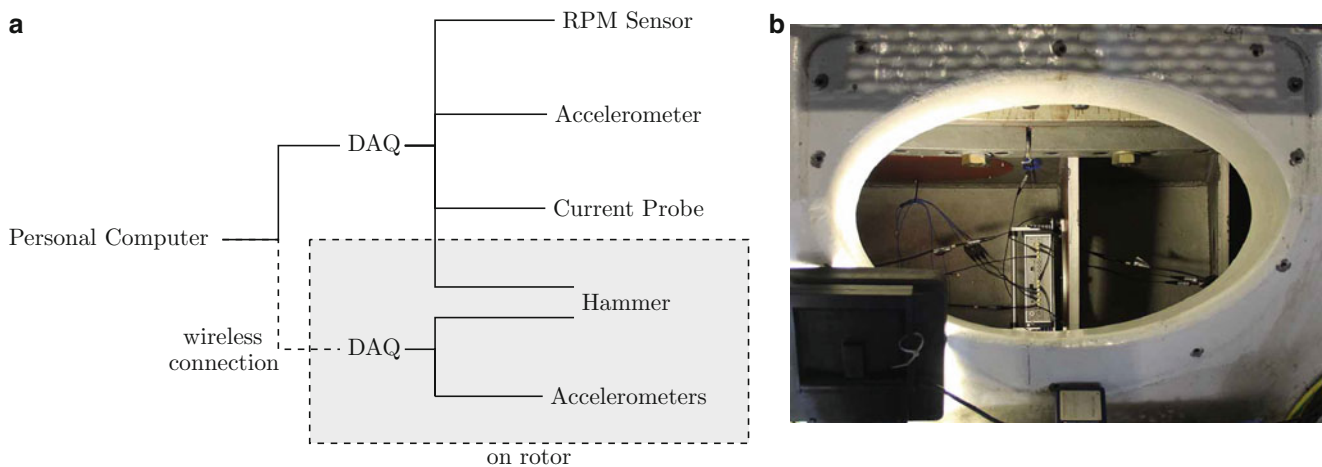**Fig. 15.2** Accelerometer positions in rotor stiffener

Fig. 15.3 Measurement set up for the XD-115. (**a**) Schematic of the measurement set up. (**b**) The Data Acquisition system mounted in the turbine

15.2.1 Sensor Positions

In total 11 channels were used for acceleration measurements on the rotor. Figure 15.2 shows the sensor positions of the accelerometers in the rotor of the XD-115. The position of the sensors where chosen in such a way that bending modes can be distinguished from tilting modes.

15.3 Measurement Methods

Various Measurement methods were used to identify the dynamic behaviour and modal parameters of the generator rotor. In the previous study [3] hammering tests and operational modal analysis were mainly evaluated. However, the results were not satisfactory and thus further measurements and other methods needed to be applied to identify the modal parameters of the turbine. These methods and their results are presented hereafter.
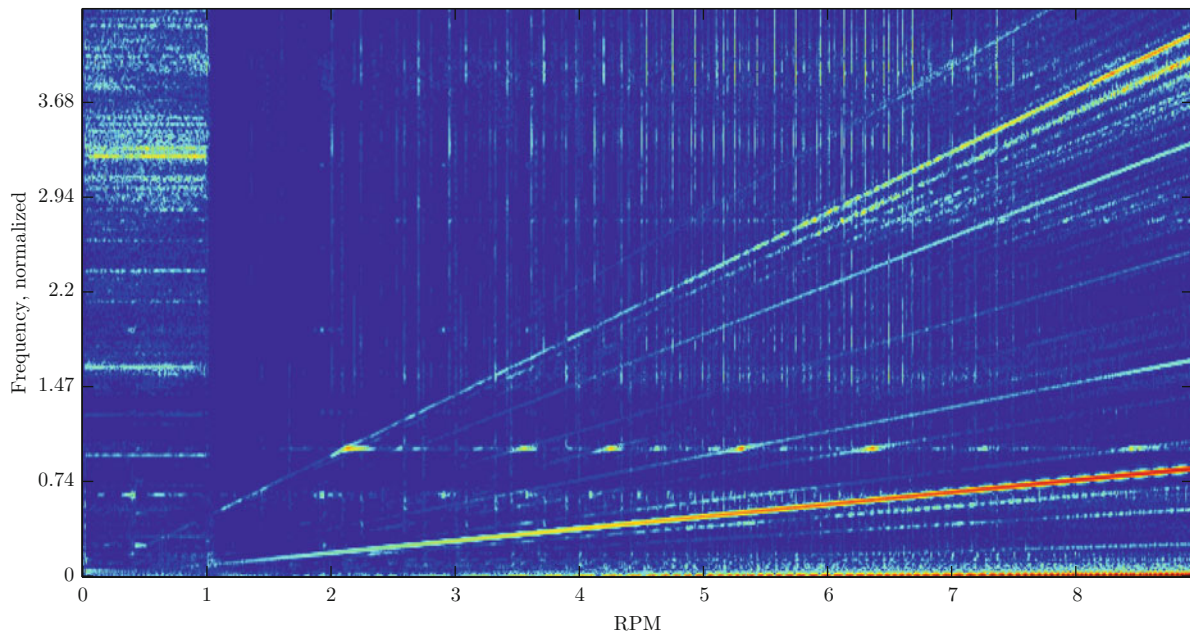
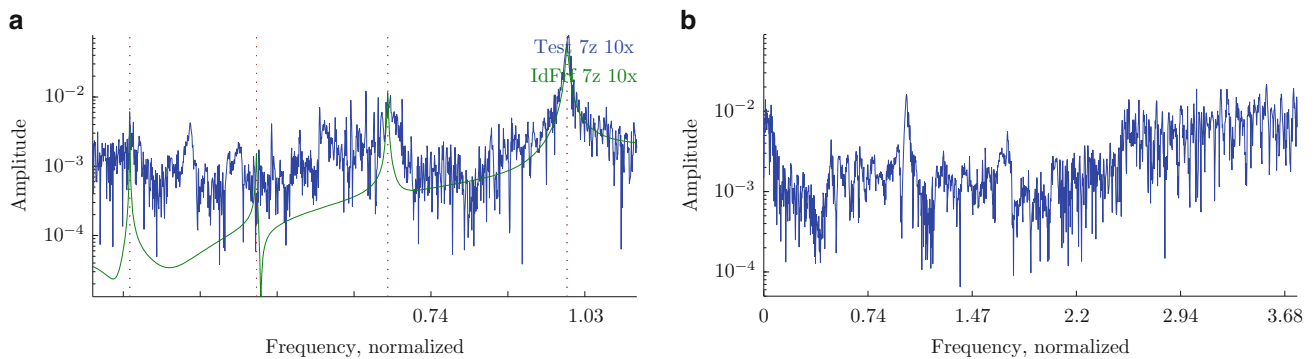**Fig. 15.4** Orderplot of the run up of the XD-115

Fig. 15.5 Orderplot of the 640th order of the rotation speed and its modal fit on the *left*. The 1920th harmonic of the rotation speed on the *right*. The most prominent excited frequency is at frequency= 1. (**a**) Order plot of the 640th harmonic of the rotation speed. (**b**) Order plot of the 1920th harmonic of the rotation speed

15.3.1 Order-Based Modal Analysis

This Order-Based Modal Analysis (OBMA) method (details can be found in [1]) assumes that during a start up or run down of the turbine, a constant sinusoidal excitation at a known frequency. The excitation acts as a sinusoidal sweep, when its frequency depends linearly on the rotation frequency. Figure 15.4 shows the vibration measurement of a sensor placed on the rotor during the run up of the XD-115. The diagonal lines represent an excitation which depends linearly on the rotation speed. During a start up of the turbine such an excitation harmonic excites various frequencies. When the excitation frequency coincides with a resonance frequency the measured amplitude of the vibration increases. Order tracking will extract such an order and its response from the measured system. The excitation can be seen as a sinusoidal sweep of the system where the excitation is generated by the operation itself. The frequency is known as it depends on the rotation frequency which was measured. The amplitude of the excitation, however, is unknown. A modal analysis method can be applied to these frequency response functions and the modal parameters can be extracted.

For this measurement a Vold-Kalman order tracking method [4] has been used to extract the orders from the measurements. Figure 15.5 shows the extracted orders against the frequency at which they were excited for the 640th and 1920th harmonic.
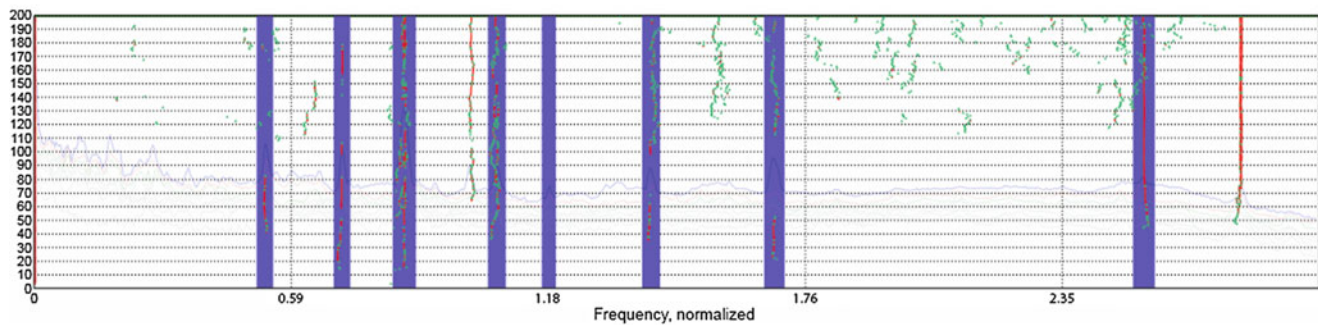
Fig. 15.6 Stability diagram of the SSI-CVA method for the measurement at constant speed

For the extraction of the phase information the RPM signal was used as reference. Assuming that the excitation force was a sinusoidal force with a magnitude of unity the transfer function is the same as the recorded frequency response function. These transfer functions can be used in any single input multiple output modal parameter estimation algorithm. Because the magnitude of the force is not know, the scaling of the modes is not possible. Assuming that the excitation force amplitude is the same for every frequency, the parameters of interest, i.e. the mode shapes, frequencies and damping, can be derived.

In this case only the parameters of the mode at ω has been extracted. The higher modes are nor excited to an extend that a parameter identification is possible as can be seen in Fig. 15.5b. The mode at $\omega = 1$, however, is clearly visible on the order plots.

15.3.2 Operational Modal Analysis at Constant Speed

In the previous study [3], the strongly changing harmonic excitation frequencies were a major problem during the Operational Modal Analysis were. The measurements were thus repeated at constant speed to eliminated this variation. However, a constant rotation speed needs to be actively maintained by the controller of the XD-115 as the turbine is designed to operate at variable speeds. The intended rotation speed of 9 RPM is, therefore, not perfectly reached and there are some slight deviations from this target rotation speed.

The plot in Fig. 15.7b shows the results of the operational modal analysis at constant speed. The singular value decomposition (SVD) plot in Fig. 15.7d indicates that there might be modes at $\omega = 0.1$, $\omega = 0.17$, $\omega = 0.27$, $\omega = 1$ and $\omega = 1.34$. The other peaks at $\omega = 0.52$, $\omega = 0.7$, $\omega = 0.84$, $\omega = 1.05$, $\omega = 1.18$, $\omega = 1.41$, $\omega = 1.69$ and $\omega = 2.53$ are generated by harmonics.

Peculiar is the peak at $\omega = 2.78$ as at that peak all singular values increase, which usually indicates that the peak is created by a harmonic. However, at that frequency there is no harmonic. It was also shown in [3] that the peak also exists when the structure is excited by a hammer. It was therefore identified as a mode.

For identifying the modal parameter two different Stochastic Subspace Identification (SSI) methods were applied to the measurements data: Stochastic Subspace Identification-Canonical Variate Analysis (SSI-CVA) and Stochastic Subspace Identification-Principal Component (SSI-PC). However, the SSI-PC method did not find any stable modes when applied to the measurement. Further the Enhanced Frequency Domain Decomposition (EFDD) method was employed.

Figure 15.6 shows the stability plot of the SSI-CVA method with the Modal indicator parameters as shown in Table 15.1. Most harmonics (indicated by a blue vertical line) are identified as modes by the algorithm. Besides that there are two stable modes at $\omega = 1$ and $\omega = 2.78$. There are five modes identified around the frequency $\omega = 2.78$.

The SSI-CVA method identifies only the modes at $\omega = 1$ and $\omega = 2.78$. These are the modes that were identified in the previous modal analysis at varying speeds in [3]. The constant measurement therefore did not yield any further results.

Table 15.1 Acceptance criteria for the operational modal analysis

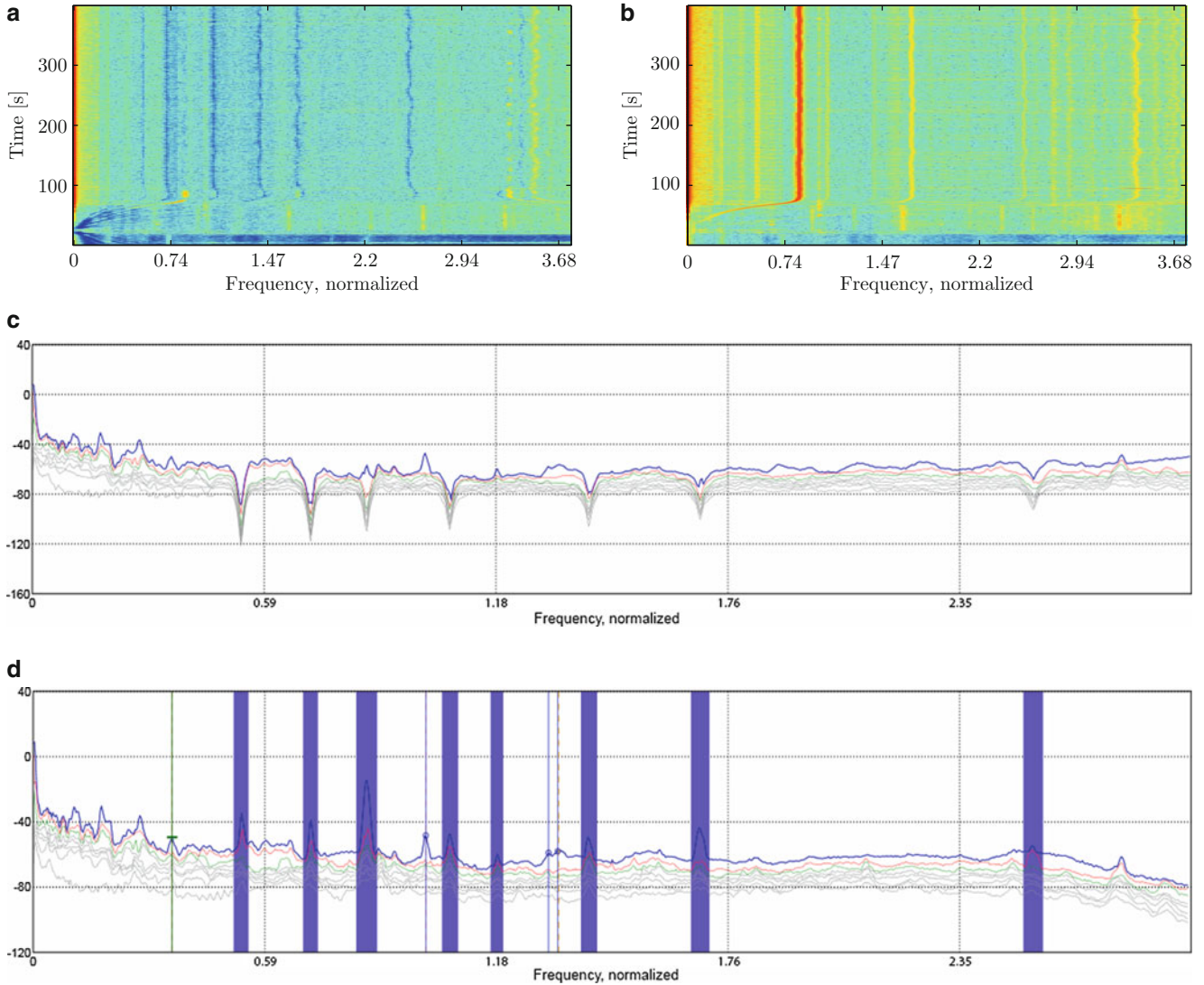| Parameter name	Parameter values CVA	Parameter values PC
Maximum deviation of parameters		
Frequency [Hz]	0.05	0.1
Damping [%]	2	1.2
Mode shape MAC	0.01	0.2
Expected range of damping		
Min [%]	0.05	0.05
Max [%]	2	2

Fig. 15.7 The spectrograms and SVD plots of filtered and unfiltered measurements. The harmonics generated by the generator were filtered out. (**a**) Spectrogram of Vold-Kalman Filtered measurement. (**b**) Spectrogram of unfiltered measurement. (**c**) SVD-Plot of Vold-Kalman filtered measurement. (**d**) SVD Plot of unfiltered measurement

15.3.3 Vold-Kalman Filtered Operational Modal Analysis

The Vold-Kalman Filter introduced in [4] is a method for order tracking. It can also be used to eliminated certain frequencies from a signal. In this case, it was used to filter out the harmonics excitations in the measurement before applying an operational modal analysis. This procedure eliminates the peaks created by the harmonic excitations in the singular value decomposition plot and thus makes it easier to identify peaks resulting from modes. Figure 15.7 shows the plots of the
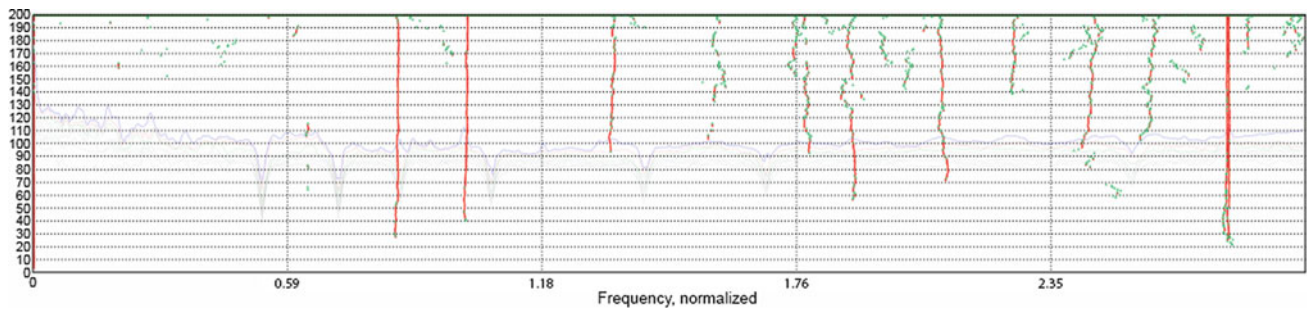
Fig. 15.8 The stability plot of the SSI-CVA method applied to the Vold-Kalman filtered measurements

Table 15.2 Overview over identified damping values by the Operational Modal Analysis (OMA) and the Order-Based Modal Analysis (OBMA) for various resonance frequencies and methods

Frequencies, normalized	0.1	0.17	0.27	1	1.34	1.88	2.09	2.25	2.78
Method	Damping values [%]								
OBMA	–	–	–	0.18	–	–	–	–	–
Constant speed measurement EFFD	2.065	1.639	1.173	0.346	1.827	–	–	–	0
Constant speed measurement SSI-CVA	–	–	–	1.23	–	–	–	–	0.073
Vold-Kalman filtered OMA EFFD	2.6	1.97	1.35	0.387	1.762	0.49	0.796	0.772	0.081
Vold-Kalman filtered OMA SSI-CVA	–	–	–	1.11	0.941	0.891	1.334	1.274	0.246

operational modal analysis. On the left hand side it shows the spectrogram of the Vold-Kalman filtered measurements. On the right hand side the same measurement is shown before the filter is applied. The harmonics that are still present on the right hand side disappeared. This can also be seen in the SVD plots. At the location where the peaks were that resulted from the harmonic excitation the singular value decomposition values approach zero (Fig. 15.8c).

The Vold-Kalman filter makes it easier to identify modes as the peaks resulting from the harmonics are no longer present in the measurement. Looking at the SVD plot possible modes could be at the same locations that were identified in the measurement at constant speed. Additionally, there could be mode at $\omega = 1.88$, $\omega = 2.09$ and $\omega = 2.25$. The automatic mode detection of the SSI-method now detect more modes because the peaks from the harmonic excitation are missing. The stability diagrams of the methods now show more stable modes with the same setting as before. The identified modes and damping values for this method are listed in Table 15.2.

15.3.4   Yawing Test

During yawing, the nacelle is moved around the center axis of the tower. Because the center of gravity of the generator is not aligned with this axis, it experiences a movement. When this movement is stopped inertia forces are generated acting on the rotor. The time distribution of this force resembles an impulse force used for the hammering test. Measuring the response to this force makes the identification of the modal parameters of the system possible. This method is especially suited to excite the lower structural modes because the high frequency content of the excitation is low and this method can introduce much energy into the system. Furthermore, the applied inertia forces excite the structure everywhere instead of locally as it is done for the hammering measurements. The excitation generated this way cannot be measured. That is why an output only parameter identification method needs to be employed. To identify the modal parameters the Least Square Complex Exponential method (LSCE) (see for instance [5] for an explanation) has been used. Figure 15.9 shows the stability plot and the spectrogram of the measurement. In the spectrogram the noise generated by the yawing motion and engines is clearly visible. After the movement stops at around 21 s some frequencies seem to be excited. Those could be resonance frequencies.

From Fig. 15.9a it can be seen that the lower frequencies that were mainly excited by this method are relatively unstable. Even the mode at $\omega = 1$ which is easily identifiable in the other methods is not stable. Only some modes around $\omega = 0.05$ seem to be stable. However, those frequencies are too low to be of interest in the scope of this paper.
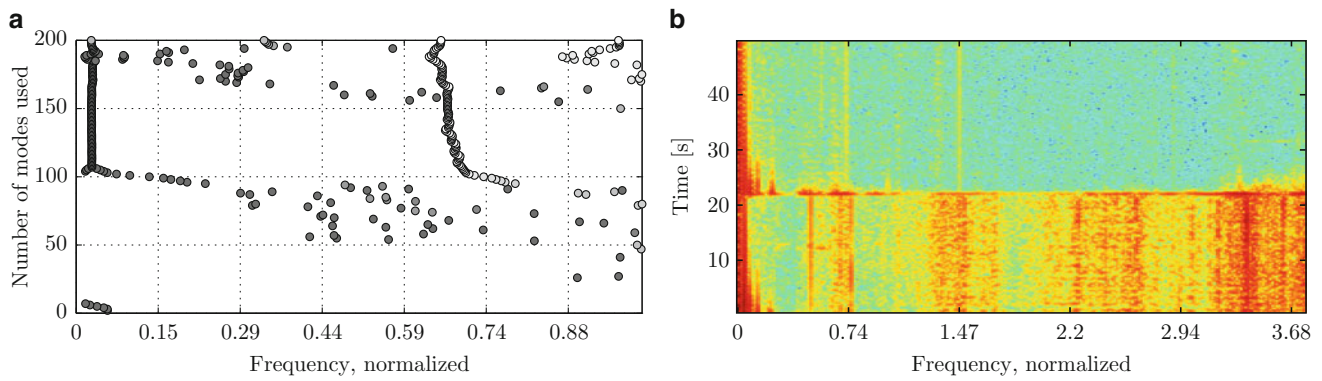
Fig. 15.9 Stability plot of The LSCE method (**a**) Stability plot of the Least Square Complex Exponential method applied to the yawing measurement. (**b**) Spectrogram of the yawing excited measurement
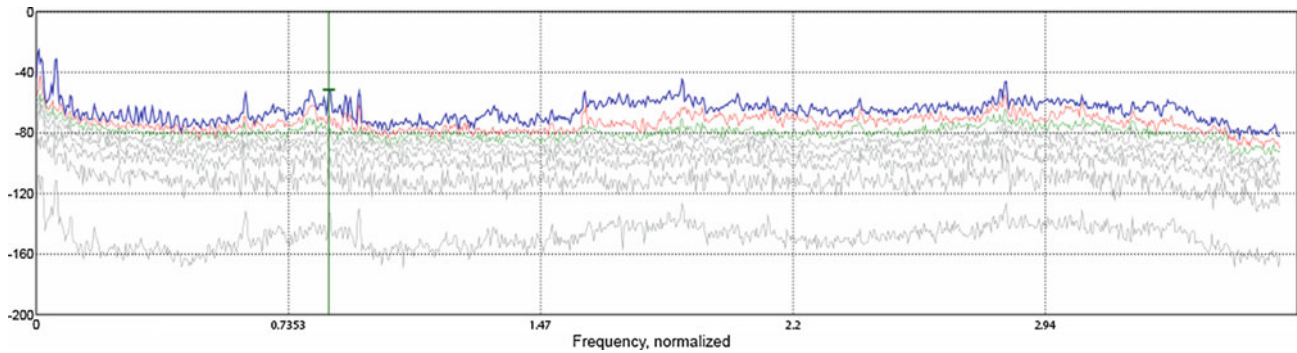

Fig. 15.10 Singular value decomposition plot of the yawing noise analysis

15.3.5 Operational Modal Analysis of Yawing Noise

In Fig. 15.9b the spectrogram of the measurement during the yawing of the turbine can be seen. The measurement during the yawing of the turbine seems to be relatively white noise. Therefore, it can be analysed by an operational modal analysis assuming the excitation to be perfect white noise. Figure 15.10 shows the singular value decomposition plot of this measurement. The plot shows no significant peaks that could be used to analyse modes of the turbine generator structure. Therefore, the analysis was stopped after the evaluation of the singular value decomposition.

15.4 Discussion

Table 15.2 presents the damping values of several resonance frequencies identified and various methods employed. For resonance frequencies that were not identified by a certain method a "-"was used. The operational modal analysis methods give similar damping values for the same resonance frequency. Which method is used for the subspace identification has a minor effect on the identified damping parameters. However, filtering the harmonics from the measurement made it possible to identify more resonance frequencies than before.

All presented identification methods leave some uncertainty regarding the modes identified. For this uncertainty, there are several possible explanations. The probable main reason for this lack of uncertainty is the fact that the modes of interest are not properly excited during operation of the turbine. In the spectrograms in Fig. 15.7a and b only the modes at $\omega = 1$ and $\omega = 2.87$ are visible. These two modes are excited and thus their identification is more reliable. For a more reliable identification of the modal parameters an excitation methods has to be used that excites all modes. This will proof difficult with a structure that is as big as the generator structure of the XD-115.

Comparing the results of the identification methods used, it becomes apparent that the strong harmonic excitation in the frequency range of interest poses a large problem for the operational modal analysis methods. Filtering them before applying the method yields better results. However, only the excitation methods that are directly present in the generator seem to excite the modes of the generator structure. All other excitation techniques such as yawing noise failed to excite the modes of interest.

The mode shapes for the identified resonance frequencies were extracted and compared. Because the mode shapes of the various methods matched, they were not shown in this paper.

15.5 Conclusion and Outlook

It could be shown that including some more techniques for modal parameter identification it was possible to extract more modes from the data or get more certainty about modes that were already identified without the techniques presented here.

In order to get more accurate modal parameter estimations operational modal analysis is not the method of choice. Measurements using an external excitation mechanism that excite all modes of interest promise to yield better results. These measurements will be linked to a larger amount of effort as the excitation techniques need further equipment. Especially the use of falling weights or inertial shakers seem promising.

References

1. Di Lorenzo E, Manzato S, Vanhollebeke F, Goris S, Peeters B, Desmet W, Marulo F (2014) Dynamic characterization of wind turbine gearboxes using Order-Based Modal Analysis. In: ISMA 2014
2. Kirschneck M, Rixen D, Polinder H, van Ostayen RA (2014) Electro-magneto-mechanical coupled vibration analysis of a direct-drive off-shore wind turbine generator. J Comput Nonlinear Dyn . . ISSN 1555-1415. doi: 10.1115/1.4027837. URL http://computationalnonlinear.asmedigitalcollection.asme.org/mobile/article.aspx?articleid=1881888
3. Kirschneck M, Rixen DJ, Polinder H, van Ostayen R (2014) Modal analysis of a large direct-drive off-shore wind turbine generator rotor. In: ISMA 2014
4. Leuridan J, Kopp GE, Moshrefi N, Vold H (1995) High resolution order tracking using kalman tracking filters - theory and applications. Technical report, URL http://papers.sae.org/951332/
5. Maia NMM, Silva JMMA (1997) Theoretical and experimental modal analysis. Research Studies Press. ISBN 0863802087
6. Shrestha G, Polinder H, Bang D-J, Ferreira JA (2010) Structural flexibility: a solution for weight reduction of large direct-drive wind-turbine generators. IEEE Transactions on Energy Convers 25(3):732–740, ISSN 0885-8969. doi: 10.1109/TEC.2010.2048713. URL http://ieeexplore.ieee.org/lpdocs/epic03/wrapper.htm?arnumber=5484469

Chapter 16
Effect of Radial Confinement on Wave Propagation and Vibrational Response in Bars

Jacob C. Dodson, Jason R. Foley, Janet C. Wolfson, Jonathan Hong, Vincent Luk, Alain Beliveau, and Alexander Idesman

Abstract It is currently beyond the state-of-the art to accurately predict the instantaneous dynamic response of a structure with rapidly changing boundary conditions. In order to establish a basic understanding of changing boundary conditions, we examine the wave propagation through a bar subject to mechanical confinement. The Air Force Research Laboratory has conducted several experiments investigating the effect of non-traditional boundary conditions, such as mid-structure confinement, on the local and global dynamic response of rods using a modified Hopkinson Bar configuration with radial clamping. We have shown that the wave velocity in the mechanically clamped area is significantly lower than that in a stress free bar. This paper presents the experimental results and analytical modeling of the effect of radial confinement on dynamic response in bars.

Keywords Wave propagation • Confined effects • Hopkinson bar • Dispersion • Experimental mechanics

Nomenclature

Symbol	Description	Units
ρ	Density	kg/m^3
λ, μ	Lamé constants	Pa
σ	Stress	Pa
ω	Angular/radian frequency	Rad/s
r	Radial Direction of cylinder	m
ψ	Phase	Rad
A	Area	m^2
E	Dynamic elastic modulus	Pa
V	Material velocity	m/s
i	Imaginary number	–
c_j	Elastic wave velocity ($j = ph, 0, d, t$)	m/s
κ	Wavenumber	m^{-1}
Λ	Wavelength	m
t	Time	s
$u, \mathbf{u}$	Displacement	m
$J_0 (\cdot)$	Bessel function, zeroth order	–
$J_1 (\cdot)$	Bessel function, first order	–

J.C. Dodson (✉) • J.R. Foley • J.C. Wolfson
Air Force Research Laboratory/RWMF, 306 W. Eglin Blvd., Bldg. 432; Eglin AFB, FL 32542-5430, USA
e-mail: jacob.dodson.2@us.af.mil

J. Hong • V. Luk • A. Beliveau
Applied Research Associates, Valparasio, FL, USA

A. Idesman
Texas Tech University, Lubbock, TX, USA

16.1   Introduction

Radial confinement of a free bar is typically used to create a clamped end condition. We will change the way we look at the traditional clamped boundary condition by examining the wave propagation through a mechanically clamped area. Ultimately, we want a better understanding of how a changing area of mechanical clamping will affect the dynamics of our system. We will look at the changes in the wave velocity and amplitude due to a clamp on a long bar. The properties of elastic waves in stress-free bars are well documented, but the elastic wave velocity of the same waves in a bar with an applied clamp has not been thoroughly explored. In this paper we review wave propagation in stress-free bars, develop a simple theory to explain wave velocity in constrained bars, review how the addition of a clamp on a bar will change the wave amplitude, explain the experimental setup and computational model, and finally discuss the results of the confinement effect as seen in the experiment and numerical model.

16.2   Theory

The theory describing wave propagation in a stress-free or unconstrained bar is well known and we review the theory for comparison against the experimental and numerical results to validate our unconfined setup and model. Additionally, the theoretical 1-D wave velocity and transmission and reflection ratios for waves in a clamped bar are independently developed and later compared against the experimental and numerical data. We use the theory for baseline information and help explain some of the expected and unexpected experimental results.

16.2.1   Wave Propagation in a Bar

The 3-D theory of wave propagation allows a non-uniform distribution to exist over cross-sectional area of the bar. Pochhammer and Chree independently developed the relations for longitudinal waves in an infinite cylindrical bar in 1876 and 1889 respectively [1, 2]. The solution for governing the wave velocities of longitudinal waves in cylindrical bars has come to be known as the Pochhammer-Chree equation. Using the longitudinal assumptions, the harmonic forms of the displacements, and the stress-free boundary conditions on the surface of a cylinder with radius R that is infinitely long, we arrive at the dispersion equation governing the wave velocity as a function of frequency given by

$$\left(2\frac{\partial}{\partial r^2}J_0(hr) - \frac{\lambda\omega^2\rho}{\mu(\lambda+2\mu)}J_0(hr)\right)\left(\frac{\omega^2\rho}{\mu}-2\kappa\right)J_1(mr)\Bigg|_{r=R} = -4\kappa^2\frac{\partial}{\partial r}J_0(hr)\frac{\partial}{\partial r}J_1(mr)\Bigg|_{r=R} \tag{16.1}$$

Where λ and μ are Lamé's elastic constants, ρ is the density, $J_0(\cdot)$ is the Bessel function of the zeroth order and $J_1(\cdot)$ is a first order Bessel function and

$$h^2 = \frac{\omega^2}{c_d^2} - \kappa^2 \text{ and } m^2 = \frac{\omega^2}{c_t^2} - \kappa^2$$

where $\kappa = \frac{\omega}{c_{ph}}$ is the wavenumber, c_{ph} is the phase velocity, ω is the angular frequency. The dilatational velocity c_d and the transverse velocity c_t are defined as

$$c_d = \sqrt{\frac{\lambda+2\mu}{\rho}} \text{ and } c_t = \sqrt{\frac{\mu}{\rho}}.$$

The dispersion equation above can be numerically solved for the wavenumber κ and corresponding phase velocity c_{ph} as a function of frequency. In the three-dimensional case, the stress wave velocity is frequency dependent creating dispersive waves [1, 2]. As a result, a propagating wave shape will *disperse* and the wave will change shape as its various frequency components travel at different speeds.

Using the Pochhammer-Chree equation given above and assuming that $hr \ll 1$ and $mr \ll 1$, the dispersion equation could be approximated by only using the first term of the Bessel power series expansion. Substituting the approximated Bessel series into the Pochhammer-Chree Dispersion equation and simplifying yields

$$\frac{\omega^2}{\kappa^2} = \frac{E}{\rho},$$

where E is Young's modulus and the non-dispersive (or one-dimensional) phase velocity can be written as

$$c_0 = \frac{\omega}{\kappa} = \sqrt{\frac{E}{\rho}}.$$

For long wavelengths, Λ, when $\frac{R}{\Lambda} < 0.1$, the Pochhammer-Chree phase velocity, c_{ph}, of longitudinal waves has very little variance from the one-dimensional phase velocity c_0 [3]. For the titanium bar used in this experiment the Young's modulus is approximately 104 GPa and the density is 4,430 kg/m^3 which gives an estimated 1-D wave velocity of $c_0 = 4{,}845$ m/s. We will use this full Pochhammer-Chree theory and the one-dimensional approximation for the analysis of the numerical and experimental data later in the paper.

16.2.2 One Dimensional Wave Propagation with Mass Loading

As mentioned in the section above, the typical wave velocity in the bar is for the stress-free conditions. Here we will address the case when we have a clamp on the bar with length, L. In this case, the bar is titanium and the clamp is steel. To ensure a one-dimensional response, we assume that the incoming wave has very long wavelengths to eliminate interaction with the clamp length, $\Lambda \gg L$. Examining the forces acting on a differential element with width dx, in Fig. 16.1, we can determine the 1-D axial equation of motion.

Summing the forces acting on the differential element yields

$$\left(\rho^{ti} A^{ti} + \rho^{st} A^{st} \right) \frac{\delta^2 u_{xx}}{\delta t^2} dx = \left(\sigma_{xx}^{ti} A^{ti} + \frac{\delta \sigma_{xx}^{ti}}{\delta x} A^{ti} dx + \sigma_{xx}^{st} A^{st} + \frac{\delta \sigma_{xx}^{st}}{\delta x} A^{st} dx \right) - \sigma_{xx}^{ti} A^{ti},$$

after some simplification

$$\left(\rho^{ti} A^{ti} + \rho^{st} A^{st} \right) \frac{\delta^2 u_{xx}}{\delta t^2} dx = \frac{\delta \sigma_{xx}^{ti}}{\delta x} A^{ti} dx + \sigma_{xx}^{st} A^{st} + \frac{\delta \sigma_{xx}^{st}}{\delta x} A^{st} dx,$$

Now examining the limit as $dx \to 0$ yields

$$\lim_{dx \to 0} \left(\rho^{ti} A^{ti} + \rho^{st} A^{st} \right) \frac{\delta^2 u_{xx}}{\delta t^2} dx = \lim_{dx \to 0} \left[\frac{\delta \sigma_{xx}^{ti}}{\delta x} A^{ti} dx + \sigma_{xx}^{st} A^{st} + \frac{\delta \sigma_{xx}^{st}}{\delta x} A^{st} dx \right],$$
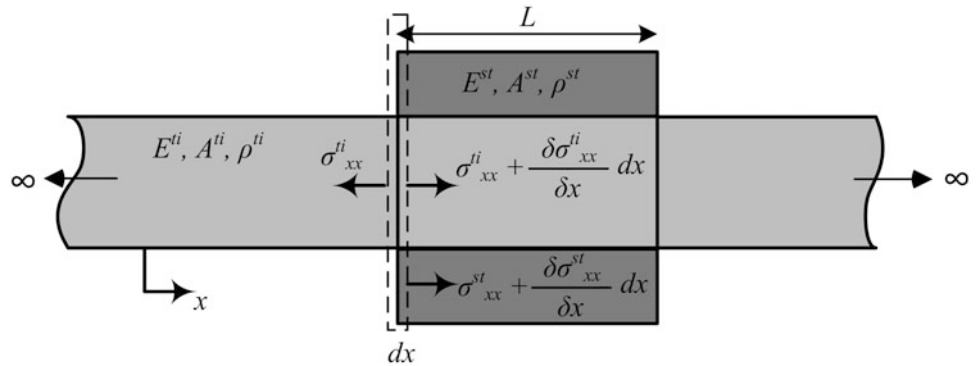

Fig. 16.1 Longitudinal vibration in the x-direction in a rod with a clamped area

then $0 = \sigma_{xx}^{st} A^{st}$ and therefore $0 = \frac{\delta \sigma_{xx}^{st}}{\delta x} A^{st}$. Using the zero stresses in the steel and simplifying, the equation of motion becomes

$$\frac{\left(\rho^{ti} A^{ti} + \rho^{st} A^{st}\right)}{A^{ti}} \frac{\delta^2 u_{xx}}{\delta t^2} = \frac{\delta \sigma_{xx}^{ti}}{\delta x}.$$

Substituting the linear stress-strain relation, $\sigma_{xx}^{ti} = E^{ti} \frac{\delta u_{xx}^{ti}}{\delta x}$, into the equation of motion above, it can be written as $\rho_{eff} \frac{\delta^2 u_{xx}}{\delta t^2} = E^{ti} \frac{\delta^2 u_{xx}}{\delta x^2}$ or $\frac{\delta^2 u_{xx}}{\delta t^2} = c_{eff}^2 \frac{\delta^2 u_{xx}}{\delta x^2}$ where the effective density is $\rho_{eff} = \frac{\left(\rho^{ti} A^{ti} + \rho^{st} A^{st}\right)}{A^{ti}}$ and the effective one dimensional wave velocity is

$$c_{eff} = \sqrt{\frac{E^{ti}}{\rho_{eff}}}. \tag{16.2}$$

This formulation indicates that the wave velocity is much slower in the region of the clamp than the stress-free sections. This slower effective wave velocity is used in when examining the experimental data in the following sections. The next section derives the transmitted and reflected wave amplitude in a bar from the clamped area.

16.2.3   Reflected and Transmitted Wave Amplitude

The wave velocity of the elastic wave in the clamped region has been discussed, now we will analytically develop the amplitude relationship of a compressive wave passing through the same clamped area. To investigate the change in amplitude of the waves as they travel along the stress-free bar and encounter the clamped region, we will examine the change in amplitude due to mechanical impedance induced by the steel clamp. A diagram illustrating the titanium bar with the attached steel clamp can be found in Fig. 16.2 below.

16.2.3.1   Assumptions

1. The bar length is significantly larger than the bar diameter in Fig. 16.2 to ensure one-dimensional wave propagation along the bar.
2. The radial confinement is applied by a steel ring with length, L, which is adequately long so that there is no wave interference between the Interfaces A and B.
3. The bar section that is subjected to radial confinement enclosed by the steel ring does not experience any cross-sectional area change. If this change of the bar section is available from the test setup, the reduced cross-sectional area of this bar section can be incorporated in the model.
4. The density of the titanium bar section subjected to radial confinement remains unchanged.
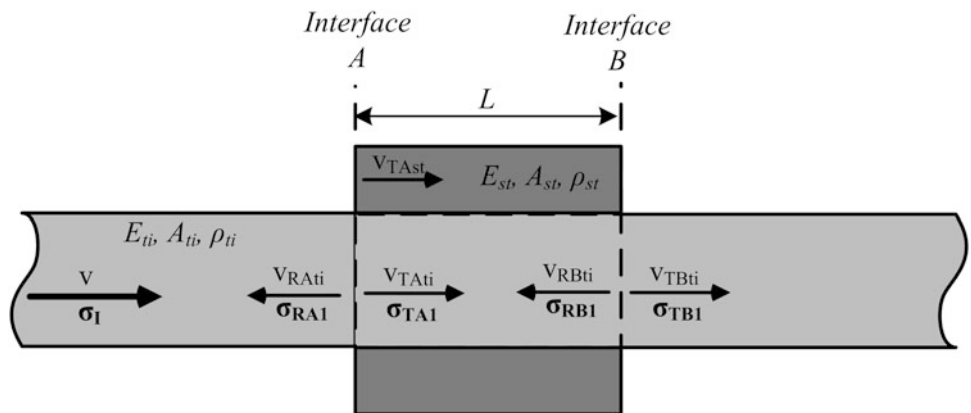

Fig. 16.2 First pass of wave transmission and reflection of a titanium bar subjected to radial confinement by a steel ring

16.2.3.2   Model Development

Consider the first pass of a pulse at the Interface A in Fig. 16.2, two conditions must be satisfied:

1. The forces in both bar sections at the interface must be equal,

$$A_{ti} \left(\sigma_I + \sigma_{RA1} \right) = \left(A_{ti} + A_{st} \right) \sigma_{AT1} \tag{16.3}$$

2. Particle velocities at the interface must be continuous,

$$V_I - V_{RAti} = V_{TAti} + V_{TAst} \tag{16.4}$$

Using $\sigma = \rho c V$, where ρ is density and c is wave velocity, Eq. (16.4) becomes

$$\sigma_I - \sigma_{RA1} = \sigma_{TA1} \left(1 + \frac{\rho_{ti}}{\rho_{st}} \sqrt{\frac{E_{ti} \rho_{st}}{E_{st} \rho_{ti}}} \right)$$
$$\sigma_{TA1} = \left(\sigma_I - \sigma_{RA1} \right) \left(1 + \frac{\rho_{ti}}{\rho_{st}} \sqrt{\frac{E_{ti} \rho_{st}}{E_{st} \rho_{ti}}} \right)^{-1} \tag{16.5}$$

Substituting σ_{TA1} in Eq. (16.5) into Eq. (16.3) yields

$$\sigma_I + \sigma_{RA1} = \left(\sigma_I - \sigma_{RA1} \right) \left(1 + \frac{A_{st}}{A_{ti}} \right) \left(1 + \frac{\rho_{ti}}{\rho_{st}} \sqrt{\frac{E_{ti} \rho_{st}}{E_{st} \rho_{ti}}} \right)^{-1}.$$

After some manipulations, we nondimensionalize the equations by letting $\alpha = \frac{A_{st}}{A_{ti}}$, $\beta = \frac{E_{st}}{E_{ti}}$, $\gamma = \frac{\rho_{st}}{\rho_{ti}}$, and $\xi = \sqrt{\frac{\beta}{\gamma}}$, and get

$$\sigma_{RA1} = \frac{\alpha \gamma \xi - 1}{1 + (2 + \alpha)\, \gamma \xi} \, \sigma_I \tag{16.6}$$

$$\sigma_{TA1} = \frac{2 \gamma \xi}{1 + (2 + \alpha)\, \gamma \xi} \, \sigma_I. \tag{16.7}$$

Considering the force balance and particle velocities at the Interface B in Fig. 16.2, we get

$$\left(A_{ti} + A_{st} \right) \left(\sigma_{TA1} + \sigma_{RB1} \right) = A_{ti}\, \sigma_{TB1} \tag{16.8}$$

$$V_{TAti} + V_{TAst} - V_{RBti} = V_{TBti} \tag{16.9}$$

From Eq. (16.9), $\sigma_{TB1} = \sigma_{TA1} \left(\frac{1 + \gamma \xi}{\gamma \xi} \right) - \sigma_{RB1}.$ Substituting σ_{TB1} into Eq. (16.8) yields

$$\left(1 + \alpha \right) \left(\sigma_{TA1} + \sigma_{RB1} \right) = \sigma_{TA1} \left(\frac{1 + \gamma \xi}{\gamma \xi} \right) - \sigma_{RB1}$$

After some manipulations, we get

$$\sigma_{RB1} = \frac{2 \left(1 - \alpha \gamma \xi \right)}{\left(2 + \alpha \right) \left[1 + (2 + \alpha)\, \gamma \xi \right]} \, \sigma_I \tag{16.10}$$

$$\sigma_{TB1} = \frac{2 \left(1 + \alpha \right) \left(1 + 2 \gamma \xi \right)}{\left(2 + \alpha \right) \left[1 + (2 + \alpha)\, \gamma \xi \right]} \, \sigma_I. \tag{16.11}$$

The one-dimensional wave propagation model developed above will be used to investigate the dynamics of a compressive wave propagating along a titanium bar subjected to a radial confinement caused by a steel ring. The analytical model is formulated using the change of mechanical impedance in terms of changes in cross-sectional areas utilizing the material properties of both the bar and the clamp.

Equations (16.6) and (16.11) are used to calculate the 1-D theoretical reflected and transmitted wave amplitudes for the clamped region of the bar. These values will represent the change in wave amplitude caused by the analytical mechanical impedance change and will be compared with the experimental and numerical values later in the paper. We will discuss the experimental and numerical setups in the next sections followed by the analysis and discussion of the results.

16.3 Experiment

The experiment consists of a modified direct impact Hopkinson pressure bar test apparatus at the AFRL Shock Dynamics Laboratory. The system consists of a 96″ titanium bar which is instrumented with semiconductor strain gages. A steel mechanical clamp was applied in the center of the bar to test the effect of changing the mechanical boundary condition.

In the experimental effort discussed here, the primary measurements are the strain time history in the bar on both sides of the confinement. Uniaxial strain gages are mounted to the bar at a four locations along the bar: 24″, 42″, 54″ and 72″ from the point of impact as shown in Fig. 16.3. The axial distribution allows tracking of the stress wave propagating through the system. The gages are oriented axially on the bar in diametrically opposed pairs to allow bending and/or extensional cancellation. This is feasible since the data acquisition system has sufficient number of phase-matched channels to independently capture the output from individual gages: the bending and extension are calculated from the axial strain in post-processing. Semiconductor strain gages are used on the incident bar; these have resistances of 120 or 350 Ω with a fast response time ($\sim$10 ns) and correspondingly higher bandwidth ($\sim$10 MHz) than foil gages (typically $\sim$300 kHz [4]). The gage length is typically $\sim$1 mm and the gage factor is about 150, [5] providing orders-of-magnitude improvement in sensitivity. The traditional disadvantage of semiconductor gages being strongly temperature dependent is not a concern for these dynamic tests since the circuits can be balanced immediately prior to a test or run in an AC-coupled mode because minimal temperature variation between data acquisition arming and trigger is expected.

The confining rings that were used are heavy duty shaft collars that were machined in-house. They were arranged such that the steel collar (1.875 in long, 0.625 in thick) was centered on the titanium bar. The collar applied 4,000 psi (27.6 Mpa) of pressure to the bar. This was experimentally determined through the use of Prescale pressure sensitive film shown in Fig. 16.3b [6]. This film had a maximum pressure of approximately 7,100 psi. As pressure is applied, the paper turns pink. The more pressure applied, the darker the color. Fuji Film Pressure Distribution Mapping Software (FPD-8010E) [6] was utilized to measure the actual pressure distribution on the film, and the pressure applied was fairly uniform with minor fluctuations on the ends.

Analog signal conditioning for the strain gages, (i.e., regulated constant-current excitation, analog filtering at 700 kHz, and amplification), is accomplished via a Precision Filters 28000 chassis with 28144A Quad-Channel Wideband Transducer
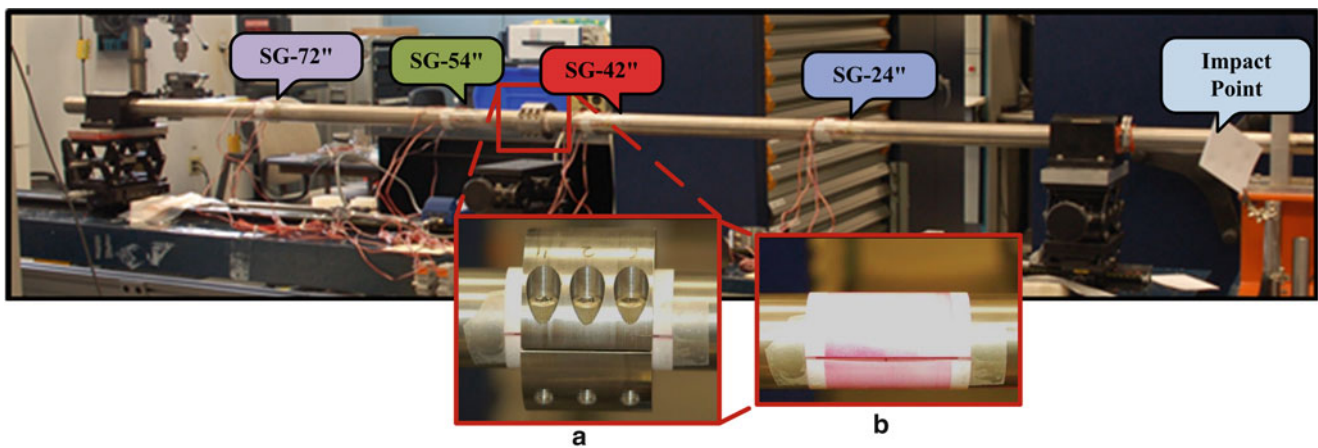

Fig. 16.3 Photos of the instrumented titanium bar, (*a*) the steel clamp, and (*b*) the pressure sensitive film under the clamp
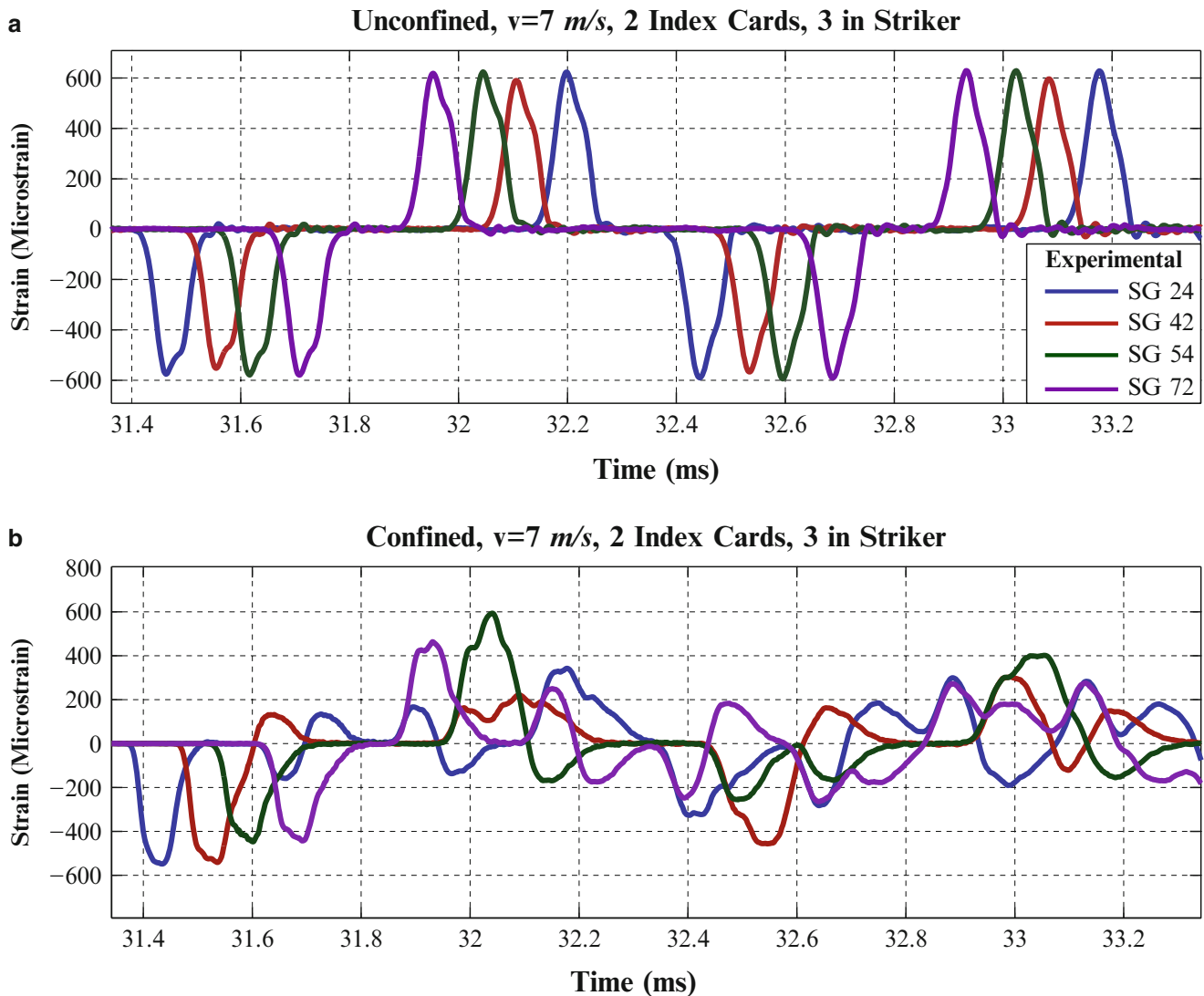
a

b

Fig. 16.4 Strain time history in the titanium bar for the two different experimental configurations ($x_i = 24$, 42, 54, and 72 in.); (**a**) Unconfined and (**b**) Confined

Conditioner with Voltage and Current Excitation cards.[7] A high rate instrumentation system using a National Instruments chassis paired with PXI-6133 multifunction input/output cards is used to digitize the analog data. The PXI-6133 samples at 2.5 MSa/s with 12 bits of vertical resolution [8]. A typical strain time history is shown in Fig. 16.4.

16.4 Numerical Model

We have simulated the experiments described in the previous section by the numerical solution of the corresponding 2-D axisymmetric elastodynamics problems. One of the main issues in the numerical modeling of wave propagation problems is the appearance of spurious high-frequency oscillations in numerical solutions. We have used a new numerical finite-element technique based on the two-stage time integration approach with basic computations in the finite element analysis program (FEAP) and the filtering stage [9, 10]. With this approach, there is no need for the assumptions related to the user-defined amount of artificial viscosity or numerical dissipation used in existing numerical approaches for the suppression of spurious oscillations. For example, our results show that this amount should depend on the order of finite elements, the size of finite elements, the observation time, the numerical dispersion and other factors. This modeling approach yields numerical results

Table 16.1 Material Properties used in elastodynamic numerical simulation

	Young's modulus (E) [GPa]	Density (ρ) [kg/m^3]	Poisson's ratio (ν)[−]
Steel	205	7850	0.29
Titanium	104	4430	0.29

Table 16.2 TRAC values for the comparison of numerical and experimental data for both the unconfined and confined cases

	TRAC values			
	SG-24	SG-42	SG-54	SG-72
Unconfined	0.996	0.994	0.995	0.994
confined	0.815	0.879	0.875	0.856

converging to exact solutions with increasing mesh refinement. Using this approach, finite elements codes can be used as 'black boxes' for wave propagation problems.

The numerical technique used is based on the fact that for linear elastodynamics problems, there is no necessity to filter spurious oscillations at each time increment because the errors in high frequencies do not affect the accuracy of low frequencies during time integration [10]. In basic computations, known explicit or implicit time-integration methods with zero numerical dissipation (zero artificial viscosity) can be used with sufficiently small time increments. This means that the numerical results in basic computations are close to the exact solution of the semi-discrete equations and are practically independent of a time integration method used and time increments. The numerical results in basic computations may contain large spurious oscillations.

For the filtering of spurious oscillations, the implicit TCG method with large numerical dissipation developed in Ref. [10] is used at the filtering stage. For all elastodynamics problems, we use $N = 10$ uniform time increments (five positive plus five negative time increments) at the filtering stage. This means that there is no real time integration at the filtering stage (the sum of 10 time increments used at the filtering stage is zero). As shown in Ref. [10], this procedure is equivalent to the multiplication of each velocity and displacement of the uncoupled system of the semi-discrete equations by a frequency dependent factor and does not require the modal decomposition and the calculation of eigen-frequencies.

The problem was solved on a uniform mesh with square linear elements with reduced numerical dispersion. The mesh includes 12 elements in the radial direction. The elastic values used for the computation are presented in Table 16.1. The evolution of the axial strain in the four gages is shown in Fig. 16.5 for the experiments and for the numerical simulation for both confined and unconfined cases. As can be seen for the unconfined case in Fig. 16.5a, we have a surprisingly good agreement between experiments and calculations not only for large oscillations but also for the following small oscillations; see solid lines and circles. We should emphasize that in our approach we selected the velocity V(t) at the impact face that allows us to fit the experimental and numerical results just for the first big oscillations in SG-24 for a short time. Then, all other numerical results for long observation time in SG-24 and the results in SG-42, SG-54, SG-72 represent an accurate numerical solution of the wave propagation problem for the selected boundary conditions.

The time response assurance criterion (TRAC) [11] is used to evaluate the accuracy of the numerical simulation. The TRAC determines the correlation between the experimental data and the numerical data. The TRAC is defined by

$$TRAC = \frac{\left[\{Exp(t)\}^T \{Num(t)\}\right]^2}{\left[\{Exp(t)\}^T \{Exp(t)\}\right]\left[\{Num(t)\}^T \{Num(t)\}\right]}$$

The TRAC is the correlation for the n$^{\text{th}}$ strain gage over all time for the numerical data, {*Num(t)*}, compared to the actual measured experimental data, {*Exp(t)*}. The TRAC values for the four strain gage locations are shown in Table 16.2.

As seen in Table 16.2, the TRAC values for the unconfined condition are all above 0.99, and have excellent correlation (with perfect correlation being a TRAC value of 1). The TRAC values for the confined case are all above 0.81 again indicating good correlation and the simulation captures the overall behavior with only a slight increase on the reflected pulses from the ring. Now that we have shown the experimental and elastodynamic simulation results agree; in the next section we will process and compare the data with the theory discussed above.

16.5 Analysis and Discussion

This section will compare and discuss various aspects of the theory, experimental data, and numerical results. We will first compare the transmission and reflection amplitudes of the first pulse passing through the clamped region of the bar. Next we will compute and discuss the elastic frequency-dependent phase velocity of the different results for both the unconfined and
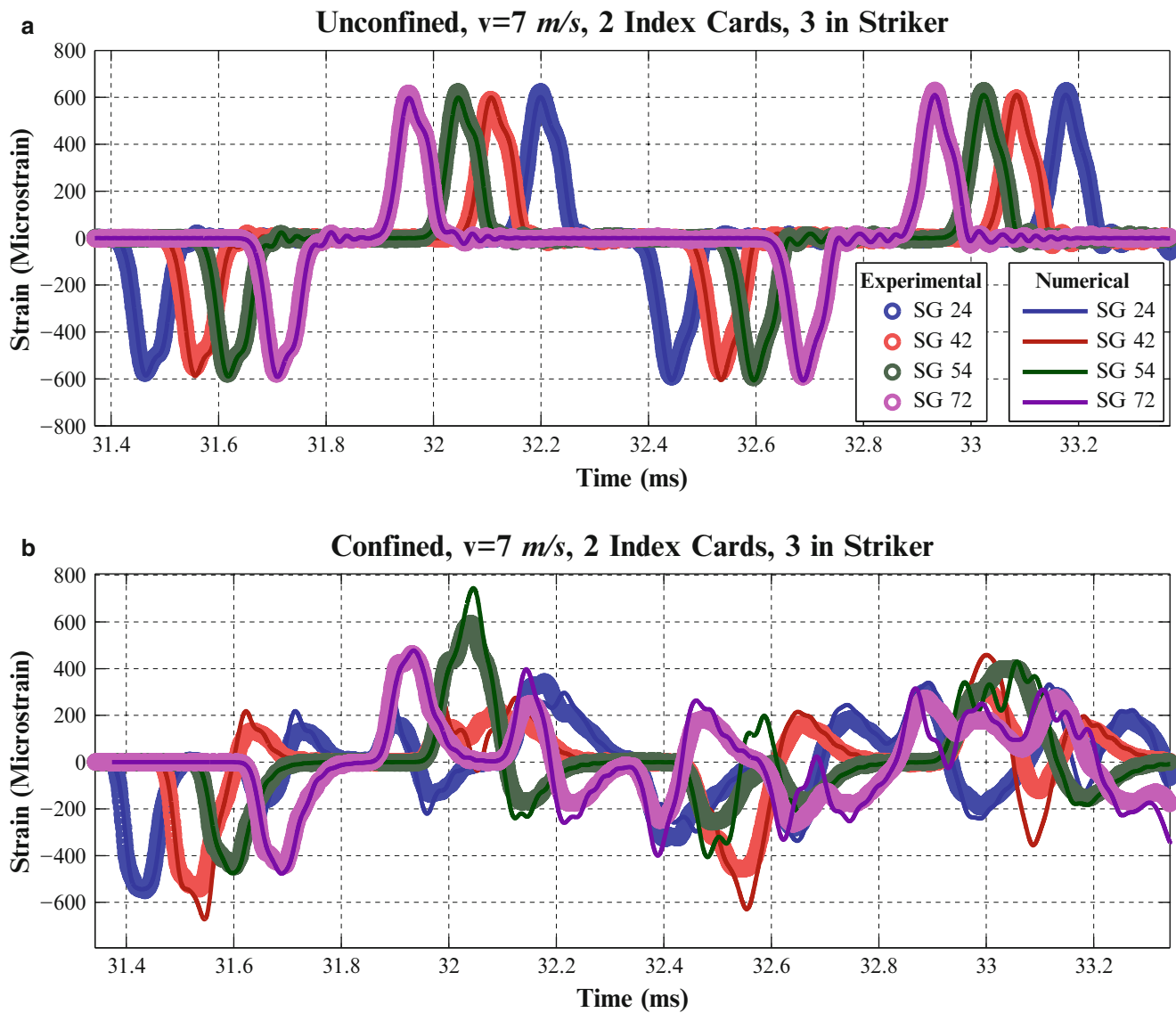
Fig. 16.5 Strain time history in the titanium bar for the two different experimental configurations with numerical results ($x_i = 24$, 42, 54, and 72 in.); (**a**) Unconfined and (**b**) Confined

confined cases. Finally, we calculate and compare the vibrational natural frequencies present in the experimental data and numerical results.

16.5.1   Comparison of Reflected and Transmitted Amplitudes

The first comparison of the theory, numerical simulation, and experimental data is the amplitude ratios of the first pulse as it encounters the clamped region of the bar. Due to the change of the mechanical impedance due to the change of mass and area, we expected there to be a reflected and transmitted wave. We calculated the analytical transmission and reflection amplitudes of the first pulse encountering the clamped area (only calculated for the clamped condition) by using the equations (16.6) and (16.11), and the material property values given in Table 16.1. The numerical and experimental reflection and transmission ratios are the ratios of the maximum values of the reflected and transmitted pulses to the incident pulse respectively. The calculated reflected and transmitted ratios calculated using the analytical relations, the experimental data, and the numerical results are presented in Table 16.3.

Table 16.3 Comparison of the reflected and transmitted amplitudes from the clamped area of the bar for the analytical equations, experimental data, and numerical results

	Analytical	Experimental	Numerical
R_1	0.373	0.241	0.400
T_3	0.798	0.816	0.874

The calculated magnitudes of the transmitted and reflective waves compare reasonably well with the test data from the Hopkinson bar experiment. The numerical and analytical values align very well with only a 7 % difference for the computation of R_1 and a 9 % difference for T_3. Note that both the numerical model and theoretical calculations share the assumption of a perfect interface (shared displacement) between the steel clamp and the titanium bar. The experimental data has a 35 % variation from the analytical calculation for the reflection ratio (R_1) and only a 2 % difference for the transmission ratio. The reflection ratio has the most variance for the different methods which was unexpected and we hypothesize that the reflection ratio is fairly sensitive to the interface condition. The experimental interface has a layer of pressure sensitive film between the titanium bar and steel clamp which most likely affects the amplitude of the reflected pulse from the clamped area. These effects of this interface will be further explored in future technical work.

16.5.2 Elastic Phase Velocity in the Bar

The elastic wave velocity in cylindrical bars with stress-free boundaries is well characterized. In order to establish baseline phase velocities, we calculate the velocity of the dispersive waves from the frequency-dependent phase changes of signals in the unconfined case. The theoretical phase velocities were found by numerically solving the Pochhammer-Chree dispersion equation in (16.1) for a range of frequencies. For the experimental and numerical cases we calculated the phase velocity using the first pulse of the strain responses at SG-24 and SG-54 locations. Knowing the distance between the two sensing locations, Δx, and calculating the phase change, $\Delta \psi$, between the two signals we can determine the frequency dependent phase velocity $v_{exp}(\omega)$, the relation is [12]

$$v_{exp}(\omega) = \frac{\Delta x * \omega}{\Delta \psi}. \tag{16.12}$$

The phase velocity for the unclamped titanium bars for the various cases are shown in Fig. 16.6 up to 50 kHz. The experimental, numerical and analytical results are similar to each other and are all around 5,010 m/s for low frequencies (<5 kHz). The phase velocities illustrate the dispersive behavior and decline with higher frequencies; the phase velocity is ~4,945 m/s at 47 kHz for all three methods. The overlapping of the predicted values of the experimental, numerical and theoretical methods was the expected result and we were pleased that the different methods matched so well.

The same phase velocity calculation was conducted for the case with the confining ring on the bar using the first pulse of the strain response at the SG-24 and SG-54 locations for both the experimental and numerical data and we saw that the velocity had decreased in comparison to the unconfined case. To eliminate the averaging of the elastic phase velocity over some stress-free sections and the clamp section, we used the theoretical Pochhammer-Chree phase velocity and phase velocity dispersion correction techniques [13, 14] with 8,192 frequency bins to propagated the SG-24 first pulse response to the location to the front of the clamped area and SG-54 first pulse response to the back of the clamped area. The phase velocity of the confined area was calculated using the estimated strain responses from the front and back of the clamped region in the titanium bar and is shown in Fig. 16.7. The phase velocity in the clamped region is approximately 1,800 m/s for frequencies below 5 kHz for both the numerical and experimental results. Additionally, we calculated the 1-D wave velocity in a clamped area using equation (2) and the values in Table 16.1 to be around 2,100 m/s. There is about a 14 % difference between the clamped phase velocity given by the data and the 1-D clamped theory and generally describes the behavior for low frequencies (<5 kHz). The elastic wave velocity has a 51 % decrease from the 1-D stress free case (5,010 m/s) to the 1-D clamped case (2,100 m/s), this is significant and depending on the length of confinement can significantly shift the natural frequencies of the system. The next section further expands on this and examines the change in vibrational response of the bar due to the clamp.
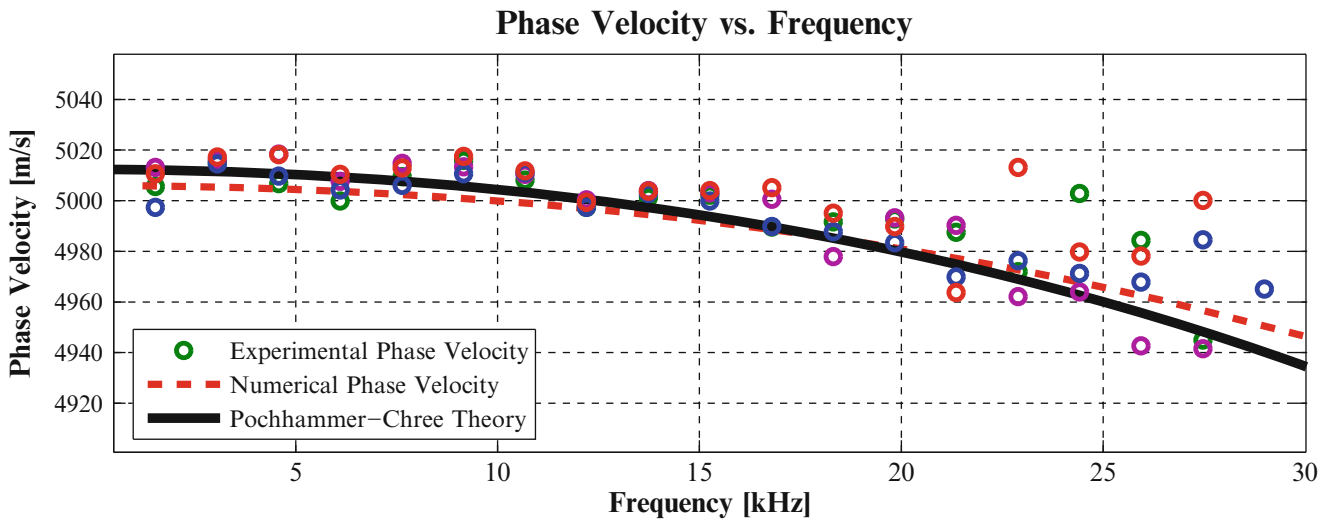
Fig. 16.6 Frequency-dependent phase velocity for the unconfined case computed using the Pochhammer-Chree theory, experimental data, and numerical results
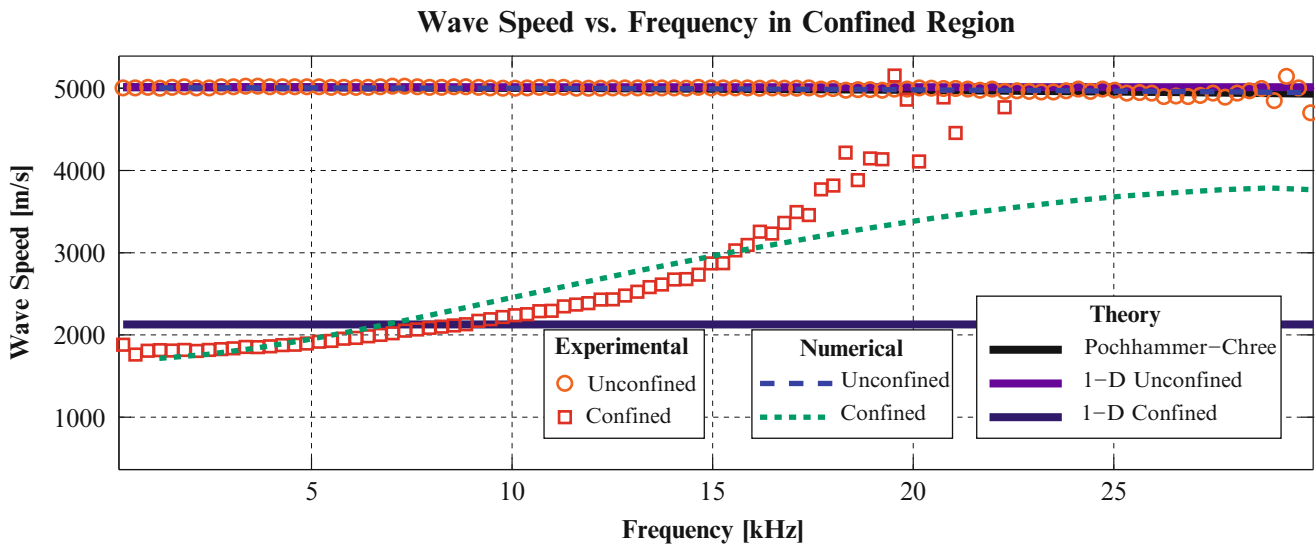

Fig. 16.7 Frequency-dependent phase velocity for both the unconfined case and confined cases computed using the Pochhammer-Chree theory, 1-D confined theory, experimental data, and numerical results

16.5.3   Vibrational Response

The vibrational response is the overall time response of the system. A small segment of the numerical data (approximately four reflections in the bar) was used. The analysis presented here for both the experimental data and numerical results was limited to length of the numerical results (7,610 points with a constant time step of 0.4 μs). The linear spectra of SG-24 time response was calculated via the fast Fourier transform for both the experimental data and numerical results for both the unconfined and confined cases; this data is shown in Fig. 16.8.

Comparing the linear spectra for the unconfined case (Fig. 16.8a) and the case when the confining ring is applied (Fig. 16.8b) we see the reduction in amplitude or elimination of natural frequencies at 4 and 10 kHz and a shifting the natural frequency which was originally just greater than 6 kHz. This illustrates that the clamp is eliminating or shifting (softening) the dynamic modes with the maximum displacement (of the unclamped case) in the center of the bar, which is the location of the steel clamp.

For the unconfined case (Fig. 16.8a), the experimental and numerical linear spectra overlay on each other and confirms that the numerical model did an excellent job capturing the wave propagation in the unconfined case. In the case of the
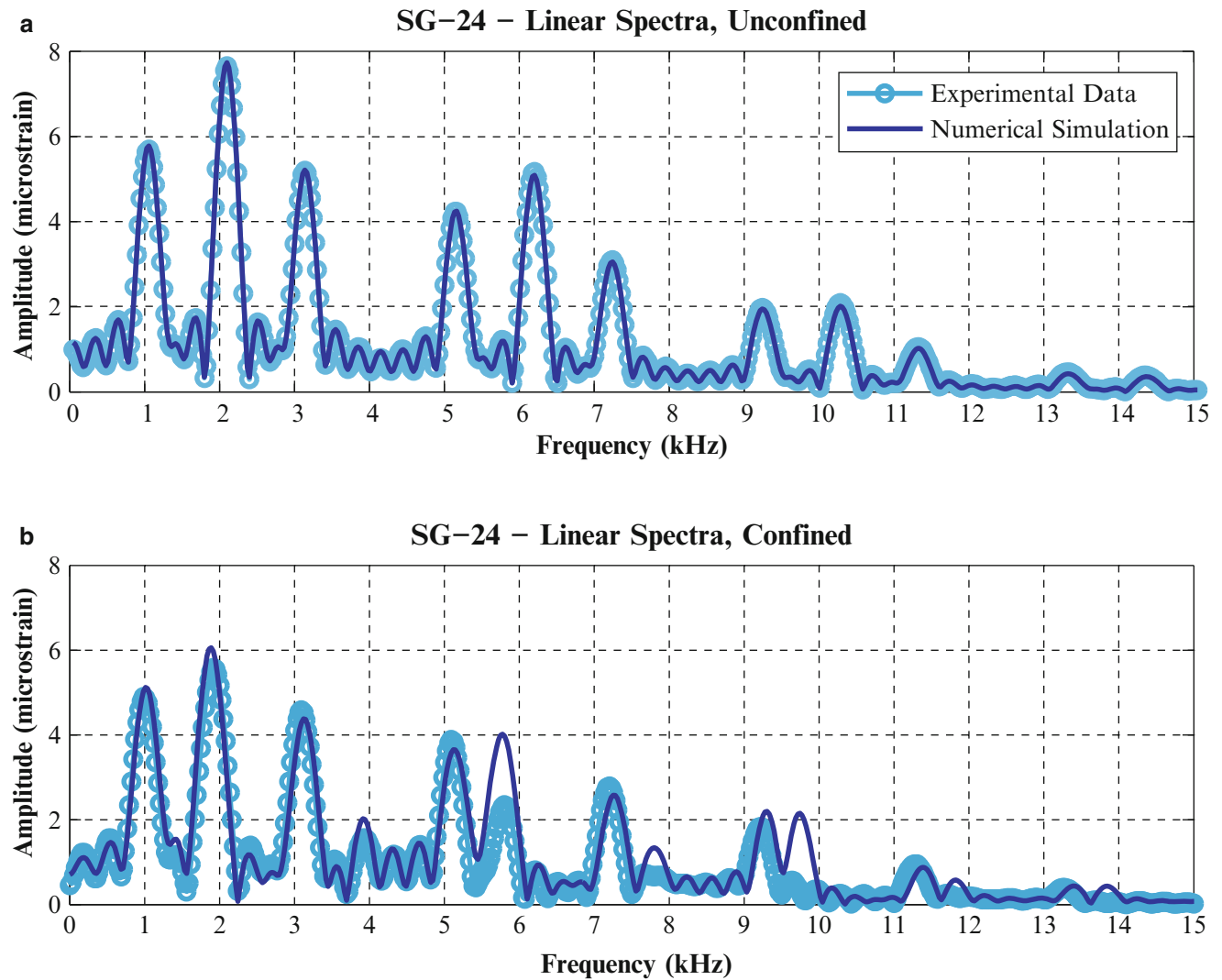
Fig. 16.8 The linear spectra of the experimental and numerical data of SG-24 using the first 7,610 points of the dynamic response for the (**a**) unconfined and (**b**) confined cases

applied clamp (Fig. 16.8b), the numerical results do not follow the experimental results as well as they did for the unconfined case. While the numerical and experimental linear spectra for the confined case are very similar up to 5 kHz, the numerical results start to overestimate the peaks (∼6 kHz) or predict peaks that are not there at all in the experimental data (∼10, 12, and 14 kHz). This discrepancy can be traced back to the differences in the transmission and reflection ratios discussed earlier.

16.6 Summary

The clamped area on the bar had both expected and unexpected changes to the dynamic response of the system. The expected results were that the reflected and transmitted amplitudes of the first pulse confirmed that there were notable changes to the area and mass in the clamped area of the titanium bar. The fact that the phase velocity decreases by over half due the clamp contributing to a mass loading effect was unexpected. We showed a 1-D theoretical derivation to explain this mass loading effect for very low frequencies ($\Lambda \ll L$) which agrees with the experimental and numerical phase velocity estimates. Future work includes deriving the 3-D dispersion relation that relates the length of the clamp to the higher frequency phase velocities.

References

1. Pochhammer L (1876) On the propagation velocities of small oscillations in an unlimited isotropic circular cylinder. J fur die Reine Angew Mathematik 81:324–326
2. Chree C (1889) The equations of an isotropic elastic solid in polar and cylindrical coordinates, their solutions and applications. Trans Camb Philos Soc 14:250–369
3. Kolsky H (1963) Stress waves in solid. Clarendon Press, Oxford
4. Ueda K, Umeda A (1998) Dynamic response of strain gages up to 300 kHz. Exp Mech 38(2):93–98
5. 2001, Kulite Strain Gage Manual, Kulite Semiconductor Products
6. Prescale Pressure Sensitive Film, 6 Oct 2014, http://www.fujifilm.com/products/prescale/prescalefilm/
7. 2009, Precision 28144 quad-channel wideband transducer conditioner with voltage and current excitation (datasheet). Precision Filters, Ithaca
8. 2003, NI PXI-6133 Specifications, National Instruments, Austin
9. Idesman AV, Mates SP (2014) Accurate finite element simulation and experimental study of elastic wave propagation in a long cylinder under impact loading. Int J Impact Eng 71:1–16
10. Idesman AV (2011) Accurate time integration of linear elastodynamics problems. Comput Models Eng Sci 71(2):111e48
11. Van Zandt T (2006) Development of efficient reduced models for multi-body dynamics simulations of helicopter wing missile configurations. Master's thesis, University of Massachusetts Lowell
12. Dodson J, Inman D (2014) Investigating thermally induced acoustoelastic effect in isotropic media with lamb wave. J Acoust Soc Am 136:2532–2543
13. Doyle JF (1997) Wave propagation in structures: spectral analysis using fast discrete fourier transforms. Springer, New York
14. Follansbee P, Frantz C (1983) Wave propagation in the split Hopkinson pressure bar. J Eng Mater Technol 105(1):61–66

Chapter 17
Component Qualification Using 3D Laser Vibrometry and Transmissibility Models

D.J. Macknelly and P.R. Ind

Abstract This paper details the application of 3D laser vibrometry in the qualification of a lightweight cable structure for operational usage under a number of vibration environments. The paper describes how transmissibility models were developed, based on laser vibrometry, and applied to numerous vibration environment specifications in order to reduce the number of ground-based testing sequences required. The paper also describes how a spatially dense measurement model removed the requirement to develop a detailed finite element model and the associated expensive material dataset.

Keywords Qualification • Laser doppler vibrometry • Electrodynamic shaker • Transmissibility

17.1 Introduction

During a refurbishment activity of a complex mechanical system, a cable component was swapped for an upgraded specification version, resulting in a change of build standard of the overall system. The resulting design review highlighted the possibility of unwanted dynamic interaction between the new cable and another component during the system's operational life. The structural dynamics group were tasked with characterising the response of the cable system to a number of vibration environments and establish the likelihood of component interaction.

Figure 17.1 shows a diagrammatic representation of the cable system. It should be noted that this was a non-trivial dynamic system with complex material properties, geometry and boundary conditions.

17.2 Certification Methodology

Typically when certifying geometrically simple or homogeneous components over a range of vibration environments, a mixture of Finite Element (FE) modelling and verification tests would be utilised. Low and mid amplitude environments would be physically tested, with component performance measured and then compared to FE models. This is done in order to validate their accuracy in predicting component performance at high amplitude environments, which may not be possible or safe to physically test and would therefore utilise the predictive FE models.

For this methodology to be successful it is imperative to accurately model the system under test to reduce to a minimum the uncertainties inherent in any simulation model; material properties, geometric configuration and boundary conditions. In this case study whilst accurate geometry was available it was not possible to obtain sufficiently accurate material models and boundary condition information within the project timescales.

Instead of using FE simulations as a predictive model, it was proposed to use a test-based model utilising vibration measurements to predict component response over a range of environments as illustrated in Fig. 17.2.

D.J. Macknelly (✉) • P.R. Ind
Structural Dynamics, AWE Aldermaston, Reading, Berkshire RG7 4PR, UK
e-mail: david.macknelly@awe.co.uk

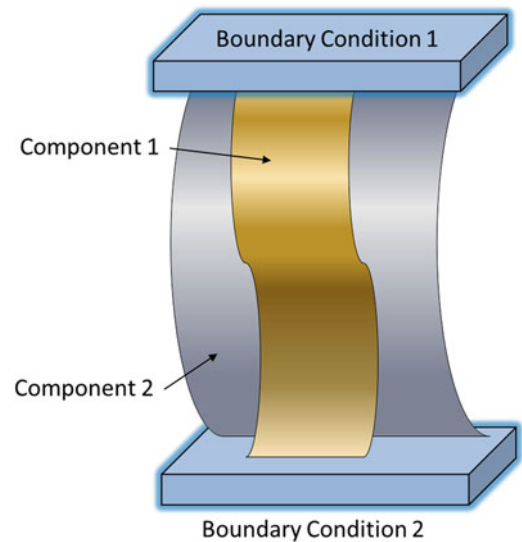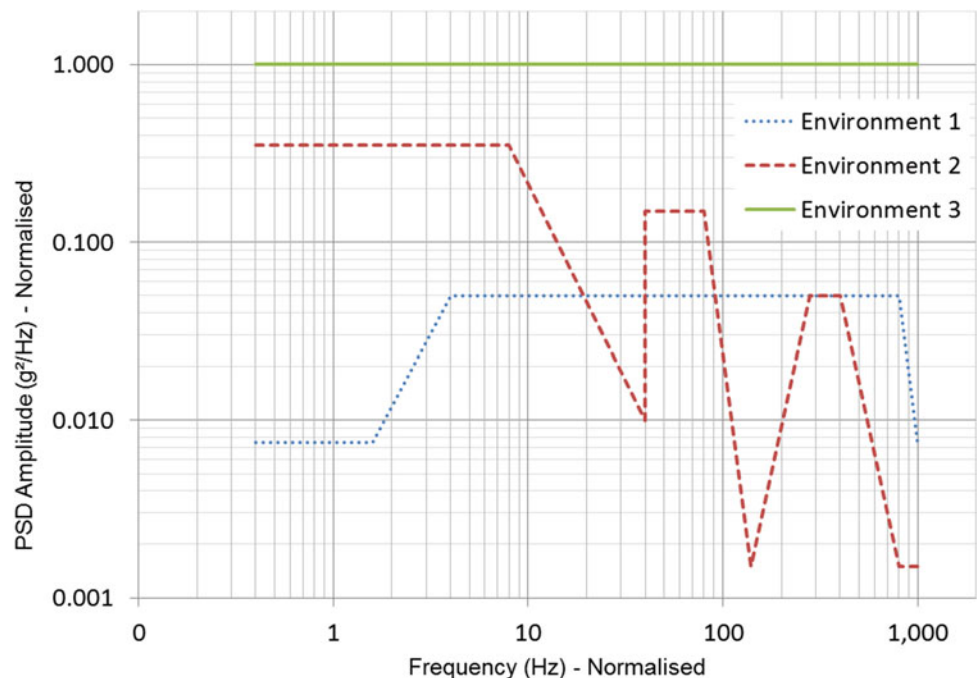**Fig. 17.1** Diagrammatic representation of components of interest

Fig. 17.2 Range of vibration PSD's that represents the system's operational environment

In order to create high quality, spatially dense measurements on the thin and light components of interest, a non- contact technique was essential. To this end, a 3D Scanning Laser Doppler Vibrometer (SLDV), as shown in Fig. 17.3, was utilised to make the measurements of the two components of interest whilst they were assembled in a service configuration in order to exactly replicate the complex boundary conditions.

Whilst the non-contact nature of the 3D SLDV enabled measurements with zero mass-loading, the 'raster scan' nature of the instrument, where it scans each discrete measurement point sequentially, posed significant problems for the higher intensity vibration environments. In order to achieve a sufficient spatial density of measurements, a large number of points were required which, when combined with frequency range and resolution requirements, significantly increased the overall test duration. This increases the risk of fatigue damage in high amplitude vibration environments to unacceptable levels, making these measurements unachievable.

Fig. 17.3 Example of 3D
Scanning Laser Doppler
Vibrometer used for
measurements

17.3   Transmissibility Methodology

To reduce the risk of damage to an acceptable level, the 3D SLDV measurements were made at a vibration level that was assessed to be safe for long durations. These measurements could then be used to create a predictive model for higher amplitude environments.

The predictive model was based on the concept of transmissibility (17.1) measurements between the base acceleration input and the displacement measurement output on the components of interest [1].

$$_i T_{jk}\left(\omega\right) = \frac{H_{ji}\left(\omega\right)}{H_{kj}\left(\omega\right)} \tag{17.1}$$

Figure 17.4 shows a diagrammatic representation of the test setup, with reference to the transmissibility methodology, where an electro-dynamic shaker is connected to a hydraulic slip table which applies a base excitation to the system under test. Each measurement point, as defined by the 3D SLDV, is then scanned sequentially and referenced to the base acceleration, creating a series of transmissibility-like[1] measurements. The test was repeated in a number of directions in order to find the worst-case response.

Once the series of transmissibility measurements had been made the selection of environmental PSD's that represent operational environments of interest were converted to acceleration spectrums and multiplied together in the frequency domain, resulting in predicted displacements. This process is shown as a flowchart in Fig. 17.5.

In order to use the transmissibility model in a predictive nature and extrapolate displacements for high-amplitude vibration environments that were untested, the assumption of linearity is necessary. In order to validate this assumption a number of vibration tests were performed at increasing vibration amplitudes, with the resulting acceleration normalised displacements overlaid.

Figure 17.6 shows the comparison of linearity tests at increasing vibration levels (Level 1 up to Level 3) and shows increasing damping, lowering peak response, at higher vibration amplitudes. This proves that whilst the assumption of linearity may be conservative, it is valid for this application.

---

[1]These are not true transmissibility measurements, as they are actually displacement/base acceleration.

Fig. 17.4 Diagram of test setup with reference to transmissibility methodology
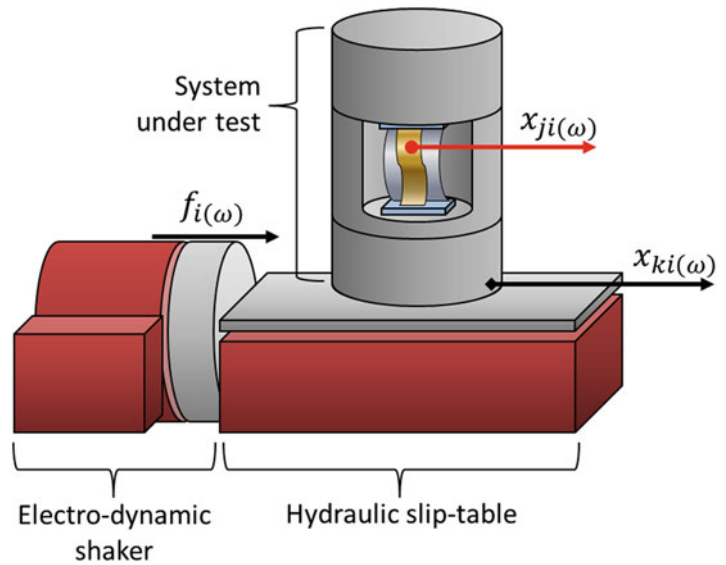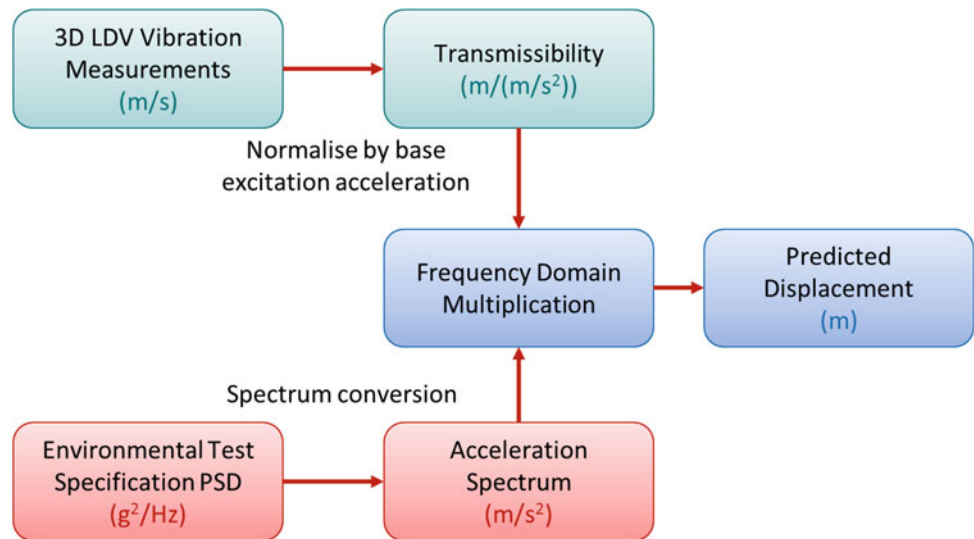

Fig. 17.5 Flowchart describing the transmissibility model methodology

To ensure that an accurate characterisation of the dynamics of the components of interest was made, a spatially dense measurement grid was created using the 3D SLDV. However, only a single estimate of the worst-case displacement of the components of interest was required for qualification purposes. In order to achieve this, the areas of maximum deflection at a given excitation frequency were identified, as illustrated in Fig. 17.7. A spatial average was then performed to remove local variations and outliers.

As with any prediction model, it was important to test the validity of the method to ensure correct estimates of displacement were produced. In order to achieve this, the PSD of the broadband Gaussian random excitation signal was fed back into the resulting transmissibility measurements. The estimated displacement from the spatially averaged area of maximum deflection was compared to the raw displacement measurements from the 3D SLDV[2] in the same area and found to be a good match.

---

[2]Whilst a Laser Doppler Vibrometer measures velocity, the software provided by the manufacturer provides the ability to convert to both acceleration and displacement values.

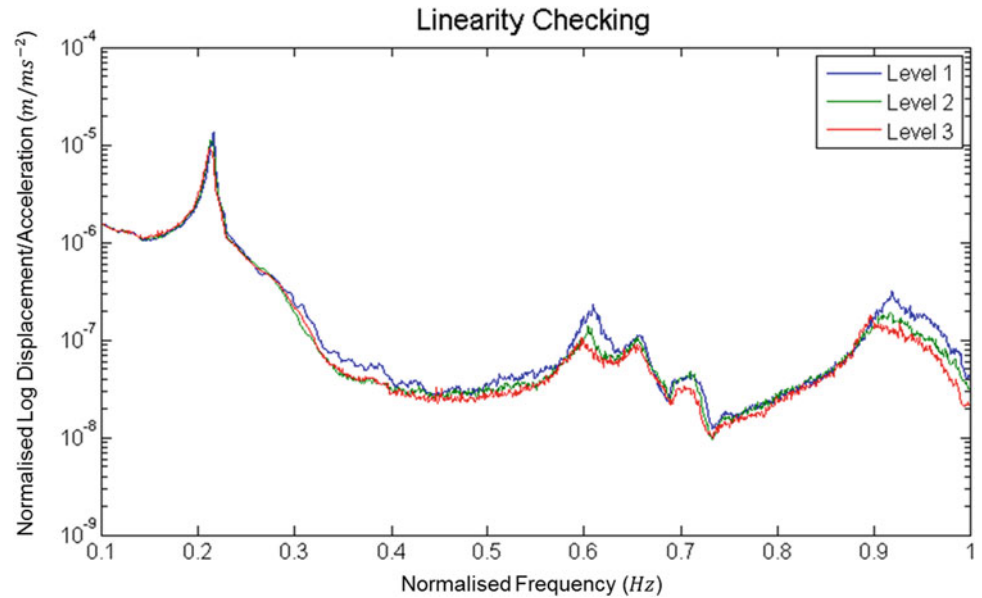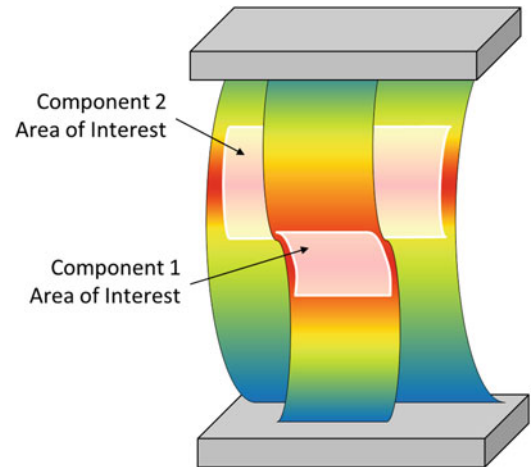**Fig. 17.6** Plot assessing the validity of the linearity assumption

Fig. 17.7 Maximum response locations at a given excitation frequency

17.4 Boundary Condition Modification

After reviewing the predicted displacements from a number of vibration environments it was decided that an alteration to the boundary condition of the cable component was required, this is illustrated in Fig. 17.8. In order for this design change to pass qualification it was necessary to quantify the difference it had made to the dynamic response of the cable component.

In order to quantify the effect of the boundary condition change, the transmissibility methodology was again used to provide a comparison of predicted displacements in the different vibration environments. Figure 17.9 shows a comparison between the two boundary conditions, with the new condition (plotted in red) displaying lower response amplitudes for the majority of the frequency range, particularly in the 0.05 Hz (normalised) region.

In addition to the plots of average displacement in areas of concern over the entire frequency range, the single- point displacement estimates were also used to provide headline values to the design review team, satisfying their certification requirements.

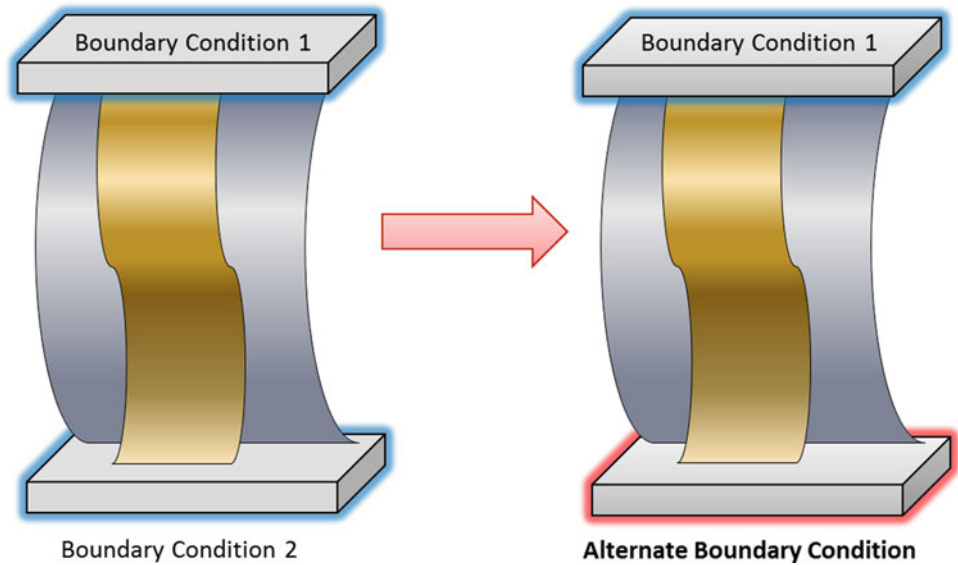**Fig. 17.8** Illustration indicating change of boundary conditions to the components of interest
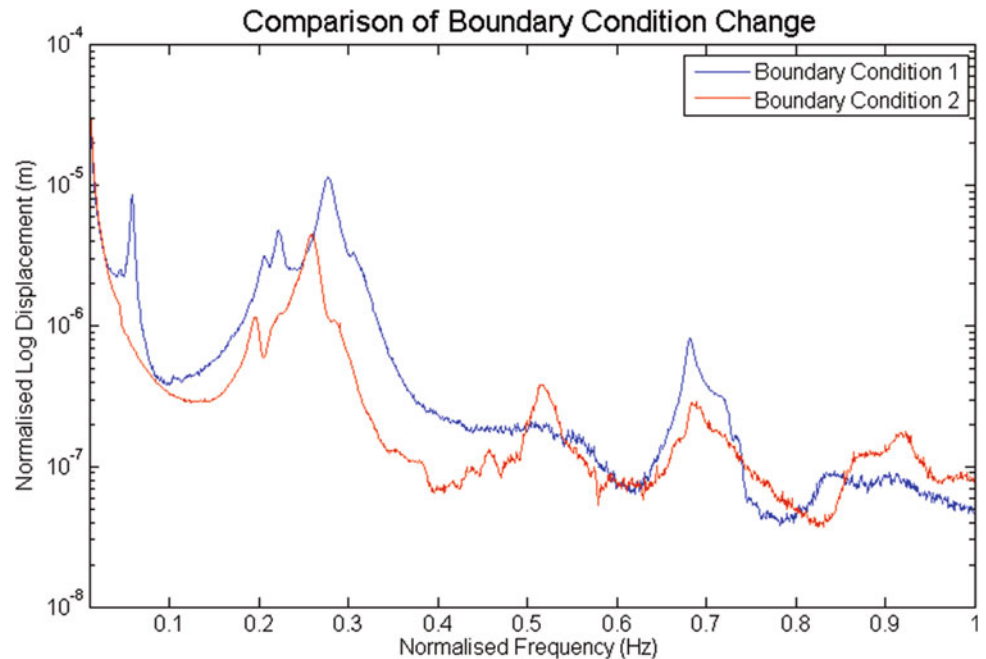

Fig. 17.9 Comparison of maximum response location between two boundary condition tests

17.5 Conclusion and Methodology Advantages

This paper has demonstrated a methodology that allows 3D SLDV transmissibility measurements to be successfully utilised to form a predictive model capable of estimating displacements under a range of different simulated PSD vibration environments. Using these predicted displacements, a component change and associated modification to its boundary conditions were successfully qualified for operation in a compressed timescale compared to traditional qualification tests and high fidelity FE analysis.

Whilst it should be noted that this particular technique is reliant on the linear (or conservative non-linear) response of the item under test to the vibration environments of interest, the technique presents some distinct advantages over traditional test techniques:

- Safeguards expensive test items by removing the requirement to test in high amplitude vibration environments
- Reduces overall test time by removing entire test runs

- Reduces operator risks such as exposure to hazardous materials and those inherent with manual handling operations
- Removes uncertainties associated with FE simulations, such as material models, geometric configuration and boundary condition definitions

Reference

1. Ewins DJ (2000) Modal testing – theory, practice and application, 2nd edn. Research Studies Press Ltd, Baldock

Chapter 18
Exploiting Continuous Scanning Laser Doppler Vibrometry and Wavelet Processing for Damage Detection

P. Chiariotti, G.M. Revel, and M. Martarelli

Abstract The present paper proposes a novel damage detection approach based on the exploitation of the simultaneous time and spatial sampling provided by CSLDV and the feature extraction capabilities of wavelet-domain processing. Superficial defects are analysed in the paper. The damage detection procedure is presented and its performances studied in a simulated application on a plate with different crack scenarios (varying crack depth ratio). Both line and area scans are analysed, considering also the influence of measurement noise. The method shows promising results, since cracks are identified in all severity conditions. An example on a sub-surface defect on a carbon-fiber panel is also presented.

Keywords Laser Doppler vibrometry • Continuous scan laser Doppler vibrometry • Damage detection • Wavelet processing • Non-destructive diagnostics

18.1 Introduction

Damage detection and location, together with condition assessment of structures, has always represented a productive working field for scientists. The use of Laser Doppler Vibrometry (LDV) has grown widely in the last decade, being a well-established method for non-intrusive vibration measurements with potentials for many different applications, ranging from vibroacoustics to biomedical applications [1–4]. Several attempts have been made for developing fast and reliable methods for structural health assessment (e.g. [5]). The presence of damages that modify the modal behavior of the structure under analysis can be assessed by LDV, both in Discrete (SLDV) and Continuous Scanning (CSLDV) approach.

The Continuous Scanning Laser Doppler Vibrometry (CSLDV) method was introduced by Ewins et al. [6] as an alternative to conventional Scanning Laser Doppler Vibrometry (SLDV). This characteristic rises from the possibility to recover Operational Deflection Shapes (ODSs) from a unique time history acquired by the Laser Doppler Vibrometer (LDV) while the laser beam scans, in a continuous way, all over the vibrating surface. With respect to Discrete Scanning Laser Doppler Vibrometry, CSLDV presents the following advantages:

- extremely high spatial resolution,
- compact data structure (e.g. a single time history contains both time and spatial information),
- limited duration of the experiment (e.g. acquisition time only depends on the required frequency resolution).

When a vibration measurement is performed by CSLDV, the time history appears as an amplitude-modulated signal whose modulation is due to the Operational Deflection Shapes excited during the experiment. CSLDV has recently started to be applied for different applications (e.g. [7]). All these aspects make CSLDV extremely suitable also for damage detection in structural health assessment tests. In 1997 Stanbridge et al. [8] and later on in 2000 Khan et al. [9] demonstrated the effectiveness of using CSLDV for detecting cracks when the crack produces a localized mode shape discontinuity. The approach proposed by Khan et al. consisted in applying a standard demodulation technique, multiplying the digitised CSLDV signal, point by point, by a sine wave at the excitation frequency, and passing the result through a low-pass filter. This approach, however, has some drawbacks, since the choice of the low pass-filter cut-off frequency might seriously affect the possibility of locating a discontinuity in the mode shape; moreover, the use of a demodulation approach implies several trials

P. Chiariotti (✉) • G.M. Revel
Università Politecnica delle Marche, via Brecce Bianche, Ancona 60131, Italy
e-mail: p.chiariotti@univpm.it

M. Martarelli
Università degli Studi e-Campus, via Isimbardi, Novedrate, CO, Italy

in order to identify the best case scenario that is able to enhance the defect (e.g. if the defect is located on a nodal line for certain mode shapes it cannot be recovered by demodulation).

The approach proposed in this paper exploits Wavelet-domain processing to extract features related to the damage in the CSLDV signal. Wavelet processing has been intensively investigated in the last decade for structural health assessment [10–12]. Some examples that report the use of wavelet-processing on mode shapes extracted by SLDV are also present in literature (e.g. [13]). However, the conventional Discrete Scanning Vibrometry requires the acquisition of several points all over the surface, and the efficiency of the wavelet processing in extracting the damage information (either from the modal curvature or from a discontinuity in the mode shape) is strongly dependent on the dimension of the damage with respect to the spatial sampling used in the experiment.

In this sense, CSLDV overcomes these limits, since it provides a single time history which inherently contains the ODSs information with an almost infinite spatial resolution.

The paper is organized as follows: the Damage Detection procedure proposed is discussed in Sect. 18.2, where also a description of the virtual experiment used to test the procedure is provided; Sect. 18.3 shows the results obtained on different crack scenarios; an application of the approach to a sub-surface damage is presented in Sect. 18.4, while main conclusions are summarized in Sect. 18.5.

18.2 Damage Detection Procedure

This paper presents a feasibility study for the joint exploitation of CSLDV and wavelet-processing for superficial cracks identification. The method and the main assumption it is based on, however, can be extended, with targeted modification, to sub-surface defects. An example of such application is also presented in Sect. 18.4.

A vibration signal acquired by CSLDV will show an amplitude modulation related to the ODSs excited during the vibration test. Since the laser spot continuously scans the surface of the test specimen, the possibility of passing on a superficial crack is highly realistic. The presence of a crack can introduce discontinuities on certain mode shapes of the structure, and therefore the modulating signal will reflect this discontinuity as well. Moreover, if dealing with superficial damages as cracks, the discontinuity in the mode shape will also introduce further complex phenomena linked to the interaction of the laser light with the defect edges, as diffraction, speckle noise in the optical signal coming back to the detector active area and eventually signal drop-outs (depending on the extension of the crack in the scan direction). Such effects will be stronger the more relevant is the discontinuity introduced.

Speckle noise which naturally affects CSLDV [14] has also to be taken into account. However, while the latter is periodic in nature and strongly related to the scan frequency, the phenomena related to light-defect interaction are still periodic but dependent on the transits of the laser spot over the crack. Wavelet-processing can therefore be exploited to enhance these discontinuities in the signal and to localize them in time domain. When using wavelet packet analysis to decompose the vibration signal acquired, approximations will retain the low frequency content related to the mode shapes, while details will enhance discontinuities. Since in CSLDV time and space are related by the signals the LDV mirrors are driven with, identify discontinuities in the time history analysed is equal to spatially-localize the damage on the structure under test. The approach is also less sensitive to measurement noise with respect to standard demodulation, since this noise, which is generally Gaussian in nature, is uniformly spread throughout the wavelet space.

The main issue in applying a wavelet-processing consists in choosing the mother wavelet, especially considering that there are not reference deterministic approaches in literature suggesting a guideline for that. In this paper the mother wavelet was chosen by testing several and checking the correlation between the approximation and the original signal: the one providing the highest level of correlation is able to enhance discontinuities in the most fruitful way. The best performing was the Db8 (Daubechies 8) wavelet.

Once the original signal is decomposed by wavelet-processing a threshold has to be defined in order to localize discontinuities in the details signal. The authors propose to calculate the threshold (t) as the product of Stein's Unbiased Estimate of Risk (SURE) [15] criterion threshold and the RMS (Root Mean Square) of the absolute value of detail:

$$t = \sqrt{\frac{1}{N}\sum_{n=1}^{N} x(n)^2} \cdot \sqrt{2\ln\left(\frac{N\ln N}{\ln 2}\right)} \tag{18.1}$$
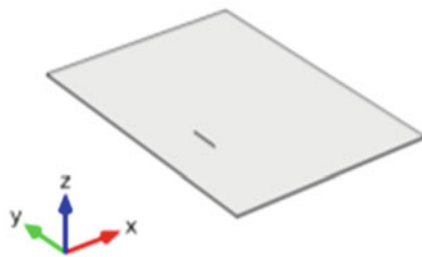
Crack scenario	Crack depth ratio ($\xi_c = d/D$)
I	1
II	0.5
III	0.25

plate dimension: $0.210 \times 0.297 \times D$ [m], $D = 0.002$ [m]
defect dimension: $0.0003 \times 0.03 \times d$ [m]

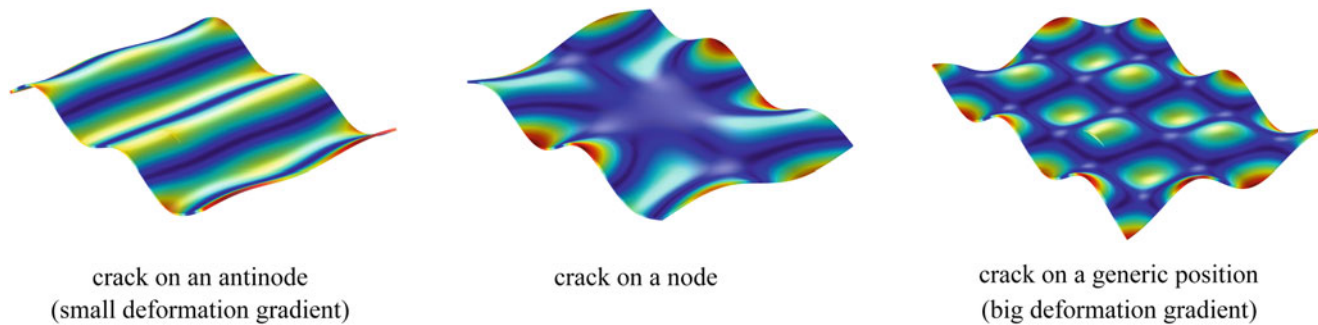**Fig. 18.1** Geometrical model and crack scenarios used in damage detection tests

crack on an antinode
(small deformation gradient)

crack on a node

crack on a generic position
(big deformation gradient)

Fig. 18.2 Mode shapes selected for synthetizing CSLDV signal

where:

- x: detail velocity signal;
- N: number of samples of the detail velocity signal;
- ln: natural logarithm.

18.2.1 CSLDV Signal Synthesis

The approach was tested on a simulated test case representing a steel plate with several crack scenarios, as reported in Fig. 18.1. Crack scenario I refers to a through-thickness damage.

The CSLDV signal was synthetized by extracting the mass normalized mode shapes from a FEA (Finite Element Analysis) of the steel plate. The shapes to be used as amplitude-modulating functions for the vibration signal were extracted on a simulated scan path reproducing the laser spot scanning the surface at a scan frequency (f_{scan}) of 1 Hz. The digital signal was generated simulating a sampling frequency (f_s) of 100 kHz and a recording time (T) of 20s. Three main modes, each involving the crack in a different way, were selected for the analysis. These modes, ranging from 1 to 2 kHz, were mixed and selected in order to test the influence of the shape with respect to the crack position/orientation (Fig. 18.2).

Since it is expected that the laser signal is affected by light-crack interaction, this event was reproduced, to a first approximation, by considering noise at the time samples corresponding to the crossing of the crack by the laser spot. Measurement noise was also added to the signal, in order to have a Signal to Noise Ratio (SNR) of 30 dB. Figure 18.3 reports the synthetized CSLDV signal and its spectrum for a line scan crossing the crack. The crack scenario addressed in Fig. 18.3 refers to $\xi_c = 1$.

Fig. 18.3 Synthetized CSLDV signal for a line scan crossing the crack: (**a**) time domain representation within the time interval 0 s ÷ 1 s; (**b**) frequency domain representation within the frequency range 1 kHz ÷ 2.2 kHz
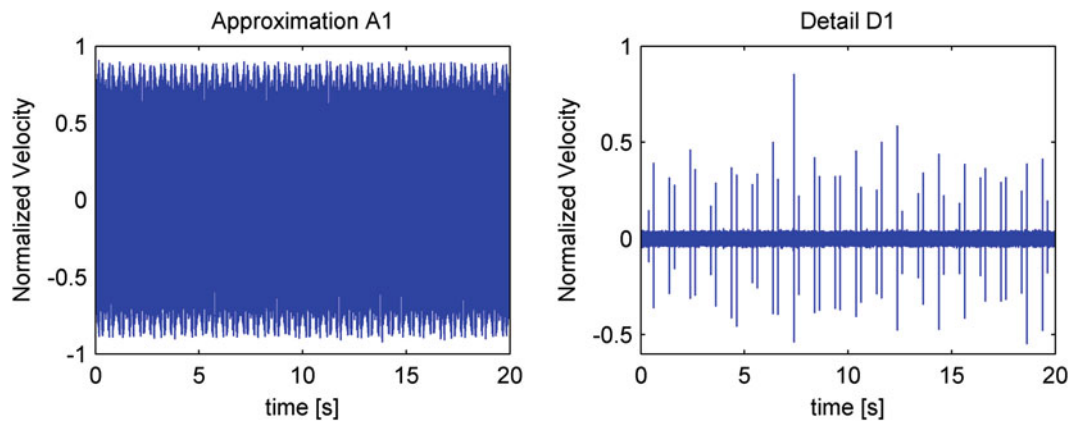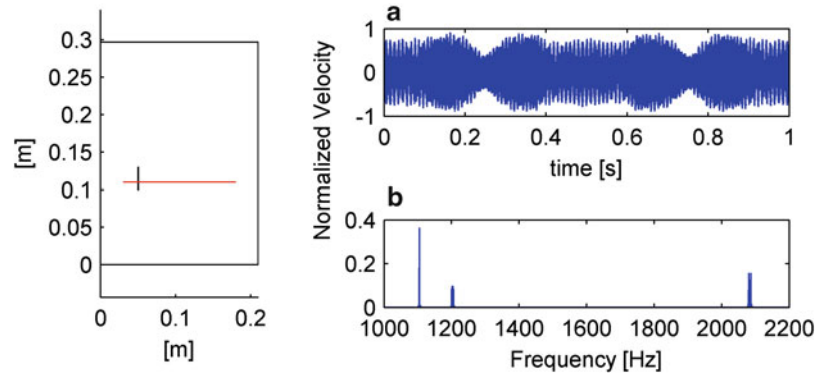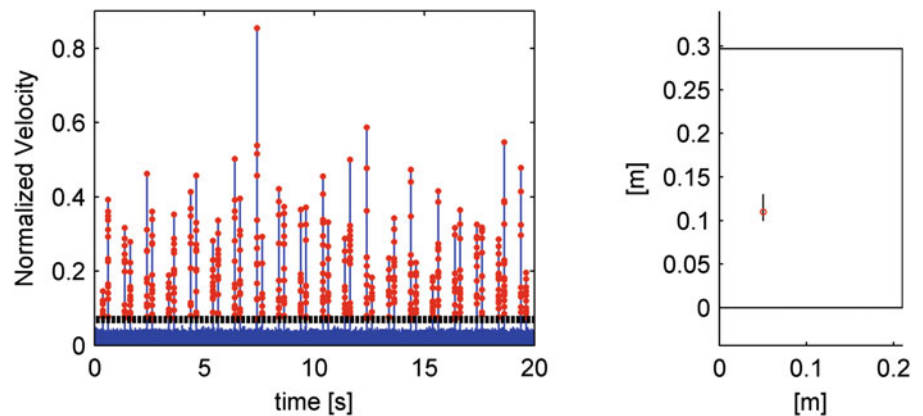
Fig. 18.4 Wavelet decomposition of CSLDV signal from a line scan crossing the crack: Approximation (*left*) and Detail (*right*)

Fig. 18.5 Crack identification by thresholding operation on the modulus of the detail signal

18.2.2 Results for a Line Scan Over the Damage

The result of wavelet-processing on the synthetized CSDLV signal is reported in Fig. 18.4, were approximation and detail for a level 1 wavelet decomposition are reported. It can be easily seen that detail signal contains information about the high frequency content which is directly related to the presence of the crack.

By applying the thresholding procedure proposed in Eq. (18.1) the spatial location of the crack can be easily identified, as can be seen in Fig. 18.5. The threshold is identified in Fig. 18.5 as the black dashed line, while samples above the threshold are pictured as red (in colour version only) markers.

The effectiveness of the approach is verified by checking that no cracks are identified in the undamaged plate. Figures 18.6 and 18.7 report, respectively, the wavelet decomposition and the thresholding result for such condition. It can be easily seen that detail does contain only randomly distributed noise, and therefore no samples are identified above the threshold as reported in Fig. 18.7.
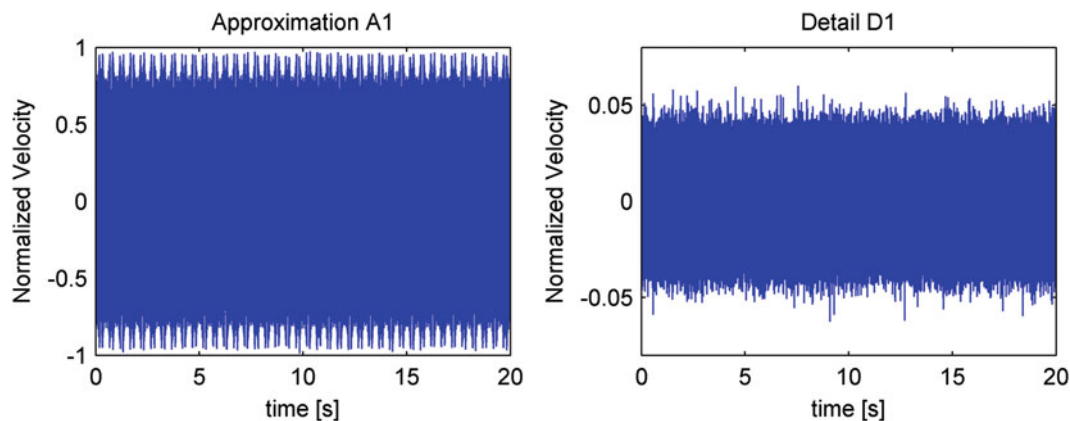
Fig. 18.6 Wavelet decomposition of CSLDV signal from the line scan reported in Fig. 18.3 performed on an undamaged plate: Approximation (*left*) and Detail (*right*)

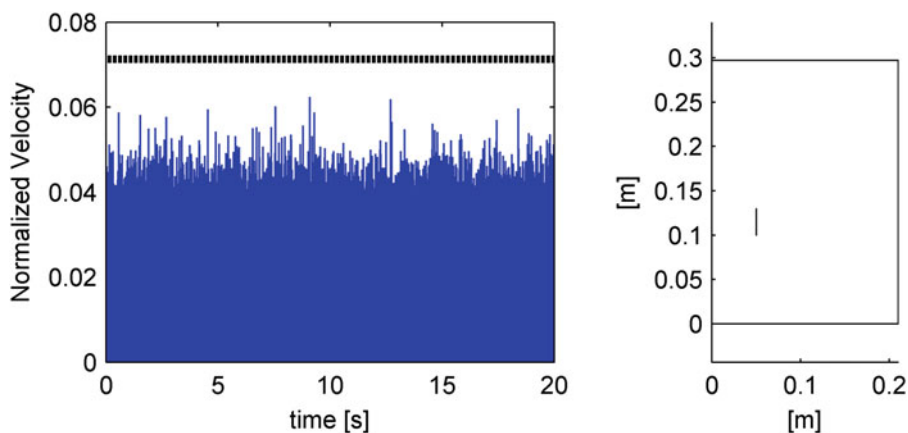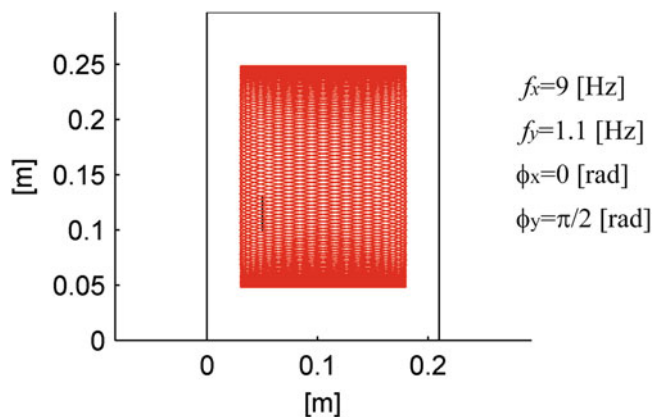**Fig. 18.7** Thresholding operation on the modulus of the detail signal for an undamaged plate

Fig. 18.8 Lissajous pattern used to virtually perform an area scan on the test plate

$f_x=9$ [Hz]
$f_y=1.1$ [Hz]
$\phi_x=0$ [rad]
$\phi_y=\pi/2$ [rad]

18.3   Results for an Area Scan

This section discusses results obtained applying the proposed damage detection approach on the crack scenarios reported in Fig. 18.1. In a real case scenario the crack location is never known a priori, therefore it is necessary to perform a 2D scan, rather than a line scan. An area scan obtained by creating the Lissajous pattern reported in Fig. 18.8 was used to build the synthetized CSLDV signal discussed in this section.

Figures 18.9, 18.10, and 18.11 report the processed data of the crack scenarios of Fig. 18.1. As in Fig. 18.5, the threshold is always identified as the black dashed line, while samples above the threshold are pictured as red (in colour version only) markers.

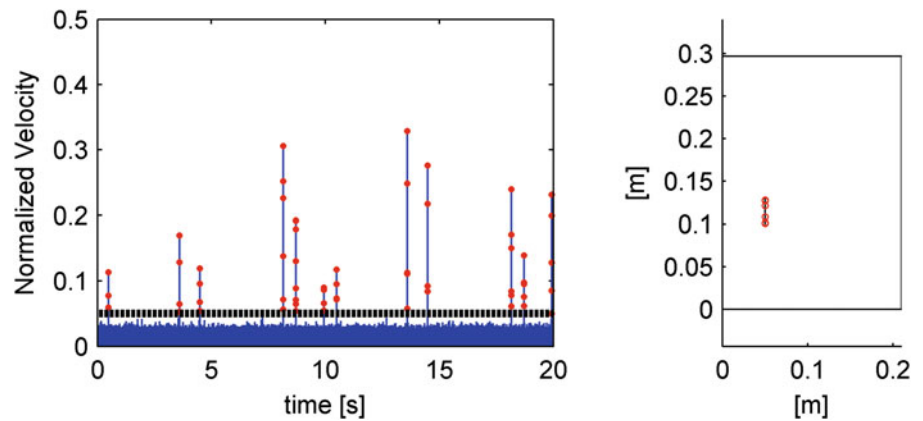**Fig. 18.9** Crack scenario I: crack depth ratio $\xi_c = 1$

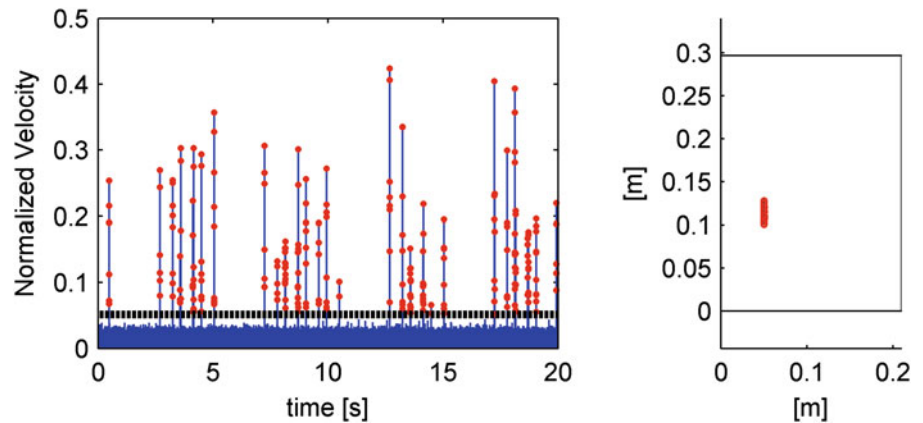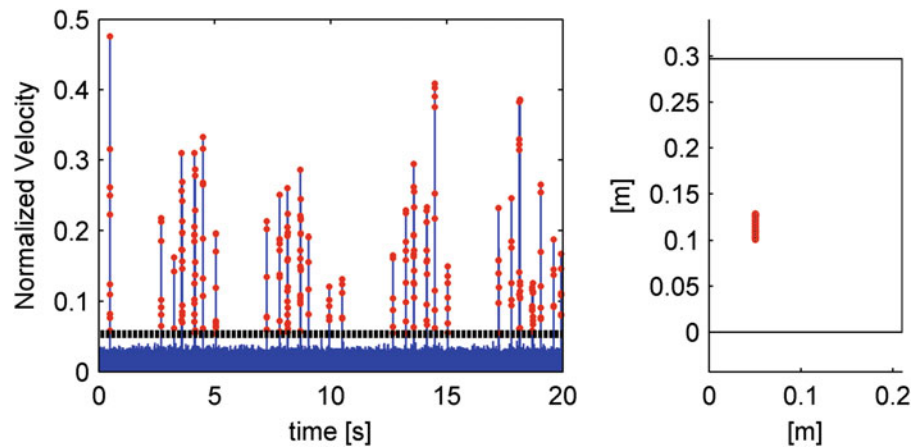**Fig. 18.10** Crack scenario II: crack depth ratio $\xi_c = 0.5$

Fig. 18.11 Crack scenario III: crack depth ratio $\xi_c = 0.25$

The proposed approach is able to identify correctly the cracks in different severity scenarios. It is interesting to notice, however, that the crack scenario I, the one with the crack depth ratio $\xi_c = 1$, therefore with highest severity level, shows the worst performances of the method. The approach does not perfectly reconstruct the damage extension in the y direction as happens for the other cases. This phenomenon could be due to the orientation of the defect with respect both to mode shapes excited and to the CSLDV scanning pattern.

18.4   Application of the Method on a Sub-surface Defect

The performances of the method discussed in the previous section were also tested on a virtual experiment reproducing a carbon-fibre composite panel ($0.210 \times 0.297 \times 0.005$ [m], fibre orientation 45°) characterized by a damage consisting in an
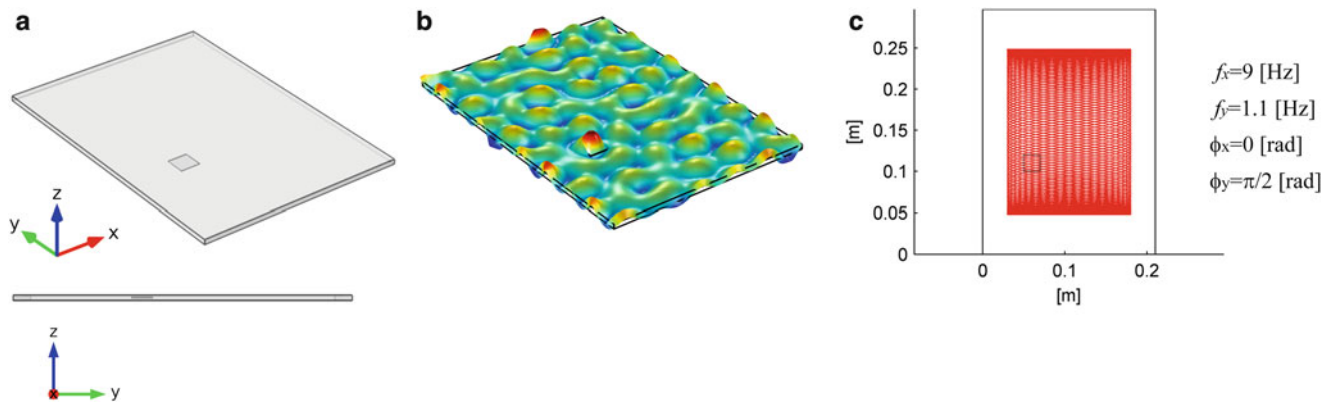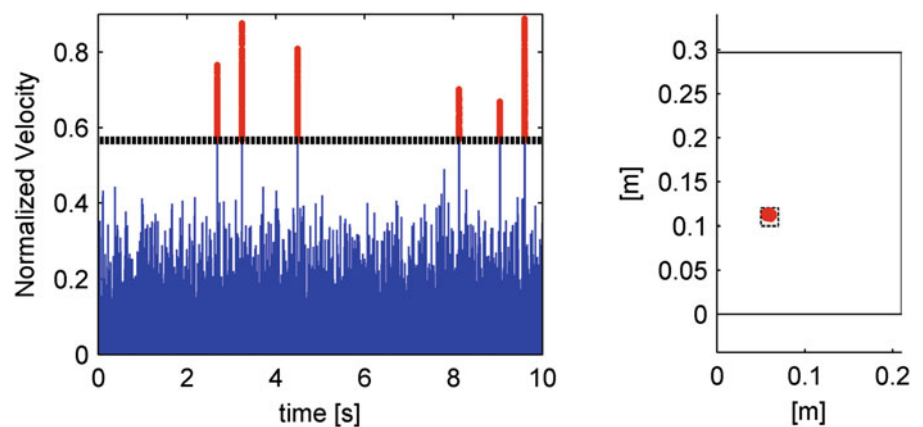
Fig. 18.12 Virtual experiment on a composite panel: geometry (**a**); mode shape @ 54,189 Hz (**b**); Lissajous pattern used to virtually perform an area scan on the test panel (**c**)

Fig. 18.13 Sub-surface defect on a carbon-fibre composite panel: results of CSLDV and wavelet-processing

air inclusion of $0.020 \times 0.020 \times 0.0005$ [m] at a depth of 0.00025 m with respect to the panel surface. The geometry of the panel is shown in Fig. 18.12a.

The CSLDV signal was synthetized using the approach discussed in Sect. 18.2.1, namely using as amplitude-modulating function for the CSLDV vibration signal the mass-normalized mode shape shown in Fig. 18.12b. The choice to work on such high frequency range was due to the need of avoiding contributions due to high-energy global modes (low frequency modes). Since the defect is a sub-surface one only measurement noise was added to the CSLDV synthetized signal in order to have a SNR of 30 dB. The scan pattern used was the Lissajous one reported in Fig. 18.12c.

Db8 wavelet was used to decompose CSLDV signal. The Detail of wavelet decompositions at level 3 contains the information associated to the presence of the defect. Indeed by applying the thresholding method of Eq. (18.1) the spatial position of the defect can be well localized, as reported in Fig. 18.13. As in previous figures reporting processing results, the threshold is always identified as the black dashed line, while samples above the threshold are pictured as red (in colour version only) markers.

18.5 Conclusions

A damage detection approach based on CSLDV and wavelet-processing has been presented and discussed throughout the paper. The inherent characteristic of CSLDV of giving as output a signal which is amplitude modulated by the mode shapes of the structure makes this technique extremely sensitive to shape discontinuities. Moreover, when dealing with superficial damages as cracks, the deformation gradient will produce a further discontinuity in the time signal which is due to complex phenomena linked to the interaction of laser light with the defect edges, therefore dealing with a technique that shows an almost infinite spatial resolution increase the possibility of crossing the damage and then in locating it. The processing based on wavelet decomposition has resulted efficient in identifying these discontinuities, especially if used together with a

thresholding approach based on the combined use of SURE criterion and the RMS of the decomposed signal extracted from a wavelet packet decomposition. The procedure was tested on a simulated test case for different crack scenarios (varying crack depth ratio). The method showed promising results, since cracks were identified in all severity conditions. An application on a sub-surface scenario for a carbon-fibre composite panel was discussed as well. Again the method was able to localize the defect with good accuracy. With respect to previously proposed approaches, the one addressed by the authors does not need any analysis on the mode shapes of the structure, neither any foreknowledge of the undamaged structure.

References

1. Castellini P, Revel GM, Tomasini EP (1998) Laser Doppler vibrometry: a review of advances and applications. Shock Vib Dig 30(6):443–456
2. Di Sante R, Revel GM, Rossi GL (2000) Measurement techniques for the acoustic analysis of synchronous belts. Meas Sci Technol 11(10):1463–1472
3. Revel GM, Martarelli M, Chiariotti P (2010) A new laser vibrometry-based 2D selective intensity method for source identification in reverberant fields: Part I. Development of the technique and preliminary validation. Meas Sci Technol 21(7), 075107
4. Marchionni P, Scalise L, Ercoli I, Tomasini EP (2013) An optical measurement method for the simultaneous assessment of respiration and heart rates in preterm infants. Rev Sci Instrum Am Inst Phys 84:121705
5. Castellini P, Revel GM (2000) Laser vibration measurements and data processing for structural diagnostic on composite materials. Rev Sci Instrum Am Inst Phys 7:207–215
6. Stanbridge AB, Martarelli M, Ewins DJ (2000) Measuring area vibration mode shapes with a continuous-scan LDV, measurement. In: 4th international conference on vibration measurements by laser techniques: advances and applications, Ancona, June 2000
7. Chiariotti P, Martarelli M, Revel GM (2014) Exploiting continuous scanning laser Doppler vibrometry (CSLDV) in time domain correlation methods for noise source identification. Meas Sci Technol 25(7):075204. doi:10.1088/0957-0233/25/7/075204
8. Stanbridge AB, Khan AZ, Ewins DJ (1997) Fault identification in vibrating structures using a scanning laser Doppler vibrometer. In: Proceedings of the international workshop on structural health monitoring, Stanford, pp 56–65, 18–20 Sept 1997
9. Khan AZ, Stanbridge AB, Ewins DJ (2000) Detecting damage in vibrating structures with a scanning LDV. Opt Lasers Eng 32:583–592
10. Chukwujekwu Okafor A, Dutta A (2000) Structural damage detection in beams by wavelet transforms. Smart Mater Struct 9:906. doi:10.1088/0964-1726/9/6/323
11. Kim H, Melhem H (2004) Damage detection of structures by wavelet analysis. Eng Struct 26:347–362
12. Radzieński M, Krawczuk M (2009) Experimental verification and comparison of mode shape-based damage detection methods. J Phys Conf Ser 181:012067. doi:10.1088/1742-6596/181/1/012067
13. Cao M, Xu W, Ostachowicz W, Zhongqing S (2014) Damage identification for beams in noisy conditions based on Teager energy operator-wavelet transform modal curvature. J Sound Vib 333:1543–1553
14. Martarelli M, Ewins DJ (2006) Continuous scanning laser Doppler vibrometry and speckle noise occurrence. Mech Syst Signal Process 20:2277–2289
15. Donoho DL, Johnstone IM (1995) Adapting to unknown smoothness via wavelet shrinkage. J Am Stat Assoc 90:1200–1224

Chapter 19
Use of 3D Scanning Laser Vibrometer for Full Field Strain Measurements

Jesus M. Reyes and Peter Avitabile

Abstract A relatively new technique to identify full field strain uses extensions of a 3D scanning laser vibrometer measurement. The technique was studied on several structures to understand the benefits and usefulness of the technique. One structure is a simple cantilevered beam which can be used to study the results of the 3D scanning laser vibrometer and quantify the results with a well-known solution. The other structure is a wind turbine blade which is more complicated in geometry and strain distributions. The two structures are subjected to dynamic testing and the results of the 3D scanning laser vibrometer are compared to strain gage results. Each of the sets of results are discussed and compared. The advantages and limitation of the technique are discussed in the paper.

Keywords 3D scanning laser Doppler vibrometer • Dynamic strain measurements • Strain gages • Wind turbine blade • Experimental techniques

19.1 Introduction

Identifying areas where the strain is maximum in a structure is key for a structural engineer. This will enable him to forecast the location where the structure most likely will tend to present failures or critical damage due to resonance vibrations. Another critical reason why having knowledge about the dynamic strain distribution is vital is because it is required for fatigue testing. Additionally, in order to corroborate a finite element model, a precise full field strain distribution is desired for any dynamic stress analysis. Usually, the engineer mounts transducers and a large number of strain gages to identify the strain distribution.

The use of strain gages is, by far, one of the most common techniques to acquire strain measurements. One advantage of strain gages is they are capable of measuring small strain levels. However, the gages are only able to get strain data at discrete points which means that a full field distribution is not available. In addition to this, their installation is very time consuming. Moreover, for light structures, the weight of the gages plus their cabling may lead to mass loading effects. The use of the technique which uses measurements of a 3D Scanning Laser Doppler Vibrometer (3D SLDV) system can generate full field strain distributions [1].

Photogrammetry is also one of the new technologies that have been recently used to extract full-field dynamic strain on structures during vibration. Carr et al. [2, 3] used digital image correlation to measure dynamic strain on several structures and correlated the results to strain gage measurements. Poozesh et al. [4] used this method to extract the dynamic strain over a large area of a utility-scale wind turbine blade. More recently, researchers have used a point-tracking algorithm in conjunction with a modal expansion technique to extract full field dynamic strain on rotating and non-rotating structures [5–8].

This work focuses in the application of the 3D scanning laser vibrometer to measure full field strain for a dynamic testing. This paper focuses in the preparation of the 3D SLDV system for the acquisition of data which is processed to compute the actual strain distribution. The description of the test and the structure is also presented. To show the benefits of the proposed technique, the results of common strain gage measurements will be compared to the strain distribution obtained via 3D-SLDV system.

This study is divided in two stages: confirmation of the proposed methodology and application of the proposed technique. A simple beam like structure is used for the confirmation of the test and applied methodology. The goodness of the beam structure is that the strain distribution is well known. The beam is a simple structure which is easy to describe its behavior

---
J.M. Reyes (✉) • P. Avitabile
Structural Dynamics and Acoustic Systems Laboratory, University of Massachusetts Lowell, One University Avenue, Lowell, MA 01854, USA
e-mail: jesus_reyesblanco@student.uml.edu

from a test and model standpoints. As the beam has a well-known solution, the comparison of the results provides reliability to the proposed technique. In the second part of this work, the methodology is applied to a Southwest Windpower turbine blade. This structure represents a more complicated geometry and strain distributions. The objective of this work is to prove that the 3D SLDV system can acquire full field strain distributions in complicated structures as wind turbine blades.

19.2　Theoretical Background

The basis of the Polytec Strain evaluation has its roots in basic solid mechanics, theory of elasticity and finite element modeling; for completeness, this material is shown in Appendix.

19.3　Technique Description

For this work the 3D Scanning Laser Vibrometer system (a Polytec PSV-400-3D), shown in Fig. 19.1, is used as the main measuring instrumentation and this is described next.

19.3.1　3D Scanning Laser Vibrometer System

The 3D Scanning Laser Doppler Vibrometer system measures vibrations at discrete points. The 3D SLDV system acquires the 3D dynamic motion vectors at those points. Then, the raw vibration data is treated using stand-alone post processing software developed by Polytec, the Polytec Strain Processor, which processes the acquired data to calculate strain as well as stress distributions.

　　The 3D-SLDV works on a predefined grid, which consists of connected points forming triangular elements. At these points, the system acquires velocity measurements for every single point in the grid. All these non-contact measurements are obtaining while the structure is being driven at a particular frequency. For every defined point on the grid, the three laser beams are aligned via VideoTriangulation. This feature of the system corrects the drifting in the laser beams cause by warm up effects. VideoTriangulation makes the system capable of performing high precision measurements to obtain a detailed geometry of the structure and more accurate 3D dynamic motion vectors. In Fig. 19.2a, the three red lines represent the laser beams. This shows how the lasers are not aligned exactly at the same point which is not desirable for a measurement. Figure 19.2b presents how the VideoTriangulation feature places the three laser beams accurately in one

Fig. 19.1 Experimental arrangement of the 3D scanning laser Doppler vibrometer system
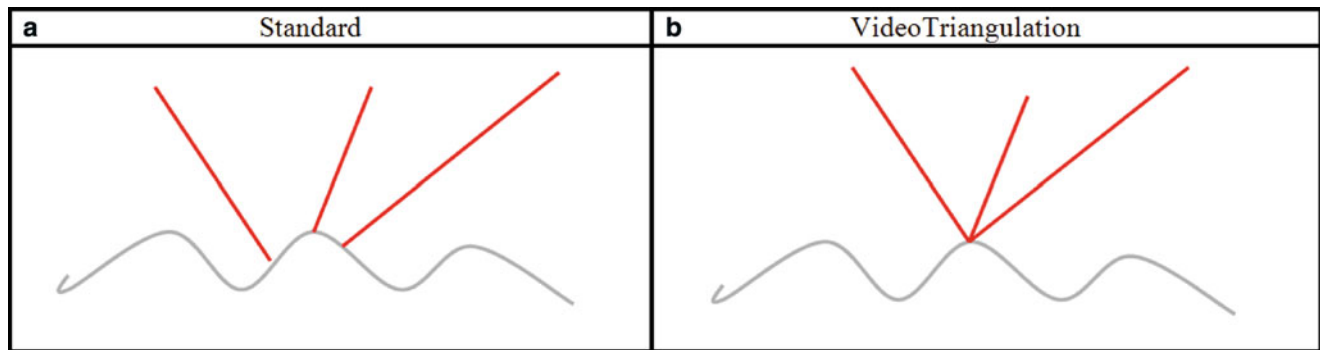
Fig. 19.2 Beam positioning accuracy – standard (**a**) and video triangulation (**b**) [9]
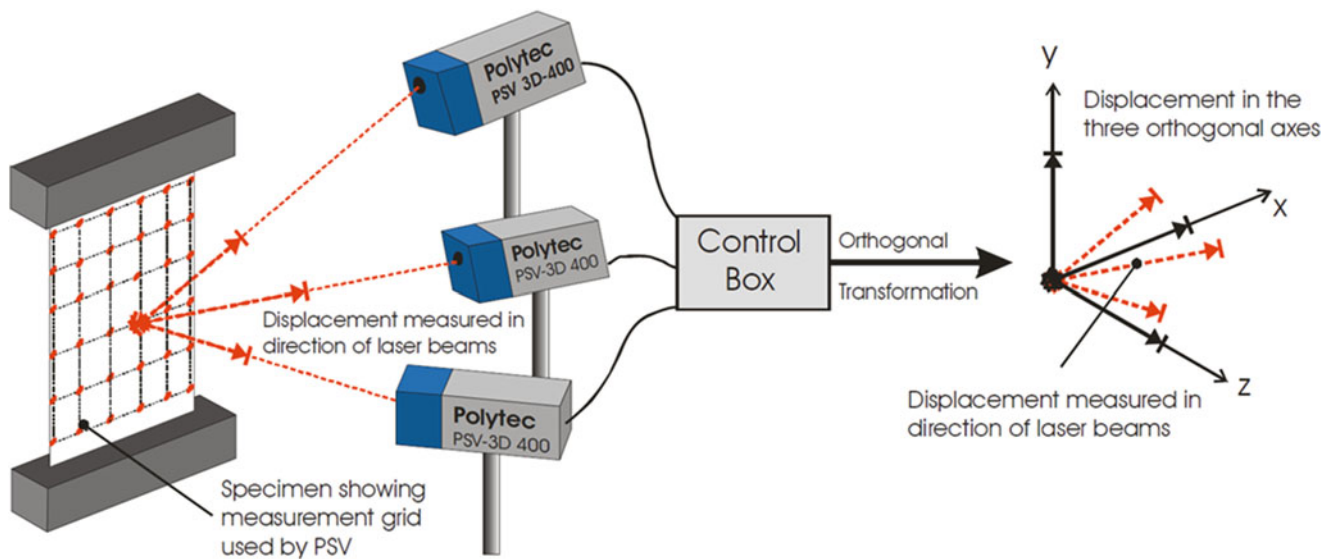

Fig. 19.3 Sketch of setup for measurement of displacement field on a flat plate [10]

single point. In addition, one of the advantages of the proposed technique is that the measurement grid can be set manually according to the structure or be imported from an existing Finite Element Model (FEM).

The 3D-SLDV system employs the three laser heads to measure the instantaneous vibratory velocity in the direction of each laser and works based on the Doppler principle. A factor that has to be taken in consideration is the scattering of the laser beam on uneven surfaces because these types of measurements generate speckle noise. However, this noise can be automatically decreased using a procedure called Speckle Tracking which can be activated through the software of the system allowing the laser beams to slightly change their position to remeasure a point in order to improve the signal-to-noise ratio (SNR) during the measurement. As shown in Fig. 19.3, from every velocity measurement, the displacement of the scanned point can be computed and through an orthogonal decomposition the displacement components in three orthogonal directions are acquired.

19.4   Structure Description and General Testing Information

Two structures were examined; a simple 5-ft cantilever aluminum beam type structure and 7.5-ft turbine blade provided by Southwest Windpower. First, testing was performed on the beam because it is a simpler structure in order to prove that the methodology works. The cross-section of the beam is a rectangular tube with dimensions of 1-in. by 2-in. and a thickness of 1/8-in. The beam was clamped in a fixture specially designed for testing a wind turbine blade [2]. The beam is very simple to characterize from a test and model standpoint and the results provide more credibility for the proposed approach.
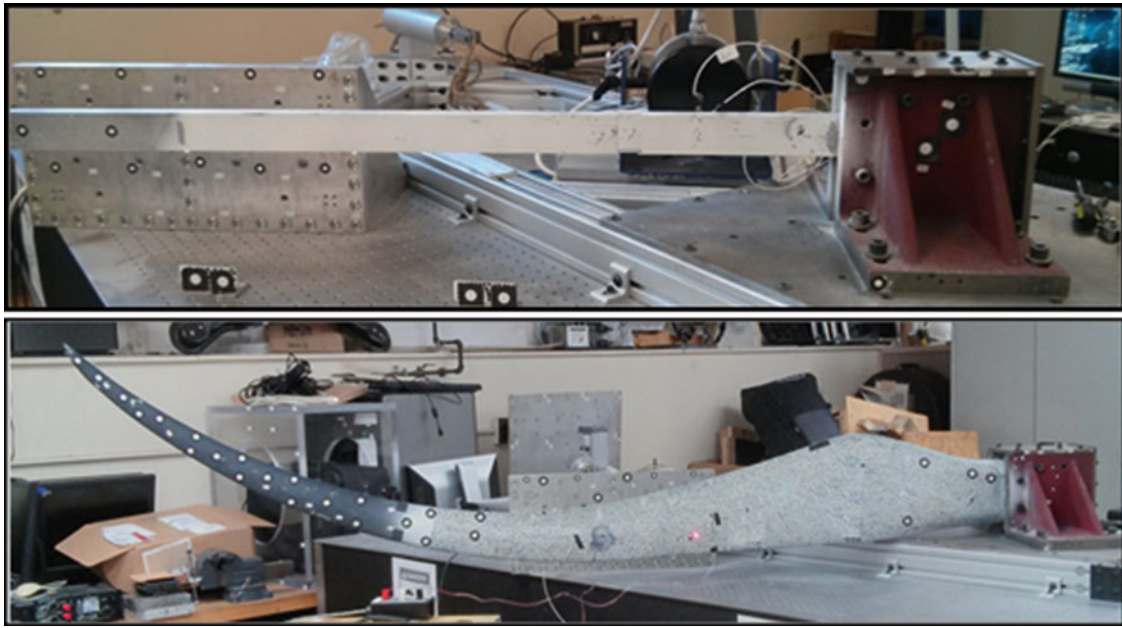
Fig. 19.4 Test setups – aluminum beam (*top*) and turbine blade (*bottom*)

After, the testing of the beam, a wind turbine blade was tested using the same techniques. Figure 19.4 shows an overview of the test setup for both structures.

As previously discussed above, two structures were tested to compute the dynamic strain distribution; an aluminum beam and a wind turbine blade, both being fixed at one end. First tests were performed on the beam due its simple geometry and well-known solution.

For the acquisition of the tridimensional velocity components, a grid has to be created. The points in the grid define the scan points, where the Polytec system acquires the desired data at every single point. After, the output file is processed through the Polytec Strain Processor. For the strain calculation, a spatial filtering size has to be defined, which is defined in millimeters. Polytec documentation recommends [9] that spatial filter size should be similar to the smallest Spacing Between Scan Points (SBSPs).

For the beam, the entire process was straight forward since the grid and spatial filter size specifications that Polytec suggests were capable of producing accurate results. In the other hand, for the turbine blade, further analysis was needed and performed to determine the proper distance of the SBSPs and the size of the spatial filter for the computation of a precise strain distribution.

19.5 Beam Testing

To validate the technique, a sinusoidal dynamic test was performed on the beam. This dynamic testing was done using a shaker with a sine wave at the first natural frequency of the cantilevered beam. Using the 3D-SLDV system, a Frequency Response Function (FRF) was measured to determine that the first natural frequency of the beam found to be 14.8 Hz. Throughout the test, the shaker was located six in away from the base. Velocity measurements were acquired for every scanned point defined by the grid shown in Fig. 19.5. The area covered by the grid represents one third of the total area of the beam; this area is located near the base. The grid consisted in 630 scan points with a SBCPs of 5 mm. The size of the spatial filtering was 5 mm also.

The generated output file was processed using the Polytec Strain Processor to obtain the strain distribution along the area covered by the grid. Strain gage data was collected at the same time as the 3D-SLDV system measured the scan area. Two strain gages were mounted on the surface of the beam. Strain Gage 1 and Strain Gage 2 were located exactly at the middle of the surface of the beam at 2.1 and 10.7 in. away from the base. Figure 19.6 shows the strain distribution on the beam as well as the location of the strain gages is presented.
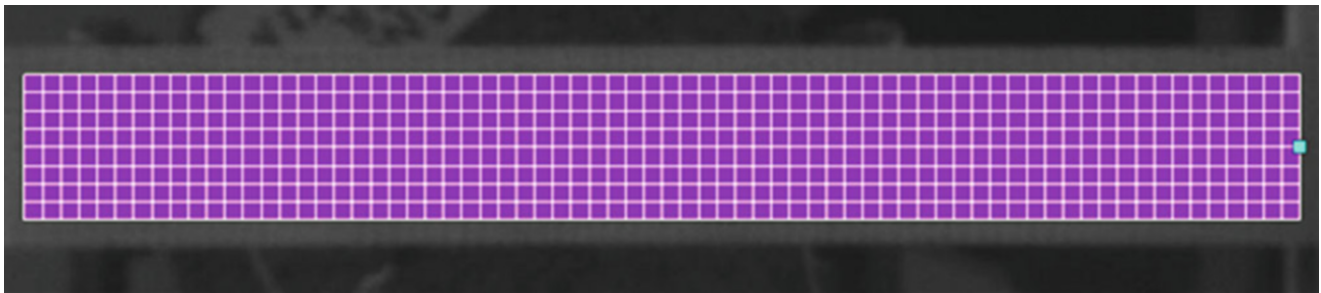
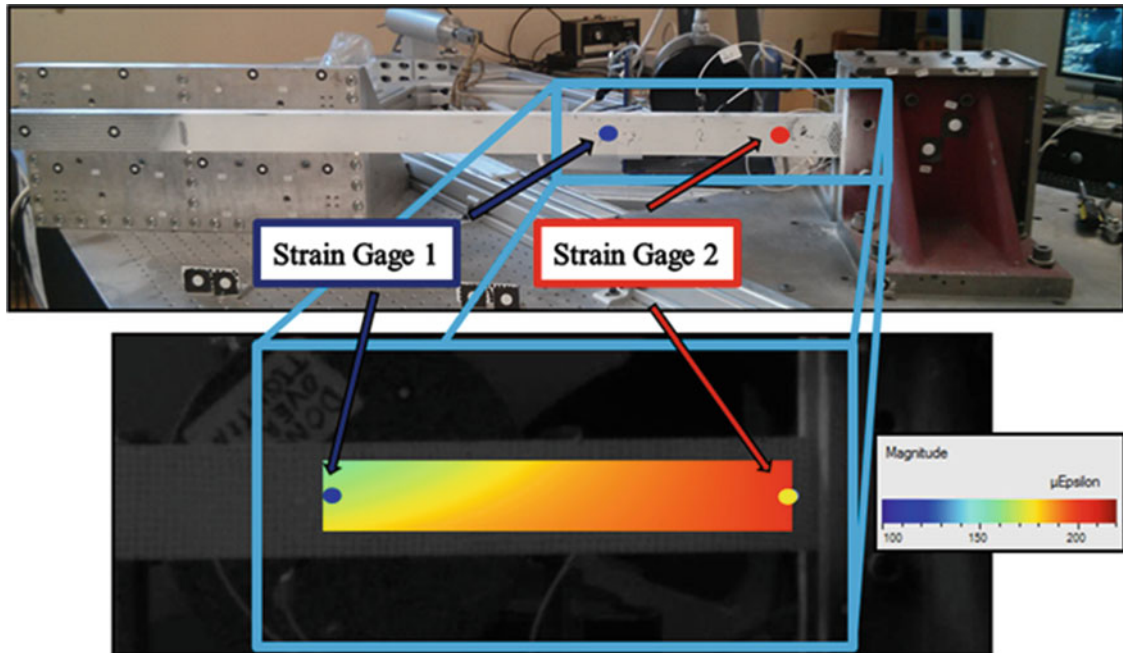**Fig. 19.5** Grid defining the scanned points in the surface of the beam

Fig. 19.6 Strain distribution on the beam

Table 19.1 Comparison of the full field 3D-SLDV system and the strain gage data from the beam

Strain [$\mu\varepsilon$]			
Location	Exp. strain gage data	PSV-400-3D	Difference (%)
Strain gage 1 (near base)	202	200	1
Strain gage 2 (near tip)	165	162	2

The results of the 3D-SLDV system showed good agreement to the strain gage data as expected. In Table 19.1, a comparison between the discrete points on the grid corresponding to the location of the strain gages and the respective strain gage locations is showed.

19.6   Blade Testing

For the validation of the Polytec system, measurements were taken on the 7.5-foot wind turbine blade to calculate the strain distribution. The strain was compared to strain gage measurements. The strain gages were, Strain Gage 2 (SG #2) and Strain Gage 3 (SG #3) located at 20 and 38 in. away from the base of the blade, respectively as shown in Fig. 19.7. Dynamic testing was performed using a shaker which drove the turbine blade throughout all tests at its first resonance frequency the levels of input force were varied also. The input force was measured using a force gage attached to the stinger of the shaker. This
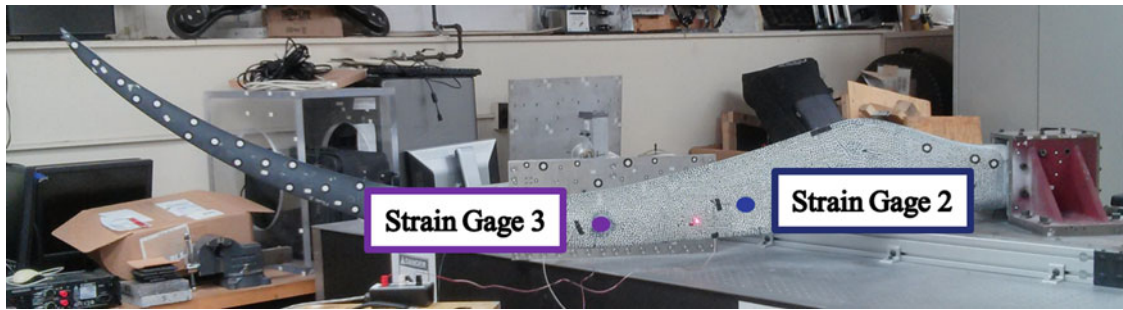
Fig. 19.7 Strain gages location for SG #3 and SG #2

frequency was determined using a FRF measurement. The first resonance frequency of the blade was found to be at 5.5 Hz. For this dynamic test, the shaker was located 11 in apart from the base.

The testing performed was divided into three parts; influence of the spatial filtering applied, grid density sensitivity during the acquisition of measurements and presentation of the results with the proper parameters result of the filtering and mesh sensitivity analysis.

19.6.1 Spatial Filtering Analysis

Two locations were tested, SG # 3 and SG #2. At SG #3, the strain values at 4 discrete points (points 158, 159, 173 and 174) were selected adjacent to the strain gage and plotted against the level of filtering applied. For SG #2, the points selected were 176, 177, 189 and 190. These points were located right on the surface of the corresponding strain gage. The size of the filter was varied from 0 mm to 10 times the SBSPs. Also, three levels of force were used – 17, 34 and 51 N. The collected data was plotted and shown in Fig. 19.8.

Figure 19.8 shows that for SG #3 (first column), the value of the strain tends to converge when a 4-time-SBSPs-size filter is applied. Also, the data for SG #2 showed that a trend starts to emerge when a 2-time-SBSPs-size filter is used and converges to the value of the strain acquired through the strain gages mounted on the blade.

In this analysis, several sizes of spatial filtering were used during the computation of the strain. The study showed that the proper filter size value is in between the length of 2-time-SBSPs to 4-time-SBSPs. Once, the values for the filtering process were known, a grid refinement study was performed.

19.6.2 Grid Density Sensitivity Analysis

During the grid sensitivity analysis, three cases were studied to understand the effect of the variation of the number of scan points during the acquisition of data for the computation of the strain distribution via Polytec system. Case 1 and 2 focus on the area over SG #2. An initial test is performed and the strain values are compared to strain gage data. Then, a percentage error is computed to show the convergence of the data. Also for these cases, two more tests are run; one test over a smaller area than the initial test one and one more keeping the same area than the initial one but now with a higher number of scan points. Case 3 shows a set of three tests that are done over an area covering SG #2 and SG #3 and compared to strain gage data in the same fashion as was done for the rest of the cases.

Case 1 The initial measurement covered an area of 24 in.^{2} where SG #2 is located (4 in. width by 6 in. height) using 221 scan points and its area is shown by the red rectangle in Fig. 19.9. The results from the measurement were compared to strain gage data and had a 24 % error. Then, a second test was performed; its grid is represented by the blue mesh in Fig. 19.9 and its corresponding covered area was 12 in.^{2} (4 in. width by 3 in. height), which means a reduction of 50 % of the area of the preliminary test, and 221 scan points were also used. This second measurement presented a 4 % error in comparison to the strain gage data.

Case 2 Then, a test with 603 scan points in a rectangular grip arrangement over the 24-in.^{2} area of the initial measurement was run on the SG #2 zone (Fig. 19.10). The results were compared to the strain gage data and shown a 21 % error.
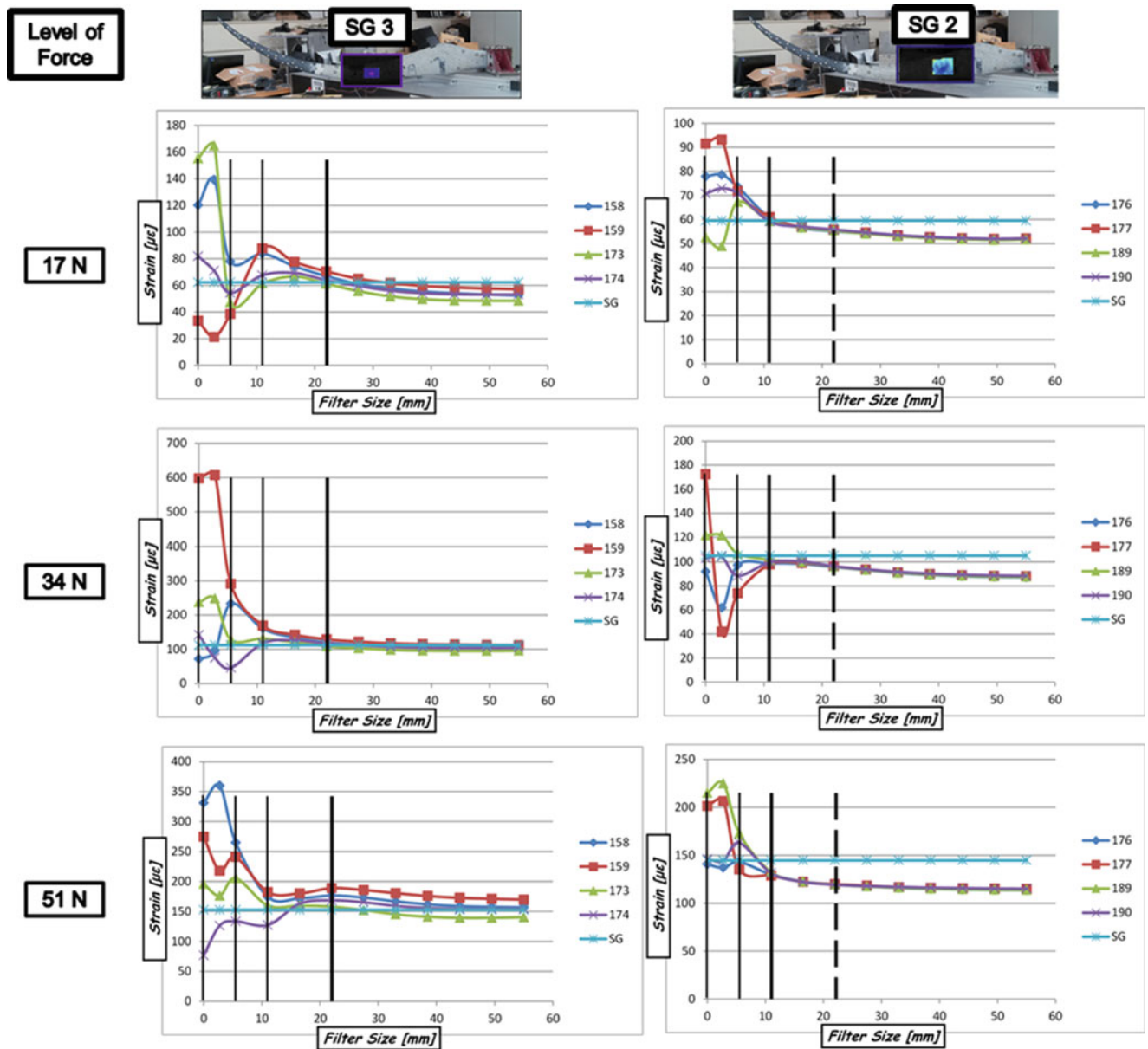
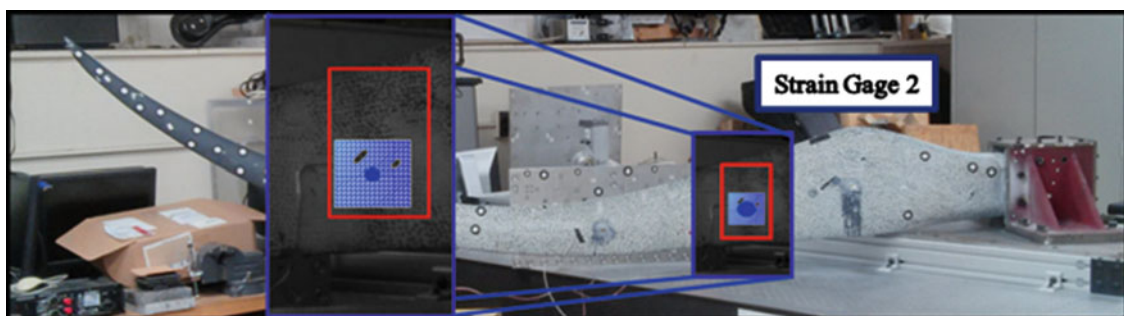**Fig. 19.8** Spatial filtering size analysis – strain values for different levels of input force

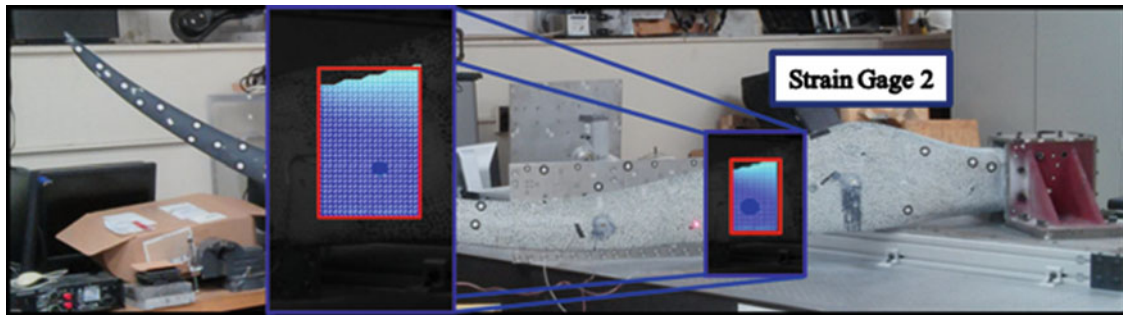**Fig. 19.9** A 221 scan point grid used at the location of SG #2

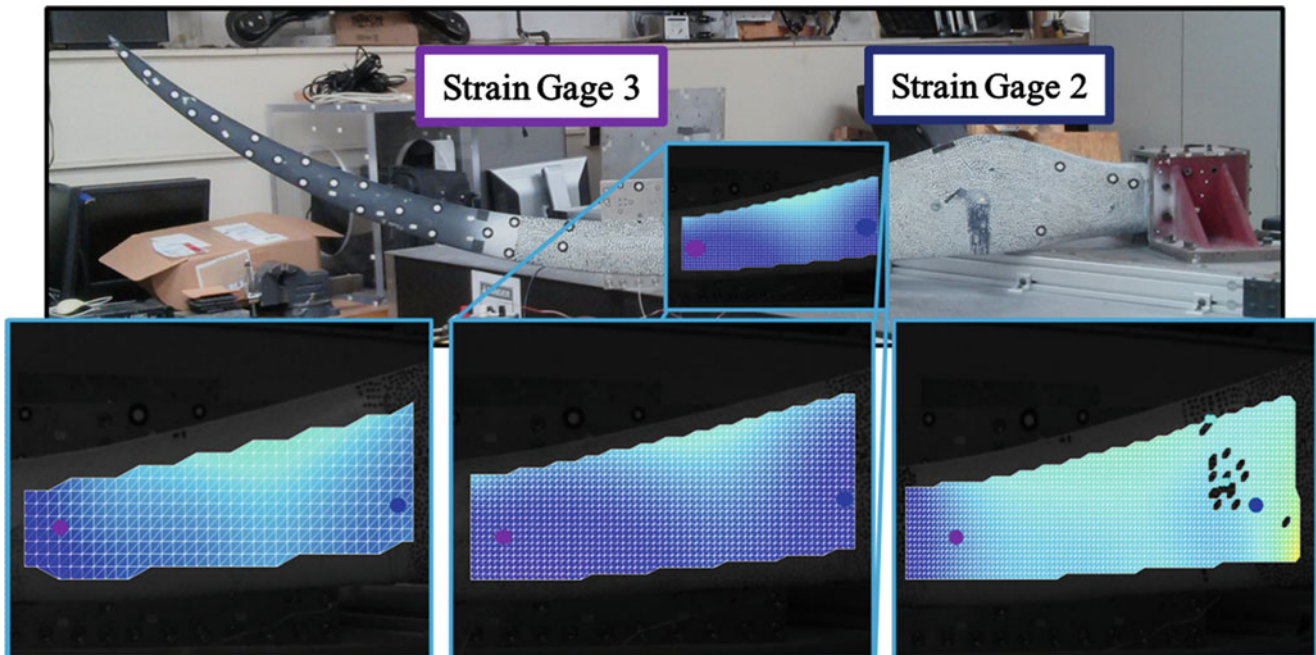**Fig. 19.10** A 603 scan point grid used at the location of SG #2

Fig. 19.11 Grids with 344, 1,397 and 1,944 scan points, respectively

Table 19.2 Grid sensitivity analysis – comparison of the strain distribution results to strain gage data

Strain [$\mu\varepsilon$]									
	Mesh #1 (344 Scan points)			Mesh #2 (1,397 scan points)			Mesh #3 (1,944 scan points)		
Location	Strain gage	Polytec	Diff. (%)	Strain gage	Polytec	Diff. (%)	Strain gage	Polytec	Diff. (%)
SG #2	42.86	36.37	15	44.35	43.24	2.5	41.22	25.10	39
SG #3	46.02	45.02	2	47.84	41.05	14	43.11	40.88	18

The improvement in the measurement was only of 3 % after increasing the number of scan points by three over the same initial area.

Case 3 Three tests were run. The number of scan points for the tests were 344, 1,397 and 1,949 as shown in Fig. 19.11. The grid for these tests covered an area of 64 in.^{2} (16 in width by approx. 5 in. height), which was capable of taking data on both strain gages location making possible the simultaneous comparison of them with the Polytec system. The results shown in Table 19.2 summarize the comparison between the data computed by Polytec and the strain gages.

The results do partially show an improvement but overall the trend is not uniform. Due to the high number of scan points, the time duration of the test may have had a significant effect on the results; over a long period of time there could have been slight shifting of frequencies, change in temperature, and other factors that may not have been consistent throughout the
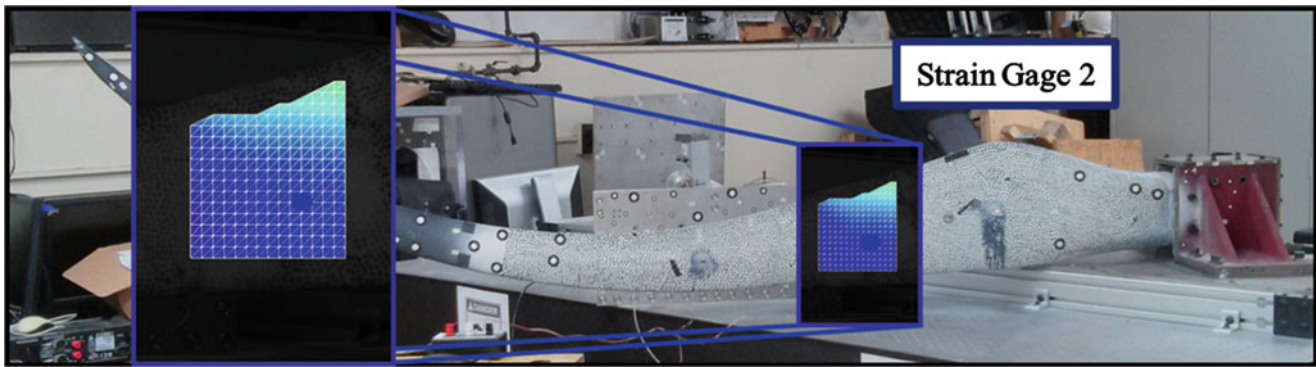
Fig. 19.12 Applied grid during measurement over the SG #2 area

Table 19.3 Strain Gage #2 data – results comparison between Polytec system and strain gage data

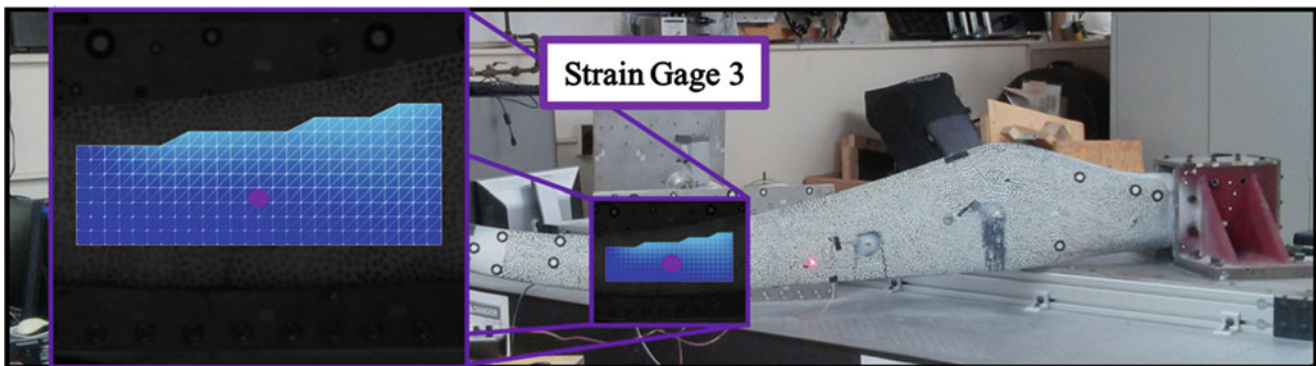|	Strain [$\mu\varepsilon$]		
Level of force [N]	Strain gage	Polytec	Diff. (%)
6	8.55	6.76	21
16	22.75	15.81	30
32	45.10	32.66	27

Fig. 19.13 Applied grid during measurement over the SG #3 area

entire test time. These results are not totally conclusive and additional testing is needed to draw more concrete conclusions. Where the results of the beam tests were very clear and straightforward, the results from the blade test were not as clear.

19.6.3 Results

Once the grid and spatial filtering analysis were performed, sufficient data was gathered to determine the proper characteristics of the grid and the size of the spatial filter. A spatial filtering of 4-SBSP (24 mm) was selected for the acquired data and at the same time the number of scan points was minimum. The same methodology applied on the beam is used in the wind turbine blade to perform the strain analysis through the 3D-SDLV system. Then, the computed strain distribution will be compared to the strain gage measurements as done for the beam.

The first set of data was collected using a 220 scan point grid (Fig. 19.12) over the area of SG #2. After the acquisition of the data a spatial filtering of 4-time-SBSPs was used by the Strain Processor software. This level of filtering was used along the following sets of data. Table 19.3 shows the values of the strain for this test in comparison to the strain gage data.

A second set of data was acquired over the area surrounding SG #3 location (Fig. 19.13). The number of scan points used in this measurement was 249. An effort was done to create a grid which had exactly the same number of scan points as the previous measurement performed for SG #2 but the grid was generated automatically using the software tools. The results were compared and are presented in Table 19.4.

Table 19.4 Strain Gage #3
data – results comparison
between Polytec system and
strain gage data

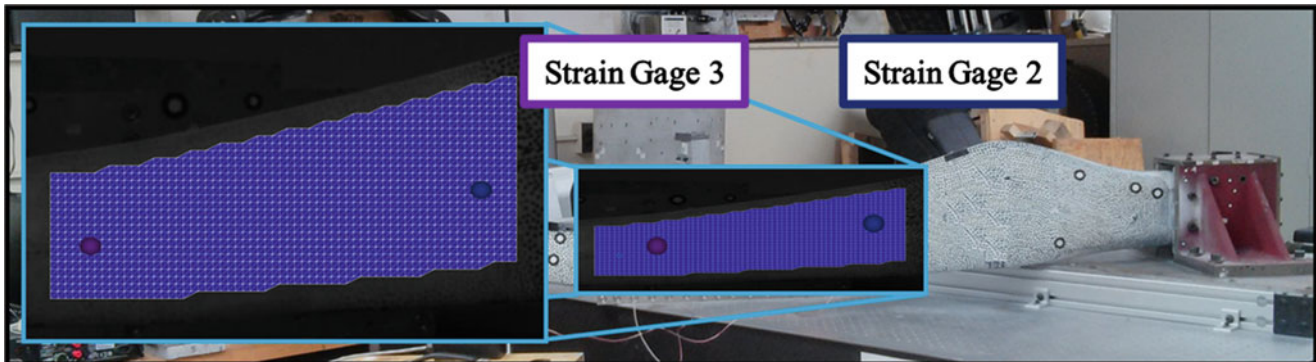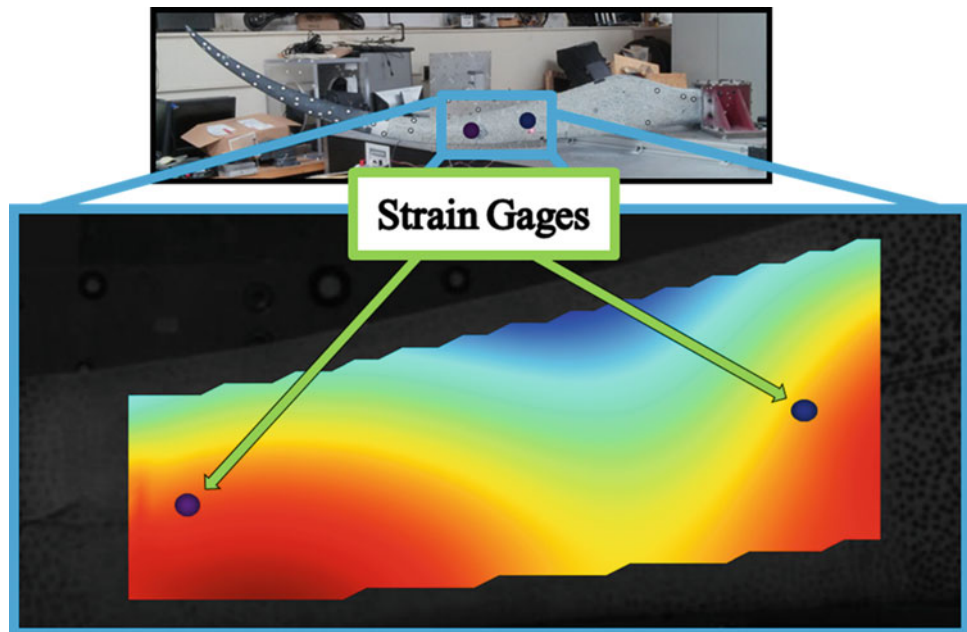| Level of force [N]	Strain [µε]		
	Strain gage	Polytec	Diff. (%)
6	8.64	7.01	18
16	22.84	21.21	7
32	47.32	46.72	1

Fig. 19.14 Applied grid during measurement over SG #2 and #3 areas

Fig. 19.15 Strain distribution on
the wind turbine blade at level of
force of 32 N

The last set of data was collected using a grid which covered the area surrounding both strain gages as shown in Fig. 19.14. 590 scan points were used for this measurement.

Once velocity measurements are obtained, as similarly was done for the beam, the output file can be processed using the Polytec Strain Processor to compute the strain distribution. Figure 19.15 shows the location of the strain gage and the strain distribution for a level of force of 32 N the defined area. Finally, a comparison between the measured values through the 3D-SLDV system and the data collected with the strain gage is shown in Table 19.5.

The strain distribution computed over the area of SG #3 by the Polytec system shows good agreement in comparison with its corresponding experimental strain gage value. But this is not the case for SG #2 which showed more error. However, reviewing the results of (table or fig), the spatial filtering was seen to have a very positive effect on strain gage #3 but the results for strain gage #2 were not improved as well. This may be part of the reason for the lack of correlation for strain gage #2 in this study. Further testing is needed to provide additional data to confirm these results. There may be many factors that have contributed to the poor results in SG#2 and will be the focus of future work.

Table 19.5 Comparison of the full field 3D-SLDV system and the strain gage data for the wind turbine blade

Level of force [N]	Location	Strain [μɛ]		
		Strain gage	Polytec	Diff. (%)
6	SG #2	8.29	6.35	23
	SG #3	9.02	7.05	21
16	SG #2	21.43	14.70	31
	SG #3	23.33	22.31	4
32	SG #2	44.75	28.68	35
	SG #3	48.61	44.67	8

19.7   Conclusion

A Polytec 3D SLDV was used to evaluate strain distributions for two structures – one an academic cantilever beam and the other a wind turbine blade. Studies were performed on mesh density, mesh area on structure, and spatial filter parameters to understand their effect on the results obtained from the data. The trends on these parameters were very useful in subsequent test set up evaluations for the blade test results.

The results for the beam were good overall and the application of the technique was very straightforward. However, the results on the turbine blade were generally good but there were some inconsistencies in the results for several cases studied. These results may have been the consequence of long test durations with high number of scan points where test conditions may not have been completely stable over the test duration thereby affecting the results. The results overall were generally good for the initial studies performed, but additional tests are needed to completely understand the variance seen in a few of the tests performed. This will be further studied in future testing.

Appendix: Polytec Strain Processor Theory

The PSV Strain Processor software computes strain based on three-nodded elements. As shown in [10] for a three-nodded element, the strain finite element shape functions for a planar structure will derived as well.

This analysis could be used for 3D structures. The interpolation equation for a three-nodded linear element as shown in Fig. 19.16 can be written as

$$\phi(x, y) = \alpha_1 + \alpha_2 x + \alpha_3 y \tag{19.1}$$

Equation 19.1 shows how a value, for this case the displacements u and v, can change along the element. The α_i parameters represent the real weights and these are in function of the values of ϕ at each of the three nodes (ϕ_1, ϕ_2 and ϕ_3) defined by [10] as

$$\alpha_1 = \frac{1}{2A} \left(a_1 \phi_1 + a_2 \phi_2 + a_3 \phi_3 \right) \tag{19.2}$$

$$\alpha_2 = \frac{1}{2A} \left(b_1 \phi_1 + b_2 \phi_2 + b_3 \phi_3 \right) \tag{19.3}$$

$$\alpha_3 = \frac{1}{2A} \left(c_1 \phi_1 + c_2 \phi_2 + c_3 \phi_3 \right) \tag{19.4}$$

A in Eqs. 19.2, 19.3 and 19.4 is the area of the triangular element, computed by

$$A = \frac{1}{2} \begin{vmatrix} 1 & x_1 & y_1 \\ 1 & x_2 & y_2 \\ 1 & x_3 & y_3 \end{vmatrix} = \frac{1}{2} \left(x_1 y_2 + x_2 y_3 + x_3 y_1 - x_1 y_3 - x_2 y_1 - x_3 y_2 \right) \tag{19.5}$$

Fig. 19.16 Two-dimensional triangular element [10]
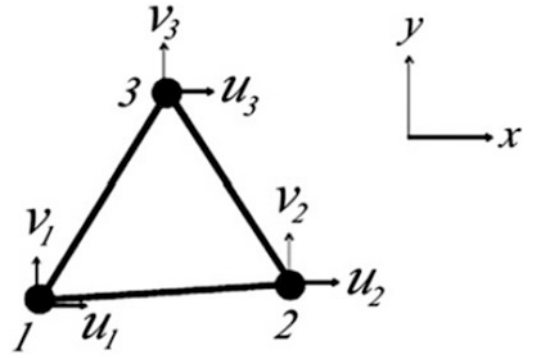
and the a_i, b_i and c_i parameters can be computed with

$$
\begin{aligned}
a_1 &= x_2 y_3 - x_3 y_2; \quad b_1 = y_2 - y_3; \quad c_1 = x_3 - x_2 \\
a_2 &= x_3 y_1 - x_1 y_3; \quad b_2 = y_3 - y_1; \quad c_1 = x_1 - x_3 \\
a_3 &= x_1 y_2 - x_2 y_1; \quad b_3 = y_1 - y_2; \quad c_1 = x_2 - x_1
\end{aligned}
\tag{19.6}
$$

Rewriting Eq. 19.1 in matrix form

$$
\phi(x, y) = N(x, y)\, \Phi
\tag{19.7}
$$

Where N is the Finite Element shape function vector defined by

$$
N = [N_1(x, y) \quad N_2(x, y) \quad N_3(x, y)] \quad \text{with } N_i = (1/2A)(a_i + b_i x + c_i y)
\tag{19.8}
$$

The interpolation function vector Φ is given by

$$
\Phi = \begin{bmatrix} \phi_1 & \phi_2 & \phi_3 \end{bmatrix}^T
\tag{19.9}
$$

being Φ a column vector.

Now, at an arbitrary location (x, y), the displacement $[u, v]^T$ is considered. The displacement is defined by the product of the shape function equations at the location and the vector holding the displacements at the nodes:

$$
\begin{bmatrix} u(x, y) \\ v(x, y) \end{bmatrix} = N(x, y)\, U
\tag{19.10}
$$

$N(x, y)$ defines the shape function matrix as

$$
N = \begin{bmatrix} N_1 & 0 & N_2 & 0 & N_3 & 0 \\ 0 & N_1 & 0 & N_2 & 0 & N_3 \end{bmatrix}
\tag{19.11}
$$

The nodal displacements U is defined by the following column vector

$$
U = \begin{bmatrix} u_1 & v_1 & u_2 & v_2 & u_3 & v_3 \end{bmatrix}^T
\tag{19.12}
$$

Via differentiation of the displacement vector the 2D strain can be computed. This can be expressed as

$$
\begin{aligned}
\varepsilon_x &= \frac{\partial u}{\partial x} \\
\varepsilon_y &= \frac{\partial v}{\partial y} \\
\gamma_{xy} &= \frac{\partial u}{\partial y} + \frac{\partial v}{\partial x}
\end{aligned}
\tag{19.13}
$$

The relationship between the strains and the nodal displacements vector U can be defined as

$$
\begin{bmatrix} \varepsilon_x \\ \varepsilon_y \\ \gamma_{xy} \end{bmatrix} = BU
\tag{19.14}
$$

Fig. 19.17 Principle of strain calculation [11]
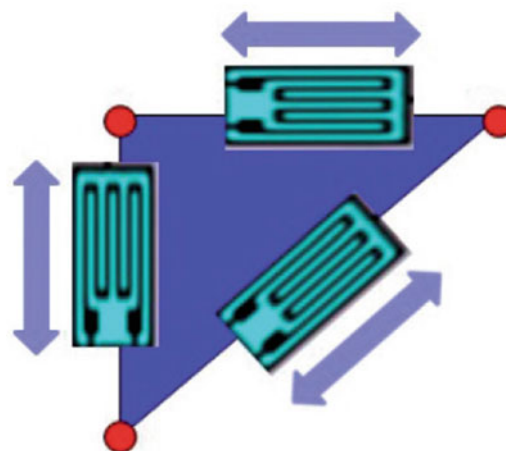
being B the strain matrix given by

$$B = \frac{1}{2} \begin{bmatrix} b_1 & 0 & b_2 & 0 & b_3 & 0 \\ 0 & c_1 & 0 & c_2 & 0 & c_3 \\ c_1 & b_1 & c_2 & b_2 & c_3 & b_3 \end{bmatrix} \tag{19.15}$$

The triangular element is known as the constant strain element since the strains across linear triangular elements are uniform.

Once the 3D-SLDV acquires the displacement field, the PSV Strain Processor software package will compute the strain, which is computed based on the previously stated equations using three-nodded triangular elements [1]. The strain measurement principle can be explained by making the assumption that strain gages are placed at each edge of a triangle as shown in Fig. 19.17.

Using the difference in displacement along the edge divided by the length of the edge is how strain is calculated for each triangle edge. Actually, for the strain calculation, for each surface triangle the displacement measurements are converted into two in-plane components and one out-of-plane component. Thereby, two linear strain values ε_x, ε_y and one shear value δ_{xy} are computed [11]. Then, the surface strain values are transformed back into the global coordinate system.

References

1. Vuye C, Wildy S, Codrington J, Kotousov A, Schuessler (2008) Scanning laser vibrometer for non-contact three-dimensional displacement and strain measurements. In: Proceedings of ACOUSTICS 2008, Geelong, 24–26 Nov 2008
2. Carr J, Baqersad J, Niezrecki C, Avitabile P, Slattery M (2012) Dynamic stress-strain on turbine blade using digital image correlation techniques Part 1: static load and calibration. In: Proceedings of IMAC 31, a conference on structural dynamics, Jacksonville, pp 215–220
3. Carr J, Baqersad J, Niezrecki C, Avitabile P, Slattery M (2012) Dynamic stress-strain on turbine blades using digital image correlation techniques Part 2: dynamic measurements. In: Proceedings of IMAC 31, a conference on structural dynamics, Orlando, Jacksonville, p 221–226
4. Poozesh P, Baqersad J, Niezrecki C, Harvey E, Yarala R (2014) Full field inspection of a utility scale wind turbine blade using digital image correlation. In: Proceedings of CAMX, Orlando
5. Baqersad J, Poozesh P, Niezrecki C, Avitabile P (2015) Predicting full-field strain on a wind turbine for arbitrary excitation using displacements of optical targets measured with photogrammetry. In: Proceedings of IMAC 33, a conference on structural dynamics, Orlando
6. Avitabile P, Baqersad J, Niezrecki C (2014) Using digital image correlation and three dimensional point tracking in conjunction with real time operating data expansion techniques to predict full-field dynamic strain. In: AIP conference proceedings, Ancona, Italy, pp 3–22
7. Carr J, Baqersad J, Niezrecki C, Avitabile P, Slattery M (2013) Predicting dynamic strain on wind turbine blade using digital image correlation techniques in conjunction with analytical expansion methodologies. In: Proceedings of IMAC 32, a conference on structural dynamics, Garden Grove, pp 295–302
8. Baqersad J, Niezrecki C, Avitabile P (2014) Predicting full-field dynamic strain on a three-bladed wind turbine using three dimensional point tracking and expansion techniques. In: SPIE Smart Structures and Materials Nondestructive Evaluation and Health Monitoring, International Society for Optics and Photonics, pp 90612P-90612P-90613
9. Polytec (2011) PSV-3D: dynamic strain measurements. Technical presentation, Polytec GmbH, July 2011
10. Cazzolato B, Wildy S, Codrington J, Kotousov A, Schuessler M (2008) Scanning laser vibrometer for non-contact three-dimensional displacement and strain measurements. In: Proceedings of ACOUSTICS 2008, Geelong, 24–26 Nov 2008
11. Polytec (2011) Optical measurement of dynamic stress and strain. Polytec data sheet: technical report, Polytec GmbH, Apr 2011

Chapter 20
Inline Measurements of Rail Bending and Torsion Through a Portable Device

S. Bionda, F. Braghin, D. Milani, and E. Sabbioni

Abstract Structural condition of railway track can be quantified by considering the deflection of the track under load, since it is related to system stiffness. However measuring track deflection and torsion in working conditions represent a challenging task. In the present paper, the design and testing of a portable device for assessing rail bending and torsion as well as the relative wheel-rail position is presented. The proposed portable device is based on laser sensors, since they do not require any operations on the rails (contactless sensors) and allow placing the sensors at a reasonable distance from both the rail and the passing by wheel. The first bending eigenfrequency of the device is above 100 Hz in order not to dynamically amplify rail bending motions. Moreover the device can be easily mounted on different track sections in order to assess also the influence of vehicle type and speed. The portable device was used to measure rail banding and torsion during tests performed on a dedicated test track in Czech Republic both at low speed (20 km/h on a 150 m radius curve) and at medium speed (90 km/h on a 600 m radius curve) with two axle and four axle wagons. Installation was extremely easy and acquired signals were post-elaborated to assess rail vertical and lateral bending as well as torsion.

Keywords Portable device • Rail bending and torsion monitoring • Contactless sensors • Inline measurements

20.1   Introduction

Structural condition of railway track can be quantified by considering the deflection of the track under load [1–2], since it is related to system stiffness [3–4]. However static loading does not adequately represent real working conditions induced by train passage. Thus measurements of dynamic deflections are required [5]. Current methodologies for measuring track deflection/deformation often require significant railway possession time and thus result expensive. To address this issue two different track displacement monitoring system are proposed in [6]. The first system combines remote video monitoring with particle image velocimetry (using a webcam and a small telescope). The second system uses geophones to measure sleeper velocities (or ground motions), which can be filtered and integrated to calculate track dynamic deflections. Although these devices allow to measure track deflections, they are not able to measure rail torsion.

A device for measuring rail bending and torsion as well as the relative wheel-rail position is presented in this paper. It is based on laser sensors (contactless sensors) and it can be easily mounted in different track sections without the requirement of any operations on the rails.

Within the EU Project D-RAIL (Development of the future rail freight system to reduce the occurrences and impact of derailment), the designed measurement device was used during several tests performed on Velim test track in Czech Republic. Tests were performed at low speed (up to 20 km/h) on a flat 150 m radius curve and at medium speed (up to 90 km/h) on a 600 m radius curve characterized by a rail super-elevation of 153 mm. Tests were repeated with two-axle and four-axle wagons (loaded and empty).

Results of tests will be used to setup and validate the results of a FE model of the rail for prediction of its fatigue life, which specifically will investigate the influence of lateral bending on the loading of a rail foot crack.

S. Bionda • F. Braghin (✉) • D. Milani • E. Sabbioni
Department of Mechanical Engineering, Politecnico di Milano, Via La Masa 1, Milano, MI 20156, Italy
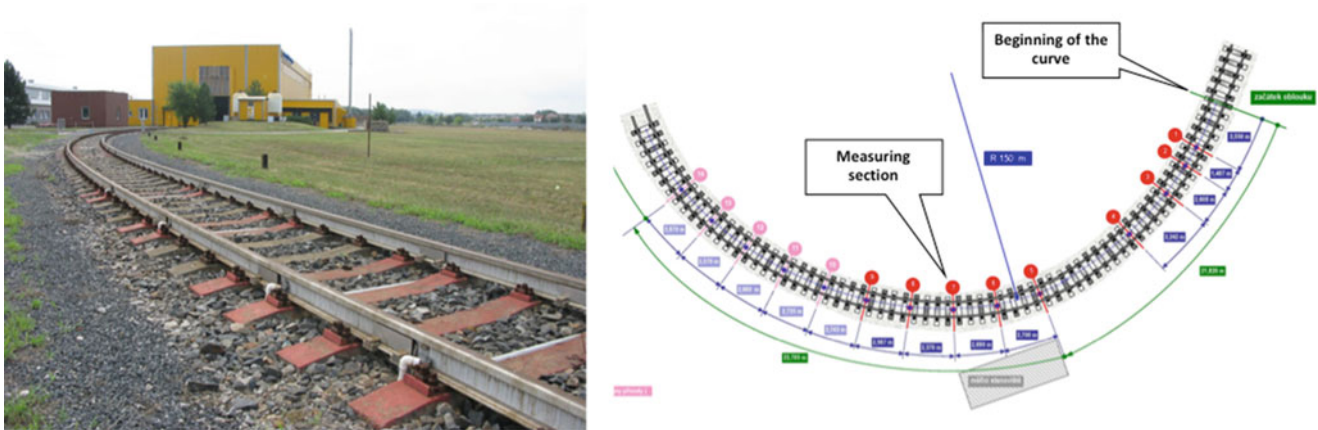e-mail: francesco.braghin@polimi.it

Fig. 20.1 Flat curve of radius 150 m

Fig. 20.2 Small test ring 600 m curve

20.2 Test Site

The measurements were carried out in the VUZ Test Centre Velim (Czech Republic) on the 150 m radius flat curve (Fig. 20.1) and on the 600 m radius curve of the small test ring (Fig. 20.2).

The 150 m radius curve is equipped with nine measuring sections for measuring the guiding and wheel forces on both rails. Four sections are located at the beginning of curve and five of them in the middle (Fig. 20.1). The curve is being used for measurements in accordance with european norm EN 14 363 in order to determine the safety against derailment of vehicles. Strain gauges for measuring vertical and transversal forces are stuck in each measuring section. There are two pairs of strain gauges and four strain gauge rosettes stuck on the rail web.

For this test section No. 7 in the middle of the curve was selected (Fig. 20.1).

On the small test ring, tests were performed in correspondence of the 600 m radius curve (Fig. 20.2), which is characterized by a super-elevation of 153 mm.

20.3 Tested Vehicles

In order to compare the behaviour of two-axle and four-axle wagon the following two types of test freight wagons were selected. Both types are open. The first one was class Es (two-axle, Fig. 20.3) and the other one was class Eas-u (four-axle, Fig. 20.4) equipped with Y25 bogies. The main technical parameters of the wagons are given in Table 20.1.

Fig. 20.3 Two-axle wagon class Es

Fig. 20.4 Four-axle wagon class Eas-u

Table 20.1 Technical parameters of tested wagons

	Two-axle wagon class Es	Four-axle wagon class Eas-u
Gauge	1.435 m	1.435 m
Length over buffers	10.0 m	14.040 m
Wheelbase	6.0 m	9.0 m
Bogie wheelbase	–	1.8 m
Wheel diameter	1.0 m	0.92 m
Unladen weight	12,980 kg	22,570 kg
Load	22,000 kg	42,000 kg

20.4 Test Conditions

In order to investigate different loading conditions, tests both on the 150 m radius flat curve and on the 600 m radius curve of the small ring were repeated varying wagon type (two-axle or four-axle), load conditions (wagon empty or loaded) and vehicle speed.

More in particular, tests on the 150 m radius flat curve were performed in the following conditions:

- two wagons: two-axle wagon class Es, four-axle wagon class Eas-u (see Figs. 20.3, 20.4 and Table 20.1);
- two loading conditions: wagons empty and loaded (see Table 20.1);
- three different speeds: 5, 10 and 15 km/h;
- in all the tests wagons were pushed into the curve by VUZ diesel locomotive (Fig. 20.5a);
- all the tests were carried out on dry rails;
- for each variant three measurements were carried out.

Tests on the 600 m radius curve were performed in the following conditions:

- two-axle wagon and four-axle wagons both trailed by VUZ locomotive (Fig. 20.5b);
- empty wagons;

Fig. 20.5 (**a**) Diesel locomotive was pushing the wagon class Es into the 150 m radius curve; (**b**) Locomotive trailing the wagons on the 600 m radius curve

1 - Laser for wheel-passage detection
2 - Laser for rail head lateral displacement
3,4 - Lasers for rail foot vertical displacement
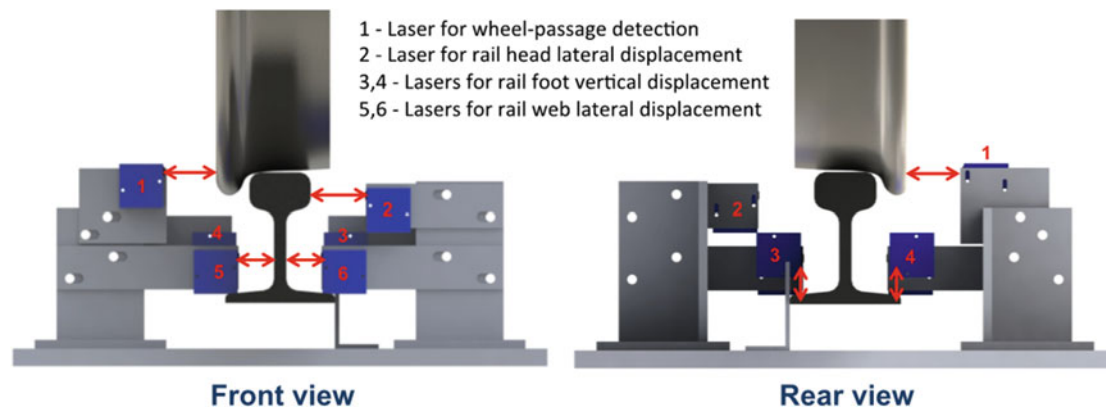5,6 - Lasers for rail web lateral displacement

Fig. 20.6 Portable measurement device

- four different speeds: 30, 60, 80 and 90 km/h;
- all the tests were carried out on dry rails;
- for each variant three measurements were carried out.

20.5 Rail Bending and Torsion Measurement

A portable device for assessing rail bending and torsion as well as the relative wheel-rail position was designed and used during the tests.

The device was designed so that its first eigenfrequency is well above the first bending eigenfrequency of the rail in order not to dynamically amplify rail bending motions. Specifically a first bending frequency of 100 Hz was achieved.

The scheme of the designed portable device is shown in Fig. 20.6. As it can be seen it is based on six laser sensors so that no operations on the rail are required (contactless sensors). Position of lasers can be adjusted to properly place the sensors with respect to the rail.

More in details the measurement device allows to measure:

- lateral bending of rail head (laser 2, see Fig. 20.6)
- lateral bending rail web (lasers 5 and 6, see Fig. 20.6)
- vertical bending of rail foot (lasers 3 and 4, see Fig. 20.6)

Moreover wheel-passage is detected so that vehicle speed can be identified during the passage on the instrumented section of the rail.
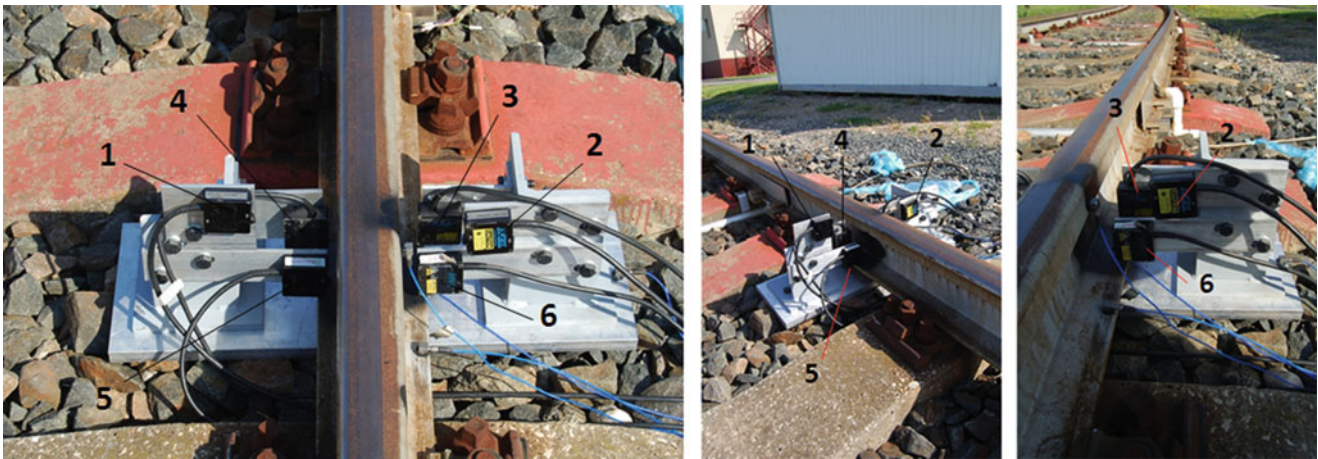
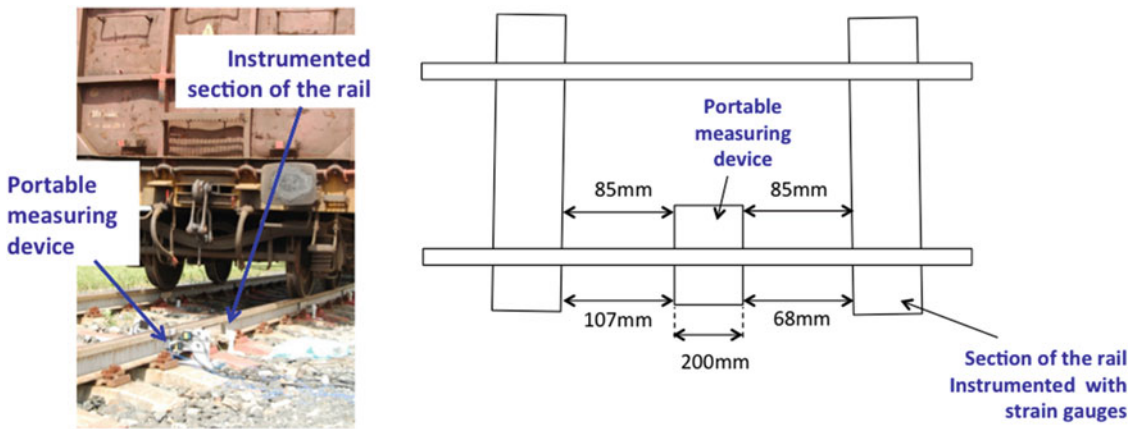**Fig. 20.7** Portable measurement device placement during 150 m flat curve tests

Fig. 20.8 Portable measurement device placement during 150 m flat curve tests

Fig. 20.9 Portable measurement device placement during 600 m radius curve tests

During the tests on the 150 m radius flat curve, the measuring device for rail bending and torsion measurement was placed in the middle between two sleepers at the beginning of section No. 7 (Figs. 20.7 and 20.8), in correspondence of the outer rail.

During the tests on the 600 m radius curve of the small ring, the measuring device for rail bending and torsion measurement was placed in the middle between two sleepers, in correspondence of the outer rail (Fig. 20.9).

20.6   Results

In this section results concerned with the tests carried out on the 150 m radius flat curve and the 600 m radius curve are presented.

Data acquired using the portable device for measuring rail deformations were post-processed to obtain:

- outer rail vertical bending: z (Fig. 20.10);
- outer rail lateral bending: y (Fig. 20.10);
- outer rail torsion: θ (Fig. 20.10);
- vehicle speed while passing over the instrumented section of the rail.

Lateral bending of the rail was estimated averaging lateral displacement of rail web. In the same way, vertical bending was gained averaging vertical displacement of rail foot. Torsion was instead estimated based on difference between displacements of rail foot. Finally, vehicle speed was identified based on wheel passage detection, being known the wheelbase of wagon/bogie (see Figs. 20.11, 20.12, and 20.13).

As an example of obtained results, Fig. 20.11 through Fig. 20.13 show measured rail bending and torsion for the different tested vehicles and the considered loading conditions for a nominal vehicle speed of 15 km/h. Specifically, Fig. 20.11 compares the empty two-axle vehicle with empty the four-axle vehicle equipped with Y25 bogies. Figure 20.12 shows the effect of the load for the two-axle vehicle, while Fig. 20.13 compares rail deformations for empty and loaded four-axle vehicle. As it can be seen, although nominal speed was 15 km/h in each test, real vehicle speed is actually more close to 18–20 km/h.

Comparing the empty two-axle and four-axle wagons, it can be seen that obviously the vertical load is more uniformly distributed on the four-axle wagon and this leads to lower vertical bending of the rail. Lateral rail bending and torsion are instead comparable and however small. In both cases, the rail is bended towards the outside of the track with respect to centreline.

For the two-axle wagon, an increase of the load leads to a more uniform vertical bending of the rail between the two axles (Fig. 20.12).

Both in the case of the two-axle wagon and of the four-axle wagon, increasing the load leads to higher lateral bending of the rail, but while for the two-axle vehicle lateral bending is comparable for the first and the second axle, for the four-axle wagon lateral bending due to the passage of the first and third axles is much higher than the one due to passage of the second and fourth axle.

Torsion of the rail is very small in all the tests, except in the case of the loaded four-axle wagon. In this case (Fig. 20.13b), it can clearly seen that the passage of the first and of the third axle makes the rail rotate towards the outside of the track.

Figure 20.14 shows the results for the tests carried out on the 600 m radius curve of the small test ring. Tests concerned with vehicle speed of 30 km/h (Fig. 20.14a) and 90 km/h (Fig. 20.14b) are reported. As previously said, during these tests, the empty two-axle and the empty four-axle wagons were simultaneously trailed by the locomotive (see Fig. 20.5b). As it can be seen, higher bending of the rail is always associated to the passage of the locomotive, due to the higher load per axle.

Comparing the lateral bending induced by the passage of the locomotive and the wagons, it can be noticed that the rail is always bended towards the outside of the track with respect to centreline. Moreover, while lateral bending of the rail due to the passage of the two-axle vehicle is almost null at 30 km/h, it becomes comparable to the one of the four-axle wagon at 90 km/h. This may suggest that these wagons are more prone to rail climbing than Y25 bogie.

Torsion of the rail due to the locomotive appears to be higher at low speeds than at medium-high speeds, while it remains almost constant and small due to the passage of the two and four axle wagons. Torsion of the rail produced by the two wagons is comparable at both speeds.
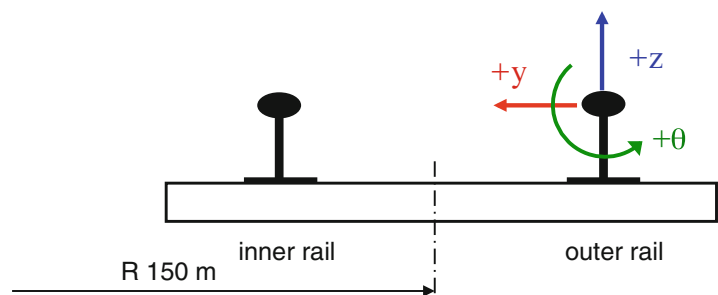

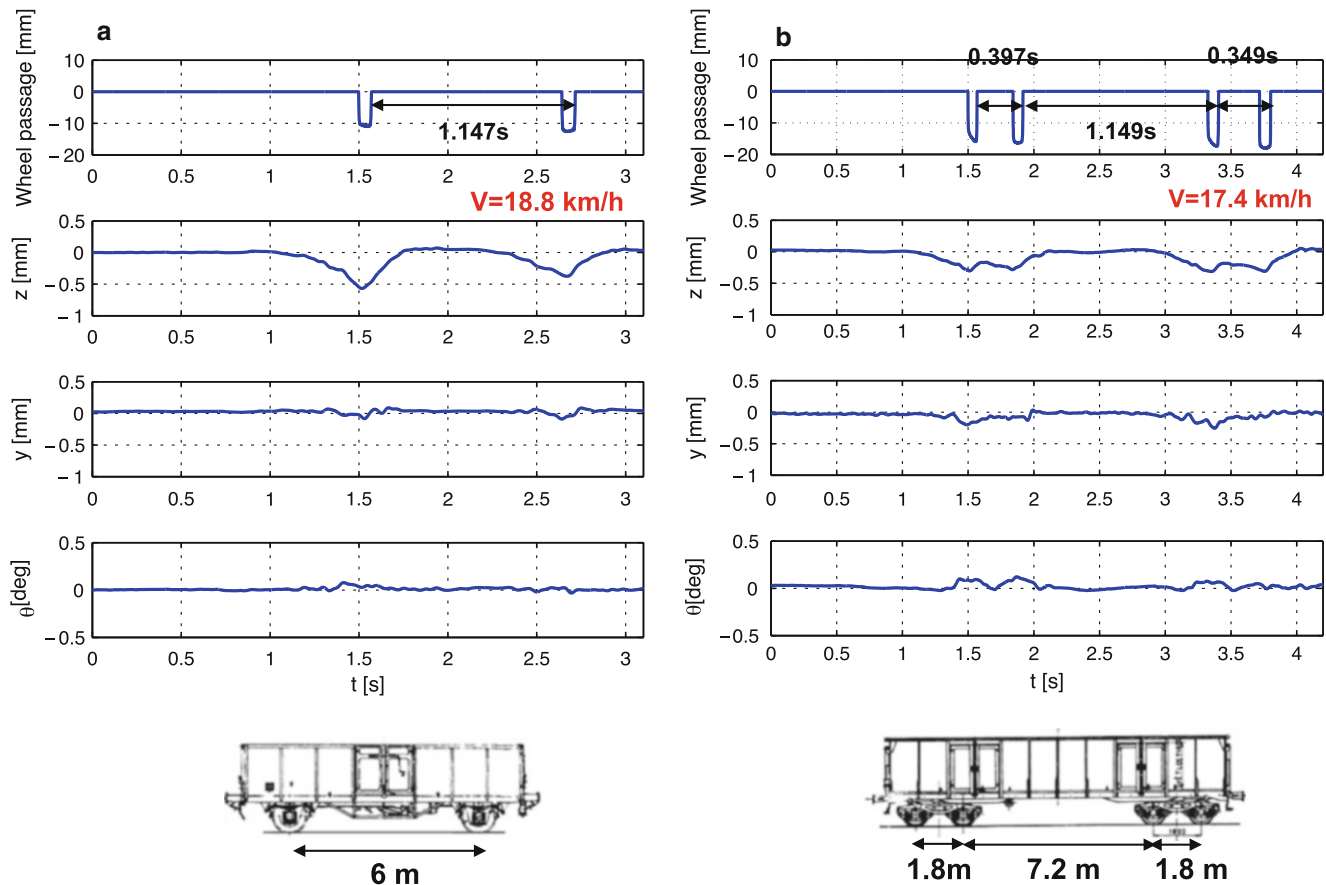**Fig. 20.10** Reference system for rail bending and torsion

Fig. 20.11 Tests of the 150 m radius flat curve, speed 15 km/h. Wheel-passage detection, rail bending and torsion: (**a**) two-axle wagon empty, (**b**) four-axle wagon empty

20.7   Concluding Remarks

A portable device for assessing rail bending and torsion as well as the relative wheel-rail position was designed and tested on the Velim test track. Tests were performed on a 150 m radius flat curve and on a 600 m radius curve with a super-elevation of 153 mm. Tests were carried out considering different wagons (two-axle and four-axle wagons), different loading conditions (empty and loaded) and different vehicle speeds.

Analysing the results of the tests on the 150 m radius flat curve, the following considerations can be drawn:

- comparing the empty two-axle and four-axle wagons, it can be seen that obviously the vertical load is more uniformly distributed on the four-axle wagon and this leads to lower vertical bending of the rail. Lateral rail bending and torsion are instead comparable and however small. In both cases, the rail is bended towards the outside of the track with respect to centreline;
- for the two-axle wagon, an increase of the load leads to a more uniform vertical bending of the rail between the two axles (Fig. 20.12);
- both in the case of the two-axle wagon and of the four-axle wagon, increasing the load leads to higher lateral bending of the rail, but while for the two-axle vehicle lateral bending is comparable for the first and the second axle, for the four-axle wagon lateral bending due to the passage of the first and third axles is much higher than the one due to passage of the second and fourth axle (Fig. 20.13);
- torsion of the rail is very small in all the tests, except in the case of the loaded four-axle wagon. In this case (Fig. 20.13b), it can be clearly seen that the passage of the first and of the third axle makes the rail rotate towards the outside of the track.

Tests on the 600 m radius curve confirm that the rail is bended towards the outside of the track with respect to centreline for both the tests wagons and the considered speeds. Moreover, while lateral bending of the rail due to the passage of the

Fig. 20.12 Tests on the 150 m radius flat curve, speed 15 km/h. Wheel-passage detection, rail bending and torsion: (**a**) two-axle wagon empty, (**b**) two-axle wagon loaded

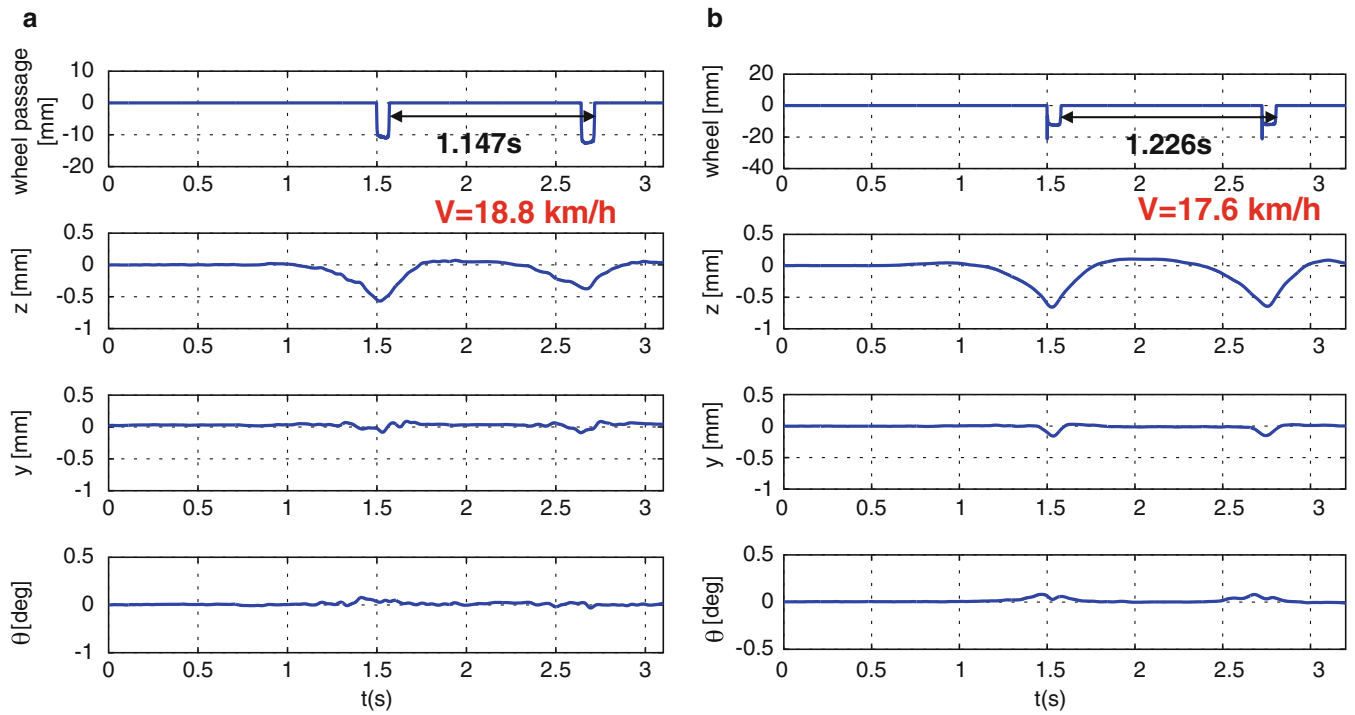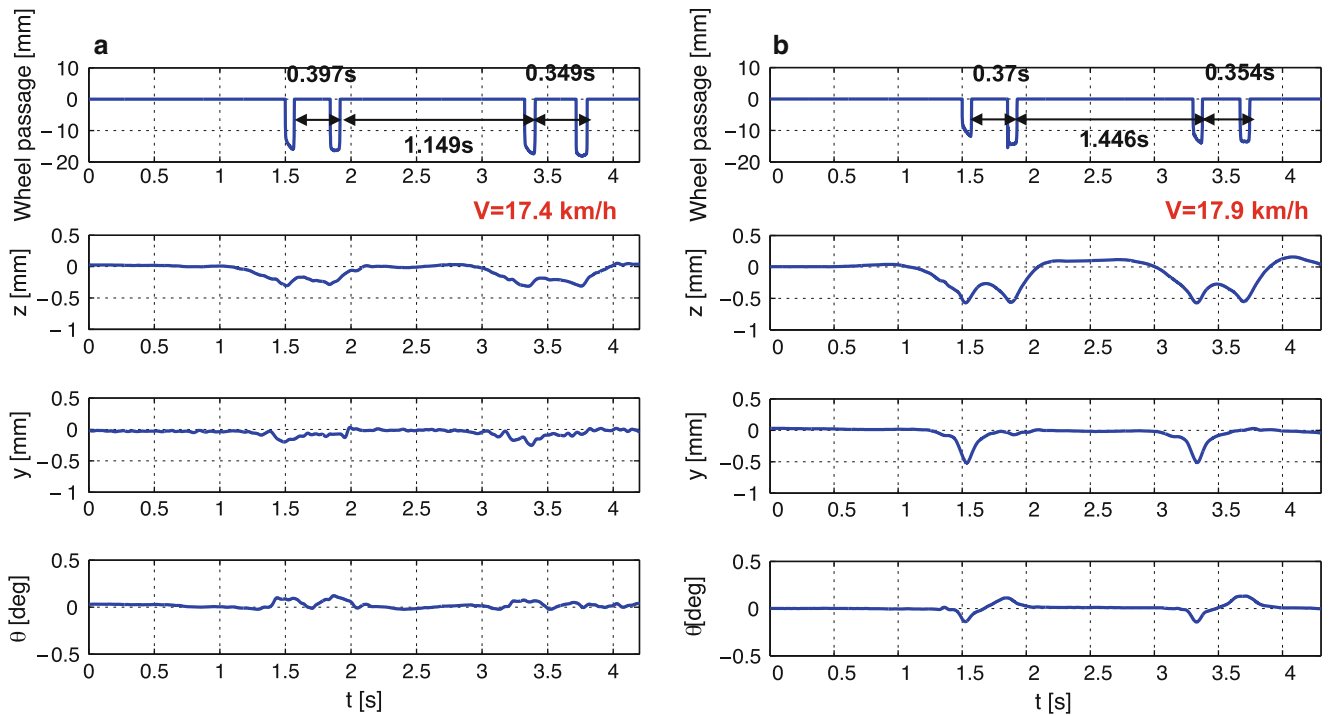**Fig. 20.13** Tests on the 150 m radius flat curve, speed 15 km/h. Wheel-passage detection, rail bending and torsion: (**a**) four-axle wagon empty, (**b**) four-axle wagon loaded
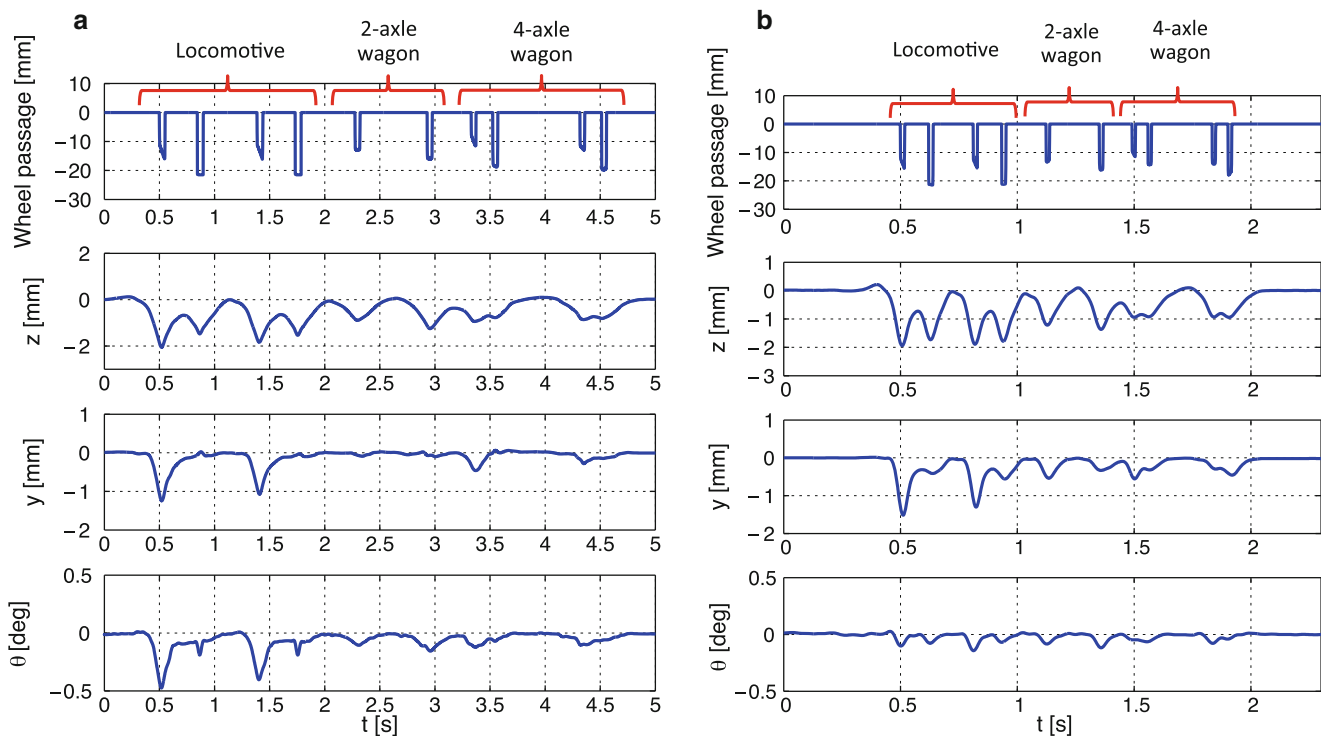
Fig. 20.14 Tests on the 600 m radius curve. Wheel-passage detection, rail bending and torsion: (**a**) V = 30 km/h, (**b**) V = 90 km/h

two-axle wagon is almost null at 30 km/h, it becomes comparable to the one of the four-axle wagon at 90 km/h. This may suggest that these wagons are more prone to rail climbing than Y25 bogie.

References

1. Brown SF (1996) Soil mechanics in pavement engineering. Geotechnique 46(3):383–426
2. Sussman TR, Ebersohn W, Selig ET (2001) Fundamental nonlinear track load-deflection behaviour for condition evaluation. Trans Res Rec 1742:61–67
3. Cai Z, Raymond GP, Bathurst RJ (1994) Estimate of static track modulus using elastic foundation models. Trans Res Rec 1470:65–72
4. Read D, Chrismer S, Ebersohn W, Selig ET (1994) Track modulus measurement at the Pueblo soft subgrade site. Trans Res Rec 1470:55–64
5. Brown SF, Selig TE (1991) The design of pavement and rail track foundations. In: O'Reilly MP, Brown SF (eds) Cyclic loading of soils: from theory to design. Blackie, Glasgow, pp 249–305
6. Bowness D, Lock AC, Powrie W, Priest JA, Richards DJ (2007) Monitoring the dynamic displacements of railway track. Proc Inst Mech Eng Part F J Rail Rapid Transit 221:13–22

Chapter 21
Forty Years of Use and Abuse of Impact Testing: A Practical Guide to Making Good FRF Measurements

David L. Brown, Randall J. Allemang, and Allyn W. Phillips

Abstract Impact testing first came into common use over 40 years ago, once the fast Fourier transform (FFT) was commercially available. Over this period of time, implementation of impact testing has evolved but some of the same problems seem to reoccur. This paper documents the practical guidelines that have evolved, along with some practical examples of what happens when the guidelines are not followed, particularly with respect to overload detection and related errors. In particular, the ADC hardware differences are noted and the distortion problem associated with overloads is thoroughly reviewed. Other issues that are discussed include factors that affect force spectrum, impact hammer calibration, double impacting, use, application and correction for exponential windows and understanding how the time truncation causes leakage for a realistic case involving a lightly damped structural system.

21.1 Introduction

Impact testing and other related transient testing methods have now been utilized for over 40 years. Throughout that time, a few general guidelines have evolved regarding how to handle the common problems that arise from using transient signals. The specific problems of a force signal that has a very high peak to RMS characteristic and a response signal that may have similar characteristics but for most applications have signals that do not decay in the observation time window. These attributes contribute to problems with adjusting the frequency content of the impact excitation and thus the response to the transient excitation, auto-ranging the digital signal processing hardware and software, capturing the peak signals without the distortion that arises if an overload occurs, double impacts by the force hammer and correctly chosen and applied windows on both force and response signals to identify the primary issues. Many of the guidelines were developed in the 1970s and have evolved to the present time without much recognition that the digital signal processing software and hardware has evolved significantly. While the software and hardware evolution has not changed the guidelines, the impact of the changes in hardware and software greatly affects the use of impact testing, particularly with respect to overloads and overload detection. If good frequency response functions (FRFs) are the goal, recognition of these hardware and software changes must be understood.

21.2 Background

The development of impact testing predates the first commercial Fourier analyzer system. In the mid-1960s, the mathematical properties of the integral and discrete Fourier transform were well known but its applications were limited until the fast Fourier transform (FFT) was developed and published. Much research work had already been done and published information regarding digital signal processing (DSP) and windowing had begun to be available from groups like the US Air Force Research Lab (US-AFRL). The equations for the numerical estimation of FRFs and coherence functions along with most DSP concepts, including windowing, were already known. In the mid-1960s, the potential use of an impact as an excitation signal was being evaluated at the University of Cincinnati via available equipment.

D.L. Brown • R.J. Allemang (✉) • A.W. Phillips
Structural Dynamics Research Lab, Department of Mechanical and Materials Engineering, College of Engineering and Applied Science,
University of Cincinnati, Cincinnati, OH 45221-0072, USA
e-mail: Randall.Allemang@UC.EDU

In the 1966–1967 time period, a project to develop a transient testing procedure for measuring frequency response functions was initiated as part of a MS thesis. In this initial effort, an impact hammer was used to excite a machine tool structure, with the measurement of the transient input and response on an FM tape recorder. Tape loops of the transient responses were played into a transfer function analyzer (TFA). The input and response signals were processed by using the tracking filters in the TFA to filter and ratio the response to the input signal, thereby estimating the frequency response between the input signal and the response signal. This method proved to be impractical due to signal-to-noise problems.

At about the same time, a single channel, prototype Real Time Analyzer (RTA), made available by Spectral Dynamics, was used to estimate the response spectrum to an impact on the machine tool structure. This spectrum measurement had good agreement with the response spectrum estimated from the measured FRF using the current test standard, the TFA methodology using analog sinusoidal excitation. Based upon this result, a serious effort was initiated to develop a measurement process which would use the newly developed FFT algorithm to estimate an FRF from the FFTs of the digitized input and response signals.

Once the FFT algorithm was published, a hybrid computer, located in Department of Electrical Engineering at the University of Cincinnati was used to develop a software program which used the analog part of the hybrid computer to digitize the force and the response (accelerometer) signals, recorded on an FM Tape recorder, measured by testing a machine tool base. The digital part of hybrid computer was used to compute FRFs and coherence functions using the FFT algorithm. These measurements were compared to FRF functions measured with the analog TFA equipment with good agreement. Unfortunately, the hybrid computer filled a complete room. As a result, only small test objects could be taken into the computer room to be tested in real time. For large test articles, the measurement data had to be recorded on an AM and/or FM tape recorder and this recorded data were processed with the hybrid computer.

Finally, in the late 1960s and early 1970s, small minicomputer based systems, manufactured by Hewlett Packard and the Time Data Corporation, became available. These systems included analog to digital converters (ADCs) along with the mini-computer and a proprietary software operating system that processed the digitized data with the FFT. These systems were portable and could be located next to the test article, making laboratory and field testing practical. These systems made impact testing possible and practical leading to one of the first publications in 1972 regarding the approach to testing a mechanical structural system [1, 2].

21.2.1 Impact Testing Development

Impact testing was investigated during the 1970s [1–4], becoming a mainstream testing technique for the experimental analysis of vibration and acoustics. The portability of the excitation established impact testing as a testing method well suited for trouble-shooting vibration and noise problems, including the development of single reference and multi-reference, experimental modal analysis methodologies. The paper by Halvorsen and Brown [5] in Sound and Vibration Magazine in 1978 summarized many of the practical issues associated with impact testing. Most of the issues highlighted in that article (force spectrum characteristics, specialized windows, multiple impacts, overloads and overload detection, etc.) remain the focus of current impact testing technique. The only commonly used method today not reviewed in the article is the use of a pre-trigger which was not available in hardware of that era. However, it is important to understand that the hardware and software technology of the 1970s has changed and those changes make some of the issues even more important with respect to current hardware and software. The next section will document some of those changes.

21.2.2 Evolution of Impact Testing Hardware/Software

Impact testing hardware and software involves a number of concepts/issues that need to be considered. This includes anti-aliasing filters, the location and purpose of the anti-aliasing filters, the number of bits in the ADC that are available to quantify the amplitude of the time domain signal, the detection of signals that are too large for the input gain chosen (overloads), the location of the detection of the overloads and the number of simultaneous channels.

The year 1980 is chosen as the crossover point where the hardware began moving toward fewer sampling frequencies with fewer analog filters to the design of the current delta-sigma (or sigma-delta) ADC technology with only one sampling frequency and one analog anti-aliasing filter, relying increasingly on digital filtering. By 1980, most hardware systems had added the ability to pre- and post-trigger, the last piece of hardware and software technology that is commonly used in impact testing today.

Fig. 21.1 Historical ADC design
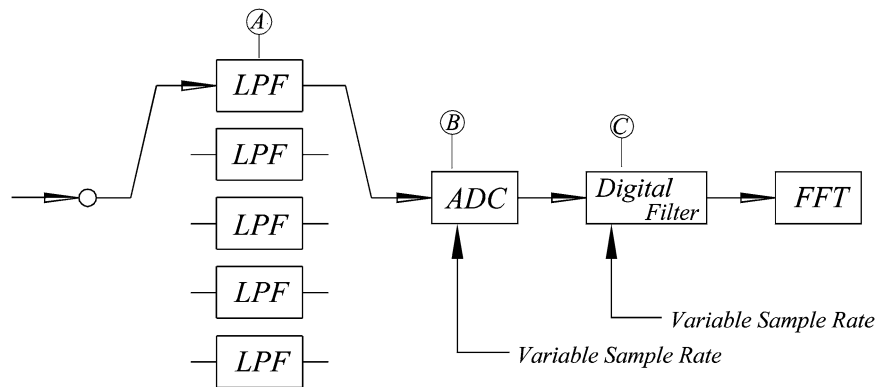
21.2.2.1   Historical Impact Testing Hardware/Software (Pre-1980)

Figure 21.1 gives a block diagram of the typical hardware that was used prior to 1980 for each channel of the data acquisition. It is important to note that there were generally not more than four channels of simultaneous data acquisition in the Fourier transform analyzers of this time period. From the first commercial Fourier transform analyzers, the traditional frontend hardware input utilized a user selectable, low-pass filter (LPF) that was placed before the analog gain portion of the ADC to protect against the aliasing error (noted by location A in Fig. 21.1). This filter was not generally part of the Fourier analyzer during this time period and the user had to choose the LPF based upon the Nyquist frequency that would be used in the ADC. The general rule was to choose the cutoff frequency of the LPF around 80 % of the Nyquist frequency to eliminate the frequency information above the Nyquist frequency, thus avoiding the aliasing error.

Several design issues are important to note. The analog, anti-aliasing LPF needs to have significant roll-off to prevent the aliasing error based upon the 80 %, Nyquist frequency rule and the same filter must be applied to all channels of data acquisition to prevent phase mismatch between channels. This requires an instrumentation quality filter to be both adjustable and to have the desirable pass band characteristics. The overload detection was generally a visual indicator on each channel (LED) but the software interface with the hardware rarely provided any feedback to the user. The overload detection circuitry that triggered the visual indicator was in the output of the analog gain section of the ADC or in the input of the digital section of the ADC (location B in Fig. 21.1). The ADC typically had only 10–12 bits together with numerous input gain settings to allow for optimization of the analog signal to the ADC. The digital filter (noted by location C in Fig. 21.1) was limited by the computer performance of the mini-computers available in these data acquisition systems (computer speed, computer word size, computer memory, etc.). For this reason, the digital filter was only used to perform banded frequency analysis within the chosen Nyquist frequency bandwidth.

With respect to impact testing, it is important to note that the analog, anti-aliasing LPF performed a secondary function that is distinctly different in the current ADC design. Since the cutoff frequency of the LPF filter was always set at 80 % of the desired Nyquist frequency, this filter removed the frequency information (energy) above the Nyquist frequency on every signal before the signal entered the analog gain section of the ADC (at location B). This allowed the input gain to be set according to the signal frequency content that was in the user's frequency band of interest. Note that in the mid-1980s, when DSA manufacturers first integrated the LPF into the frontend, it was not uncommon for the manufacturer to choose a 50 % cutoff frequency to protect the quality of the user's data through an additional guard-band.

The high cost of this ADC design had a significant cost per channel that prohibited multiple channel designs. The high cost was a function of both the design of the ADC itself and the requirement for an instrumentation quality filter for each ADC channel.

21.2.2.2   Current Impact Testing Hardware/Software (Post-1995)

Figure 21.2 gives a block diagram of the typical hardware that is now used for each channel of the data acquisition. The delta-sigma design currently used allows for a digital signal analyzer to have a much lower cost per channel since this design takes advantage of the delta-sigma ADC/DAC design that is widely used throughout many consumer electronics devices (CD and DVD players, HD-TV systems, etc.). The delta-sigma ADC design uses a different process that takes advantage of the bundling of the operations into a single electronics chip along with increased computer speed, computer word size and computer memory to give a superior final result (24 bits) at a much lower cost. This means that more channels can be made

Fig. 21.2 Current ADC design
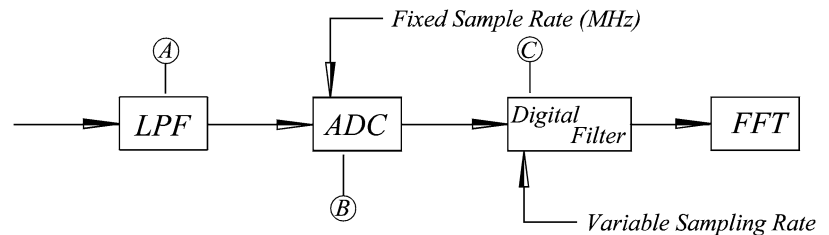
available at a lower and lower cost per channel. The changes in the design concept give the same final result but the operation is a bit different.

In Fig. 21.2, the significant difference in the delta-sigma design is the single sampling rate that is required. The ADC is a one-bit ADC with a sampling rate at a very high frequency when compared to structural testing, or even acoustic testing, requirements. The actual sampling rate is often in the 5–10 MHz region (noted by location B in Fig. 21.2), and is generally chosen at 128 times the *effective sampling rate* associated with the highest *effective Nyquist frequency*. Note that other oversampling rates are used in specialized application areas when the decimated frequency may be chosen to match a particular application need; for example in audio applications where the effective sampling rate is chosen to match the CD audio data rate. As an example, if the highest desired Nyquist frequency is 25 kHz, then the highest effective sampling rate would be 50 kHz. The actual sampling rate would then be 6.4 MHz. The 24 *effective bits* of the delta-sigma ADC, at the highest effective sampling rate, comes via the digital filtering and down-sampling that occurs in the delta-sigma ADC chip beginning with the one bit sampling that occurs at 6.4 MHz. The *user selected Nyquist frequency* is determined by the digital filter characteristics (noted by location C in Fig. 21.2).

The difference in the delta-sigma ADC design that affects impact testing comes from the analog, anti-aliasing LPF that is utilized (noted by location A in Fig. 21.2). Note that the analog, anti-aliasing LPF (at location A) is positioned early in the signal processing and separated from the digital filter that is set by the user selected Nyquist frequency (at location C). In the example cited above, the cutoff frequency of the LPF can be chosen anywhere between 80 % of the highest effective Nyquist frequency (25 kHz) up to 80 % of the actual Nyquist frequency (3.2 MHz). Since the digital filter (at location C) removes the high frequency energy in the signal *after* the input gain and quantization, the input gain cannot be optimized as in the historical ADC design. In order to make sure that the characteristics of the LPF do not affect the magnitude and phase characteristics of any data in the frequency range up to the effective Nyquist frequency, vendors will often choose a less aggressive anti-aliasing filter design set at a frequency that is well above the effective Nyquist frequency. This gives an effective anti-aliasing design at a minimum cost per channel.

Regardless of the oversampling rate, the type of anti-aliasing filter that is used and/or the cutoff frequency chosen by the vendor in a delta-sigma design, the anti-aliasing filter no longer limits the higher frequency energy that may be present in impact testing. At a minimum, this cutoff frequency would be at 80 % of the highest Nyquist frequency (25 kHz) in a digital signal analyzer. Most structural testing involving impact testing is at 1 kHz or below. While there are no issues involving the aliasing error, the anti-aliasing LPF now allows this high frequency energy from the impact input or response to reach the ADC.

The overload detection in a delta-sigma ADC design occurs at the same location as in the historical ADC design. The overload is detected at the output of the analog gain section of the ADC or in the input of the digital section of the ADC. The problem for impact testing is that the data signals now have energy in the frequency range well above the actual Nyquist frequency desired (100–500 Hz). This means that the analog, input gain on each channel will be set using the higher energy level of the frequency range up to the analog, anti-aliasing LPF. This is distinctly different from the historical ADC design. As an example, the delta-sigma ADC may require that the input gain be set to a plus/minus 10 V range to satisfy the high frequency characteristics in the data (25 KHz or above) but the final time waveforms may be only a volt or less once the digital filter reduces the data to the desired Nyquist frequency (100 Hz). This means that the choice of the hammer and hammer tip, to limit the frequency content above the desired Nyquist frequency, is critical. This will be discussed further in a later Section concerning auto-ranging, overloads and overload detection.

There are a number of other issues concerning the delta-sigma ADC design that affect impact testing. With the move to a delta-sigma ADC design with 24 *effective bits* (more dynamic range than previous designs), most manufacturers have reduced the number of input gain settings as the number of effective bits in the ADC have increased. Figure 21.3 summarizes the ADC characteristics of a number of current and past ADC configurations. While the need for fewer input ranges may be true for most steady state testing situations, it is another complication for impact testing since there are fewer input ranges to choose from to avoid the overload problem.

Card	ADC Info	Dynamic Range	Channels Card	Fmax (lowest)	Fmax (highest)	Vmax (lowest)	Vmax (highest)	Number Ranges
HP-35652-A	14-16 bit, conventional	30 dB	1	.195 Hz	51.2 kHz	.0013 V	40 V	46
HP-35652-B	14-16 bit, conventional	75-80 dB	1	.195 Hz	102.4 kHz	.0013 V	40 V	46
HP-35655-A	14-16 bit, conventional	72 dB	8	0.0625 Hz	12.8 kHz	.005 V	10 V	34
HP-35655-B	14-16 bit, conventional	72 dB	4	0.0625 Hz	12.8 kHz	.005 V	10 V	34
Agilent/VTI-1432A	15 bit, delta sigma	80-90 dB	16	10 Hz	23 kHz	0.1 V	10 V	7
Agilent/VTI-1433B	15 bit, delta sigma	74-90 dB	8	0.0954 Hz	75.8 kHz	5 mV	10 V	11
VTI 1435 (1436)	24 bit, delta sigma	112 dB	8 (16)	244 µHz	46 kHz	0.1 V	20 V	8
NI-4462	24 bit, delta sigma	106-110 dB	4	400 Hz	81.92 kHz	0.316 V	42.4 V	6
NI-PXI-4472	24 bit, delta sigma	118-130 dB	8	453.5 Hz	23.2 kHz	10 V	10 V	1
NI-PXIe-4499	24 bit, delta sigma	104 dB	16	435 Hz	92.9 kHz	0.316 V	10 V	4
VTI-EMX-4350	24 bit, delta sigma	125 dB	4	0.864 Hz	270 kHz	0.1 V	20 V	4

Fig. 21.3 ADC characteristics of various current systems

Other changes that are common in current ADC designs involve a number of trends. Most systems have more channels than previously with 8–16 channels very common. More channels means that visual checking of each channel for overload or undesirable characteristics is often overlooked or compromised. To reduce this problem, most overload detection is now integrated with the software so that a hardware overload is communicated to the data acquisition software. This allows for a software auto-ranging algorithm to assist the user in detecting overloads. Current data acquisition designs also offer the ability to pre- and/or post-trigger to make sure that the initial portion of transient signals, like those involved in impact testing, is not missed.

21.3 Practical Guidelines

There are a number of impact testing guidelines that have evolved that need to be reviewed in light of the hardware and software evolution over the last forty used. In general, the same guidelines still applied but the importance of adherence to the guidelines has changed. The choice of the impact hammer and impact hammer characteristics is still the primary focus but the overload and overload detection issues are maybe more important when trying to make the best impact testing measurement of FRFs. Other concepts/issues that will be quickly reviewed include the application, use and correction of force and impact windows applied to the time domain data, minimizing multiple impacts, being careful with DC voltage shifts and the impact of various background noises on the data.

21.3.1 Impact Testing Force Spectrum

The factors that affect the force spectrum of the impact hammer are well known, have been thoroughly documented in the past and will only be reviewed briefly in the following discussion. Note, however, that the characteristics of the force spectrum will in general include energy above the user selected Nyquist frequency that is no longer reduced by the anti-aliasing filter of the current, delta-sigma ADC design.

The force spectrum of the impact hammer is controlled by a number of factors. First and foremost, the characteristic of the removable tip used in the impact hammer will define the primary usable force spectrum. A soft tip will spread the applied energy over a longer time period and thus give a lower maximum frequency that can be used. A hard tip will concentrate the applied energy over a shorter time period and thus give a higher maximum frequency. Any characteristic of the impact hammer that affects these pulse characteristics in the time domain will contribute to altering the force spectrum. Common changes are adding mass to the back of the impact hammer, using a "dead-blow" impact hammer (with mass beads inside the impact hammer head), using a larger impact hammer and imparting different velocities with a specific impact hammer will all affect the frequency content. Note that the compliance and surface characteristics of the object that is being impacted will also affect the force spectrum. In particular, a compliant structure with light damping will often make it more difficult to get a single impact. The subject of multiple impacts is discussed in the next Section.

It is important to note that the characteristic of the force spectrum need not be flat in the frequency range of interest as long as (a) there is some excitation and (b) the structure being tested is essentially linear. An order of magnitude variation in the force spectrum across the frequency range of interest is not uncommon and perfectly acceptable. This is essentially more of a signal to noise ratio (SNR) than anything else. While impact testing can be used for nonlinear system, it is generally not advisable due to the difficulty in getting a repeatable impact. However, for nonlinear systems involving nonlinear damping mechanisms, a single ensemble of an impact and response can be useful for understanding the damping characteristics when a sliding window of data analysis is applied in the time domain.

Figure 21.4 represents the force spectrum for three different hammer tip compliances. Each would have been considered to be suitable for the test object chosen. For this comparison, the same sampling frequency range and input voltage range was chosen for each of the three examples showing the response captured for two different Nyquist frequencies. Based upon Fig. 21.4, it becomes obvious that the informational/energy content that is passed through to the ADC is not limited by the analog LPF and must be removed via the digital filtering process. In addition to the primary energy lobe, significant energy is contained in the signal well above the desired Nyquist frequency.

As the frequency domain plot in Fig. 21.5 (lower) reveals, the system response includes significant out-of-desired band energy which must be removed by the digital filtering process associated with the user selected Nyquist frequency. However, the voltage range set in the ADC must accommodate this out of band energy. As a result, the use of suitable tip with appropriate compliance and frequency domain characteristics becomes even more critical if optimal sampled/digitized dynamic range data is to be obtained.

21.3.1.1 Multiple Impacts

From a theoretical viewpoint, multiple impacts can be utilized if the user is very careful and if windows are adjusted appropriately. The practical view, however, is to avoid multiple impacts by previewing the impact and response signals and rejecting any ensembles that show signs of a multiple impact.

Figure 21.6 shows a typical double impact characteristic in the time and frequency domains for a single ensemble of the force. When double or multiple impacts occur within the acquired data block, zeros in the resulting force spectrum are introduced. In this case, the magnitude ripple or oscillation in the force spectrum is due to the double impact within the block. While the power spectrum (and resulting response spectrum, Fig. 21.7) could theoretically be used in the averaging process, practically, due to leakage, the power spectra are distorted and the ripple effect tends to become visible in the resulting frequency response functions (FRFs). The double impacts manifest themselves as both magnitude and phase distortions in the frequency domain. While no force window was used in this case, the use of a force window when double impacts are present might eliminate the second impact from the measured signal but not from the actual energy that is applied to the structure and not from the response signal.

With respect to the response to a double impact, shown in Fig. 21.7, the deleterious effect is primarily associated with extending the exponentially decaying response in the time domain. This would increase the truncation of the response signal which would directly affect the leakage.
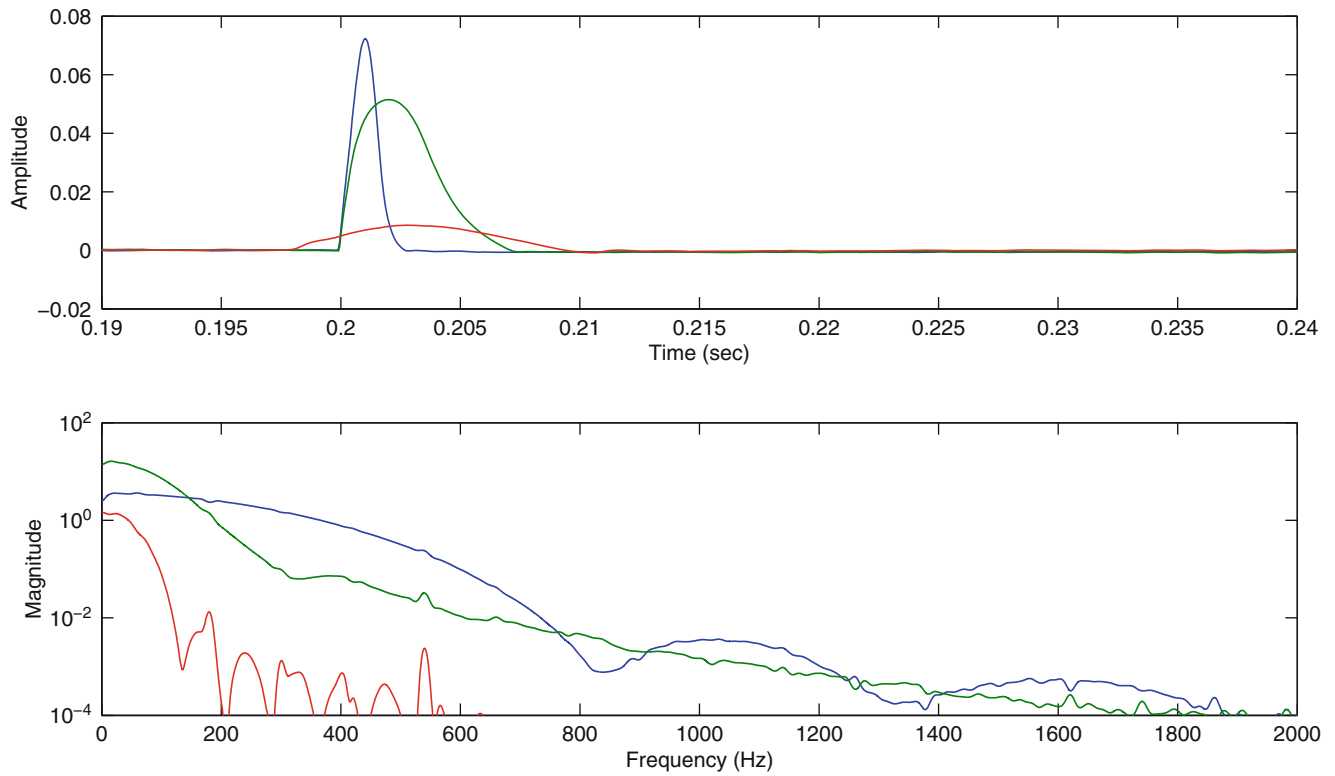
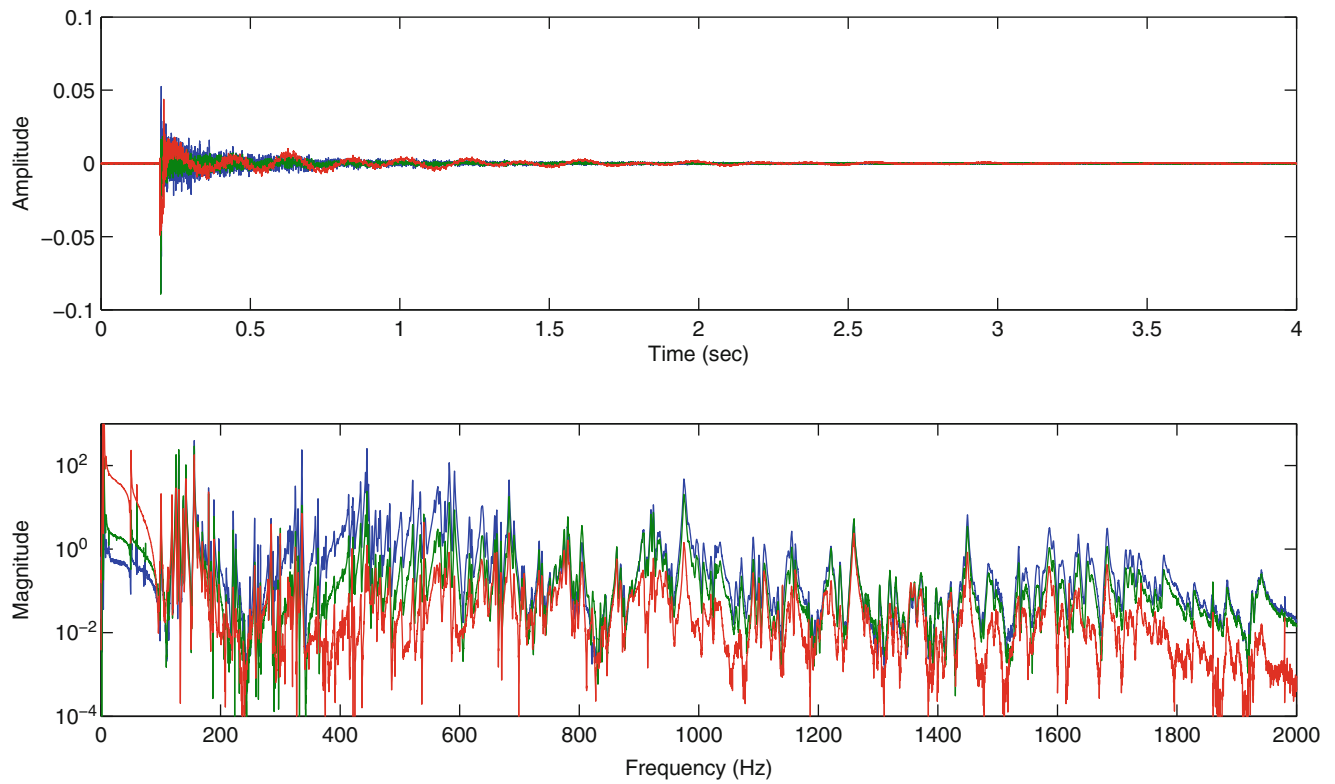**Fig. 21.4** Comparison of single impact energy distribution

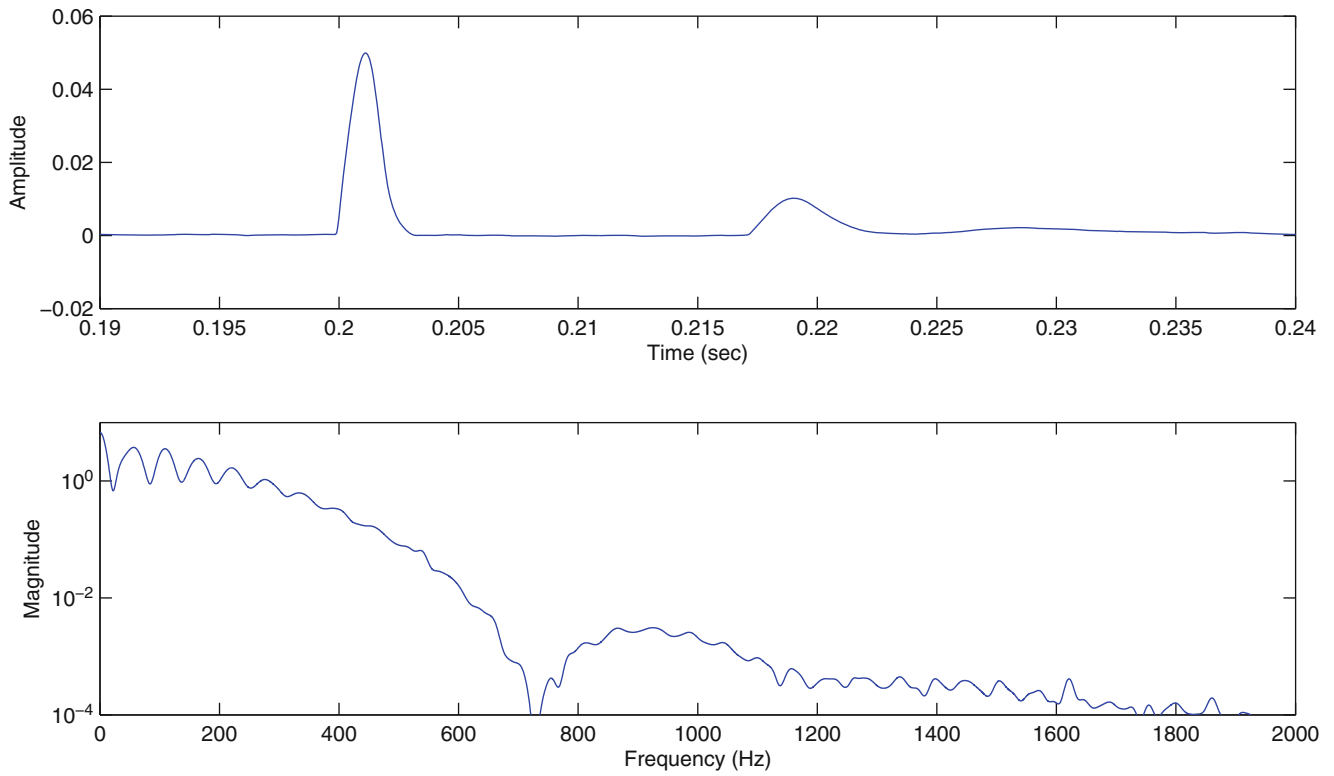**Fig. 21.5** Comparison of single response energy distribution

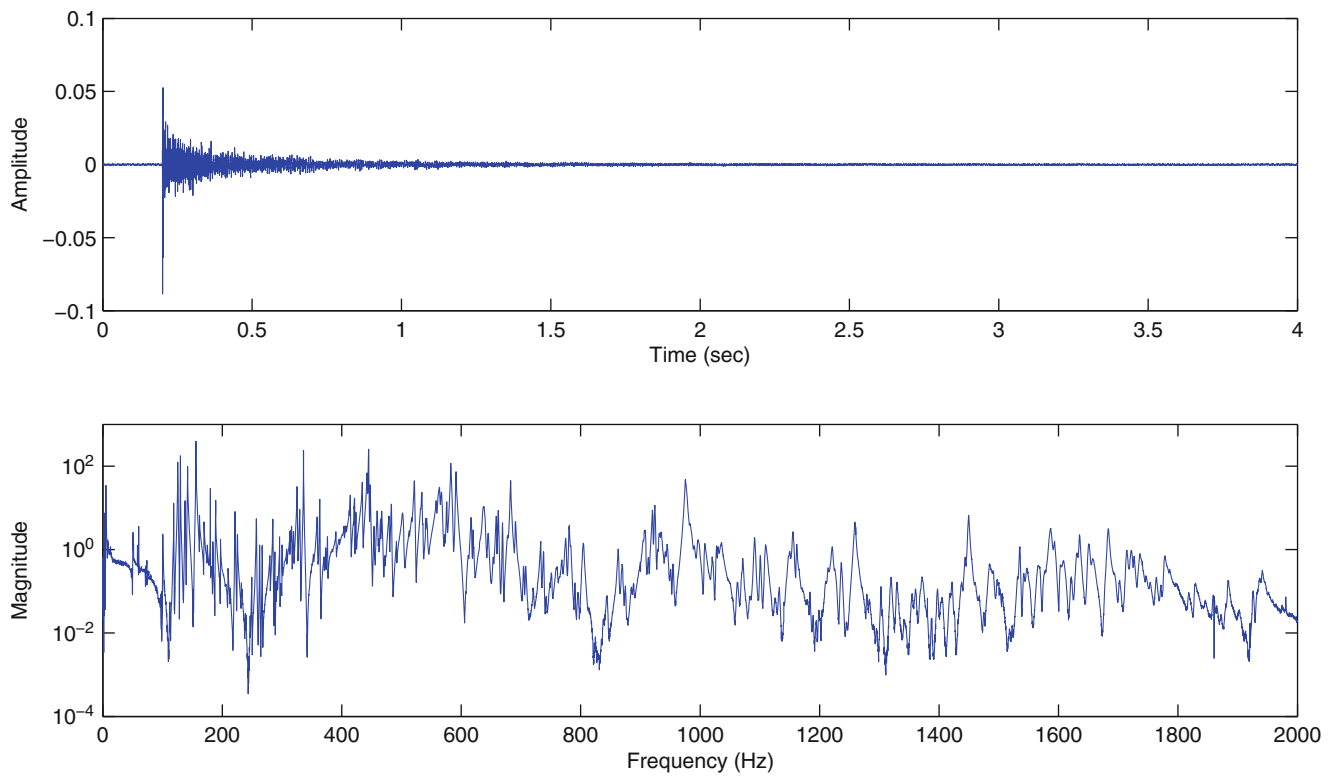**Fig. 21.6** Force spectrum to double impact

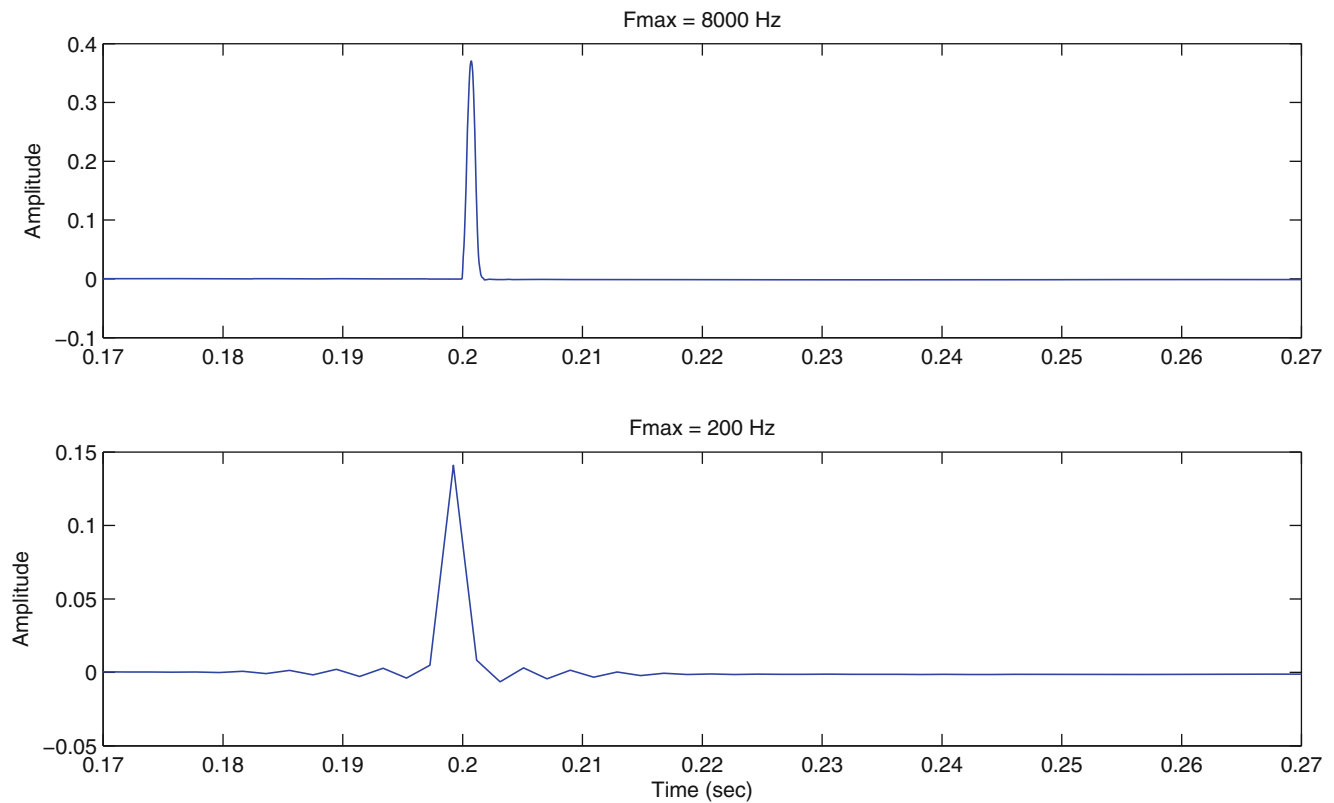**Fig. 21.7** Response spectrum to double impact

Fig. 21.8 Triggering on the impact force – pre-triggering

21.3.2 Triggering Issues

It is common to trigger the data acquisition for the impact testing case based upon the characteristic of the force signal. The trigger condition is normally set to a positive voltage and positive slope for the force channel to initiate data acquisition on *all channels*. In order to reduce the possibility of inadvertent triggers to minimal hammer motion and to make sure that all of the force pulse is captured, a pre-trigger is utilized to capture data that happens before the trigger condition is met. If a pre-trigger is utilized, the same pre-trigger should be applied to all channels to avoid the introduction of a time delay between channels and the resulting phase error. The exception to this is when impact testing is used with acoustic response. Based upon different spatial positions of any the microphones, the pre-trigger may need to be different, response channel by response channel, due to the time delays associated with the different distances between the impact location and the microphones.

The top plot in Fig. 21.8 is the force pulse captured with a pre-trigger which in this case is around 0.2 s. The amount of the pre-trigger should be kept to a minimum but does not need to be too exact. There are two reasons for this. First of all, the bottom plot of Fig. 21.8 is the impact force after it has been digitally filtered to the user defined Nyquist frequency. Note the oscillation before and after the digitally filtered force. This is part of the energy that should be retained to properly capture the characteristics of the force pulse in the band of interest.

The second reason for allowing the pre-trigger to be longer than the minimum is that this region of the force and response signals is often used for DC offset removal. If a force and/or exponential window will be applied to the data, it is important to remove any DC signal prior to the application of the windows. Otherwise, the window characteristics will distort the DC signal into energy that occurs across the frequency band.

21.3.3   Overload Issues

The overload problem is one area that has been greatly affected by the delta-sigma ADC design that is now being used in current data acquisition analyzers. Eliminating ensembles that include overloads is one of the most difficult tasks for impact testing with both historical and current data acquisition analyzers. Impact testing generates a high peak to RMS transient input and associated exponentially decaying response signals that may have significant amplitudes in response to the impact. Unless the hammer characteristics and the force spectrum of the hammer are chosen carefully, overloads will occur. Current delta-sigma ADCs no longer limit the frequency content of either signal to the frequency range of interest which contributes to overloads which may be difficult to understand. The difficulty in trapping *near overload* conditions in delta-sigma ADC designs contribute to frequency domain distortion errors that give non-physical FRF data on occasion. This means that relying on the overload detection and auto-ranging algorithms may still allow some significant data errors to occur.

A common pretest procedure, established with the historical ADC design, is to impact at the selected input location and observe the measured time histories of the input and response(s), sampled at a very high Nyquist frequency (essentially setting the digital filter in the current, delta-sigma ADC design to a very high cut-off frequency). In this configuration, the digital signal analyzer is acting as a digital oscilloscope and, with experience, this procedure may make it possible to visually identify some overload conditions. However, in the current, delta-sigma ADC design, it is often difficult to detect the overload visually and it is possible that the hardware and software overload detection will miss the *near overload* condition. This near overload condition may result in a distortion error that can be observed in the resultant FRF data, if the user is carefully watching for it. Unfortunately, the use of larger and larger number of channels in impact testing causes the users to increasing rely on the auto-ranging algorithm and the associated overload detection software and hardware.

However, the current, delta-sigma ADC design makes this overload situation difficult to detect visually. Therefore, users rely on the data acquisition hardware to detect an overload and interact with the software to flag the problem, possibly rejecting the data automatically and/or setting the input gain higher or lower as appropriate. This all begins with the auto-ranging process which will need to be repeated for each time the impact force is moved to a new point. In order to start the auto-ranging and overload detection process, a continuous series of impacts are applied at the input point. This allows the data acquisition to be set to levels that will reduce the potential for overloads. Obviously, during this auto-ranging phase, if a large input occurs, the overload detection hardware allows the data acquisition software to detect the overloads and to reset the input gain on each channel appropriately.

Once the actual measurement cycle begins, if the force channel overloads, then all the channels have to be rejected for that ensemble. If the any of the response channels overload, then the normal procedure is to reject all channels as well. However, if a response channel overloads, then only that ensemble for that channel needs to be rejected. This results in each response channel potentially having a different number of averages. This approach has been evaluated but is rarely implemented as it requires more user interaction.

This potential overload problem is documented in the following figures. Currently, it appears that high frequency overloads (overloads due to energy above the user's frequency range of interest) are causing distortion errors in measured FRFs in most digital data acquisition systems. This phenomenon has been observed in hardware and software systems from more than one vendor.

As an initial example shown in Fig. 21.9, the overload distortion problem can be observed in a typical FRF measurement even when some care is taken in detecting overloads by visually observing the time domain signals. Note the difference in the definition of the anti-resonance noted at location A in the two measurements. More important to note is the phase distortion at location B in the two measurements. The distorted FRF shows a phase loss at the anti-resonance which, physically, should be a phase gain. This was particularly troublesome and notable when trying to work with the characteristics of a physical system in this low frequency region. At first this was thought to be just a graphical plotting mistake involving phase wrapping and unwrapping but this is not the case.

21.3.3.1   Overload Issues Test Cases

The following figures represent a series of test cases investigating the effect of overload. The data was captured simultaneously by replicating one force (input) channel and one response (output) channel to multiple frontend channels set to different voltage ranges and different frequency spans. Two voltage ranges were chosen, 0.1 v and 1.0 v, and two frequency spans, 200 Hz and 8,000 Hz. The result is that the four different voltage/span cases for each channel were captured simultaneous.
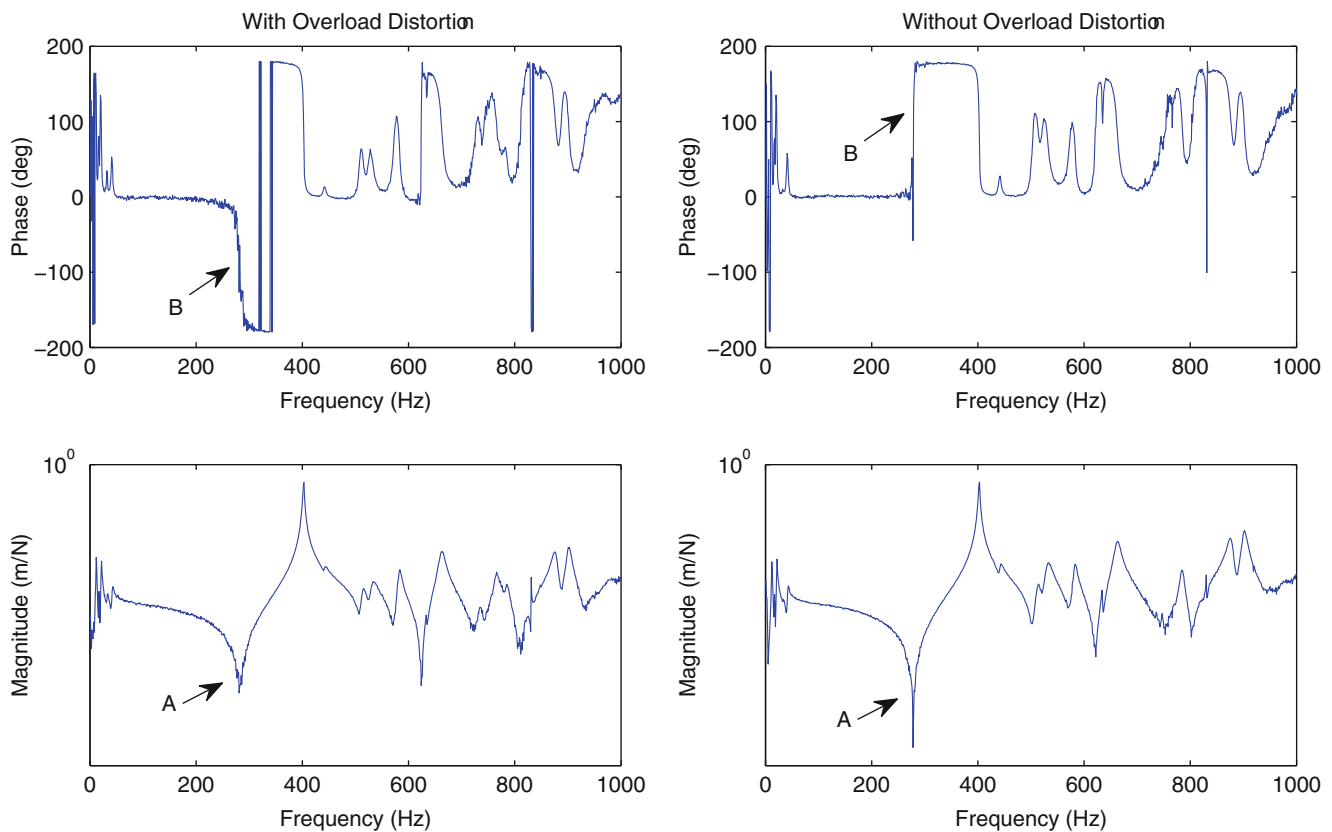
Fig. 21.9 FRF measurement exhibiting overload distortion

Figures 21.10 and 21.11 represent the time and frequency domain results of the 8,000 Hz and 200 Hz spans without overload. The markers A and B on each plot represent the region of the plot that will be emphasized in the following overload figures (Figs. 21.12, 21.13, 21.14, 21.15, 21.16, and 21.17). In many cases, the difference between the overloaded and the non-overloaded measurements will be very slight. In some cases, the difference will only be practically detectable on the full 8,000 Hz span. Unfortunately, unless the user explores frequency ranges other than the frequency range of interest, this distortion is not observable. In all FRF cases, only one ensemble is shown to make sure that the resultant distortion is linked to the time domain overload. This results in more noise on the FRF data but clearly shows the distortion in both FRF magnitude and phase.

21.3.4 Impact Hammer Calibration

Current impact hammers involve a load cell that is embedded in the head of the hammer. Even with ideal placement of the load cell, the force that is measured is not exactly the force that enters the structure at the hammer tip. The force measured by the load cell is the force acting across the load cell, which is not equal to the external force acting on the tip of the hammer during the impact.

In order to calibrate an impact hammer, a free-free, rigid mass is impacted with the force vector acting through its center of mass. The external force acting on the mass is equal to external force acting on the hammer tip which is equal to external force acting on the hammer. The force acting on the rigid mass is equal to the mass of calibration mass times is acceleration (Newton's Second Law, f = ma). The acceleration of the rigid mass is measured with an accelerometer. The mass line of the (acceleration over force) FRF is equal to the reciprocal of the mass of the calibration mass, in whatever units are desired.
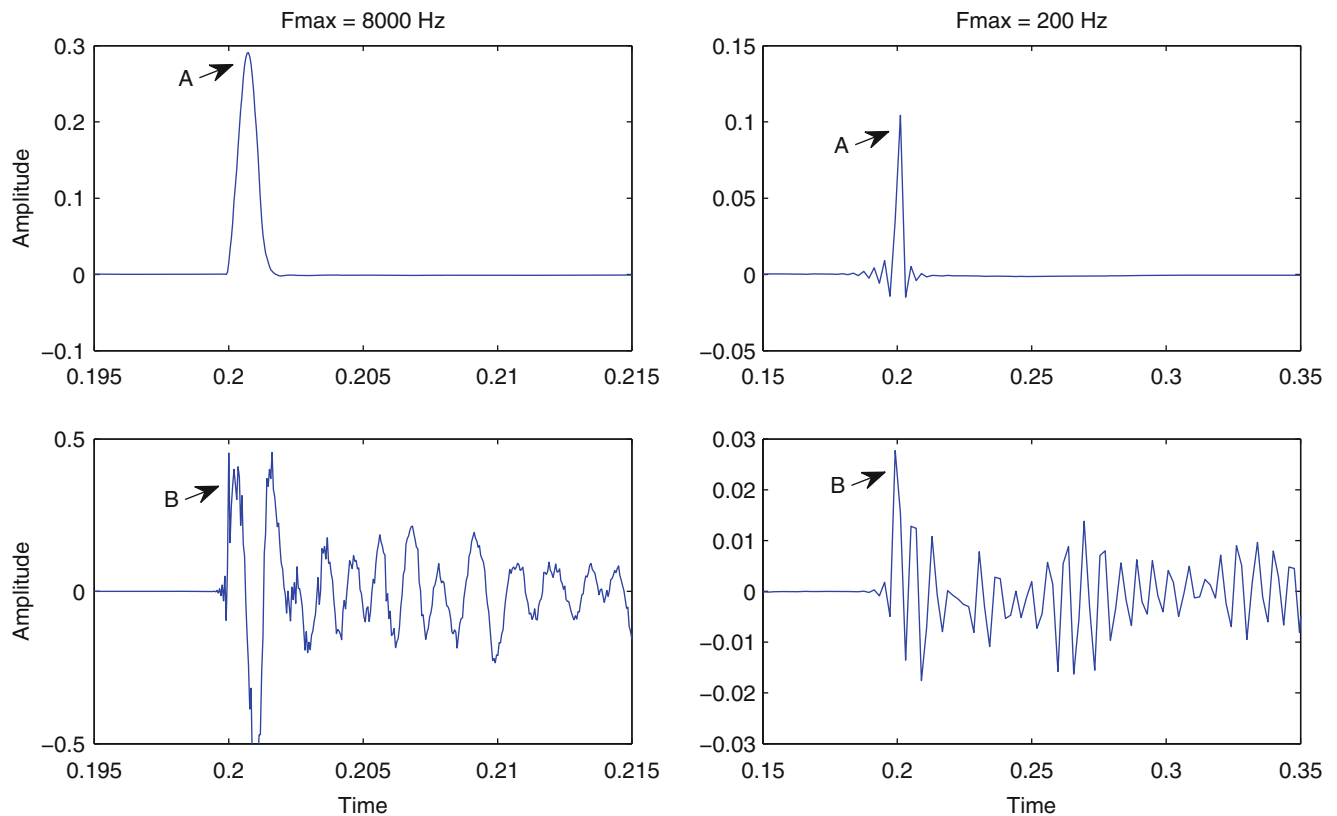
Fig. 21.10 System input/response without overload

It is common to adjust the hammer tip characteristics to allow for a drop of 10–20 dB (factor of 10–100) in force spectrum magnitude over the frequency range of interest. As long as the structure being tested is linear, this does not pose any problems and minimizes the energy that excites system dynamics above the user's frequency range of interest. This will allow the channels gains to be set as optimally as possible during the auto-ranging procedure.

If the accelerometer calibration is known (or updated with a separate calibration method), then the true calibration of the force from the impact hammer, at a level that is appropriate for the test involved, can be determined in order to get the correct value for the calibration mass. It should be noted that it is not necessary for the load cell and the accelerometer to be calibrated individually as long the two sensors are always used in pairs (for example, if the testing procedure is to mount the accelerometer at a fixed point of the structure and rove the hammer to points of interest on the structure). While this is a possible approach, it is common practice to first calibrate the accelerometer and then calibrate the hammer with a known calibration mass (Fig. 21.18).

21.3.5 Force and Response Windows

In the early 1970s, the most important signal processing development for impact testing was the development of force and exponential windows. The shift theorem states that multiplying a time function by an exponential function will shift the damping and/or frequency axis in the transformed domain. In other words, the apparent damping of system can be changed in a predictable way, simply by multiplying the unit impulse response measurement of a system by a damped exponential. Inversely, it became apparent that this could be used as a window to eliminate errors due to the time domain truncation of the response signal (leakage) and to improve the signal-to-noise of impact measurements. As result, an exponential window can be applied to both the input force and the output response signal. An additional force window can be applied to the force signal to eliminate noise on the force channel after the impact since this noise is not actual input energy that excites the system being tested. These windows have been documented in a number a references [4–7]. Figure 21.19 shows an example of the force and response (exponential), time domain windows that are used in impact testing. It should be noted that if an
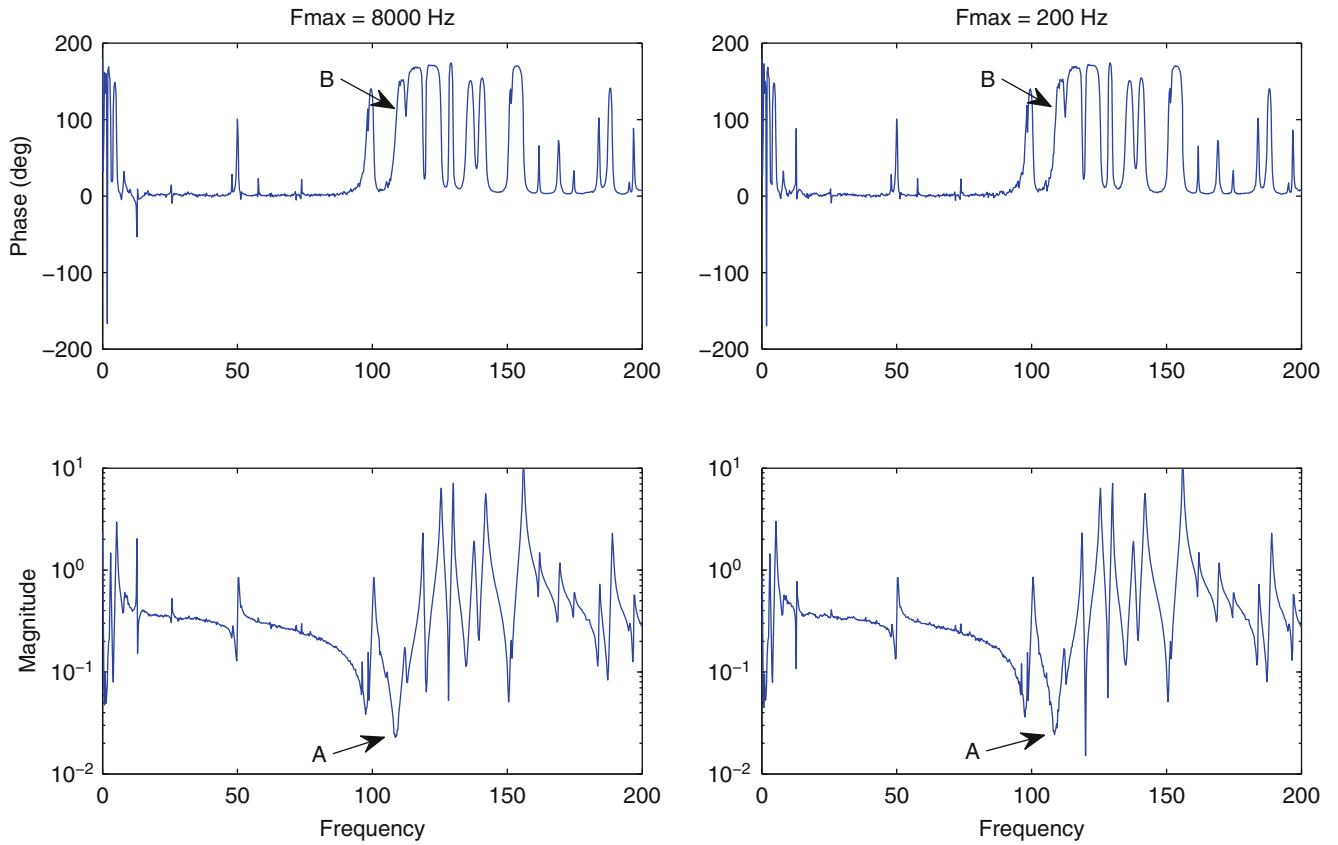
Fig. 21.11 System FRF without overload

exponential window is applied to the response, the same exponential window must be applied to the force window to allow for the proper damping correction [7].

The damping effect of the exponential window can easily be corrected in the frequency domain once the damping is estimated from an FRF. Primarily, the response (exponential) window may add significant damping to the resultant frequency response function. This can only be corrected after the modal damping for each mode is found.

$$h_{pq}(t) = \sum_{r=1}^{2N} A_{pqr} e^{\lambda_r t}$$

$$e^{\beta t} h_{pq}(t) = e^{\beta t} \sum_{r=1}^{2N} A_{pqr} e^{\lambda_r t}$$

$$e^{\beta t} h_{pq}(t) = \sum_{r=1}^{2N} A_{pqr} e^{\beta t} e^{\lambda_r t}$$

$$e^{\beta t} h_{pq}(t) = \sum_{r=1}^{2N} A_{pqr} e^{(\lambda_r + \beta) t} = \sum_{r=1}^{2N} A_{pqr} e^{\widehat{\lambda_r} t}$$

$$\widehat{\lambda}_r = \widehat{\sigma}_r + j\widehat{\omega}_r = (\sigma_r + \beta) + j\omega_r$$

$$\widehat{\sigma}_r = \sigma_r + \beta$$

$$\sigma_r = \widehat{\sigma}_r - \beta$$

$$\omega_r = \widehat{\omega}_r$$

Note that, while the damping correction of the exponential window is possible, the use of the exponential window for lightly damped systems may cause modal parameter estimation problems when the lightly damped modes are close in frequency. The added numerical damping provided by the exponential window may make it more difficult to identify and estimate the
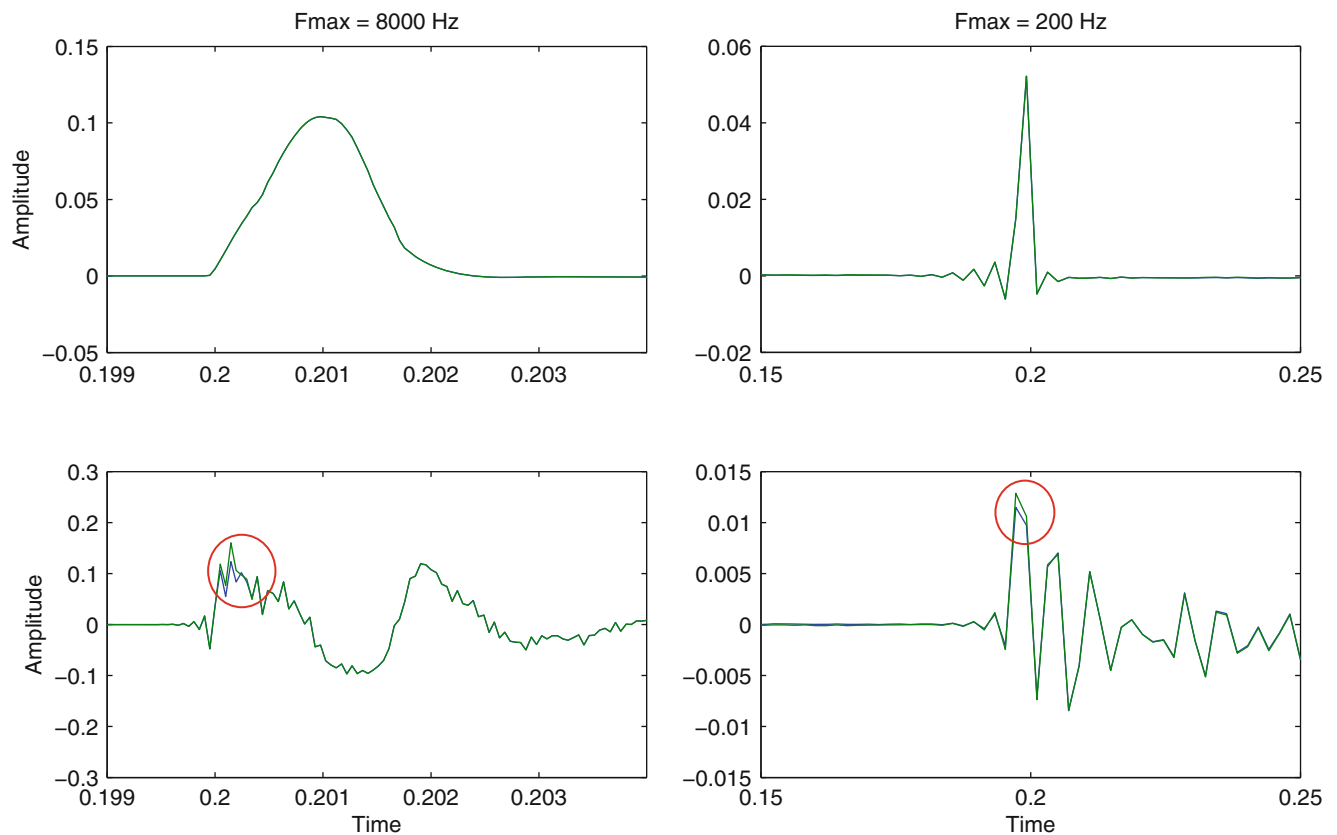
Fig. 21.12 System input/output exhibiting minimal overload distortion

individual frequency and damping values for each mode. If these estimates are inaccurate due to this numerical damping distorting the FRF measurement or there is noise on the data, when the damping correction is applied, the corrected estimate of the damping factor can become slightly positive (physically, a passive structural system must have negative damping factors). This must be recognized as a numerical error and treated accordingly. Since the alternative is an incorrect damping estimate due to the leakage error, this issue is normally considered a reasonable problem to be accommodated.

21.3.6 Other Common Issues

Another frequent source of error, or loss of measurement quality, which is not related to either DSP or system noise, is an inconsistency in force input location or direction due to either user lapse of attention or extreme difficulty of access to a particular input location. It is not uncommon to have an intermediate measurement result that is clean and then, in the process of looking from the test article to the computer screen and back to the article again, to hit a location or direction close to, but not identical with, the previous averaged ensembles. The result is to average in a data ensemble with slightly different input–output characteristics. Because impact testing generally uses only a few ensembles in its averaging process, the effect upon the computed FRF and Coherence is generally quite dramatic. The anti-resonances tend to fill in and there a general loss of coherence. Figure 21.20 provides an example of this error where the first three ensembles were hit with a consistent location and direction. Then a fourth ensemble was added which represents a user lapse where a wrong, but nearby, location was hit.
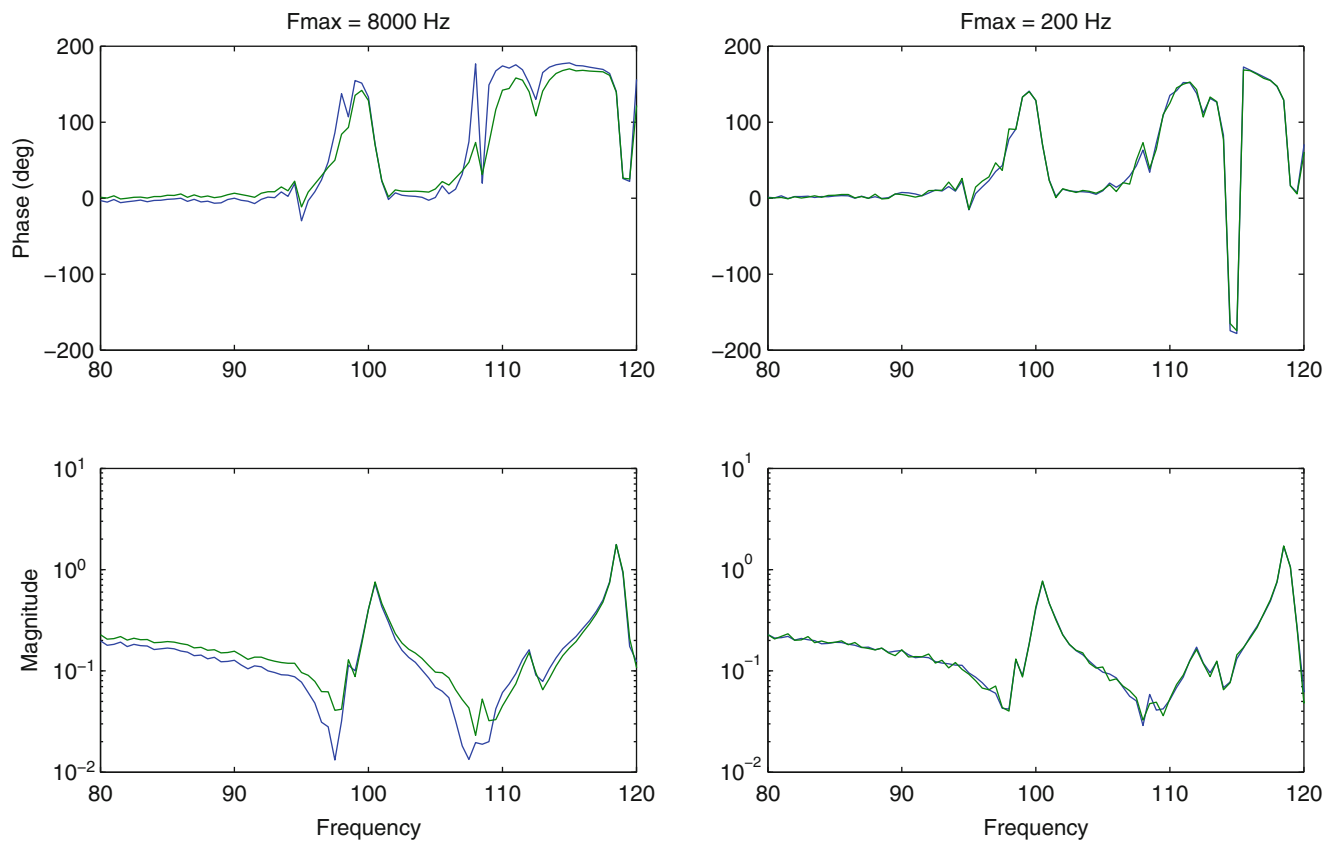
Fig. 21.13 System FRF exhibiting minimal overload distortion

21.3.7 *Reducing External Noise and Non-linear Effects*

One of the negative aspects of the exponential impact window is that periodic noise (periodic noise with respect to the length of the time domain FFT window) components and/or DC offsets are smeared by the exponential window over a frequency range centered on the frequency of the periodic noise. The DC component and frequency components due to noise (like 60 Hz) that were periodic in the window were filtered by taking the FFT of both the input and response channels and setting the Fourier coefficient of the noise components to the mean values of the adjacent Fourier coefficients. The DC component could be removed by removing the zero frequency Fourier coefficient in this process. The data were then transformed back into the time domain. The force/exponential window could then be applied to the filtered force and response signals. Once pre-triggering was available (around 1980), the DC offset could be determined from the pre-triggered section of the data and removed directly in the time domain by subtracting the offset from the data.

For noise signals which are not periodic in the window, a technique which has been used with some success is to use a full block pre-trigger, process this block for periodic and non-periodic noise components and then generate a time block of noise which can be subtracted from the data block being processed. This must happen before any windows are applied to the impact data. This has been used with some success on rotating systems, particularly large steam turbine generator sets.
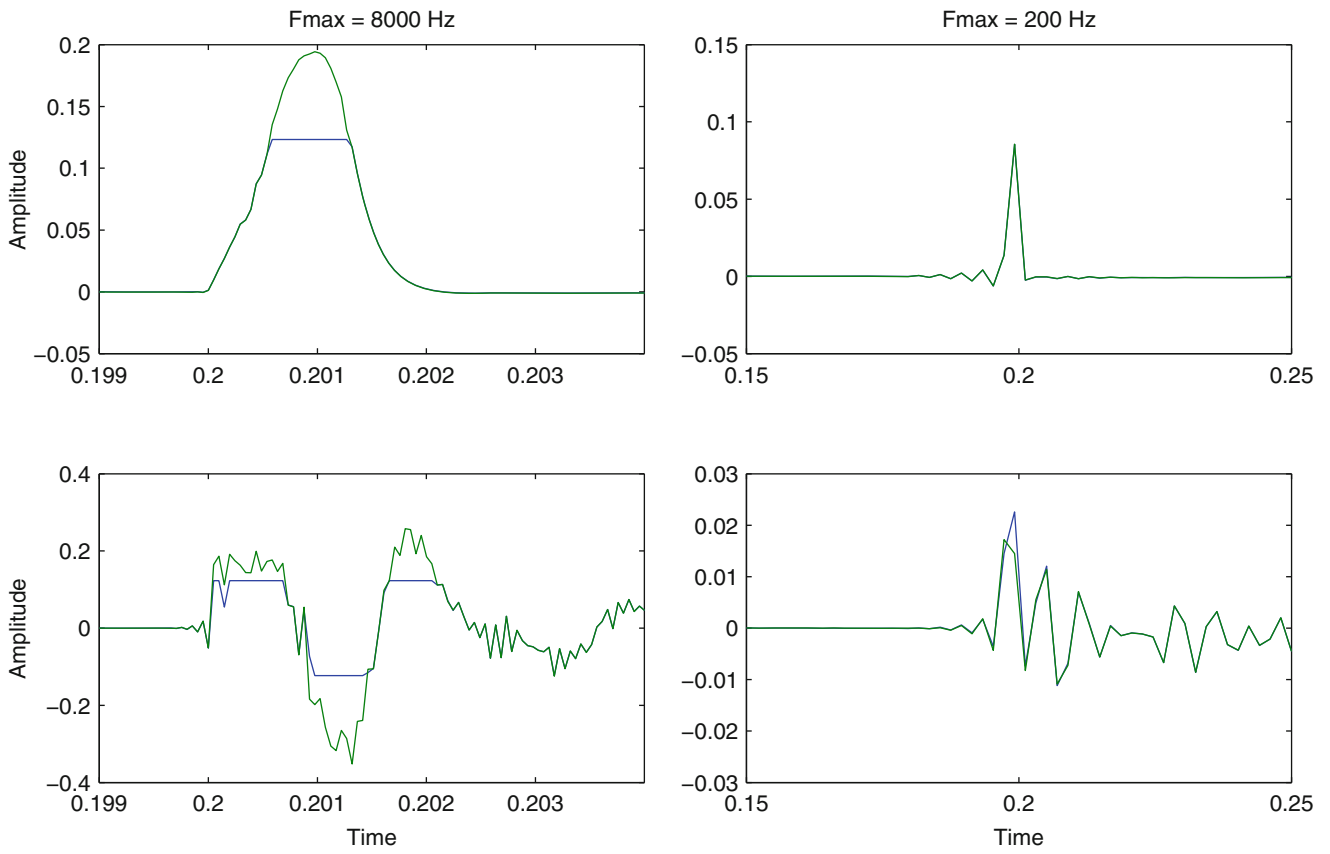
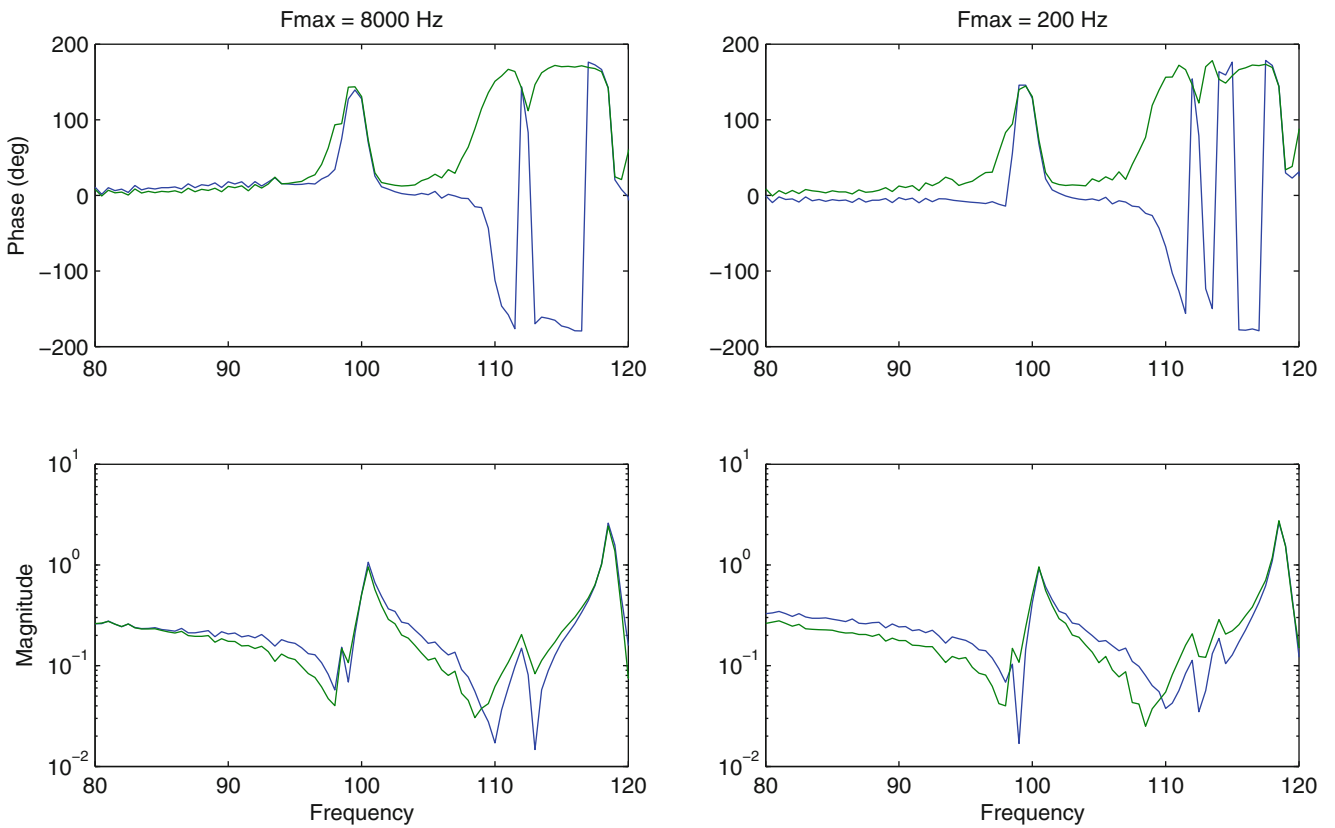**Fig. 21.14** System input/output exhibiting overload distortion

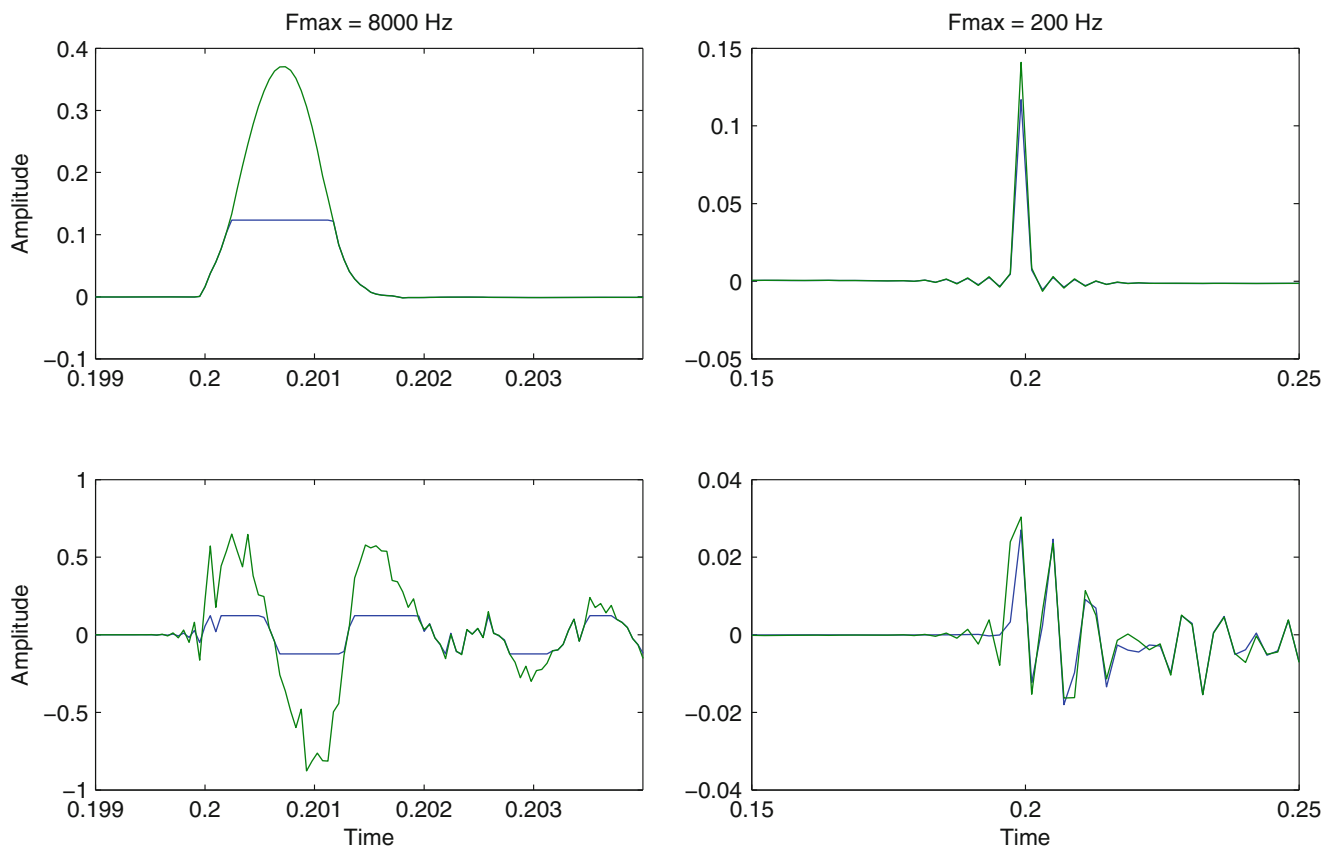**Fig. 21.15** System FRF exhibiting overload distortion

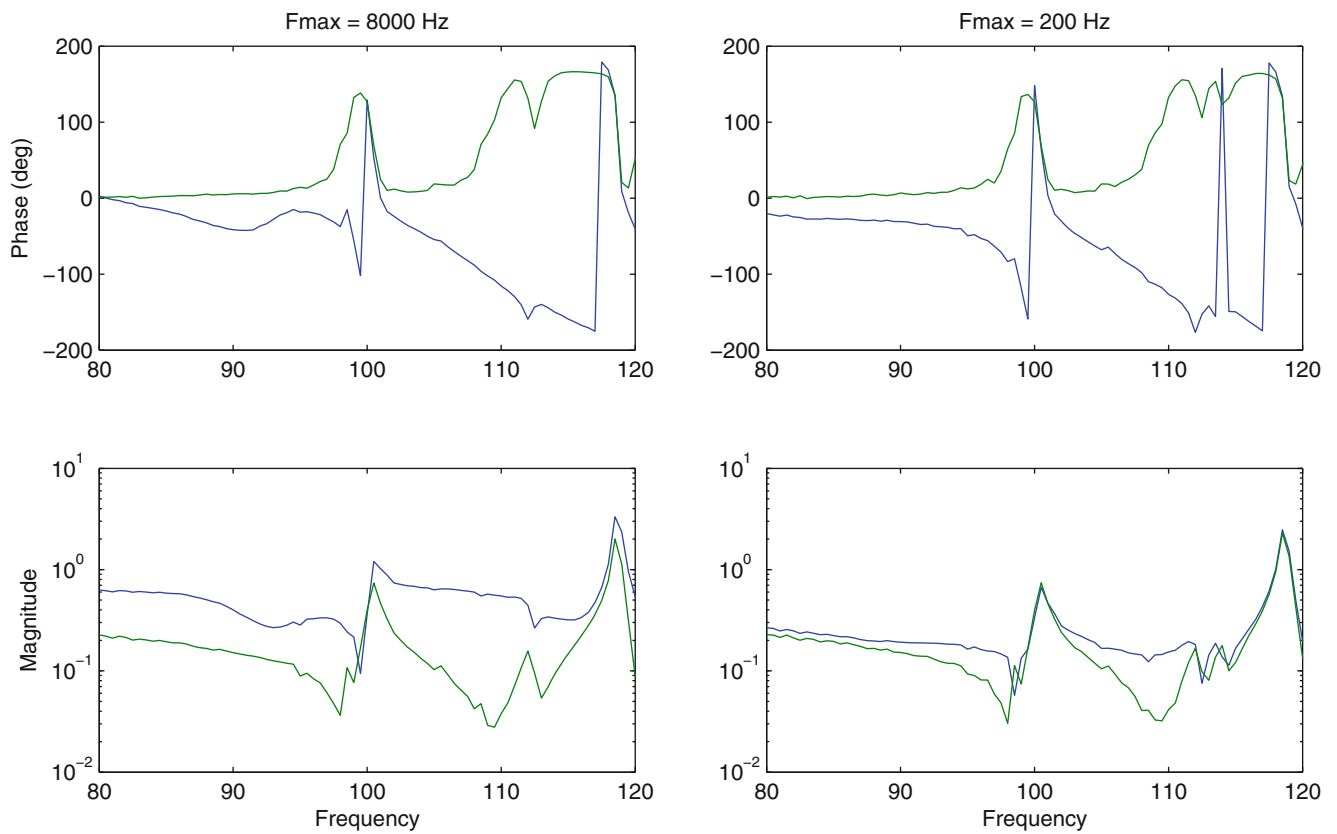**Fig. 21.16** System input/output exhibiting significant overload distortion

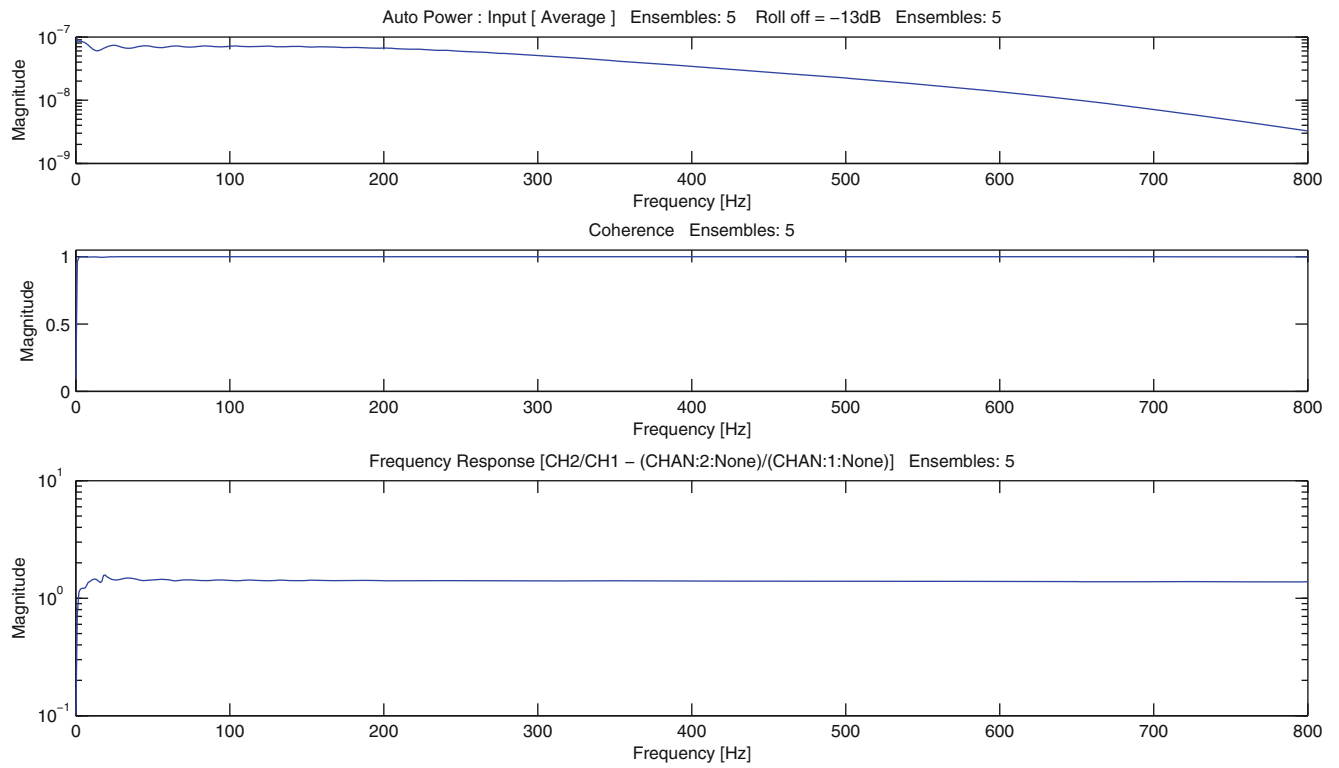**Fig. 21.17** System FRF exhibiting significant overload distortion
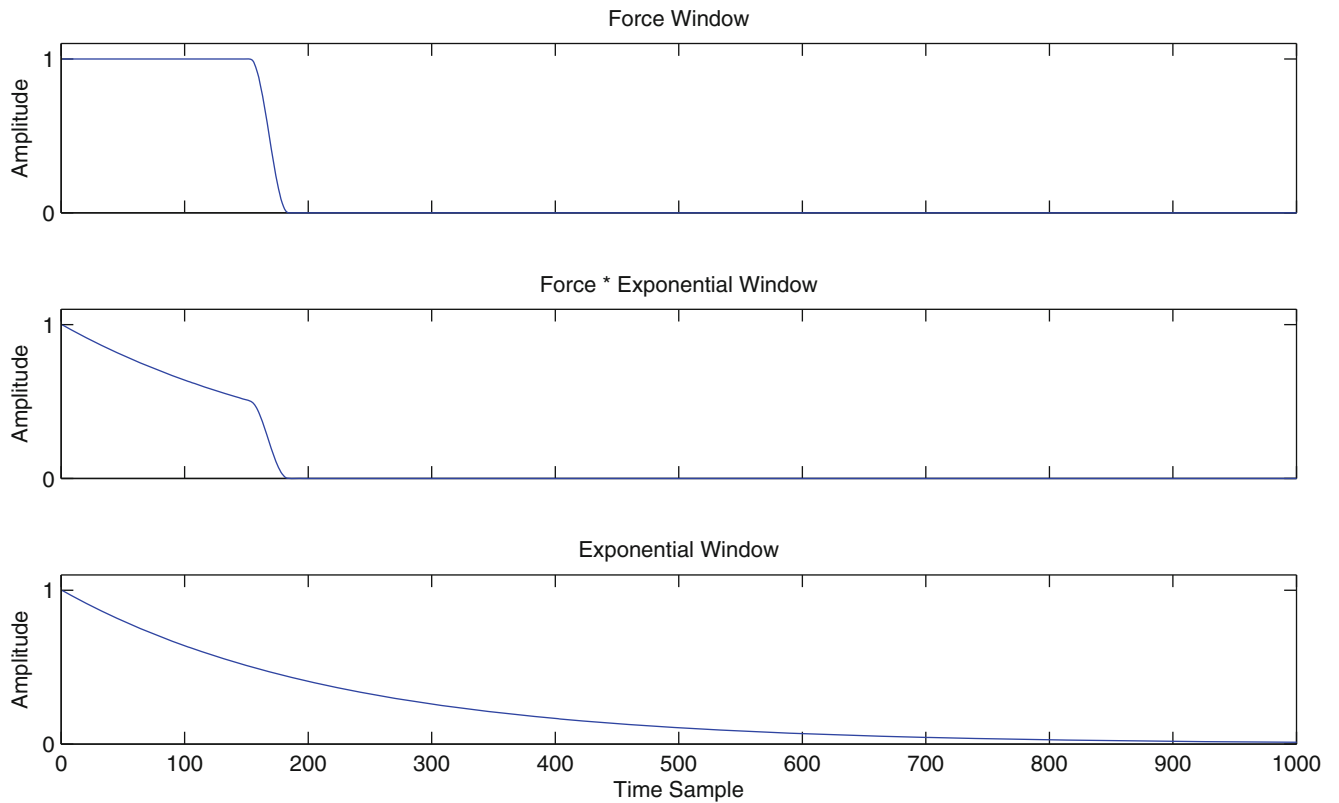
Fig. 21.18 Ratio calibration example

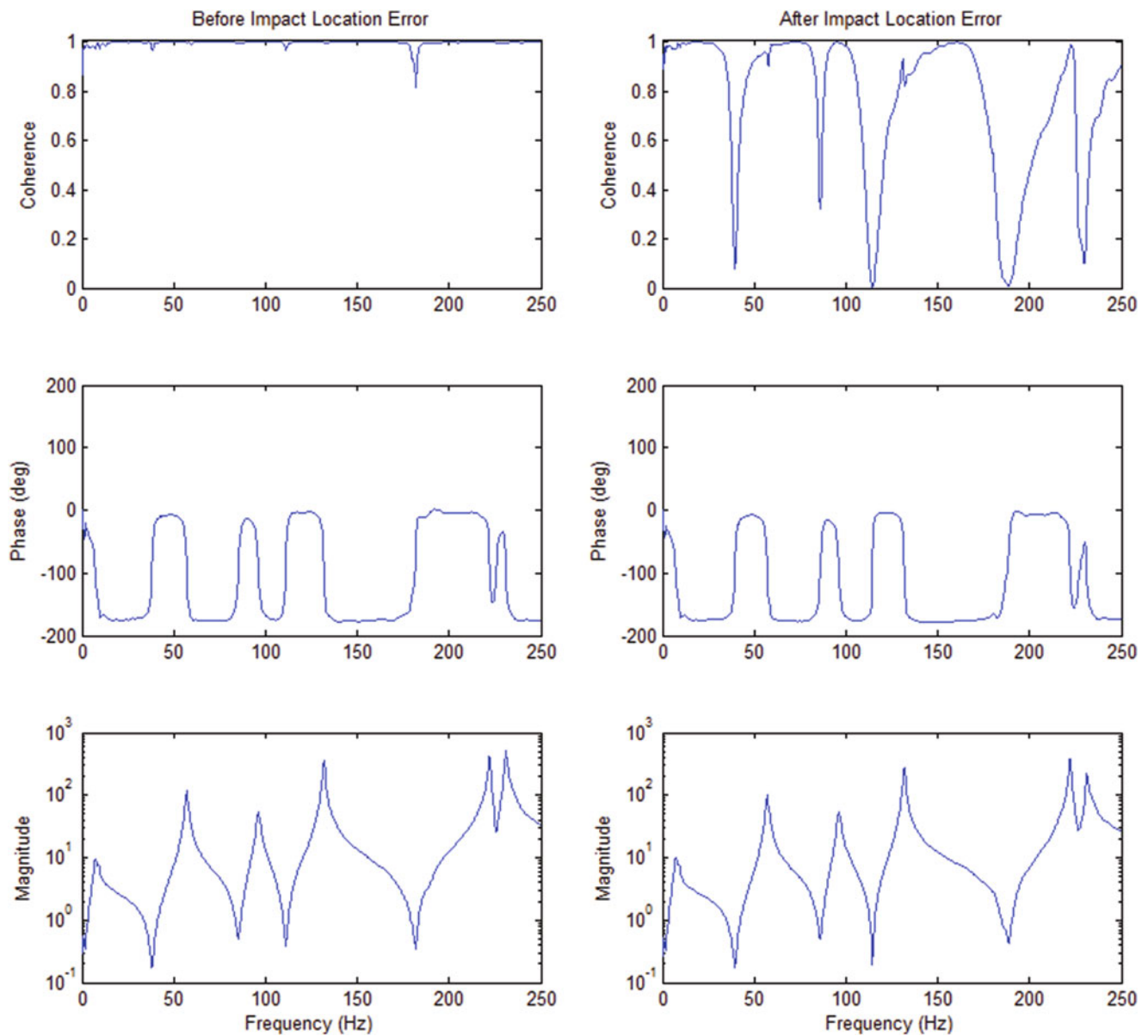**Fig. 21.19** Typical force and response windows

Fig. 21.20 Comparison of FRF/COH before and after ensemble with impact location error

However, in many cases the ambient noise in the testing environment is too large and the methods mentioned above cannot be reasonably applied. In this case, one possible solution is to shut down most or all the ambient, environmental noise sources. This technique has been used in a number of industrial situations by conducting the test during a third shift, on the weekend or a holiday.

21.4 Summary/Conclusions

Impact testing is an important testing methodology that has evolved over the last 40 years. While impact testing appears to be a very simple method, obtaining good FRF measurements, compared to other test methodologies is not trivial. Great attention must be paid to the details, particularly due to the transient nature of the signals. The process begins with force spectrum adjustment via the hammer size and tips and continues through properly pre-triggering and recording the time domain signals, careful inspection of both time and frequency domain data for the possibility of overloads, estimation of

FRFs in the presence of ambient noise and finally correcting any damping estimation in response to the application of exponential windows. While many of these issues remain the same with only minor refinement over the last 40 years, it is particularly important to recognize the difference in the data acquisition hardware has resulted in the need to pay particular attention to the overload problem.

References

1. Morse IE, Shapton WR, Brown DL, Kuljanic E (1972) Application of pulse testing for determining dynamic characteristics of machine tools. In: 13th international machine tool design and research conference, University of Birmingham, Birmingham
2. Hewlett Packard Corporation (1972) Dynamic testing of mechanical systems using impulse testing techniques. HP Application Note 140–3
3. Allemang RJ, Graef T, Powell CD (1974) Dynamic characteristics of rotating and non-rotating machine tool spindles. ASME paper number 73-DET-29, ASME Trans J Eng Ind Ser B 96(1):343–347
4. Brown DL (1976) Grinding dynamics. PhD dissertation, Department of Mechanical Engineering, University of Cincinnati
5. Halvorsen WG, Brown DL (1977) Impulse technique for structural frequency response testing. Sound and Vibration Magazine, Nov 1977, pp 8–21
6. Fladung WA (1994) Multiple-reference impact testing. MS thesis, Department of Mechanical Engineering, University of Cincinnati
7. Fladung WA, Zucker AT, Phillips AW, Allemang RJ (1999) Using cyclic averaging with impact testing. In: Proceedings of the SEM-IMAC, 7 pp

Impact Testing Bibliography[1]

Agardh L (1994) Impact excitations of concrete highway bridges. In: Proceedings, SEM-IMAC
Ahn SJ, Jeong WB, Yoo WS (2004) Unbiased expression of FRF with exponential window function in impact hammer testing. J Sound Vib 277(4–5):931–944
Berman MS, Li TH (2001) High-energy modal excitation technique utilizing powder-actuated impact tool. In: Proceedings, SEM-IMAC
Bissinger G (1993) Merging microphone and accelerometer hammer-impact modal analysis measurements: working example -the violin bow. In: Proceedings, SEM-IMAC
Bissinger G, Chowdury M (1990) Comparison of modal analysis measurements with microphone and accelerometer on hammer-impacted structures. In: Proceedings, SEM-IMAC
Bono RW, Lally MJ, Hunt VJ, Aktan AE, Brown DL (1996) Portable, controllable impact excitation for civil infrastructure. In: Proceedings, SEM-IMAC
Brandt (2010) Impact excitation processing for improved frequency response quality. In: Proceedings, SEM-IMAC, pp 7
Brown DL (1679) The weaknesses of impact testing. In: Proceedings, SEM-IMAC, pp 1672–1676
Brown DL, Witter MC (2010) Review of recent developments in multiple-reference impact testing. Sound Vib Mag, pp 8–16 In: Proceedings, SEM-IMAC, pp 18
Brown DL, Carbon GD, Ramsey K (1977) Survey of excitation techniques applicable to the testing of automotive structures. SAE Paper Number 770029, pp 16
Brown DL, Phillips AW, Witter MC (2011) Practical trouble shooting test methodologies. In: Proceedings, SEM-IMAC, pp 12
Carne TS, Stasiunas ET (2006) Lessons learned in modal testing-part 3: transient excitation for modal testing, more than just hammer impacts. Experimental Techniques, May/June, 2006, pp 69–79
Catbas FN (1997) Investigation of global condition assessment and structural damage identification of bridges with dynamic testing and modal analysis. Ph.D. Dissertation, University of Cincinnati, Department of Civil and Environmental Engineering
Catbas FN, Lenett M, Brown DL (1997) Modal analysis of multi-reference impact test data for steel stringer bridges. In: Proceedings, SEM-IMAC
Champoux Y, Paillard B, Machéto D (2001) Moment excitation using two synchronized impact hammers. In: Proceedings, SEM-IMAC
Chouychai T, Vinh T (1986) Analysis of non linear structure by programmed impact testing and higher order transfer function. In: Proceedings, SEM-IMAC
Chouychai, Vinh T (1987) Impact testing of non-linear structures. In: Proceedings, SEM-IMAC
Corelli DA, Brown DL (1984) Impact testing considerations. In: Proceedings, SEM-IMAC
Correlli DL, Zimmerman RD (1990) Electric impact hammer – a performance comparison between the PCB electric impact hammer and conventional impact hammers. In: Proceedings, SEM-IMAC
Dillon M, Fladung B, Brown DL (1996) Improved impact testing throughput by using a 3D digitizing system. In: Proceedings, SEM-IMAC
Doebling SW, Farrar CR, Cornwell PJ (1997) A statistical comparison of impact and ambient testing results from the Alamosa Canyon bridge. In: Proceedings, SEM-IMAC
Dong J, McConnell KG, Atfonzo M, Golovanova L (1998) Error reduction of measured impact forces and their lines of action via cross sensitivity studies. In: Proceedings, SEM-IMAC

---

[1]The following is a partial list of published articles over the last forty years that contribute to the background of the methodologies involved with impact testing. There are literally hundreds of published articles if all application examples are included. Our apologies to any author whose publication(s) have been omitted.

Fladung WA (1994) Multiple-reference impact testing. MS Thesis, University of Cincinnati, Department of Mechanical Engineering

Fladung WA (1997) Windows used for impact testing. In: Proceedings, SEM-IMAC

Fladung WA, Brown DL (1993) Multiple reference impact testing. In: Proceedings, SEM-IMAC

Fladung WA, Rost RW, Brown DL (1994) Further developments of multiple reference impact testing. In: Proceedings, SEM-IMAC

Fladung WA, Rost RW, Poland JB (1994) The modal punch: a new impacting development. In: Proceedings, SEM-IMAC

Fladung WA, Zucker AT, Phillips AW, Allemang RJ (1999) Using cyclic averaging with impact testing. In: Proceedings, SEM-IMAC

Gade S, Herlufsen H (1993) A hand-held exciter for field mobility measurements – an alternative to the impact hammer method. In: Proceedings, SEM-IMAC

Hemez FM, Doebling SW, Rhee W (2000) Validation of nonlinear modeling from impact test data using probability integration. In: Proceedings, SEM-IMAC

Hemez FM, Wilson AC, Doebling SW (2001) Design of computer experiments for improving an impact test simulation. In: Proceedings, SEM-IMAC

Ibrahim SR, Mikulcik EC (1977) A method for the direct identification of vibration parameters from the free response. Shock Vib Bull 47(4): 183–198

Keiffer J, Bissinger G (2001) Planar Grid vs. Geometry-controlled hammer-impact/scanning laser modal analysis. In: Proceedings, SEM-IMAC

Kessler CL, Kim J (1999) Application of triaxial force sensor to impact testing of spinning rotor systems. In: Proceedings, SEM-IMAC

Kim HS, Schmidtz TL (2007) Bivariate uncertainty analysis for impact testing. Meas Sci Technol, 18(11)

Kong FL, Liang Z, Lee GC (1996) Responses of a model bridge under impact and ambient excitation. In: Proceedings, SEM-IMAC

Lenett M, Catbas N, Hunt V, Aktan AE, Helmicki A, Brown DL (1997) Issues in multi-reference impact testing of steel-stringer bridges. In: Proceedings, SEM-IMAC

Lenett MS, Helmicki AJ, Hunt VJ (2000) Multi-reference impact testing of FRP bridge deck material. In: Proceedings, SEM-IMAC

Lenett MS, Hunt VJ, Helmicki AJ, Shahrooz B (2001) Influence of FRP Decking as measured through impact test data. In: Proceedings, SEM-IMAC

Mattson SG, Van Karsen CD, Blough JR, Scheifer M (2000) Design and performance of a gas actuated impact hammer. In: Proceedings, SEM-IMAC

McConnell KG, Varoto PS (1995) The effects of window functions and trigger levels on FRF estimations from impact tests. In: Proceedings, SEM-IMAC

Meyer, Wang B, Britt S, Kazi R, Adams DE (2006) Modal impact testing of ground vehicles enabling mechanical condition assessment. In: Proceedings, SEM-IMAC, 9pp

Napolitano K, Yoder N, Brillhart R (2012) A comparison of multiple impact testing methods. In: Proceedings, SEM-IMAC, pp 331–345

Pavic RL, Pimentel R, Waldron P (1998) Instrumented sledge hammer impact excitation: worked examples. In: Proceedings, SEM-IMAC

Pickrel CR, Foss GC, Phillips S, Allemang RJ, Brown DL (2004) New concepts in Aircraft ground vibration testing. In: Proceedings, SEM-IMAC, pp 6

Rezai MK, Ventura CE, Prion HGL, Lubell AS (1997) Dynamic properties of steel plate shear wall frame by impact testing. In: Proceedings, SEM-IMAC

Seth BB, Field NL (1984) Structural dynamics characteristics using impact tests. In: Proceedings, SEM-IMAC

Sohaney RC, Nieters JM (1985) Proper use of weighting functions for impact testing. In: Proceedings, SEM-IMAC

Soom, Wang BJ (1987) Frequency domain power transfer during impact testing of structures. In: Proceedings, SEM-IMAC

Soom, Wang BJ, Trachsler T (1986) Energy transfer during impact testing. In: Proceedings, SEM-IMAC

Stanbridge AB, Martarelli M, Ewins DJ (1999) The scanning laser doppler vibrometer applied to impact modal testing. In: Proceedings, SEM-IMAC

Stenger G (1979) Step relaxation method for structural dynamic excitation. Master of Science Thesis, Department of Mechanical Engineering, University of Cincinnati, 54pp

Tamhane SK (1984) Feasibility of impact technique for studying nonlinear systems. In: Proceedings, SEM-IMAC

Tretheway MW, Cafeo JA (1992) Tutorial: signal processing aspects of structural impact testing. Int J Anal Exp Modal Anal 7(2):129–149

Trethewey MW (1997) Structural impact testing force spectra. In: Proceedings, SEM-IMAC

Van Karsen CD, Little EF (1997) The strengths of impact testing. In: Proceedings, SEM-IMAC

Varghese J, Dasgupta A (2003) Test tailoring methodology for impact testing of portable electronic products. In: Proceedings, SEM-IMAC

Witter MC, Brown DL, Bono RW (1998) Broadband 6 DOF accelerometer calibration via impact excitation. In: Proceedings, SEM-IMAC

Chapter 22
Detection of Coupling Misalignment by Extended Orbits

Michael Monte, Florian Verbelen, and Bram Vervisch

Abstract In this paper a 'SpectraQuest' demonstrator is used to introduce misalignment into a rotating machinery set-up. Depending on the coupling used in the set-up, angular and/or parallel misalignment can be brought in the rotating system. Traditionally, the data captured by accelerometers is transferred into the frequency domain in order to interpret the vibrations measured by the accelerometers. The frequency domain has proven its usefulness but even the time domain can come in handy to draw the right conclusions regarding to misalignment in a rotating set-up. Orbit plots display the integrated data captured by accelerometers, in order to display the movement of the rotating shaft. The influence of the misalignment and imbalance on these orbits will be discussed.

Keywords Machinery fault • Misalignment • Imbalance • Full spectrum • Orbit

22.1 Introduction

In rotating machinery misalignment is a serious problem [1]. It can lead to stress and it can cause severe damage leading to malfunction or even breakdown. A lot of research has been done on misalignment, and is still ongoing. Several techniques have been developed to detect misalignment and other machine faults. Some techniques found in literature are vibration monitoring [2], acoustic emission [3], thermal imaging [4] and oil particle analysis [5].

The most widespread method is the use of vibration spectra. This technique is used in this paper to detect misalignment. A lot of information can be taken out of a spectrum measured by accelerometers. The time based captured data are transformed into the frequency domain and the spectra have some characteristics for detecting single faults. The problem is when several faults are in the rotating system at the same time. More advanced techniques are necessary to draw a correct conclusion based on the spectra. Full-spectra and orbits can help to detect several machine faults [6]. In this paper the orbit is extended to a third dimension. Instead of only looking at the radial direction, the axial direction also plays an important role in detecting angular and parallel misalignment.

22.2 Experiments

The set-up used for the experiments is the Machinery Fault Simulator from SpectraQuest. Three accelerometers are used to measure the vibrations, two in the radial (*x*-horizontal and *y*-vertical) and one in the axial direction (*z*-direction). The data captured by the three accelerometers are used to build up an extended orbit plot, a three dimensional representation of the double integrated data captured on the bearing close to the coupling where misalignment is introduced to the system.

M. Monte (✉) • F. Verbelen
Department of Industrial Systems and Product Design, University of Ghent, Campus Kortrijk, Graaf Karel de Goedelaan 5, B-8500 Kortrijk, Belgium
e-mail: michael.monte@ugent.be

B. Vervisch
Department of Industrial Systems and Product Design, University of Ghent, Campus Kortrijk, Graaf Karel de Goedelaan 5, B-8500 Kortrijk, Belgium

Department of Electrical Engineering, Systems and Automation, University of Ghent, Technologiepark 914, B-9052 Zwijnaarde, Belgium
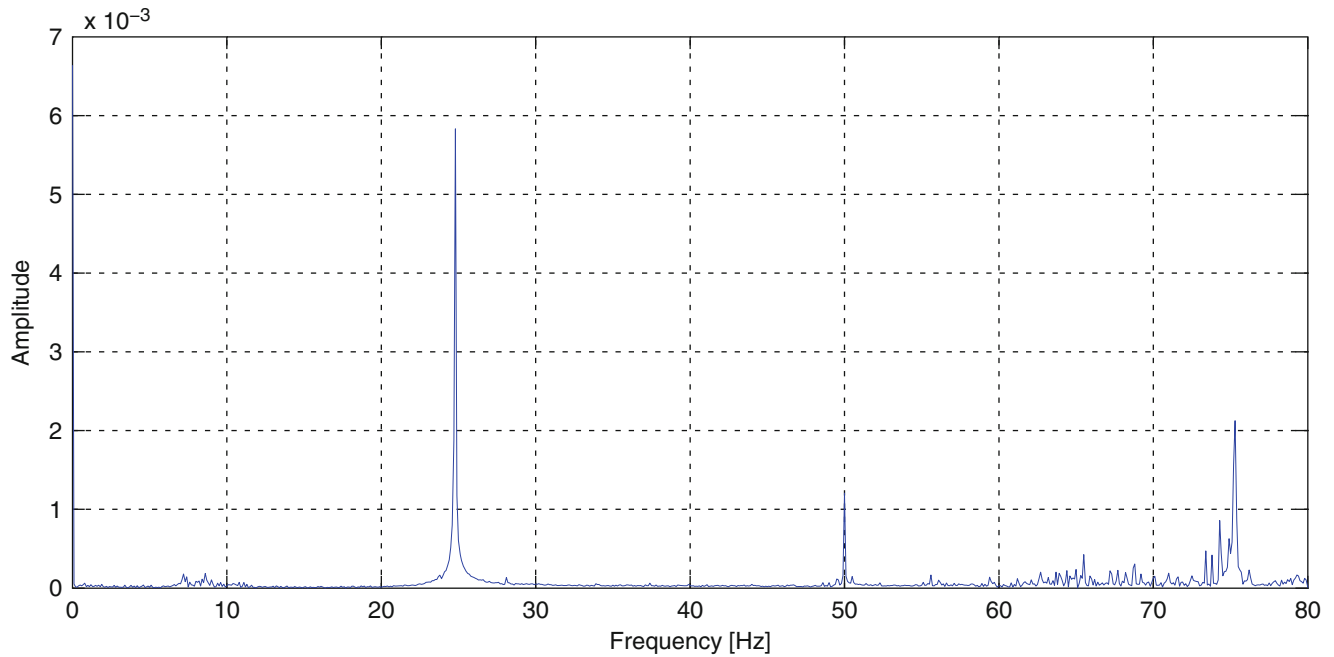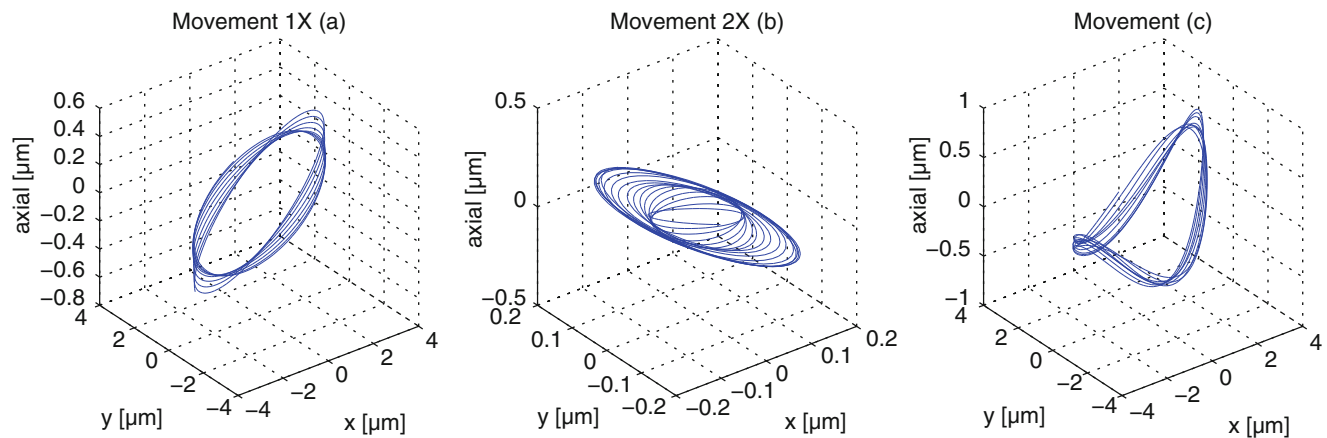
Fig. 22.1 Reference FFT at 25 Hz (horizontal)

Fig. 22.2 Three dimensional orbit at 25 Hz

A reference measurement at a rotating speed of 25 Hz from an accelerometer placed horizontal (*x* direction) is represented in Fig. 22.1. These measurements were done on a well-aligned and balanced set-up. Similar measurements were done at 35 and 50 Hz.

Subsequently a three dimensional orbit is made from the data collected from the three accelerometers (Fig. 22.2). The measurements show the movement of the 1× vibration together with the 2× vibration. The third plot is the movement of the 1× and 2× vibration together. In these plots no ellipses are shown as mentioned in previous work [6], but when the regular orbits (horizontal and vertical radial direction) are plotted ellipses appear (Fig. 22.3). It is clear that the motion in the radial direction is very limited in this set-up (Fig. 22.4).

22.2.1 Measurements on Parallel Misalignment

Next, the influence of parallel misalignment on the orbits will be discussed. On the face of it no conclusions can be made from the 3D orbit (Fig. 22.5). The shapes of the orbits are very similar and no more distortion is observed in the plot as the
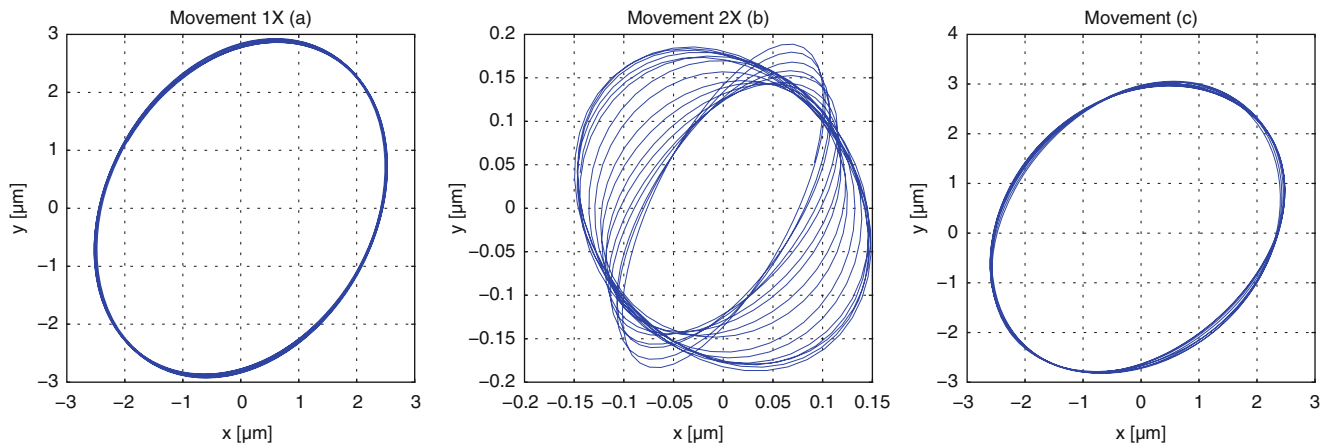
Fig. 22.3 Two dimensional orbit at 25 Hz (radial direction)
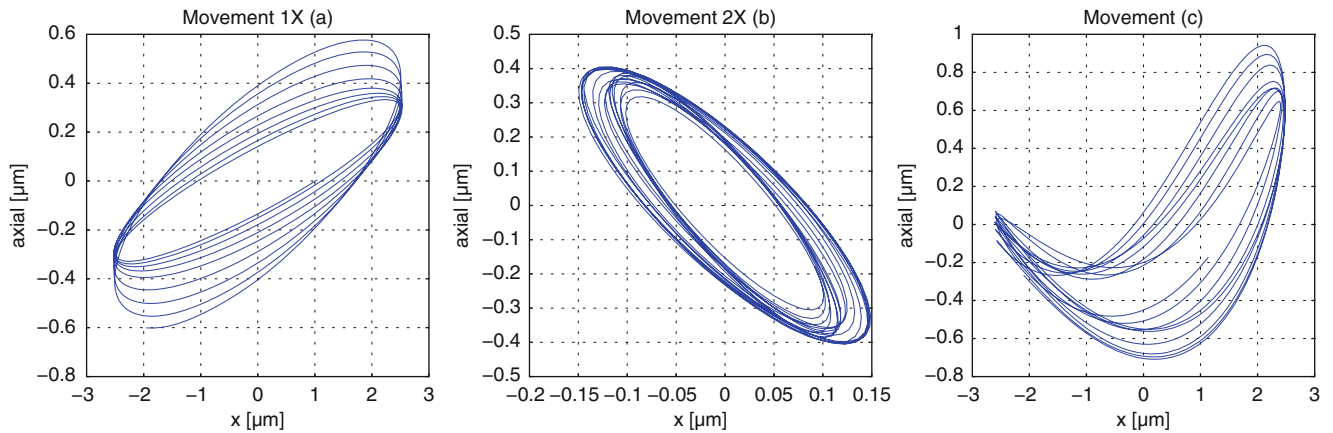
Fig. 22.4 Two dimensional orbit with a radial direction combined with an axial direction
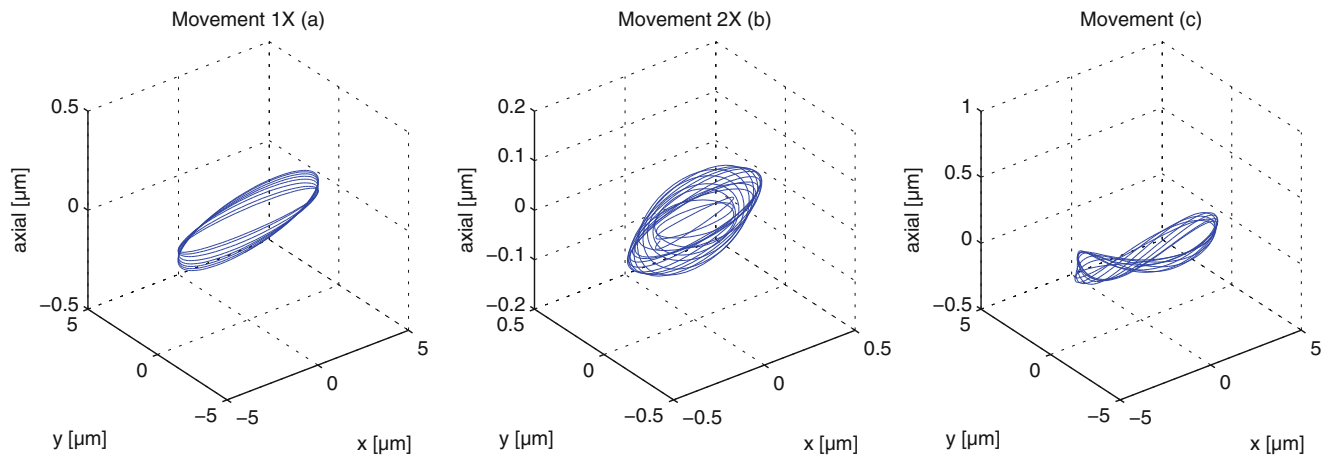
Fig. 22.5 Three dimensional Orbit at 25 Hz with parallel misalignment

misalignment in the system is very small, but when looking at the projections in the radial and axial direction, a difference is visible so as to identify parallel misalignment (Fig. 22.6). The amount of motion in the vertical direction (*y* direction) is higher when parallel misalignment is introduced. The orbit in the axial direction is very similar compared with the orbit in a well-aligned set-up (Fig. 22.7). The increase at 2× rotational speed is according to what is mentioned in literature [7].

Fig. 22.6 Two dimensional orbit in radial direction at 25 Hz with parallel misalignment

Fig. 22.7 Two dimensional orbit in axial direction at 25 Hz with parallel misalignment

Fig. 22.8 Three dimensional orbit at 25 Hz with angular misalignment

22.2.2 Measurements on Angular Misalignment

For angular misalignment an increase in the 1× peak should be noticed. When looking at the three dimensional orbit this increase is also visible (Fig. 22.8). The projection in the radial direction does not reveal any increase (Fig. 22.9) but both projections in the axial direction exhibit an increase at 1× rotational speed (Figs. 22.10 and 22.11).
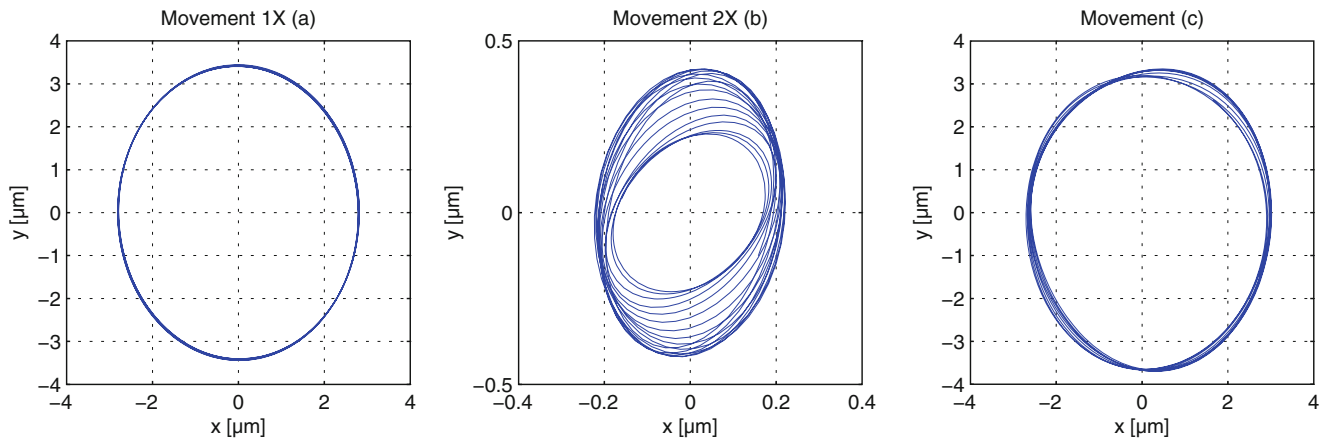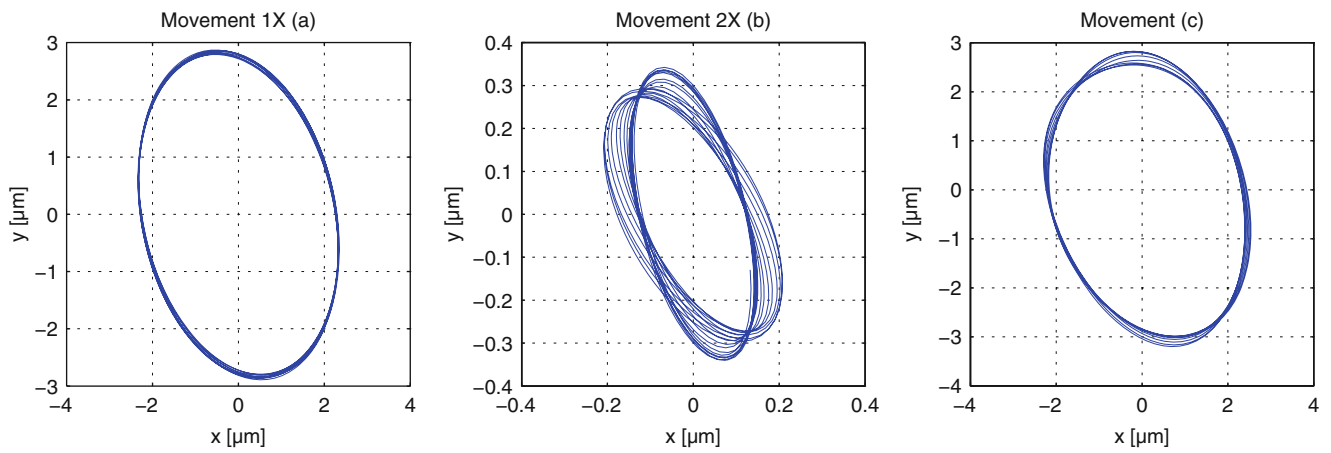
Fig. 22.9 Two dimensional orbit in radial direction at 25 Hz with angular misalignment
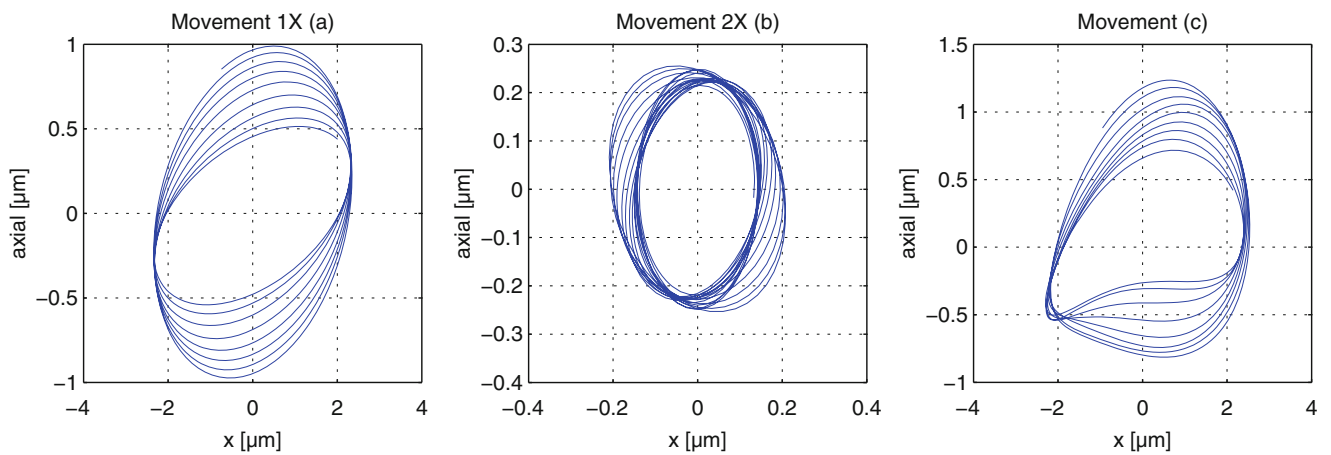
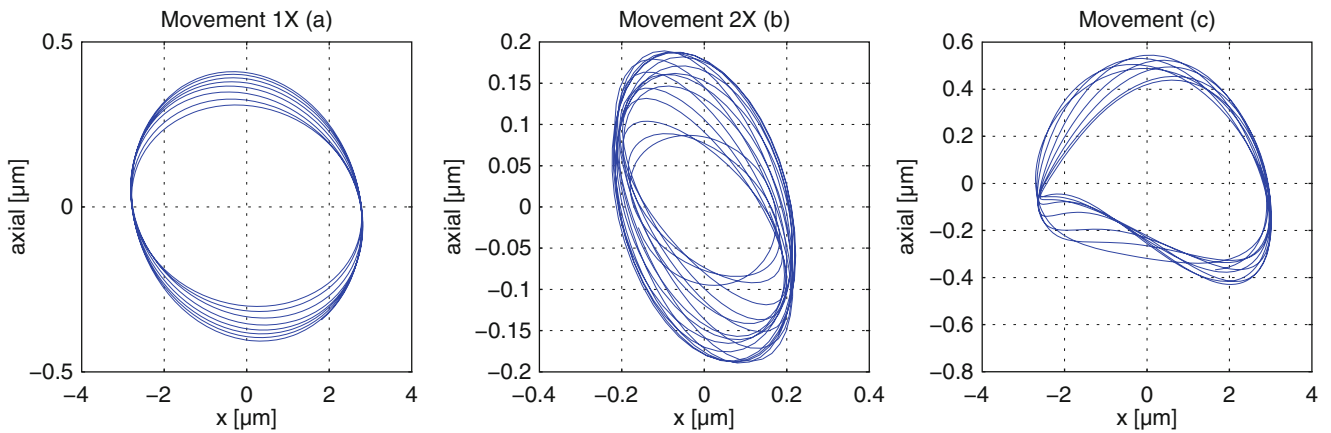**Fig. 22.10** Two dimensional orbit in axial direction at 25 Hz with angular misalignment
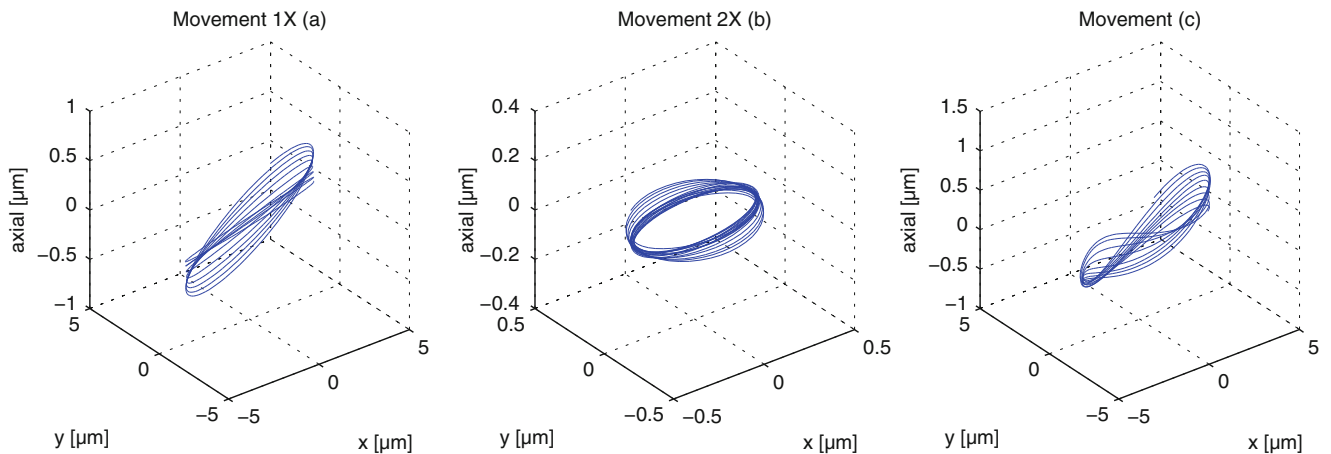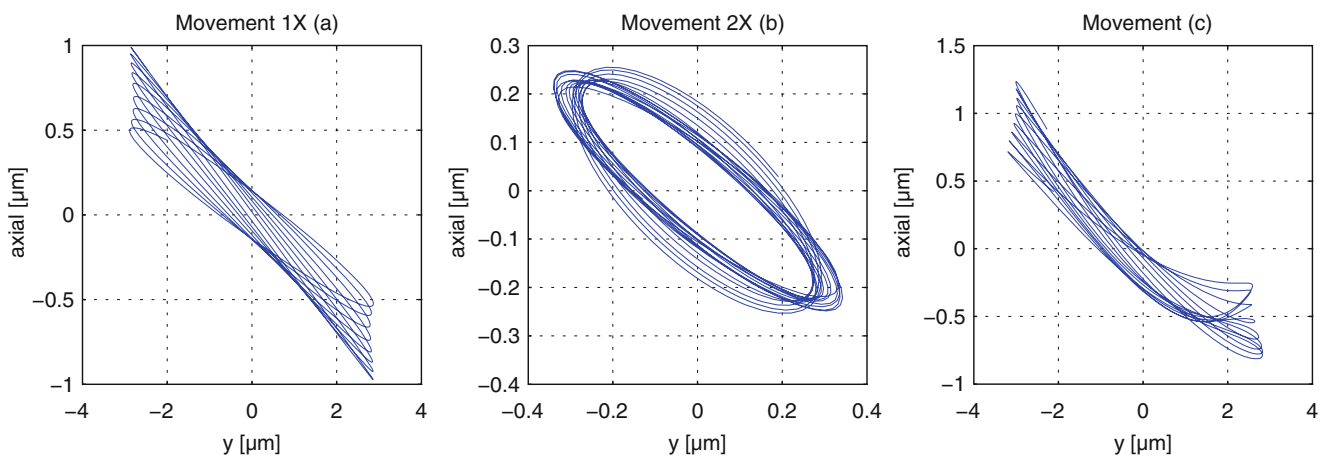
Fig. 22.11 Two dimensional orbit in axial direction at 25 Hz with angular misalignment
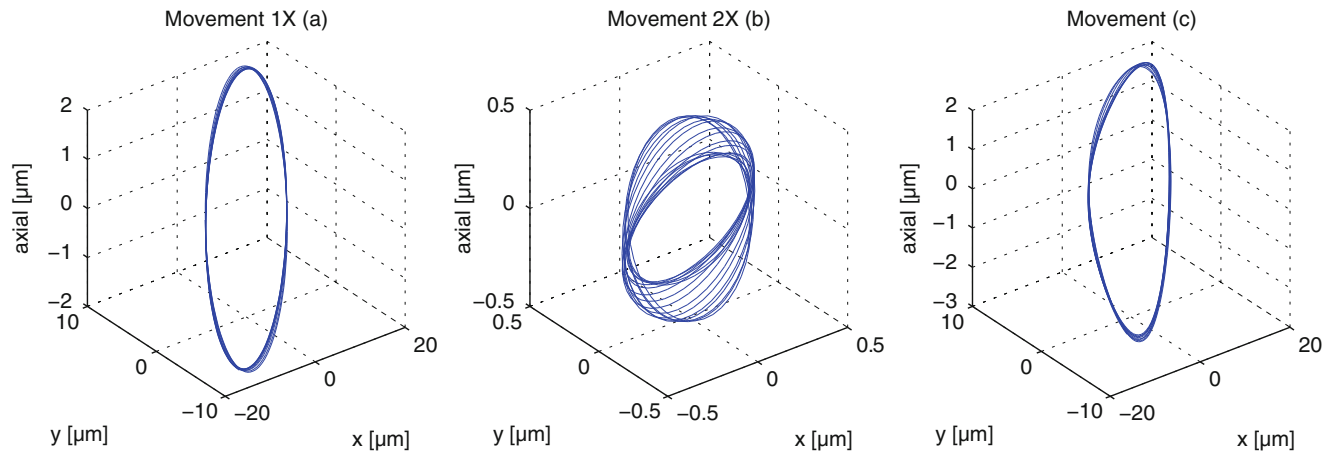
Fig. 22.12 Three dimensional orbit at 25 Hz with imbalance
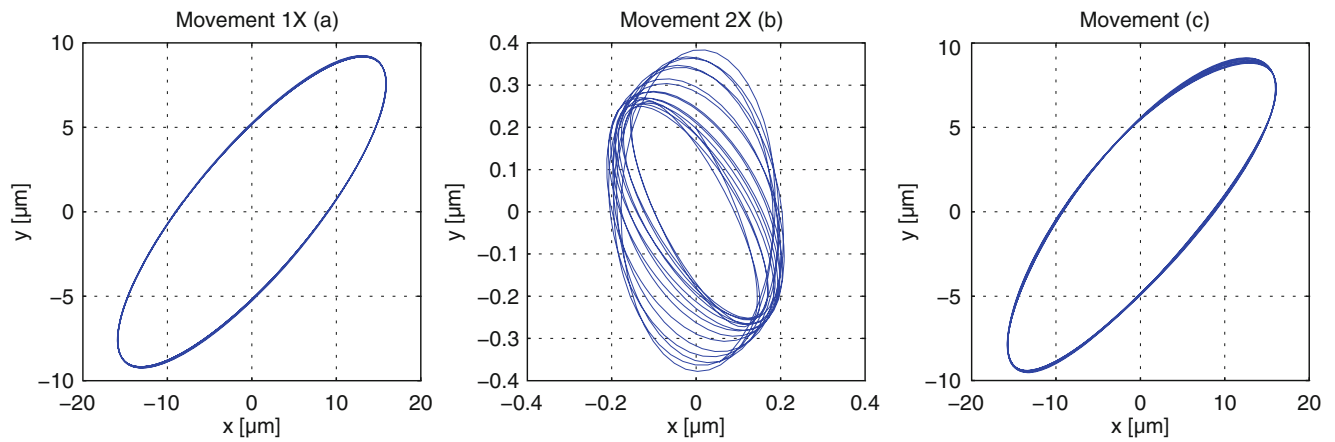
Fig. 22.13 Two dimensional orbit at 25 Hz with imbalance in radial direction
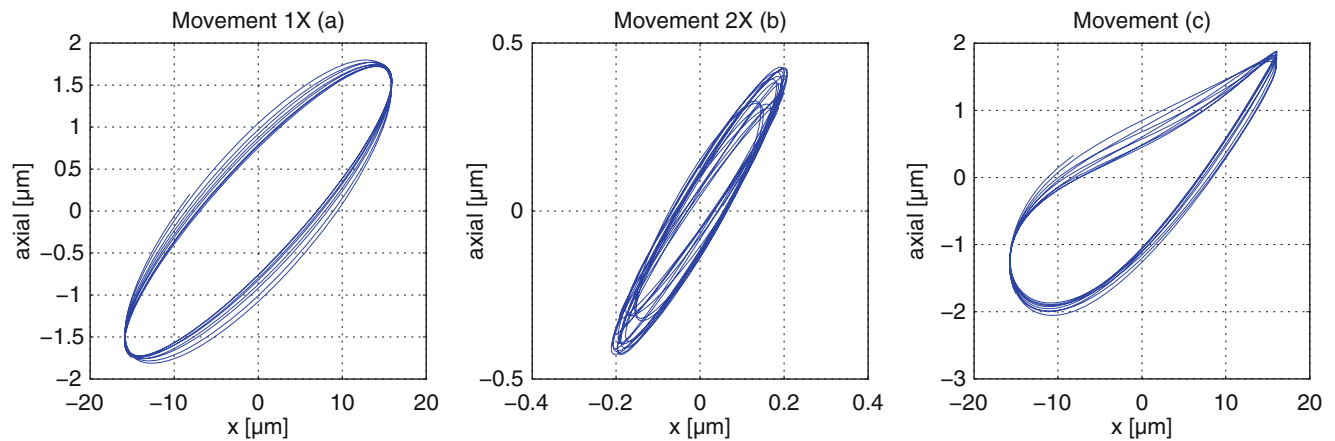
Fig. 22.14 Two dimensional orbit at 25 Hz with imbalance in radial direction

22.2.3   *Measurements with Imbalance and Combined Faults*

The introduction of imbalance to an aligned system results in an increased amplitude of the movement at 1× rotational speed, both in axial and radial direction (Figs. 22.12, 22.13, and 22.14). When parallel or angular misalignment are combined with imbalance full spectra are necessary to make the proper analysis, but with 3D Orbits it is also possible to detect the combined
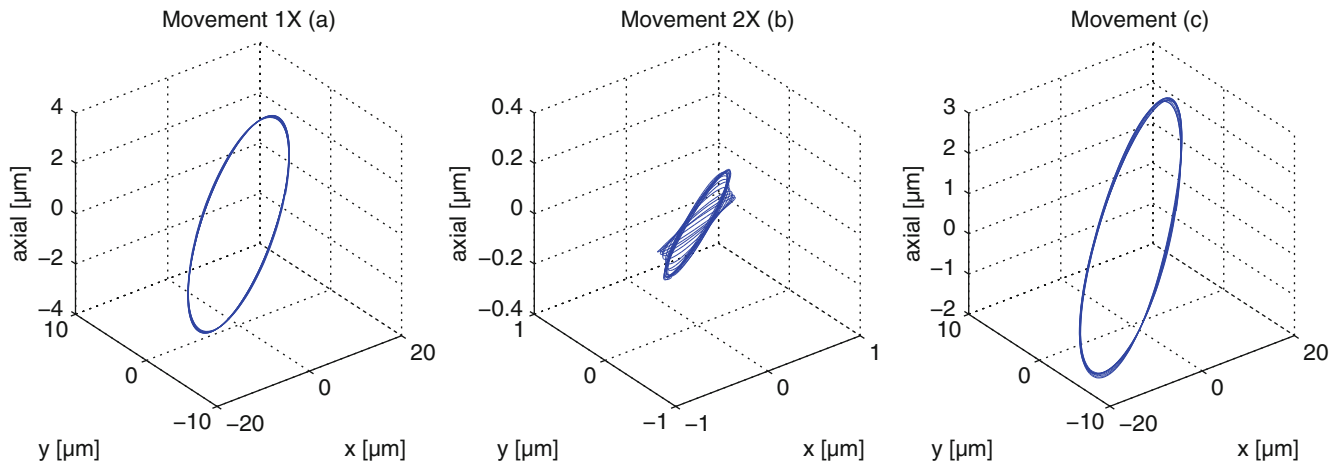
Fig. 22.15 Three dimensional orbit at 25 Hz with imbalance and parallel misalignment
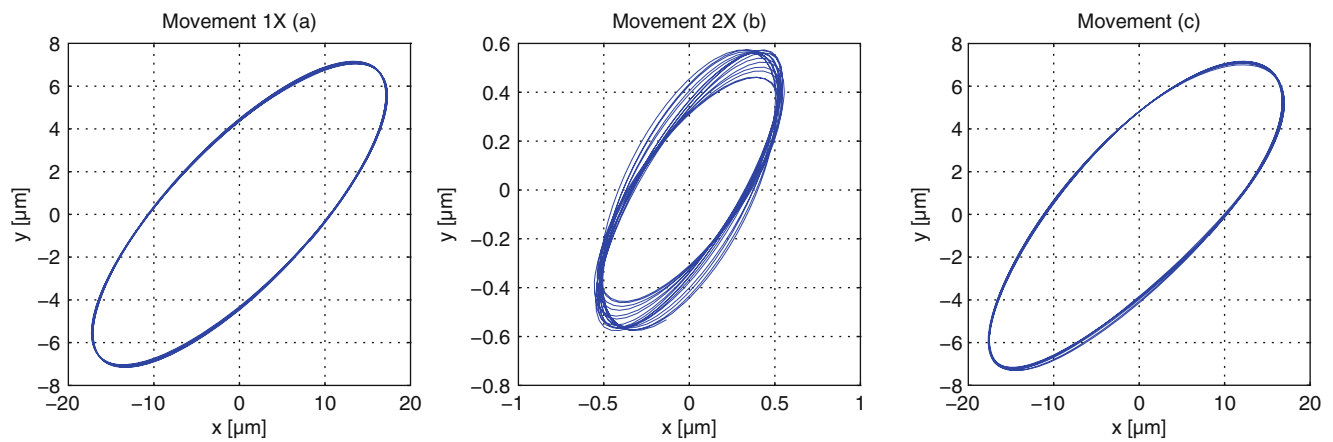
Fig. 22.16 Two dimensional orbit at 25 Hz in radial direction with imbalance and parallel misalignment

fault. In Figs. 22.15 and 22.16 an increase of the movement can be noticed at 2× rotational speed in radial direction. In the full spectrum of these measurements the parallel misalignment is not detected (Fig. 22.17). The higher peak marks the imbalance at 1× the rotational speed compared with −1×, but the peak at 2× rotational speed is very limited.

22.3 Conclusions

Orbitals and full spectra had already proven their usefulness in detecting machinery faults from vibration measurements. But by extending the orbit plot to the axial direction more information can be taken out of the time-domain data captured by accelerometers. The difference between angular and parallel misalignment is very clear when studying the three dimensional orbits. Angular misalignment can be detected by looking at the axial direction on the 1× peak, while parallel misalignment is detected in the radial direction at the 2× peak. The presence of imbalance leads to a higher excitation of the orbits. An additional advantage of three-dimensional orbits is that even a small misalignment can be detected while this is difficult to spot in a traditional spectrum.

Additional research is absolutely needed in order to confirm these findings and to compare the measurements with other couplings used in the rotating set-up. It is expected that the coupling will have a big influence on future measurements. The three-dimensional orbitals and full spectrum can be used as an additional tool when vibrational data are studied.
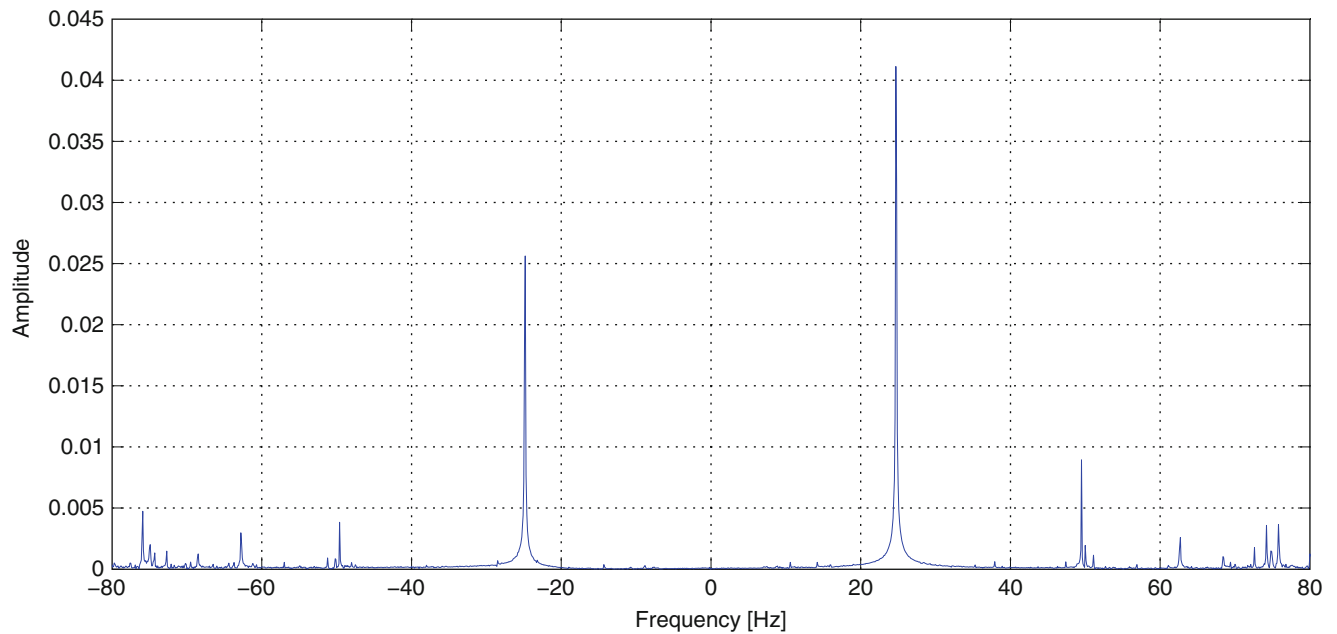
Fig. 22.17 Full spectrum at 25 Hz in radial direction with imbalance and parallel misalignment

References

1. Piotrowski J (2007) Shaft alignment handbook. 3rd edn. CRC Press, Boca Raton. http://marc.crcnetbase.com/isbn/9781420017878
2. Kumar SS, Kumar MS (2014) Condition monitoring of rotating machinery through vibration analysis. J Sci Ind Res 73:258–261
3. Ferrando Chacon JL, Artigao Andicoberry E, Kappatos V, Asfis G, Gan T-H, Balachandran W (2014) Shaft angular misalignment detection using acoustic emission. Appl Acoust 85:12–22
4. Ciang CC, Lee J-R, Bang H-J (2008) Structural health monitoring for a wind turbine system: a review of damage detection methods. Meas Sci Technol 19(12):122001
5. Newell GE (1999) Oil analysis cost-effective machine condition monitoring technique. Ind Lubr Tribol 51(3):119
6. Monte M, Verbelen F, Vervisch B (2014) The use of orbitals and full spectra to identify misalignment. Struct Health Monit 5:215–222. http://link.springer.com/chapter/10.1007/978-3-319-04570-2_24
7. Sekhar AS, Prabhu BS (1995) Effects of coupling misalignment on vibrations of rotating machinery. J Sound Vib 185(4):655–671

Chapter 23
Linear and Nonlinear Response of a Rectangular Plate Measured with Continuous-Scan Laser Doppler Vibrometry and 3D-Digital Image Correlation

David A. Ehrhardt, Shifei Yang, Timothy J. Beberniss, and Matthew S. Allen

Abstract Dynamic measurement of real structures, such as panels, can be difficult due to their low mass and complicated deformations under large amplitude loading conditions. These conditions bring to light shortcomings of traditional sensors such as accelerometers, strain gauges, displacement transducers, etc. A majority of these sensors require contact with the structure under test which tends to modify the dynamic response of these light structures. In contrast, a few recently developed techniques are capable of measuring the response over a wide measurement field without contacting the structure, which is ideal for these structures. Two techniques are considered here: continuous-scan laser Doppler vibrometry (CSLDV) and high speed three dimensional digital image correlation (3D-DIC). Both techniques can be used to return real-time deformation shapes under certain conditions; however, measurements will be obtained using post processing here. The linear and nonlinear deformations of a clamped flat plate under steady state sinusoidal loading will be measured using both techniques and compared with a finite element model to assess the relative merits of each measurement approach.

Keywords Continuous scan • Laser Doppler vibrometer • Digital image correlation • Nonlinear deflection

23.1 Introduction

With the development of high performance light weight structures there is an increasing need for experimental techniques capable of measuring the response at a large number of measurement degrees of freedom without modifying the structural response significantly. Techniques such as Continuous-Scan Laser Doppler Vibrometry (CSLDV) and high-speed Three Dimensional Digital Image Correlation (high-speed 3D-DIC) have been developed to meet this need. Both CSLDV and high-speed 3D-DIC are non-contact, non-destructive, and capable of measuring the response at thousands of points across the surface of the test specimen. However, these techniques involve additional processing to extract velocities or displacements from measured signals when compared with traditional measurement techniques. Both techniques are capable of providing "real-time" measurements; however this has seen limited to no implementation. In the case of 3D-DIC, the computations and amount of data to be handled are significant enough to make this challenging, and limits its application to sampling frequencies of 100 Hz. In principle CSLDV could be performed in real time with the implementation of the harmonic power spectrum, but this has not been done yet. For this work, the data acquired with both methods was analyzed in a post-processing step.

CSLDV is an extension of traditional Laser Doppler Vibrometer (LDV) measurements, where the laser point, instead of dwelling at a fixed location, is continuously moving across a measurement surface. This added motion requires the measurement to be treated as time-varying, but the motion also provides an increased measurement resolution with a drastically decreased measurement time when compared with traditional LDV measurements. Several algorithms have been

D.A. Ehrhardt (✉)
Department of Engineering Physics, University of Wisconsin-Madison, 1500 Engineering Drive, Madison, WI 53706, USA
e-mail: dehrhardt@wisc.edu

S. Yang
Praxair Inc, 175 East Park Drive, Tonawanda, NY 14150, USA

T.J. Beberniss
Structural Sciences Centers, Aerospace Systems Directorate, Air Force Research Laboratory, Wright-Patterson AFB, Ohio, OH 45433, USA

M.S. Allen
Department of Engineering Physics, University of Wisconsin-Madison, 1500 Engineering Drive, Madison, WI 53706, USA

devised to process CSLDV measurements so the vibration shapes of a test piece along the laser scan path can be determined. For example, Ewins et al. treated the operational deflection shape as a polynomial function of the moving laser position [1–5]. They showed that harmonics appear in the measured spectrum separated by the scan frequency, and the amplitudes of these harmonics can be used to determine a polynomial's coefficients that describe the operating deflection shape along the scan path. Allen et al. later presented a lifting approach for impulse response measurements [6, 7]. This approach groups responses at the same location along the laser path so the responses appear to be from a set of pseudo sensors attached to the structure. Conventional modal analysis routines can then be used to determine modal properties of the structure. Recently, algorithms based on Linear Time Periodic (LTP) system theory [8–12] were used to derive input-output transfer functions from CSLDV measurements allowing virtually any input to be used with CSLDV. The algorithms based on LTP system theory will be used in this investigation to identify the natural frequencies and modes shapes of a clamped rectangular plate.

Displacements measured with 3D-DIC are obtained by matching a measurement point, consisting of a pixel area, in each image between each camera for the duration of the experiment. For sample rates greater than 100 fps, deformations are measured using post processing. Schmidt et al. [13] presented early work on the use of high-speed digital cameras to measure the deformation and strain experienced by test articles under impact loadings. Tiwari et al. [14] used two high-speed CMOS cameras in a stereo-vision setup to measure the out of plane displacement of a plate subjected to a pulse input. Results compared favorably with work previously published and showed the capability of the 3D-DIC system in a high-speed application, although over a short time history. Niezrecki et al. [15], Helfrick et al. [16], and Warren et al. [17] obtained linear mode shapes using 3D-DIC with different test articles using discrete measuring points. Niezrecki et al. and Helfrick et al. also combined accelerometers, vibrometers, and dynamic photogrammetry to compare results obtained with DIC analyzed at discrete measurement locations. Each technique provided complimentary results between all single point measurement techniques showing the capability of 3D-DIC. Since 3D-DIC has the capacity to measure thousands of 3D displacements on a surface, a further comparison can be made with full field measurements if sensor arrays are available; however, handling the large amount of data in conjunction with the image files and measurement locations can prove to be difficult.

These methods are also desired as a tool for nonlinear model updating, where a geometrically nonlinear finite element model (FEM) of the structure is updated to reflect the nonlinear response of the test article [18, 19]. For example, in [19] Allen and Weekes found that the nonlinear response of a finite element model exhibited coupling between two of the linear modes and that the degree of coupling influenced how the resonance frequency changed with amplitude. However, measurements were only available at one point so the FEM could not be confidently updated to reflect the behavior of the test article.

This work seeks to expand on a previous comparison [20] between CSLDV and high-speed 3D-DIC by examining the suitability of these measurements in the linear and nonlinear dynamic response regimes of a 177 mm × 228 mm clamped aluminum plate. The linear response of the plate was measured when it was excited with a sinusoid at the first and fourth natural frequency. The nonlinear response of the plate was measured when it was excited at high amplitude near the first resonance. CSLDV measurements were processed with the harmonic transfer function and used to identify the mode shapes and natural frequencies. 3D-DIC measurements were processed using a commercial software Aramis [21] and its Real Time Sensor extension [22]. Then a transfer function is assembled and used to identify the mode shapes and natural frequencies of the structure. The quality of the measurements was compared as well as practical considerations that may limit the applicability of the methods.

23.2 Measurements

23.2.1 Introduction to CSLDV

CSLDV measurements are acquired by moving the point of a laser-doppler vibrometer (LDV) across a surface using a two dimensional pattern. Patterns can range from simple lines and circles to complex Lissajous curves, but, if the pattern is periodic, the same technique can be used to extract velocities along the pattern no matter what the shape. Note that this work considers only periodic scan patterns, but if the methods developed by Ewins are used then the laser may scan non-periodically over the surface extracting the deformation over a very dense grid [1–5]. In this work, a pattern is scanned across a surface using a single point fiber optic LDV and external mirrors offset from the measurement surface as shown in Fig. 23.1. Retro-reflective tape cut in the shape of the scanning pattern is also added to reduce signal contamination from the speckle pattern needed for 3D-DIC and improve measurement feedback. With the completion of the scan, the LDV measurement is now a collection of time-varying velocities of the surface deformation in the defined z-direction. The measured data are analyzed using the harmonic transfer function concept from linear-time periodic (LTP) systems, which is derived by defining an exponentially modulated periodic signal, and using the general solution for the response of a linear time varying

Fig. 23.1 CSLDV system diagram: the laser beam was redirect by a pair of mirrors to continuously scan on the test article
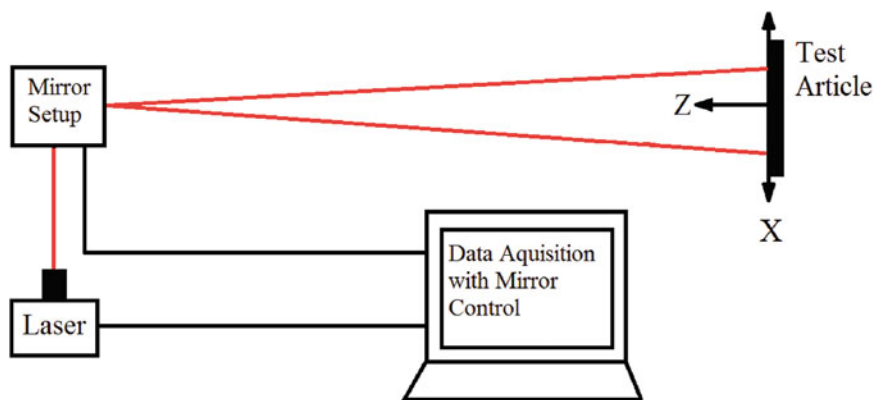
system [23]. This allows the user to employ LTP algorithms that are analogous to the transfer function of linear time invariant (LTI) systems, and can be written in a modal summation form in terms of the modal parameters of the structure. For further discussion, the reader is referred to [11, 24, 25].

This method of mode shape extraction has previously been successfully applied to 1-D single frequency line scans on beams [20, 25], and is readily applied to CSLDV measurements with a more complicated scanning pattern, provided the scan pattern is periodic. Here, a Lissajous curve is used, which defines the x- and y-coordinate of the pattern as a system of parametric equations shown in Eq. 23.1. The x- and y-coordinates oscillate at separate frequencies, f_x and f_y, and are defined as 90° out of phase. The result is a closed periodic scan pattern allowing the use of the previously mentioned LTP algorithms. The period of the Lissajous curve can then be defined as the smallest period within which both f_x and f_y have an integer number of cycles as shown in Eq. 23.2, where T_x and T_y are the periods of the x- and y- positions of the laser. Using this definition, N_x and N_y are defined based on the ratio of the selected x- and y-coordinate frequencies, as shown in Eq. 23.3. The selection of scan frequencies involves considerations of the measurement area to be covered, the measurement noise (which generally increases with the speed of the moving laser), the expected spatial density of the deformation, and level of damping and modal density of the structure. The level of damping and modal density is especially important when using broad band methods of excitation [25], which is not used here. In this work, the x-coordinate frequency is set as 3 Hz and the y-coordinate frequency is set as 4 Hz to keep feedback noise from the laser low while providing enough measurement signal to distinguish complex deformation shapes. The result is a Lissajous curve, shown in Fig. 23.3a, with a period of 1 Hz.

$$x(t) = A_x \cos\left(2\pi * f_x t\right)$$
$$y(t) = A_y \sin\left(2\pi * f_y t\right) \tag{23.1}$$

$$T_{Lissajous} = N_x * T_x = N_y * T_y = N_x * \left(\frac{1}{f_x}\right) = N_y * \left(\frac{1}{f_y}\right) \tag{23.2}$$

$$\frac{N_x}{N_y} = \frac{f_x}{f_y} \tag{23.3}$$

23.2.2 Introduction to 3D-DIC

For digital image correlation, two cameras are used to image the test article as it deforms and then the 3D displacements of the surface can be determined using digital image correlation (DIC) algorithms, which match portions of the surface from image to image and use that to calculate the displacements. As schematically shown in Fig. 23.2, the two cameras are placed at a specific distance along the Z-axis from the test article to allow the surface to be captured simultaneously in each camera and establish a field of view. A pan angle, Θ_p, is specified based on a desired depth of view or the range of out-of-plane displacements expected. Once the stereo camera setup is assembled and fixed, photogrammetric principles of triangulation and bundle adjustment are used to establish each camera's position and the experimental measurement volume by capturing images of a known pattern or calibration panel [26]. With this calibration, displacement accuracy is not limited to the pixel size of the imaged surface, but allows for accuracies on the sub pixel level (eg. 0.1 pixels). Prior to testing, a high-contrast random speckle pattern is applied to the measurement surface to increase image texture and improve image correlation.

Fig. 23.2 3D-DIC system diagram. The 3D-DIC system diagram shows Camera 1 (*left camera*) and Camera 2 (*right camera*) set to a specified pan angle, Θ_p
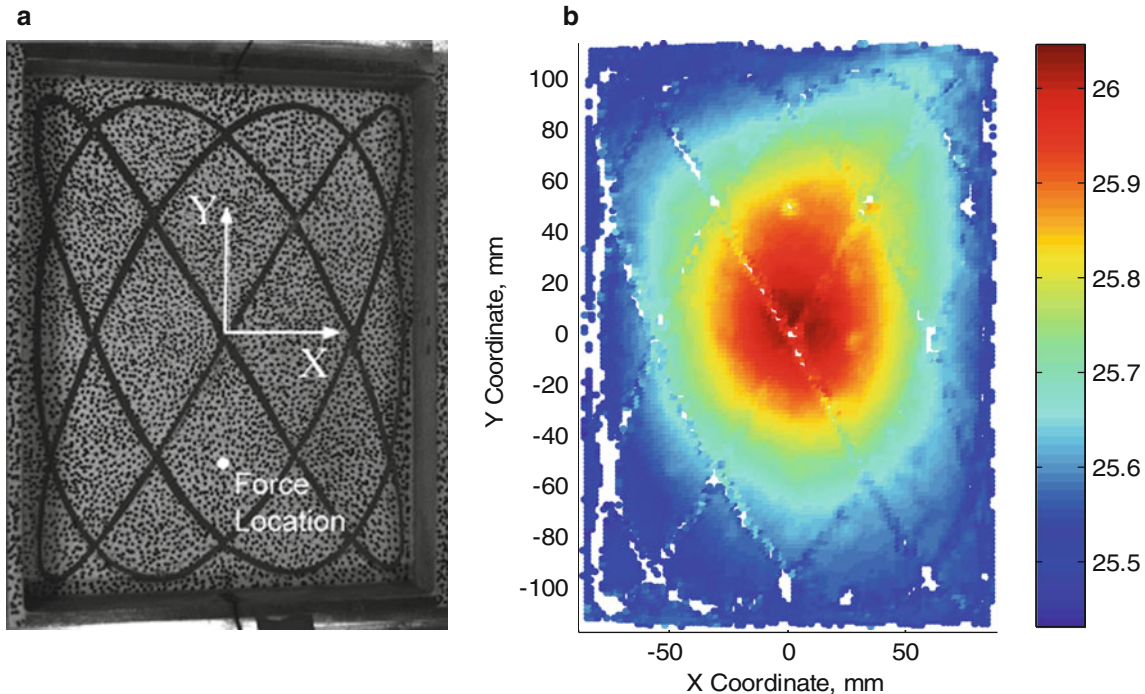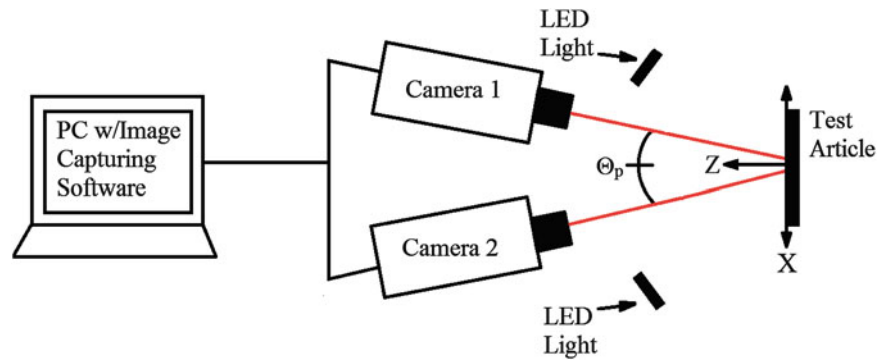
Fig. 23.3 Images of rectangular plate: (**a**) Final prepared surface, (**b**) Measured initial curvature

In this work, a commercial software (Aramis [21]) is used to calibrate and analyze displacements of the measurement surface. The high-contrast random speckle pattern is applied to the surface using the best practice discussed in [27] based on the desired field of view. The use of retro-reflective tape for CSLDV measurements results in contamination of 3D-DIC measurements where the tape covers the speckle pattern as seen in the static 3D-DIC measurements in Fig. 23.3b. So, results for dynamic 3D-DIC presented in this paper will be from a selection of measurement points around this Lissajous scan pattern.

23.3 Test and Analysis Description

23.3.1 Test Specimen and Finite Element Model

The device under test for this investigation is a nominally flat clamped aluminum plate. As summarized in Table 23.1, the tested plate had an effective length of 177 mm, an effective width of 228 mm, and a thickness of 0.5 mm. The plate was then clamped between two mounting frames with adhesive as further described in [28]. After being fixed between the mounting frames, the plate was painted with a white base coat, and a speckle pattern was applied using a marker and spray paint to

Table 23.1 Plate geometric and material properties

Length = 177 mm	Width = 228 mm	Thickness = 0.5 mm
E = 71.7 GPa	υ = 0.33	ρ = 2.76*10³ kg/m³

increase the imaged surface texture and improve tracking for both 3D-DIC systems. Once the plate had dried, a pattern of retro-reflective tape cut from a printed Lissajous stencil was added to increase feedback to the CSLDV laser while providing room for 3D-DIC measurements. The final prepared plate is shown in the clamping fixture in Fig. 23.3a. For an accurate description of the initial conditions of the plate, static 3D-DIC images were captured after the plate was fully clamped. An initial deflection of 0.613 mm near the center of the plate was measured, as shown in Fig. 23.3b, where the color bar segments the defined z-coordinate. This coordinate system was defined based on the front of the clamping fixture, or 25.4 mm from the clamped edge of the plate. One can see that the retro-reflective tape and the edge of the mounting frame have a negative effect on the ability of 3D-DIC to track surface deformations at certain positions, but the measurement density is high in other regions so it is not difficult to interpolate over the anomalies that these introduce. The final step of preparation was the addition of a 6 mm steel disk to the back of the aluminum plate to give allow input force from a magnetic driver, discussed in the next section. The location of this disk is shown in Fig. 23.3a.

To provide a baseline of comparison between measurement techniques for linear responses, the finite element model (FEM) described in [28] is used. A coordinate transformation established in the static 3D-DIC measurements is used to match the coordinate system in the FEM with the measurement coordinate systems for CSLDV and 3D-DIC. Low amplitude tests were performed and used to identify the linear natural frequencies and modes shapes for the first and fourth modes, and to compare the results of the two methods. For high amplitude testing, only a comparison between the measured responses is made since geometrically nonlinear simulations with the FEM exceeds time constraints for submission of this paper.

23.3.2 Experimental Setup and Description

The experimental setup is shown in Fig. 23.4. In this setup, there are five main systems: (1) exciter/controller, (2) static 3D-DIC system, (3) dynamic 3D-DIC system, (4) the CSLDV system, and (5) system for force appropriation:

1. Excitation was provided by two separate mechanisms, both controlled in an open-loop using a Wavetek Variable Phase Synthesizer. The low amplitude excitation was provided by a magnetic driver with a Piezo Amplifier. The force exerted by the magnetic driver was measured using a force transducer mounted to a solid base between the magnetic driver providing measurement of the reaction force with the base. Since the plate is aluminum, a small steel disk was added to the plate in the previously described location. High amplitude excitation was provided by shaking the frame on which the plate was mounted with a 5,000 N MB dynamics shaker and power amplifier. Excitation for this setup is provided through the mounting base at a set excitation acceleration. This type of excitation limits the ability to examine asymmetric modes and why the measurements focused on the first and fourth modes of the plate.
2. The static 3D-DIC system consists of two Prosilica GT2750 CCD cameras with a full resolution of $2,750 \times 2,200$ pixels with a maximum frame rate of 20 fps. For this experimental setup, full resolution images were selected for finer measurement resolution. The static system uses 18 mm lenses and is positioned at a standoff distance of 580 mm with a camera angle of 26°. All static displacements were determined using a commercial 3D-DIC software Aramis [17] using subsets of 31×31 pixels with a 13 pixel overlap across the entire surface of the plate. A 250 mm $\times$ 200 mm calibration panel was used to establish the measurement volume and lead to a calibration deviation of 0.032 pixels or 0.004 mm for this field of view.
3. The dynamic 3D-DIC system includes two Photron, high speed 12-bit CMOS cameras (model Fastcam SA5 775 K-M3K). Each camera has 32GB of memory onboard with a maximum resolution of $1,024 \times 1,024$ pixels. For this experimental setup, images of 704×768 pixels were used to fit as much of the plate in the frame of both cameras as possible. The dynamic system uses 85 mm lenses at a stand off distance of 1,370 mm with a camera angle of 24.4°. All dynamic displacements were determined using a software extension of Aramis called IVIEW Real Time Sensor [18] using subsets of 15×15 pixels. In order to minimize the heat generated and remove the 60 Hz noise produced by the halogen lamps that are typically used in high-speed DIC systems, two 305×305 LED light panels were used. The cameras and the data acquisition system were simultaneously started using an external TTL trigger. Measurement points were selected to avoid the retro-reflective tape, so there is no overlap of measurements between CSLDV and 3D-DIC. This was done to reduce the measurement noise previously seen in the static measurements and provide better tracking for the DIC algorithm. A 250 mm $\times$ 200 mm calibration panel was used to establish the measurement volume and lead to a calibration deviation of 0.02 pixels or 0.007 mm for this field of view.
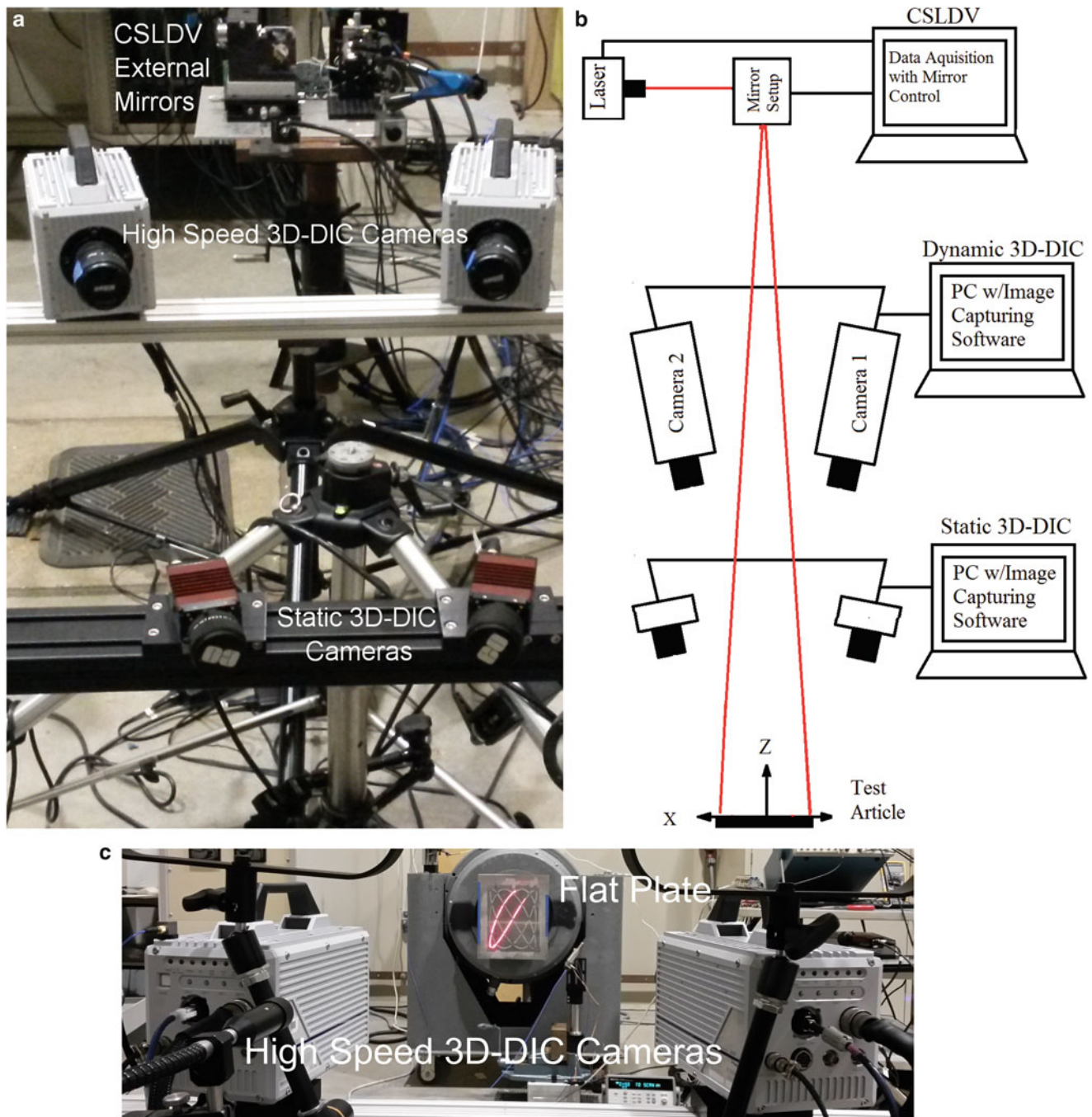
Fig. 23.4 Experimental setup. (**a**) Measurement systems, (**b**) Complete experimental schematic, (**c**) Close-up of rectangular plate

4. The continuous-scan mechanism was built using a Polytec OFV-552 fiber optic laser vibrometer with a sensitivity of 125 mm/s/V and the same external mirror system that was used in [24, 29]. The mirrors were positioned at a stand off distance of 2.4 m, which was selected to minimize the scan angle (5.4° in y-direction) and maintain the specified standoff distance. The external mirror system consisted of two galvanometer scanners in open-loop control; each scanner had a position detector that measured the instantaneous rotational angle, allowing precise and accurate control and measurement of the laser position. The control and data acquisition system was built using a National Instruments PXI system. A LabVIEW program was developed to integrate several the features including the function generator, data acquisition, and signal processing. As previously mentioned, the Lissajous pattern used for this investigation has a x-direction scan

frequency of 3 Hz and a y-direction scan frequency of 4 Hz with a maximum amplitude of 162 mm in the x-direction and 211 mm in the y-direction. The starting point for the laser, based on the coordinate system set in Fig. 23.3, was at x = 162 mm and y = 0. Data was collected at a sampling frequency of 10,240 Hz for 2 min.

5. A second single point laser is used to measure the response of the plate as it is subjected to a single frequency sinusoid at a set excitation amplitude. Additionally, the voltage input to the exciter was measured, as well as the input force for the magnetic driver and the base acceleration for the shaker. The velocity response and input voltage signals were analyzed in real time using a Onosoki FFT Analyzer to track the phase between the signals. Here, the input voltage was used instead of the measured force/acceleration to limit noise contamination from the measurement sensors. However, the measured force/acceleration signals were compared after measurement to ensure the correct phase relationship between input and response was maintained. Natural frequencies could then be determined by adjusting the frequency until the input voltage and response velocity are 180° out of phase.

23.4 Results

23.4.1 Modal Hammer Test

Single input and single output modal hammer tests were performed on the plate pre- and post-test for each level of excitation to check consistency of the plate's boundary conditions and detect damage throughout testing. Analyzing the frequency response functions (FRFs) obtained from hammer tests revealed that each method of excitation affected the dynamic response of the plate differently. For instance, a consistent reduction of 1 Hz in the first natural frequency, was observed with the placement of the magnetic driver in range of the excitation location. Also, 140 Hz noise from shaker cooling fan was measured when the shaker was turned on. Even with these effects a maximum frequency shift of 1.8 % was observed in the first natural frequency of the plate, the natural frequency that showed the highest percent change, showing the plate did not change significantly with time. The natural frequencies (f_n) and damping ratios (ζ) from the measured FRFs from each hammer test were averaged and are presented in Table 23.2. Additionally, the natural frequencies from the FEM are included, which show good agreement with the test frequencies as seen with the calculated percent errors. Although, the added mass from the paint and retro-reflective tape were not included, which could account for the consistently lower values of the natural frequencies.

23.4.2 Linear Mode Shape

Force appropriation was used to drive the plate at the first and fourth natural frequency and the steady state response was measured using both CSLDV and high-speed 3D-DIC. Figure 23.5 shows an example of the spectrum from the CSLDV signal with the Lissajous frequency of 1 Hz when the plate was driven at 106.9 and 277.7 Hz. For mode 1 and mode 4, the sideband harmonics higher than the 14th and 32nd order, respectively, are in the noise of the signal, as seen in the power spectral density (PSD) plots in Fig. 23.5a, b, and hence no harmonics above these orders were used when constructing the mode shapes.

Figure 23.6 compares the mode shapes obtained by CSLDV and 3D-DIC for the two linear steady state experiments. Figure 23.6a, b contain the mode shape at 106.9 Hz and show good agreement between both measurement techniques and the FEM with a MAC of 0.9385 for CSLDV and 0.9274 for 3D-DIC. One difference between the measured and calculated mode shapes is a notable skew in the maximum deformation of the mode 1 shape, seen most clearly in Fig. 23.6b. This skew is most likely due to the addition of the magnetic disk, as it is skewed toward the disk location, but could also be from the

Table 23.2 Modal comparison

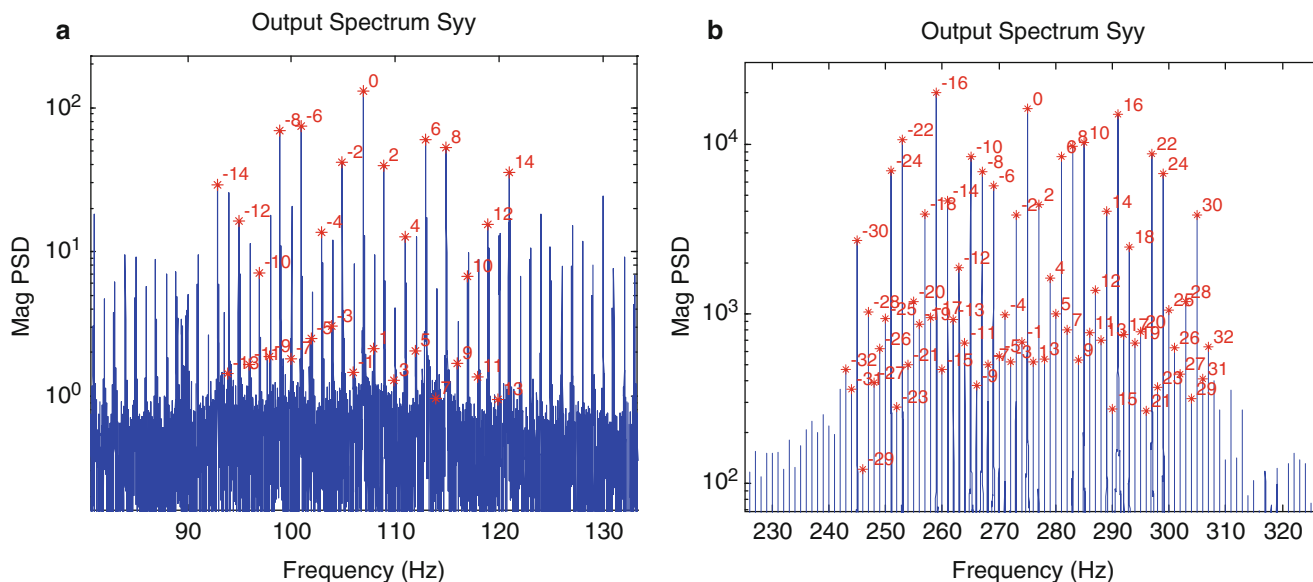| Mode		1	2	3	4	5	6	7	8	9
Test	f_n, Hz	106.1	159.4	236.9	276.6	307.8	420.5	436.4	458.9	532.9
	ζ, −	0.79 %	1.27 %	0.66 %	0.66 %	0.41 %	0.65 %	0.41 %	0.68 %	0.59 %
FEM		113.74	195.90	263.75	330.07	339.53	466.90	492.35	512.83	565.4
% error		−6.72 %	−18.63 %	−10.18 %	−16.20 %	−9.35 %	−9.94 %	−11.36 %	−10.52 %	−5.75 %

Fig. 23.5 Power spectra of CSLDV signals for (**a**) mode 1 and (**b**) mode 4

initial curvature previously discussed or a difference in clamping at the boundaries of the plate. Hence, there are most likely systematic differences between the FEA and measured mode shapes, so the fact that the MACs are not unity is not necessarily an indication of experimental error but information that will be useful when updating the FEM. On the other hand, since the linear measurement pertains to small displacements one would expect the noise for 3D-DIC to be higher. The focus of this work was on modes of the plate that would be excited with the use of symmetric loading, so the next linear mode examined was mode 4. Since mode 4, is symmetric it can be excited with base excitation from the larger shaker. Figure 23.6c, d contain the mode shape at 277.70 Hz and again show good agreement between measurement and analysis with a MAC of 0.9408 for CSLDV and 0.9672 for 3D-DIC. There are again noticeable differences in the location of the maximum and minimum deformations of mode 4.

It is important to note that while the smooth nature of the CSLDV mode shapes seems to suggest that they are infallible, they are in fact an approximation of the true mode shapes obtained by expanding them in a Fourier series of the time-varying scan pattern. As mentioned previously, 28 clearly dominant harmonics (i.e. n = −14 . . . 14) were observed for the first mode. The neglected harmonics were an order of magnitude smaller than the dominant ones, so one would be inclined to have high confidence in that shape, but any feature that is too small to be represented in a 28-term Fourier series would not be captured. Another check of measurement confidence comes from the reconstruction of the Lissajous curve since the laser is scanning along a fixed pattern. When the measurements are noisy, the overlapping parts of the pattern tend to differ giving an indication of the error. Due to the complexity of the 2-D pattern, this is difficult to visualize here but when the 3D shapes are rotated it becomes apparent. An additional consideration for the accuracy of CSLDV comes as the mode shapes become more complicated, since more harmonics are needed accurately reconstruct the mode shape. This is evident in the mode 4, where even though more than twice as many side bands were used to reconstruct the shape, it appears to not have reconstructed the mode shape as accurately as 3D-DIC.

23.4.3 Nonlinear Deflection Shapes

As the magnitude of input excitation to a structure is increased such as this, geometric nonlinearity becomes more noticeable in the response. With the use of single-sine (or mono-harmonic) force appropriation, nonlinearity can be visible in the PSD of the response as harmonics of the mode frequency being excited [30]. This is illustrated in Fig. 23.7a, b where the PSD of the 308 3D-DIC measurement locations and the CSLDV measurement for the response of the plate when excited in the first
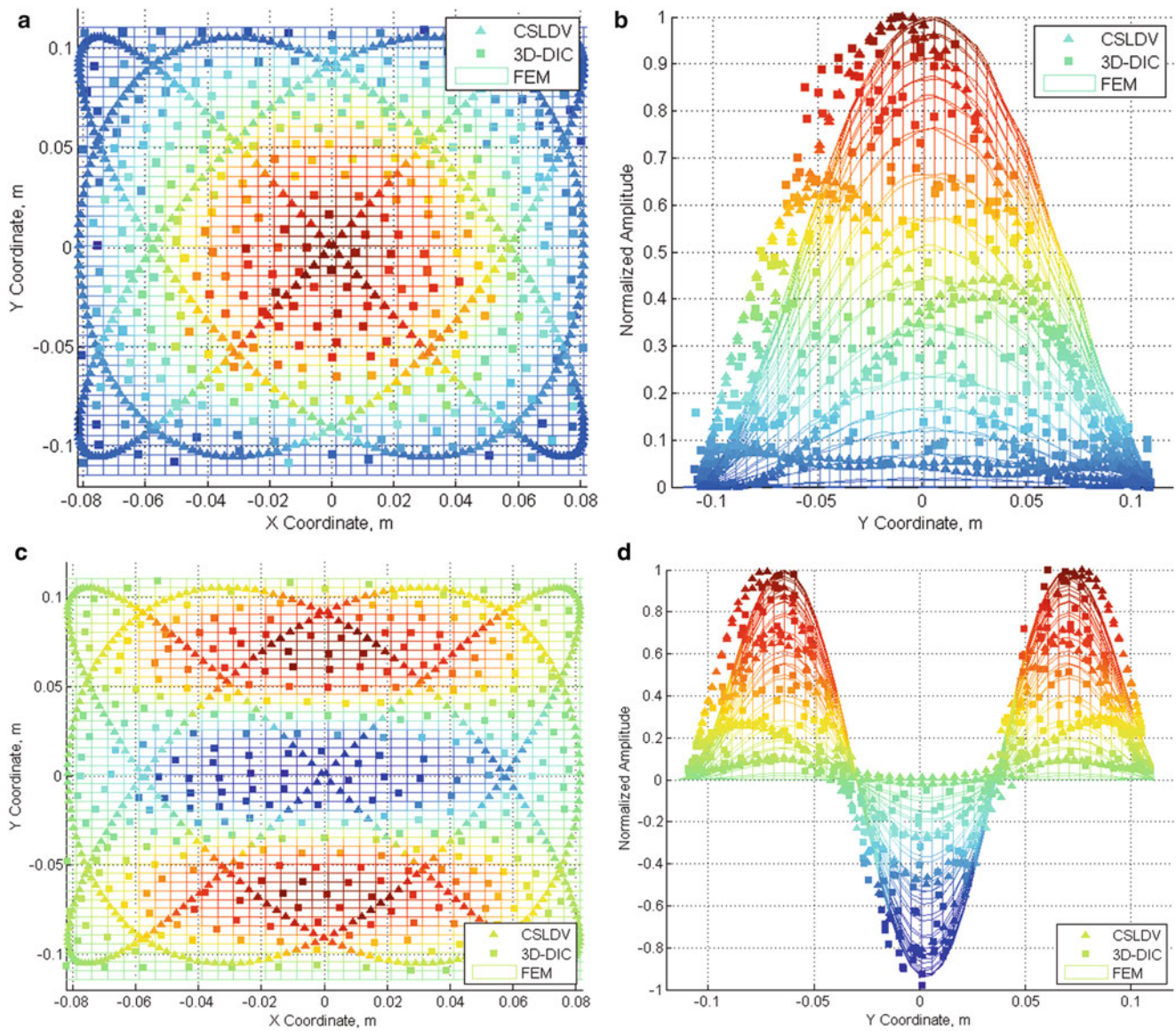
Fig. 23.6 Mode shape comparison between CSLDV, 3D-DIC, and FEM: (**a**, **b**) Mode 1, (**c**, **d**) Mode 4

mode at 1.21 g's of base acceleration is shown. The geometric nonlinearity of the plate for the first mode takes the form of spring hardening, where the natural frequency increases with increasing force amplitude. For instance, the linear frequency for mode 1 was 106.9 Hz and this has increased to 160.8 Hz (a 53.9 Hz shift in natural frequency!) for this high amplitude excitation. In addition to the change in frequency, higher harmonics are seen at integer multiples of the forcing frequency and the deformation of the plate can be different at each of these harmonics. After transforming the measured deformations with 3D-DIC and CSLDV to the frequency domain the plate deformation at each of these harmonics of the forcing function can be examined.

Here, the deformation shapes at each harmonic are reconstructed with CSLDV using 32 sideband harmonics, the same number that was used previously with the 4th linear mode shape. As is generally the case for a structure such as this [31], the primary harmonic of the measured nonlinear response, at 160.8 Hz, resembles the first linear mode of the plate, as shown in Fig. 23.8a, b. Both measurement systems capture this deformation well and are in good agreement with each other. The second harmonic of the nonlinear response, at 321.6 Hz is shown in Fig. 23.8c, d and was found to resemble the third linear mode of the plate. This deformation shape is unexpected since the base excitation that was used should theoretically not
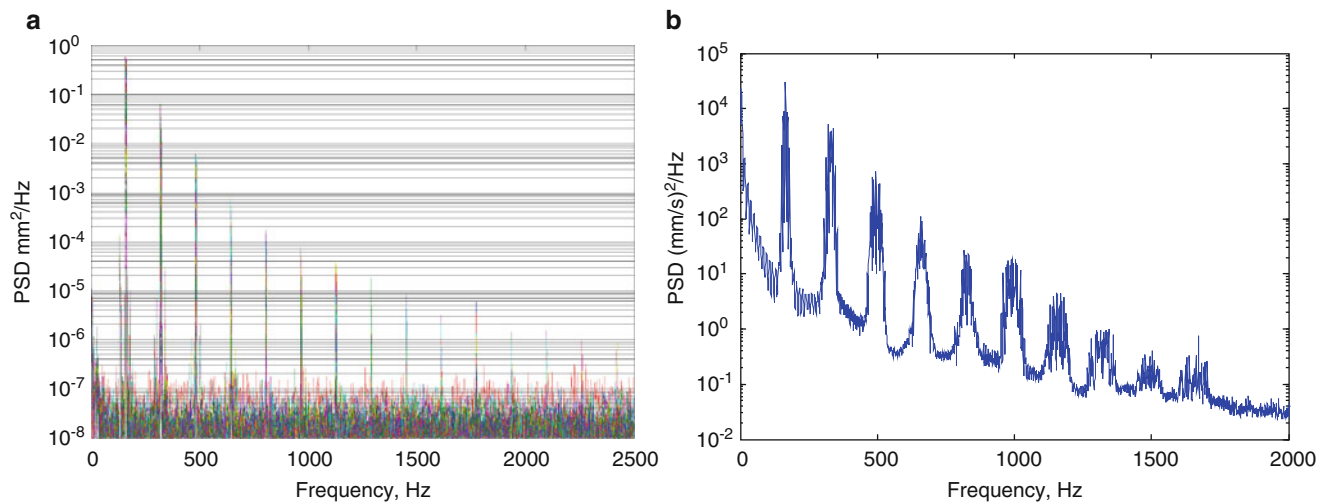
Fig. 23.7 Power spectral density of (**a**) All 3D-DIC measurements, (**b**) CSLDV vibrometer measurement

be able to directly excite an asymmetric mode such as this. Furthermore, the nonlinear normal modes [32] of a symmetric structure are typically all either purely symmetric or anti-symmetric [31, 33], so this measurement suggests that asymmetry is important to the nonlinear response and this information will be critical when modeling the structure. One should also note that asymmetric motions such as this are frequently observed in initially curved structures so the initial curvature of the plate should be modeled in the FEM. Again, both measurement systems are able to capture this slightly more complicated mode shape.

The third harmonic, at 482.4 Hz, was found to resemble a rotated version of the 5th linear mode of the FEM as seen in Fig. 23.9. This type of response is again unexpected as the characteristic shape is asymmetric in the y-coordinate. Again, both measurement systems capture the deformation shape well confirming the validity of this unexpected deformation shape. The fourth and the fifth harmonics showed similar results. The next harmonic examined is the sixth harmonic. Interestingly, the sixth harmonic's deformation shape, at 964.8 Hz, resembles the 21st mode of the FEM. Here, the deformation shape is far more complicated, calling into question the accuracy of a CSLDV shape based on only 39 Fourier terms. The shape does not agree with itself at several of the points where the lines of the Lissajous figure cross. Additional terms could easily be added when post processing the measurement, but the sideband harmonics greater than 39 at the sixth harmonic do not stand out from the noise sufficiently to warrant adding additional terms. The accuracy of the deformation shape with 3D-DIC is also called into question since the deformation at this frequency is small. An examination of Fig. 23.9a shows small differences between adjacent measurement points that is more prominent at the peaks of deformation giving an indication of measurement error. However, this error is hard to fully define.

23.5   Conclusion

In this investigation, the dynamic response of a nominally flat clamped aluminum plate was examined. Between each test, the natural frequencies and damping ratios were identified using a single-input single-output modal hammer test in order to monitor the consistency of the plate, and they were found to exhibit minimal variation. The mode shapes and natural frequencies of the first and fourth modes of the plate were also identified using force appropriation, with full-field dynamic deformations measured using CSLDV and high speed 3D-DIC. The results showed good agreement between the indentified linear frequencies and mode shapes and those calculated with the FEM. In addition to these linear measurements, nonlinear deformations of the first mode are also presented. Under nonlinear response conditions, full-field measurements allow the identification of nonlinear harmonics and the associated deformation shapes. This information is expected to be critical when
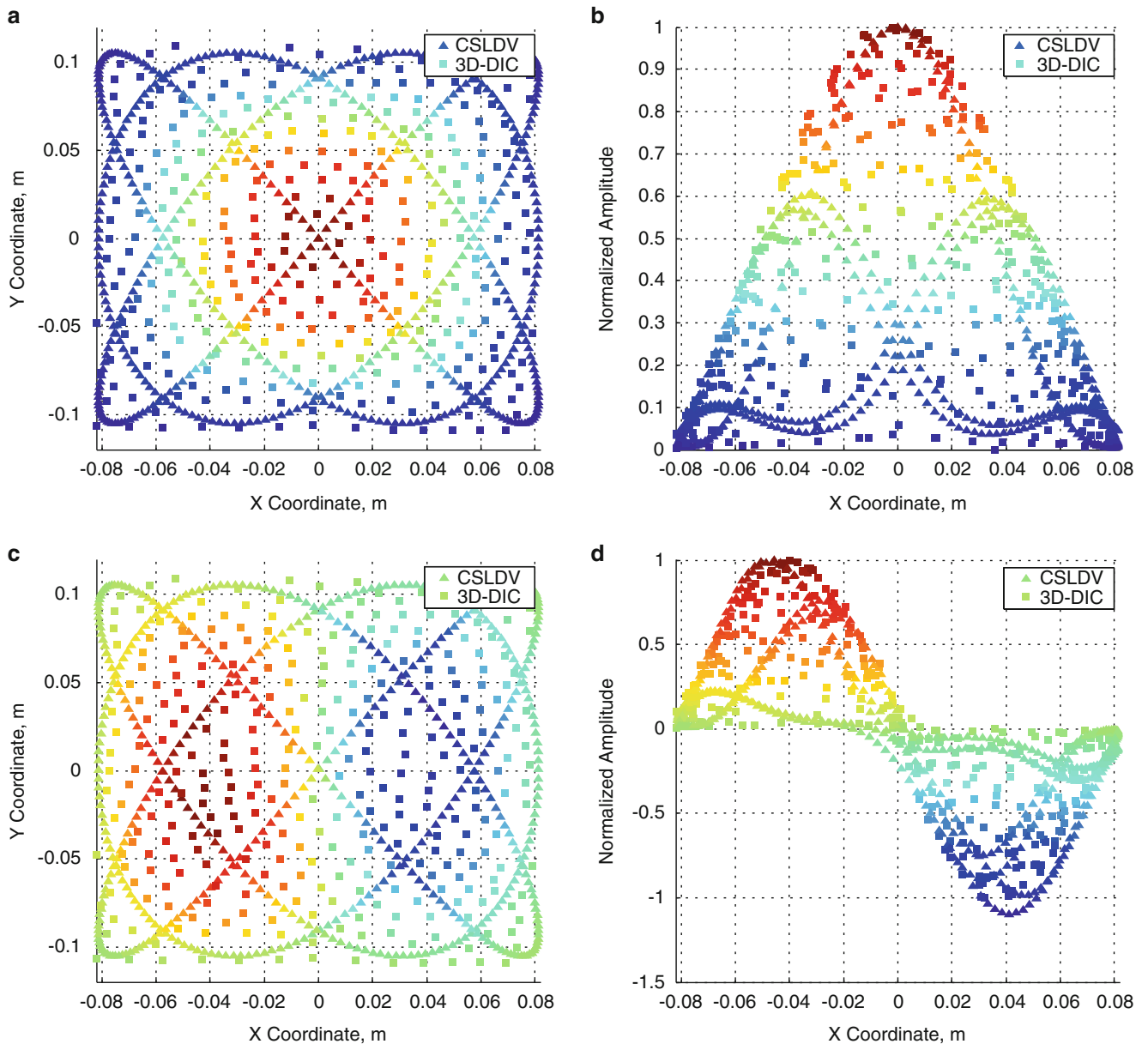
Fig. 23.8 Deformation shape of CSLDV and 3D-DIC: (**a**, **b**) 1st harmonic, (**c**, **d**) 2nd harmonic

seeking to update a nonlinear FE model of the structure, as the authors have begun to explore in [18], because there are often many ways in which the model may be updated to match the linear natural frequencies but nonlinear response predictions will not be accurate unless it also reproduces the correct nonlinear couplings between modes and the correct frequency-energy dependence for each mode.

Both techniques have shown the ability to provide dense measurements along surfaces, as long as each technique can "see" the surface throughout the deformation. To improve measurement accuracy, additional surface preparation is required, unless the material used for the test piece fulfills specific requirements (eg. a random pattern for 3D-DIC and a sufficiently reflective pattern for CSLDV). For DIC, this surface preparation is especially important when response levels are small, or in a structure's linear range. For CSLDV, surface preparation becomes more important when the vibration amplitude becomes small relative to speckle noise, and also as the laser standoff distance (or field of view) increases.

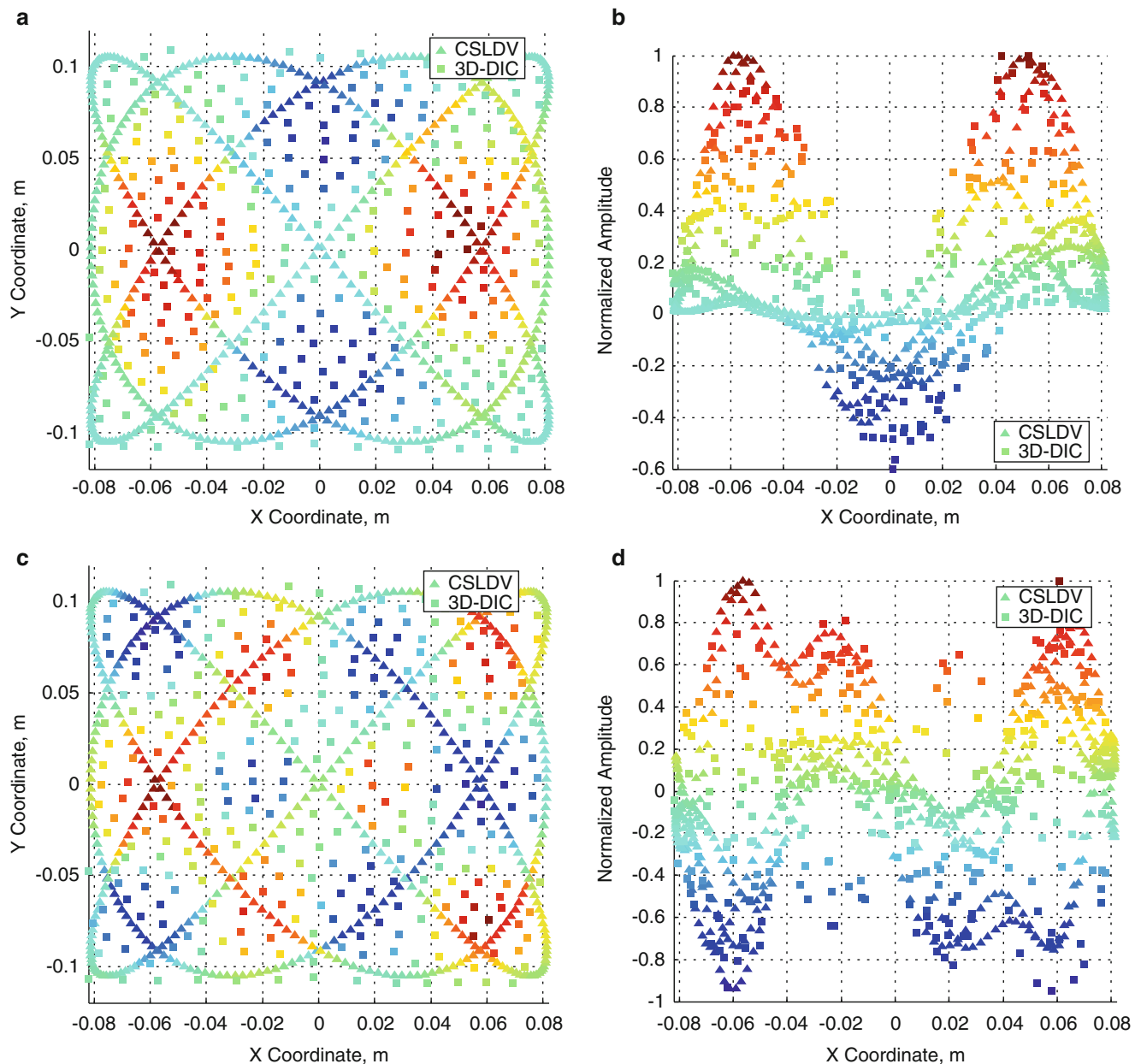**Fig. 23.9** Deformation shape of CSLDV and 3D-DIC: (**a**, **b**) 3rd harmonic, (**c**, **d**) 6th harmonic

References

1. Schwingshackl CW, Stanbridge AB, Zang C, Ewins DJ (2007) Full-field vibration measurement of cylindrical structures using a continuous scanning LDV technique. In: Presented at the 25th international modal analysis conference (IMAC XXV), Orlando
2. Stanbridge AB, Ewins DJ (1999) Modal testing using a scanning laser Doppler vibrometer. Mech Syst Signal Process 13:255–270
3. Stanbridge AB, Martarelli M, Ewins DJ (2004) Measuring area vibration mode shapes with a continuous-scan LDV. Measurement 35:181–189
4. Martarelli M (2001) Exploiting the laser scanning facility for vibration measurements. PhD, Imperial College of Science, Technology & Medicine, Imperial College, London
5. Stanbridge AB, Khan AZ, Ewins DJ (2000) Modal testing using impact excitation and a scanning LDV. Shock Vib 7:91–100
6. Allen MS (2009) Frequency-domain identification of linear time-periodic systems using LTI techniques. J Comput Nonlinear Dyn 4:1–6
7. Yang S, Sracic MW, Allen MS (2012) Two algorithms for mass normalizing mode shapes from impact excited continuous-scan laser Doppler vibrometry. J Vib Acoust 134:021004
8. Wereley NM (1991) Analysis and control of linear periodically time varying systems. PhD, Department of Aeronautics and Astronautics, Massachusetts Institute of Technology, Cambridge

9. Wereley NM, Hall SR (1991) Linear time periodic systems: transfer functions, poles, transmission zeroes and directional properties. Presented at the proceedings of the 1991 American control conference, Boston

10. Wereley NM, Hall SR (1990) Frequency response of linear time periodic systems. Honolulu, pp 3650–3655

11. Yang S (2013) Modal identification of linear time periodic systems with applications to continuous-scan laser Doppler vibrometry. PhD, Engineering Physics, University of Wisconsin-Madison

12. Yang S, Allen MS (2014) Harmonic transfer function to measure translational and rotational velocities with continuous-scan laser Doppler vibrometry. J Vib Acoust 136:1–11

13. Schmidt TE, Tyson J, Galanulis K, Revilock DM, Melis ME (2005) Full-field dynamic deformation and strain measurements using high-speed digital cameras, 26th International Congress on High-Speed Photography and Photonics, Bellingham, WA, pp 174–185

14. Tiwari V, Sutton MA, Shultis G, McNeill SR, Xu S, Deng X, Fourney WL, Bretall D (2009) Measuring full-field transient plate deformation using high speed imaging systems and 3D-DIC. In: Proceedings of the society for experimental mechanics annual conference, Albuquerque

15. Niezrecki C, Avitabile P, Warren C, Pingle P, Helfrick M (2010) A review of digital image correlation applied to structural dynamics. AIP Conf Proc 1253:219–232

16. Helfrick M (2011) 3D digital image correlation methods for full-field vibration measurement. Mech Syst Signal Process 25:917–927

17. Warren C, Niezrecki C, Avitabile P, Pingle P (2011) Comparison of FRF measurements and mode shapes determined using optically image based, laser, and accelerometer measurements. Mech Syst Signal Process 25:2191–2202

18. Ehrhardt DA, Harris RA, Allen MS (2014) Numerical and experimental determination of nonlinear normal modes of a circular perforated plate. In: 32nd international modal analysis conference (IMAC XXXII), Orlando

19. Allen MS, Weekes B (2015) Nonlinear model updating of a flat plate and a stiffened skin panel from a lynx helicopter. Presented at the scitech 2015, 56th AIAA structures, structural dynamics and materials conference, Kissimmee

20. Ehrhardt D, Yang S, Beberniss T, Allen M (2014) Mode shape comparison using continuous-scan laser Doppler vibrometry and high speed 3D digital image correlation. In: XXXII international modal analysis conference, Orlando

21. G. mbH, "Aramis," 6.3.0 ed. Braunschweig, Germany, 2011

22. G. mbH, "IVIEW Real Time Sensor," 6.3.0 ed. Braunschweig, Germany, 2011

23. Wereley NM, Hall SR (1991) Linear time periodic systems: transfer function, poles, transmission zeroes and directional properties. In: American control conference, Boston, pp. 1179–1184

24. Yang S, Allen MS (2014) Lifting approach to simplify output-only continuous-scan laser vibrometry. Mech Syst Signal Process 45:267–282

25. Yang S, Allen MS (2012) Output-only modal analysis using continuous-scan laser Doppler vibrometry and application to a 20 kW wind turbine. Mech Syst Signal Process 31:228–245

26. Sutton MA, Orteu JJ, Schreier H (2009) Image correlation for shape, motion, and deformation measurements: basic concepts, theory, and applications. Springer Science and Business Media LLC, New York

27. Ehrhardt DA, Beberniss TJ (2013) Experimental investigation of dynamic out of plane displacement error in 3D digital image correlation. In 54th AIAA/ASME/ASCE/AHS/ASC structures, structural dynamics and materials conference, Boston, 8–11 Apr 2013

28. Gordon RW, Hollkamp JJ (2006) Nonlinear random response of a clamped plate: a well characterized experiment. Presented at the 47th AIAA/ASME/ASCE/AHS/ASC structures, structural dynamics, and materials conference, Newport

29. Gasparoni A, Allen MS, Yang S, Sracic MW, Castellini P, Tomasini EP (2010) Experimental modal analysis on a rotating fan using tracking-CSLDV. Presented at the 9th international conference on vibration measurements by laser and noncontact techniques, Ancona

30. Peeters M, Kerschen G, Golinval JC (2011) Modal testing of nonlinear vibrating structures based on nonlinear normal modes: experimental demonstration. Mech Syst Signal Process 25:1227–1247

31. Kuether RJ, Allen MS (2014) A numerical approach to directly compute nonlinear normal modes of geometrically nonlinear finite element models. Mech Syst Signal Process 46:1–15

32. Kerschen G, Peeters M, Golinval JC, Vakakis AF (2009) Nonlinear normal modes. Part I. A useful framework for the structural dynamicist. Mech Syst Signal Process 23:170–194

33. Gordon RW, Hollkamp JJ (2011) Reduced-order models for acoustic response prediction. Air Force Research Laboratory, AFRL-RB-WP-TR-2011-3040, Dayton

Chapter 24
Vibration Event Localization in an Instrumented Building

Javier Schloemann, V.V.N. Sriram Malladi, Americo G. Woolard, Joseph M. Hamilton, R. Michael Buehrer, and Pablo A. Tarazaga

Abstract In this paper, we present the preliminary results of an indoor location estimation campaign using real data collected from vibration sensors mounted throughout an instrumented smart building. The Virginia Tech Smart Infrastructure Laboratory house a unique testbed featuring a fully instrumented operational building with over 240 accelerometers permanently mounted to the steel structure. It is expected that in the future, more and more buildings will be constructed with sensors scattered about their infrastructures, in no small part due to the envisioned promises of such systems which include improved energy efficiency, health and safety monitoring, stronger security, improved construction practices, and improved earthquake resistance. One of the most promising uses of this smart infrastructure is for indoor localization, a scenario in which traditional radio-frequency based techniques often suffer. The detection and localization of indoor seismic events has many potential applications, including that of aiding in meeting indoor positioning requirements recently proposed by the FCC and expected to become law in the near future. The promising initial results of a simplistic time-difference-of-arrival based localization system presented in this paper motivate further study into the use of vibration data for indoor localization.

Keywords Smart infrastructures • Indoor localization • Vibration sensing and detection • Time-of-arrival • Time-difference-of-arrival

24.1   Introduction

The electronics and communications revolution has completely changed life in the modern world. A new frontier in this revolution is the massive instrumentation of modern infrastructure or *smart buildings*. Smart buildings promise to exploit advanced building instrumentation and control to bring benefits such as improved energy efficiency, health and safety monitoring, stronger security, improved construction practices, and improved earthquake resistance, among others.

One promising use of increased building instrumentation is the localization of events causing vibrations. When specific floor vibrations (e.g., footsteps) can be localized, it becomes possible to locate individuals moving throughout the building. This leads to several important applications which may be realized. Specifically, locating individuals within buildings has strong applications in many important areas such as emergency response, personnel monitoring, building security, improved energy efficiency, etc. Energy savings may be realized if heating/cooling systems can be adjusted based on precise knowledge of building occupancies. A recent DOE report [1] suggests that advanced occupancy sensors such as those we are considering are capable of increasing building efficiencies by 18 %, as opposed to the 5.9 % increase realizable using common occupancy sensors. An emergency response (e.g., building evacuation) may be greatly improved if the number and locations of individuals within the building is known to security personnel. Furthermore, the response times of first-responders can be dramatically improved if the locations of individuals is known at the room level when 911 is called from a mobile phone. Thus, there are many ways in which vibration event detection and localization can bring to fruition the potential benefits of smart buildings. We also note that, recently, the FCC, citing the fact that a majority of E911 wireless calls now come from indoor locations, published a Third Notice of Proposed Rulemaking recommending future location accuracy requirements

---

J. Schloemann • R.M. Buehrer
Department of Electrical and Computer Engineering, Blacksburg, VA 24061, USA

V.V.N. Sriram Malladi (✉) • A.G. Woolard • J.M. Hamilton • P.A. Tarazaga
Department of Mechanical Engineering Virginia Tech, Virginia Tech Smart Infrastructure Laboratory (VTSIL),
Virginia Polytechnic Institute and State University, Blacksburg, VA 24061, USA
e-mail: sriram@vt.edu

for indoor mobile phone calls [2]. Some cellular providers are quite pessimistic about the chances of RF-based localization to meet these proposed requirements. The work explored herein (especially when integrated with cellular networks) may allow for the localization of individuals to accuracies much better than those being suggested by the FCC.

The study of vibrations deals with the propagation of waves in materials (e.g., traveling or standing). The propagation of waves in solids has been studied for several reasons including, but not limited to, structural health monitoring, signaling, and earthquake analysis/propagation. Usually these studies involve the analysis of in-plane and out-of-plane waves in a dispersive medium. Sometimes referred with different nomenclature (i.e., P and S, in-phase and out-of-phase, etc.) these waves are distinguished by a pair of wave types where one type travels faster and carries less energy and the other travels slower, but carries most of the energy. In-plane waves can be used to announce the arrival of out-of-plane waves, which in earthquake situations can alert the onset of a larger event. The dispersive nature of waves in a solid leads to difficulties in using techniques such as time-of-arrival to perform simple trilateration. In this work, we apply common multilateration procedures for impact localization in a highly-instrumented building environment.

There has been considerable research done over the past 30 years in the areas of RF-based and acoustic-based localization [3–9]. The previous work has largely focused on either distance-based measurements (e.g., time-of-arrival (TOA), time-difference-of-arrival (TDOA), received signal strength (RSS)) or angle-based measurements (e.g., angle-of-arrival (AOA)), although substantial work has also been done with pattern-matching approaches (e.g., [10]). The work herein is interested in localization in 2-dimensional space in which emissions are due to vibration events and occur at unknown initial times. A brief summary of methods for footstep source localization is presented by Lee in [11] which includes three well known methods: (1) the amplitude attenuation over a distance between sensors (analogous to RSS), (2) the difference in arrival times for a given signal (TDOA), and (3) the orthogonality relationship of particle motion for P and S waves. These methods are discussed in more detail by Bahroun [12], where it is asserted that wave reflections, dispersion, and flexural mode dominance in an indoor environment generally make these methods inaccurate for localization. To get around these issues, a grid of sensors are used to establish an order-of-arrival matrix, which is used to determine from what area the source came from. Time difference and particle motion techniques are used to track personnel in an outdoor environment in [13] with relatively low accuracy, attributed to the dispersive nature of seismic waves. In [14], the TDOA method proved to be superior to bearing estimation due to the characteristics of seismic waves. From a building point of view, it is possible that occupation may be of a greater concern than personnel tracking. Researchers at Carnegie Mellon University in Pittsburgh have recently developed a system to accurately estimate the number of occupants in a room using sparsely distributed vibration sensors [15]. However, despite all of this past work, there have been no studies in a fully instrumented operational building, and thus there remain several open problems related to practical localization via vibration tracking.

In this project, the authors investigate the use of advanced building instrumentation to provide person location and tracking through the localization of hammer impacts in an instrumented corridor. While the concept of using seismic disturbances to localize footsteps has been proposed previously, it is still a very immature area of research. Further, the application to buildings remains unsolved, primarily because the appropriate testbed did not exist. The work presented here leverages such a testbed, Virginia Tech's newly-constructed Goodwin Hall, the most instrumented public building in the world for vibrations.

24.2 The Smart Building Testbed: Goodwin Hall

The research work presented in this paper is enabled by the instrumentation of a new building on the campus of Virginia Tech. The instrumentation of Virginia Tech's Goodwin Hall has been spearheaded by Dr. Pablo Tarazaga, Founder & co-director of the VT Smart Infrastructure Lab (VT-SIL), which has the mission of advancing research and education in areas that utilize sensor information in order to improve the design, monitoring, daily operation, and human-structure interactions in civil and mechanical structures. The centerpiece of VT-SIL is a full-scale living laboratory in this new 160,000 ft^2 building. In conjunction with the Virginia Tech College of Engineering, VT-SIL designed this living laboratory to comprise over 136 welded mounts for accelerometers (3 axis-per-mount capability), along with other types of sensors. It is believed that this is the most instrumented public building in the world for vibrations. Currently, the data collection system features five distributed VTI Instruments data acquisition units, connecting 241 PCB accelerometers via 55,000 ft of Dytran cable throughout the building to create a fully wired and synchronized system. The sensors are located throughout the structure, including the buildings major corners, corridors, laboratories, and office floors. The sensor distribution has been carefully designed to create a multidisciplinary research testbed that enables a great diversity of applications. This testbed is set in an academic environment, giving the team full control of the structure for experimentation: the team can design specific scenarios to rigorously validate the proposed algorithms over time. The present work is a result of the preliminary tests conducted on this building with the aim of localizing a specific vibration source in a highly-complex environment.

24.3 Experimental Setup

The research presented in this paper aims to study the use of time-based techniques to locate the source of an impact on a concrete floor. An experimental setup was designed such that the response of a building floor to a hammer strike is recorded with the help of a large number of accelerometers installed throughout the floor. A Kistler modal hammer (model: 9727A500) is used to impact the fourth floor of Goodwin Hall (GH). The structural waves generated by the impact are captured by sixteen PCB shear accelerometers (model: 393B04) mounted underneath the floor of the 4th floor. The 4th floor of GH large amount of floor sensors dedicated to this specific application. The relative locations of the impact strikes and the sensors are placed such that some sensors are in direct line-of-contact with the source of the vibrations while others have obstacles such are walls, doors, equipment, etc. in between. The locations of the sensors are plotted in Fig. 24.1 and their global coordinates are tabulated and presented in Table 24.1. The floor is impacted such that the maximum vibration amplitude is sensed by accelerometers C4-C7. The relative location of various hammer hits w.r.t the sensors is shown in Fig. 24.2. In Fig. 24.5, the location of the hammer strike is represented by a green diamond and the sensor locations are represented by cyan squares (note that there are many additional vibration sensors in the building, but only the sensors used for this experiment have been shown in the figure). Each sensor is labeled based on the corresponding channel number in the data acquisition system. The location of one of the sensors (C-10) is assumed to be the global origin for the floor against which the coordinates of the other sensors is measured. The wave propagation in the floor is studied with the help of hammer impacts employing two types of tips, a steel-tip and a nylon tip, while all hammer strike experiments were repeated ten times in order to facilitate multiple localization attempts.
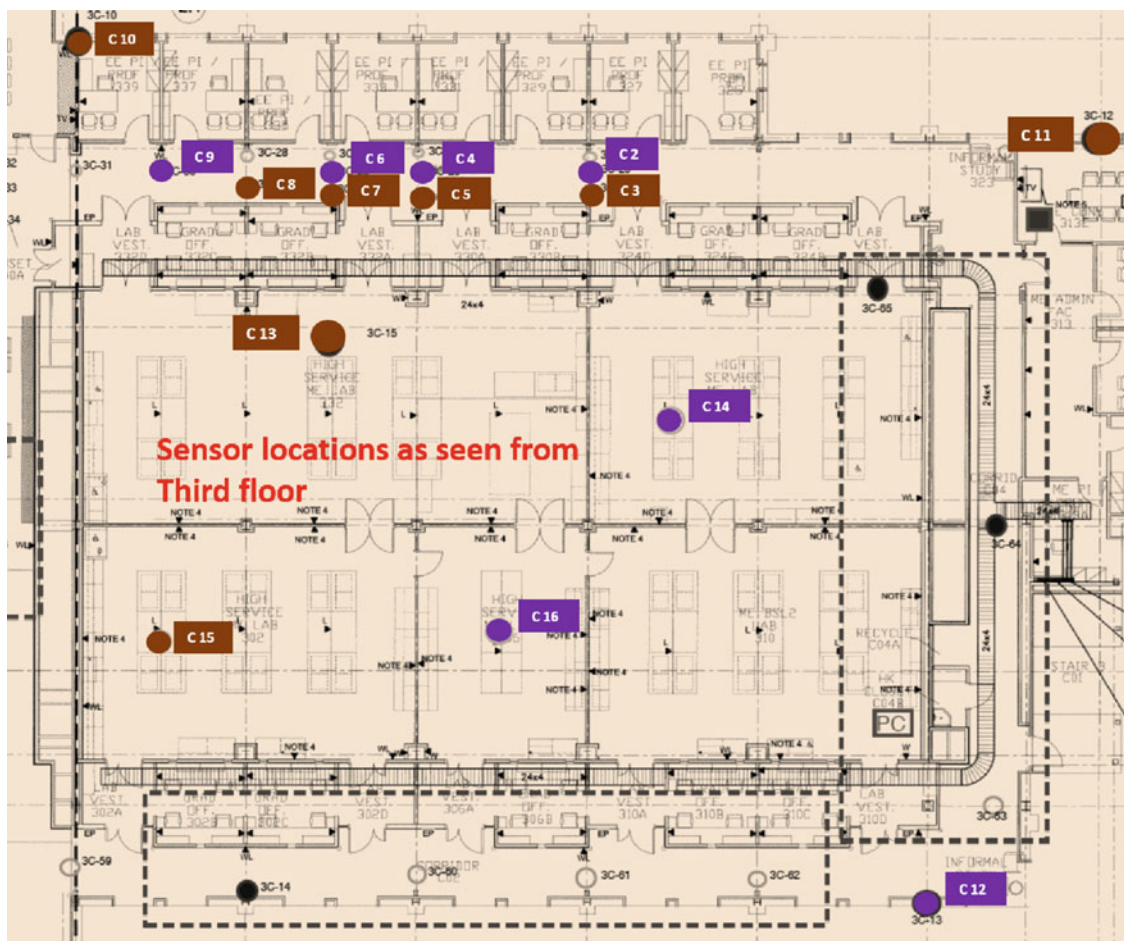

Fig. 24.1 Location of sensors and their labels

Table 24.1 Global coordinates

| Sensor label	Coordinates (ft)		Sensor label	Coordinates (ft)	
	x	y		x	y
C − 2	63.99	−15.36	C − 12	104.7	−105.8
C − 3	63.92	−17.49	C − 13	28.90	−31.63
C − 4	43.08	−51.21	C − 14	76.36	−46.63
C − 5	42.86	−17.67	C − 15	10.63	−73.09
C − 6	32.60	−15.25	C − 16	55.36	−72.54
C − 7	32.50	−17.64	ImpactPointA	37.84	−14.97
C − 8	22.07	−17.78	ImpactPointB	37.84	−16.47
C − 9	10.77	−15.10	ImpactPointC	37.84	−17.97
C − 10	0	0	ImpactPointD	40.84	−16.47
C − 11	126.0	−12.54	ImpactPointE	34.84	−16.47
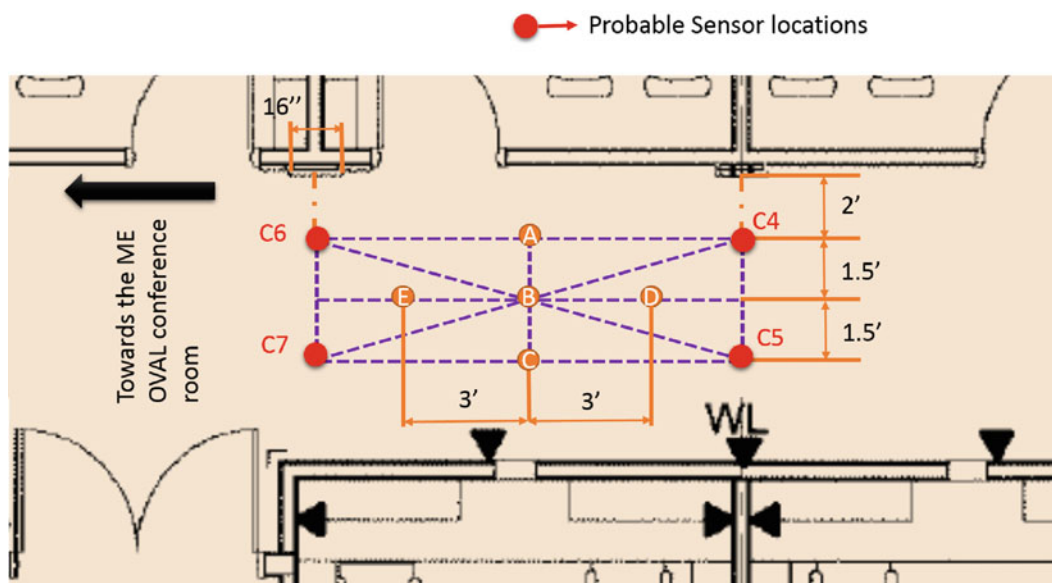
Fig. 24.2 Location of various hammer hits on the floor (zoomed version of the floor plan with hammer locations)

24.4 Localization

In this section, we briefly describe the localization method used to obtain the preliminary results. Since Goodwin Hall contains a highly synchronized recording system, the vibration sensors are inherently synchronized in time. However, the impact time is unknown and thus estimating a true time-of-arrival metric is not possible since the time origin is not available. Instead, an arbitrary reference time may be chosen resulting in all TOA estimates containing the same fixed timing offset. In this scenario, time-differences-of-arrival may be calculated which eliminate the constant timing offsets in the TOA estimates at the cost of one fewer observation (since one of the TOA estimates must be used as the differencing measurement). Geometrically, the difference between a TOA and TDOA estimate is as follows: whereas a TOA estimate places the position of the impact on a circle centered at the reference sensor, a TDOA estimate places the impact point on a hyperbola where the two reference sensors used in the TDOA calculation are its focal points as shown in Fig. 24.3. The approach described above is the one implemented to obtain the preliminary results presented here. Note that another common technique for determining the time differences uses the locations of the cross-correlation peaks of the received signals at different pairs of sensors. However, it is known that the performance of this technique degrades significantly in dispersive, multipath channels [16] and our preliminary results using this approach were not promising and are thus omitted from this paper. The TOA estimates were calculated using a simple peak detection algorithm on the sensors' vibration response magnitudes and the sensor with the strongest overall peak (presumed to be the most reliable) was used as the reference sensor. In Fig. 24.4, we present an example of a seismic wave from a single steel-tipped hammer impact with vibration response shown at the top arriving at two sensors, C-6 (middle) which is closer and C-8 (bottom) which is farther from the impact point. Note that the
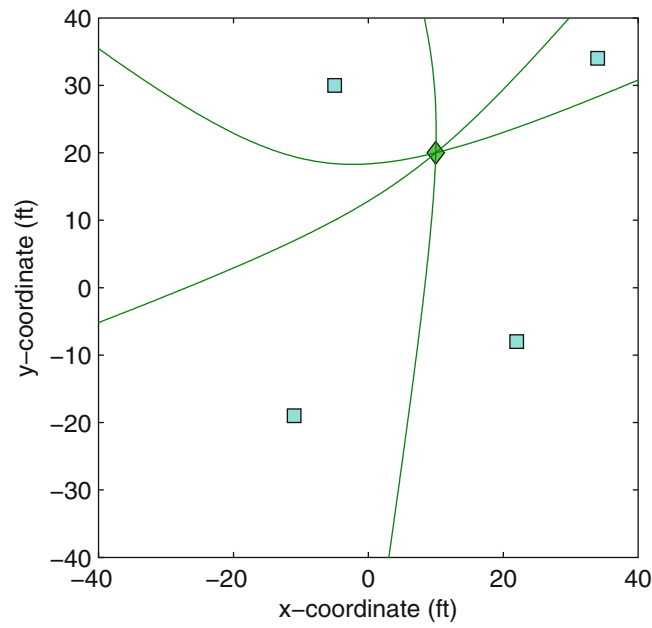
Fig. 24.3 An example of target positioning using TDOA observations in the absence of noise. The true target location is at the intersection of the hyperbolae
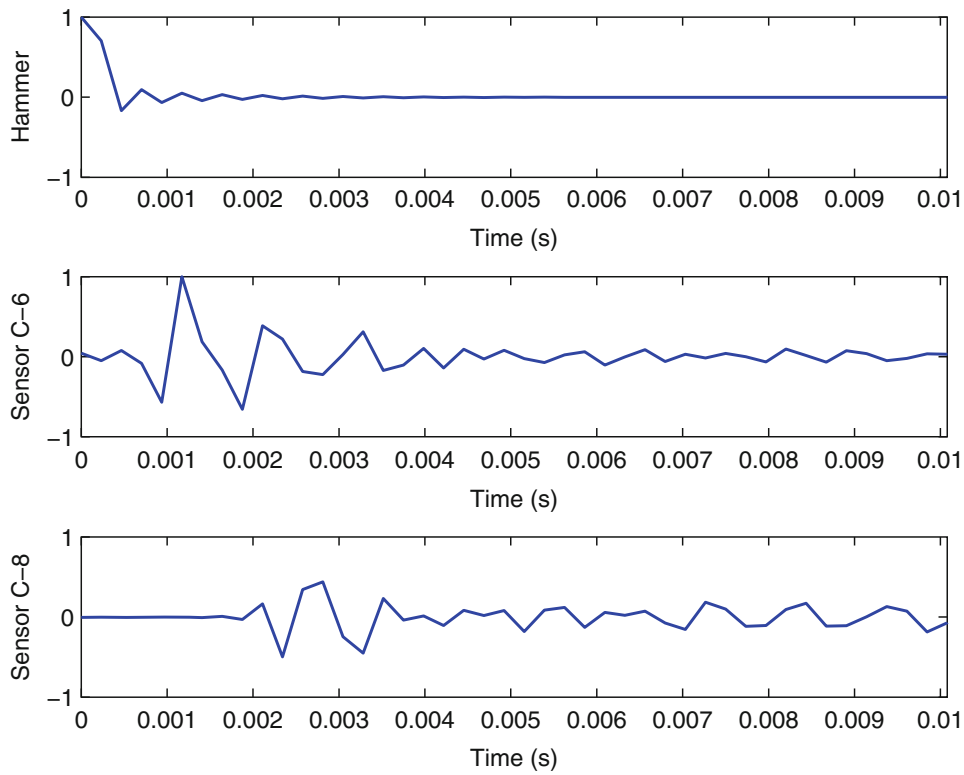

Fig. 24.4 Examples of the time-delayed and attenuated responses at two vibration sensors with different separations from the hammer impact at time zero

hammer impact, occurring at time zero, is recorded at the closer sensor C-6 earlier in time and with a greater magnitude than the same impact recorded at the more distant sensor C-8 (the two topmost plots have been normalized such that the maximum response is unity, while the plot for sensor C-8 is shown with the same normalization as used for sensor C-6). In this work, a total of 15 sensors were used for localization (C-2 to C-16) resulting in a total of 14 TDOA observations. These observations along with the sensor locations were then used to calculate the hammer impact locations using the well-known Chan & Ho TDOA algorithm presented in [6] with a preliminary propagation speed estimate for the seismic waves of 3,000 ft/s. The final result is an approximation of the maximum likelihood estimator and the position estimate

$$\hat{\theta}_{\mathrm{ML}} = \underset{\theta}{\mathrm{argmax}} \ f(\mathbf{z} \mid \theta),$$

where $\mathbf{z}$ represents the collection of TDOA observations, θ is the true impact location, and $f(\cdot)$ represents the probability density function of its argument. In other words, the final position estimate is the location which best explains the measured TDOA data.

24.5 Preliminary Results

We now present the results of several initial experiments designed to collect real vibration data in Goodwin Hall on a relatively quiet traffic day. Primarily, the results serve as a proof-of-concept of the ability to perform localization using the sensors installed in this smart building and motivate the continued study of vibration-based localization and tracking.

First, we present the results of the TDOA positioning system for the scenarios concerning hammer impact point B. For all ten simulations, the resulting TDOA position estimates are shown in Fig. 24.5 as red crosses for both the (a) steel-tipped and (b) nylon-tipped hammer impacts. A visual inspection reveals that these initial results are very promising. Using the steel-tipped hammer, the root mean square errors (RMSE) in the x and y directions was found to be $\mathrm{RMSE}(x) = 1.99$ ft and $\mathrm{RMSE}(y) = 3.17$ ft, respectively, resulting in an overall root mean square position error of

$$\mathrm{RMSE} = \sqrt{\mathrm{RMSE}^2(x) + \mathrm{RMSE}^2(y)} = 3.74 \ \text{ft}.$$

Using the nylon-tipped hammer, the resulting RMSE of the position estimates over the ten simulations was clearly higher: $\mathrm{RMSE} = 6.45$ ft. The RMSEs in both the x and y directions as well as the overall positioning RMSEs over all ten simulations carried out for each of the various experimental scenarios is tabulated in Table 24.2. We note that in general, better positioning performance was obtained using the steel-tipped hammer. Although the nylon-tipped hammer is expected to yield an impact more similar to a footstep, it should be mentioned that the results were generated using simplistic techniques (e.g., peak
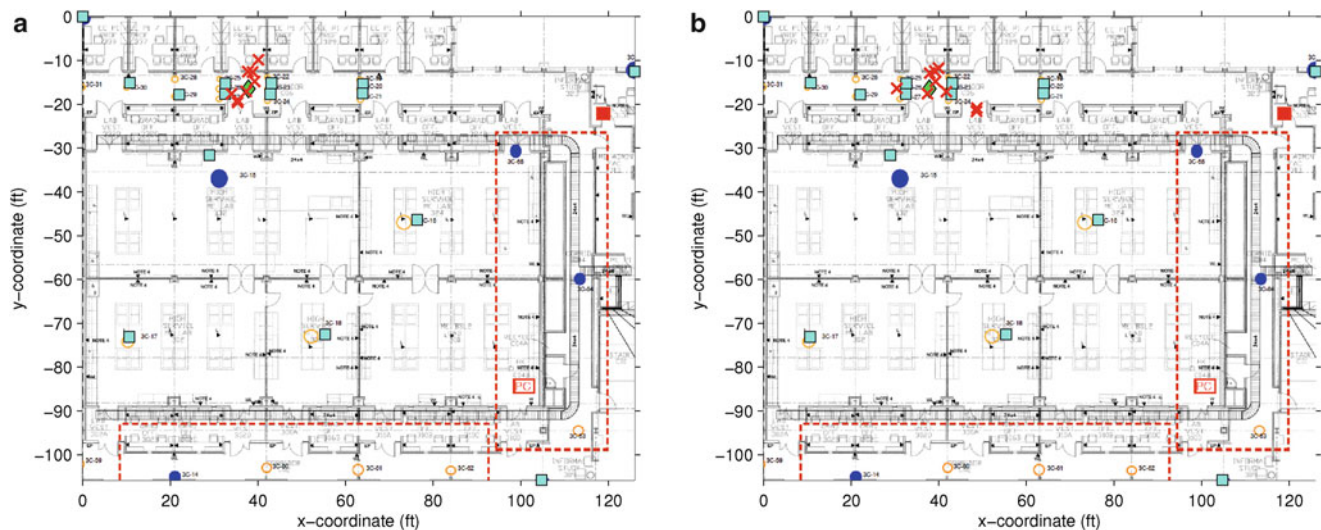

Fig. 24.5 TDOA position estimates (*red crosses*) of the hammers with different tips at impact point B (*green diamond*) using data collected at 15 vibration sensors (*cyan squares*). (**a**) Steel-tipped impact. (**b**) Nylon-tipped impact (Color figure online)

Table 24.2 Preliminary positioning results

Position error performance (ft)	Experimental Scenario							
	A		B		C	D	E	
	Steel	Nylon	Steel	Nylon	Nylon	Nylon	Steel	Nylon
RMSE(x)	4.97	6.88	1.99	5.59	6.28	4.51	4.33	3.19
RMSE(y)	8.74	7.79	3.17	3.20	6.44	5.41	3.46	6.63
OverallRMSE	10.1	10.4	3.74	6.45	9.00	7.04	5.55	7.36

detection, a simple TDOA algorithm, a coarse estimate of wave propagation speed). Thus, even as the experiments are made more realistic (e.g., footfalls instead of hammer strikes, more interference from other vibration sources), there is still much room available for countering the expected degradation from these less favorable conditions using more sophisticated techniques for both signal detection and localization.

24.6 Conclusion

This paper presents preliminary results of TDOA-based target localization using real vibration data collected in a cutting-edge smart building. The test are conducted in the Virginia Tech Smart Infrastructure Laboratory which houses the most instrumented public building in the world for vibrations with over 240 accelerometers. While simplistic techniques were used, the results are promising and prompt further study into the use of vibration data for indoor localization, an environment in which typical positioning methods, such as RF-based GPS positioning systems, oftentimes struggle. The development of this technology will be a key driver allowing smart buildings to reach their full potential, promising enhanced energy efficiency through automated environmental controls as well as enhanced emergency responsiveness, both in terms of evacuating buildings in times of emergency as well as locating specific individuals in distress, a very difficult problem with life-threatening implications in large buildings.

References

1. Zhang J, Lutes RG, Liu G Brambley MR (2013) Energy savings for occupancy-based control (OBC) of variable-air-volume (VAV) systems, vol. PNNL-22072, Pacific Northwest National Laboratory
2. Federal Communications Commission, Wireless E911 Location Accuracy requirements: third further notice of proposed rulemaking, PS Docket No. 07-114, February 21 2014
3. Torrieri DJ (1984) Statistical theory of passive location systems. IEEE Trans Aerosp Electron Syst AES-20(2):183–198
4. Stein S (1981) Algorithms for ambiguity function processing. IEEE Trans Acoust Speech Signal Process 29(3):588–599
5. Stein S (1993) Differential delay/Doppler ML estimation with unknown signals. IEEE Trans Signal Process 41(8):2717–2719
6. Chan YT, Ho KC (1994) A simple and efficient estimator for hyperbolic location. IEEE Trans Signal Process 42(8):1905–1915
7. Patwari N, Ash JN (2005) Locating the nodes: cooperative localization in wireless sensor networks. IEEE Signal Process Mag 22(4):54–69
8. Zekavat R, Buehrer RM (2012) Handbook of position location: theory, practice, and advances. Wiley, New York
9. Buehrer RM, Anderson CR, Martin RK, Patwari N, Rabbat MG (2014) Introduction to the special issue on non-cooperative localization networks. IEEE J Sel Areas Signal Process 8(1):2–4
10. Nerguizian C, Despins C, Affes S (2006) Geolocation in mines with an impulse response fingerprinting technique and neural networks. IEEE Trans Wireless Commun 5(3):603–611
11. Lee H, Park JW, Helal A (2009) Estimation of indoor physical activity level based on footstep vibration signal measured by MEMS accelerometer in smart home environments. Springer, Berlin
12. Bahroun R, Michel O, Frassati F, Carmona M Lacoume J (2014) New algorithm for footstep localization using seismic sensors in an indoor environment. J Sound Vib 333:(3):1046–1066
13. Richman MS, Deadrick DS, Nation RJ, Whitney S (2001) Personnel tracking using seismic sensors. Aerospace/defense sensing, simulation, and controls, International Society for Optics and Photonics, pp. 14–21
14. Pakhomov A, Sicignano A, Sandy M Goldburt ET (2003) Single-and three-axis geophone: footstep detection with bearing estimation, localization, and tracking. AeroSense 2003, International society for optics and photonics, pp. 155–161
15. Pan S, Bonde A, Jing J, Zhang L, Zhang P, Noh, HY (2014) BOES: building occupancy estimation system using sparse ambient vibration monitoring, SPIE Smart Structures and Materials+ Nondestructive Evaluation and Health Monitoring, International Society for Optics and Photonics, pp. 90611O–90611O
16. Gezici S (2008) A survey on wireless position estimation. Wirel Pers Commun 44(3):263–282

Chapter 25
Loading Effect on Induction Motor Eccentricity Diagnostics Using Vibration and Motor Current

Ganeriwala Suri

Abstract Diagnostics of an induction motors is serious issue for improving plant reliability. Air gap eccentricity between rotor and the stator can lead to power loss, decrease in efficiency, current spikes, and other complications leading to premature failure of a motor. Motor current signature analysis (MCSA) and vibration data are commonly used for diagnosing induction motor problems. However, the effect of mechanical loading on the fault signature is not clear. This paper will present a comparison of vibration and motor current signals for induction motor subjected to different levels of torque, unbalance and misalignment loading air gap eccentricity fault signatures. Experiments were performed on intentionally faulted motor with varying degrees of static air-gap eccentricity. Different levels of mechanical torque, unbalance and misalignment loadings were applied to the rotor side. The data was analyzed using both vibration and motor current sensors. Results indicate significant components in motor current signature to due rotor eccentricity and torsional mechanical loadings. Vibration spectra do not provide a clear picture air gap eccentricity fault. But vibration data provide a better indication of mechanical faults than the motor current data. The results suggest that both motor current and vibration measurements are required for more complete diagnostics of induction motors.

Keywords MCSA • Condition monitoring • Diagnostics • Vibration analysis • Motor current signature analysis

25.1 Introduction

Diagnostics and condition monitoring in industrial rotating machinery can avoid machine downtime, and save time and money. Faults in rotating equipments can generate vibration of mechanical parts or change the power quality of the motor. Also, electrical faults in induction motor can change the behavior of the motor reflecting in motor currents. Motor current signature analysis (MCSA) techniques process motor currents to diagnose the machine. Therefore, a comprehensive study of motor current/voltage and vibration response under faults is needed for such diagnostics. Induction motors are critical components of many industries and are considered to be the 'power horses' of the industry. This paper focuses on the application of Motor Current Signature Analysis (MCSA) to diagnose faults in three-phase induction motors. MCSA has the advantages of non-invasive and online monitoring techniques [1]. A review of publications in the field of MCSA reveals inverse relationship between fault detection ease and importance to the user of that fault detection [2]. Also the amount of literature available on the application of MCSA on broken rotor bars is considerably high compared to the other faults [11]. This article studies effects of mechanical loading induction motor fault due to air gap eccentricity on machine vibration and motor current spectrum.
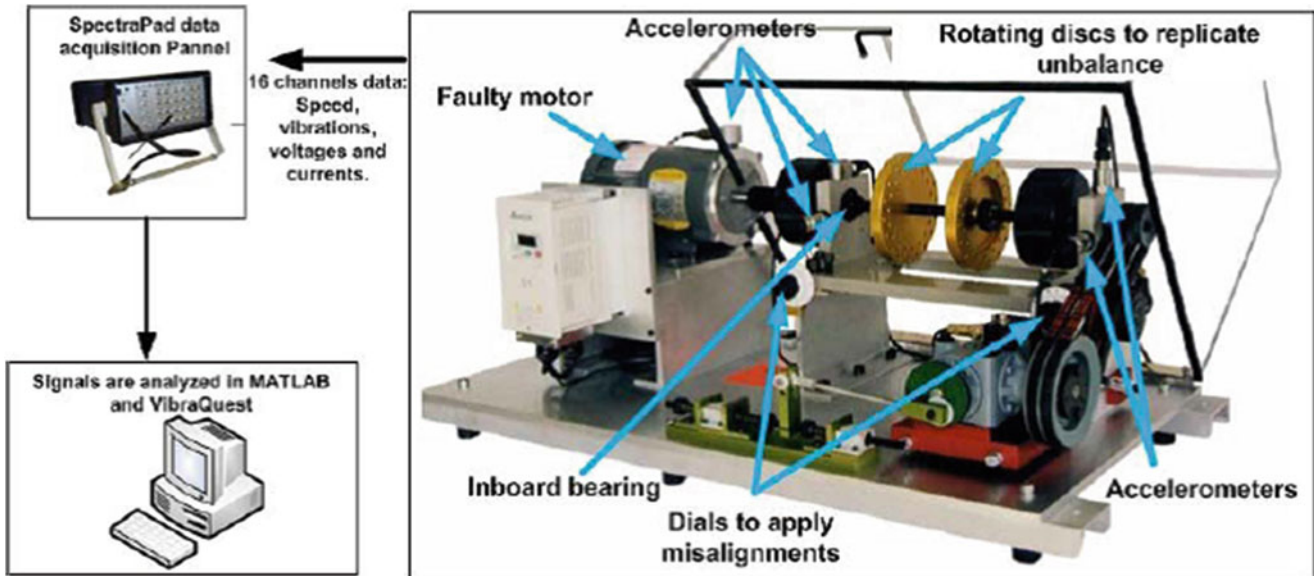
25.2 Experiment Setup

Experiments were performed on the Machinery Fault Simulator (MFS) made by SpectraQuest Inc. Table 25.1 shows the specification of the MFS (Fig. 25.1).

G. Suri (✉)
SpectraQuest Inc., 8227 Hermitage Rd, Richmond, VA 23228, USA
e-mail: suri@spectraquest.com

Table 25.1 Experiment parameters and specifications

Parameter	Value	Parameter	Value
Induction motor, Marathon	0.5 HP	Rolling element bearings	MB ER-10 K
Number of rotor bars	34	Number of balls	9
Number of stator slots	24	Ball dia. [mm]	7.94
Shaft diameter [in]	0.625	Outer race dia. [mm]	31.38
Shaft length [in]	21	Inner race dia. [mm]	47.26
Rotor bearings span [in]	14.1	Bearing pitch dia. [mm]	39.32

Fig. 25.1 Experimental set-up machinery fault simulator (MFS)

Table 25.2 Experiments design

| Faults	Description	16 Channels
Rolling element bearing faults	Inner Race Fault (IRF)	Tachometer
	Outer Race Faults (ORF)	Acceleration of motor, vertical
	Ball Faults (BF)	Acceleration of motor, horizontal
	Combined Faults (CF)	Acceleration of inboard bearing, vertical
Eccentricity faults	Level I: 25 %	Acceleration of inboard bearing, horizontal
	Level II: 50 %	
	Level III: 75 %	Acceleration of outboard bearing, vertical
	Level IV: 100 %	
Mechanical imbalance	Static imbalance	Acceleration of outboard bearing, horizontal
	Coupled imbalance	Acceleration of gearbox, axial
		Acceleration of gearbox, vertical
Misalignment	Parallel and angular	Acceleration of gearbox, horizontal
		Currents (3 phase)
		Voltages (3 phase)

Vibrations of the motor, inboard bearing and outboard bearing were measured. Shaft speed was measured with tachometer. Voltages and currents were measured with the V/I Transducer made by SpectraQuest. For each fault, machine started up from rest and reached steady state and sixteen channels of data were acquired simultaneously sampling rate of 5,120 Hz (Table 25.2).

Three major issues/faults including (1) bearing faults, (2) mechanical imbalance, (3) misalignment faults have been introduced to the Machinery Fault Simulator (MFS) at various levels of static rotor eccentricity. For each fault, 16 channels of data including vibration, voltages, currents, and tachometer signals were recorded. Each channel has been analyzed and the results of channels with distinct aberrations are presented. Results can be used for detection, isolation and assessment of induction motor faults. First, induction motors fundamental equations and fault components for each fault are introduced.

Experiment setup is detailed. For each fault, vibration signals are investigated first. Then, motor current signals are studied in time- and frequency domain to find fault components. Results associated with each fault are presented in terms of graph and tables.

25.2.1 Air Gap Eccentricity

Airgap Eccentricity: Airgap is not a Uniform Radial Length between Rotor surface and Stator bore. It creates a non-uniform electro-dynamic force resulting in uneven torque. This is measured using motor current and indirectly vibration. A depiction of the imbalance and theoretical formulation is given below [7–10].
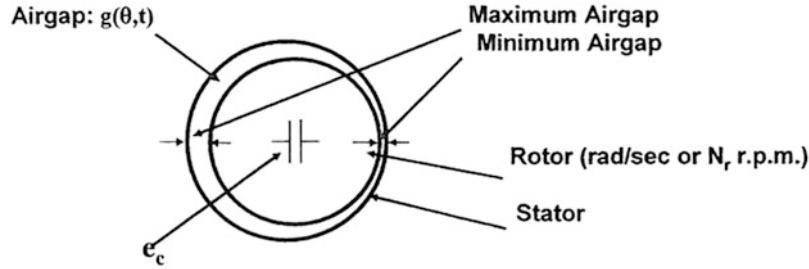
For completeness the airgap length as a function of both static (e_s) and dynamic eccentricity (e_d) can be expressed as :

$$g_{(\theta,t)} = g(1 - e_s \cos\theta - e_d \cos(\omega_r t - \theta)) \tag{25.1}$$

Air gap eccentricity can either be dynamic or static:

- Dynamic eccentricity is created when the rotor axis is shifted to one side while rotational axis still lies on stator axis. This fault causes whirling motion of the rotor.
- Static eccentricity: both rotor and rotational axes are shifted to one side.

The frequency fault equations are given below for both types of eccentricity.

$$f_{ec} = \left\{ 2\,(R.k \pm n_d)\left(\frac{1-s}{p}\right) \pm v \right\} f_1 \tag{25.2}$$

f_{ec} = frequency components of eccentricity faults
k = positive constant or zero
n_d = 0 for underline *static* eccentricity and 1,2,3 ... for dynamic eccentricity
R = number of rotor bars
v = 1,3,5 ... denotes for line frequency sideband harmonics
p = 2, & static eccentricity & $k = 1 \Rightarrow f_{ec} = R.f_r \pm vf_1$

25.3 Results and Discussion

25.3.1 Rolling Element Bearing Faults

Bearing faults (ORF, IRF, BF) were introduced at the inboard bearing. Vibration and currents signals were measured for each case and results are presented here. For comparison in time-domain, Kurtosis value of the bearing vibration in vertical direction, k, and RMS of the current in steady state, I_{ss}, are calculated and presented in Table 25.3. For frequency analysis, fault components should be calculated [3–6]. The induction motor with two poles and line frequency of 60 Hz has the synchronous speed of $f_s = 60$ (Hz). Bearing *multipliers, M, running speed and bearing frequency components, M. f_r, are obtained for* each case and shown in Table 25.3 (Fig. 25.2).

Table 25.3 Effect of bearing faults on motor current

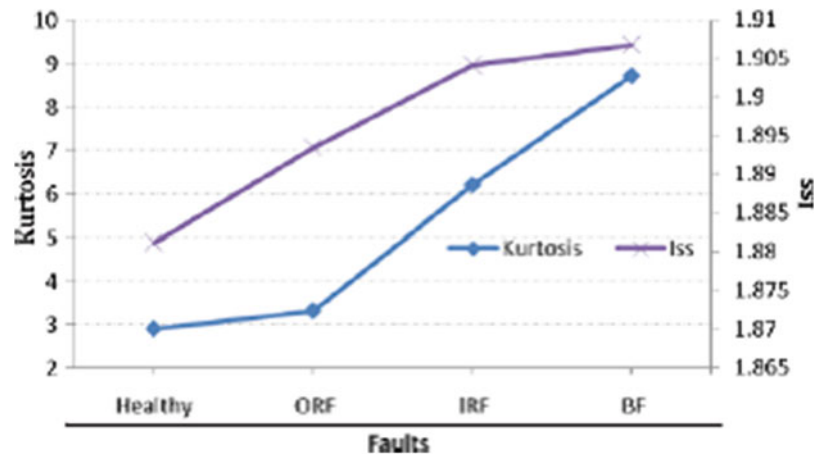|	f_r [Hz]	M	$M. f_r$ [Hz]	k	I_{ss} [A]
Baseline	59.626	–	–	2.90	1.881132
ORF	59.609	3.052	181.92	3.31	1.893456
IRF	59.571	4.948	294.76	6.19	1.904126
BF	59.602	3.984	237.45	8.71	1.906715
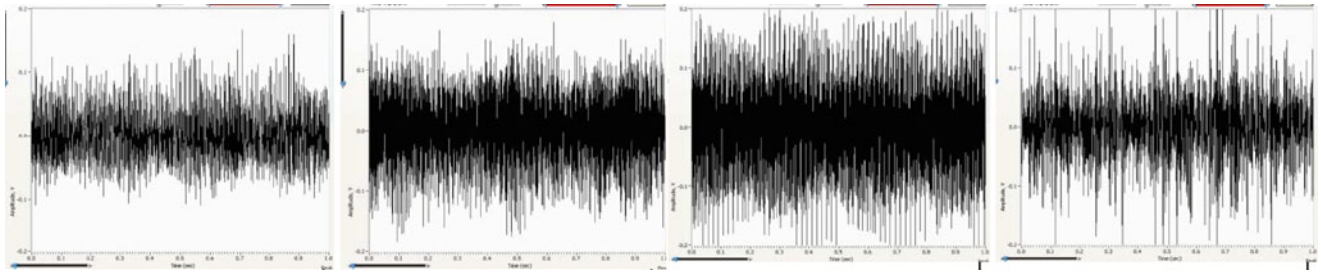
Fig. 25.2 Bearing faults increase both vibration Kurtosis and motor startup currents

Fig. 25.3 Steady State current and kurtosis of bearing with different faults

Kurtosis values, a measure of the 'peakedness' of the vibration data, and motor currents are plotted in Fig. 25.3 below for each fault. Bearing faults generate periodic impacts in bearings which increase Kurtosis values. Also, as shown in Figure, motor currents are slightly increased with presence of faults. Figure 25.3 shows bearing vibrations for different faults. Increase in the level of vibration due to bearing faults is clearly observed.

In the current spectrum, sidebands of line frequency around center frequency harmonics of $M. f_r$ are expected. Figure 25.4b plots frequency spectrum of motor currents for different faults. Line frequency harmonics are clearly observed through the spectrum. However, the fault components, f_{bg}, are not clear. For few cases sidebands of 60 Hz are observed around center frequency harmonics of $M. f_r$ which are highlighted in Fig. 25.4.

25.3.2 Motor with Eccentric Rotor

Table 25.5 shows motor running speed, slip speed, rms values of motor vibration, rising time and motor current values as obtained from experiments with different levels of motor static eccentricity. Also these results are plotted in Fig. 25.4 above. As the severity of eccentricity increases, motor slip and motor vibration increase. However, bearing vibration levels are not increased much compared to the motor vibration. This effect can be used in can be used for the fault isolation. Also, eccentricity faults in induction motors increase motor rising time as well as motor running currents as shown in Fig. 25.5 below.
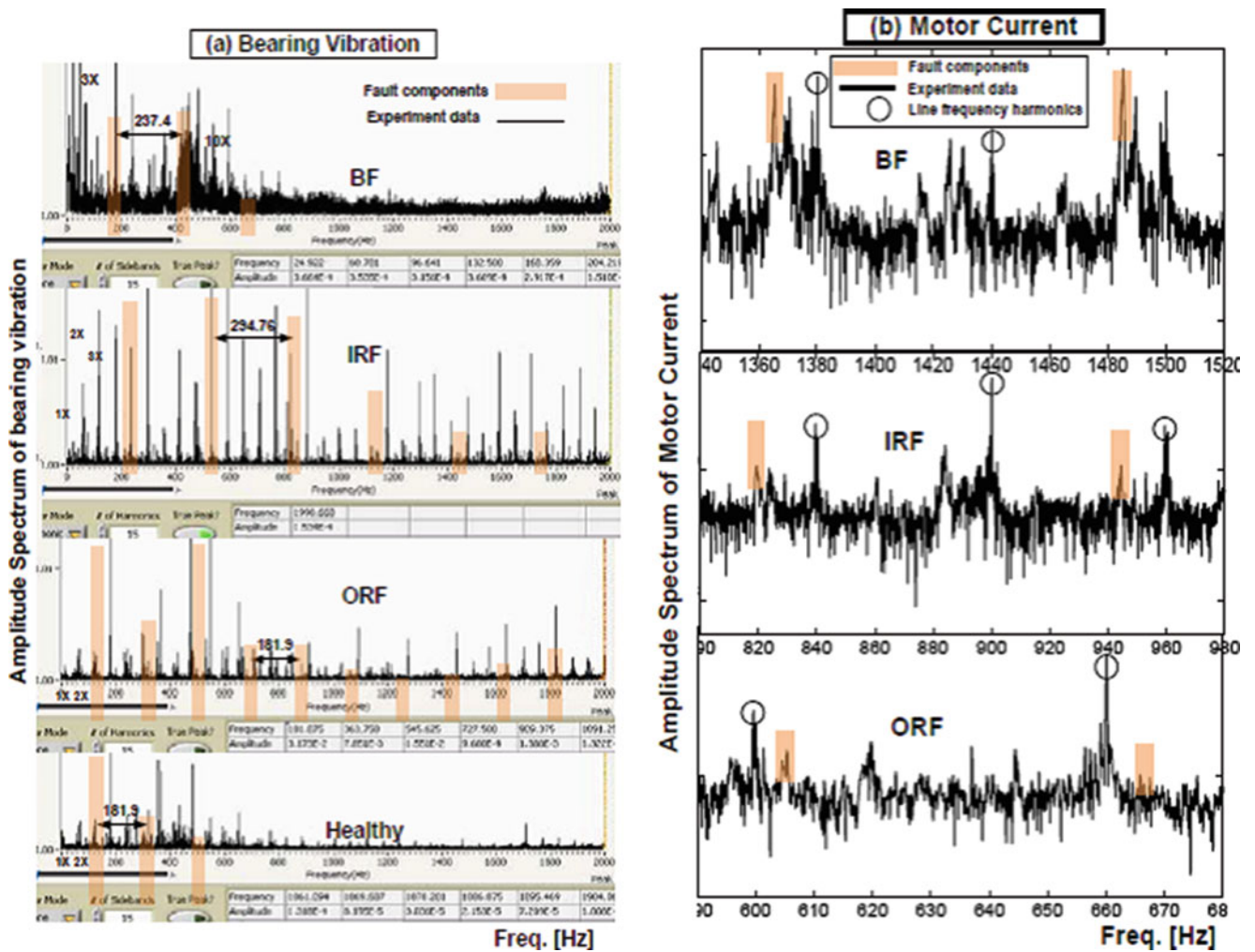
Fig. 25.4 Frequency spectrum of vibration signals (**a**), and frequency spectrum of motor currents (**b**) for different bearing faults

Table 25.4 Effect of static rotor eccentricity faults on motor parameters

	f_r [Hz]	S [Hz]	Motor vibration, RMS	I_{max} [A]	T_r [sec]	I_{ss} [A]
Baseline	58.95	1.047	0.069	5.66	2.05	2.64
Eccentric rotor, Level I	58.99	1.006	0.068	5.73	2.08	2.60
Eccentric rotor, Level II	59.00	1.000	0.070	5.55	2.15	2.59
Eccentric rotor, Level III	58.89	1.114	0.072	5.59	2.33	2.67
Eccentric rotor, Level IV	58.27	1.726	0.163	5.55	2.43	3.07

Figure above plots frequency spectrum of motor currents for different severity levels of eccentricity faults. As expressed in Eq. (2) the sidebands of $\pm vf_1$ around center frequency of $R. f_r$ in motor current spectrum are expected for faulty motor. These sidebands are clearly observed in the spectrum as fault components. However, the magnitude of fault components are not affected by the fault and even in the healthy case, the fault components are observed. Therefore, the results of this study cannot validate expected fault components in motor current spectrum.

It can be seen from the data that eccentricity signature is affected by mechanical loads which is torsional in nature. The torsional loading increases the slip and magnitude of the current. It also produces large number of harmonics and side-band frequencies associated with the slip frequencies [5–7]. This must be due to the non-linearity in the system. The vibration data is inconclusive at this moment. It appears that eccentricity associated with the torsional affect is easy to see the signature in torsional vibration. This requires further investigation into this phenomenon. It can also be seen the effects of non-stationary loading is much more complicated.

The effect of misalignment mechanical load is dominated by the spectra of the misalignment and it obscures the effect on the current signature [12]. This will be investigated further in the next paper.
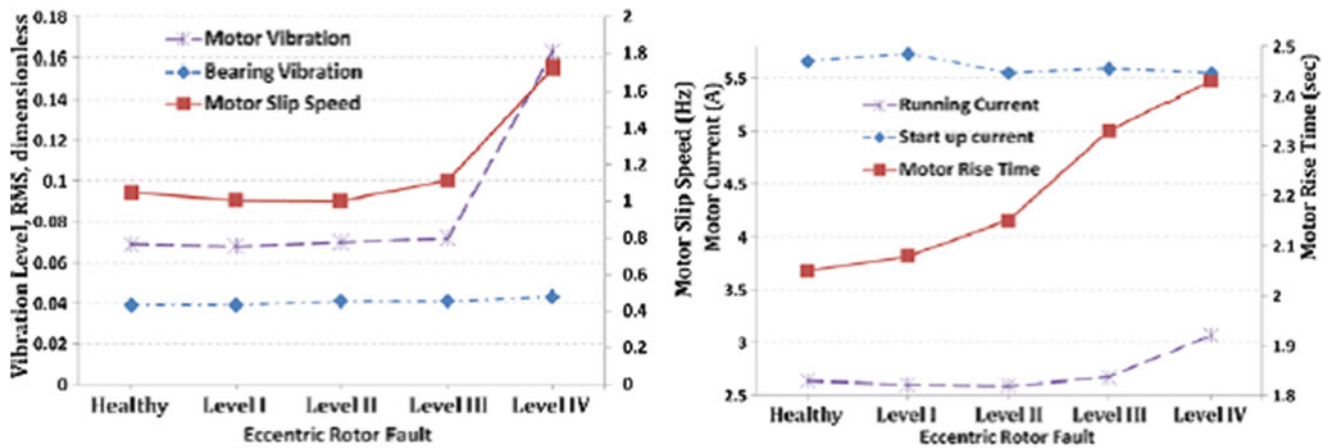
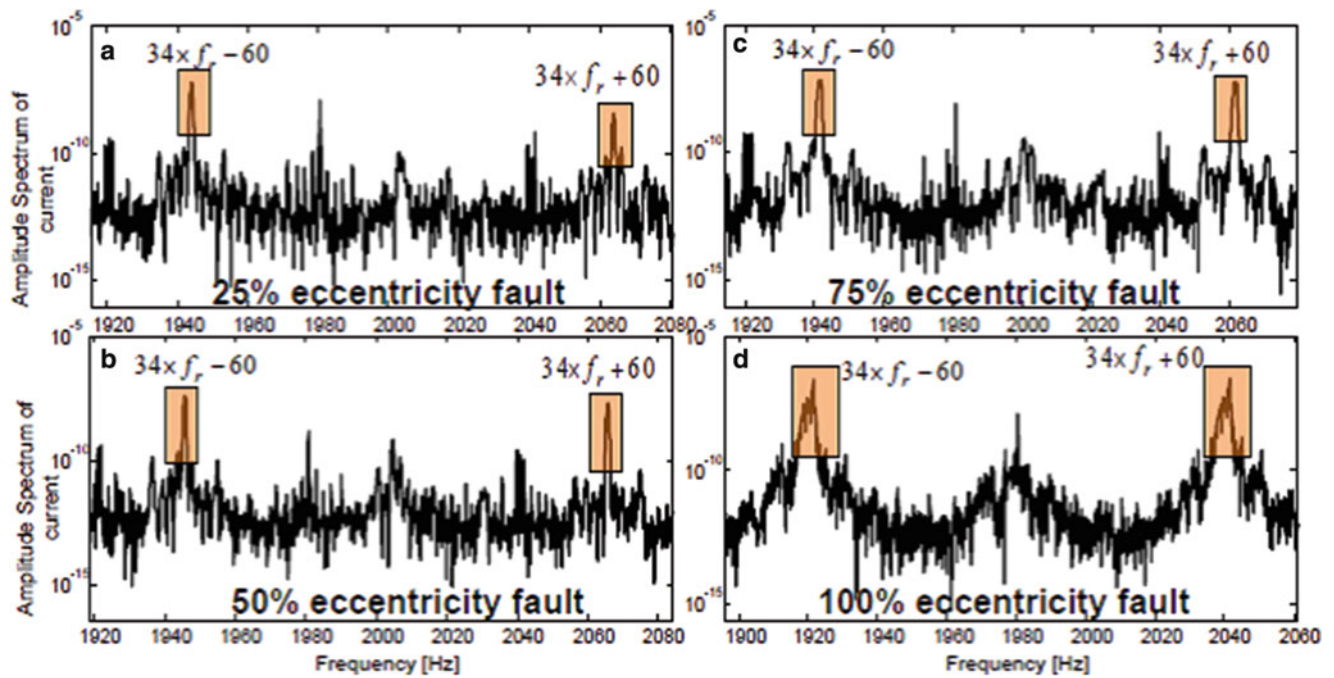**Fig. 25.5** Effect of eccentricity on vibration and motor slip speed

Fig. 25.6 Current spectrum of motor with eccentricity faults. (**a**) 25 % eccentricity, (**b**) 50 eccentricities, (**c**) 75 % eccentricity, (**d**) 100 % eccentricity
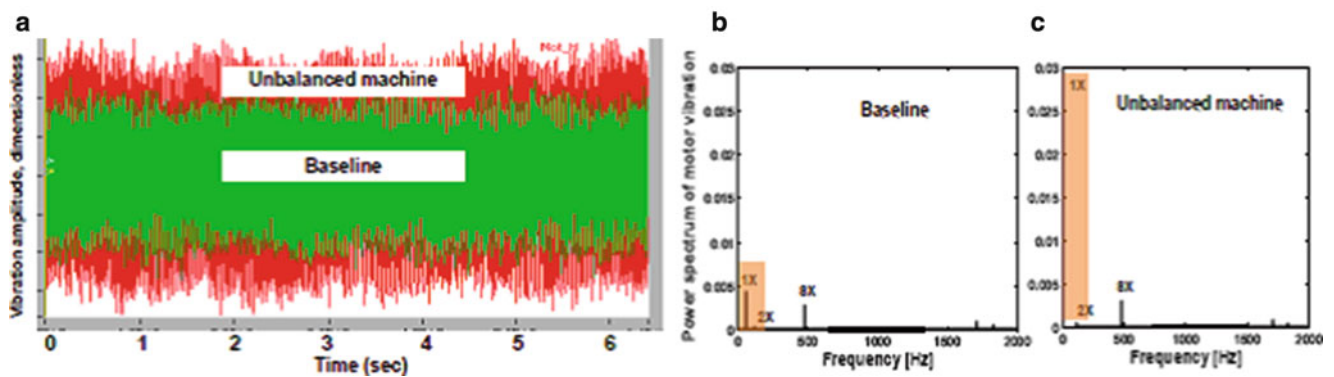

Fig. 25.7 Effect of rotor imbalance on motor vibration (**a**) vibration time signals: baseline vs. imbalance, (**b**) frequency spectrum: baseline, (**c**) frequency spectrum: unbalanced machine

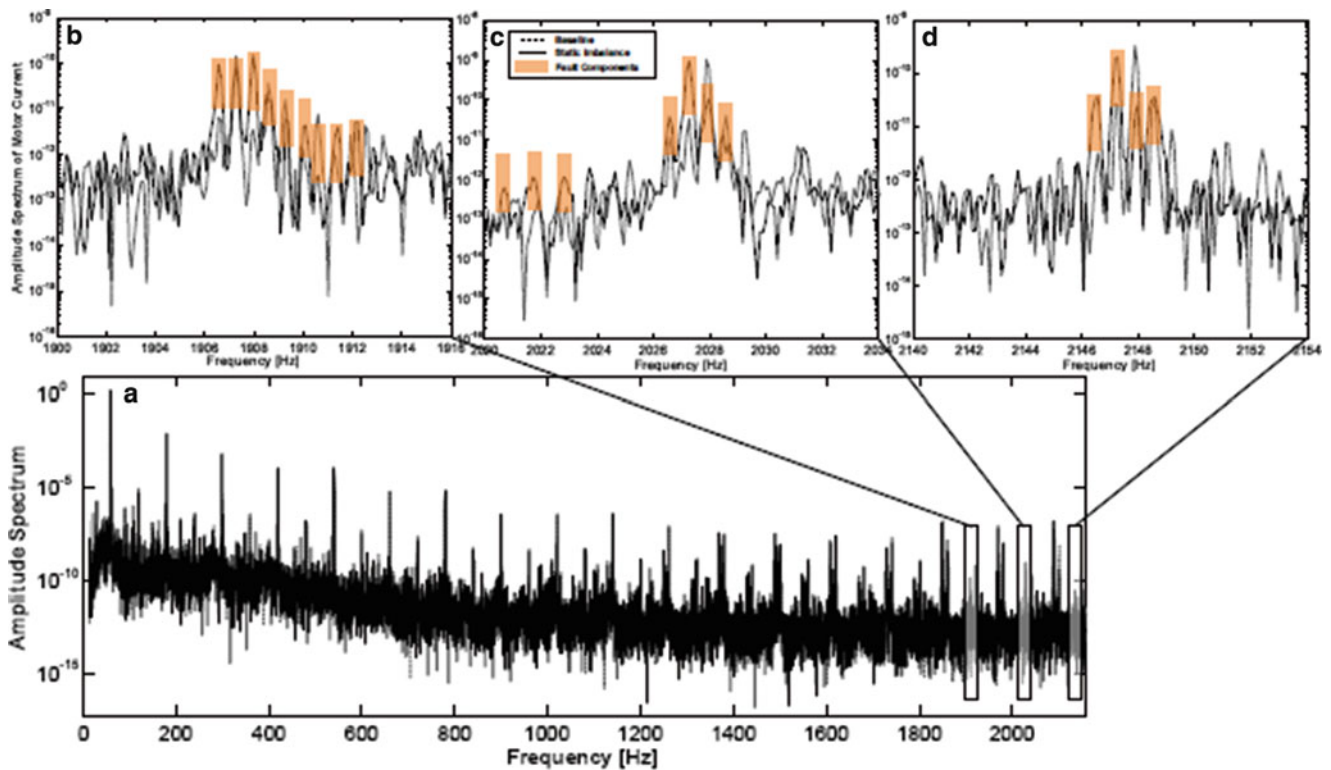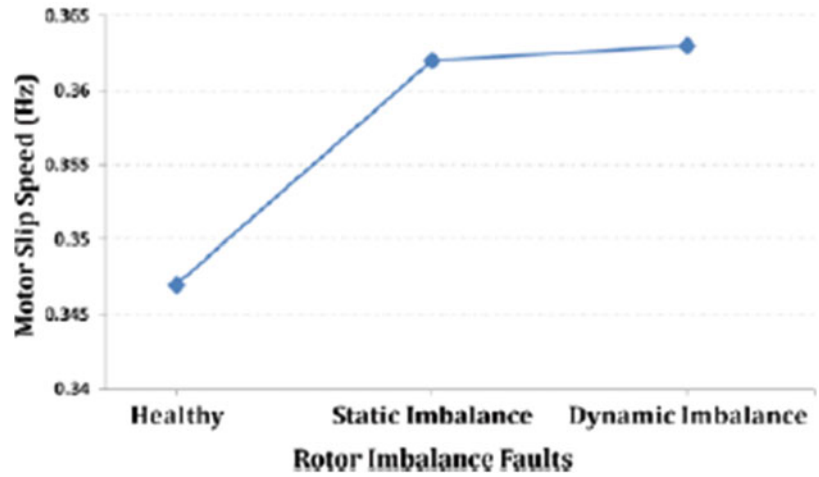**Fig. 25.8** Motor slip is slightly increased when rotor imbalance is introduced

Fig. 25.9 Frequency spectrum of motor current I1 for healthy motor and motor with mechanical imbalance faults. (**b**), (**c**), and (**d**) are magnified portions of the plot (**a**)

25.3.3 Mechanical Imbalance

The effect of mechanical imbalance on the machine vibration is very strong and significant. The level of vibration is increased in unbalanced machine as shown in Fig. 25.6a, the slip speed of the motor is increased as shown in Fig. 25.7 and 1X frequency component of vibration is significantly increased as shown in Fig. 25.6c (Fig. 25.8).

As described before, mechanical imbalance can cause lateral movement of the shaft or bending of the rotor of the motor. In the case of bending, mechanical imbalance is treated as dynamic eccentricity faults in MCSA and fault components are expected in current spectrum as described in [11]. Figure 25.9a plots frequency spectrum of the motor current I1 and three portions of the spectrum containing fault components are zoomed in Figs. 25.9b–d. Also, each plot is overlaid with baseline plots for the comparison. Fault components are slightly increased with introducing the faults. However, these components are observed even in the baseline spectrum showing the presence of dynamic eccentricity in the healthy motor.

25.4   Conclusion: Eccentricity Faults

- No Load: In MCSA, fault signals are not strong and advanced signal processing techniques.
- Not much is seen in vibration data.
- Loading Effect: Torsional mechanical Loading has strong effect on motor current signature
- Rotor slip increases with torsional load and current signal gets stronger producing a large number of harmonicas and side bands of line frequency
- Not much is seen in vibration data.
- Effects of non-stationary torsional loading is more complicated

References

1. Benbouzid MEH (2000) A review of induction motors signature analysis as a medium for faults detection. IEEE Trans Ind Electron 47(5): 984–993
2. Nandi S, Toliyat HA, Li X (2005) Condition monitoring and fault diagnosis of electrical motors – a review. IEEE Trans Energy Convers 20(4):719–729
3. Nakhaeinejad M, Bryant MD (2009) Measurements of faulty and healthy rolling element bearings. In: ASME/STLE international joint tribology conference, Memphis
4. Penrose HW (2005) Practical motor current signature analysis taking the mystery out of MCSA. All-Test Pro Inc. Tech note, Saybrook
5. Schlensok C, van Riesen D, Hameyer K (2006) Structure-dynamic analysis of an induction machine with eccentric rotor movement. In: 17th international conference on electrical machines, ICEM, Crete Island, Greece
6. Ganeriwala S (2014) The effect of loading on induction motor air gap eccentricity fault signature using vibration and motor current signature analysis (MCSA), BINDT-CM2014 conference, Manchester, UK
7. Thomson WT (2003) Keep motors turning via motor current signature analysis. In: IMC-2003, the 18th international maintenance conference, Clearwater
8. Thomson WT (2001) On-line MCSA to diagnose shorted turns in low voltage stator windings of 3-phase induction motors prior to failure. In: Proceedings of IEEE conference on electrical machines and drives (IEMDC), Boston
9. Thomson WT (1999) A review of on-line condition monitoring techniques for three-phase squirrel-cage induction motors – past, present, and future. IEEE symposium on diagnostics for electrical machines, power electronics and drives, Gijon, pp 3–18 (opening keynote address)
10. Thomson WT, Frenger M (2001) Current signature analysis to detect induction motor faults. IEEE Ind Appl Mag 7(4):26–34
11. Spectra Quest Tech Note (2006) Diagnostics of induction motor with broken bars Using motor current signature analysis (MCSA). Jan 2006
12. Nakhaeinejad M, Ganeriwala S (2009) Experimental study of misalignment in rotating machinery. In: Power-Gen international conference 2009, Las Vegas